N° d'ordre :4326

THESE

Présenté à

L'UNIVERSITÉ BORDEAUX 1

École doctorale des sciences chimiques

par

IGOR SIRETANU

Pour obtenir le grade de

DOCTEUR

SPÉCIALITÉ : Chimie – Physique

Nanostructuration contrôlée de films de polymères

Date de soutenance: 21 Octobre 2011

Après avis de:	**M.**	**Yves GROHENS**	**Rapporteur**
	M.	**Günter REITER**	**Rapporteur**

Devant la commission d'examen formée de :

M.	Yves Grohens	Professeur, Université de Bretagne-Sud	Rapporteur
M.	Günter Reiter	Professeur, Université de Freiburg	Rapporteur
M.	Carlos Drummond	Chargé de recherches, CNRS	Directeur de thèse
M.	Eric Papon	Professeur, Institut Polytechnique de Bordeaux	Directeur de thèse
M.	Jean-Paul Chapel	Chargé de recherches, CNRS	Invité
M.	Philippe Richetti	Directeur de recherches, CNRS	Examinateur
M.	Etienne Barthel	Directeur de recherches, CNRS	Examinateur

Thanks to …

… all the people I spent time with during the last three years of my PhD work. As everyone contributes something - in many different forms - it is difficult to list everybody.

First and foremost, I would like to express my deepest and sincerest gratitude to my supervisor, **Dr. Carlos Drummond** for his teaching, guidance, expertise and the ideal learning atmosphere over the past three years. His originality, calm and generosity to share his knowledge has triggered and nourished my intellectual maturity, and built my curiosity, love and admiration for scientific work. He has taught me "the magic" of SFA and AFM techniques and, in general, the process of doing high-quality research and the importance of clear and concise writing. Thank you, **Carlos**, for giving me the opportunity to develop this experience and challenging me every day to make me a better scientist. During my work, I was discouraged sometimes with the complexity of the project and I was wondered about irrelevant tangents, but you have always been there to motivate me and guide me back to a reasonable path. Your door was always open for me. **Carlos**, I am grateful in every possible way and hope to keep up our collaboration in the future. I wish you all the best in your personal life and scientific carrier.

I would like to thank to **Prof. Eric Papon**, who provided confidence and guidance at key moments in my work while also allowing me to work independently the majority of the time.

I gratefully acknowledge **Dr. Jean-Paul Chapel** for his advices, supervision, and crucial contribution, which made him a backbone of this research, and consequently of this thesis. It has been a pleasure to work with you, **Jean-Paul**. You always provided a positive - dynamic spirit and friendly mannerism to our collaboration. I thank you for the time you dedicated to follow my work progress through meetings and discussions and for your constructive feedback.

My sincere thanks are conferred to the PhD committee members, **Prof. Yves Grohens**, **Prof. Günter Reiter**, **Dr. Etienne Barthel** and **Dr. Philippe Richetti**, for their patience analyzing this work, detailed review, constructive criticism, excellent comments, discussions and suggestions.

Indeed, no good work can be done in "a vacuum", so I would like to thank the former and current members of the SFA research team for training, knowledge sharing, motivating discussions and ensuring a positive and friendly ambiance of work. I am very grateful to **Joanna**, who taught me everything about ellipsometry in my first year. I thank for numerous hours spend in constructive discussions. I have also been lucky to receive much guidance on this project concerning AFM from **Hassan Saadaoui**. Without him, I would never been able to have so many nice AFM images or dynamic measurements in temperature. Consequently, I owe him "a cart" of croissants and "a ton" of coffee for his time, efforts and French lessons over the years. I enjoyed the friendship and support from **Jeanne-Marie Granger-Lagleize**, who helped me with French translations, cleaving of mica and my first steps in SFA room. It was a real pleasure for me to work with you, **Jeanne-Marie**, and to share the same lab, SFA, AFM and other devices. More enjoyable were your delicious "canelette" (I

hope to ever taste them). I wish you, **Philippe** and your **future baby** all the best in the world. I would like to express my sincere gratitude to my team-mates: **Sribharani**, **Emeline**, **Anne-Sophie**. I wish you all good luck in your present and future life.

I also would like to thank Centre of Research Paul Pascal (CRPP) for accepting me as a part of this glorious institution and providing all kinds of necessary support to find a foothold inside the sea of knowledge which will always be with me as a stamp on my heart. CRPP led by Philippe Richetti as the laboratory director with all his departments is truly unique in that it fosters a friendly collaborative atmosphere among the graduate students. I wish to thank all services who work in the background but are very essential. Thank to **Corinne** for indispensable help and unfailing efficiency to solve any problem dealing with administration and bureaucratic matters during my stay in France. Thank to the management service and especially **Marie-Christine** and **Beatrice** who took care of travel funds and our comfort in all our missions. Thank to **Nadine**, the guardian of the library. Thank also to the instrumentation and machine shop cells, **Ahmed**, **Lionel**, **Pascal**, **Philippe**, **Jean-Yves** and **Emmanuel**, and informatics service, **Jean-Luc**, **Philippe**, **Anne** and **Sandrine** for their help in everyday life.

My friends have made my life happy and helped me to succeed during difficult periods. I would like to express my appreciation to: **Octavian**, **Igor**[2], **Rodica**, **Dmitri**, **Liubov**, **Oleg**, **Tatiana**, **Julien**, **Andie**, **Sergiu**, **Mihai**, … - you all have been wonderful friends. I really enjoyed our coffee breaks, lunches and talks during the day. I will always cherish my association with you in France. Also I would like to thank my best friend **Ion Samson** from Moldova.

Where would I be without my family? My family, particularly my parents **Sergiu** and **Zinovia**, has guided me through many challenging times, for which I am grateful, and I would not be the person I am today without them. They deserve special mention for their inseparable support and love, showing me the joy of intellectual pursuit ever since I was a child. My heartiest thanks to my brother, **Ion**, my sister, **Ina**, my brother in law **Alexei** and their wonderful little son, **Maximca**.

Last, but not least, I thank my wife **Diana**. She is the person who listens to my stories, complaints, and celebrations on a daily basis, even though she may have her own issues on her mind. **Diana** was there to support me while writing my thesis, to celebrate with me the after passing of my defense, and to explore with me during the past three years. We have had many great adventures together and I look forward to a lifetime full of many more great moments and adventures. I love you. Therefore, I am also thanking **Codreanu** family for accepting me as a member of the family, warmly encouraging me for my scientific work.

Finally, I would like to thank everybody who was important to the successful realization of this thesis, as well as expressing my apologies that I could not mention personally one by one.

Thank you all – Merci à tous – Mulţumesc tuturor

Igor Siretanu

Pessac, October 2011

Abstract

Naturally formed patterns have been a source of fascination for scientists and nonscientists during centuries. Examples of patterns can be found everywhere in Nature. The importance and the applications of surface structuration in Nature and in technology are widespread. Simple patterns, such as surface waves, are indispensable in some natural processes and may have direct application to technological innovations. For example, in Nature, self–cleaning of leaves are based on random patterns of microscopic wax crystals. Periodic arrays might lead to colorful optical properties; butterflies used their colored wings in courtship or to warn birds or other predators. In technology, structured films are often used in sensors, self-cleaning surfaces, memory storage devices, among many other examples.

Conventional methods used to create micrometer scale structures such as optical lithography, which have been used for a hundred of years, are reaching its inherent limitations determined by the wavelength of light. This has led scientists to look for original patterning methods. Surface patterning is known to impact optical, adhesive, and wetting properties of materials, particularly soft materials. Carefully controlling each of these properties is important for technological applications such as biomaterials, microfluidics or coatings. For example, in designing devices for biological applications it is important to tune the adherence properties. In microfluidic devices, surface topography influences the hydrophobicity of a surface. The appearance of coated materials is dictated by the light reflection properties of the coating, which is strongly influenced by the surface topography. The immense area of technological applications and the great deal of research and understanding that needs to be conducted to achieve technical control of surface structure and functionality at nanoscale level inspire new developments and enthusiasm.

This thesis deals with patterning of polymer surfaces. Two distinctive techniques based on the same physical principle are described. In the first part of this study, I describe a significant variation of a method that has been amply documented for structuration of polymer films: the use of externally applied electric fields. Most of the methods reported in the literature for structuring glassy polymer films involve pattern formation at elevated temperatures followed by quenching the structured sample at room temperature. We show that even at room temperature is possible to structure glassy polystyrene films under the application of an electric field. Besides simplifying the operational conditions of the process, this method allows a more expedite production of shorter wavelengths. These results confirm the presence of a layer of enhanced mobility at the surface of glassy polystyrene films, which can be restructured under external stimuli. The characteristic wavelength and resulting morphology of the pattern can be controlled by varying the applied field. This method is described in Chapter III.

The second and most important part of this study is also focused on methods of structuring glassy hydrophobic polymers films at room temperature. We developed a novel way to induce and control submicron structures on hydrophobic substrates by a single, simple treatment step based on treating the substrate with degassed aqueous solution. This nanostructuration is the result of close adsorption of charged species on the hydrophobic polymeric surface building a high electric field,

which, combined with the mobility of the polymer surface, induces the deformation of the polymer substrate. I describe in Chapter IV how this process depends on parameters such as pH, temperature, polymer nature, molecular weight, supporting substrate, amount of gas dissolved in aqueous and ions presents in solution.

The technique of electrostatic pressure induced nanostructuration presented here is straightforward and does not need any specialized equipment or chemicals. In a laboratory or technological application, this method of structuration can be easily achieved just by controlling with precisely the degassing process. This water induced self-assembly of hydrophobic polymer surfaces is an indirect validation of three controversial subjects i) the presence of a low density layer at the interface between a hydrophobic surface water, ii) the adsorbtion certain ions at the surface of hydrophobic surfaces iii) the presence of a zone of enhanced mobility at the outermost surface of a glassy polymer film. In addition, I believe that the phenomena are relevant for the interface between water and any hydrophobic object, and should be considered in the description of processes a diverse as protein folding, surfactant aggregation, friction or adhesion. This process may find applications in many different scientific and technological fields like nanolithography, microfluidics or flexible electronics.

The third section of this work focuses on the description of interfacial dynamics of thin polymer films using this novel patterning technique. The formation and relaxation of the patterns were thoroughly studied. The process of formation of self-assembled nanostructure reveals a number of surprising features. By using different substrates, it is shown that the developing of bumps in the first few nanometer of the surface is affected by the substrate, and this effect can propagate as far as film thickness of the order of the size of the polymer molecules. This study is presented in Chapter V.

In the final section of this study we used the nano surface bumps formation and relaxation technique to investigate the near free surface dynamics of PS films. It is shown that the near free surface region of PS films has enhanced molecular mobilities. We study the influence of temperature and polymer molecular weight on this enhanced dynamics. These results are presented in Chapter VI.

Table of contents

Chapter I

Generalities and Context

Table of contents for Chapter I:

This thesis deals with structuration strategies of hydrophobic polymer surfaces: causes and implications. In this introductory Chapter I briefly outline some concepts that will help the understanding of the results described in following chapters. Some notions of polymers and polymer physics will be presented. Then the glass transition will be introduced, focused on polymer films. Later, the stability of polymer films and some structuration strategies will be discussed. Finally, previous work on the behavior of hydrophobic polymer surfaces in contact with water will be reviewed. This last topic is highly relevant for the structuration strategy that constitutes the main body of this thesis.

A. Polymer generalities.

A.1. Polymers

Polymer are molecules composed of many repeating units (sometimes hundreds of thousands of them) called monomers, which link together with covalent bonds and form long molecular chains. The term "*polymer*" is the combination of the Greek roots "poly" (many) and "meros" (part). Figure I.1 shows the chemical structure of some common polymers polyethylene (PE), polystyrene (PS), and poly(methylmethacrylate) (PMMA).

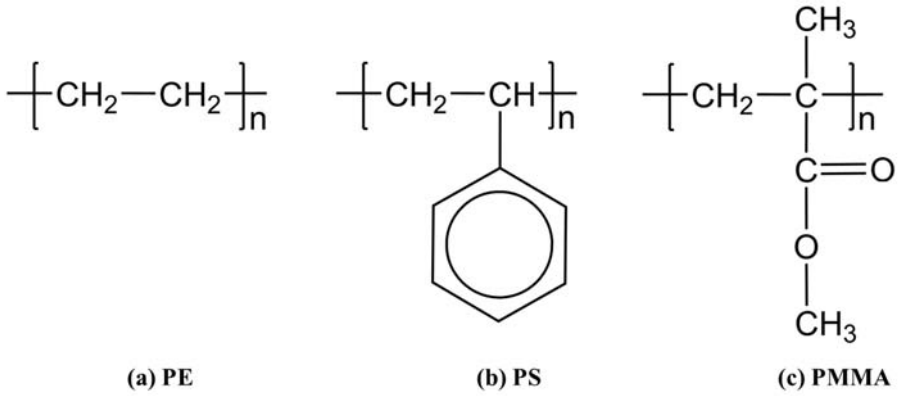

Figure I.1: Chemical structures of some common polymers

A large variety of natural and synthetic materials are polymers. They are almost everywhere in our daily life. Natural polymers such as proteins, nucleic acids and cellulose serve us as food, medicine and many other useful materials. In 1909 the first wholly synthetic polymer, Bakelite, was invented by Dr. Leo Baekeland [1]. Ever since, a huge variety of synthetic polymers has been manufactured, finding applications in almost every area of modern life. Synthetic macromolecules serve to make various fibers, our clothes, and numerous materials we use for housing or traveling equipments. Despite the importance of polymers, details of their molecular structure remained a mystery until 1922, when Hermann Staudinger proposed the correct structural model of polymer molecules [2]. He was awarded the Nobel Prize for this discovery. Since then, polymer science has experienced a rapid development and six Nobel prizes have been awarded in this area.

A.2. Molecular weight of polymer molecules

The number of chemical repeat units of a polymer molecule is called *degree of polymerization, N*. The molar mass *M* of a polymer molecule is therefore equal to the degree of polymerization *N* times the molar mass $M_{monomer}$ of its chemical repeat unit (monomer). If all molecular chains of a polymer sample have the same molecular weight, the sample is *monodisperse.* Strict monodispersity can be found in some biopolymers, where molecular chains are copies of a template. In most cases not all molecular chains are of the same length. Synthetic polymers usually contain a mixture of chains of different lengths (different molecular weights) as a result of the process of polymerization. Two variables are commonly used to characterize the size/weight of a polymer: number average molecular weight M_n and weight-average molecular weight M_W [3], which are defined as:

$$M_n = \int p(m)m\,dm \tag{1.1}$$

$$M_W = \frac{\int p(m)m^2\,dm}{\int p(m)m\,dm} = \frac{\int p(m)m^2\,dm}{M_n} \tag{1.2}$$

In the above equations, *p(m)* is the probability distribution function of polymer chains with molecular weight *m*. M_W is always larger than M_n. An useful parameter used to describe the width of the molecular weight distribution of a polymer is the *polydispersity index.*

$$r_{PDI} = \frac{M_W}{M_n} \tag{1.3}$$

r_{PDI} is unity if all polymer chains have a uniform molecular length, but for most synthesized polymers $r_{PDI} > 1$.

A.3. Homochain polymers and heterochain polymers

In the case of polyethylene the backbones of the molecular chains are built up by carbon (*C*) atoms. However, this isn't always the case. In some polymers the backbones are constructed by atoms of another element, or even by atoms of several elements.

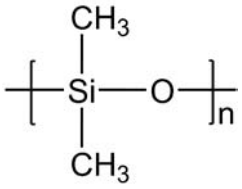

Figure I.2: polydimethylsiloxane

For example, Polydimethylsiloxane (PDMS) contains silicon Si and oxygen O atoms besides carbon (C). If the backbone is formed by atoms of one single element, the polymer is called *Homochain polymer*. On the contrary, if the backbone is formed by atoms of two or more elements, the polymer is called *Heterochain polymer* [3]. In the present work mostly polymers with just carbon atoms in the backbone were studied.

A.4. Homopolymers and heteropolymers

Homopolymers are polymers built up of one type of monomers, while *Co-polymers* are those containing two or more types of monomers. Copolymers can be alternating, random, block or graft depending on the sequence in which their monomers are bonded together, as shown in Figure I.3. Polymers containing two blocks are called *diblock copolymers*. Polymers with three blocks are called *triblock copolymers*, and with many alternating blocks *multiblock copolymers*.

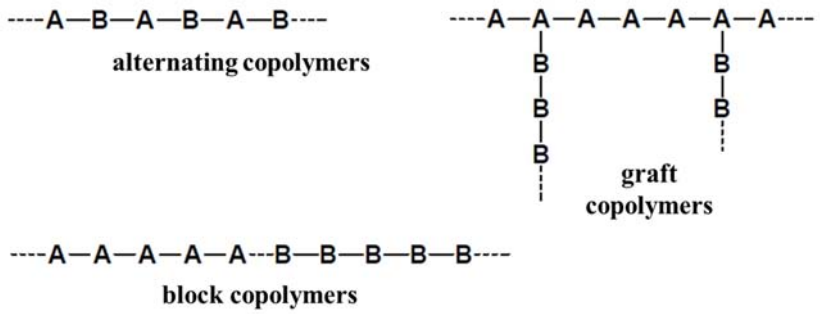

Figure I.3: Types of copolymers

Homopolymers are often classified by *tacticity*. Consider for example polystyrene. As illustrated in Figure I.4, the pendant phenyl groups may appear at one or the other side of the molecular chain. The detailed structure is determined by the coupling of the monomers. If they are coupled in such a way that the side groups are always on the same position relative to the backbone, the polymer is called *isotactic.* If monomers are coupled in an irregular way, the polymer is said to be *atactic. Syndiotacticity* describes coupling of monomers which is non-unique but varies in a regular way.

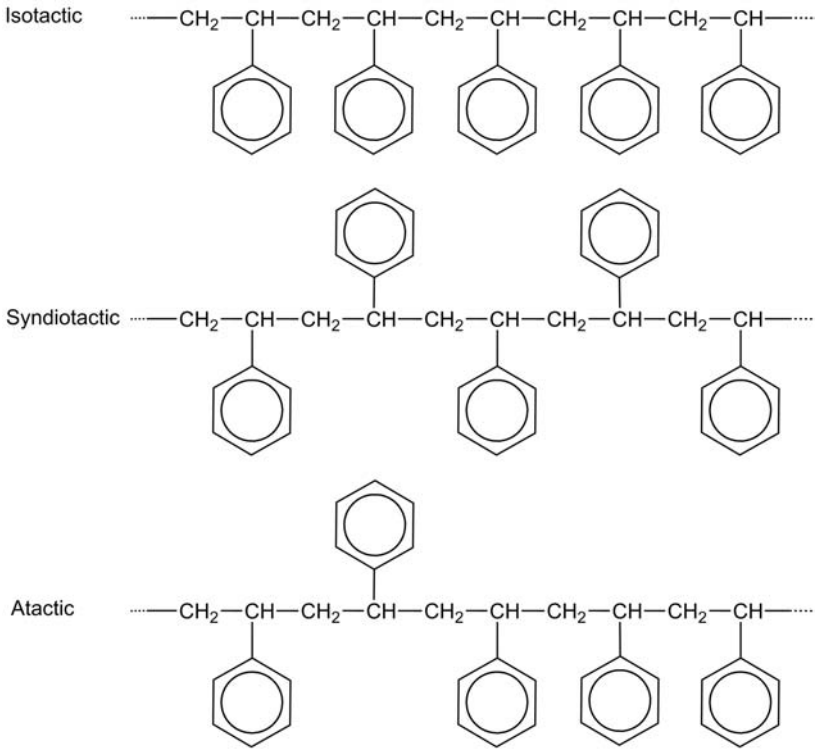

Figure I.4: Schematic representation of three isomers of polystyrene.

A.5. Architecture/microstructure of polymeric chain molecules

Another important feature of polymeric systems is their architecture. Many important polymers have some *side groups* attaching to the macromolecular backbone. In some polymers, there are also some short chains attached to the main chain backbone. Based on the chemical *architecture,* polymers can be classified as (Figure I.5):

Linear polymer— without side chains (but there might be side groups);

Branched polymer— with side chains attached to the main chain backbone;

Network polymer— polymer chains interconnected with each other by chemical or physical crosslinking

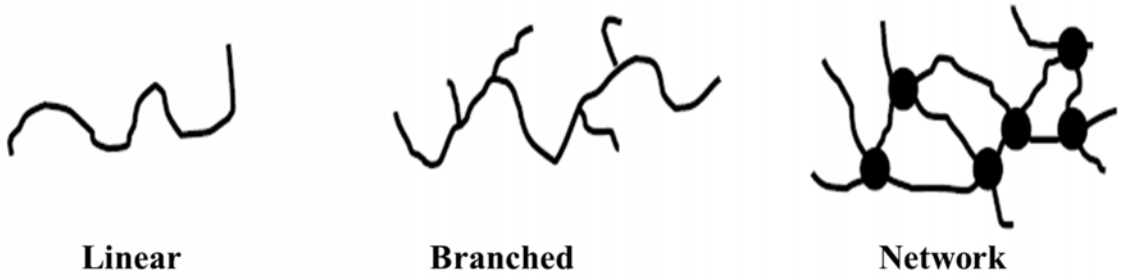

Figure I.5: Schematic architectures of different polymers.

The architecture and microstructure of a polymer is fixed after the process of polymerization. To change them it is necessary to break and reform covalent bonds in the macromolecule. In many studies of polymer systems there is no chemical reaction involved, and only physical treatments - such as changing of temperature, volume, pressure, or exposing to electric fields - are applied.

A.6. Thermoplastics and thermosetting plastics

Based on their behavior when exposed to heat, polymers can be classified into two categories, *thermoplastics* and *thermosetting* plastics. Thermoplastics, such as polyethylene, nylon and polystyrene are mixture of molecules that can be heated up to liquid state and remolded. Thermosetting plastics such as vulcanized rubber and epoxy resin have highly cross-linked molecular structures: the molecules are chemically bonded together to form a percolating network. If thermosetting plastics are heated up they will decompose before becoming liquids. In this thesis only thermoplastics were studied.

A.7. Size of the polymers

Some concepts to be discussed in the present work are related to the size and weight of polymer molecules. Polymer chains consist of atoms that are connected by covalent bonds. These covalent bonds are usually capable of adopting a large number of conformations. It is, therefore, difficult to define the shape of a polymer chain. Several concepts to describe the size of the polymer molecule are currently used.

A.7.1 Contour length

For a linear polymer chain, the maximum end-to-end distance is named *contour length*. The contour length of a polymer chain is equal to the sum of the lengths of all monomer segments. Figure I.6 shows the contour length of a polyethylene molecule.

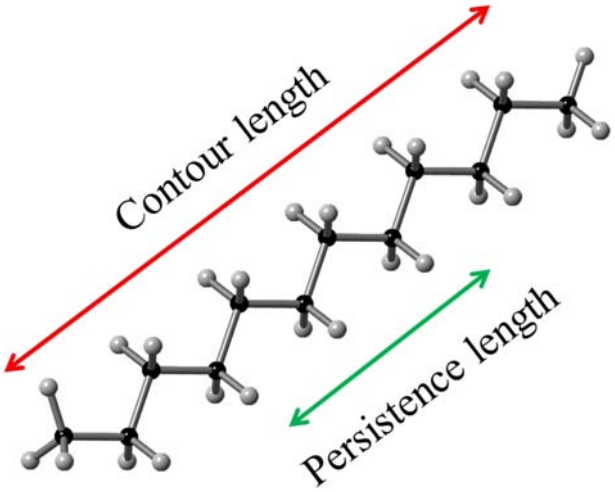

Figure I.6: Contour and the persistence lengths of a short polyethylene molecule.

A.7.2. Persistence length

The *persistence length* quantifies the stiffness of polymer molecular chains: large persistence length values indicate rigid molecular chains. For example, the persistence length of a double-helical DNA molecule is about 50 nm, which is quite large and makes the double-helical chain very stiff. On the contrary the persistence length of polyethylene is only 0.65 nm (Figure I.6) [4]; this molecule is very flexible. The persistence length of a polymer molecule depends on temperature.

A.7.3. End-to-End distance

The end-to-end distance, R_{EE}, is the distance that connects the two terminal atoms of the polymer chain. If the chain forms a tight ball, which is the case in a poor solvent, the R_{EE} will be small. On the contrary R_{EE} will be larger in a good solvent, as the polymer ball is inflated and the terminal groups are widely separated. In dilute solutions of ideal (Gaussian) chains or in polymer melts the molecular chain can be described by the model of "random walk". Using this model R_{EE} can be evaluated as $l\sqrt{n}$, where n represents the number of covalent bonds along the backbone of the chain and l represents the length of each covalent bond. R_{EE} is a function of molecular weight, and increases with increasing molecular weight [5].

A.7.4. Gyration radius

The end-to-end distance is difficult to measure. Instead, the *radius of gyration*, R_g, is often used since this quantity can be measured by light scattering techniques. R_g is the average distance from the center of gravity to the chain segments.

R_g is defined as [3,5]:

$$R_g^2 = \frac{1}{N}\sum_{k=1}^{N}(r_k - r_{mean})^2 \quad (1.4)$$

where N is the number of the repeating units of a molecule, r_k is the position of a given unit, and

$$r_{mean} = \sum_{k=1}^{N} r_k \quad (1.5)$$

Rg is also defined by:

$$R_g^2 = \frac{1}{2N^2}\sum_{i,j}(r_i - r_j)^2 \quad (1.6)$$

The above two definitions are equivalent. Figure I.7 schematically shows a linear polymer molecule chain and its gyration radius.

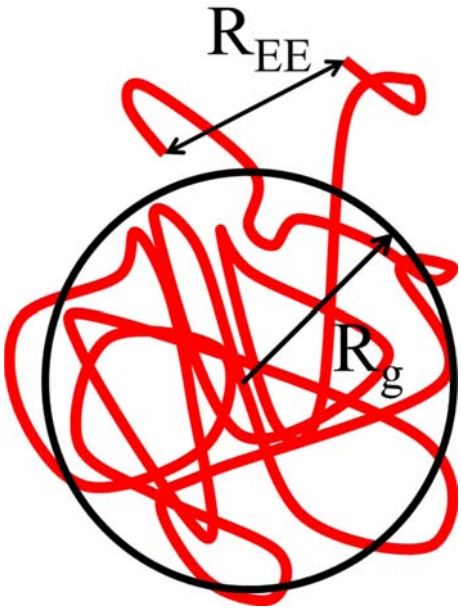

Figure I.7: A linear polymer molecule chain that is randomly distributed in space. The black arrow shows its gyration radius.

The mean-square value of R_g can be related to the mean-square value of R_{EE} by:

$$\langle R_g^2 \rangle = \frac{1}{6}\langle R_{EE}^2 \rangle \quad (1.7)$$

For ideal chains, R_g of a polymer in a poor solvent is smaller than in a good solvent. The radius of gyrations for the same polymer with and without branching is different even for the same molecular weight. To evaluate the degree of branching, the *g-factor* is defined as:.

$$g = \frac{\langle R_g^2 \rangle (branched\ polymer)}{\langle R_g^2 \rangle (linear\ polymer)} \quad (1.8)$$

A.7.5. Stokes radius

The *Stokes radius* of a polymer molecule is defined as the radius of a hypothetical hard sphere that diffuses at the same rate as the polymer molecule.

A.8. Types of polymeric substances

A.8.1. Polymeric liquids

There are two types of polymeric liquids: polymer melts and polymer solutions. Polymer solutions can be obtained by dissolving a polymer in a solvent. Examples of polymeric liquids are wood protectants and floor shines. Polymer solutions are classified depending on the polymer *mass concentration* (*c)* (Figure I.8), the ratio of total mass of polymer dissolved in a solution and the volume of the solution. An alternative measure of concentration is the volume fraction ϕ, the ratio of occupied volume by the polymer molecules and the volume of the solution. These two quantities are related through the polymer density ρ.

$$\phi = \frac{c}{\rho} = c\frac{v_{mon}N_{Av}}{M_{mon}} \tag{1.9}$$

A typical monomer volume $v_{mon} \approx 100\ Å^3$ and the corresponding monomer molar volume is $v_{mon}N_{Av} \approx 60\ cm^3$.

The pervaded volume V is the volume of solution spanned by the polymer chain.

$$V \approx R^3 \tag{1.10}$$

where R is the size of the chain.

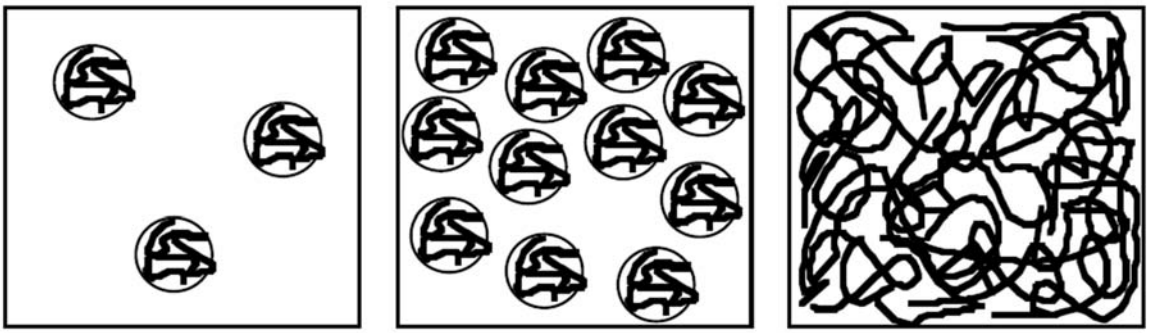

Figure I.8: Solution regimes of flexible polymers.

In the absence of a solvent, macromolecules can form a bulk liquid state, called *polymer melt*. Polymers melts are neat polymeric liquids above their glass transition and melting temperature. A macroscopic piece of a polymer melt remembers its shape and has elasticity on short time scales, but exhibits liquid flow (with a high viscosity) at long times. Such time-dependent mechanical response is called viscoelastic because it combines viscous flow at long times and elastic response at short times.

A.8.2. Polymer solids

There are several different types of polymeric solids. If a polymer melt is cooled, it can either be transformed into a semicristaline solid below its melting temperature T_m or into a glass below its glass transition temperature T_g. Semicristalline solids consist of crystalline regions, called lamellae, in which sections of chains are packed parallel to each other, and of amorphous regions between these lamellae.

Macromolecules with more random configuration, such as atactic homopolymers or random copolymers, tend to transform upon cooling into transparent yet brittle glassy state (e.g. polymethylmethacrilate and polystyrene). This transition will be extensively discussed later.

A.9. Viscoelastic properties of polymers

If one applies a stress to deform a perfect elastic material within a suitable range, the work done on it is stored as the energy of deformation. The energy will be completely released when the applied stress is removed. This mechanism can be well described by Hooke's law of elasticity

$$\sigma \equiv c\varepsilon \tag{1.11}$$

where σ denotes the stress, ε denotes the strain and c denotes the modulus, for example the tensile or shear modulus, conventionally represented by E and G respectively.

On the other hand, if one applies a stress to a perfect viscous liquid, the work done on it is dissipated as heat due to the friction between molecules and there is no tendency for the liquid to recover its original state. This mechanism can be described by Newton's law of viscosity

$$\sigma = \eta\frac{d\varepsilon}{dt} \tag{1.12}$$

where η is the viscosity of the liquid. However, for polymers, within an intermediate range of temperatures or frequencies (e.g. in a dynamic measurement, where an oscillating field is applied to the sample), a complex combination of elastic and viscous properties is usually observed. That is to say, polymers behave neither like perfect elastic nor like viscous materials, but rather somewhere in between. This phenomenon is called viscoelasticity [3]. If the applied strain or rate of strain to the polymers is very small, the resulting stress will be *linearly* dependent on ε. This behavior is called *linear viscoelasticity*. From the previous section, we have already seen that long chain polymer molecules have very complex structures and they can adopt a large number of conformation states. To change a polymer from one state to another, for example by thermal or mechanical treatments, there are many kinds of rotational and translational motions involved. Different molecular motions and complex structures of polymers are at the origin of the phenomena of viscoelasticity.

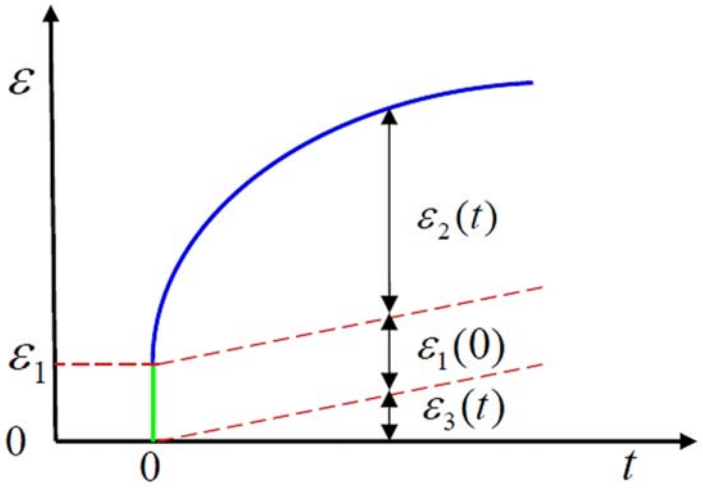

Figure I.9: Schematic representation of viscoelasticity phenomenon

Figure I.9 shows a schematic representation of viscoelasticity. If one applies a small stress at time 0, then a viscoelastic polymer will have an instantaneous elastic response strain ε_1, shown as the vertical green line in Figure I.9; some energy is then stored in the material. With time elapses, the response strain ε_2 of this material develops gradually, shown as the upper blue curve; in this process, called *retarded elasticity*, there is also some energy stored, which is recoverable. The third mechanism involved is related to the viscous flow behavior, shown as ε_3, in which a small amount of energy is dissipated as heat; for crosslinked polymers (often called viscoelastic solids) the amount of dissipated energy due to viscous flow is very small and can be neglected, but for uncrosslinked polymers (often called viscoelastic liquids) there is an amount of energy dissipated. If the applied stress is removed at a specific moment, then the previous stored energy in the elastic and retarded elastic processes will be released and the viscoelastic material partially recover its original shape.

The viscoelastic properties can be modeled by the well-known Maxwell and Kelvin (or Voigt) models [5], in which the combination of *elastic springs* and *viscous dashpots* is considered, or different combinations of both models. In the Maxwell model a spring and a dashpot are in series; in the Kelvin model, the two components are in parallel. Schematic representations for the two models are shown in Figure I.10.

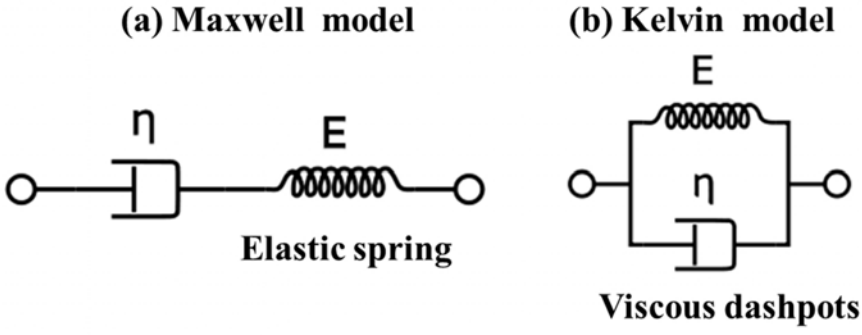

Figure I.10: Schematic representations for two common models of viscoelastic materials.

Using eqs. (1.11) and (1.12), the Maxwell model predicts

$$\sigma = \sigma_0 \exp\left(-\frac{ct}{\eta}\right) = \sigma_0 \exp(-\frac{t}{\tau}) \tag{1.13}$$

where $\tau = \eta/c$ is the characteristic relaxation time. Similarly, the Kelvin model predicts

$$\varepsilon = \frac{\sigma_0}{c}\left[1 - \exp(-\frac{t}{\tau})\right] \tag{1.14}$$

From Eq. (1.13) and Eq. (1.14), we see that in both models σ and ε follow exponential laws.

A.10. Superposition principles for viscoelastic polymers

Most experimental set-ups are only useful for limited ranges of frequency or time, making it difficult to investigate effects occurring at widely different scales with the same instrument. One method commonly used to overcome this limitation is the Time-Temperature Superposition (TTS) method [6]. TTS states that for viscoelastic material time and temperature are essentially equivalent. That is, one can determine long time behavior of a variable of interest (e.g. relaxation modulus, storage or loss moduli or creep compliance) by performing the experiment at higher temperature and viceversa. When using TTS one assumes that if the entire experiment were performed at a single temperature, the resulting curve would be the same as the curve composed of the superposition of many experiments performed at different temperatures. TTS assumes that the viscoelastic behavior at one temperature can be related to another temperature by a simple change in time scale. A material for which TTS is found to be valid is called rheologically simple.

Figure I.11-(a) shows a particularly elegant set of experimental data [7] in which the storage compliance of poly(n-octyl methacrylate) is plotted against log frequency at a number of temperatures.

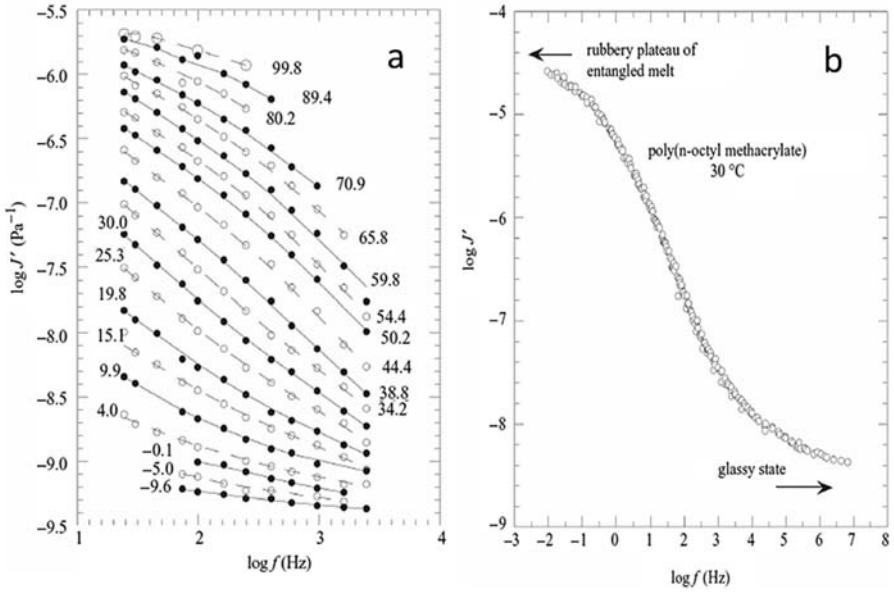

Figure I.11: (a) Poly(n-octyl methacrylate): dynamic storage compilance J' at the temperatures shown (°C). Data from Ferry [7]. (b) Time–temperature reduction of the data from (a) to 30°C.

To unifying the data, a given temperature is chosen as the reference temperature and then all other curves are shifted by a factor a_T, along the t or ω axes, respectively, in order to get the superposition of the curves, as demonstrated in Figure I.11-(b). Here the reference temperature was chosen as 30°C. The quantity a_T is therefore called the *shift factor*. The curve obtained after the shifts have been applied is a *master curve*. The important thing about this curve is that it effectively gives the response of the polymer over a much wider range of time/frequencies than a single apparatus is able to provide.

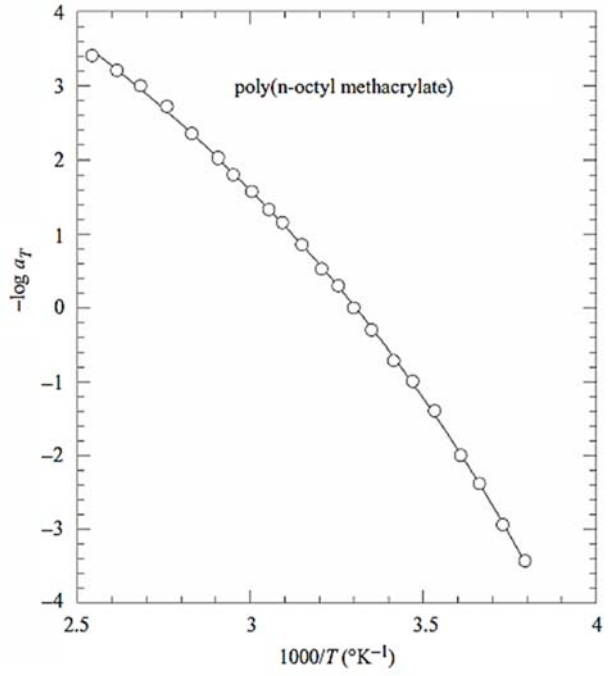

Figure I.12: Temperature dependence of the shift factors used in Figure I.11. The solid curve is a fit of the VF equation.

The master curve presented in Figure I.11-(b) was constructed from a finite set of experimental curves. Thus, a set of shift factors exist for the temperatures of the experiments. If the shift factors were parameterized as a continuous temperature function then dynamic data over the entire time/frequency region at any temperature could be inferred. Time–temperature superposition is intimately associated with the temperature behavior of a central relaxation time, τ_0. Relaxation times in general are associated with rate processes and, as such, suggest a temperature dependence appropriate to an activated process. A frequency shift factor from temperature T to the reference temperature T_0 is defined as $\log a_T = \log f(T) - \log f(T_0)$. In Figure I.12, $-\log a_T$ is plotted versus $1/T$ for the data of Figure I.11. In this representation a straight-line suggest a simple Arrhenius-like thermally activated process: the slope would then be proportional to the activation energy. However, it is apparent that the plot is not a straight line and distinct curvature is observed. The slope magnitude increases as $1/T$ increases (or T decreases). This non-Arrhenius behavior is characteristic of processes connected with the glass transition region in amorphous polymers, and in fact for vitrifying liquids in general.

An Arrhenius plot for a generic rate constant is based on a functional relationship of the form

$$k_{rate} = A_f e^{-\Delta E^*/RT} \tag{1.15}$$

$$lnk_{rate} = lnA_f - -\Delta E^*/RT \tag{1.16}$$

where E^* is an activation energy and A_f is a frequency factor.

A relaxation time behaves as the inverse of a rate constant, $\tau \equiv 1/k_{rate}$, so that if Arrhenius behavior prevailed, the appropriate function form would be:

$$-log\tau = A - B/T \tag{1.17}$$

where A, B are constants typically obtained by data fitting. It has been found that a simple empirical modification of eq. (1.17) allows data to be fitted quite well, as those in Figure I.11. Specifically, the functional form is,

$$-log\tau \quad = A - \frac{B}{T-T_\infty} \tag{1.18}$$

where T_∞ is an additional parameter. This form is often called the Vogel–Fulcher (VF) or Vogel–Fulcher–VanTammen equation [8].

The shift factors in Figure I.12 were calculated with 30°C as the base temperature. In the context of time–temperature superposition it is useful to parameterizes the shift factor not in terms of T_∞ but in terms of the base temperature (T_0). Thus if

$$-loga_T = A - \frac{B}{T-T_\infty} \tag{1.19}$$

and at $T = T_0$, the reference temperature, where the shift factor $a_{T0} = 1$, then

$$0 = A - \frac{B}{T-T_\infty} \tag{1.20}$$

Subtraction of the above two relations and rearrangement gives

$$-loga_T = -\frac{B}{T-T_\infty} + \frac{B}{T-T_\infty} \tag{1.21}$$

$$loga_T = log\frac{\tau(T)}{\tau(T_{ref})} = \frac{-C_1(T-T_{ref})}{C_2+(T-T_{ref})} \tag{1.22}$$

where $c_1 = B/(T_0 - T_\infty)$ and $c_2 = T_0 - T_\infty$. This formulation is known as the Williams–Landel–Ferry or WLF equation [9,10].

The WLF equation is typically used to describe the time/temperature behavior of polymers in the glass transition region. The equation is based on the assumption that above the glass transition temperature, the fractional free volume increases linearly with respect to temperature [10]. The model also assumes that as the free volume of the material increases, its viscosity rapidly decreases [11].

B. Glass transition

Simply stated, the glass transition describes the transition from a liquid to a glassy or amorphous solid as a material is cooled. Almost all materials on earth can undergo glass transition if we cool them fast enough from the liquid state [12]. Materials will change from the liquid or rubbery state (in the case of a polymer) with low viscosity, e.g., on the order of 10^{-3} Pa·s for a typical liquid, to the glassy state with much higher viscosity (of the order of 10^{13} Pa·s) without major structural changes. Glasses are amorphous solids with liquid-like structures. Conventionally, the glass transition temperature is defined as the temperature where the viscosity of glass forming materials reaches 10^{13} Pa·s or the temperature where the molecular relaxation of the sample materials is approximately 100 seconds.

Many important physical properties change drastically at the glass transition temperature. The variation of these properties with temperature is a convenient method for determining T_g. Some of the test methods include the temperature variation of specific volume (dilatometry), refractive index (refractometry), or specific heat (calorimetry, DSC or DTA). Others methods include temperature-induced changes in vibrational energy levels (infrared spectroscopy), proton environment (nuclear magnetic resonance or NMR), dipole moment (dielectric constant and loss), elastic modulus (creep or stress relaxation), and mechanical energy absorption (dynamic mechanical analysis, DMA).

As mentioned before, a convenient method to determine T_g is to measure the volume or heat capacity as a function of temperature (Figure I.13). Typically, one observes an abrupt change in the slope of the temperature dependence of the volume at a certain temperature, which is identified as T_g. It is usually found that the T_g measured in such an experiment depends on the cooling or heating rate (Figure I.13), as well as on the thermal history of the sample. For example, the green curve in Figure I.13 represents a measurement performed at a lower cooling rate compared with the upper blue curve. Higher cooling rates usually result in higher T_gs. A sample which is cooled faster falls out of equilibrium at a higher temperature, resulting in a T_g value that is higher than the one observed at slower cooling rates.

Because of the dependence of T_g on time or history, the glass transition is not a true thermodynamic phase transition, but it is rather a kinetic transition in which the motion of the molecules is slowed so dramatically upon cooling that, at sufficiently low temperatures, no appreciable molecular motion can occur.

The slowing of the dynamics upon cooling can be observed directly by a dramatic increase in the viscosity of the liquid [13]. For example, the viscosity of *o*-terphenyl, a simple glass-former, increases by nine orders of magnitude in the 30°C temperature range above T_g [3,5]. Unlike the large structural changes observed during the formation of a crystal upon cooling, only very subtle structural changes are observed during the formation of a glass, with the structure of the high temperature liquid effectively frozen with rapid cooling.

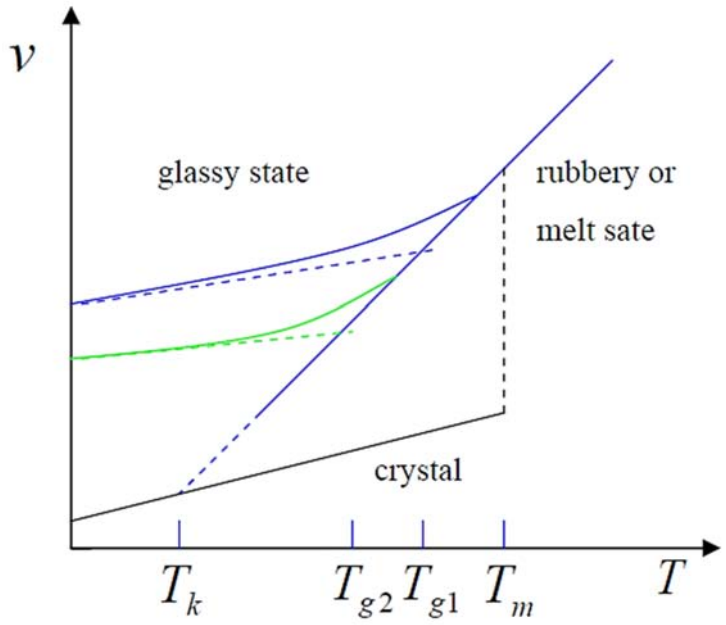

Figure I.13: Volume *V* versus temperature *T* for a glass-forming material for two different cooling rates. The slope change in the υ=f(T) curve is common used to define T_g.

We can understand the frequency (or time) dependence of the measured T_g values if we consider structural relaxation of the material near T_g. If we consider a simplified material that has a single characteristic relaxation time τ at a given temperature, then for short times (or correspondingly high frequencies), no significant structural relaxation can occur during the experiment so that the material appears to be solid-like [6]. For times that are much longer than τ (or correspondingly low frequencies), the material fully relaxes during the experiment so that it appears to be liquid-like. If τ increases strongly with decreasing temperature, then below a certain temperature, relaxation for that mode is effectively frozen. For a glass-forming material, physical quantities such as volume or index of refraction will relax in response to a change in an experimental parameter such as temperature. At a given temperature, the relaxation function $\Phi(t)$ can be described by a so-called stretched exponential (Kohlrausch-Williams-Watt or KWW) function [14]:

$$\phi(t) \sim exp\left[-(t/\tau)^{\beta}\right] \tag{1.23}$$

The relaxation function is shown schematically as a plot of Φ versus t/τ in Figure I.14 for two different values of β. For $\beta = 1$, the decay is a single exponential; for $\beta < 1$, which is typical for glass-forming materials, the decay is nonexponential and is "stretched" in time compared with the exponential decay. The nonexponential behavior has two possible explanations: either the sample is homogeneous, with each molecule obeying the same nonexponential relaxation; or the sample is dynamically heterogeneous, consisting of regions with different dynamics, each one obeying nearly exponential relaxation, with different regions having significantly different relaxation times. In recent work, experimental results seem to support dynamic heterogeneity.

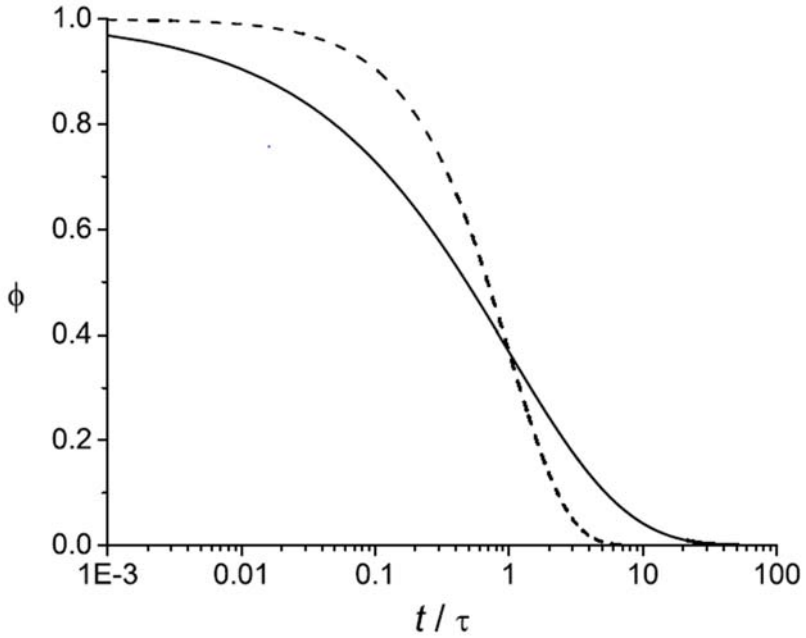

Figure I.14: Relaxation function ϕ versus t/τ for an idealized glass-forming material characterized by a single relaxation time τ (dashed line, $\beta = 1$) and stretched exponential (solid line $\beta = 0.5$)

The fundamental nature of the glass transition is still unclear. It is a complex process that involves equilibrium, thermodynamic and kinetic factors. Despite impressive efforts, no complete theory of the glass transition exists today. However, there are few models that have been useful in trying to explain the dramatic reduction in molecular mobility with decreasing temperature. The thermodynamic approach is based on entropy considerations of the glassy state, while the kinetic theory of the glass transition considers the relaxation phenomena associated with it. Each approach gives only a partial explanation to the observed behavior of polymers. We now briefly discuss these theories along with the free volume theory, a phenomenological approach.

B.1. Glass transition theories

B.1.1. Kinetic theory

The kinetic concept of glass transition considers the glass transition as a dynamic phenomenon since the position of the T_g depends on the rate of heating or cooling [15,16]. It predicts that the value of T_g measured depends on the time scale of the experiment in relation to that of the molecular motions arising from the perturbation of the polymer system by temperature changes. A number of models have been proposed. One approach considers the process of vitrification (glassification) as a reaction involving the movement of chain segments (kinetic units) between energy states. For the movement of a chain segment from one energy state to another to occur, a critical “hole” or empty space must be available. To create this hole, sufficient energy must be available to overcome both the cohesive forces of the surrounding molecules and the potential energy barrier associated with the rearrangement. The

temperature at which the number of holes of sufficient size is great enough to permit flow is considered as T_g. This theory permits a description of the approach to thermodynamic equilibrium. When a polymeric material above T_g is cooled, there is sufficient molecular motion for equilibrium to be achieved. However, the rate of approach to equilibrium, and hence T_g, depends on the cooling rate employed.

B.1.2. Equilibrium theory

In 1965, Adam and Gibbs [17] developed a molecular kinetic theory based on describing the temperature dependence of time relaxation behavior of glass forming liquids in terms of the variation of the configurational entropy of *cooperatively rearranging regions* (CRR).

This equilibrium concept treats the ideal glass transition as a true second-order thermodynamic transition, which has equilibrium properties. However, the ideal state cannot be obtained experimentally since its realization would require an infinite time. According to the theory of Gibbs and DiMarzio [18], the glass transition process is a consequence of the changes in conformational entropy with changes in temperature. The reduced level in molecular reorganization observed near the transition temperature is attributed to the reduction in the number of available conformations as the temperature is lowered. The equilibrium conformational entropy becomes zero when a thermodynamic second-order transition is ultimately reached. In this condition the conformations are essentially "frozen in" since the time required for conformational changes becomes virtually infinite. The glass transition temperature, T_g, therefore approaches true transition temperature as the time scale of experiment becomes longer. Based on this reasoning and using a statistical thermodynamics treatment that utilizes a quasi-lattice theory, Gibbs and DiMarzio developed quantitative predictions of the second-order phase transition that are in agreement with experiment [18].

B.1.3. Free Volume theory

A most useful and popular theory of glass transition is the *free volume* model of Fox and Ferry and, later, of Williams, Landell, and Ferry [19,20,21]. Free volume theory is one of the first theories that successfully explained some aspects of glass formation such as the dramatic slowdown of the dynamics near the glass transition. This theory is also attractive because it provides an intuitive representation of glass transition that can be really useful in understanding different phenomena. Normally, there is some free space between polymer monomers even in melt. In general, one can distinguish between the total volume and the occupied volume. This theory considers the free volume of a substance as the difference between its specific volume, V, and the space actually occupied by the molecules, V_0, where V_0 is expressed as:

$$V_0 = V' + \alpha_g T \tag{1.24}$$

where V' is the extrapolated volume of glass at absolute zero and α_g is the thermal expansion coefficient of the glass.

The amount of the free volume changes with temperature, so this model further defines the free volume fraction, f, at temperature T as

$$f = f_g + \alpha_f (T - T_g) \tag{1.25}$$

$$\alpha_f = \alpha_1 - \alpha_g = \frac{1}{V_f}\frac{dV_f}{dT} \tag{1.26}$$

where f_g is the free volume fraction at T_g, α_1 the thermal expansion coefficient above T_g, and α_g the thermal expansion coefficient below T_g. For most amorphous polymers, the free volume fraction at the glass transition temperature is found to be constant, with a value of 0.025 [22]. Amorphous polymers, when cooled, are therefore supposed to become glassy when the free volume fraction attains this value.

Various techniques, including electro-chromic and photo-chromic florescent probes, nuclear magnetic resonance, small-angle X-ray scattering, density measurement and positron annihilation spectroscopy, have been applied for the measurement of free volume in polymers [23,24,25].The mean volume of a single hole has been reported to be about 0.02-0.07 nm^3.

A simple approach to the concept of free volume, which is popular in explaining the dynamic mechanical properties, is the crankshaft mechanism [26]. The crankshaft model treats the molecule as a collection of mobile segments that have some degree of free movement. As the free volume of the chain segment increases, its ability to move in various directions also increases. This increased mobility results in a greater compliance (lower modulus) of the molecule. These movements have been studied and Heijboer [27] classified α, and β transitions by their type of motions.

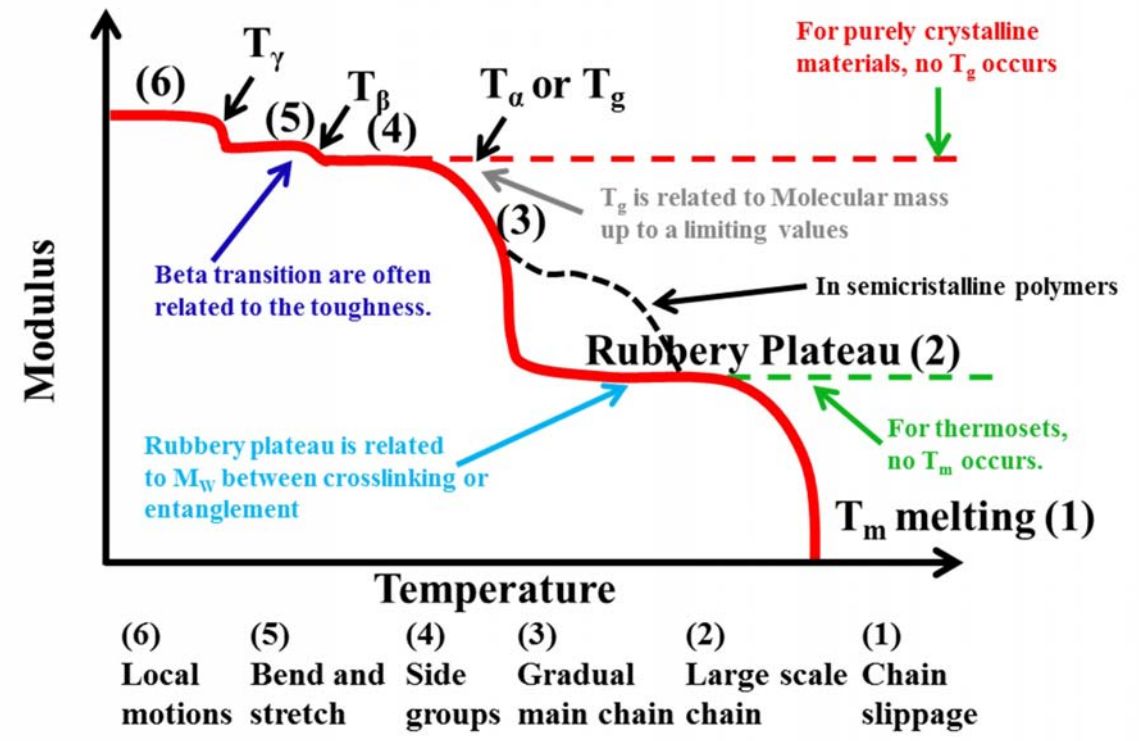

Figure I.15: Schematic representation of the effect of temperature on the modulus E of an amorphous polymer and the corresponding chain conformations (numbers 1-6) associated with each transition region. The sub-T_g β and γ transitions occur at T_β and T_γ.

Taking advantage of this model, it is possible to simply describe the various transitions seen in polymers. When the free volume accessible to the movement of atoms is small ($T<T_g$), segments of the main chain or side group elements can rotate or stretch around their axes without changes in the bond angle or can bend with small changes in the bond angles. When the free volume is largely increased ($T> T_g$), segments of one main chain can move in a coordinated fashion while segments of another main chain or whole polymer chains can slip past one another.

When a polymer is heated up, the free volume of the chain segment increases and the ability of the chain segments to move in various directions also increases. This increased mobility in either side chains or small groups of adjacent backbone atoms results in various transitions, affecting several properties of the polymer, e.g. mechanical and dielectric properties. Figure I.15 schematically shows the effect of these transitions on the modulus E as a function of temperature and the chain conformations associated with each transition according to the crankshaft model. From very low temperature, as the polymer heats up and expands, the free volume increases so that localized bond movements (rotating, bending and stretching) and side chain movements can occur. This is the *gamma* transition at T_γ. As the temperature and the free volume continue to increase, the whole side chains and localized groups of 4-8 backbone atoms begin to have enough space to move and the material starts to develop some toughness. This transition is called the *beta* transition T_β. Often it is the T_g of a secondary component in a blend or a specific block in a block copolymer.

Region **4** indicates the glass state. In this region polymer is glassy and frequently brittle. Typical examples at room temperature include polystyrene and poly(methyl methacrylate). It has been found that for a wide range of polymers the Young's modulus remains constant throughout this temperature range, with value of several GPa. Local vibrations and short-range rotational motions prevail in molecular motions in this state. Some studies [28,29] have reported that coordinated molecular motions involves typically less than 4 main chain atoms. As the free volume continues to increase with increasing temperature, the glass transition T_g occurs when large segments of the chains start moving. The third region is the glass transition region. The Young's modulus decreases by a factor of 1000 in a 20° to 30°C range. In this region long-range, coordinated molecular motions become significant.

The next region is called rubbery plateau region, where the modulus becomes almost constant. A typical value of the modulus is 10^6 Pa. At this region the mechanical dynamics is different for different polymers. Linear amorphous polymers exhibit rubber elasticity and the plateau slowly drops off as temperature increases. For cross-linked polymers, the modulus follows the green discontinued line. For crystalline materials there would not be T_g, and for semi-crystalline polymers the modulus follows the black dashed line.

On continued heating, the melting point, T_m, is reached. The melting point is where the free volume has increased up to a point that the chains can slide past each other and the material flows. This is also called the terminal region. In the molten state, the ability to flow depends on the molecular

weight of the polymer. In the region between rubbery the plateau and the terminal region (area), polymers exhibit a viscoelastic behavior. In short-time scale polymers are predominantly elastic materials, because the molecular chains have not enough time to rearrange themselves. In long-time scale, polymers behave more like viscous materials, because the molecular chains have sufficient time to move around. There is no such region for cross-linked polymers.

B.2. Glass transition, dynamics and structure studies in thin polymers films.

As already mentioned in the previous sections, our understanding of the glass transition is still limited and the nature of such phenomenon remains a challenge in the field of condensed matter physics. Polymers are good candidates for studying the glass transition. Polymers are easily available products since nowadays, chemists can produce polymers by routine polymerization methods and there is a great variety of different polymers available. In addition, due to the high viscosity of polymers, one can make polymer glasses in a variety of dimensions from several micrometers to a few nanometers using some conventional methods, such as polymer solution dipping or spin-coating. The studies of polymers on the mesoscopic scale, where finite size and/or chain confinement effects may dominate, make it possible to investigate the local dynamics and some characteristic correlation length scales involved in the glass transition. In addition a good deal of effort has involved the study of ultrathin polymer films due to their increasing technological importance, sensors, dielectric layers, lubricants and bio-compatible materials.

B.3. Glass transition in thin polymer films

B.3.1. Supported films

The first study of the glass transition of thin polymer films was conducted by Beaucage, Composto and Stein [30] in 1993. In this study the authors monitored the glass transition temperature for polystyrene films ~300nm thick on silicon wafers using a novel technique at that time, ellipsometry. In this technique the refractive index and thickness of polymer films can be measured as a function of temperature and specific cooling or heating procedures. In a later work, Keddie, Jones and Cory [31], found that in films thinner than 40nm the T_g was significantly reduced below the bulk value. The authors proposed an empirical relation for the behavior of T_g as a function of film thickness h

$$T_g(h) = T_g(\infty)\ 1 - (A/h)^{\delta}] \tag{1.27}$$

in which $T_g(\infty)$ is the glass transition temperature of bulk polystyrene ($h \rightarrow \infty$) and the constant A (= 3.2 nm) is related to a length scale of a near free surface region with enhanced molecular mobility due to the relaxation of constraints to molecular motions. They found that A has no molecular weight dependence. This was the first time that the existence of a near free surface mobile region with a role

in the on-average enhanced dynamics in ultra-thin polymer films was suggested. The idea that there can be a mobile layer at the free surface of a polymer has since fascinated numerous researchers who have devised some most ingenious experiments to verify its existence [32,33,34,35,36,37,38,39, 40,41].

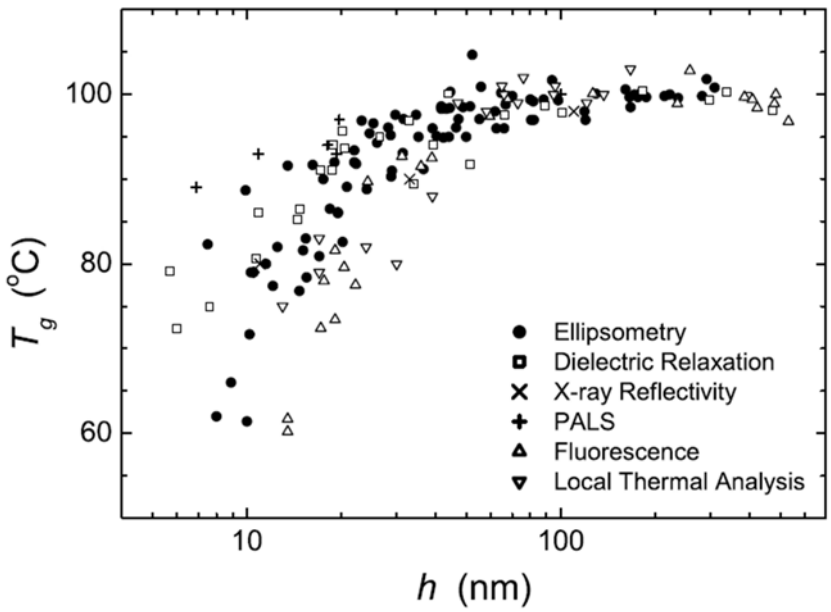

Figure I.16: Glass transition temperature T_g as a function of film thickness h measured for polystyrene (PS) of different molecular weights M_W supported on a variety of substrates using six different techniques: ellipsometry [31,43,44,45], dielectric relaxation [46,47], X-ray reflectivity [48], positron annihilation lifetime spectroscopy (PALS) [49], fluorescence intensity [50], and local thermal analysis [51], (Graph from [42]).

A compilation of results obtained for T_g studies on PS films on a variety of substrates using numerous experimental techniques is shown in Figure I.16. Results obtained by ellipsometry [31,43,44,45], dielectric spectroscopy [46,47], X-ray reflectivity [48], positron annihilation lifetime spectroscopy (PALS) [49], local thermal analysis [50] and probe fluorescence intensity [51,52] are reunited. From this figure we can see that all measurements observe a film thickness dependence of T_g (negative T_g shifts) in particular for films thinner than ~40 nm. Since similar results are obtained for PS films on different substrates, one could conclude that the PS films interact only weakly with the underlying substrates. But this is not always the case. The importance of the effect of the polymer-substrate interaction on the measured T_g value was first observed for the case of poly (methyl methacrylate) (PMMA) films on Au surfaces and the native silicon oxide layer of silicon wafers. It was observed that T_g decreased with decreasing film thickness for PMMA films on Au; the opposite is true for films on silicon oxide [53]. Later, evidence for a strong attractive interaction between poly-(2)-vinylpyridine and silicon oxide layer was observed in x-ray reflectivity measurements, which correlates with an increase in T_g with decreasing thickness [54].

In summary, from the above studies we see that when polymer films are thinner than a few tens of nanometers T_g changes from the bulk value. As the film thickness decreases the contribution of the free surface region to the overall dynamical properties of the whole film is more important. In the case of systems with a vacuum(air)-polymer interface and a weak substrate-polymer interaction, the average dynamics is enhanced compared with the bulk and the glass transition temperature is reduced. The opposite may be true if there is a strong polymer-substrate interaction.

As can be seen from the data presented in Figure I.16, there are different experimental techniques that have been used to measure T_g in supported thin polymer films. Most of these techniques probe the material properties averaged across the thickness of the film, yielding an average T_g value. However, it is important to determine whether each of these techniques measures the same physical quantity, e.g. is the T_g value measured by ellipsometry and dielectric relaxation (DR) the same physical quantity?

To exclude doubts concerning technical particularities it has been recently suggested that attention should be focused on measurements of the distribution of T_g values across the thickness of the film, rather than measurements of the average T_g value [55]. In response to this suggestion, Ellison and Torkelson applied a probe fluorescence technique [51] to multilayer films incorporating thin layers which contained small quantities of fluorescent probes (either probe molecules or probe-labeled polymer molecules) [52]. By using the multilayer geometry and varying the position of the fluorescently-tagged layer within the film, the authors were able to obtain the distribution of T_g values across the thickness of the film. They found a decrease in T_g near a free surface which extends several tens of nanometers into the film.

Several other studies have focused on measuring the distribution of α-relaxation times in thin polymer films, using the techniques of second harmonic generation (SHG) [56] and dielectric relaxation (DR) spectroscopy [45,46,47]. These studies have allowed a detailed determination of the τ-relaxation time distribution in the films. The SHG experiments, performed on a copolymer of isobutyl methacrylate and dye-functionalized methacrylate monomer, revealed no change in the average α-relaxation time with decreasing film thickness (the interaction between the large amounts of dye labels and the substrate may have caused the invariance of the average α-relaxation time with film thickness). On the contrary, in studies of PS, poly(vinyl acetate) and atactic PMMA using DR spectroscopy [57] the average α-relaxation temperature T_α was observed to decrease with decreasing film thickness, but only below a threshold film thickness that was small compared with values for which T_g reductions were observed using other techniques.

B.3.2. Freely-standing films

The experimental data obtained for polymer films supported on substrates indicate that the presence of the free surface tends to decrease T_g, whereas the presence of the underlying substrate can increase T_g. The T_g value measured for a particular polymer-substrate combination will depend on which interface dominates. To clarify the role of the free surface on the measured T_g, the underlying

substrate was removed and freely-standing polymer films, with air-polymer interfaces on both sides of the film, have been studied [43,58,59,60,61]. A very detailed review of studies of freely standing polystyrene films has been reported by Forrest et al. [62]. Here I just briefly outline the major observations of such studies. Figure I.17 shows the combination of the measured glass transition temperatures of freely standing polystyrene films within a wide molecular weight range. One may readily notice that the magnitude of the shift in $T_g(h)$ is about twice as large as that found in supported PS films (Figure I.16). These results provide additional evidence to support the theory postulated by Keddie et al [31].

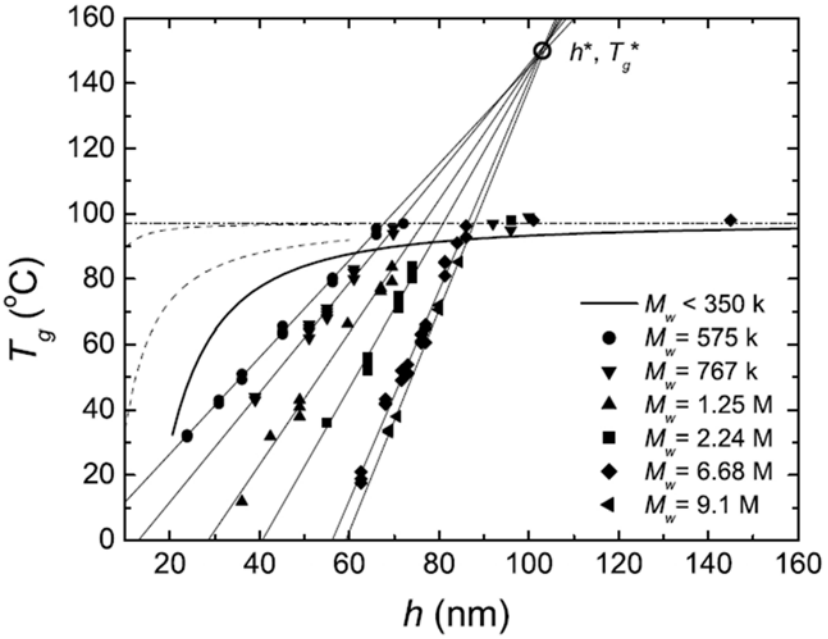

Figure I.17: Glass transition temperature T_g as a function of film thickness h for freely-standing polystyrene films of different molecular weights. High M_w data, measured using ellipsometry, are displayed using a different symbol for each M_w value [51], and data for M_w < 350 kDa, measured using Brillouin light scattering, are indicated by the thick solid line [50]. The dashed lines for h < 60 nm represent the spread and uncertainty in the T_g data for supported PS films (Figure I.16). The small circle indicates the common intersection point (h^*, T_g^*) of the straight line fits to the Tg data for the high M_w films. The plot is taken from reference [42]

Some studies on free-standing films reported some contradictory results, which suggests that the mechanism underlying this phenomenon is probably more complex [60,58,61,60,36]. In Keddie's study of supported films [31], it was found that the molecular weight has no effect on the thickness dependence of T_g; they concluded that the confinement is not the at the origin of T_g reduction. This was confirmed by Ellison et al. who studied supported PS films in a broad M_W range (5K-3000K g/mol). However, further studies on free-standing PS films [60,58,61,60,36] revealed that if there is no molecular weight dependence of T_g reduction when M_n < 514 K, this was no longer true for larger molecular weights. This is illustrated in Figure I.17. We can observe that for M_W > 514 K, the molecular weights have a strong effect on the thickness dependence of T_g. Further quantitative analysis shows that the threshold film thickness at which T_g reductions start to occur is roughly equal to R_{EE},

which increases with increasing molecular weight, as discussed in section A.7. This strongly suggests that for the samples with larger molecular weights, the chain confinement becomes the dominant origin of the thickness dependence of T_g in free standing films.

This dependence of T_g on h can be interpreted as the interplay between two types of mobility: the bulk mechanism, which dominates for sufficiently thick films, and a new mode of mobility which becomes more efficient than the bulk mechanism for sufficiently thin films, resulting in reduced T_g values. Several models which attempt to describe this behavior will be discussed later [63].

B.3.3. The role of the substrate

The first study of T_g of PS thin films [31], in which the vacuum (air)-polymer interfacial effects were supposed to be the cause of the T_g deviations from the bulk materials, motivated more research on the role played by interfaces in the overall dynamics of thin polymer films. [44,64,65,66,67,68,69,70]. As mentioned before, it has been found that when the interaction between polymers and substrates is very strong, a positive T_g shift in thin polymer films can be observed; in contrast, negative T_g shifts were often measured in polystyrene films, which have a weak interaction with the substrates. Positive T_g shifts measured in poly(methyl methacrylate) (PMMA) [65,66,68,71] and tetramethylbisphenol-A polycarbonate (TMPC) [64] films suggest that the substrate-polymer effects overwhelm the vacuum (air)-polymer effects and the overall dynamics is slower than in the bulk materials.

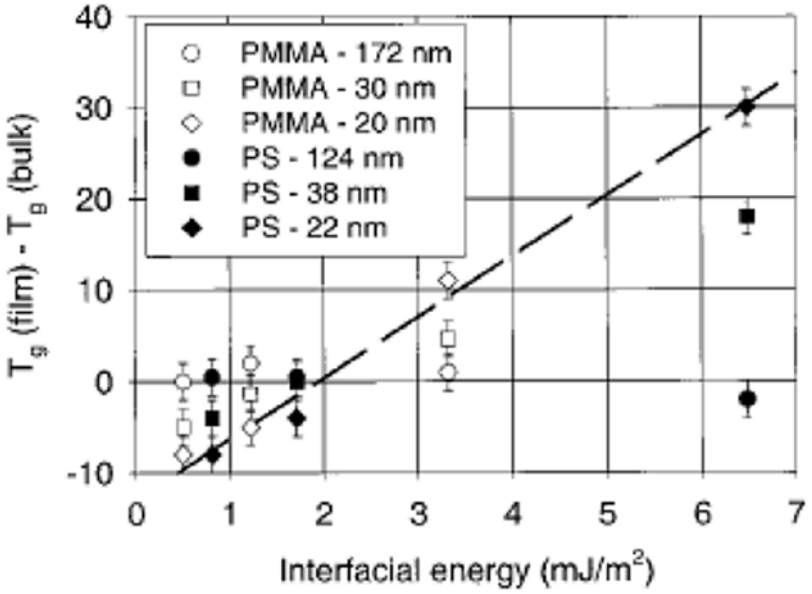

Figure I.18: Compiled results of T_g deviations from the bulk value for PS and PMMA films of three thicknesses as a function of polymer-substrate interaction energies, Graph from [66].

Fryer and co-workers [68], studied the T_g of thin films of PS and PMMA as a function of substrate-polymer interaction energy. The substrates used were silicon wafers coated with thermally stable self-assembled films of octadecyltrichlorosilane (OTS). In Figure I.18, it can be observed: (1)

For both PS and PMMA films, the measured T_g deviations are almost a linear function of polymer-substrate interaction energy (for a constant film thickness). (2) The T_g deviations can be negative or positive depending on the strength of the polymer-substrate interaction energy. (3) The T_g deviations are a function of film thickness: For thinner films, the T_g deviations are larger. These results show that the measured T_gs are a combining results of both substrate-polymer and (vacuum/air)-polymer interface effects.

Tsui and co-workers [44] studied the glass temperature of thin PS films by modifying the substrate interactions. They used ~3 nm thick (PS-r-MMA) brushes anchored on silicon wafers. The homopolyer/copolymer interactions are modified by changing the styrene fraction. When the styrene fraction of the copolymer brushes was larger than 0.75, the measured T_g should have a linear dependence on the homopolyer/copolymer interaction in agreement with [66]. Tsui and co-workers noticed that the sole substrate interaction energy is not sufficient to describe the observed T_g deviations and instead proposed a model incorporating the chain density variations in the interfacial regions. According to this model, a small variation in chain segment density in the interfacial regions (<1.4%) can result in T_g shifts of ~20 °C.

In the foregoing sections we have seen that there seems to be an experimental consensus about film thickness dependence of T_g in thin polymer film. There is strong evidence that this is related to enhanced dynamics in the near free surface region. Since the interfacial effects may play a key role for such observations, a variety of studies focusing on investigating the effects of both the vacuum (air)-polymer and substrate-polymer interfaces on the T_g of thin polymer films have been conducted. In order to study the length scale over which the interfacial effects can influence the dynamics of thin polymer films, the glass transition temperature distributions in thin polymer films have been measured and a length scale of several tens of nanometers is often observed. However, the glass transition temperature is an indirect measure of the dynamics in nanometer confined glass forming materials. In addition, several mechanisms are coupled to the T_g in different glass forming systems; even for a single glass forming materials there might be different mechanisms contributing to some dynamical or mechanical variable in different temperature windows. Therefore, local dynamic studies are necessary to improve our understanding of the glass transition mechanism in confined glass forming materials. The importance of such measurements was highlighted by de Gennes [63] who noted that "Future experiments should not aim at the determination of a single T_g, but at distribution of T_g's". As mentioned before, and as I will discuss in greater detail in Chapter VI, reports of such measurements have recently begun to appear.

B.4. Models addressing T_g anomalies in thin polymer films

One general observation in the past 15 years of dynamics studies of thin polymer films is that the measured T_g deviate from the bulk values, which indirectly means that the dynamic in polymers confined at the nanometer scale is different from the one of the bulk materials. The sign of T_g deviation can be negative for thin polymer film systems with weak polymer-substrate interactions, or positive for systems with strong polymer-substrate interactions. Some theoretical models have been proposed to interpret such observations. Three of those models (which are not system or polymer specific) are outlined below.

B.4.1. Layer model

The simple layer model can successfully explain some aspects of the T_g reduction in thin polymer films. The basic idea behind it is that a length scale of cooperative motion exists, and that a layer of similar thickness near the free surface has enhanced mobility [31]. Therefore, it is reasonable to consider that the interface mobility plays a key role for the T_g deviation phenomena observed in polymer systems on the nanometer scale. Keddie, Jones and Cory [31] were the first to suggest the existence of a liquid-like layer at the free polymer surface; the model was further developed by Forrest and Mattsson [72], by incorporating the idea of cooperative dynamics to describe the length scale of the interfaces with molecular mobility different from that of the bulk. The dynamics of the polymer films are then *heterogeneous on average*: the interface may have different dynamics compared with the rest of the system, but the whole system might be described by one averaged T_g. For nanometer scale polymer systems, the dynamics of the near free surface region (with enhanced molecular mobility) play a key role in determining the experimentally measured average dynamical properties.

The major success of the layer model is that it incorporates the dynamically different interface layer with a temperature-dependent length scale, and it can quantitatively estimate the average T_g of thin polymer films. However, this model does not specify the physical origin of the temperature dependence of the interface length scale. In addition, it is applicable only if $M_w \leq 378$ k for polystyrene.

B.4.2. Sliding chain model

de Gennes [63] proposed a sliding mechanism to explain the reduced glass transition temperature in thin polymer films, which also explains the linear dependence of T_g reduction in freely-standing films. The model considers the sliding motion of loops of polymer chains along their own contour. Only those loops with the two end points in contact with the polymer-air interface considered, so that the barrier to the motion at the end points could be ignored, as shown in Figure I.19. By arguing that is those loops that are long enough to reach the mid-plane of the film that have the most influence on the T_g of the film, he predicted at a glass transition temperature, T_g(slide), that is linear in h. The glass transition temperature of the film would be determined by the sliding motion if T_g(slide) < $T_g(\infty)$. This condition occurs when the film thickness is smaller than a threshold value that is of the

order of the end-to-end distance, R_{EE}, of the polymer. The model provides a good description for the experimental result of the high-M_W freely-standing films (Figure I.17). However, it does not predict a M_W - dependence in the slope of $T_g(h)$ as observed in experiment nor predicts a crossover from a high-M_W to low-M_W behavior (Figure I.17). This suggests there could be an additional mechanism for the enhanced molecular mobility that competes with the sliding chain mechanism.

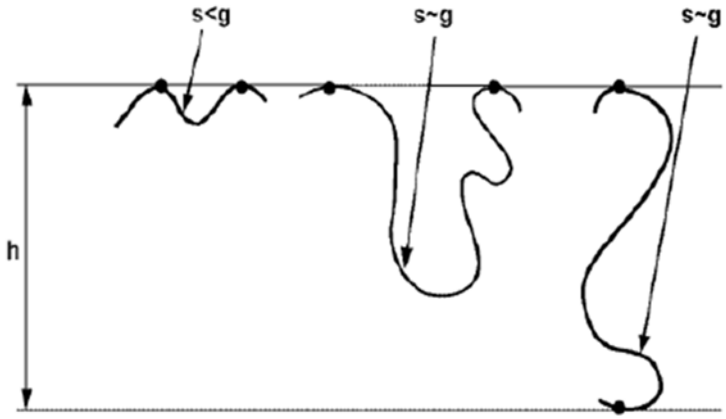

Figure I.19: Illustration of polymer loops with various loop lengths, *s*, sliding about the polymer-air surface. Only those loops with $s\sim g \sim (h/a)^2$ and thus extend to the mid-plane of the film can have an impact on the T_g of the film. Figure was reproduced from ref. [63]

B.4.3. Percolation model

Long and Lequeux proposed a density fluctuation model to explain T_g reduction in thin films [73]. In this model thermally induced density fluctuations are assumed to be responsible in producing dynamical heterogeneity with zones of different mobility. The glass transition appears when a percolation happens between more rigid areas. The T_g reduction in thin films is explained by a transition from a three-dimensional percolation to a two-dimensional percolation. The model predicts a universal exponent equal to $\delta = 1.5$. This model cannot predict why the T_g reduction in free standing films starts at a larger thickness compared to supported films, or why a profile of T_g's is observed in multi-layer films: the model completely ignores the fact that heterogeneity exists normal to the plane of the film, which does not vanish if averaged over time. For example, the free standing films are stable at temperatures above their T_g and start dewetting only at temperatures above bulk T_g. If the film were uniform, one would expect it to dewet once the temperature is increased above their measured T_g.

B.5. Methods Probing Polymer Motions and Transitions

B.5.1. Bulk Methods

There are many experimental methods for probing motions, relaxations and transitions in polymers which can be broadly classified in two approaches. The response of some thermodynamic or physical propriety can be measured as function of temperature, or one can look at a resonance response to externally applied oscillations, be they mechanical, electrical, or other. We will briefly describe several widely used methods.

B.5.1.1. Differential scanning calorimetry (DSC)

Differential scanning calorimetry consists in measuring the heat take up (endothermic) or given off (exothermic) by a polymer sample as a function of temperature. The glass transition temperature is manifested as a change in the slope of the heat capacity *vs.* temperature curve. Side chain and order of relaxation phenomena in polymers are very difficult to detect by this technique. Efremov et al. [74,75] used nano-calorimetry to measure the glass transition of PS, poly(2-vinyl pyridine) (PVP) and PMMA thin films supported on platinum substrates. In order to get a reasonable signal, different cooling/heating rates were used. The measured T_g of films with different thicknesses (PS) (100–4 nm) and polymethylmethacrylate (PMMA) (400–10 nm) was determined to be the same, within the experimental error (± 5 K). Huth et al. [76] used differential and AC calorimetry to measure the T_g of thin PS films at different cooling rates/frequencies. The fact that the cooling rate is inversely proportional to the relaxation time was used to produce the Arrhenius plot of the relaxation for PS films in the frequency range of 0.6 to 1280 Hz.

B.5.1.2. Dynamic Mechanical Analysis (DMA)

DMA is a technique used for studying the viscoelastic behavior of polymers. It measures elastic modulus (or storage modulus, E'), viscous modulus (or loss modulus, G') and damping coefficient ($tan\ \delta$- the ratio of loss to the storage moduli) as a function of temperature, frequency or time. Results are typically provided as plots of E', G', and $tan\ \delta$ versus temperature. Different transitions in materials can be identified as changes in the E' or $tan\ \delta$ curves. Those include not only the glass transition and the melting, but also other transitions that occur in the glassy or rubbery plateau. DMA measure subtle changes in the material and can recognize small transition regions that are beyond the resolution of DSC.

Values of dynamic moduli for polymers range from 0.1 MPa to 100 GPa depending upon the type of polymer, temperature, and frequency. Typically the Young's modulus of an amorphous polymer in its glassy state is of the order of few GPa. Mechanical relaxation is characterized by large modulus change that are best represented on a logarithmic scale.

B.5.1.3. X-ray and visible light scattering measurements

The relaxation time τ of a polymer film can be determined from the exponential decay of the intensity autocorrelation of the X-ray beam that is totally externally reflected from the film surface. Using this technique, Kim et al. [77,78] measured the dynamic response of the top 10 nm of polystyrene films from the free surface. The authors found viscosity inhomogeneities close to surface region for different film thickness, and reduction of T_g was attributed to the existence of a thin liquid-like surface where segments of the polymer chains bear higher mobility than those in the bulk.

Erichsen and coworkers used XPCS to measure the T_g of thin films [79]. T_g reduction was observed in thin films, but they concluded that this effect cannot be due to the free surface and XPS technique can be used only to measure glass transition in the bulk of thin films.

Forrest and Svanberg [80] used dynamic light scattering to measure the relaxation time of very thin PS free standing films of high molecular weight. They reported a reduction of T_g and a complete relaxation at temperatures above T = 297K (about 80 degrees below the bulk T_g value of PS).

B.5.1.4. Dielectric Relaxation Spectroscopy (DRS) measurements

Dielectric spectroscopy (sometimes called impedance spectroscopy), measures the dielectric proprieties of the medium as function of frequency or temperature. This technique has been used in a large fraction of the dynamical measurements of polymer films, and produced some of the most elaborate data for $\tau(T)$. DRS measurements provide more details about the relaxation properties over a wider range of relaxation times and temperatures above bulk T_g, compared with X-ray and visible light photon correlation measurements.

In this technique, the $\tau(T)$ of a film is typically obtained by measuring the dielectric loss peak from a frequency (temperature) scan at different temperatures (frequencies). For PS films, it was found that when the film thickness decreases, the dielectric loss peak is broadened and at the same time shifted to higher frequencies or lower temperatures. Fukao and coworkers [81,82,83,84] used dielectric relaxation and thermal expansion spectroscopy to study the behavior of PS films ($3{,}6 \times 10^3 < M_w < 1.8 \times 10^6$). They observed that dynamics in the films become more heterogeneous and chains become more mobile on average with decreasing film thickness. The T_g of the films estimated as the temperature at which the relaxation time is equal to 100 seconds: it seemed to be molecular weight dependent, a result which is not observed in any other dielectric relaxation studies or other measurements using different techniques. However, for dielectric measurements, it is necessary to sandwich a polymer between metal electrodes, making it difficult to study the effect of free surface on the molecular of the polymer films. To make these films, the upper electrode is deposited onto the polymer by thermal evaporation. The effect of evaporated metals on the properties of thin films has been studied by Sharp and Forrest [85]. They observed that covering a thin film of polystyrene with an evaporated Au layer eliminates the T_g reduction as expected if the free surface is the cause of T_g reductions in thin films. However, covering it with an evaporated Al layer did not change the

measured T_g of the film. They dissolved the polymer films and looked at the metal-polymer interface using contact mode AFM and observed qualitative differences between the interfaces produced by the two different types of metals. The interface of Al-PS seemed to be sharper, while the gold layer had penetrated about 4 nm into the polymer film, and also showed large clusters. This observation shows clearly that understanding the results of the dielectric measurements needs a comprehensive understanding of the metal-polymer interactions. A novel procedure avoiding evaporation of metals was reported by Sharp and Forrest [85]. Instead of evaporating Al on the PS film they made one h thick film by fusing two $h/2$ thick supported films. Contrary to previous dielectric measurements, they found that the T_g reduction effect disappeared, thus confirming the importance of the existence of the free surface.

The experiments described above measures changes in a physical property of the material as the surface to volume ratio is increases, T_g. For the case of PS, these techniques strongly suggest a reduced surface T_g value. To determine the cause of T_g reduction, we need to perform more detailed studies. Considering the reported works [86,87,90 88,89,90] which provide strong evidences about the important role of the free surface in T_g reduction, it seems reasonable to study the surface directly and try to define its dynamics in a way that is minimally affected by the bulk of the film.

B.5.2. Polymer Surface Dynamics

Only a handful of techniques are available for study motions and relaxations of polymer molecules in vicinity of the surfaces or interface. In this section I will describe some of them.

B.5.2.1. Atomic Force Microscopy

Dynamical studies employing AFM techniques generally probe the surface of the polymer samples. AFM-based experiments involve monitoring the response of the material to a surface perturbation. This perturbations can be oscillatory, as in the case of AFM surface rheology experiments [91,92], or it can be applied and then allowed to relax over time [93,94,95]. Because of the large number of factors that can influence the measurements, the conclusion can often depend on the interpretation adopted for the data, which may explain contradictory AFM results reported by different groups.

AFM studies of polymer films started in 1992 when Meyers et al. tried to answer the question, "*Is the Molecular Surface of Polystyrene Really Glassy*?" [96]. It was observed that if the surface of a glassy PS film is measured using contact mode atomic force microscopy (AFM), the motion of the AFM tip produced morphology changes on the surface uncompatible with a glassy material that depends on the molecular weight of the sample.

By using forced modulation microscopy (FMM) and lateral force microscopic (LFM) measurements of monodisperse polystyrene (PS), Kajiyama and Tanaka [97,98] showed that the surface of PS is already in a viscoelastic state even at room temperature. In monodispersed PS with M_W = 40kDa, Hammerschmidt et al. [91] also observed a modest reduction in the surface T_g (< 10 K)

by friction force microscopy (FFM), which is consistent with Kajiyama's observations. On the other hand, Ge and coworkers [92] measured no change or a slight increase in the T_g of monodispersed supported PS with $3k \leq M_W \leq 6.7$ MDa and freely-standing PS films with $M_W = 697K$ Da and $32 \leq h \leq 140$ nm by using shear modulation force microscopy (SMFM).

The conflicting results may be due to the fact that for all these experiments it is necessary to introduce a surface perturbation, causing a stress. Likewise, in many experiments involving AFM tips are in contact with the sample, subjecting it to a very large stress. This stress should be as small as possible and should certainly be smaller than the yield stress of PS ($\sim 3 \times 10^7$ Pa).

To reduce the stress on the polymer surface, Forrest and coworkers proposed the use of embedding nanoparticules. Gold nanoparticles are usually used as nano-indentors to study the properties of polymer surfaces. In such cases, embedding of the gold on the surface can be problematic, because it partially covers the free surface, and it is not exactly clear how this can affect the dynamics. There is also a difference between the embedding of evaporated gold and colloidal gold, which makes it more complicated to interpret the results [99,100,101,102,103].

AFM experiment and embedding experiments has been successful in showing the existence of enhanced dynamics near the surface, but defining the exact shape of relaxation function and its temperature dependence in the vicinity of the surface is nearly impossible. The viscoelastic nature of the polymer surface and the fact that at different depths the relaxation times could be different makes it hard to separate different modes of motion.

B.5.2.2. Surface roughness experiments

One way to measure surface relaxations is to introduce a perturbation on the surface and monitor the relaxation of the perturbed surface at different temperatures. An example of such experiment is the work of Kerle et al. [104]. In their study, artificial roughness on Si substrate was produced using CaF_2 salt. The salt surface was covered with a thin layer of Aluminum. A polystyrene film with a thickness of 10 microns was placed on top of this rough surface. The film was reversed and the salt and Aluminum were removed using HCl. The initial roughness (RMS) obtained by this method is about 4.5 nm at room temperature. The films were then annealed at temperatures between 65 to 105 °C. The temperature dependent relaxation process derived by Laplace pressure was followed using AFM. At $T \geq T_g$ a full relaxation of the asperities were observed and the aspect ratio of the final roughness to the initial roughness decayed to zero. But at $T < T_g$, only a partial relaxation of surface roughness was observed and the aspect ratio was larger than zero. At 70 °C the final aspect was about 0.4.

Surface roughness measurements are also useful for showing the existence of enhanced dynamics near the surface, but to define the exact shape of relaxation function and its temperature dependence in the vicinity of the surface some important details should be taken into account. The relaxation times of the motions driven by surface tension are inversely proportional to the radius of curvature. In a rough surface, curvatures of many length scales exist, which could have relaxation

times much longer than the time scale of the experiment. So it is important to perform experiments where surface perturbations have a constant length scale, which makes possible the correct estimation of relaxation.

The work of Papaleo et al. is an example of such experiments [105,106,107]. High energy ion bombardment was used to produce deformations on the surface. In the point of ion contact there is a plastic deformation due to high temperature of the impact point. Away from this point, the shock waves of the impact produce bumps at the surface, with a size that depends on the molecular weight of the polymer. These bumps can be annealed at different temperatures above and below bulk T_g. The relaxation of these structures at different temperatures showed that above T = 67°C (T_g (bulk) = 116°C) the relaxation looked like a stretched exponential with β=0.4. Below this temperature, annealing still happens, but the relaxation looks like a single exponential relaxation with an Arrhenius temperature dependence of the characteristic relaxation times. These results show that not only the dynamics of the surface is enhanced compared to the bulk, but the behavior of the system is changed. It should be noted that the nano-deformations were produced by a very high-energy process. The bombardment could produce high local stress, radiation-induced cross-links, or chemical changes. Unfortunately, it is not clear how this will affect the results. Clearly more work is needed to confirm these results.

An extended set of experiments was performed by Fakhraai and Forrest [108]. To make nano-deformations (holes) with constant depth and radius of curvature, gold spheres (approximately 20 nm in diameter) were put on the surface of spin-cast PS films (thickness 100 nm, M_W = 641 K Da) and were embedded above T_g (105°C) for different periods of times to get different embedding depths. The embedding times were selected to produce average embedding values of ~2 to 4 nm. The temperature of the samples was then brought back to room temperature and the gold spheres were dissolved using mercury. To probe the surface dynamics, they measured the time-dependent relaxation of these surface deformations (holes) as a function of temperature from 4 to 96 °C. Surface relaxation was observed at all temperatures, providing strong direct evidence for enhanced surface mobility. The deviation from bulk α relaxation became more pronounced as the temperature was decreased below the bulk glass transition temperature.

In summary, the studies of the polymer dynamics in local nanometer confined regions are relatively new and require various experiments to confirm the temperature and/or chain size dependence in the near free surface regions of thin polymer films. More theoretical considerations for such dynamical features in nanometer scale confined polymer systems are also necessary. An important part of the work of this thesis is devoted to this aspect.

C. Structuration of liquid polymer films by capillary instability

Thin polymer films are being increasingly used in a wide variety of technological applications ranging from barrier layers in microelectronics to protective coatings and adhesives. In the continual push toward miniaturization of devices and minimization of material costs, the thickness of the films used in these applications has been, and will continue to be, reduced. It is important to understand the physical properties of the polymer molecules confined to very thin films and, in particular, to determine if they differ from those in bulk. A particularly important property is the stability of the thin films. To be useful in technological applications, polymer films should have a morphology that either remains stable within an acceptable range of temperatures, or undergoes a transformation in morphology that is desirable, controllable and predictable. It has been found that large changes in the films can be produced by relatively weak external stimuli such as the application of an external field or a change in temperature. For example, modest temperature changes near room temperature can produce dramatic changes in the mechanical properties and the self-assembly of polymers. Some of these aspects will be briefly described in this section.

C.1. Stability of thin films

Considerable experimental and theoretical efforts have been devoted to understand the stability of thin films supported by solid substrates. This topics have been addressed by many authors [109,110,111,112,113,114] who tried to explain the different rupture mechanisms, as well as the large number of factors that influence this process. A strong motivation for this type of experiments is the large number of different patterns that are generated by the break–up mechanism [115]. This opens a door for many application based on surface patterning. However, it is first necessary to understand the processes governing the dynamics of thin films at a fundamental level. Thin polymer films have proven to be ideal model systems for these studies due to their low vapor pressure and their high viscosity that facilitates the study of their dynamic behavior. The generic experimental system is represented in Figure I.20. A thin polymer film is deposited onto a substrate and liquefied by heating above its glass transition temperature T_g. Liquid surfaces are never completely flat: the molecular motion of the liquid at finite temperatures causes a spectrum of capillary waves at the liquid surface. Perturbations of the free interface which generate flow in the film can be described using a hydrodynamic approach [110,111] based on the Navier–Stokes equation, which balances the macroscopic forces at the interface.

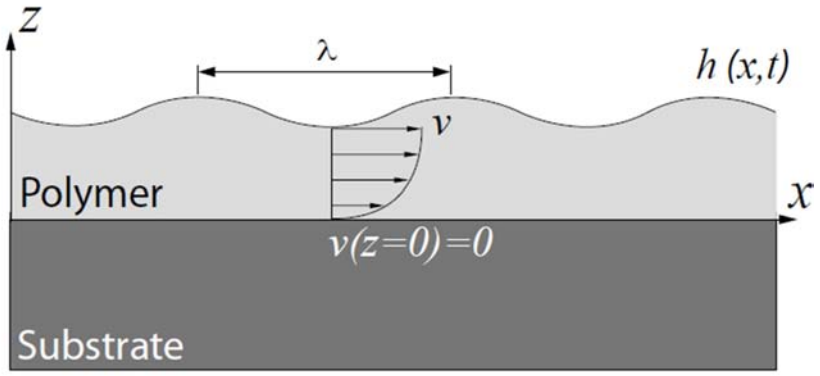

Figure I.20: The generic experiment used to study the influence of external factors on the stability of thin liquid polymer films. The *z*-position of the interface is described by the function h(x, t) with the lateral coordinate *x* and time *t*.

The stability of the film is determined by the transient behavior of the capillary waves, which can be observed using sensitive scattering techniques (e.g. light scattering). Although the capillary waves are created by a spontaneous process caused by thermal motion, their relaxation is described by macroscopic laws, if their wavelength is larger than molecular dimensions. If additional forces are present, undulations might either be suppressed or amplified. Examples of such forces are gravity, surface-tension forces, van-der-Waals forces, forces due to external fields (e.g. electric or magnetic), radiation pressures, or temperature variations of material properties resulting in stresses at the interface. Since the basic equations describing to the problem are generic for many experimental conditions, a complete derivation of them is helpful in order to understand the physical mechanisms behind the instabilities covered in the following chapters.

C.2. Pattern formation by capillary instability

A destabilizing interfacial pressure can be generated at the surface of liquid film, e.g. with the help of electric fields or temperature gradients. If the external pressure overcomes the stabilizing effect of the surface tension, it drives the film towards dewetting. The external field can be applied by placing the polymer film between two electrodes in a capacitor geometry, including also an air gap. The developing morphology can be controlled by laterally varying the applied field with the help of a structured electrode.

To theoretically describe the behavior of capillary waves one can model them as sinusoidal perturbation of a flat interface [116].

$$h(x,t) = h_p + \zeta \exp(iqx + \frac{t}{\tau_q}) \tag{1.28}$$

where ζ is the amplitude of the capillary wave and h_p is the position of the planar surface ($\zeta = 0$). For negative values of τ_q, the mode with wave vector q is damped. For positive τ_q values the surface is destabilized by the exponential growth of this mode.

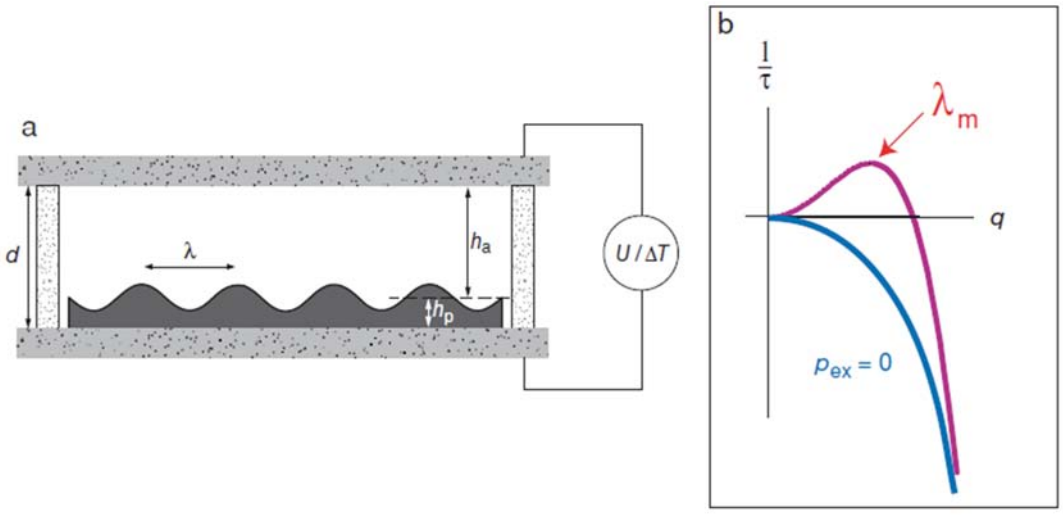

Figure I.21: (a) Schematic representation of the device used to study capillary surface instabilities. A polymer air bilayer of thicknesses h_p and h_a, respectively, is formed betwen two planar silicon wafer held at a separation d. A capillary instability with wavelength $\lambda = 2\pi/q$ is observed upon applying a voltage U or a temperature difference ΔT. (b) Dispersion relation (prediction of Eq. 1.33). While all modes are damped ($\tau < 0$) in the absence of an interfacial pressure, the application of an interfacial force gradient may lead to the amplification of a range of λ-values, with λ_m the fastest growing mode.

The formation of a surface wave (Figure I.21-a) requires the lateral displacement of matter. Assuming a non-slip boundary condition at the substrate surface (lateral velocity $v(z=0) = 0$), and in the absence of normal stresses at the liquid surface a parabolic velocity profile (half-Poiseuille profile) in the film will be developed

$$v(x,z) = \frac{1}{2\eta} z(z-2h)\partial_x p \tag{1.29}$$

where η is the viscosity of the liquid and ∂_i represents the partial derivative with respect to i . $\partial_x p$ is the lateral pressure gradient that drives the liquid flow in the film. In the one dimensional case considered here, the lateral flow causes an averaged flux $j = hv$ through the film cross section h, given by

$$j = -\frac{h^3}{3\eta}\partial_x p \tag{1.30}$$

The third necessary ingredient for the model is the continuity equation for the non-volatile polymer melt

$$\partial_t h + \partial_x j = 0 \tag{1.31}$$

Inserting Eq. (1.29) into Eq. (1.30) yields the equation of motion

$$\partial_t h = \frac{1}{3\eta}\partial_x (l^3 \partial_x p) \tag{1.32}$$

Eq. (1.31) describes the response of a liquid film to an applied pressure p together with the Eq. (1.32). The resulting differential equation is usually solved in the limit of small amplitudes $\zeta << h \approx h_p$ and only terms linear in ζ are kept ("linear stability analysis"). This greatly simplifies the differential equation. The pressure inside the film $p = p_L + p_{ex}$ consists of the Laplace pressure $p_L = -\gamma\partial_{xx}h$, minimizing the surface area of the film, and an applied destabilizing pressure p_{ex}, which does not have to be specified at this point. This leads to the dispersion relation

$$\frac{1}{\tau} = \frac{h_p^3}{3\eta}(\gamma q^4 + q^2 \partial_l p_{ex}) \tag{1.33}$$

The predictions of Eq. (1.33) are schematically shown in Figure I.21-b. For $p_{ex} = 0$, $\tau < 0$ for all values of q. This confirms that films are stable in the absence of a destabilizing pressure. If a (possibly externally imposed) force is switched on, so that $\partial_h p_{ex} < 0$, $\tau > 0$ if q is smaller than a critical value q_c and has a maximum for $0 < q_m < q_c$. Qualitatively, modes with a large wave vector q (corresponding to surface undulations with short wavelengths $\lambda = 2\pi/q$) are suppressed ($\tau < 0$), since the amplification of such waves involves a large increase in liquid-air surface area. On the opposite end of the spectrum, long wavelength (small q) modes, while allowed, amplify slowly due to the large lateral transport of material involved in this process. As a consequence, the mode with the highest positive value of τ_m is maximally amplified:

$$\lambda = \frac{2\pi}{q_n} = 2\pi\sqrt{-\frac{2\gamma}{\partial_h p_{ex}}} \tag{1.34}$$

$$\tau_m = \frac{3\eta}{\gamma h_p^3} q_m^{-4} \tag{1.35}$$

Eq. 1.34 is a generic equation describing film instabilities in the presence of an applied pressure. It describes the film instabilities driven by van der Waals forces, or forces caused by electrostatic or temperature gradient, as discussed below. Eq. (1.34) also illustrates that film instabilities are determined by the forces that cause them. The systematic study of film instabilities can therefore be used to quantitatively measure surface forces.

C.2.1. Van der Waals forces

The case $p_{ex} = 0$ is purely academic, since van der Waals interactions are omnipresent and are known to affect the stability of thin films. In the non-retarded case, the van der Waals disjoining pressure can be described as [110,117]:

$$p_{vdW} = \frac{A}{6\pi h^3} \tag{1.36}$$

where A is the effective Hamaker constant for the liquid film sandwiched between the substrate and a third medium (usually air). Depending on the sign of A, p_{vdW} can have either a stabilizing ($A < 0$) or a destabilizing ($A > 0$) effect. Eqs. (1.34) and (1.36) yield the well-known dewetting equations [118]

$$\lambda = 4\pi\sqrt{\frac{\pi\gamma}{A}}h^2 \tag{1.37}$$

Dewetting driven by van-der-Waals forces has been observed by many workers [119,120]. It is characterized by a wave pattern, as opposed to heterogeneously nucleated film break-up caused by imperfections in the film, leading to the formation of isolated holes that cause the dewetting.

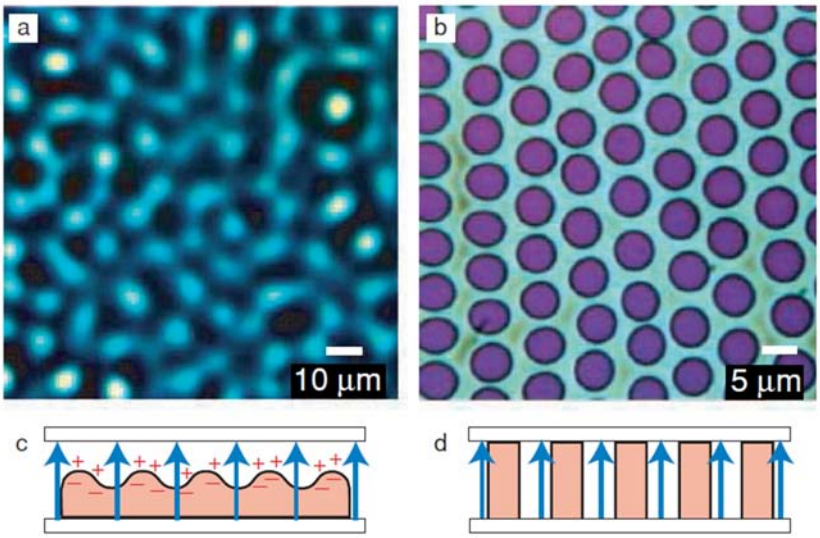

Figure I.22: Electrohydrodynamic instability of a polymer film. Applying a voltage at the capacitor in Fig. 1.21a results in the amplification of a surface undulation with a characteristic wavelength λ (a). This leads to the formation of hexagonally ordered columns (b). The origin of the destabilizing pressure p_{el} is schematically shown in (c): the electric field causes the energetically unfavorable build-up of displacement charges at the dielectric interface. (d) The alignment of the dielectric interface parallel to the electric field lines lowers the electrostatic energy. Adapted from [126].

C.2.2. Electrostatic forces

Films can be also destabilized by applying an electric field perpendicular to surface. The physical basis for the deformation of a liquid surface by an electric field has been known for more than a century. In 1879 Rayleigh [121] observed that a liquid jet breaks-up as a consequence of a capillary instability that is characterized by a wavelength larger than the jet's circumference. Later, in 1894, Bassett [122] showed how electric charges destabilize liquid cylinders and drops. Until the 1960s most of the work was focused on study the behavior of different varieties of liquids under electric field. Good conductors (e.g. mercury) and perfect dielectrics (e.g. apolar liquids such as benzene) have been studied [123,124]. Later studies were more focused on poorly conducting liquids and leaky dielectrics. Particular attention has been paid to the structuring effect at an externally applied electric field on polymer systems [125,[126]. At the base of these experiments is a very simple concept related to the fact that at the interface between two media a density gradient is always present, which corresponds to a gradient in the dielectric constant at the interface. When a voltage is applied between two planar electrodes the gradient in the dielectric constant translates into a gradient in the electric field across the interface. Any field gradient, translates into a corresponding pressure. This electrostatic pressure serves to amplify fluctuations at the interface.

This process was first called lithographically-induced self-assembly (LISA), but in more recent publications it has been named more generally as electric-field-induced pattern formation and is called electrohydrodynamic (EHD) patterning. In EHD patterning, schematized in Figure I.22, a glassy polymer, often poly(methyl methacrylate) (PMMA) or polystyrene (PS), is spin-coated on to a

electrode known as the substrate. This thin polymer film is allowed to dry flat, forming a glassy polymer film. Then, another electrode mask is placed at a small distance above the top of the film, leaving a gap which can be filled with air or another liquid. The system is then heated above the glass transition temperature (T_g) of the polymer, allowing it to flow. The mask and the substrate are then electrically connected and a constant electrostatic potential is applied between them. As the electric field is applied, the interface of the polymer film destabilizes, first forming cone-shaped undulations which eventually grow in amplitude across the entire domain until the polymer film hits the upper electrode, producing columns with characteristic separation distances and diameters. After the pillars reach a steady-state configuration, the temperature is quickly lowered to lock the polymer into a glassy state and the mask is removed, leaving the desired pattern of pillars on the polymer film.

The destabilizing effect arises from the fact that the electrostatic energy of the capacitor device is lowered for a liquid conformation that spans the two electrodes (Figure I.22-d) compared to a layered conformation (Figure I.22-c). The corresponding electrostatic pressure p_{el} is obtained by the minimization of the energy stored in the capacitor (constant voltage boundary condition) $F_{el} = QU = 1/2\ CU^2$, with the capacitor charge Q and the applied voltage U. The capacitance *C* is given in terms of a series of two capacitances. This leads to a destabilizing pressure

$$p_{el} = -\varepsilon_0(\varepsilon_2 - \varepsilon_1)E_1E_2 \tag{1.38}$$

with ε_1 and ε_2 the dielectric constants of the two media and the corresponding electric fields

$$E_i = \frac{\varepsilon_j}{\varepsilon_1 h_2 + \varepsilon_2 h_1} \ (i,j = 1,2; i \neq j) \tag{1.39}$$

ε_0 is the permittivity of the vacuum. Making use of Eq. (1.34), we obtain [125]

$$\lambda_{el} = 2\pi\sqrt{\gamma U \frac{\sqrt{\varepsilon_2\varepsilon_1}}{\varepsilon_0(\varepsilon_2-\varepsilon_1)^2}(E_1E_2)^{-\frac{3}{4}}} = 2\pi\sqrt{\frac{\gamma(\varepsilon_1 h_2+\varepsilon_2 h_1)^3}{\varepsilon_0\varepsilon_1\varepsilon_2(\varepsilon_2-\varepsilon_1)^2U^2}} \tag{1.40}$$

For a double layer consisting of a polymer layer ($\varepsilon_2 = \varepsilon_p$) with film thickness $h_2 = h_p$ and an air gap (ε_1=1), we obtain:

$$\lambda_{el} = 2\pi\sqrt{\frac{\gamma U}{\varepsilon_0\varepsilon_p(\varepsilon_p-1)^2}}E_p^{-\frac{2}{3}} \tag{1.41}$$

C.2.2.1. Previous studies and research

The formation of periodic arrays of pillars from a thin, uniform polymer film was first observed in 1999 by Chou, Zhuang and co-workers [127,128], who postulated that internal charges created an internal electric field in the film which served as the driving force for pillar creation. Almost simultaneously, Schaffer and co-workers found that the application of an external electric field enhances the instability, leading to the formation of well-defined arrays of smaller pillars [129].

In the experiments of Chou and coworkers, pillars with diameters of 1 μm were generated. Replicated patterns of Schaffer were nearly perfect [130], and smaller feature sizes were also achieved, with pillar diameters nearing 100 nm. After these seminal works, researchers have focused on controlling the patterns and decreasing their size using externally applied electric fields and patterned mask.

Lin et al. decrease the interfacial tension and the Laplace pressure by replacing the air layer with a liquid, leading to a substantial reduction in feature size. Nearly 50 times faster growing of the pillars in comparison to the polymer/air case was observed [131,132]. In 2008, Bae and coworkers [133] present a new method of making smaller features. Their strategy consisted in increasing the electrostatic stress at the interface by enhancement the dielectric contrast between bottom and top layers. Polystyrene-capped gold nanoparticles were incorporated into a polystyrene film, increasing the effective dielectric constant from 2.6 (for the pristine polymer) to □3.2, which resulted in □20% reduction of the spacing between pillars. Additional shapes, such as arrays of holes [132], 100 nm periodic gratings [134], rosettes [129], and concentric rings [135] have also been reported. In experimental and theoretical work Morariu and coworkers (2003), Bandyopadhyay and Sharma (2007, 2009) have extended these results to a trilayer geometry, which has led to even more complicated novel structures such as hollow pillars [136,137,138].

Over the past 10 years, electric-field-induced pattern formation has been extensively studied both experimentally and through modeling. A recent review article by Wu and Russel 2009 nicely summarizes much of experimental research work in patterning of thin films by using electrodynamic instabilities and proposes some challenges and future directions in pattern formation by the electric field [139].

Besides the experimental work, many researchers have sought to understand the above phenomena through mathematical modeling. In the 1960s, G. I. Taylor introduced the leaky dielectric model to explain the behavior of droplets deformed by a constant electric field [140,141]. Melcher adopted this model in a study of planar interfaces [142]. In the Taylor-Melcher model, a fluid is assumed to be weakly conducting (leaky) to the extent that a bulk charge density does not exist, but a surface charge density can develop at the interfaces [143]. From these first theories on the rupture of liquid films by an externally electric field two qualitatively different cases can be distinguished. Film instabilities can be caused (i) by free charges at a liquid/air or liquid/liquid interface, or (ii) by polarization charges in the liquid. The first is achieved, for instance by exposing a thermoplastic surface to a discharge or by the accumulation of charges at the interface (leaky dielectrics).

The theoretical treatment of thin film pattern formation using the leaky dielectric model was first considered by Pease and Russel in 2002 [144]. They utilized standard linear stability techniques under the lubrication approximation to analyze the effect of conductivity and surface properties on the size of formed patterns. They found that the growth rates and wavenumbers calculated using the leaky dielectric model were significantly larger than for perfect dielectrics and those obtained experimentally data by Schaffer et al [130] and Lin et al [131]. To improve previous analyses, which used the lubrication approximation, Pease and Russel in 2003 presented a generalized linear stability analysis that relaxed this approximation [145]. They showed that as surface tension decreased and the electric field is increased, the wavelength of the pillars (surface structure) decreased. Additionally, Shankar and Sharma in 2004 [146] studied the effect of an external applied electric field on the stability of the interface between two thin leaky dielectric fluid films using a linear stability analysis in

the long-wave limit. They used asymptotic expansions to derive the coupled nonlinear evolution equations of the position of the interface between the fluids and the interfacial free charge distribution. They found two parameters to be important: the thickness ratio and the viscosity ratio. Larger thickness ratios lead to larger scale structures while viscosity ratio has a significant effect on the fastest growing wavelength. A reduction in the viscosity ratio by a factor of 100 can decrease the wavelength by a factor of 5. They also found that the feature size scales as $\beta^{-\alpha}$, where β the ratio of the thicknesses of the two fluid layers and α depends only on the ratio of the conductivities. Further investigation into the dynamics of pattern formation induced by electrostatic field has been conducted by 3D nonlinear simulation by Verma, Sharma et al. in 2005 [147]. They studied the morphology of the final pattern features, along with the evolution of those features, for both homogeneous and heterogeneous electric fields in a perfect dielectric fluid. Wu and co-workers [148,149] used a combination of weakly and fully nonlinear evolution equations to investigate how nonlinear effects govern the growth of the instability and determine the final patterns. Through Fourier expansions, they showed that second- and third-order nonlinearities favor the growth of hexagonal patterns in agreement with experimental findings. Additionally, the effect of patterned masks was investigated, showing that the geometry of the self-assembled patterns conform to the mask patterns.

The majority of theoretical studies presented above have only considered the flow of Newtonian fluids, while in the experiments is typically are used the polymer polystyrene or poly (methyl methacrylate) are typically used. It is well established that polymer melts that are above their T_g exhibit strong non-Newtonian behavior, often viscoelastic.

Instabilities in the flows of viscoelastic fluids has been widely studied in other configurations, as nicely summarized in a review article by Larson [150]. A majority of these studies were for bulk flows without free interfaces, with the exception of a section on gravity-driven viscoelastic flows down inclined planes. Chen [151] and Balmforth [152] also reviewed some of the literature on interfacial instabilities of viscoelastic fluids in shear flows.

Non-Newtonian models have also been used to study electric-field-induced pattern formation. Wu and Chou [153] was the first to attempt this by modeling the liquid layer as a leaky dielectric fluid utilizing the Oldroyd-B viscoelastic constitutive equation, finding that the addition of elasticity further destabilized the interface. This elasticity could also couple with the dynamics of the free charge, creating a resonance that produced a bi-modal growth rate curve with two most-unstable wavenumbers. The model used in this study, however, ignored the effect of inertia, which led to curious singularities in the growth rate curves. Tomar [154] later included inertia in the formulation using the Maxwell model, showing that the singularity described by Wu and Chou [153] was an artifact of their neglect of inertia. Alternatively, inertia could be ignored if a solvent viscosity was included instead by using the Jeffreys model.

More recently Shankar and Sharma 2010 presented a general unified theory of field (van der Waals, electric, etc.)-induced surface instabilities in thin viscoelastic films. Their theory covers the instability and its different regimes in films ranging from elastic to viscous, from adhesive (confined)

to wetting (free surface), and from short- to long-wave instabilities. They found that critical conditions for the onset of instability strongly dependent on elastic properties, such as the shear modulus of the film, but the dominant wavelengths are strikingly independent of the film rheology. Different regimes based on a nondimensional parameter ($\gamma/\mu h$) are uncovered, where γ is the surface energy, μ is the elastic shear modulus, and h is the film thickness. A short-wave, elastic like response with wavelength $\lambda \approx 2.96h$ was obtained for $\gamma/\mu h < 0.1$ (elastic limit), whereas for $\gamma/\mu h > 1$ (viscous limit)a long waves that depend nonlinearly on the field strength and surface energy were obtained [155].

Elastic solids under the effect of electric fields have also been studied, beginning with the work of Yang and Song [156]. This approach considered the mechanics of the solid using contributions of surface energy, elastic energy, and electrostatic energy to the overall chemical potential of the interface. They showed that for elastic solids there is a critical electric field strength above which the interface will destabilize with a characteristic wavelength. Sarkar et al. [157] later used a more rigorous model for the elastic solid, which extended the analysis to include the glassy and transition regimes of the polymer behavior. They reported, primarily using 2-D nonlinear simulations, that the pattern length scale depends only on the initial film thickness, regardless of the rheological properties of the material. Experiments were conducted by Arun et al. [158] to specifically study the effect that viscosity and elasticity have on pillar formation. They reported two distinct regimes of behavior, one that behaves much like a liquid, displaying long wavelengths that are governed by the electric field and material properties, and a second that behaves like a solid, where the length scale is relatively unaffected by the material properties. The transition region between these two regimes is very narrow and depends on the storage modulus.

A more detailed theoretical description of electric field induced instability in soft liquid, solid and visco-elastic thin films will be presented in Chapter III.

D. Contact between water and hydrophobic polymer films. (How water meets a hydrophobic polymer surface)

Water is one of the most important and ubiquitous chemicals on earth. It surrounds and permeates our lives; making up over 60% by volume of our bodies, and covering over 70% of the earth's surface. Still for all its importance, water is not well understood, and exhibits many anomalous behaviors when compared to other fluids. For example water has a much higher surface tension and heat capacity than comparable liquids. The origins of many of the unusual aspects of water are due to its unique liquid structure. In its liquid form, water consists of an ever-changing three-dimensional network of hydrogen bonds.

Water presents an even more puzzling behavior near hydrophobic surfaces. Loosely speaking, one can define hydrophobicity as the tendency to of a substance to repel water. Usually hydrophobic surfaces do not form hydrogen bonds. When water is placed in contact with a hydrophobic surface, its hydrogen-bonding network must be disrupted. This drives the minimization of the area of contact between water and hydrophobic substances. For this reason, a drop of water placed on a hydrophobic surface will ball up instead of spreading out. The angle made between the solid and the liquid surface at the point of contact is a good measure of the hydrophobicity of the solid. This angle is called the contact angle (θ). Water placed on a hydrophobic surface will form a drop with θ larger than 90°. However, what happens when water is forced into contact with a hydrophobic surface? Some researchers have argued that an ultra-thin low-density region forms near the surface [159,160,161, 162,163]. However the microscopic details of how water meets a hydrophobic surface is still highly debated in literature. There is not general consensus as to whether or not such a depleted region exists. An overview of the experimental work performed on water-vapor and water-solid interfaces can be found in the review article of Verdauger et al. [85].

The existence of sub-microscopic gas bubbles on solid surfaces immersed in water was first proposed to account for the unexpected long-ranged attractive force between hydrophobic surfaces in water.[164,165] Since then, results collected from different techniques has been presented in support their existence at the water/hydrophobe interface, [166,167,168,169,170,171,172;173,174,175, 176,177,178,179,180,181] including direct imaging of nanobubbles by tapping mode atomic force microscopy (AFM) [167,168,169,170,171,173], ellipsometry [179,180,181], neutron and X-ray reflectivity [174,175,176,177,178]. Thermoreflectance measurements across solid-water interfaces were performed by Ge et al. [182]. They found a significantly reduced heat conductance at hydrophobic substrates compared to hydrophilic samples. Assuming that the thermal conductance of an interfacial depletion layer is similar to water-vapor, an upper limit of 2.5Å for the size of the interfacial gap was estimated. Other than these experiments on single solid-water system, other techniques as the surface forces-apparatus (SFA) [183,184,185,186], colloidal stability [166], and infrared spectroscopy measurements (ATR-FTIR) on the aggregation of hydrophobic particles [187] have been used to study the interaction of hydrophobic objects in water.

Theoretical efforts have also been developed on this topic. In 1973, Stillinger presented a theory to qualitatively explain what happens to water near hydrophobic objects [188]. Based on calculations from scaled particle that explicitly include "the strong and directional hydrogen-bonding forces in water", he suggested that large hydrophobic objects will be surrounded by a "thin film of water vapor". He predicted that the water in direct contact with the object would have a density that is 50,000 times less than that of bulk water. Furthermore, if the external pressure is close to the saturated vapor pressure for the given temperature, the film could be thick on the molecular scale because there is "essentially no driving force to eliminate the vapor film"[188]. Lum, Chandler and Weeks have developed a theory of hydrophobicity that predicts the existence of a gas-like layer between two extended hydrophobic planar surfaces in water [189]. Many computer simulations have been performed to try to uncover the causes of the different hydrophobic effects, as gas and dewetting behavior between two hydrophobic planar surfaces and even in a two-domain protein immersed in water [190,191,192].

The experimental results are still disputed. Part of continuous debate is focused on whether the gas at the liquid/solid interface is in the form of bubbles or as a continuous gas layer. Two major difficulties argue against the presence of nanobubles. First, thermodynamics indicates that the bubbles cannot be in equilibrium because their internal pressure would be too high. The internal gas pressure of a 10 nm bubble would be 140 atm, according to the Laplace equation. Such a high pressure should force the nanobubbles to quickly dissolve. The lifetime of those nanobubbles predicted by conventional thermodynamics ranges from several picoseconds to hundreds of microseconds [193], which is too short to be experimentally detectable (e.g. AFM). The second objection is that the AFM techniques used to image these bubbles may in fact be nucleating the bubbles or breaking up a continuous vapor layer. In a neutron reflectivity study, Doshi et al. pointed out that the density reduction of water at the hydrophobic silane-water interface depended on the dissolved gases in water, whereas pre-existing nanobubbles were excluded [178]. As can be observed in Figure I.23, a reduced density layer adjacent to a hydrophobic OTS surface is present, with thickness determined by the gasses dissolved in water. Ambient water produced an 11 Å depletion layer, while the OTS surface with degassed water bubbled with argon had a 2 Å depletion layer.

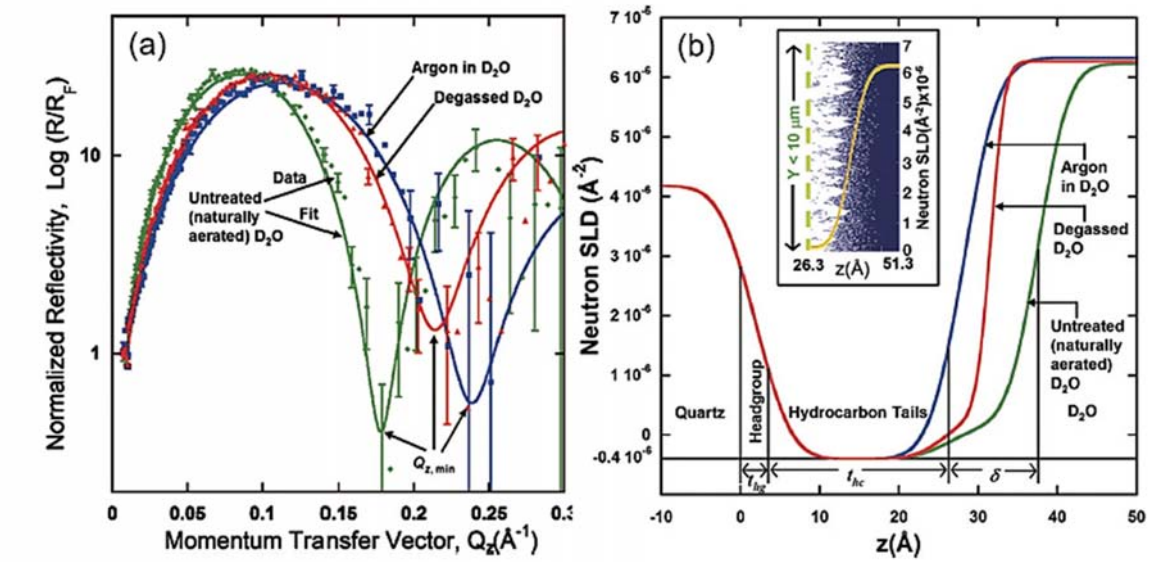

Figure I.23: Neutron scattering experiments at the OTS–water (D_2O) interface (compilation from Doshi et al. [178]). (a) Neutron reflectivity R normalized by the Fresnel reflectivity R_F together with calculated curves (solid lines) from the parameter refinement of a slab model versus the vertical momentum transfer q_z. Doshi et al. found a strong dependence on the gas content in the water (naturally, green; degassed, red; argon, blue). (b) Scattering length density (SLD) profiles obtained from the neutron reflection pattern. The extracted structure depends highly on the water preparation.

Some years ago, Attard and Tyrrell [170,194] suggested that long-range hydrophobic attraction is caused by the presence of nanobubbles and reported some images obtained using tapping mode Atomic Force Microscopy (AFM). The size of the observed bubbles was 20-30 nm; the surface coverage is so high that it is hard to see the bare substrate. They observed that the size of the nanobubbles is comparable to the distance at which the hydrophobic surfaces jump into contact. In a more recent study Attard et al [194] insisted that nanobubbles were responsible for the long-range attractive force measured by AFM between hydrophobic surfaces immersed in water. In their view, as two hydrophobic surfaces approach one another the nanobubbles can bridge the distance and the bridging meniscus then pulls the surfaces together. Figure I.22 shows AFM measurements performed by Tyrrell et al. [170] and a more recent study by Simonsen et al. [173].

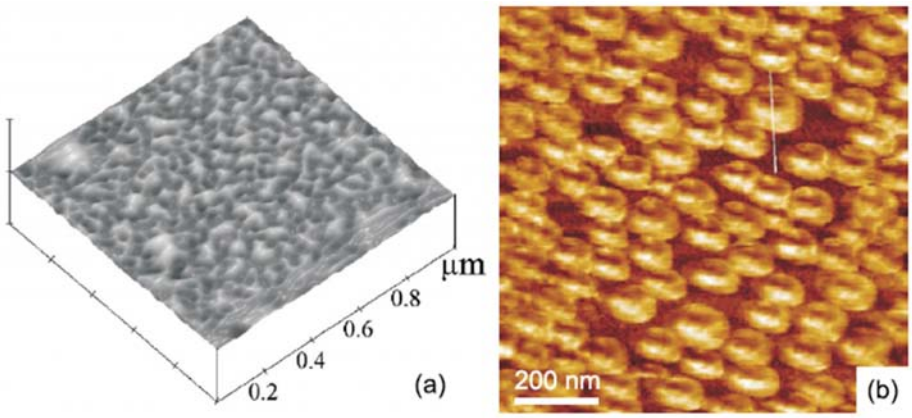

Figure I.24: Compilation of taping-mode AFM measurements on hydrophobic solid substrates immersed in water. (a) Hydrophobic glass surface in water taken from Tyrrell et al. [170] (heigh image, peak-to-valley scale: 30 nm). (b) AFM phase image of the polystyrene-water interface taken from Simonsen et al. [173].

Recent X-ray reflectivity measurements seem to show that the depletion layer between the water and a hydrophobic surface cannot be explained by nanobubbles [195]. On the other hand, Zhang et al. have reported that the gas nanobubbles [175,196] and gas pancakes [197] can be formed with high reproducibility by the solvent exchange method.

Despite of the long list of seemingly contradictory results around the nature depletion of the layer between the water and a hydrophobic surface, consensus is slowly emerging around the idea that a boundary layer of reduced density is indeed present. This is not the only unexpected effect related to the contact between water and hydrophobic surfaces [198]. In many areas of biological, environmental, or technological interests the aqueous phase is not pure water, but comprises a number of ions including those associated with the acidity or alkalinity of the solution. For this reason exploring the behavior of aqueous solution of salts, acids and bases in contact with hydrophobic surfaces and understanding the behavior of different ions is a topic of interests.

Since hydrophobic surfaces are by definition "water hating", one might assume that solvated ions would avoid a hydrophobic surface. Simple electrostatic considerations suggest that solvated ions would rather be located in the high dielectric constant environment of bulk water that at the interface with low dielectric medium. Yet experiments reveal that solid hydrophobic polymers, hydrophobic assembled structures, and even gas bubbles are usually negatively charged in contact with water at neutral or basic pH [199,200,201,202,203,204] and become positively charged in acidic solutions [205,206]. Most hydrophobic polymers do not have reactive surface groups or a strong affinity for ions (inert surfaces), but often exhibit electrokinetic potentials of the same order of charged hydrophilic surfaces (such as glass), and have similar pH dependence. In neutral solutions this inert surfaces show a negative surface charge and isoelectric point (IEP) close to pH = 4 (Figure I.25).

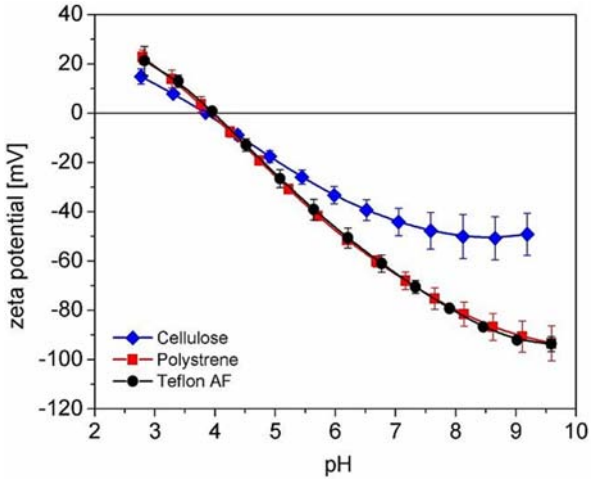

Figure I.25: Zeta potential of non-oxidized cellulose, polystyrene, and Teflon® AF thin films in dependence of the solution pH in KCl solution (1 mM). Figure was reproduced from ref. [206]

An IEP of about 4 has been reported for many hydrophobic surfaces [206]. As represented in Figure I.25, the zeta potential, ζ is negative above the IEP and decreases with increasing pH, while positive zeta potentials are observed at pH<IEP. Polymer surfaces of different hydrophobicities have different ζ, the magnitude of ζ is similar for polystyrene and Teflon® AF films within the probed pH range (contact angle of Teflon and PS is 121° and 93°), while ζ values of non-oxidized cellulose films (contact angle is 35°) were considerably lower. This measurements show that water ions preferentially adsorb at the highly hydrophobic polymer surfaces: detailed analysis of the pH dependence led to attribute the surface charges to hydroxide (OH^-) and hydronium (H^+) ions [205,206]. Moreover, since hydroniums dominate only at low pH, it was concluded that they have a lower hydrophobic surface affinity than hydroxides [205]. The presence of water ions at hydrophobic interfaces is further supported by spectroscopic studies in highly concentrated solutions, which show that the O−H stretching modes in the vicinity of the liquid−vapor interface are affected by both OH^- and H^+ ions, albeit more substantially by the latter.

The origin of charge at water hydrophobe interfaces is debated. The mechanisms and driving forces that charge interfaces in the absence of dissociative processes are not well understood. Disagreement comes from the fact that majority of experiments suggest a preferential adsorption of hydroxide ions [199,205,206,204,203,207,208,209,210,211,212]. An opposite picture has emerged from experiments analyzing molecular structures and MD simulations [213,214,215,216,217,218]; which concluded that the concentration of hydronium ions, but not hydroxide ions, is enhanced at the gas/water interface. Moreover, MD simulations have even suggested a weak depletion of hydroxide ions in the topmost water layer in 1.2 M NaOH solution [218]. These divergent results are currently a subject of discussion in the scientific community and require further clarification. According to ref. [101] two reasons are at the origin of contradictory results. One possibility is related to fundamental differences in experimental design and data interpretation. Electrokinetic and surface force measurements provide integral information, and continuum models have been used to derive the molecular structure of the interface. In contrast, surface-sensitive spectroscopic techniques and MD simulations explore interfacial structures and properties at the molecular level. Another reason of the incompatible results can be the different concentration levels used for the experiments. In MD simulations, ion concentrations of 0.1 M or higher are typically used, which restricts the studies to either very high or very low pH values. In contrast, the majority of the experiments are performed at intermediate pH values (pH = 2–11) in solutions of ionic strength lower than 0.1 M.

In the literature we find different explanations for the surface charge at polymer-water interfaces. But before discussing the origins of charges at water-hydrophobic polymer interfaces, I will present a brief summary of the physical processes at the origin of surface charge in general.

D.1. Origins of surface charge

Interfaces can be charged by a variety of different processes. At solid surfaces, charges are often caused by ionization of functional groups, (e.g. carboxylic acid or amino groups), preferential adsorption of ions or desorption or substitution of lattice ions.

D.1.1. Ionization of surface groups

Many surfaces behave as weak acids or basis in aqueous solutions, owing to reactivities of surface groups, e.g., amines, carboxylic acids, or oxides. Glass is a particularly well-studied example of such a system. In glass substrates, surface silanol groups can be deprotonated in aqueous environment leaving a negative surface charge:

$$SiOH \overset{K_a}{\Leftrightarrow} SiO^- + H^+$$

The pK_a for this reaction is approximately 4.7 [219]. In cases like this where protonation/deprotonation of surface groups is the origin of charge, the charge-determining ions are H^+ and OH^-, and the electrokinetic properties of the system are a strong function of pH [220].

D.1.2. Differences in affinity for ions between the solid and liquid phases

Differences in affinity between the liquid phase and the solid phase for particular ions lead to charge separation by (i) preferential adsorption of ions from an electrolyte solution onto the surface and/or (ii) preferential solution of ions from the crystal lattice of an ionic salt [221]. Many Nernstian surfaces exhibit mechanism (ii), leading to a surface potential that is well defined as a function of the salt concentration. Silver halides, such as AgI, are examples of Nernstian surfaces. Their surface potential, ζ, as a function of the silver ion concentration, $[Ag^+]$, is defined by [220]

$$\zeta = \frac{k_B T}{ze} ln \frac{[Ag^+]}{[Ag^+]_{pzc}} \tag{1.42}$$

where k_B is the Boltzmann constant, T is the temperature, z is the valence of the ion ($z = 1$ for AgI), e is the elementary charge, and *pzc* refers to the point of zero charge. Equation (1.42) assumes that as the bulk activity of Ag^+ ions is altered, the activity of surface Ag^+ ions remains constant. Nernstian surfaces can be useful in studying electrokinetics, since their surface electrical potential boundary conditions are well-defined.

D.1.3. The electrical double layer

The net charge density at fluid-solid interfaces causes an electrical potential and ion distribution structure within the fluid, known as the electrical double layer (EDL). The surface charge generates an electric field, which pulls oppositely charged ions (counterions) toward the surface, and pushes like charges (co-ions) away from it. Counterions preferentially concentrate near the surface, effectively shielding the bulk solution from the surface charge. The shielding layer is often referred to as the Debye layer. A schematic diagram of the EDL is shown in Fig. 1.

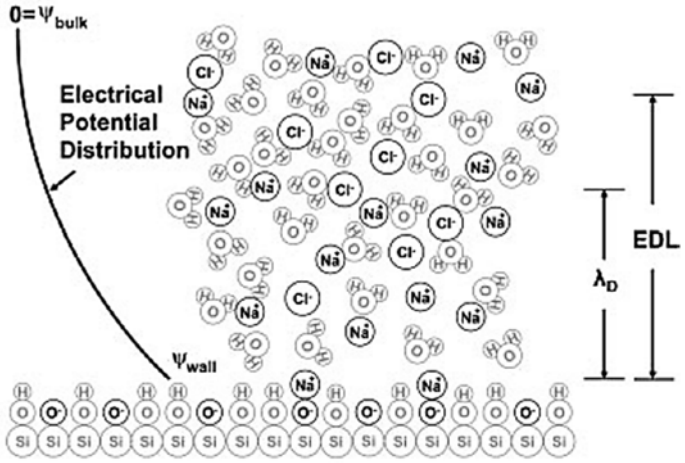

Figure I.26: Scheme of the electrical double layer.

More detailed descriptions of the internal structure of the EDL and electrokinetic phenomena will be described in Chapter II.

D.2. The origin of charge at water hydrophobe interface

As was already mentioned, the origin of surface charge in common hydrophobic surfaces is not well-understood, still debated and difficult to measure. Most hydrophobic materials are considered chemically inert, and are not expected to have reactive charge-forming surface groups or a strong affinity for ions. Nevertheless, different hydrophobic materials, including PDMS, PS, PE, Zeonor, and PTFE have been shown to have significant surface charge [220]. The hypothesis regarding the source(s) of charge include: (i) surface impurities present owing to the manufacturing process, which undergo charge-forming chemical reactions when in contact with water; (ii) anions are specifically adsorbed, owing to differences in affinity or hydration energy; and (iii) water ions are specifically adsorbed, owing to water orientation at a hydrophobic interface.

D.2.1. Impurities

Some researchers attribute the origin of electrical charge at polymer water interfaces to residual plasticizers, cross-linkers, and initiators from the manufacturing/polymerization process which are capable of getting charged by chemical reactions such as acid-base dissociation [222,223,224]. The prevalence of trade secrets in the polymer industry often leads to uncertainty as to the makeup and concentration of these impurities. It is possible that impurities may affect the electrokinetic performance of some hydrophobic materials used in microsystems, but they cannot explain the majority of the observed data. More than this, many hydrophobic materials show consistent electrokinetic properties independent of the manufacturing process [225]. In fact, there is little, if any, support for the postulate that impurities are a primary source of charge in any polymeric microfluidic system. However few experiments have been conducted to detect the role of impurities.

D.2.2. Specific adsorption of (salt) ions

Is known that specific adsorption of ions may affect many surfaces; for example, divalent cations, if present at high concentrations, have been shown to change the sign of the electrokinetic potential on glass surfaces at high pH. While adsorption is critical for large surfactant molecules and large ions, for small salt ions things are more complicated. For an ion to be able to adsorb to a surface, water molecules must be removed, so less-hydrated ions tend to preferentially adsorb as compared to more hydrated ions. A number of spectroscopic and molecular dynamics (MD) studies have provided direct evidence for the adsorption of electrolyte ions at liquid-gas interfaces [226,227,228,229], which serve as model hydrophobic interfaces. Sum frequency generation (SFG) measurements of air-water systems indicate enhanced anion concentration at the interface at high (0.1 M) salt concentrations [226]. Recent XPS experiments performed at water-vapor interfaces with very high salt concentrations demonstrated similar behavior [229]. Second harmonic generation (SHG) data for these interfaces across a range of salt concentrations (1 mM - 1 M) showed that ion adsorption follows Langmuir adsorption kinetics [227]. On the contrary electrokinetic experiments involving hydrophobic surfaces and lower salt concentrations (0.1 - 1 mM) does not conclusively support ionic adsorption [230,231,232]. Measurements of electrophoretic mobility as a function of the counterion concentration have been described by Gouy-Chapman-type double layer shielding effects and are in general independent of the particular buffer ions used for a variety of hydrophobic substrates [230,231]. The electrophoretic mobility of oil droplets was also found to be buffer-independent, and to behave consistently with double layer shielding [232]. The divergence between the spectroscopic measurements and the electrokinetic measurements may come from the fact that spectroscopic measurements has been performed at high salt concentrations while electrokinetic tests are usually conducted at low concentrations of salt. However, the data in [227], which covers a concentration range between those studied in microfluidics and other spectroscopic measurements (1mM–1M), shows that the degree of interfacial salt adsorption decreases rapidly as the salt concentration decreases. This suggests that at low concentrations anion adsorption is less important, and may be very difficult to observe in the presence of other chemical processes (e.g., surface reactions or hydroxyl or hydronium adsorption).

D.2.3. Specific adsorption of water ions

The specific adsorption of hydroxyl ions onto hydrophobic interfaces has also been proposed as the origin of surface charge in hydrophobic polymer materials [204,205,206]. Even though hydroxyl ions tend to be more hydrated as compared to hydronium or salt ions [233], they are believed to preferentially adsorb onto aqueous-hydrophobic interfaces resulting in a net negative surface charge density [199]. This interfacial charging mechanism is consistent with experimental data for most hydrophobic surfaces, which have pH-dependent electrokinetic potentials that become increasingly negative with increasing pH [231]. However, as was mentioned before, these results differ from MD

simulations; moreover; simple models based solely on hydroxyl ion adsorption fail to explain positive charges on hydrophobic polymer surfaces [230] at low pH conditions.

Other authors [234,235] attribute the phenomenon of water-ions adsorption to specific properties of the ions and not to the characteristics of the interface. Kudin and Car [235] concluded that both water ions behave like amphiphilic surfactants that adsorb to a hydrophobic hydrocarbon surface with their hydrophobic side. It was suggested that this behavior originates from the asymmetry of the molecular charge distribution, resulting in a strongly hydrophobic and a hydrophilic surface side of the ions [235].

References

[1] Rob Perree. Bakelite. Cadre, 1997.

[2] Mülhaupt, R. Hermann Staudinger and the origin of macromolecular chemistry. *Angew. Chem. Int. Ed. Engl* **43**, 1054-1063 (2004).

[3] Rubinstein, M. & Colby, R.H. *Polymer Physics*. (Oxford University Press, USA: 2003).

[4] Yamakawa, H. Stiff-Chain Macromolecules. *Annu. Rev. Phys. Chem.* **35**, 23-47 (1984).

[5] Bower, D.I. *An introduction to polymer physics*. (Cambridge University Press: 2002).

[6] Sperling, L.H. *Introduction to physical polymer science*. (John Wiley and Sons: 2006).

[7] Ferry, J.D. *Viscoelastic properties of polymers. Second Edition*. (John Wiley & Sons Inc: 1970).

[8] H. Vogel, J. *Phys. Z*. **22**, 645 (1921); G. S. Fulcher, *J. Amer. Ceram. Soc*. **8**, 339 (1925); G. Tammann and W. Hesse, Z. *Anorg. Allg. Chem*. **156**, 245 (1926).

[9] Williams, M.L., Landel, R.F. & Ferry, J.D. The Temperature Dependence of Relaxation Mechanisms in Amorphous Polymers and Other Glass-forming Liquids. *Journal of the American Chemical Society* **77**, 3701-3707 (1955).

[10] Ferry, J.D. *Viscoelastic properties of polymers*. (John Wiley and Sons: 1980).

[11] Doolittle, A.K. & Doolittle, D.B. Studies in Newtonian Flow. V. Further Verification of the Free-Space Viscosity Equation. *J. Appl. Phys.* **28**, 901 (1957).

[12] G.B. McKenna, On the physics required for prediction of long term performance of polymers and their composites. *J. Res. Natl. Inst. Stand. Tech.* **99** 2, 169–189 (1994).

[13] Ediger, M.D., Angell, C.A. & Nagel, S.R. Supercooled Liquids and Glasses. *The Journal of Physical Chemistry* **100**, 13200-13212 (1996).

[14] Williams, G. & Watts, D.C. Non-symmetrical dielectric relaxation behaviour arising from a simple empirical decay function. *Trans. Faraday Soc.* **66**, 80 (1970).

[15] Chow, T.S. Molecular kinetic theory of the glass transition. *Polymer Engineering & Science* **24**, 1079-1086 (1984).

[16] Shukla, P. Model of the glass transition and the glassy state. *Z. Physik B - Condensed Matter* **52**, 179-184 (1983).

[17] Adam, G. & Gibbs, J.H. On the Temperature Dependence of Cooperative Relaxation Properties in Glass-Forming Liquids. *J. Chem. Phys.* **43**, 139 (1965).

[18] DiMarzio, E.A. & Gibbs, J.H. Chain Stiffness and the Lattice Theory of Polymer Phases. *The Journal of Chemical Physics* **28**, 807 (1958).

[19] M. D. Ediger, Spatially Heterogeneous Dynamics in Supercooled Dynamics, *Annu. Rev. Phys. Chem*. **51**, 99-128 (2000).

[20] Hoffman, J.D. Anelastic and dielectric effects in polymeric solids. By N. G. McCrum, B. E. Read, and G. Williams, Wiley, 1967, 617, , Lib. Congress Card 67:29334. *Journal of Polymer Science Part A-2: Polymer Physics* **7**, 750-750 (1969).

[21] Jackle, J. Models of the glass transition. *Rep. Prog. Phys.* **49**, 171-231 (1986).

[22] Bouda, V. Structure and ductility of glassy polymers. *Polymer Bulletin* **7**, (1982).

[23] Kluin, J.E. et al. Ortho-positronium lifetime studies of free volume in polycarbonates of different structures: influence of hole size distributions. *Macromolecules* **26**, 1853-1861 (1993).

[24] Song, H.H. & Roe, R.J. Structural change accompanying volume change in amorphous polystyrene as studied by small and intermediate angle x-ray scattering. *Macromolecules* **20**, 2723-2732 (1987).

[25] Forsyth, M., Meakin, P., MacFarlane, D.R. & Hill, A.J. Free volume and conductivity of plasticized polyether-urethane solid polymer electrolytes. *J. Phys.: Condens. Matter* **7**, 7601-7617 (1995).

[26] McCrum, N.G. *Anelastic and Dielectric Effects in Polymeric Solids*. (Dover Publications: 1991).

[27] Heijboer, J. Secondary Loss Peaks in Glassy Amorphous Polymers. Int. J. of Polymeric Mat. 6, 11-37 (1977).

[28] Katz, D. & Salee, G. Crosslinked oligoethylene glycols: Correlation between their structure and some rheological properties. Journal of Polymer Science Part A-2: Polymer Physics 6, 801-811 (1968).

[29] Katz, D. & Zewi, I.G. Correlation between molecular structure and some bulk properties of highly crosslinked polysiloxanes. Journal of Polymer Science: Polymer Symposia 46, 139-148 (1974)

[30] Beaucage, G., Composto, R. & Stein, R.S. Ellipsometric study of the glass transition and thermal expansion coefficients of thin polymer films. Journal of Polymer Science Part B: Polymer Physics **31**, 319-326 (1993).

[31] Keddie, J.L., Jones, R.A.L. & Cory, R.A. Size-Dependent Depression of the Glass Transition Temperature in Polymer Films. *Europhys. Lett.* **27**, 59-64 (1994).

[32] Xie, L. et al. Positronium Formation as a Probe of Polymer Surfaces and Thin Films. *Phys. Rev. Lett.* **74**, 4947 (1995).

[33] Kajiyama, T., Tanaka, K. & Takahara, A. Depth Dependence of the Surface Glass Transition Temperature of a Poly(styrene-block-methyl methacrylate) Diblock Copolymer Film on the Basis of Temperature-Dependent X-ray Photoelectron Spectroscopy. *Macromolecules* **28**, 3482-3484 (1995).

[34] Ellison, C.J. & Torkelson, J.M. The distribution of glass-transition temperatures in nanoscopically confined glass formers. *Nat Mater* **2**, 695-700 (2003).
[35] Hammerschmidt, J.A., Gladfelter, W.L. & Haugstad, G. Probing Polymer Viscoelastic Relaxations with Temperature-Controlled Friction Force Microscopy. *Macromolecules* **32**, 3360-3367 (1999).
[36] Ge, S. et al. Shear Modulation Force Microscopy Study of Near Surface Glass Transition Temperatures. *Phys. Rev. Lett.* **85**, 2340 (2000).
[37] Tsui, O.K.C., Wang, X.P., Ho, J.Y.L., Ng, T.K. & Xiao, X. Studying Surface Glass-to-Rubber Transition Using Atomic Force Microscopic Adhesion Measurements. *Macromolecules* **33**, 4198-4204 (2000).
[38] Wang, X.P., Xiao, X. & Tsui, O.K.C. Surface Viscoelasticity Studies of Ultrathin Polymer Films Using Atomic Force Microscopic Adhesion Measurements. *Macromolecules* **34**, 4180-4185 (2001).
[39] Liu, Y. et al. Surface Relaxations in Polymers. *Macromolecules* **30**, 7768-7771 (1997).
[40] Wallace, W.E., Fischer, D.A., Efimenko, K., Wu, W.-L. & Genzer, J. Polymer Chain Relaxation: Surface Outpaces Bulk. *Macromolecules* **34**, 5081-5082 (2001).
[41] Fukao, K. & Miyamoto, Y. Glass transitions and dynamics in thin polymer films: Dielectric relaxation of thin films of polystyrene. *Phys. Rev. E* **61**, 1743-1754 (2000).
[42] Dutcher, J.R. & Marangoni, A.G. *Soft materials: structure and dynamics*. (Marcel Dekker: 2005).
[43] Forrest, J.A., Dalnoki-Veress, K. & Dutcher, J.R. Interface and chain confinement effects on the glass transition temperature of thin polymer films. *Phys. Rev. E* **56**, 5705 (1997).
[44] Tsui, O.K.C. & Zhang, H.F. Effects of Chain Ends and Chain Entanglement on the Glass Transition Temperature of Polymer Thin Films. *Macromolecules* **34**, 9139-9142 (2001).
[45] Kawana, S. & Jones, R.A.L. Character of the glass transition in thin supported polymer films. *Phys. Rev. E* **63**, 021501 (2001).
[46] Fukao, K. & Miyamoto, Y. Glass transition temperature and dynamics of α-process in thin polymer films. *Europhys. Lett.* **46**, 649-654 (1999).
[47] Fukao, K. & Miyamoto, Y. Glass transitions and dynamics in thin polymer films: Dielectric relaxation of thin films of polystyrene. *Phys. Rev. E* **61**, 1743 (2000).
[48] Tsui, O.K.C., Russell, T.P. & Hawker, C.J. Effect of Interfacial Interactions on the Glass Transition of Polymer Thin Films. *Macromolecules* **34**, 5535-5539 (2001).
[49] DeMaggio, G.B. et al. Interface and Surface Effects on the Glass Transition in Thin Polystyrene Films. *Phys. Rev. Lett.* **78**, 1524 (1997).
[50] Fryer, D.S., Nealey, P.F. & de Pablo, J.J. Thermal Probe Measurements of the Glass Transition Temperature for Ultrathin Polymer Films as a Function of Thickness. *Macromolecules* **33**, 6439-6447 (2000).
[51] Ellison, C.J. & Torkelson, J.M. Sensing the glass transition in thin and ultrathin polymer films via fluorescence probes and labels. *Journal of Polymer Science Part B: Polymer Physics* **40**, 2745-2758 (2002).
[52] Ellison, C.J. & Torkelson, J.M. The distribution of glass-transition temperatures in nanoscopically confined glass formers. *Nat Mater* **2**, 695-700 (2003).
[53] Keddie, J.L., Jones, R.A.L. & Cory, R.A. Interface and surface effects on the glass-transition temperature in thin polymer films. *Faraday Disc.* **98**, 219 (1994).
[54] van Zanten, J.H., Wallace, W.E. & Wu, W.-li Effect of strongly favorable substrate interactions on the thermal properties of ultrathin polymer films. *Phys. Rev. E* **53**, R2053 (1996).
[55] de Gennes, P.G. Glass transitions in thin polymer films. *Eur. Phys. J. E* **2**, 201-205 (2000).
[56] Hall, D.B., Miller, R.D. & Torkelson, J.M. Molecular probe techniques for studying diffusion and relaxation in thin and ultrathin polymer films. *Journal of Polymer Science Part B: Polymer Physics* **35**, 2795-2802 (1997).
[57] Fukao, K., Uno, S., Miyamoto, Y., Hoshino, A. & Miyaji, H. Dynamics of alpha- and beta- processes in thin polymer films: poly(vinyl acetate) and poly(methyl methacrylate). *Phys. Rev. E*. **64**. (2001).
[58] Forrest, J.A., Dalnoki-Veress, K., Stevens, J.R. & Dutcher, J.R. Effect of Free Surfaces on the Glass Transition Temperature of Thin Polymer Films. *Phys. Rev. Lett.* **77**, 2002 (1996).
[59] Dalnoki-Veress, K., Nickel, B.G., Roth, C. & Dutcher, J.R. Hole formation and growth in freely standing polystyrene films. *Phys. Rev. E* **59**, 2153 (1999).
[60] Mattsson, J., Forrest, J.A. & Börjesson, L. Quantifying glass transition behavior in ultrathin free-standing polymer films. *Phys. Rev. E* **62**, 5187 (2000).
[61] Dalnoki-Veress, K., Forrest, J.A., Murray, C., Gigault, C. & Dutcher, J.R. Molecular weight dependence of reductions in the glass transition temperature of thin, freely standing polymer films. *Phys. Rev. E* **63**, 031801 (2001).
[62] Forrest, J.A. & Dalnoki-Veress, K. The glass transition in thin polymer films. *Advances in Colloid and Interface Science* **94**, 167-195 (2001).
[63] Gennes, P.G. de Glass transitions in thin polymer films. *The European Physical Journal E* **2**, 5 (2000).
[64] Pham, J.Q. & Green, P.F. The glass transition of thin film polymer/polymer blends: Interfacial interactions and confinement. *J. Chem. Phys.* **116**, 5801 (2002).

[65] Grohens, Y., Brogly, M., Labbe, C., David, M.-O. & Schultz, J. Glass Transition of Stereoregular Poly(methyl methacrylate) at Interfaces. *Langmuir* **14**, 2929-2932 (1998).
[66] Fryer, D.S. et al. Dependence of the Glass Transition Temperature of Polymer Films on Interfacial Energy and Thickness. *Macromolecules* **34**, 5627-5634 (2001).
[67] Bernazzani, P. & Sanchez, R.F. Effect of substrate interactions on the melting behavior of thin polyethylene films. *The European Physical Journal E - Soft Matter* **26**, 8 (2008).
[68] Fryer, D.S., Nealey, P.F. & de Pablo, J.J. Thermal Probe Measurements of the Glass Transition Temperature for Ultrathin Polymer Films as a Function of Thickness. *Macromolecules* **33**, 6439-6447 (2000).
[69] van Zanten, J.H., Wallace, W.E. & Wu, W.-li Effect of strongly favorable substrate interactions on the thermal properties of ultrathin polymer films. *Phys. Rev. E* **53**, R2053 (1996).
[70] Torres, J.A., Nealey, P.F. & de Pablo, J.J. Molecular Simulation of Ultrathin Polymeric Films near the Glass Transition. *Phys. Rev. Lett.* **85**, 3221 (2000).
[71] Priestley, R.D., Broadbelt, L.J. & Torkelson, J.M. Physical Aging of Ultrathin Polymer Films above and below the Bulk Glass Transition Temperature: Effects of Attractive vs Neutral Polymer−Substrate Interactions Measured by Fluorescence. *Macromolecules* **38**, 654-657 (2005).
[72] Forrest & Mattsson Reductions of the glass transition temperature in thin polymer films: probing the length scale of cooperative dynamics. *Phys Rev E Stat Phys Plasmas Fluids Relat Interdiscip Topics* **61**, R53-56 (2000).
[73] Long, D. & Lequeux, F. Heterogeneous dynamics at the glass transition in van der Waals liquids, in the bulk and in thin films. *The European Physical Journal E* **4**, 17 (2001).
[74] Efremov, M.Y., Olson, E.A., Zhang, M., Zhang, Z. & Allen, L.H. Glass Transition in Ultrathin Polymer Films: Calorimetric Study. *Phys. Rev. Lett.* **91**, 085703 (2003).
[75] Efremov, M.Y., Olson, E.A., Zhang, M., Zhang, Z. & Allen, L.H. Probing Glass Transition of Ultrathin Polymer Films at a Time Scale of Seconds Using Fast Differential Scanning Calorimetry. *Macromolecules* **37**, 4607-4616 (2004).
[76] Huth, H., Minakov, A.A. & Schick, C. Differential AC-chip calorimeter for glass transition measurements in ultrathin films. *Journal of Polymer Science Part B: Polymer Physics* **44**, 2996-3005 (2006).
[77] Kim, H. et al. X-ray photon correlation spectroscopy on polymer films with molecular weight dependence. *Physica B: Condensed Matter* **336**, 211-215 (2003).
[78] Kim, H. et al. Hydrodynamic surface fluctuations of polymer films by coherent X-ray scattering. *Thin Solid Films* **515**, 5536-5540 (2007).
[79] Erichsen, J., Dolgner, K., Zaporojtchenko, V. & Faupel, F. Glass Transition Temperature in Thin Polymer Films Determined by Thermal Discharge in X-ray Photoelectron Spectroscopy. *Macromolecules* **37**, 8813-8815 (2004).
[80] Forrest, J.A. et al. Relaxation dynamics in ultrathin polymer films. *Phys. Rev. E* **58**, R1226 (1998).
[81] Fukao, K. & Miyamoto, Y. Slow dynamics near glass transitions in thin polymer films. *Phys. Rev. E* **64**, 011803 (2001).
[82] Fukao, K. & Miyamoto, Y. Dielectric and dilatometric studies of glass transitionsin thin polymer films. *Le Journal de Physique IV* **10**, 4 (2000).
[83] Priestley, R.D., Broadbelt, L.J., Torkelson, J.M. & Fukao, K. Glass transition and alpha -relaxation dynamics of thin films of labeled polystyrene. *Phys. Rev. E* **75**, 061806 (2007).
[84] Priestley, R.D., Broadbelt, L.J., Torkelson, J.M. & Fukao, K. Glass transition and alpha -relaxation dynamics of thin films of labeled polystyrene. *Phys. Rev. E* **75**, 061806 (2007).
[85] Sharp, J.S. & Forrest, J.A. Free surfaces cause reductions in the glass transition temperature of thin polystyrene films. *Phys. Rev. Lett* **91**, 235701 (2003).
[86] Keddie, J.L., Jones, R.A.L. & Cory, R.A. Size-Dependent Depression of the Glass Transition Temperature in Polymer Films. *Europhys. Lett.* **27**, 59-64 (1994).
[87] Sharp, J.S. & Forrest, J.A. Free Surfaces Cause Reductions in the Glass Transition Temperature of Thin Polystyrene Films. *Phys. Rev. Lett.* **91**, 235701 (2003).
[88] Keddie, J.L., Jones, R.A.L. & Cory, R.A. Size-Dependent Depression of the Glass Transition Temperature in Polymer Films. *Europhys. Lett.* **27**, 59-64 (1994).
[89] Sharp, J.S. & Forrest, J.A. Free Surfaces Cause Reductions in the Glass Transition Temperature of Thin Polystyrene Films. *Phys. Rev. Lett.* **91**, 235701 (2003).
[90] Ellison, C.J. & Torkelson, J.M. The distribution of glass-transition temperatures in nanoscopically confined glass formers. *Nat Mater* **2**, 695-700 (2003).
[91] Hammerschmidt, J.A., Gladfelter, W.L. & Haugstad, G. Probing Polymer Viscoelastic Relaxations with Temperature-Controlled Friction Force Microscopy. *Macromolecules* **32**, 3360-3367 (1999).
[92] Ge, S. et al. Shear Modulation Force Microscopy Study of Near Surface Glass Transition Temperatures. *Phys. Rev. Lett.* **85**, 2340-2343 (2000).
[93] Schwab, A.D. & Dhinojwala, A. Relaxation of a rubbed polystyrene surface. *Phys. Rev. E* **67**, 021802 (2003).

[94] Kerle, T., Lin, Z., Kim, H.-C. & Russell, T.P. Mobility of Polymers at the Air/Polymer Interface. *Macromolecules* **34**, 3484-3492 (2001).
[95] Gasemjit, P. & Johannsmann, D. Thickness of the soft layer on glassy polystyrene surfaces. *Journal of Polymer Science Part B: Polymer Physics* **44**, 3031-3036 (2006).
[96] Meyers, G.F., DeKoven, B.M. & Seitz, J.T. Is the molecular surface of polystyrene really glassy? *Langmuir* **8**, 2330-2335 (1992).
[97] Kajiyama, T., Tanaka, K. & Takahara, A. Surface Molecular Motion of the Monodisperse Polystyrene Films. *Macromolecules* **30**, 280-285 (1997).
[98] Tanaka, K., Takahara, A. & Kajiyama, T. Rheological Analysis of Surface Relaxation Process of Monodisperse Polystyrene Films. *Macromolecules* **33**, 7588-7593 (2000).
[99] Du, B., Tsui, O.K.C., Zhang, Q. & He, T. Study of Elastic Modulus and Yield Strength of Polymer Thin Films Using Atomic Force Microscopy. *Langmuir* **17**, 3286-3291 (2001).
[100] Du, B., Tsui, O.K.C., Zhang, Q. & He, T. Study of Elastic Modulus and Yield Strength of Polymer Thin Films Using Atomic Force Microscopy. *Langmuir* **17**, 3286-3291 (2001).
[101] Weber, R. et al. X-ray reflectivity study on the surface and bulk glass transition of polystyrene. *Phys. Rev. E* **64**, 061508 (2001).
[102] Rudoy, V.M. et al. Metal Nanoparticles on Polymer Surfaces: 1. A New Method of Determining Glass Transition Temperature of the Surface Layer. *Colloid Journal* **64**, 746-754 (2002).
[103] Hutcheson, S.A. & McKenna, G.B. Nanosphere Embedding into Polymer Surfaces: A Viscoelastic Contact Mechanics Analysis. *Phys. Rev. Lett.* **94**, 076103 (2005).
[104] Kerle, T., Lin, Z., Kim, H. & Russell, T. Mobility of Polymers at the Air/Polymer Interface. *Macromolecules* **34**, 3484-3492 (2001).
[105] Papaléo, R., de Oliveira, L., Farenzena, L., de Araújo, M. & Livi, R. Probing thermomechanical behavior of polymers at the nanometer scale with single-ion bombardment and scanning force microscopy. *Phys. Rev. B* **62**, 11273-11276 (2000).
[106] Papaléo, R., de Oliveira, L., Farenzena, L., de Araújo, M. & Livi, R. Probing thermomechanical behavior of polymers at the nanometer scale with single-ion bombardment and scanning force microscopy. *Phys. Rev. B* **62**, 11273-11276 (2000).
[107] Farenzena, L.S., Livi, R.P., de Araújo, M.A., Garcia Bermudez, G. & Papaléo, R.M. Cratering and plastic deformation in polystyrene induced by MeV heavy ions: Dependence on the molecular weight. *Phys. Rev. B* **63**, 104108 (2001).
[108] Fakhraai, Z. & Forrest, J.A. Measuring the Surface Dynamics of Glassy Polymers. *Science* **319**, 600 -604 (2008).
[109] Guyon, É. *Physical hydrodynamics*. (Oxford University Press: 2001).
[110] Israelachvili, J. N. Intermolecular and surface forces. Academic Press, London, (1991)
[111] Kalliadasis, S., Thiele, U. & Sciences, I.C. for M. *Thin films of soft matter*. (Springer: 2007).
[112] Jacobs, K., Herminghaus, S. & Mecke, K.R. Thin Liquid Polymer Films Rupture via Defects. *Langmuir* **14**, 965-969 (1998).
[113] Reiter, G. Dewetting of thin polymer films. *Physical Review Letters* **68**, 75-78 (1992).
[114] Sharma, A. & Khanna, R. Pattern Formation in Unstable Thin Liquid Films. *Phys. Rev. Lett.* **81**, 3463 (1998).
[115] Reiter, G. The Artistic Side of Intermolecular Forces. *Science* **282**, 888 -889 (1998).
[116] Landau, L.D. (Lev D., Lifshitz, E.M. (Evgenii M. & Landau, L.D. (Lev D. *Fluid mechanics / by L.D. Landau and E.M. Lifshitz ; translated from the Russian by J.B. Sykes and W.H. Reid*. (Pergamon Press ; Addison-Wesley: London : Reading, Mass. :, London : Pergamon Press ; Reading, Mass. : Addison-Wesley, c1959.).
[117] Steiner, U. Structure Formation in Polymer Films From Micrometer to the sub-100 nm Length Scales. *Nanoscale Assembly* 1-24 (2005)
[118] Vrij, A. Possible mechanism for the spontaneous rupture of thin, free liquid films. *Discuss. Faraday Soc.* **42**, 23 (1966).
[119] Reiter, G. Dewetting of thin polymer films. *Phys. Rev. Lett.* **68**, 75 (1992).
[120] Seemann, R., Herminghaus, S. & Jacobs, K. Structure Formation in Thin Liquid Films: Interface Forces Unleashed. *Thin Films of Soft Matter* **490**, 1-24 (2007).
[121] Rayleigh, Lord J. W. S., "On the instability of jets," Proc. London Math.Soc., 10, 4 (1879).
[122] A. Basset, ''Waves and jets in a viscous liquid,'' Am. J. Math.16, 93 (1894).
[123] Swan, J. W. Stress and other effects produced in resin and in a viscid compound of resin and oil by electrification. Proc. R. Soc. (London) 62, 38–46 (1897). 31
[124] Tonks, L.A theory of liquid surface rupture by a uniform electric field.Phys. Rev. 48, 562–568 (1935).
[125] Lin, Z. et al. Electric field induced instabilities at liquid/liquid interfaces. *J. Chem. Phys.* **114**, 2377 (2001).
[126] Schaffer, E., Thurn-Albrecht, T., Russell, T.P. & Steiner, U. Electrically induced structure formation and pattern transfer. *Nature* **403**, 874-877 (2000).

[127]Chou, S. Y., Zhuang, L., 1999, Lithographically induced self-assembly of periodic polymer micropillar arrays. Journal of Vacuum Science and Technology B 17 (6), 3197–3202
[128]Chou, S. Y., Zhuang, L., Guo, L., 1999, Lithographically induced self-construction of polymer microstructures for resistless patterning. Applied Physics Letters 75 (7), 1004–1006.
[129]Schaffer, E., Thurn-Albrecht, T., Russell, T. P., Steiner, U., Feb. 2000. Electrically induced structure formation and pattern transfer. Nature 403 (6772), 874–877.
[130]Schaffer, E., Thurn-Albrecht, T., Russell, T. P., Steiner, U., 2001. Electrohydrodynamic instabilities in polymer films.EurophysicsLetters 53 (4), 518–524.
[131] Lin, Z., Kerle, T., Baker, S. M., Hoagland, D. A., Schaffer, E., Steiner, U., Russell, T. P.,2001. Electric field induced instabilities at liquid/liquid interfaces. Journal of ChemicalPhysics 114 (5), 2377–2381
[132] Lin, Z., Kerle, T., Russell, T., Schaffer, E., Steiner, U., 2002.Structure formation at the interface of liquid/liquid bilayer in electric field.Macromolecules 35 (10), 3971–3976.
[133] J. Bae, E. Glogowski, S. Gupta, T. Emrick and T.P. Russell, "Effect of nanoparticle on the electrohydrodynamic instability of polymer/nanoparticle thin film," *Macromolecules***41**(7), 2722-2726 (2008).
[134] Lei, X., Wu, L., Deshpande, P., Yu, Z., Wu, W., Ge, H., Chou, S. Y., 2003. 100 nm periodgratings produced by lithographically induced self-construction. Nanotechnology 14 (7),786–790.
[135]Chou, S., JUL 2001. Nanoimprint lithography and lithographically induced self-assembly. MRS Bulletin 26 (7), 512–517.
[136] Morariu, M. D., Voicu, N. E., Schaffer, E., Lin, Z., Russell, T. P., Steiner, U., Jan. 2003. Hierarchical structure formation and pattern replication induced by an electric field.Nature Materials 2 (1), 48–52.
[137] Bandyopadhyay, D., Sharma, A., Jul. 2007. Electric field induced instabilities in thin confined bilayers. Journal of Colloid and Interface Science 311 (2), 595–608.
[138]Bandyopadhyay, D., Sharma, A., Thiele, U., Reddy, P. D. S., Aug. 2009. Electric-fieldinduced interfacial instabilities and morphologies of thin viscous and elastic bilayers.Langmuir 25 (16).
[139] Wu, N., Russel, W. B., 2009.Micro- and nano-patterns created via electrohydrodynamic instabilities. Nano Today 4, 180–192.
[140] Taylor, G. I. and McEwan, A. D.The stability of a horizontal fluid interface in a vertical electric field. J. Fluid Mech. 22, 1–15 (1965).
[141] Taylor, G., 1966.Studies in electrohydrodynamics. I. the circulation produced in a drop by electrical field. Proceedings of the Royal Society of London.Series A 291 (1425), 159–166.
[142] Melcher, J. R. and Smith, C. V. Electrohydrodynamic charge relaxation and interfacial perpendicular-field instability.Phys. Fluids 8, 1193 (1969).
[143] Melcher JR, Taylor GI. (1969). Electrohydrodynamics: a review of the role of interfacial shear stresses Annu. Rev. Fluid Mech. 1:111–46
[144] Pease, L. F., Russel, W. B., Feb. 2002. Linear stability analysis of thin leaky dielectric films subjected to electric fields. Journal of Non-Newtonian Fluid Mechanics 102 (2), 233–250.
[145] Pease, L. F., Russel, W. B., 2003.Electrostatically induced submicron patterning of thin perfect and leaky dielectric films: A generalized linear stability analysis. Journal of Chemical Physics 118 (8).
[146] Shankar, V., Sharma, A., Jun. 2004. Instability of the interface between thin fluid filmssubjected to electric fields. Journal of Colloid and Interface Science 274 (1), 294–308.
[147] Verma, R., Sharma, A., Kargupta, K., Bhaumik, J., 2005. Electric field induced instabilityand pattern formation in thin liquid films. Langmuir 21 (8), 3710–3721.
[148] Wu, N., Russel, W. B., 2005. Dynamics of the formation of polymeric microstructuresinduced by electrohydrodynamic instability. Applied Physics Letters 86 (24), 241912.
[149] Wu, L., Chou, S. Y., Jan. 2005. Electrohydrodynamic instability of a thin film of viscoelastic polymer underneath a lithographically manufactured mask. Journal of Non-Newtonian Fluid Mechanics 125 (2-3), 91–99.
[150] Larson, R.G. Instabilities in viscoelastic flows. *Rheologica Acta* **31**, 213-263 (1992).
[151] Chen, K. P,. Interfacial instabilities in stratified shear flows involving multipleviscous and viscoelastic fluids. Applied Mechanics Reviews 48, 763–776 (1995).

[152] Balmforth, N.J., Craster, R.V., Rust, A.C. & Sassi, R. Viscoplastic flow over an inclined surface. *Journal of Non-Newtonian Fluid Mechanics* **142**, 219-243 (2007).
[153] Wu, L. & Chou, S.Y. Electrohydrodynamic instability of a thin film of viscoelastic polymer underneath a lithographically manufactured mask. *Journal of Non-Newtonian Fluid Mechanics* **125**, 91-99 (2005).
[154] Tomar, G., Shankar, V., Sharma, A. & Biswas, G. Electrohydrodynamic instability of a confined viscoelastic liquid film. *Journal of Non-Newtonian Fluid Mechanics* **143**, 120-130 (2007).
[155] J. Sarkar and A. Sharma, A unified theory of insabilities in viscoelastic thin films: from wetting to confined films, from viscous to elastic films, and from short to long waves, Langmuir 26, 8464–8473 (2010).
[156] Yang, F. & Song, W. Morphological instability of elastic thin films–effect of electromechanical interaction. *Applied Physics Letters* **87**, 111912 (2005).

[157] Sarkar, J. & Sharma, A. Electric-field induced instabilities and morphological phase transitions in soft elastic films. *Physical Review E* **77**, (2008).
[158] Arun, N. *et al.* Electric-Field-Induced Patterns in Soft Viscoelastic Films: From Long Waves of Viscous Liquids to Short Waves of Elastic Solids. *Physical Review Letters* **102**, (2009).
[159] Mahnke, J., Stearnes, J., Hayes, R.A., Fornasiero, D. & Ralston, J. The influence of dissolved gas on the interactions between surfaces of different hydrophobicity in aqueous media Part I. Measurement of interaction forces. *Phys. Chem. Chem. Phys.* **1**, 2793-2798 (1999).
[160] Ishida, N., Inoue, T., Miyahara, M. & Higashitani, K. Nano Bubbles on a Hydrophobic Surface in Water Observed by Tapping-Mode Atomic Force Microscopy. *Langmuir* **16**, 6377-6380 (2000).
[161] Tyrrell, J.W.G. & Attard, P. Images of Nanobubbles on Hydrophobic Surfaces and Their Interactions. *Phys. Rev. Lett.* **87**, 176104 (2001).
[162] Yang, J., Duan, J., Fornasiero, D. & Ralston, J. Very Small Bubble Formation at the Solid−Water Interface. *The Journal of Physical Chemistry B* **107**, 6139-6147 (2003).
[163] Attard, P. Bridging Bubbles between Hydrophobic Surfaces. *Langmuir* **12**, 1693-1695 (1996).
[164] Parker, J.L., Claesson, P.M. & Attard, P. Bubbles, cavities, and the long-ranged attraction between hydrophobic surfaces. *The Journal of Physical Chemistry* **98**, 8468-8480 (1994).
[165] Carambassis, A., Jonker, L.C., Attard, P. & Rutland, M.W. Forces Measured between Hydrophobic Surfaces due to a Submicroscopic Bridging Bubble. *Phys. Rev. Lett.* **80**, 5357 (1998).
[166] Snoswell, D.R.E., Duan, J., Fornasiero, D. & Ralston, J. Colloid Stability and the Influence of Dissolved Gas. *The Journal of Physical Chemistry B* **107**, 2986-2994 (2003).
[167] Switkes, M. & Ruberti, J.W. Rapid cryofixation/freeze fracture for the study of nanobubbles at solid–liquid interfaces. *Appl. Phys. Lett.* **84**, 4759 (2004).
[168] Ishida, N., Inoue, T., Miyahara, M. & Higashitani, K. Nano Bubbles on a Hydrophobic Surface in Water Observed by Tapping-Mode Atomic Force Microscopy. *Langmuir* **16**, 6377-6380 (2000).
[169] Lou, S.-T. et al. Nanobubbles on solid surface imaged by atomic force microscopy. *J. Vac. Sci. Technol. B* **18**, 2573 (2000).
[170] Tyrrell, J.W. & Attard, P. Images of nanobubbles on hydrophobic surfaces and their interactions. *Phys. Rev. Lett* **87**, 176104 (2001).
[171] Yang, J., Duan, J., Fornasiero, D. & Ralston, J. Very Small Bubble Formation at the Solid−Water Interface. *The Journal of Physical Chemistry B* **107**, 6139-6147 (2003).
[172] Zhang, X.H. et al. Degassing and Temperature Effects on the Formation of Nanobubbles at the Mica/Water Interface. *Langmuir* **20**, 3813-3815 (2004).
[173] Simonsen, A.C., Hansen, P.L. & Klösgen, B. Nanobubbles give evidence of incomplete wetting at a hydrophobic interface. *Journal of Colloid and Interface Science* **273**, 291-299 (2004).
[174] Schwendel, D. et al. Interaction of Water with Self-Assembled Monolayers: Neutron Reflectivity Measurements of the Water Density in the Interface Region. *Langmuir* **19**, 2284-2293 (2003).
[175] Zhang, X.H. et al. Detection of Novel Gaseous States at the Highly Oriented Pyrolytic Graphite−Water Interface. *Langmuir* **23**, 1778-1783 (2007).
[176] Steitz, R. et al. Nanobubbles and Their Precursor Layer at the Interface of Water Against a Hydrophobic Substrate. *Langmuir* **19**, 2409-2418 (2003).
[177] Jensen, T.R. et al. Water in Contact with Extended Hydrophobic Surfaces: Direct Evidence of Weak Dewetting. *Phys. Rev. Lett.* **90**, 086101 (2003).
[178] Doshi, D.A., Watkins, E.B., Israelachvili, J.N. & Majewski, J. Reduced water density at hydrophobic surfaces: Effect of dissolved gases. *Proceedings of the National Academy of Sciences of the United States of America* **102**, 9458 -9462 (2005).
[179] Mao, M., Zhang, J., Yoon, R.-H. & Ducker, W.A. Is There a Thin Film of Air at the Interface between Water and Smooth Hydrophobic Solids? *Langmuir* **20**, 1843-1849 (2004).
[180] Castro, L.B.R., Almeida, A.T. & Petri, D.F.S. The Effect of Water or Salt Solution on Thin Hydrophobic Films. *Langmuir* **20**, 7610-7615 (2004).
[181] Takata, Y., Cho, J.-H.J., Law, B.M. & Aratono, M. Ellipsometric Search for Vapor Layers at Liquid-hydrophobic Solid Surfaces. *Langmuir* **22**, 1715-1721 (2006).
[182] Ge, Z., Cahill, D.G. & Braun, P.V. Thermal Conductance of Hydrophilic and Hydrophobic Interfaces. *Phys. Rev. Lett.* **96**, 186101 (2006).
[183] Israelachvili, J. & Pashley, R. The hydrophobic interaction is long range, decaying exponentially with distance. *Nature* **300**, 341-342 (1982).
[184] Israelachvili, J. & Pashley, R. The hydrophobic interaction is long range, decaying exponentially with distance. *Nature* **300**, 341-342 (1982).
[185] Christenson, H.K. & Claesson, P.M. Direct measurements of the force between hydrophobic surfaces in water. *Advances in Colloid and Interface Science* **91**, 391-436 (2001).
[186] Singh, S., Houston, J., van Swol, F. & Brinker, C.J. Superhydrophobicity: Drying transition of confined water. *Nature* **442**, 526 (2006).

[187] Gong, W., Stearnes, J., Fornasiero, D., Hayes, R.A. & Ralston, J. The influence of dissolved gas on the interactions between surfaces of different hydrophobicity in aqueous media Part II. A spectroscopic study. *Phys. Chem. Chem. Phys.* **1**, 2799-2803 (1999).
[188] Stillinger, F.H. Structure in aqueous solutions of nonpolar solutes from the standpoint of scaled-particle theory. *J Solution Chem* **2**, 141-158 (1973).
[189] Lum, K., Chandler, D. & Weeks, J.D. Hydrophobicity at Small and Large Length Scales. *The Journal of Physical Chemistry B* **103**, 4570-4577 (1999).
[190] Koishi, T. et al. Nanoscale hydrophobic interaction and nanobubble nucleation. *Phys. Rev. Lett* **93**, 185701 (2004).
[191] Huang, X., Margulis, C.J. & Berne, B.J. Dewetting-induced collapse of hydrophobic particles. *Proc Natl Acad Sci U S A* **100**, 11953-11958 (2003).
[192] Zhou, R., Huang, X., Margulis, C.J. & Berne, B.J. Hydrophobic Collapse in Multidomain Protein Folding. *Science* **305**, 1605 -1609 (2004).
[193] Ljunggren, S. & Eriksson, J.C. The lifetime of a colloid-sized gas bubble in water and the cause of the hydrophobic attraction. *Colloids and Surfaces A: Physicochemical and Engineering Aspects* **129-130**, 151-155 (1997).
[194] Stevens, H., Considine, R.F., Drummond, C.J., Hayes, R.A. & Attard, P. Effects of Degassing on the Long-Range Attractive Force between Hydrophobic Surfaces in Water. *Langmuir* **21**, 6399-6405 (2005).
[195] Poynor, A. et al. How water meets a hydrophobic surface. *Phys. Rev. Lett* **97**, 266101 (2006).
[196] Zhang, X.H., Maeda, N. & Craig, V.S.J. Physical Properties of Nanobubbles on Hydrophobic Surfaces in Water and Aqueous Solutions. *Langmuir* **22**, 5025-5035 (2006).
[197] Zhang, X.H. et al. Detection of Novel Gaseous States at the Highly Oriented Pyrolytic Graphite−Water Interface. *Langmuir* **23**, 1778-1783 (2007).
[198] Chandler, D. Interfaces and the driving force of hydrophobic assembly. *Nature* **437**, 640-647 (2005).
[199] Marinova, K.G. et al. Charging of Oil−Water Interfaces Due to Spontaneous Adsorption of Hydroxyl Ions. *Langmuir* **12**, 2045-2051 (1996).
[200] Stubenrauch, C., Schlarmann, J. & Strey, R. A disjoining pressure study of n-dodecyl-??-D-maltoside foam films. *Phys. Chem. Chem. Phys.* **4**, 4504-4513 (2002).
[201] Weidenhammer, P. & Jacobasch, H.-J. Investigation of Adhesion Properties of Polymer Materials by Atomic Force Microscopy and Zeta Potential Measurements. *Journal of Colloid and Interface Science* **180**, 232-236 (1996).
[202] Feldman, K., Hähner, G., Spencer, N.D., Harder, P. & Grunze, M. Probing Resistance to Protein Adsorption of Oligo(ethylene glycol)-Terminated Self-Assembled Monolayers by Scanning Force Microscopy. *Journal of the American Chemical Society* **121**, 10134-10141 (1999).
[203] Beattie, J.K. & Djerdjev, A.M. The Pristine Oil/Water Interface: Surfactant-Free Hydroxide-Charged Emulsions. *Angewandte Chemie International Edition* **43**, 3568-3571 (2004).
[204] Beattie, J.K. The intrinsic charge on hydrophobic microfluidic substrates. *Lab Chip* **6**, 1409 (2006).
[205] Zimmermann, R., Dukhin, S. & Werner, C. Electrokinetic Measurements Reveal Interfacial Charge at Polymer Films Caused by Simple Electrolyte Ions. *The Journal of Physical Chemistry B* **105**, 8544-8549 (2001).
[206] Zimmermann, R., Freudenberg, U., Schweiß, R., Küttner, D. & Werner, C. Hydroxide and hydronium ion adsorption -- A survey. *Current Opinion in Colloid & Interface Science* **15**, 196-202 (2010).
[207] Quinn, A., Sedev, R. & Ralston, J. Influence of the Electrical Double Layer in Electrowetting. *The Journal of Physical Chemistry B* **107**, 1163-1169 (2003).
[208] Schweiss, R., Welzel, P.B., Werner, C. & Knoll, W. Dissociation of Surface Functional Groups and Preferential Adsorption of Ions on Self-Assembled Monolayers Assessed by Streaming Potential and Streaming Current Measurements. *Langmuir* **17**, 4304-4311 (2001).
[209] Franks, G.V., Djerdjev, A.M. & Beattie, J.K. Absence of Specific Cation or Anion Effects at Low Salt Concentrations on the Charge at the Oil/Water Interface. *Langmuir* **21**, 8670-8674 (2005).
[210] Ciunel, K., Armélin, M., Findenegg, G.H. & von Klitzing, R. Evidence of Surface Charge at the Air/Water Interface from Thin-Film Studies on Polyelectrolyte-Coated Substrates. *Langmuir* **21**, 4790-4793 (2005).
[211] Creux, P., Lachaise, J., Graciaa, A. & Beattie, J.K. Specific Cation Effects at the Hydroxide-Charged Air/Water Interface. *The Journal of Physical Chemistry C* **111**, 3753-3755 (2007).
[212] Creux, P., Lachaise, J., Graciaa, A., Beattie, J.K. & Djerdjev, A.M. Strong Specific Hydroxide Ion Binding at the Pristine Oil/Water and Air/Water Interfaces. *The Journal of Physical Chemistry B* **113**, 14146-14150 (2009).
[213] Petersen, P.B. & Saykally, R.J. Is the liquid water surface basic or acidic? Macroscopic vs. molecular-scale investigations. *Chemical Physics Letters* **458**, 255-261 (2008).
[214] Winter, B., Faubel, M., Vácha, R. & Jungwirth, P. Behavior of hydroxide at the water/vapor interface. *Chemical Physics Letters* **474**, 241-247 (2009).

[215] Buch, V., Milet, A., Vácha, R., Jungwirth, P. & Devlin, J.P. Water surface is acidic. *Proceedings of the National Academy of Sciences of the United States of America* **104**, 7342-7347 (2007).
[216] Jungwirth, P. & Winter, B. Ions at Aqueous Interfaces: From Water Surface to Hydrated Proteins. *Annu. Rev. Phys. Chem.* **59**, 343-366 (2008).
[217] Vácha, R., Horinek, D., Berkowitz, M.L. & Jungwirth, P. Hydronium and hydroxide at the interface between water and hydrophobic media. *Phys. Chem. Chem. Phys.* **10**, 4975 (2008).
[218] Mucha, M. et al. Unified Molecular Picture of the Surfaces of Aqueous Acid, Base, and Salt Solutions. *The Journal of Physical Chemistry B* **109**, 7617-7623 (2005).
[219] Iler, Ralph K. The chemistry of silica : solubility, polymerization, colloid and surface properties, and biochemistry, (Wiley: New York :, New York : Wiley, c1979.).
[220] Kirby, B.J. & Hasselbrink, E.F., Jr Zeta potential of microfluidic substrates: 2. Data for polymers. *Electrophoresis* **25**, 203-213 (2004).
[221] Hunter, R.J. *Zeta Potential in Colloid Science*. (Academic Pr: 1981)
[222] Schuetzner, W. & Kenndler, E. Electrophoresis in synthetic organic polymer capillaries: variation of electroosmotic velocity and .zeta. potential with pH and solvent composition. *Analytical Chemistry* **64**, 1991-1995 (1992).
[223] Ocvirk, G. et al. Electrokinetic control of fluid flow in native poly(dimethylsiloxane) capillary electrophoresis devices. *ELECTROPHORESIS* **21**, 107-115 (2000).
[224] Ren, X., Bachman, M., Sims, C., Li, G.P. & Allbritton, N. Electroosmotic properties of microfluidic channels composed of poly(dimethylsiloxane). *Journal of Chromatography B: Biomedical Sciences and Applications* **762**, 117-125 (2001).
[225] Kirby, B.J. & Hasselbrink Jr., E.F. Zeta potential of microfluidic substrates: 2. Data for polymers. *ELECTROPHORESIS* **25**, 203-213 (2004).
[226] Liu, D., Ma, G., Levering, L.M. & Allen, H.C. Vibrational Spectroscopy of Aqueous Sodium Halide Solutions and Air−Liquid Interfaces: Observation of Increased Interfacial Depth. *The Journal of Physical Chemistry B* **108**, 2252-2260 (2004).
[227] Vrbka, L. et al. Propensity of soft ions for the air/water interface. *Current Opinion in Colloid & Interface Science* **9**, 67-73 (2004).
[228] Petersen, P.B. & Saykally, R.J. Confirmation of enhanced anion concentration at the liquid water surface. *Chemical Physics Letters* **397**, 51-55 (2004).
[229] Ghosal, S. et al. Electron Spectroscopy of Aqueous Solution Interfaces Reveals Surface Enhancement of Halides. *Science* **307**, 563 -566 (2005).
[230] Mela, P. et al. The zeta potential of cyclo-olefin polymer microchannels and its effects on insulative (electrodeless) dielectrophoresis particle trapping devices. *ELECTROPHORESIS* **26**, 1792-1799 (2005).
[231] Kirby, B.J. & Hasselbrink Jr., E.F. Zeta potential of microfluidic substrates: 2. Data for polymers. *ELECTROPHORESIS* **25**, 203-213 (2004).
[232] Franks, G.V., Djerdjev, A.M. & Beattie, J.K. Absence of Specific Cation or Anion Effects at Low Salt Concentrations on the Charge at the Oil/Water Interface. *Langmuir* **21**, 8670-8674 (2005).
[233] Israelachvili, J.N. *Intermolecular And Surface Forces*. (Academic Press: 2010).
[234] Iuchi, S., Chen, H., Paesani, F. & Voth, G.A. Hydrated Excess Proton at Water−Hydrophobic Interfaces†. *The Journal of Physical Chemistry B* **113**, 4017-4030 (2009).
[235] Kudin, K.N. & Car, R. Why Are Water−Hydrophobic Interfaces Charged? *Journal of the American Chemical Society* **130**, 3915-3919 (2008).

Chapter II

Materials, Methods and Experimental Techniques

Table of contents for Chapter II:

In this chapter the sample preparation techniques and main characterization methods are presented. The chapter starts with a description of the materials studied, substrate preparation and surface modification, followed by the description of the different sample preparation techniques. In the second half of the chapter the main characterization techniques used are presented, with discussions involving the physical principles behind the technique and its operational details.

2.1 Materials

The materials used in the studies of this thesis are linear homopolymers with a narrow molecular weight distribution (polydispersity $P_d = M_W/M_n$). The polymer used in most of the experiments described in this thesis is isotactic polystyrene (PS), but in some particular experiments polymers as polymethylmetacrylate (PMMA), polyethylene (PE) and polydimethylsiloxane (PDMS) were used. Their characteristics are summarized in Table II.1.

Table II.1: Polymers used in this work. M_w - weight-averaged molecular weight, P_d - polydispersity, γ - surface tension at 20°C, T_g - glass transition temperature, ε - dielectric constant and n - refractive index at room temperature.

Polymer	Repeating unit	M_W (kg/mol)	P_d	γ (mN/m)	T_g (°C)	ε	n
PS †‡‼	C_8H_8	7, 59, 160, 250, 500	<1.04	40.7	90-105	2.5	1.59
PMMA†	$C_5H_8O_2$	120	2	41	105	3.6	1.49
PE†	C_2H_4	125	1.32	35.7	-20	2.3	1.54

†PS of 59 and 500 kg/mol were obtained from Sigma-Aldrich

‡ PS 250 kg/mol was purchased from ACROS Organics

‼160 and 7 kg/mol were generous gifts from Dr. Eric Drockenmuller and Dr. Antoine Bosquet.

2.1.1. Polystyrene

Polystyrene (PS) is an inexpensive hard plastic which belongs to the group of standard thermoplastics, which also includes polyethylene, polypropylene and poly(vinyl chloride). A selection of PS properties relevant to the work developed in this thesis is presented in Table II.2. Polystyrene combines different properties that make it suitable for different applications. As its vapor pressure is extremely low material losses due to evaporation is not a problem. It is soluble in volatile easy to handle solvents. Typical applications take advantage of its glassy character at room temperature. Polystyrene is second only to polyethylene in our everyday life.

Polystyrene is a vinyl polymer. Structurally, it consists of a carbon backbone saturated with hydrogen, with one hydrogen in each monomer unit replaced by an aromatic ring (phenyl group) (Figure II.1). Polystyrene is usually produced by free radical vinyl polymerization, from the monomer styrene.

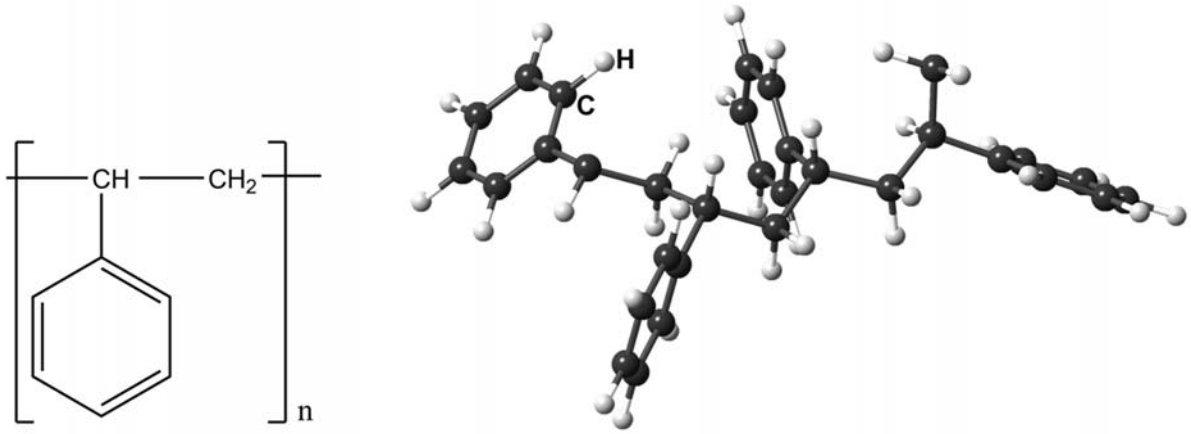

Figure II.1: Chemical structure of polystyrene.

As mentioned in previous chapter, PS exists in atactic, syndiotactic, and isotactic varieties. If all of the aromatic rings are on the same side of the chain, we say that the polymer is isotactic. In the syndiotactic variety of groups on the polymer chain are attached to alternating sides of the polymer backbone. "Normal" or atactic polystyrene has no preferential order regarding the side of the chain on which the phenyl groups are attached. Atactic PS forms a clear, amorphous structure while the regular periodicity of the syndiotactic and isotactic varieties allows them to form discrete crystalline domains from the melt, creating a semicrystalline microstructure.

Atactic polystyrene was chosen for most of the studies presented in this thesis because of its relatively simply morphology and its widespread use in polymer physics studies. The absence of a crystalline phase, make it easier to use for studies of surface mobility, instabilities in thin polymer films and structure formation.

Table II.2. Properties of polystyrene

Physical Properties	
Density	1.04-1.07 g/cm^3
Mechanical Properties	
Hardness, Rockwell M	70-74
Hardness, Rockwell R	104-120
Ultimate Tensile Strength	17.9-70 MPa
Yield Tensile Strength	25-69 MPa
Elongation at Break	1-45%
Elongation at Yield	1.5-2.2%
Elastic Modulus	3200 MPa
Poisson's Ratio	0.325-0.33
Thermal Properties	
Thermal Conductivity	0.12-0.193 W/m-K

Glass Transition Temperature	83-105°C
Optical Properties	
Visible Light Transmission	80-90%

2.2. Preparation Techniques

2.2.2. Substrate preparation

This thesis deals with structuration of supported polymer films. As will be described later, the choice of substrate is one of the factors that determine the quality of polymer films. In general, smooth and clean substrates must be used to produce good-quality films. In this work we used two different substrates: silicon wafers and freshly cleaved muscovite mica.

2.2.2.1. Silicon Wafers

We used highly polished silicon (Si) wafers (surface roughness below 5 nm) (Wafer World, Palm Beach County, Florida) with (100) lattice plane doped with boron (p–type) and resistivity 1-50Ωcm.

For our experiments, we cut pieces of 1X1 cm^2, and cleaned them with Piranha solution to remove dust and organic contaminants. Piranha solution[1], also known as piranha etch, is a mixture of concentrated sulfuric acid (H_2SO_4) and hydrogen peroxide (H_2O_2) (70 % conc. H_2SO_4 and 30% H_2O_2). Si wafers samples were immersed in them hot Piranha solution (100 to 110°C) for 1-1:30 hours. Then, samples were extensively rinsed with Millipore water and gently dried with N_2 gas. Because the piranha mixture is a strong oxidizer, it removes most organic matter, and hydroxylates the Si surfaces (adding OH groups), making them extremely hydrophilic. The oxide layer on top of the silicon substrates was approximately 2 nm thick after piranha treatment.

2.2.2.2. Mica

Mica is a phyllosilicate mineral of aluminium and potassium with chemical formula $KAl_2Si_3AlO_{10}(OH)_2$. Clay minerals are formed by two building blocks [1]: tetrahedrons of oxygen with Si^{4+} ions in their centers and octahedrons of oxygen with Al^{3+} or Mg^{2+} in their centers.

The tetrahedrons share oxygens and form hexagonal rings. Some oxygen atoms form hydroxyls, in particular when the clay is filled with Ca^{2+}. This pattern can be repeated at infinitum to form flat tetrahedral sheets. Similarly, the octahedrons are linked to form octahedral layers. The

[1]Piranha solution is **VERY DANGEROUS!,** being both a strongly acid and a strong oxidizer.
Do not attempt to use and/or mix piranha solutions without prior training and lab manager instructions. The handling of piranha solutions should be done under fume hood deck, only in **glass** containers (preferably Pyrex) and wearing protection equipment that includes: laboratory clothing (lab coat), gloves, protective eye wear, and leather shoes.
When preparing the piranha solution, always add drop by drop the peroxide to the acid. The added H_2O_2 immediately produces an exothermic reaction with gas (pressure) release. If the H_2O_2 concentration is at 50% or greater, an explosion could occur. Hot piranha should neither be stored in a closed container and nor mixed with organic compounds it may cause an explosion.
Piranha solution should be handled with extreme caution. the container must be very clearly labeled with the words "**Piranha Solution**".

tetrahedral and octahedral sheets can be stacked on top of each other in various forms to build the different kinds of clays. In mica, each sheet is composed of three layers (Figure II.2). The top and bottom layers are formed by hexagons filled with Si^{4+}. The intermediate layer is octahedral and each octahedron is filled with Al^{3+} or Mg^{2+}. The sheets are held together by cations. Since this binding is relatively weak, mica can be easily cleaved. After cleaving a clean, atomically smooth surface (R.M.S. roughness smaller than 0.5 angstroms) over large areas can be obtained. For this reason mica is a very commode substrate for coatings, microscopy, atomic force microscopy and surface forces measurements.

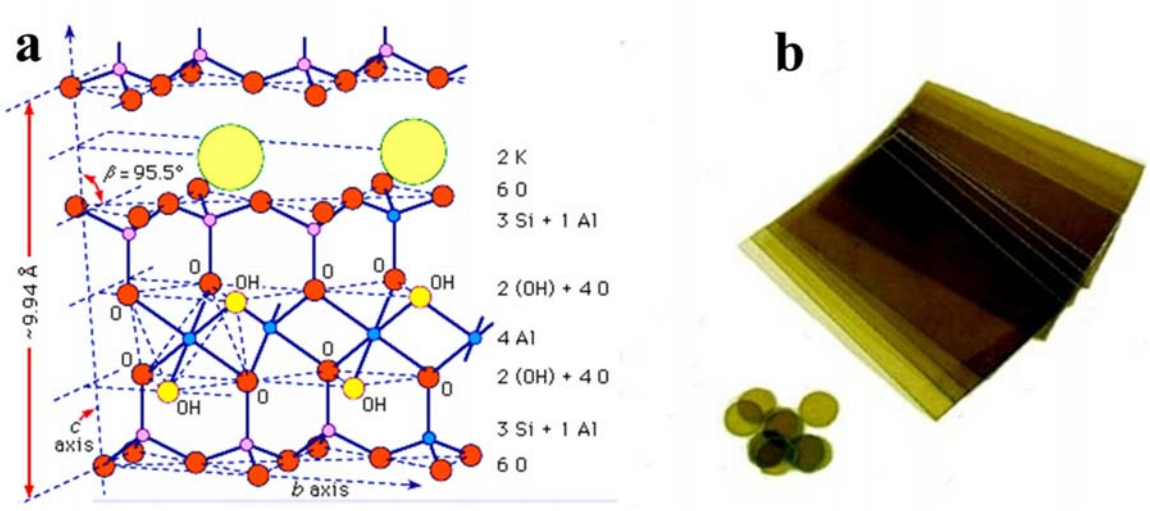

Figure II.2: Molecular structure of muscovite mica ($KAl_2Si_3AlO_{10}(OH)_2$)(a), thick mica sheets (b)

When immersed in liquids of high dielectric constant mica often gets charged by the dissolution of cations (K^+) in the liquid, leaving a negatively charged mineral behind (with one charge every 48 $Å^2$). [2,3]. In water, this charge depends somehow on the pH.

2.2.3. Sample preparation

2.2.3.1. Spin-Coating

This thesis deals with the properties of thin polymer films. They can be deposited onto a surface using various techniques, such as dip coating, capillary coating, spray coating, flow coating, chemical coating and other.

A procedure widely used to apply uniform thin polymer films is spin coating. This technique was used in all the experiments that described in this thesis (Figure II.3). A typical spin coating process starts by deposit an excess amount of a given polymer solution on top of a substrate held in place by a vacuum chuck. To obtain a smooth and defect-free film, a filtered solution (NALGENE filters pore size of 200 nm) must be used. The substrate is then rotated at high angular speeds (spin speed 1000–10 000 rotations per minute) in order to thin the film by centrifugal force. Rotation is

continued for some time (spinning time); the volatile solvent evaporate leaving behind a homogenously flat film [4].

Figure II.3: G3 series Spin Coater (Specialty Coating Systems, SCS) and representation of the spin-coating technique for the deposition of a polymer film.

Resulting film thickness, homogeneity, roughness and reproducibility (one of the most important factors in spin coating of polymer films) depend on many factors such as spin speed, polymer concentration, acceleration, spin time, viscosity, annealing time, etc. Subtle variations in the parameters that define the spin process can result in drastic variations in the quality of the coated film. For example, dispersing an insufficient amount of polymer solution results in uncoated areas (Figure II.4a). Low polymer concentrations particles on the substrate or high speed or accelerations produce streams and flares (Figure II.4b). On the contrary, if the speed or acceleration is too low or if the solvent is too volatile, non-uniform films are produced (Figure II.4c and d) [5].

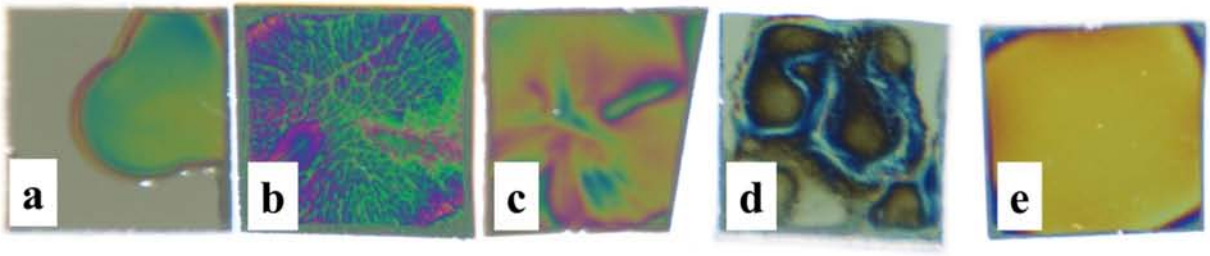

Figure II.4: Spin coated films illustrating some typical complications found in this technique.

A good balance between the choice of parameters mentioned above, and a "good" solvent (PS e.g. in toluene) permit to achieve very homogeneous films (Figure II.4e), with controlled thickness from tens of nanometers up to a few micrometers and R.M.S. roughness less than 0.5 nm (Figure II.5) the thickness of polymer films made by the spin-coating technique is a function of spin-coating speed, solution concentration/viscosity and polymer molecular weight. Quantitatively, the polymer film thickness h follows the empiric formula

$$h = k\eta_0^{\beta}\Omega^{\alpha},$$

where k and β are material specific constants, η_0 is the initial polymer solution viscosity, Ω is the spin-coating angular velocity and α is a constant with a value of around - 0.5 for most polymers.

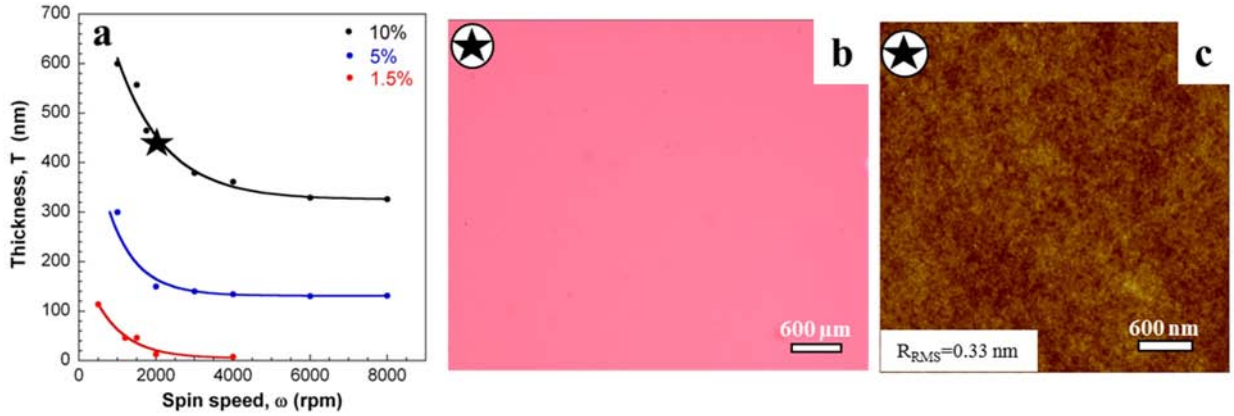

Figure II.5: (a) angular velocity dependence of the film thickness at different concentrations of 7 kDa polystyrene (PS) in toluene solution; (b) optical micrographs and (c) taping mode AFM micrograph (3 µm X 3µm) (c) of a resulting 438 nm thick coated film.

2.2.4. Surface modification

Surface chemical and physical proprieties are of primary importance in many applications, such as catalysis, drug delivery, coatings, paints, adhesives, wetting, etc. For example, it is well known that substrate surface conditions (e.g. wettability) have a direct influence on the adhesion, stability and homogeneity of thin polymer films.

For some of the experiments represented in this thesis, mica surfaces were coated with a monolayer of 10 nm diameter ceria nanoparticles and silicon wafers were hydrophobized by coating with a silane layer, in order to modify the adhesion of the polymer film on the substrates and to avoid the penetration of water between the film and the substrates.

2.2.4.1. Ceria deposition on mica by dip coating

Mica surfaces were modified by dip coating deposition of cerium oxide CeO_2 nanoparticles [6]. A 20 wt% dispersion of CeO_2 nanoparticles in water (pH ≈ 1.5) provided by RHODIA was diluted with nitric acid (HNO_3, pH = 1.5) to 0.1 wt %. The solution was further modified by addition of 0.1 M sodium nitrate ($NaNO_3$). Addition of salt does not destabilize the solution and does not change the dispersability of the nanoparticules but facilitates deposition of the particles from the solution onto the surface of the substrate. Mica samples were treated by immersion in the dispersion for 1-2 hours. Prior dipping, top and bottom dirty superficial layers of mica surfaces were removed by cleaving (using a sharp needle), or peeled off using scotch tape. After coating the plaques were removed from the solution and immersed in a nitric acid solution at pH = 1.5 for 1-5 min, rinsed twice with distilled water and gently dried with N_2 gas. The presence and quality of coating monolayers of 10 nm diameter ceria nanoparticles was verified using atomic force microscopy (AFM), Figure II.6.

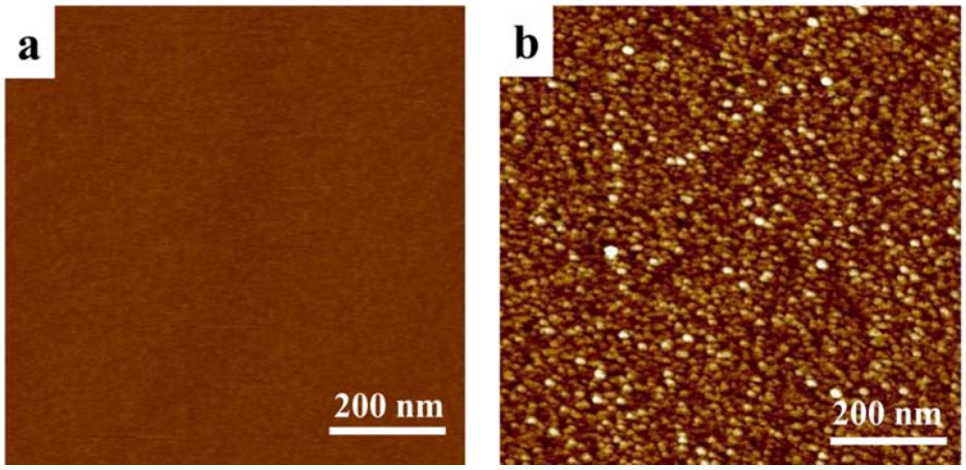

Figure II.6: Atomic force microscopy micrographs (height images) of (a) mica surface and (b) mica coated with cerium oxide nanoparticles. The presence of nanoparticles with high surface coverage is clearly evident in the height image (b). The mean diameter of the particles is 10 nm.

2.2.4.2. Molecular Self-Assembly of OTS on silicon wafers

Surface energy modification of silicon wafers was performed by coating samples with physisorbed self-assembled monolayers (SAM) of a silicon based compound with a long alkyl chain (octadecyltrichlorosilane, OTS). OTS forms covalent bonds with the oxygen groups on a (native) silicon oxide surface and self-assembles into a highly-ordered monolayer [7,8,9,10]. Direct silanization from solution was originally reported by Bigelow, Pickett and Zisman [11,12]. Later Sagiv [8] describe the application to silicon wafer surfaces.

Before silanization, the silicon surface (prepared as describe before) were cleaned with ethanol and dried with N_2 gas before and after an ultrasonic bath with double distilled water (to remove silicon flakes) and finally irradiated for 20 - 30 minutes in an UV-ozone cleaner (to activate the surface). Direct silanization was performed by immersing during 2 hours the freshly cleaned silicon wafers in a glass beaker containing solution 2 wt% of OTS in anhydrous toluene. During this time, the OTS molecules bond covalently to the silicon dioxide substrate. Then the substrates were taken out of the silane solution and rinsed with toluene, dried with dry nitrogen gas and annealed for 2-5 hours at 95°C. After annealing, the quality of the hydrophobic coating was verified by measurements of advancing and receding water contact angle. The difference of the two values gives the contact angle hysteresis, as described below. For a good hydrophobic coating, the contact angle hysteresis should be as small as possible. The roughness of the coated samples was examined by AFM. The thickness of OTS layers was measured by ellipsometry. Typical results of these measurements are summarized in Table II.3.

Table II.3: Properties of Si wafer before and after OTS coating: θ_A – advancing contact angle; θ_R – receding contact angle; $\Delta\theta$ – hysteresis; d – thickness

Sample	d [nm]	θ_A [°]	θ_R [°]	$\Delta\theta$ [°]	RMS roughness [nm]
Plane Si (native oxide)	1.6	<10	<10	-	0.21
SAM-OTS	2.3	88	81	7	0.22

In SAM method molecules adopt a define arrangement without guidance from an outside source. On the contrary, controlled grafting density of (OTS) on silicon wafers and different degrees of hydrophobicity of the surfaces can be achieved by using the Langmuir-Blodgett method of coating.

2.2.4.3. Langmuir–Blodgett (LB)

The LB trough is an apparatus which has two purposes [13].

First, it can be used to deposit one or more monolayers of specific amphiphiles onto solid substrates, as described below. Second, it can be used as an experimental device to test interfacial properties such as the surface pressure of a given system.

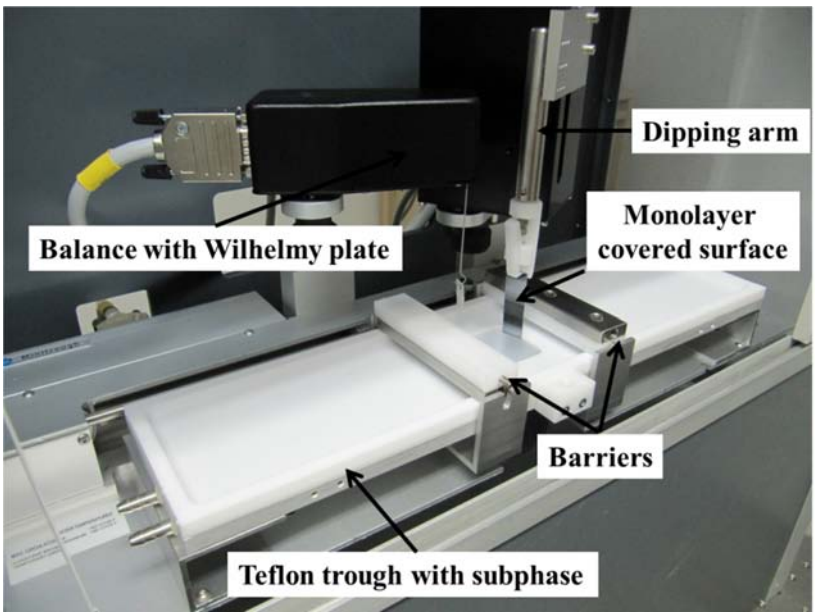

Figure II.7: Schematic illustration of a Langmuir film balance with a Wilhelmy plate electrobalance measuring the surface pressure, and barriers for reducing the available surface area.

Langmuir troughs (Figure II.7) are usually made of Teflon to prevent any leakage of the subphase over the edges. A monolayer of molecules on the subphase (usually water) is formed when a solution of a water insoluble (or sparingly soluble) amphiphile is placed on a water surface with a microsyringe; the solution then spreads rapidly to cover the available area. After solvent evaporation, movable barriers are approached to compress the monolayer at the interface. The barriers are made of Delrin, hydrophilic material, and heavy enough to prevent any leakage of the monolayer below the barriers. At the beginning of the compression amphiphilic molecules are well-separated and do not interact with each other. During compression, the barriers reduce the area available for a single

molecule increasing the intermolecular interactions. The formation of the monolayer at the aqueous surface decreases the surface tension at the air-water interface.

An experimental indicator of the properties of the surface layer is obtained by measuring the surface pressure as a function of the area available to each molecule.

Surface pressure (Π) is the difference between the surface tension of the clean subphase (γ_0) and of the surface tension at the interface covered by the monolayer (γ):

$$\Pi = \gamma_0 - \gamma \tag{2.1}$$

An isotherm is usually recorded by compressing the film (reducing the area with the barriers) at a constant rate while continuously monitoring the surface pressure. The surface pressure in the system is measured by the Wilhelmy plate-method. In this method the force due to surface tension on a suspended plate that it is partially immersed in the subphase is measured (Figure II.7). This force is then converted into surface tension (mN/m) with the help of the dimensions of the plate. The plate is often very thin and made of platinum, but even plates made of glass, quartz, mica and filter paper can be used [13]. The total force in the plate is given by:

$$F = (m_p g) + 2(t_p + \omega_p)\gamma \ \cos(\theta) - \rho_l V_p g \tag{2.2}$$

where m_p - mass of the plate, g - gravitational acceleration, t_P - thickness of the plate, ω_p - width of the plate, γ - surface tension of the liquid, θ - contact angle of the liquid on the plate, ρ_l - density of the liquid, and V_p - volume of the portion of the plate immersed in the liquid.

If the plate is completely wetted by the liquid ($cos\theta = 1$) the surface pressure is then obtained by

$$\Pi = \gamma_0 - \gamma = -\frac{\Delta F}{2(t_p + \omega_p)} = -\frac{\Delta F}{2\omega_p} \text{ if } \omega_p >> t_p. \tag{2.3}$$

A schema of a typical *Π*/*A*-isotherm is shown in Figure II.8. We can distinguish different regions or phases [14]. Initially, large monolayers exist in the gaseous state (*G*), under continuous compression a phase transition to the liquid-expanded state appears (L_1). Upon further compression, the L_1 phase undergoes a transition to the liquid-condensed state (L_2), and at even higher densities the monolayer finally reaches the solid state (*S*). If the monolayer is further compressed after reaching the S state the monolayer will collapse into three-dimensional structures. The collapse is generally seen as a rapid decrease in the surface pressure or as a horizontal break in the isotherm if the monolayer is in the liquid state.

The transfer of a monolayer from the water-air interface to a substrate is a delicate process that depends on many factors. These include the direction and speed of the substrate, surface pressure, composition, temperature, and pH of the subphase. Deposition is achieved by passing a substrate through the monolayer while simultaneously keeping the surface pressure controlled. This is achieved by using a computer controlled feedback system between the electrobalance measuring the surface pressure and the barrier moving mechanism. Consequently, the floating monolayer is adsorbed to the

solid substrate and is called Langmuir-Blodgett film. The quantity and the quality of the deposited monolayer on a solid support is measured by the transfer ratio (t.r.) defined as the ration between the decrease in the monolayer area during deposition and the area of the coated substrate.

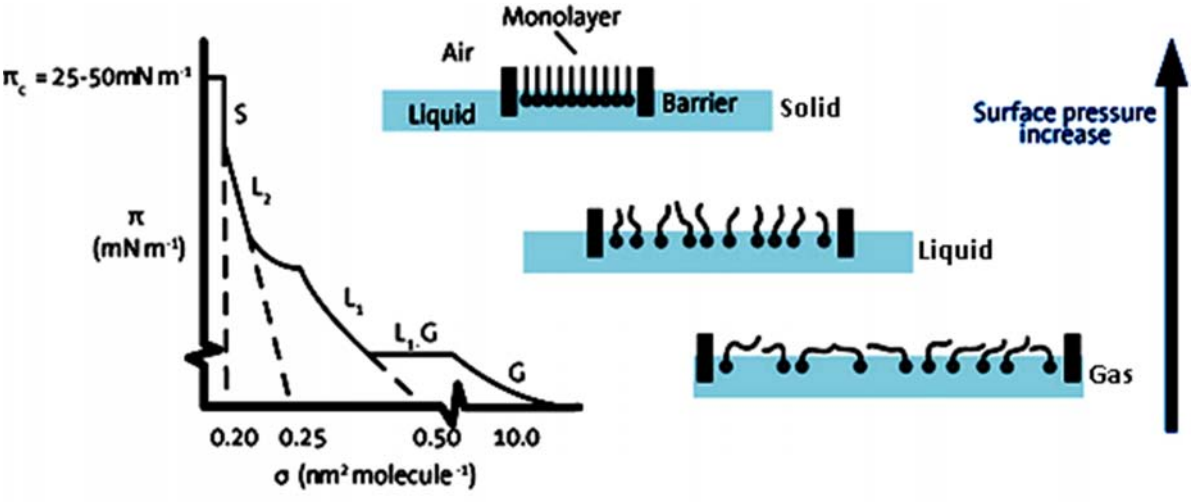

Figure II.8: Schematic *Π/A*-isotherm and orientation of the molecules in different phases [14].

The advantages of this coating technique are:

- precise control of the molecular density
- homogeneous deposition of the monolayer over large areas
- possibility to make multilayer structures with varying layer composition by successive depositions.

2.3. Characterization Techniques

In this thesis, various characterization techniques were used to study polymer thin films. In the present section, a description of the basis of the different techniques and its operation are presented.

2.3.1 Optical Microscopy of thin polymer films

A microscope is an instrument which uses visible light and a system of lenses to produce magnified images of small samples. Since his invention, the microscope has become an important research tool in many sciences such as physics, materials sciences, life sciences and biology to image objects that are too small to be seen with the naked eye [15].

We used a reflected light microscopy (Olympus Optical Microscope BX51) (Figure II.9) to qualitatively analyze the homogeneity of polymer films of thickness between 10^{-6}m and 10^{-3}m. These films appear colored due to interference of reflected white light at the polymer–air and at the polymer –substrate interface. The color of the film is then a function of its thickness, refractive index, the supporting substrate and the atmosphere. It can be used as an indication of its thickness and uniformity, as shown in Figure II.9.

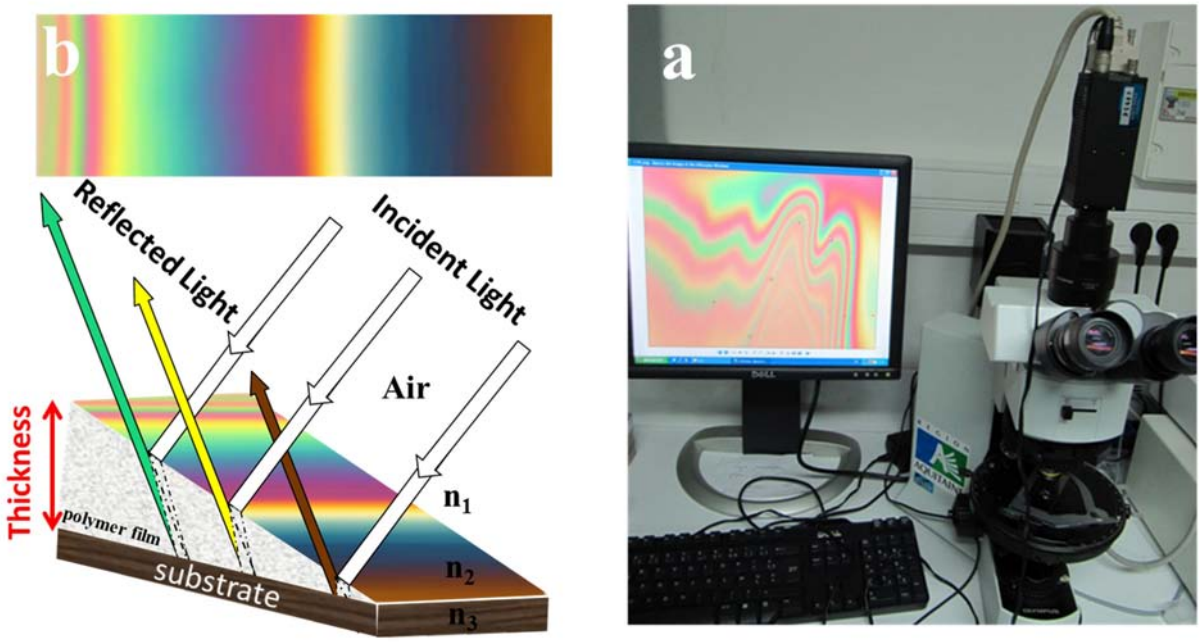

Figure II.9: Olympus BX51 microscope, equipped with several objectives (a). Interference colors from a polystyrene film on a silicon wafer (b) [16]. The film thickness changes from right to left: 20 nm (light brown), 70 nm (dark brown), 100 nm (dark blue), 140 nm (light blue) 200 nm (yellow), 250 - 280 nm (purple), 290 nm (blue), 310 nm (turquoise), 330 nm (green), 350 nm (yellow), 400 nm (light purple), 420 nm (green), 460 nm (yellow), 520 nm (pink) alternating light green and pink up to approximately 1.5 μm until it changes to a transparent gray.

2.3.2. Ellipsometry

Ellipsometry is a non-destructive optical technique used to determine the optical constants and thickness of thin films.

An ellipsometer measures the change in the polarization state of a beam of light after it is reflected from a sample. This reflection is determined by:

- Layer thickness
- Optical constants (refractive index and extinction coefficient)
- Composition
- Surface roughness

2.3.2.1. Polarization

Light, as any other electromagnetic radiation, has two components: an oscillating electric field and a magnetic field. In the direction of light propagation, both fields are sinusoidal in shape. Their field vectors are directed perpendicular with respect to each other and to the direction of propagation (Figure II.10). In any reference frame, the electric field can be split into two vectors, one along the x-axis and one along the y-axis.

$$E(z,t) = E_x(z,t) + E_y(z,t) \tag{2.4}$$

In particular, when light is reflected by a given surface, the electric field can be describe in terms of components that are parallel E_p and perpendicular E_s to the plane of incidence (plane perpendicular to the surface defined by the incident and reflected light beams) indicated by E_p and E_s, respectively.

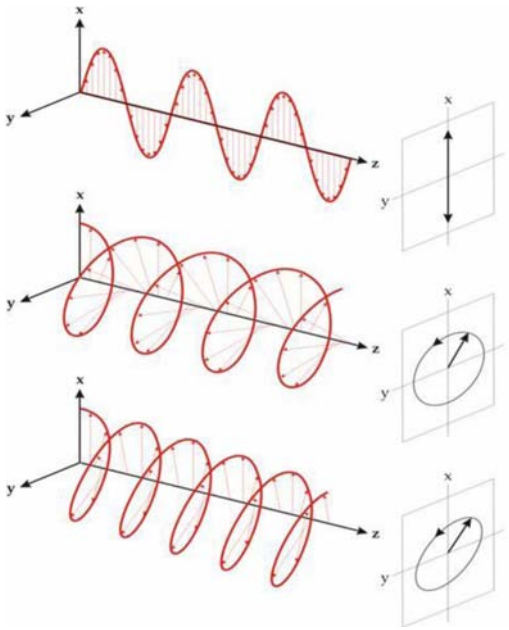

Figure II.10: Polarization state of light linearly, circularly, and elliptically [17]

The time dependent behaviour of a vector field at a fixed point in space is called polarization. Depending on the amplitude of the electric field vectors and the phase difference between them, the light is either linearly (a), circularly (b) or elliptically (c) polarized (Figure II.10). Thus, the most general polarization of (monochromatic) light is elliptical (this is the reason of the name "ellipsometry").

2.3.2.2. Ellipsometer

As we mentioned before, ellipsometry is an optical technique to characterize thin film properties such as film thickness, index of refraction and film growth. In this thesis I have used ellipsometry to measure the thickness of thin polymer films. By probing the change of the polarization state of light reflected or transmitted through film samples, the ellipsometer can be used to accurately measure film thicknesses ranging from several angstroms to several micrometers. An ellipsometer is equipped with a light source, some optical components used to modify the polarization and a detector [18]. The optical elements are classified into polarizer (analyzer), compensator (retarder), and depolarizer. The polarizer is employed to extract linearly polarized light from unpolarized light, while a compensator is used to convert linear polarization to circular polarization. The depolarizer is utilized when polarized light is changed to unpolarized light.

Figure II.11 illustrates how an ellipsometer works. If linearly polarized light with components p and s in phase is shone onto the film sample with an incidence angle θ_i, the reflected beam will have in general different amplitude and phase of both components. The two components, oscillating perpendicularly with each other with a non-zero phase difference will produce a resultant vector elliptically polarized. As shown in Figure II.11, the reflected beam is an elliptically polarized light with the resultant electric field vector *Er*. In a typical self-nulling ellipsometer as the one used in this work, the system will automatically adjust the polarization state of the incident light to a specific condition where the p and s components have amplitudes and phase differences such that the reflected beam is just linearly polarized. Conventionally, an ellipsometer uses a combination of a polarizer and a quarter wave plate to adjust the polarization state of the incidence light, and the linearly polarized light can be detected using another polarizer called analyzer. When the direction of the oscillating electric field of the reflected light is perpendicular with the transmission axis of the analyzer, there will be no light reaching the optical detector, which is called the null condition.

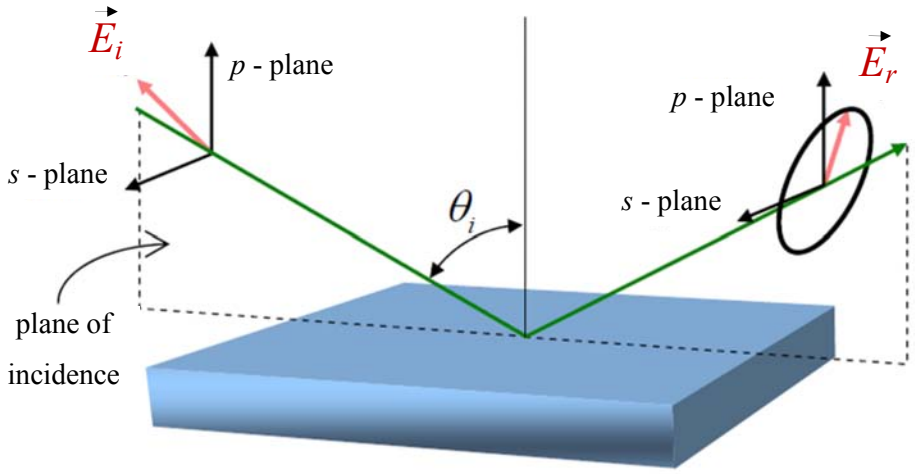

Figure II.11: Schematic geometry of the reflection ellipsometry. (Graph from [19])

From basic optics, the Fresnel reflection coefficients are given by:

$$r_P = \frac{\tilde{n}_1 \cos(\theta_2) - \tilde{n}_2 \cos(\theta_1)}{\tilde{n}_1 \cos(\theta_2) + \tilde{n}_2 \cos(\theta_1)} \tag{2.5}$$

$$r_S = \frac{\tilde{n}_1 \cos(\theta_1) - \tilde{n}_2 \cos(\theta_2)}{\tilde{n}_1 \cos(\theta_1) + \tilde{n}_2 \cos(\theta_2)} \tag{2.6}$$

In Eq.[2.5]-Eq.[2.6], r_p and r_s are reflection coefficients of *p* and *s* component respectively, subscripts 1 and 2 represent medium 1 and 2, and $\tilde{n} = n + ik$ is the complex index of refraction (n is related to the velocity and k related to the attenuation of light waves in the medium). The goal of the ellipsometric measurement is to determine the two ellipsometric parameters (relative amplitude ψ, and relative phase retardation Δ) related to the total sample reflection coefficients r_p and r_s according to [18,20,21]

$$\frac{r_P}{r_S} = \tan \Psi \, e^{i\Delta} \tag{2.7}$$

and to extract the thickness and refractive index of the films by comparing the measured parameters to a particular model, as described below. In ellipsometry one actually measures the ratio of reflection of the *p* and *s* components (to apply eq. 2.7). Therefore, it is insensitive to the absolute values of the light beam intensity and accordingly to light intensity fluctuations. This makes ellipsometry a robust and accurate technique.

2.3.2.3. The Nanofilm imaging ellipsometer

.We used an auto-nulling imaging ellipsometer Nanofilm EP^3 to characterize polymer films. All nulling ellipsometers are based on the same principle, used in the first ellipsometers 100 years ago. The operator observed the light beam reflected from the sample through an eyepiece; during observation, the polarizers and retarders were rotated by hand until the effect of the polarization was inverted and no light passed through the instrument. This is called the nulling technique. Modern nulling ellipsometers use computers to control the position of the different elements and to automatically calculate the ellipsometry signal very quickly. They use a light source, a rotating **P**olariser, a **C**ompensator plate, a **S**ample, a rotating **A**nalyser, and a detector (**PCSA** configuration) as shown in (Figure II.12). In the conventional self-nulling ellipsometer, the directly measured variables are angles of the polarizer (P), analyzer (A) and compensator (C) with fixed angle of quarter-wave-plate.

The most commonly used method is the so-called ”fixed compensator nulling scheme” which means that the compensator is fixed at a certain angle and **P** and **A** are rotated to carry out the Null condition [18]. There are four different values of P, and for each of these values the corresponding A angle which leads to a zero intensity in the detector is given by,

$$\rho = \frac{r_P}{r_S} = \tan \Psi e^{i\Delta} = -\tan A \left[\frac{\tan C - \rho_C \tan(P - C)}{1 + \rho_C \tan C \tan(P - C)} \right] \tag{2.8}$$

In the special case where C = ±π/4 which is the angle of the quarter wave plate usually used in conventional ellipsometers, one can greatly simplify eq. 2.8,

$$(C = -\pi/4) \begin{cases} P_1 = \frac{\Delta}{2} - \frac{\pi}{4}, A_1 = \psi; \\ P_3 = \frac{\Delta}{2} + \frac{\pi}{4}, A_3 = -\psi; \end{cases} \tag{2.9}$$

$$(C = +\pi/4) \begin{cases} P_2 = -\frac{\Delta}{2} - \frac{\pi}{4}, A_2 = \psi; \\ P_4 = -\frac{\Delta}{2} + \frac{\pi}{4}, A_4 = -\psi; \end{cases}$$

Accurate measurements can be performed by averaging these values (four-zone averaging). *P* and *A* are the variables measured by a nulling ellipsometer. If the measured sample is isotropic, then the

measurements in different zones will not lead to any extra information about the sample, but they are useful in eliminating systematical alignment errors in the ellipsometer. From these values, one can calculate the real and imaginary part of the ratio of the reflection coefficients.

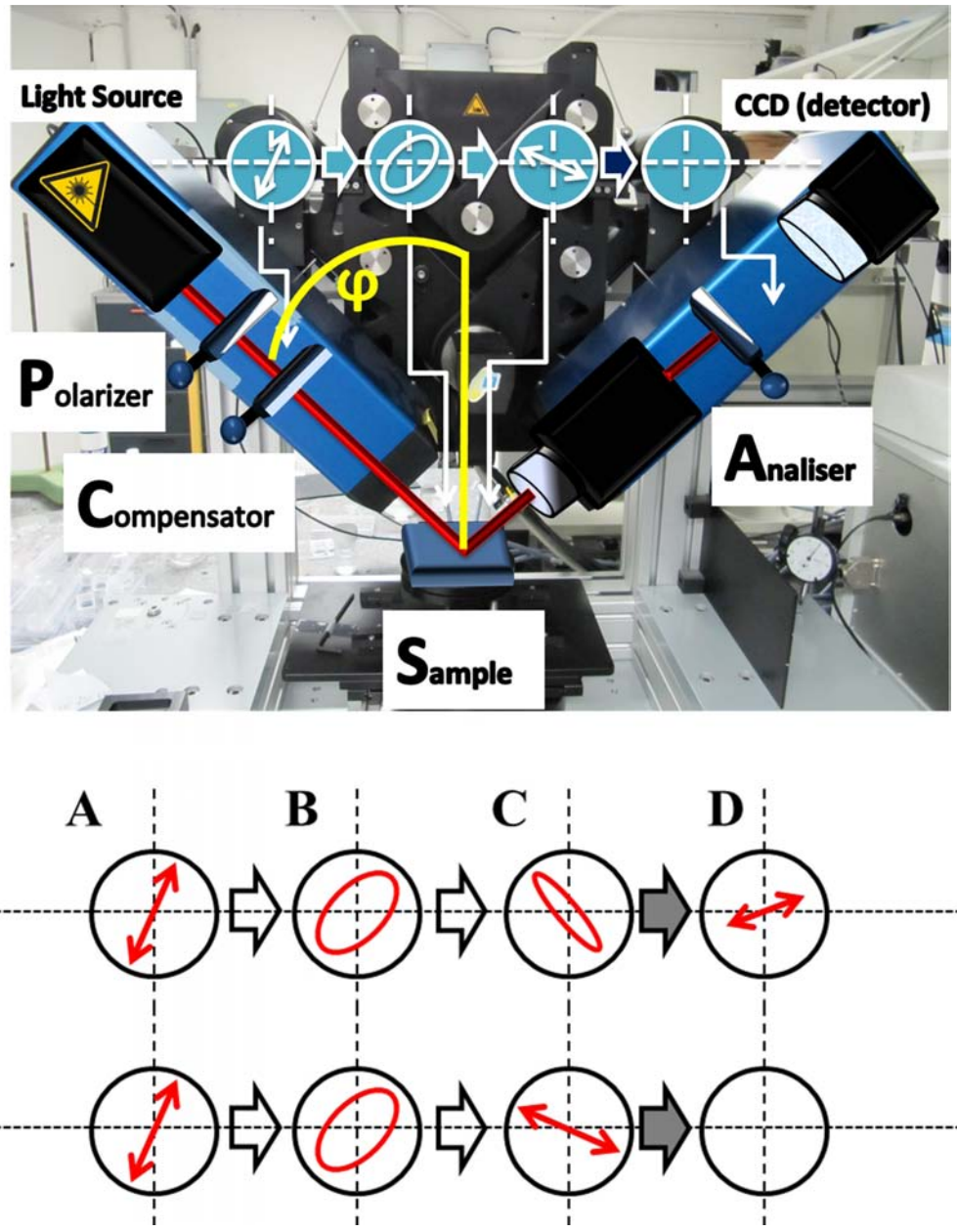

Figure II.12: (a) Standard setup of a PCSA nulling ellipsometer implemented in the Nanofilm EP3,(b) Change to the polarization of the light during its path through the ellipsometer: Top line for non-nulling condition, bottom line for perfect nulling condition. Light polarisation is shown after polarizer (A), compensator (B), sample (C) and analyzer (D).

To determine the properties of the sampel form the measured Δ and Ψ, an optical model consisting of a layered medium needs to be built, adjusting the individual layer thickness or index of refraction. An iterative computing procedure allows finding the reflective medium that matches best the experimentally measured results, as described below.

The ellipsometer Nanofilm EP^{3}has a variable angle of incidence (AOI) of 38°< φ< 90°with a continuous wave diode-pumped solid state laser with 3 wavelengths: 532nm, 635nm and 835nm.
If the measurements are done in "1-zone configuration", Δ is measured with an accuracy Δ±1° and Ψ±0.5°. The measurement takes around 20 seconds. The accuracy of determination of Δ and Ψ is increased by factor of 10 in the "four-zone configuration", but the determination requires around 1 minute [17,22].

2.3.2.4. Ellipsometric data analysis

The ellipsometric angles Δ, Ψ do not provide enough information to extract physical quantities such as film thickness. In general, it is not possible to calculate such quantities directly from the ellipsometric angles. The formulas that describe the reflection matrix R (Jones matrix used to describe mathematically the ellipsometric measurement) as a function of these parameters are too complicated and cannot be inverted. Therefore, in order to find the optical properties of a multilayer structure we need to build an optical model and fit the output of the model until fitted values match the measured values of Δ and Ψ. Simply speaking, for the case of polymer film thickness measurements we impose known values of *n* and *k* for the coating polymer, and then we change the film thickness in the model until the resulting values of Δ and Ψ are similar to the measured ellipsometric angles. A good procedure for analyzing ellipsometric data is represented in (Figure II.13).

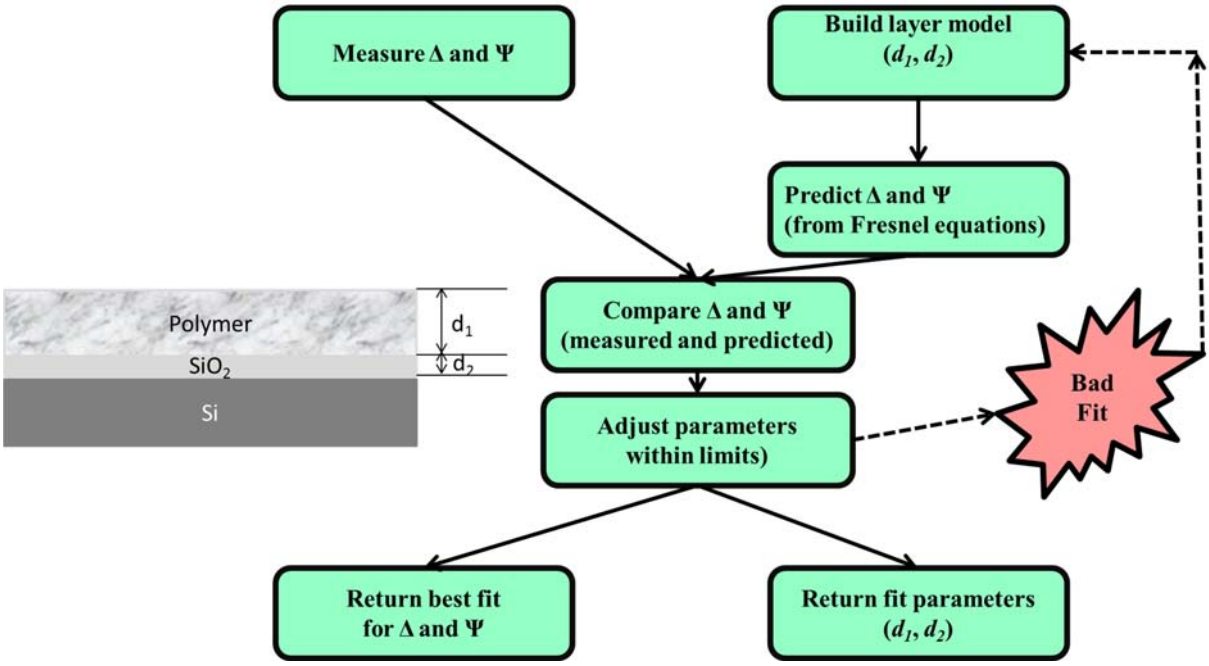

Figure II.13: Ellipsometric modeling procedure

2.3.2.5. Imaging ellipsometry

Imaging ellipsometry is a technique that combines nulling ellipsometry with optical microscopy. In imaging ellipsometry, the limitation of classical ellipsometers are overcame by the

determination of film thickness and optical properties of polymer surfaces in a two dimensional plane with a lateral resolution about at 1 µm. In this instrument a collimated parallel beam illuminates a sample and the reflected light intensity is measured by a CCD camera. Areas that have different optical properties cause different signal in the camera and will appear with different colors in the resulting image (Figure II.14). This allows building a two dimensional map of thickness and refractive index of the sample [17].

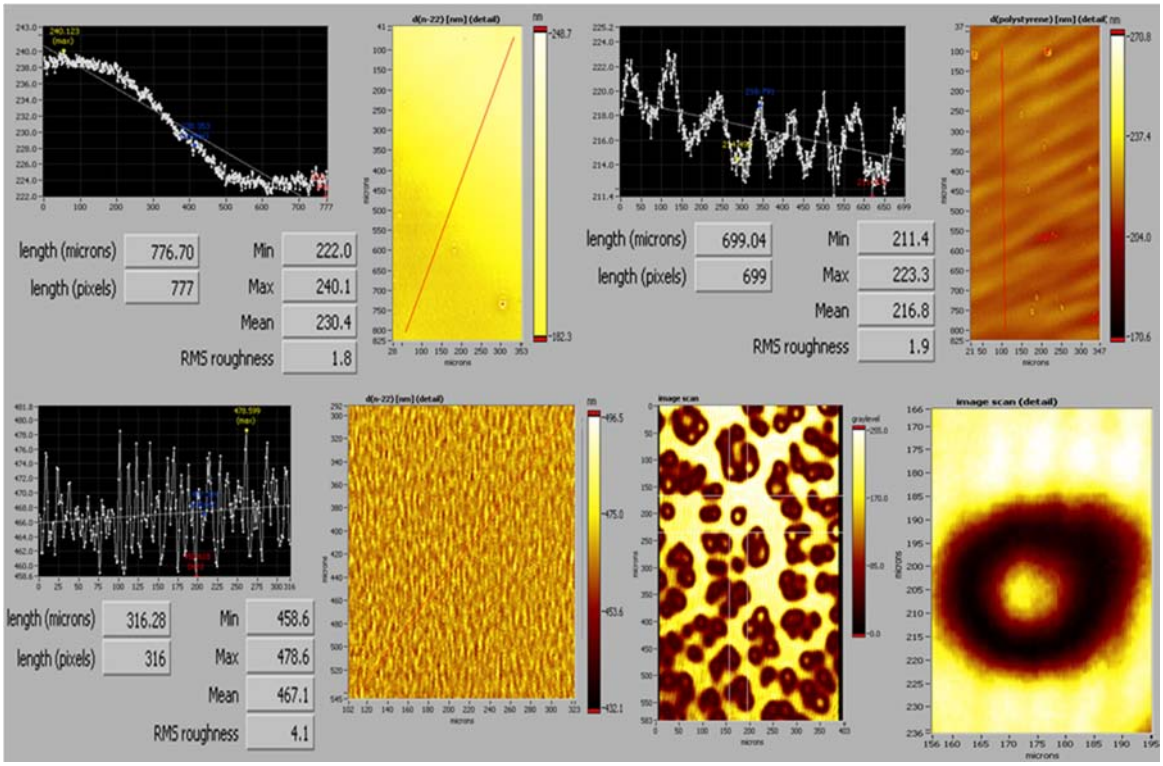

Figure II.14: imaging ellipsometry of polymer films on silicon wafers. Upper images show step or wavy structure of polystyrene films. From the left image a thickness variation from 222 to 240.1 nm is clearly visible. Lower raw, left image: the roughness of coated film was estimated; right image: patterning of the film (with lateral resolution of around 5µm) can be observed.

2.3.3. Contact angle

The contact angle θ_C is the angle at which the interface between two in miscible fluids meets a solid surface. It is a macroscopic quantity, commonly used to characterize the wetting properties of a surface. It can be related to physical and chemical proprieties of the material. The contact angle results from the interactions between the three coexisting phases that are present at the contact point: the solid, and the two fluids. It measures the competition between the cohesive forces in the liquid, which push to minimize the liquid surface area rounding the drop, and the adhesive force between the liquid and the solid, pushing the drop to spread. This competition can be described by a simple expression reflecting the mechanical equilibrium of different forces acting at the line of contact of the 3 phases (Figure II.15) known as the Young equation:

$$0 = \gamma_{SV} - \gamma_{LV} - \gamma_{SL}\cos(\theta_C) \tag{2.10}$$

So the contact angle θ_C of a liquid on a flat surface will be given by:

$$\cos(\theta_C) = \frac{\gamma_{SV} - \gamma_{LV}}{\gamma_{SL}} \tag{2.11}$$

From Eq. (2.11) it is evident that several cases are possible. If $\frac{\gamma_{SV}-\gamma_{LV}}{\gamma_{SL}}$ is close to or larger than 1, the contact angle approaches zero, meaning that the liquid wets the substrate completely. In the opposite case the angle tends to 180°, corresponding to the situation where the droplet sits as a sphere on the surface. Materials which have a water contact angle $\theta_C < 90°$ are called hydrophilic; on the contrary, if $\theta_C > 90°$ they are called hydrophobic.

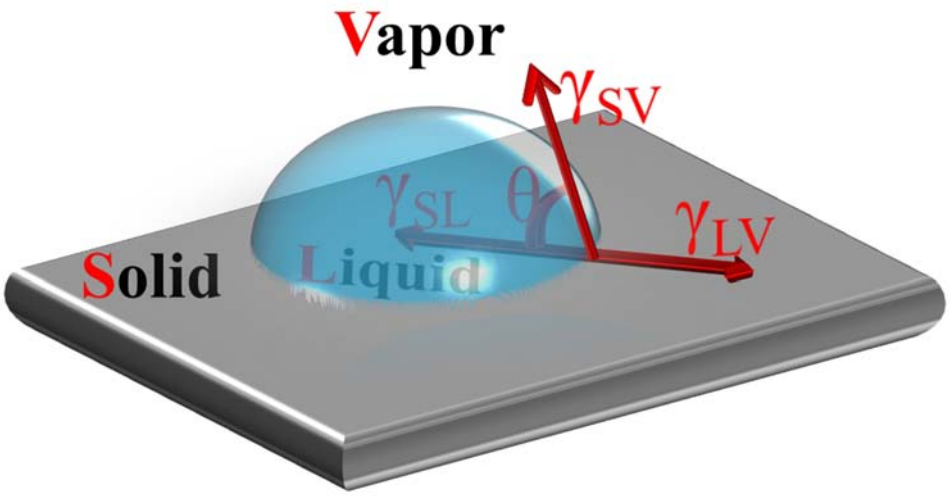

Figure II.15: Contact angle of a liquid drop on a smooth solid surface

Young's equation assumes a perfectly flat surface. However, it is well established that surface roughness may influence the wetting properties [23].Wetting of rough surfaces is more complex than the description of Young's equation. The factor of surface roughness is often embodied in the Wenzel relation. The apparent contact angle θ'_C for rough surfaces is approximated by [24]:

$$\cos(\theta'_C) = R\cos(\theta_C) \tag{2.12}$$

where R is a factor of roughness. R > 1 mean that roughness will enhance hydrophilicity as well as hydrophobicity.

- for hydrophilic solids ($\theta < 90°$), we will have $\theta' < \theta$
- for $\theta > 90°$, we will find $\theta' > \theta$

(**remark**: on certain cases (e.g. $\theta \approx 85°$) is also possible to get a higher contact angle for rough surfaces, so the theoretical limit of 90° has to be handled with caution).

Contact angle hysteresis: very often the contact angle is not a unique value. It depends on the measurement technique and the history of the sample. Surface roughness heterogeneity or adsorption processes may influence the measured value. In particular, the value measured while increasing the volume of the drop (advancing contact angle) is often different from the value measured while reducing it, the receding contact angle The physical reason for this difference is the pinning of the contact line by defects due to roughness or chemical heterogeneity. For more details see the review articles of de Gennes [25] and Quéré [24], where this phenomena is described in great detail. From the advancing and receding contact angle two important parameters are derived [26]. The average contact angle (effective water contact angle) is defined as:

$$\cos(\theta_C^0) = \frac{\theta_A + \theta_R}{2} \tag{2.13}$$

and the contact angle hysteresis $\Delta\theta$, which is provided by the difference between the maximum (advancing) and minimum (receding) contact angle values

$$\Delta\theta = \theta_A - \theta_R \tag{2.14}$$

Contact angle hysteresis helps to characterize surface heterogeneity, and roughness. For surfaces which are not homogeneous there will exist domains on the surface which present barriers to the motion of the contact line. In the case of chemical heterogeneity these domains represent areas with different contact angles. For example, when wetting with water, hydrophilic domains will pin the motion of the contact line as the liquid advances, thus increasing the contact angles. When the water recedes the hydrophilic domains will hold back the draining motion of the contact line thus decreasing the contact angle.

Two different approaches are regularly used to measure contact angles of solids: optical tensiometry (goniometry) and force tensiometry. Optical tensiometry involves the observation of a sessile or moving drop of test liquid on a solid substrate. Force tensiometry involves measuring the forces of interaction as a solid is contacted with a test liquid. In this thesis we have used optical tensiometry. The basic elements of the optical tensiometer used (TECLIS) (also called contact angle meter) include a light source, a sample stage and a CCD camera (Figure II.16).

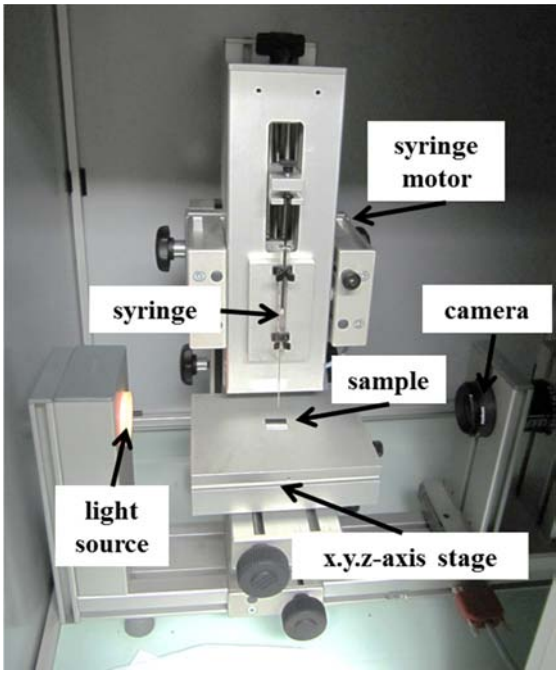

Figure II.16: Schematic illustration of TECLIS contact angle meter

The working principle of contact angle measurements is very simple: first, using a syringe, a drop of fluid is loaded on the solid sample. After this a single snap shot or a series of shots leading to a movie of image of a liquid drop is recorded with a high resolution camera At the end gray scale drop image/images are analyzed with a profile fitting method in order to determine the contact angle as a function of time. This is done by fitting the shape of the drop to the Young-Laplace equation (Figure II.17b). We measured $\Delta\theta$ by allowing the drop to evaporate, which naturally reduces its volume. The maximum angle is the advancing angle and the smallest measured angle is considered the receding angle. The difference between the advancing and receding angle gives the contact angle hysteresis (Figure II.17b).

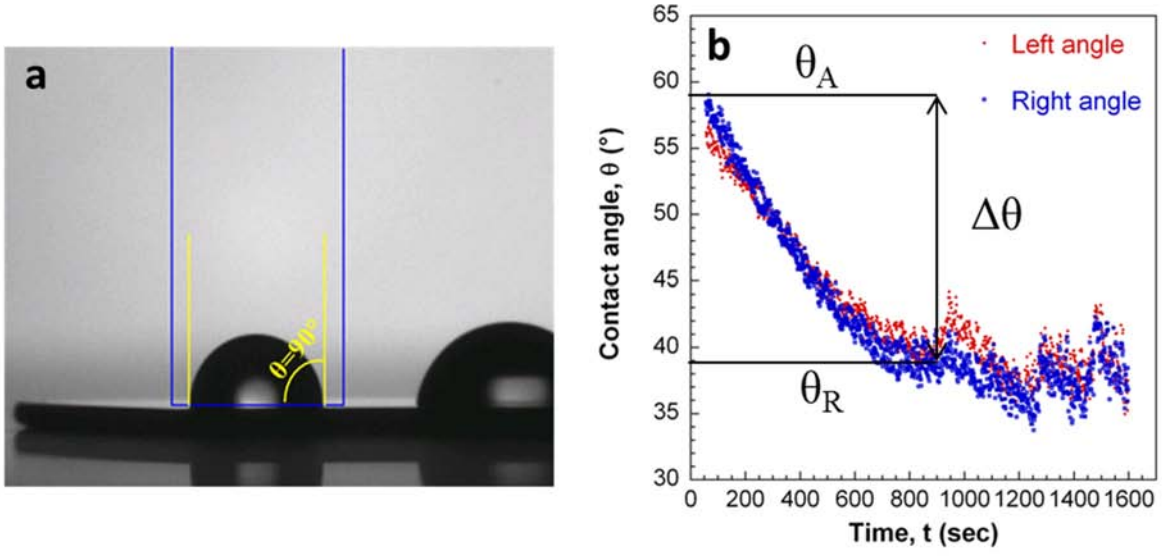

Figure II.17: (a) Static contact angle of water on a polystyrene film on silicon wafer $\theta = 90°$. (b) Contact angle as a function of time for silanized silicon wafer with 0.3 coverage density of OTS; θ_A= 58°, receding angle $\theta_R = 39°$;hysteresis $\Delta\theta = 19°$.

2.3.4. X-ray Photoelectron Spectroscopy (XPS)

X-ray Photoelectron Spectroscopy (XPS) is a powerful technique used to determine quantitative atomic composition and chemistry of surfaces. Also known as Electron Spectroscopy for Chemical Analysis (ESCA), it provides a total elementary analysis on the top 50-70 Angstroms of any surface.

The basic principle of XPS is the photoelectric effect, first outlined by Einstein in the early 1900s. This effect refers to the ejection of electrons from a surface due to photon impingement. It wasn't until the 1960s that this phenomenon began to be exploited for surface analysis [27]. XPS has been extensively used in the study of polymer surfaces, including surface modification, chemical reaction, contamination, degradation, polymer chain mobility, adhesion failure, and biocompatibility.[28,29,30,31]. XPS involves placing the sample in a high vacuum (< 10^{-8}torr) chamber and irradiating it with a monochromatic or quasi-monochromatic X-ray source (generally aluminum Al_{K_a} of 1486 eV and line width 0.85 eV or magnesium Mg_{K_a} of 1253.6 eV and line width 0.7 eV). X-ray photons interact with the atomic and molecular orbital electrons in the sample. This interaction causes a complete transfer of the photon energy to the electron (Figure II.18), which may acquire enough energy to leave the atom and escape from the surface of the sample, being subsequently collected at the analyzer. The analyzer measures the number of electrons of different kinetic energies; the information is processed to produce a spectrum of photoelectron intensity as a function of binding energy (Figure II.18 spectrum of PS). The kinetic energy E_k is related to the binding energy E_b according to

$$E_k = h\nu - E_b - \psi \tag{2.15}$$

where $h\nu$ is the quantum energy of the X-rays (h is Planck's constant and ν is the X-ray frequency) and ψ is the work function.

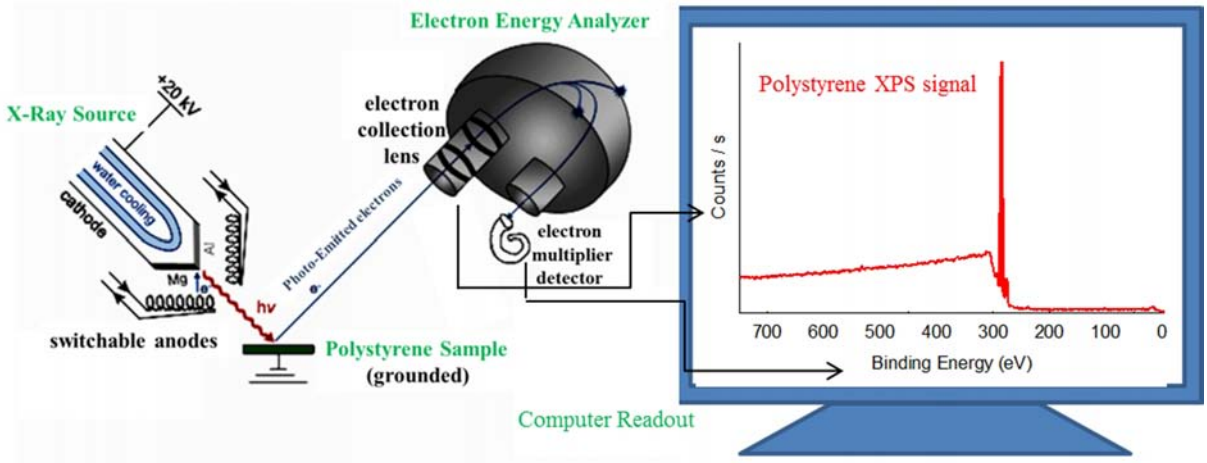

Figure II.18: Representation of the monochromatic XPS system [32] and XPS spectra of 300 nm film of polystyrene.

The binding energy of a particular shell of an atom is unique for each element which allows its identification. For example Figure II.18 shows a scan spectrum of a polystyrene film sample. Only one major feature is present – the C – 1s line at about 284.6 eV. If there are several signals, the relative proportion of different species is determined from the area under each peak. The simplest approach to rough quantification is to simply divide the peak area by the Scofild factor (also called photoionization cross section). The normalized values are then used to calculate atomic ratios or percentages [27].

2.3.5. Zeta potential

The zeta potential ζ, also known as the electrokinetic potential, is a descriptive parameter of the charge distribution at the interface between a solid surface and a surrounding liquid [33,34].
The, zeta potential is the electric potential in the interfacial double layer (DL) at the location of the slipping plane versus a point in the bulk fluid far away from the interface.

2.3.5.1. Double Layer (DL)

As mentioned in previous chapter, when a solid is in contact with a liquid it may acquire some immobilized charge on its surface by dissociation, complexation or adsorption. The immobile charge on the surface attracts an exact number of excess ions from the liquid in order to make the interface electro neutral; they form the so-called electrical double layer. The first layer is the plane of charge. The second is a spaced distribution of charges (held) near the solid by the balance between electrostatic forces and diffusion. One consequence of this charge distribution is a position-dependent electrical potential, which varies from zero far from the surface and reaches a maximum near the surface.

In 1879, Helmholtz [35] was the first to introduce a theoretical model of the electrical double layer. He described it as a simple capacitor, based on a physical model in which a single layer of ions is adsorbed at the surface. However, this simple model was not appropriate to explain observed electrokinetic effects. Later, Louis Georges Gouy [36] in 1910 and David Chapman in 1913 [37] made a significant improvement by introducing the model of the electrical DL, which considered it as a diffuse layer of counter ions whose concentration decreased with the distance from the surface. This model is also imperfect, as unrealistically high concentrations of counter ions are predicted close to the surface. The model of DL most often used combines the ideas of the above models, and is the result of research carried out by Stern [38] in 1924. In the Gouy-Stern model, the electrical double layer is viewed as consisting of two distinct regions: the excess charges in the electrolyte are distributed between a layer of counter ions situated at the shortest possible distance from the charged surface (the rigid layer), and a diffuse layer. From (Figure II.19) we can see that the double layer thus defined has a certain structure. The Inner Helmholtz Plane (IHP) is the plane cutting through the center of the adsorbed species. The Outer Helmholtz plane (OHP) is the plane cutting through the counter ions at

their position of closest approach (stern layer). There also exists a diffuse layer, which is extended from OHP into the bulk solution. The diffuse layer is ruled by Boltzmann statistics.

Several potentials can then be designed: a) the surface potential,ψ^0; b) the potential at the inner Helmholtz plane, IHP, ψ^β c) the potential at the OHP, ψ^d; and d) the electrokinetic or zeta potential at the shear plane, ζ. All these potentials are defined with respect to the potential at an infinite distance from the surface. Although the surface potential is an important parameter, the potential at the OHP is practically even more important since it represents the actual potential influencing the behavior of the charged species. However, as this potential cannot be measured directly, the zeta potential is often considered as an adequate substitute [33].

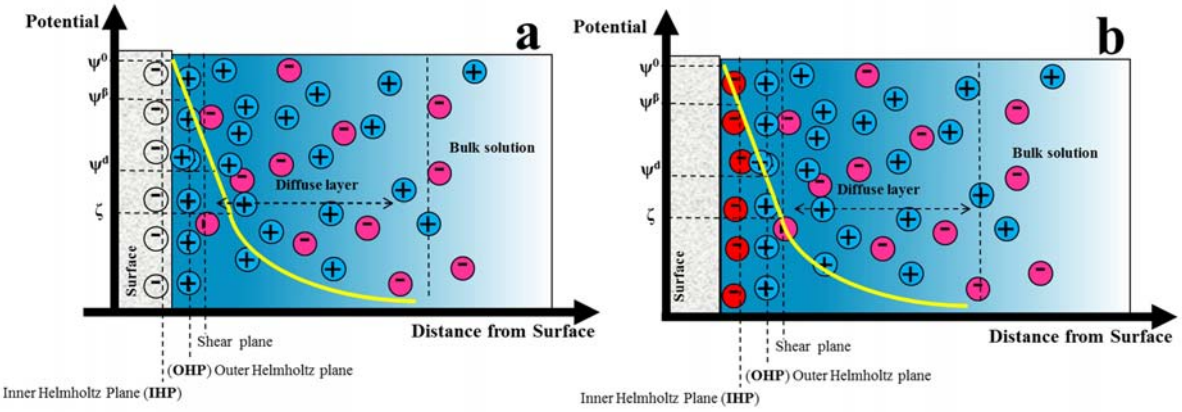

Figure II.19: Schematic representation of the decrease in potential across a double layer as a function of the distance from the surface.

Zeta potential is the charge that develops at the interface between a solid surface and its liquid medium. This potential, which is measured in MilliVolts, may arise by any of several mechanisms. Among these are the dissociation of ionogenic groups in the sample surface and the differential adsorption of solution ions into the surface region (Figure II.20-b).

Usually the, zeta potential is measured indirectly using one of three means:

- by measuring electroosmotic mobility,
- by measuring the response of a small spherical particle to an applied E-field,
- by measuring the streaming current or the streaming potential generated by pressure-driven flow through a conduit or across a channel formed by two plates.

2.3.5.2. Streaming Potential

Instead of applying an electric field to force a liquid to move through a capillary or porous plug we can force an electrolyte solution to move through a capillary, porous plug or across a channel formed by two plates by applying a pressure gradient. The excess charges near the wall are carried along channel by the liquid and their accumulation downstream causes an electric field to build-up, generating a potential difference. This potential opposes the mechanical transfer of charges, causing back-conduction by ion diffusion and electro-osmotic flow (due to the potential difference). The

transfer of charges due to these two processes is called the leak current. When equilibrium condition is attained the streaming current cancels the leak current the potential difference across the channel is called the streaming potential, denoted by *E* [34] (Figure II.20).

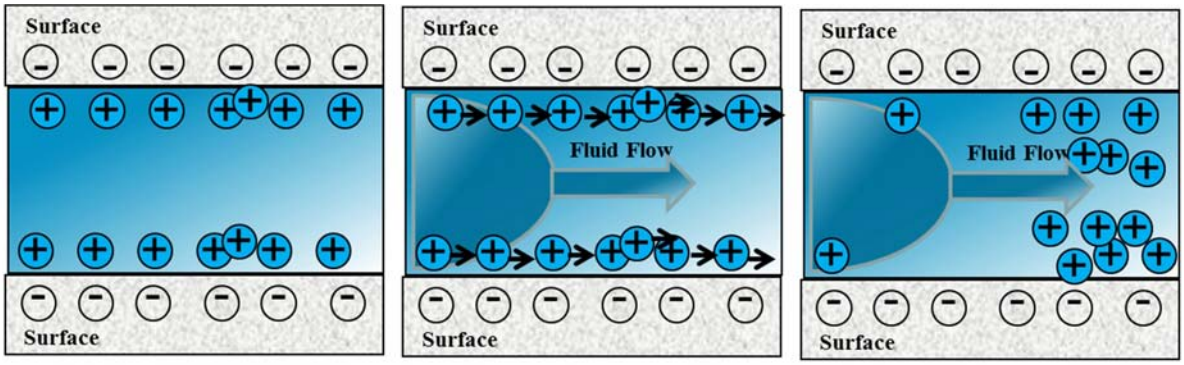

Figure II.20: Schematic representation of the streaming potential measurement. An electrical charge distribution is generated at a solid/liquid interface. The liquid flow initiates a charge separation, which leads to the formation of a potential difference, the streaming potential.

The zeta potential of a macroscopic solid surface is calculated from the slope of the linear dependence of streaming current (or streaming potential) on the differential pressure P using the classical Helmholtz-Smoluchovski formula [39],

$$\zeta = \frac{\lambda \eta E}{\varepsilon P} \quad \text{where} \tag{2.16}$$

ε - permittivity

η – viscosity of solution

λ - conductivity

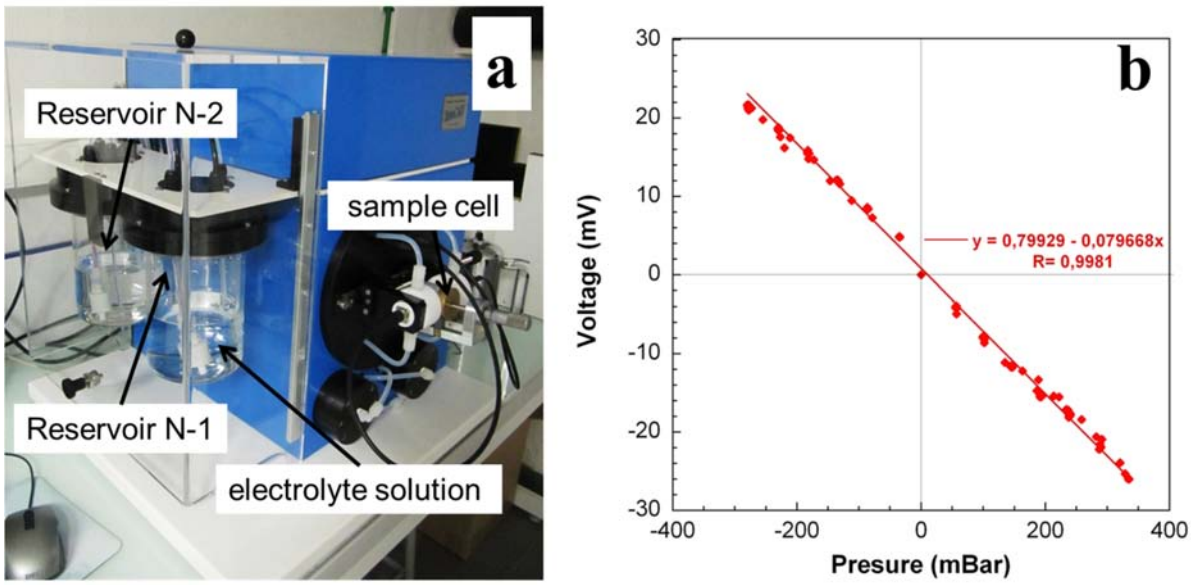

Figure II.21. (a) ZetaCAD-DC instrument, (b) linear dependence of the potential difference on the differential pressure for a polystyrene film on silicon wafer, in 10^{-3}M tetramethylammonium iodide ($(CH_3)_4N(I)$) aqueous solution. From the slope of this line and the measured conductivity the zeta potential can be calculated by using Eq(2.16).

In this thesis, measurements of streaming potential were performed using a ZetaCAD-DC instrument (Figure II.21a). It measures the electrical conductivity of the solution, the temperature and the streaming potential over a sequence of increasing pressures, in order to determine the slope *dU/dP* or *dI/dP*. When the relationship between these two variables is linear (Figure II.21b) the slope *dU/dP* is proportional to the zeta potential. In the measurements, the flow is made in both directions to remove the effect of any asymmetry through the cell from reservoir 1 to reservoir 2. The choice of the measuring cell for mounting the solid samples depends on the sample shape and size. Fibres and coarse powder samples are measured with the Cylindrical Cell. The experimental results discussed in this thesis were obtained with the cells represented in (Figure II.22.a-b). Polymer coated samples (rectangular pieces of 25mm×10mm Figure II.22.c) were mounted in the cell and the measurements were performed in the presence of different aqueous electrolyte solutions and at different pH values.

Figure II.22. (a) ZetaCAD cell with constant gap, (b) CRPP made cell with adjustable gap and (c) polystyrene coated silicon wafer sample (25mm×10mm) mounted on a cell component.

2.3.5.3. The Grahame equation

After having measured the surface potential, we might want to estimate the number of charged groups on a surface. The question is: how are surface charge σ and surface potential ψ^0related?

In 1947 Grahame derived an equation between σ and ψ^0 based on the Gouy–Chapman theory. This equation can be deduced from electroneutrality conditions. This condition imposes that the total charge (surface charge plus the charge of the ions) in the whole double layer must be equal to zero. The total charge in the double layer is $\int_0^\infty \rho_e dx$. We get [40]

$$\sigma = -\int_0^\infty \rho_e dx \tag{2.17}$$

Using the one-dimensional Poisson equation and the fact that at large distances the potential and its gradient, are zero $(d\psi / dx\big|_{z=\infty} = 0)$ we get

$$\sigma = \varepsilon\varepsilon_0 \int_0^{\infty} \frac{d^2\psi}{dx^2} dx = -\varepsilon\varepsilon_0 \left. \frac{d\ \psi}{dx} \right|_{x=0} \tag{2.18}$$

With $dy/dx = -2k\sin(h * y/2)$ and

$$\frac{dx}{dy} = \frac{d(e\psi/k_B T)}{dx} = \frac{e}{k_B T} \cdot \frac{d\psi}{dx} \tag{2.19}$$

We get the Grahame equation:

$$\sigma = \sqrt{8c_0 \varepsilon\varepsilon_0 k_B T} \cdot \sin(h)\left(\frac{e\psi_0}{2k_B T}\right) \tag{2.20}$$

For low potentials we can expand sin(h) into a series (sin(h) = $x + x^3 / 3$!+…..) we get a simple relationship

$$\sigma = \frac{\varepsilon\varepsilon_0 \psi_0}{\lambda_D} \tag{2.21}$$

where the Debye length λ_D=k^{-1} is given by $k = \sqrt{\frac{e^2}{\varepsilon\varepsilon_0 k_B T} \sum_i c_0^i Z_i^2}$. Here Z_i is valency for ith ion.

For a monovalent salt in water at 25°C, the Debye length is given by [23]:

$$\lambda_D = \frac{3.04\ \mathring{A}}{\sqrt{c_0 \frac{L}{mol}}} \tag{2.22}$$

with the concentration $c_0$in mol/L. For monovalent so-called 1:1 salts.

2.3.6. Atomic Force Microscope

Atomic force microscopy (**AFM**) is a method of measuring surface properties on a scale from angstroms to 100 microns. AFM [41] is based on Scanning Tunneling Microscopy (STM) [42], developed by Binnig and Rohrer, who were awarded the Nobel Prize in Physics in 1986. In STM, a conductive sample is investigated by measuring the tunneling of electrons from the surface atoms to the tip of an ultra sharp electrode [42]. To overcome the restrictions of STM, Binnig, Quate and Gerber [41] develop the atomic force microscope (AFM). The basic AFM mode involves measuring the topography of the sample by the use of a tip with a radius of 10-20 nm. The tip is held in contact or several nanometers away from the surface by using a feedback controlled mechanism that measures surface–tip interactions. Variations in tip position are recorded while the tip is scanned repeatedly across the sample, producing a topographic image of the surface.

In addition to basic AFM, modern instruments are capable of producing images in a number of other modes, including tapping, magnetic force, electrical force, and pulsed force. Magnetic force mode imaging utilizes a magnetic tip to enable the visualization of magnetic domains on the sample. In electrical force mode imaging a charged tip is used to locate and record variations in surface charge. In pulsed force mode, the sample is oscillated beneath the tip, and a series of force-distance curves are generated. This permits the separation of sample topography, stiffness, and adhesion simultaneously producing three independent images, or three individual sets of data.

The key element in an AFM is the microscopic force sensor, a cantilever with a sharp tip that is mounted on its end, used to sense the force between the sample and the tip. The first AFM used a diamond tip attached to a gold-foil cantilever [43]. In our days both are made using microfabrication techniques. Cantilevers are usually made from beams of silicon or silicon nitride that are 100 to 500μm long and about 0.5 to 5μm thick. Tips are usually conical or pyramidal; the radius of their apex can be as small as 1-10 nm. Besides the cantilever and the tip, AFM comprises a cantilever holder, a piezo scanner, a deflection detection system and a feedback loop. The principle of the operation of an AFM using these principal components is schematically shown in (Figure II.23).The experiment starts by placing a sample on a piezoelectric scanner tube to precisely move it in the 3 dimensions. Then the tip is brought near the surface. In order to measure the up and down movements of the tip an optical method is typically used. First, a laser beam is focused on the back of the cantilever. From there the laser beam is reflected towards a photodetector. If the cantilever is deformed due to the interaction force between the tip and the surface, the position of the reflected beam also changes. With the help of the photodetector this change is converted into an electrical signal. An electronic feedback control keeps the cantilever deflection constant by adjusting the z position of the sample. This height information of the sample is finally plotted in the xy-plane and a force map or topographic picture of the sample surface is obtained.

The deflection of the cantilever reflects the forces of interaction between tip and the surface, according to Hooke's law

$$F = k \cdot z \tag{2.23}$$

Here, *k* is the elastic constant of the cantilever and z is the vertical deflection of the end of the cantilever.

Atomic Force Microscopy has become a widely used high resolution imaging tool in different fields. True atomic resolution has been obtained on a wide range of inorganic surfaces including metals, semiconductors and insulators [44,45,46,47]. AFM has been used to image several organic surfaces, organic crystals and organic thin films deposited *via* Langmuir–Blodgett or self-assembly process [48,49,50].The AFM is an unique tool for the *in situ* investigation of biological surfaces [51], biomolecules, cell structures, or even viruses [52] due to its sensitivity to small forces and its ability to operate in liquids. AFM has opened up new possibilities of investigation of colloidal systems [53,54],

and it is contributing significantly to our understanding of the surface structure of polymers, both on a microscale and at the molecular level.

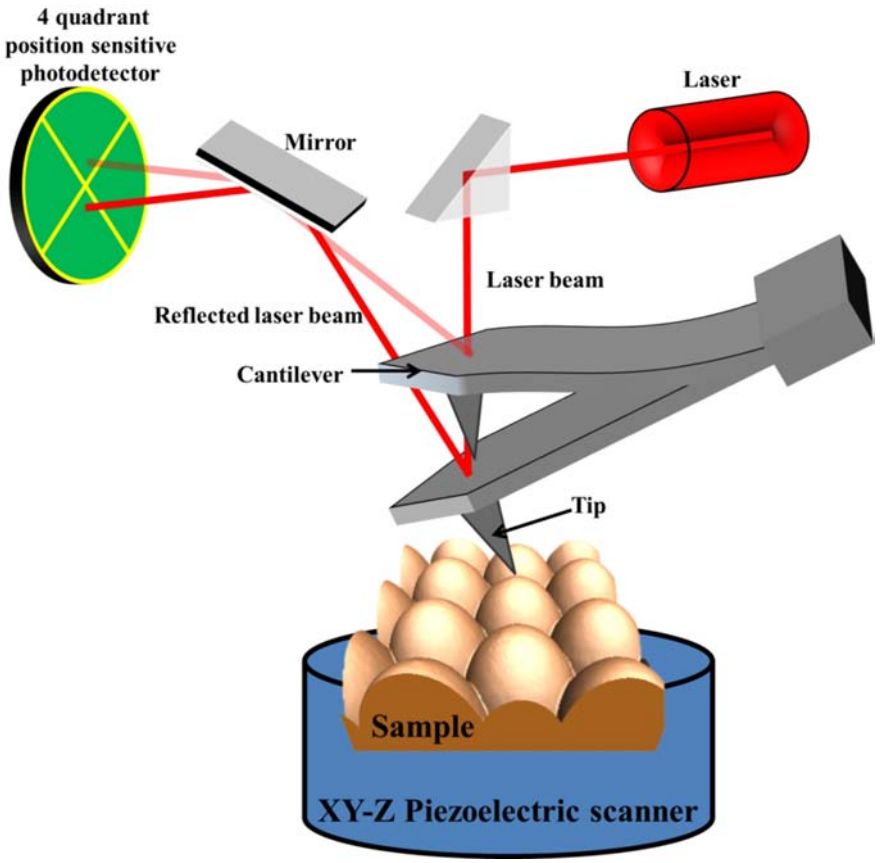

Figure II.23: Schematic setup of an atomic force microscope (AFM).

2.3.6.1. Imaging of polymer surfaces

Atomic Force Microscopy was first applied to polymer surfaces in 1988, shortly after its invention [55]. Today, these studies range from relatively simple morphology visualization to more advanced examination of polymer structures and properties at the nanometer scale. Several scanning modes can be employed to probe a sample of a polymer surface.

2.3.6.1. Contact Mode

In the so-called **contact mode**, also known as repulsive mode, the tip is brought in hard contact with the surface at all times. The tip is attached to the end of a cantilever with a spring constant between 0.001 to 100 N/m, lower than the effective spring constant holding the atoms of the sample together. As the scanner gently slides the tip across the sample surface (or the sample under the tip), a feedback mechanism is utilized to keep the deflection, of the cantilever constant (and hence force). As the cantilever is deflected the *z*-height (the position of the sample or the cantilever) is altered to cause a return to the original deflection or set point. The change in *z*-position is monitored and this information is used to create a topographical image of the sample surface as a function of the *x*,*y* position.

Contact mode is often the mode of choice when imaging a hard and relatively flat surface due to its simplicity of operation. However, there are several inconvenience of this mode. The tip is permanently in contact with the surface while scanning; hence, a considerable shear force is generated, causing damage to the surface, and contaminating the tip from material removed from the surface. Because the measurement of a static signal is predisposed to noise and drift, low stiffness (≈ 0.1 N/m) cantilevers usually are used to improve the quality of the deflection signal. Image contrast in contact mode depends on the applied force between the tip and the sample, with typically ranges from 10^{-11} to 10^{-7} N.

2.3.6.2. Taping Mode

The mode most often used in the analysis of the polymer structures in this thesis is called **tapping** or **intermittent contact mode**. In this mode, the cantilever is oscillated just below its resonance frequency (150-300 kHz) with amplitude of a few tens of nm. When the oscillations occur close to a sample surface, the probe will repeatedly engage and disengage with the surface, restricting the amplitude of the oscillation. As the surface is scanned, the oscillatory amplitude of the cantilever will change as it encounters a changing topography. By using a feedback mechanism to alter the *z*-height of the sample constant oscillation amplitude is maintained; an image of the surface topography may be obtained as in contact mode imaging.

In contrast to the contact mode, the tip only briefly hits, or "taps" the sample surface, thereby reducing the damage done to the sample surface during scanning. In proximity to the surface, the forces on the tip influence the frequency, the amplitude and the phase of the oscillation which are determined by the adhesion and stiffness of the contact. In addition to topographic information, the interaction of the tapping tip and the surface provides information on the mechanical properties of the surface material.

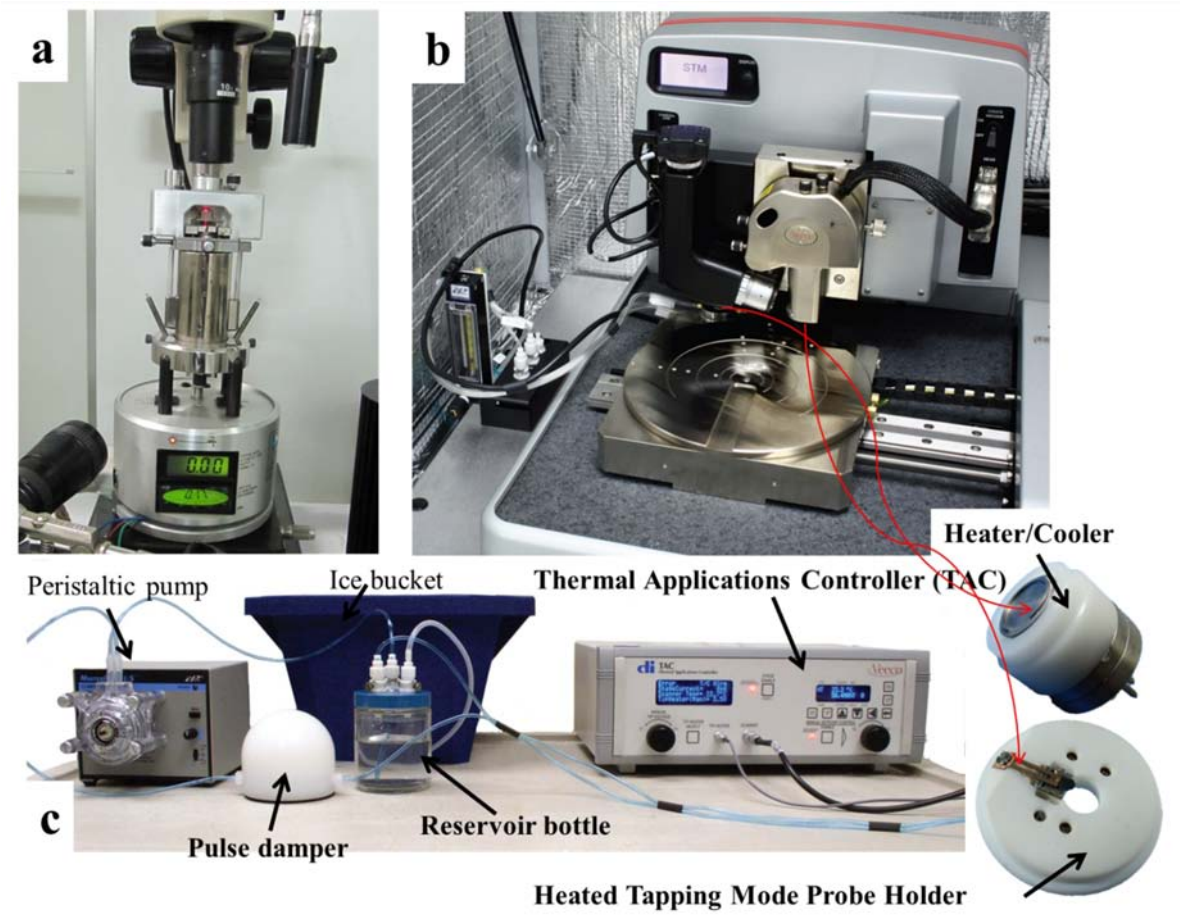

Figure II.24: (a)Atomic force microscope (Multi Mode-IIIa) from Digital Instruments, (b) Veeco's Icon P–Series AFM and (c) lower heater and cooler system components; ceramic dimension heater/cooler tip holder, heater/cooler element, Thermal Applications Controller (TAC) which set and control the sample temperature, fluid cooling system witch cools the reservoir inside the Dimension Heater/Cooler base.

A Multi Mode IIIa Digital Instruments (Figure II.24. a) was used in some of our experiments. The Multi-Mode is designed for imaging small samples (approx. 1.5 cm in size). It is equipped with the J-type scanner which has a maximum scan area of 125X125 μm^2 and Z – limit of 5 μm. The Multi-Mode is attached to an optical microscope for precise location of a desired area on a sample. For samples larger than 1.5 cm in diameter and for high temperature imaging we used Veeco's Icon P–Series AFM, with X-Y scan range 90μm X 90μm and 10μm Z range (Figure II.24. b) . Veeco's Icon P–Series AFM is equipped with heating and cooling systems. The primary components of this system include a heated probe holder, a heating element and/or a heating-cooling element and a Thermal Applications Controller (TAC) (Figure II.24). These components allow to investigate samples at temperatures up to 250°C and down to -35°C with precise control, while stepping or cycling through thermal ranges. The software controls the temperature of tip, and sample.

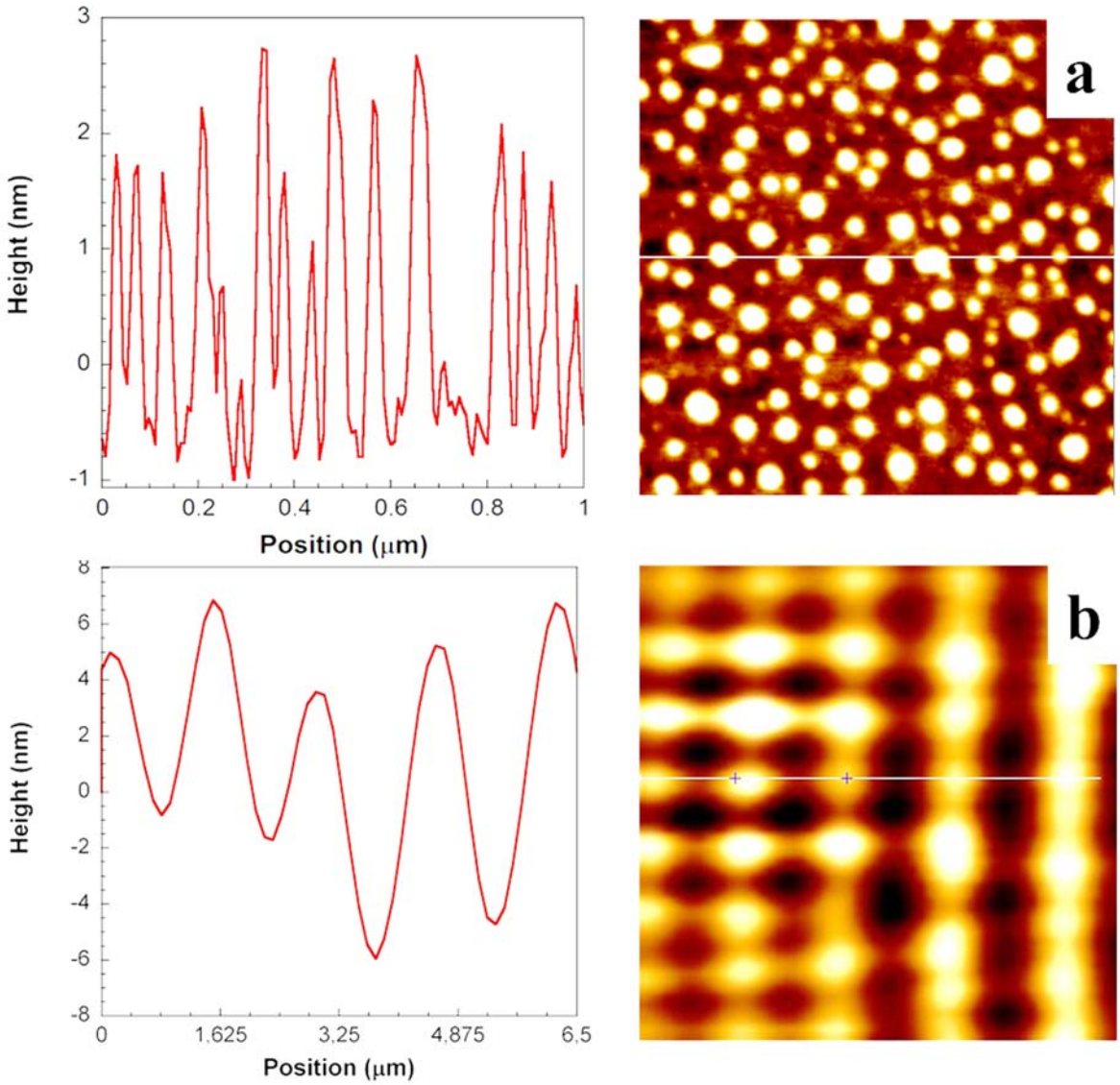

Figure II.25: (a) AFM image of a 300 nm polystyrene film exposed to degassed sodium hydroxide (NaOH) aqueous solution of pH=11.5. The presence of bumps with mean height h=3nm and mean diameter d=30nm can be observed; (b) AFM image of a 200 nm thick polystyrene film exposed to an electric field at room temperature; the cross-section show structures with an average height 7,8 nm and inter- spacing of λ= 1,55μm

AFM control and data analysis of the results presented in this thesis were done with the Nanoscope software v5.12r3 and Nanoscope software 8.00. We used these programs to characterize the morphology of polymer surface, their roughness and to characterize the patterned polymer films (Figure II.25), as will be discussed later in more detail

2.3.7. Surface Forces Apparatus (SFA)

A whole range of phenomena in interfacial science revolve around the effects of surface forces. For this reason scientists have devoted considerable effort to the understanding of surface forces and exploring pathways to influence them.

The first direct surface force measurements were made between two polished glass bodies [56]. One body was fixed, and the other was mounted on a spring. The distance between the two surfaces and the deflection of the spring were measured; the product of the spring deflection by the spring constant gave the force between the surfaces. Using of these simple early devices made it possible to verify the theoretically predicted van der Waals force for glass interacting with glass across a gaseous medium [57,58].Later, Derjaguin, Rabinovich, and Churaev measured the force between two thin metal wires, to determine the van der Waals force between metals [59]. In these early measurements several problems became obvious. The minimal distance accessible (≈ 100 nm) was rather limited; in addition experiments could not be performed in liquid environments. The development of the **Surface Forces Apparatus** (SFA) [60,61] was a big step forward; it is the first experimental technique used to successfully measure forces between surfaces as a function of their separation (force law) for distances below 100 nm. The SFA allows measurement of forces between surfaces (with accuracy of 10^{-7} N) in liquids and vapors, and of surface separation (by interferometry) with accuracy of ± 1 Å [62]. Several modified SFA models have been developed by Klein [63], Parker, [64] Israelachvili and McGuiggan [65] and Granick and coworkers [66,67] in order to improve the accuracy and simplicity of the technique. Furthermore, Tonck et al. [68] have extended the SFA method to opaque materials, replacing the optical technique for measuring distances by a capacitance method.

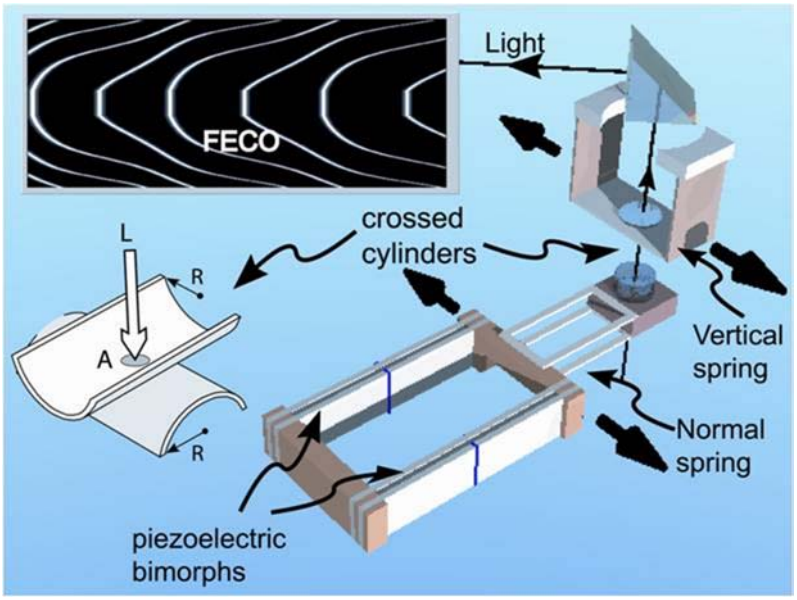

Figure II.26: The Surfaces Forces Apparatus (design by Israelachvili). Mica surfaces are supported on two hemicylindrical lenses perpendicularly oriented, and are attached to the friction sensing device and the piezoelectric bimorph slider. The samples with reflecting silver mirrors in their back-sides form a Fabry-Perot interferometer. White light passed through the surfaces generates a series of interference fringes (when it is spectrally resolved). The curvature of the fringes corresponds to the curvature of the contact region between the samples.

In the SFA instrument, the samples of interest are typically supported, coated or a adsorbed on the surfaces of very thin, atomically flat ~1–5μm thick mica sheets that are fixed to the surfaces of two

crossed hemicylindrical, silica lenses (Figure II.26). The radii of the polished hemicylinder lenses is 1–2 cm [69,62]. The cylindrical shaped of the silica disks and the placement of the disks with their axes perpendicular to each other is very important. It makes relatively easy to find an unique contact spot between the surfaces (avoiding edge effects), and to investigate different contact spots on the same pair of surfaces: in case of contamination of the surfaces during the experiment, a fresh contact zone can be readily found by laterally displacing the crossed cylinders. The accurate and absolute measurement of the distance between the surfaces, D, is central to the SFA technique. In interferometric SFAs, it is realized through an optical method called multiple beam interferometry (MBI), which has been described by Samuel Tolansky [70].

The back side of the mica surfaces is coated with reflective 40-50 nm silver films, so that the region between the silver mirrors forms the resonant cavity of a Fabry-Perot interferometer. When white light (with a continuous spread of wavelengths) is transmitted thought the stratified media between the mirrors, only the discrete wavelengths of constructive interference pass through the multilayer system. Light transmitted by the interferometer can be spectrally decomposed in a series of interference fringes of equal chromatic order (FECO) (Figure II.26), whose wavelengths are determined by the thicknesses and refractive indices of the various layers between the two silver mirrors.[71,70]. The transmitted wavelengths change continuously with changes in the surface separation D [71]. The fringes shift to longer (shorter) wavelengths with increasing (decreasing) separation.

By measuring wavelength shifts of the FECO, the thickness of the sandwiched film and its refractive index can be determined with an accuracy of 0.1 nm and 0.01 respectively. Israelachvili developed simple explicit expressions to perform these calculations [71].

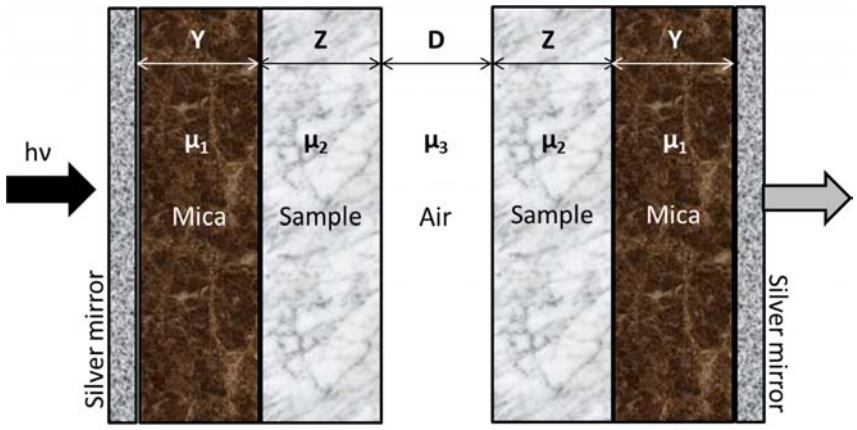

Figure II.27: Schematic representation of polymer films contained in the resonant cavity of SFA forming a 5 – layer interferometer. The five layers are mica, samples on mica surface, and air or water. The thicknesses of the layers are Y, Z and respectively D. The corresponding refractive indices are μ_1, μ_2, and μ_3.

In force measurements between coated polymer layers interacting across an air/aqueous gap, the interferometer contains five layers (Figure II.27): two mica sheets, two polymers films (samples), and the air/aqueous gap between them, with thicknesses Y, Z, and D, and refractive indices μ_1, μ_2, and

μ_3. From the calculated reflection and transmission coefficients of the interferometer, it was shown that for this five-layer interferometer (Figure II.27), [71] the wavelength shifts $\Delta\lambda_n$ (the shift in wavelength λ of the nth order fringe from the position D = 0) are related to changes in the separation ΔD by

$$\Delta D = \frac{n\Delta\lambda_n}{2\mu_1} - 2Z \text{ for odd order fringe (n odd) and} \tag{2.24}$$

$$\Delta D\mu_3^2 = \frac{n\Delta\lambda_n}{2\mu_1} - 2Z\mu_2^2 \text{ for even order fringes (n even).} \tag{2.25}$$

These analytical expressions are valid for small Z and D, and when the interferometer is symmetric (when two mica sheets and polymer films have exactly the same thickness). The problem of calculating surface separations from a given FECO pattern for asymmetric multi-layer interferometers which is more complex has been solved by applying the multilayer matrix method [72] by Clarkson [73]. Later, useful analytical expressions for asymmetric interferometers were derived by Horn et al [74].

Equation (2.24) shows that changes in the odd order fringes only depend on the known refractive index of the mica μ_1. In contrast, changes in the even order fringes depend on the refractive indices: of mica, polymer layer, and air/water (Equation 2.25). As the refractive indices of the mica and air/water are known, the refractive index or thickness of polymer films be determined from the wavelength shifts measured on even and odd order fringes using simultaneously equations (2.24) and (2.25).

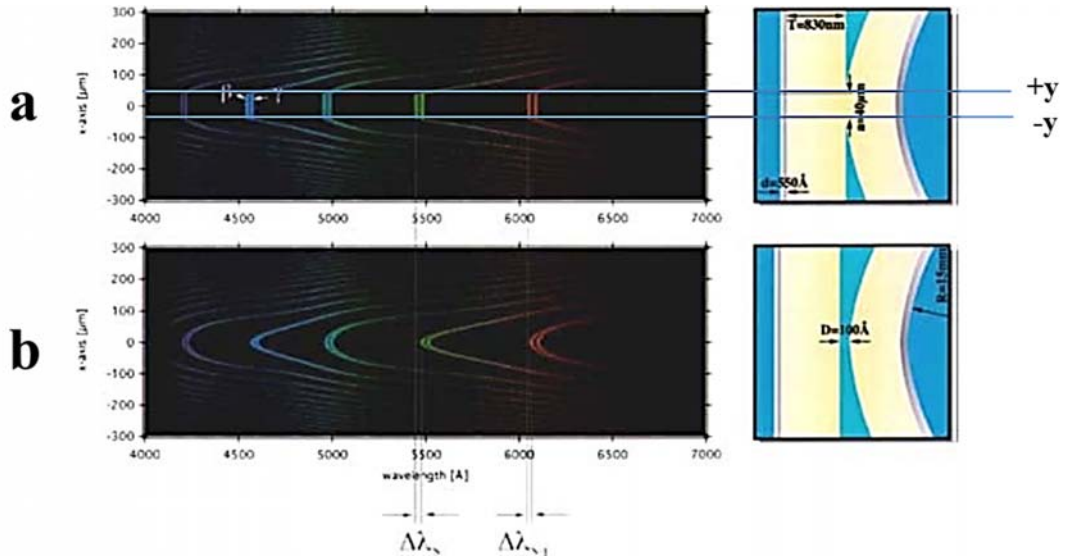

Figure II.28: Example of distortion in interference fringes resulting from surface deformation (flattening). The elastically deformed contact region appears as flattened region in the shapes of the fringes in graph (a). The distance from –y to +y is the diameter of contact area and is measured directly from the interference fringes. Once the surfaces are separated to the distance D the fringes are smoothly curved (b).The wavelength shifts are measured to calculate D and the refractive index n of the medium between the surfaces [75].

Another advantage of the interferometric technique used in the SFA is having direct access to the contact shape. Not only the surface separation can be measured precisely, but also the precise shape of the contact region can be determined. The fringes will be smooth curves when there is a gap between surfaces, as shown in (Figure II.28.b), and top-flatten when the contact zone becomes flat under load (Figure II.28.b) or under the effect of adhesion. Theories of contact mechanics (e.g., theories of Hertz or Johnson, Kendall and Roberts, JKR) can then be assessed [76,77].

The measurement of surface forces out-of-plane (normal to the surfaces) is the original purpose of the SFA technique. Given the facility for moving the surfaces toward or away from each other and independently measuring their separation, (each with sensitivity or resolution of about 0.1 nm) the force measurements become straightforward. Normal forces between the surfaces are measured by displacing the distal end of the double-cantilever with respect to the opposite surface a known amount by using a differential micrometer, motor-driven fine micrometer and/or piezo elements, and then measuring optically how much the separation between the two surfaces have actually changed. Any difference between the two values indicates a deformation of the double cantilever spring it gives the force difference between the initial and final positions when multiplied by the stiffness of the force-measuring spring. Thus, if the surfaces are initially at $Z > 0$ where the force between them is $F(D_0)$, and the piezoelectric crystal is expanded by ΔD_P so that the surface separation changes by ΔD_S to D, the force at D is related to the force at D_0 by

$$F(D) = F(D_0) + (\Delta D_P - \Delta D_S)K \tag{2.26}$$

where K is the stiffness of the force-measuring spring. Thus, if $\Delta D_P = \Delta D_S$ we have $F(D) = F(D_0)$, so that if the force is zero at D_0, it is also zero at D. However, if $\Delta D_P > \Delta D_S$ we have $F(D) > F(D_0)$ and the force at D is repulsive, whereas if $\Delta D_P < \Delta D_S$ we have $F(D) < F(D_0)$ and the force at D is attractive. In this way, by starting at some large separation where there is no detectable force and working systematically towards smaller separations both repulsive and attractive forces can be measured with a sensitivity of about 10^{-7} N and the full force-law can be obtained over any distance regime.

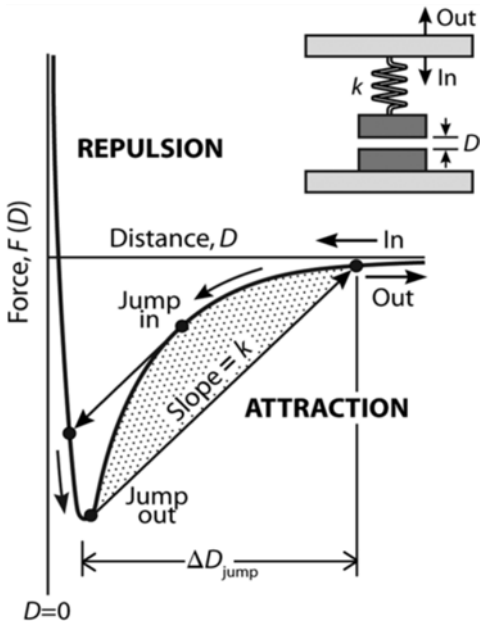

Figure II.29: Typical force law or force distance profile F(D) showing the instabilities that occur at the positions shown, manifested by jump in on approach and jump out on separation. Jump instability take place if the spring constant k is lower than the slope of the F(D) curve [78].

2.3.7.1. Adhesion Energy

Adhesion forces are measured from the force that it takes to separate surfaces (pull-off force) from adhesive contact by measuring the distance that they jump apart from contact, ΔD_{jump} (Figure II.29), and then using the following equation:

$$F_{pulloff} = k \times \Delta D_{jump} \quad (2.27)$$

where k is the spring constant. In investigations of adhesion, a key parameter is the work required to separate two surfaces, or the adhesion energy per area. Adhesion energy per unit area E_A between equivalent flat plates in the case of SFA cylindrically curved surfaces is directly proportional to the normalized pull-off force between the two surfaces normalized by their radius F_{po}/R. Exact relationship depends on the extent the surfaces deform when in contact. For large deformations under the influence of the intersurface forces or the external load, the Johnson-Kendall-Roberts theory relates the pull-off force to the adhesion energy per unit area by:

$$E_A = 2F_{po}/3\pi R \text{ [79]} \quad (2.28)$$

On the contrary, if deformations are small, the adhesion energy is better described by the Derjaguin-Müller-Toporov theory, in which

$$E_A = F_{po}/2\pi R \text{ [23]} \quad (2.29)$$

2.3.7.2. Measuring shear (friction and lubrication) forces

To measure the friction between surfaces one has to laterally drive one of the surfaces and simultaneously measure the force induced by this motion [80].

In our setup, inspired in the design of Israelachvili, lateral movement of the lower surface is driven by a BIMORPH-SLIDER (Figure II.30), which produces lateral motion when a constant slope voltage ramp is applied between the two electrodes of sectored piezoelectric bimorphs (electromechanical transducers). Sinusoidal, saw-tooth, square and other types of displacement functions can be fed to the slider, with amplitudes in the range of 0.1-40V (producing a lateral displacement of 1μm to 20μm) and a frequency range from 0.001 to 2Hz. The upper surface is itself attached to a vertical double cantilever spring, whose deflection is monitored using semiconductor strain gauges connected to form the arms of a Wheatstone bridge. This assembly is called the FRICTION DEVICE. If the displacement of the lower surface induces a viscous or friction force on the upper surface, the vertical spring will deflect. From the deflection of this spring of known spring constant *K*, the friction force between the surfaces *F* can be calculated, simply by using Hooke's law of elasticity.

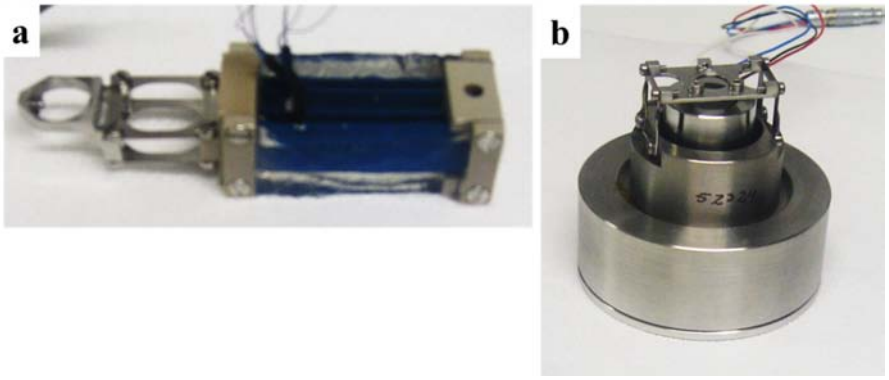

Figure II.30: (a) Bimorph, (b) Friction Device of SFA.

2.3.7.3. Experimental procedure

One very crucial factor for a successful SFA experiment is absolute cleanliness of the device and work space. Experiment usually starts with the preparation of thin mica sheets. This is a delicate process that requires some experience and often takes 1–2 days. Mica cleaving is carried out in a dust free laminar flow cabinet. Powder free gloves should be worn in order to prevent contamination of the mica surfaces.

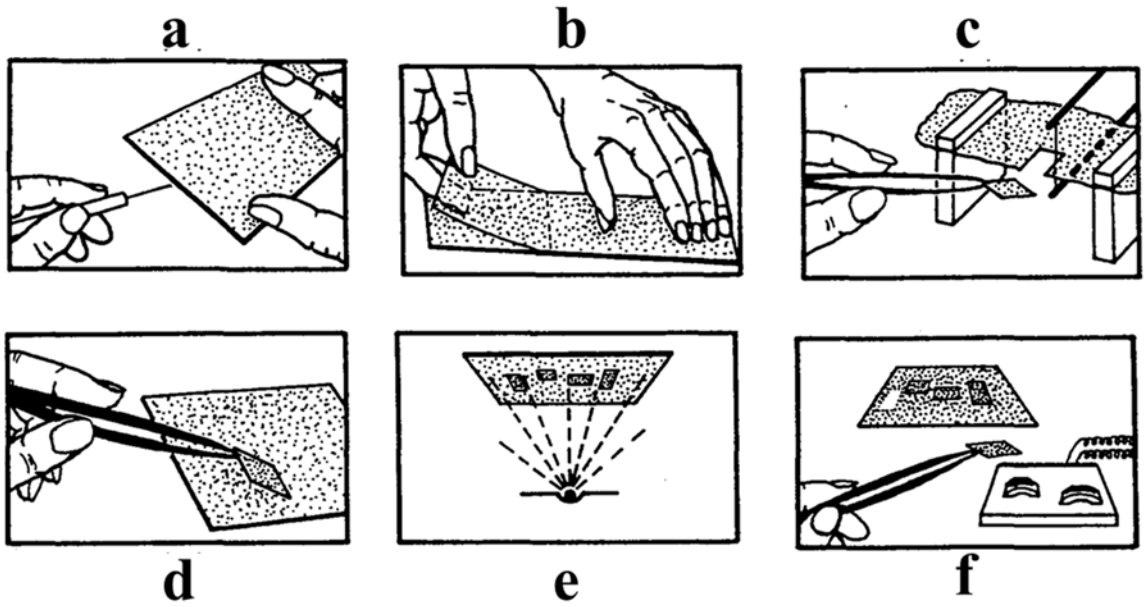

Figure II.31: Stages in preparation of mica sheets: (a)-(b) cleaving, (c) cutting, (d) placing cut sheets on baking sheet, (e) silvering, (f) gluing (placing) silvered mica sheets on silica disks.

In our experiments natural Ruby Muscovite mica was used. Muscovite mica was selected because of its high quality, hardness and excellent cleavage properties permitting it to be split into the thinnest sheets without the risk of cracking. Cleaving mica involves insertion of a sharp needle into an edge or corner of the mica sheet and strike off against the van der Waals forces between the layers. First, a large and thick mica sheet is selected and its edges are trimmed with scissors. Top and bottom dirty superficial layers should be removed by cleaving with a sharp needle. It is inserted into the edge of the thick sheets (Figure II.31.b) and moved along the cracking gap; two pieces of mica are obtained. One of the sheets is chosen as "backing sheet". The other is kept for further cleaving of much thinner and smaller sheets to be used as substrate surfaces for experiments. The procedure of cleaving thin mica sheets from a thick sheet should be done in as stress-free way possible, and usually is achieved by slowly peeling a thin sheet from a thicker one. The procedure of pealing is repeated until thin regions of 1-5 micrometres thick, step-free and several square centimetres in area are obtained. The uniform area should be at least 2 cm^2 in order to cut two rectangular pieces from it with a hot platinum wire. Subsequently, the newly cleaved film is placed across two clean metal blocks (Figure II.31.c), and held by two smaller metal blocks over its edges. A platinum wire of diameter 0.1 mm which is mounted between two parallel conducting rods and heated above the melting point of mica is used to cut the mica film into rectangular shape pieces of approximately (1 × 1) cm^2. Finally, the pieces are placed onto the backing sheet, which serves as a holder for the subsequent thermal evaporation of the silver mirrors. When several pairs of mica sheet are attached onto the backing sheet, it is ready to deposit silver on the uncovered surfaces (Figure II.31.e). We use an Edwards Auto 306 Vacuum coating system for the silver deposition. This was performed at high vacuum with a pressures below

10^{-6}torr. The silver thickness deposited on the mica film is measured with a QCM sensor. A thickness of 400 Å deposited at 1 Å/s is advised.

The next step in SFA experiment is gluing mica onto silica disks. The silica disks act as optical windows and support for mica films. Each disk has two polished surfaces with diameter of about 10 mm. One of the two surfaces is optical flat and the other is cylindrically curved, with a radius of about 2 cm. EPON RESIN 1004 was used to glue mica on the silica disks for measurements in aqueous solutions; for experiments in organic solvent such as toluene, a mixture 50%/50% of glucose and galactose was used. Before gluing the mica films the silica disks (conserved in chloroform to remove glue from previous experiments) are cleaned with chloroform, washed with ethanol, dried with dry nitrogen gas and finally irradiated for 20–30 minutes in an UV-ozone cleaner. After cleaning, the silica disks are placed on a small electrically heated hot plate (around 150°C). A tiny amount of glue in powder form (EPON RESIN or sugars) is then placed on the top cylindrically curved surfaces of the disks. As the glue melted, curved tweezers are used to spread it in uniform layers over the curved surfaces, and a small mica sheet was peeled off from the back sheet with sharp tweezers and placed on the top of the glue layer with silver coating facing down. The disk was then removed from the hot plate. The mica surface is ready for experiment, coating or further modifications. When surfaces are ready, silica disks are mounted into the disk holders of the SFA. First, the lower disk is placed into the disk holder of the Bimorph Slider with the polymer film facing up. The other silica disk is mounted in the disk holder on the Friction Device with the surface facing down. Once the silica disks are fixed by tightening the set screws, the devices are placed in the SFA chamber (Figure II.32).

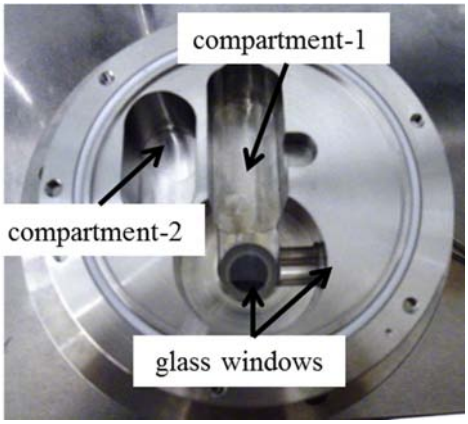

Figure II.32: SFA chamber

The SFA chamber is manufactured from stainless steel with a wall thickness of 10 mm, equipped with two glass windows (thickness: 150 μm) which allow optical measurements in transmission, and two compartments. The first one is used to place the surfaces and bathing solutions (around 350mL), in case of experiments in liquid. The second one is a special cavity where a container with drying an agent (typically phosphorus pentoxide P_2O_5) can be placed to maintain anhydrous experimental conditions.

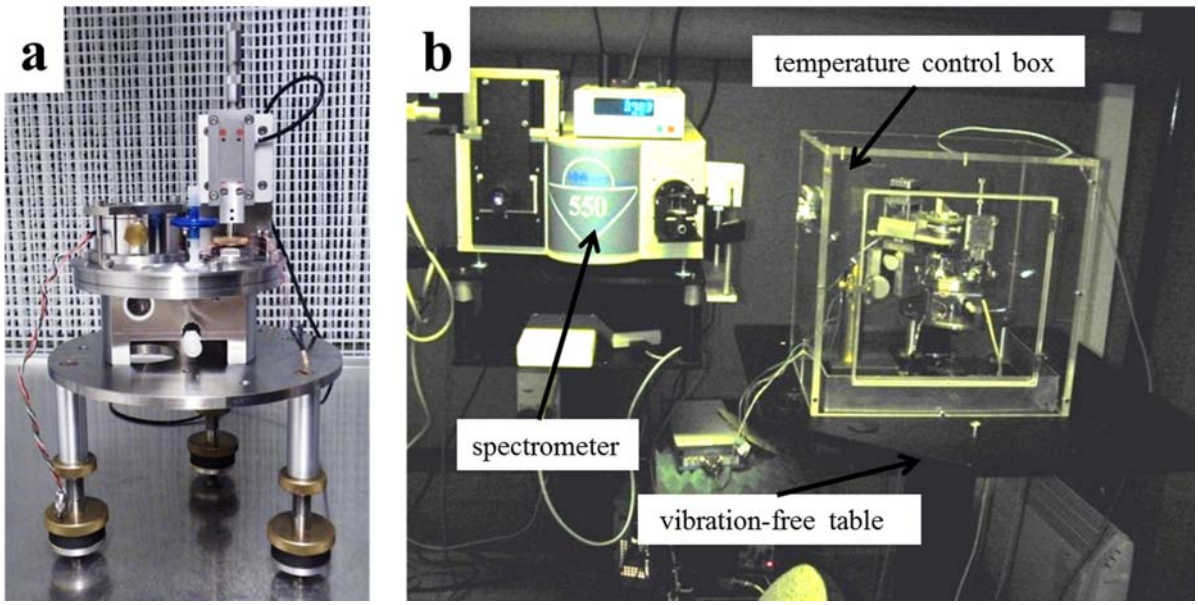

Figure II.33: (a) Assembled Surface Forces Apparatus device, (b) SFA placed on a vibration-free table inside a temperature control box.

An assembled SFA (Figure II.33.a), is placed on a vibration-free table inside a (temperature controlled box) (Figure II.33.b).

During SFA experiments, the surface separation is controlled by a coarse manual micrometer, afine manual differential micrometer and piezoelectric positioned (Physik Instruments). As already mentioned, measurements of the thickness and refractive index of polymer films are realized by MBI. The light transmitted through the sample is decomposed by a fully automated spectrometer TRIAX-550 and recorded with a digital CCD camera (EURECA, LSD-5000T1-8EPP). A spectral calibration mercury lamp with lines at λ_1 = 546.075 nm, λ_2 = 576.96 nm and λ_2 = 579.066 nm is used to calibrate the spectrometer. All major components of the SFA device are computer controlled via home written Labwindows programs.

2.4. References

[1] Gaines, G.L. & Tabor, D. Surface Adhesion and Elastic Properties of Mica.*Nature* **178**, 1304-1305 (1956).
[2] Israelachvili, J.N. &McGuiggan, P.M. Forces Between Surfaces in Liquids. *Science* **241**, 795 -800 (1988).
[3] Israelachvili, J.N. & Adams, G.E. Measurement of forces between two mica surfaces in aqueous electrolyte solutions in the range 0-100 nm.*J. Chem. Soc., Faraday Trans. 1:***74**, 975 (1978).
[4] Emslie, A.G., Bonner, F.T. & Peck, L.G. Flow of a Viscous Liquid on a Rotating Disk.*J. Appl. Phys.* **29**, 858 (1958).
[5] CEPSR. Spin Coat Theory. http://www.clean.cise.columbia.edu/process/spintheory.pdf.
[6] J.-P. Chapel, M. Morvan, PCT Int. Appl. WO 2007126925 A2 20071108 (2007)
[7] Brzoska, J.B., Azouz, I.B. &Rondelez, F. Silanization of Solid Substrates: A Step Toward Reproducibility.*Langmuir* **10**, 4367-4373 (1994).
[8] Sagiv, J. Organized monolayers by adsorption. 1. Formation and structure of oleophobic mixed monolayers on solid surfaces. *Journal of the American Chemical Society***102**, 92-98 (1980).
[9] Barrat, A., Silberzan, P., Bourdieu, L. &Chatenay, D. How Are the Wetting Properties of Silanated Surfaces Affected by Their Structure? An Atomic-Force Microscopy Study.*Europhys.Lett.***20**, 633-638 (1992).
[10] Wasserman, S.R., Tao, Y.T. &Whitesides, G.M. Structure and reactivity of alkylsiloxane monolayers formed by reaction of alkyltrichlorosilanes on silicon substrates. *Langmuir* **5**, 1074-1087 (1989).
[11] Bigelow, W.C., Pickett, D.L. &Zisman, W.A. Oleophobic monolayers : I. Films adsorbed from solution in non-polar liquids.*Journal of Colloid Science* **1**, 513-538 (1946).
[12] Silberzan, P., Leger, L., Ausserre, D. &Benattar, J.J. Silanation of silica surfaces.A new method of constructing pure or mixed monolayers.*Langmuir* **7**, 1647-1651 (1991).
[13] Roberts, G. Langmuir-Blodgett Films.*Plenum Press, New York* (1990).
[14] Gaines, G.L. Insoluble Monolayers at the Liquid-Gas Interface.*Wiley-Interscience, New York* (1996).
[15] www.wikipedia.com.
[16] Schäffer, E. PhD Thesis: Instability in Thin Films: Structure Formation and Patern Transfer. *University of Konstanz* (2001).
[17] Nano film technologie. www.nanofilm.de.
[18] Tompkins, H. Handbook of Ellipsometry.*William Andrew Inc* (2005).
[19] http://en.wikipedia.org/wiki/Ellipsometry
[20] Hiroyuki, F. Spectroscopic Ellipsometry,Principles and Applications. *John Wiley & Sons* (2007).
[21] Herman, I.P. Optical Diagnostics for Thin Film Processing.*Academic Press* (1996).
[22] Supporting manual, Operating Instruction EP3.
[23] Israelachvili, J. Intermolecular and Surface Forces.*Academic Press, London* (1992).
[24] Quéré, D. Rough ideas on wetting.*Physica A, 313 32* (2002).
[25]de Gennes, P.G. Wetting: statics and dynamics.*Rev. Mod. Phys.***57**, 827 (1985).
[26]Tadmor, R. Line Energy and the Relation between Advancing, Receding, and Young Contact Angles.*Langmuir* **20**, 7659-7664 (2004).
[27] Andrade, J.D. Surface and interfacial aspects of biomedical polymers.Vol. l.*New York: Plenum Press* (1985).
[28] Jiang J. &Kucernak A.The electrochemistry of platinum phthalocyanine microcrystals - I. Electrochemical behaviour in acetonitrile electrolytes.*ElectrochimicaActa* **45**, 2227-2239 (2000).
[29] Petersen, R. et al. Pyrolysis of Poly(ferrocenylsilanes): Synthesis and Characterization of Ferromagnetic Transition-Metal-Containing Ceramics and Molecular Depolymerization Products. *Chemistry of Materials***7**, 2045-2053 (1995).
[30] Rulkens, R. et al. Linear Oligo(ferrocenyldimethylsilanes) with between Two and Nine Ferrocene Units: Electrochemical and Structural Models for Poly(ferrocenylsilane) High Polymers. *Journal of the American Chemical Society* **118**, 12683-12695 (1996).
[31]Foucher, D.A., Tang, B.Z. & Manners, I. Ring-opening polymerization of strained, ring-tilted ferrocenophanes: a route to high-molecular-weight poly(ferrocenylsilanes). *Journal of the American Chemical Society* **114**, 6246-6248 (1992).
[32] http://www.chem.queensu.ca.
[33] Lyklema, J. Fundamentals of Interface and Colloid Science, Vols.I and II.*Academic Press, London* (1991).
[34] Hunter, R.J. Zeta Potential in Colloid Science.*Academic Press, London* (1981).
[35] Helmholtz, von H.L.F. Studienuberelectrischegrenzschichten. *Ann. Phys.***7**,337–382 (1879).
[36] Gouy, M.G. Sur la constitution de la charge electriqueala surface d'un electrolyte. *Journal de Physique et le Radium* **9**, 457-468 (1910).
[37] Chapman, D.L.A contribution to the theory of electrocapillarity.*Philos. Mag.* **25***,* 475-481 (1913).
[38] Stern, O. ZurTheorie der ElectrolytischenDoppelschicht.*Z. Electochem.* **30**, 508 (1924).
[39] Smoluchowski, M. Handbuch der Electrizität und des Magnetismus Vol. II.*Barth. Leipzig.* (1921).

[40] Grahame, D.C.The electrical double layer and the theory of electrocapillarity.*Chem. Rev* **41**, 441-501 (1947).
[41] Binnig, G., Quate, C.F. & Gerber, C. Atomic Force Microscope.*Phys. Rev. Lett.* **56**, 930 (1986).
[42] Binnig, G., Rohrer, H., Gerber, C. &Weibel, E. 7 x 7 Reconstruction on Si(111) Resolved in Real Space. *Phys. Rev. Lett.***50**, 120 (1983).
[43] Micromachined silicon sensors for scanning force microscopy.*Journal of Vacuum Science & Technology B: Microelectronics and Nanometer Structures* **9**, 1353-1357 (1991).
[44] Erlandsson, R., Olsson, L. &Mårtensson, P. Inequivalent atoms and imaging mechanisms in ac-mode atomic-force microscopy of Si(111)7 x 7. *Phys. Rev. B* **54**, R8309 (1996).
[45] Fukui, K.-ichi, Onishi, H. &Iwasawa, Y. Atom-Resolved Image of the TiO2(110) Surface by Noncontact Atomic Force Microscopy. *Phys. Rev. Lett.* **79**, 4202 (1997).
[46] Erlandsson, R., Hadziioannou, G., Mate, C.M., McClelland, G.M. & Chiang, S. Atomic scale friction between the muscovite mica cleavage plane and a tungsten tip. *J. Chem. Phys.***89**, 5190 (1988).
[47] Roark, S.E. &Rowlen, K.L. Atomic force microscopy of thin Ag films.Relationship between morphology and optical properties.*Chemical Physics Letters* **212**, 50-56 (1993).
[48] Overney, R.M. et al. Molecular surface structure of organic crystals observed by atomic force microscopy. *Ultramicroscopy* **42-44**, 983-988 (1992).
[49] Schwartz, D.K., Viswanathan, R. &Zasadzinski, J.A.N. Commensurate defect superstructures in a Langmuir-Blodgett film.*Phys. Rev. Lett.* **70**, 1267 (1993).
[50] Bourdieu, L., Ronsin, O. &Chatenay, D. Molecular Positional Order in Langmuir-Blodgett Films by Atomic Force Microscopy.*Science* **259**, 798 -801 (1993).
[51] Vansteenkiste, S.O., Davies, M.C., Roberts, C.J., Tendler, S.J.B. & Williams, P.M. Scanning probe microscopy of biomedical interfaces. *Progress in Surface Science***57**, 95-136 (1998).
[52] Ikai, A., Yoshimura, K., Arisaka, F., Ritani, A. & Imai, K. Atomic force microscope of bacteriophage T4 and its tube-baseplate complex.*FEBS Letters* **326**, 39-41 (1993).
[53] Senden, T.J., Pashley, R.M. & Ducker, W.A. Direct measurement of colloidal forces using an atomic force microscope.*Nature* **353**, 239–241
[54] Larson, I., Drummond, C.J., Chan, D.Y.C. &Grieser, F. Direct force measurements between titanium dioxide surfaces.*Journal of the American Chemical Society* **115**, 11885-11890 (1993).
[55] Albrecht, T.R. et al. Imaging and modification of polymers by scanning tunneling and atomic force microscopy. *J. Appl. Phys.***64**, 1178 (1988).
[56] Derjaguin, B.V., Titijevskaia, A.S., Abricossova, I.I. &Malkina, A.D. Investigations of the forces of interaction of surfaces in different media and their application to the problem of colloid stability. *Discuss. Faraday Soc.* **18**, 24 (1954).
[57] Rouweler, G.C.J. &Overbeek, J.T.G. Dispersion forces between fused silica objects at distances between 25 and 350 nm. *Trans. Faraday Soc.***67**, 2117 (1971).
[58] Black, W., de Jongh, J.G.V., Overbeek, J.T.G. &Sparnaay, M.J. Measurements of retarded Van Der Waals' forces. *Trans. Faraday Soc.* **56**, 1597 (1960).
[59] Derjaguin, B.V., Rabinovich, Y.I. &Churaev, N.V. Direct measurement of molecular forces.*Nature* **272**, 313-318 (1978).
[60]Tabor, D. &Winterton, R.H.S.The Direct Measurement of Normal and Retarded van der Waals Forces.*Proceedings of the Royal Society of London. A. Mathematical and Physical Sciences* **312**, 435 -450 (1969).
[61]Israelachvili, J.N. & Tabor, D.The shear properties of molecular films.*Wear* **24**, 386-390 (1973).
[62] Israelachvili, J.N. & Adams, G.E. Measurement of forces between two mica surfaces in aqueous electrolyte solutions in the range 0-100 nm.*J. Chem. Soc., Faraday Trans. 1:***74**, 975 (1978).
[63]Klein, J. Forces between mica surfaces bearing layers of adsorbed polystyrene in cyclohexane.*Nature* **288**, 248-250 (1980).
[64] Parker, J.L., Christenson, H.K. &Ninham, B.W. Device for measuring the force and separation between two surfaces down to molecular separations.*Rev. Sci. Instrum.***60**, 3135 (1989).
[65] McGuiggan, P.M. &Israelachvili, J.N. Adhesion and short-range forces between surfaces. Part I: New apparatus for surface force measurements. *Journal of Materials Research***5**, 2223-2231
[66] Van Alsten, J. &Granick, S. Molecular Tribometry of Ultrathin Liquid Films. *Phys. Rev. Lett.***61**, 2570 (1988).
[67] Peachey, J., Van Alsten, J. &Granick, S. Design of an apparatus to measure the shear response of ultrathin liquid films.*Rev. Sci. Instrum.* **62**, 463 (1991).
[68] Tonck, A., Georges, J.M. &Loubet, J.L. Measurements of intermolecular forces and the rheology of dodecane between alumina surfaces.*Journal of Colloid and Interface Science* **126**, 150-163 (1988).
[69] Israelachvili, J.N. Adhesion forces between surfaces in liquids and condensable vapours.*Surface Science Reports* **14**, 109-159 (1992).
[70] Tolansky, S. Applications of multiple-beam interferometry.*Nature* **167**, 815-816 (1951).

[71] Israelachvili, J.N. Thin film studies using multiple-beam interferometry. *Journal of Colloid and Interface Science* **44**, 259-272 (1973).
[72 Born, M. & Wolf, E. Principles of optics. Cambridge University Press: (1980).
[73] Clarkson, M.T. Multiple-beam interferometry with thin metal films and unsymmetrical systems.*J. Phys. D: Appl. Phys.* **22**, 475-482 (1989).
[74] Horn, R.G. & Smith, D.T. Analytic solution for the three-layer multiple beam interferometer. Appl. Opt. 30, 59-65 (1991).
[75]Heuberger, M. The surface forces apparatus. *Encyclopedia of Chemical Physics and Physical Chemistry - 3 Volume Set* (2001).
[76]Golan, Y., Drummond, C., Israelachvili, J. &Tenne, R. In situ imaging of shearing contacts in the surface forces apparatus. *Wear* **245**, 190-195 (2000).
[77] Luengo, G., Schmitt, F.-J., Hill, R. &Israelachvili, J. Thin Film Rheology and Tribology of Confined Polymer Melts: Contrasts with Bulk Properties.*Macromolecules* **30**, 2482-2494 (1997).
[78] Israelachvili, J. et al. Recent advances in the surface forces apparatus (SFA) technique. *Rep. Prog. Phys.* **73**, 036601 (2010).
[79] Johnson, K.L., Kendall, K. & Roberts, A.D. Surface Energy and the Contact of Elastic Solids.*Proceedings of the Royal Society of London. A. Mathematical and Physical Sciences* **324**, 301 -313 (1971).
[80] Drummond, C. &Richetti, P. Surface Forces Apparatus in Nanotribology. *Fundamentals of Friction and Wear* 15-33 (2007).

Chapter III

Electric-Field-Induced Instability in Glassy Polymer Films

Table of contents of Chapter III:

This chapter starts with a brief introduction about previous studies related to the patterning of thin films of dielectric materials by an applied electric field. It is followed by the description of the experimental setup used to investigate the electric-field-induced EFI patterns on polystyrene films at temperatures below its glass transition temperature. In the second half of the chapter experimental results concerning generation of spontaneous EFI instability are presented. Further, the morphology of the films at short and long times of exposure to electric field is described. These results support the idea of substantial mobility of polymer molecules at the surface of thin films of glassy polymer films. This mobility can be used to create self-organized patterns on polystyrene films, as will be described in this and later chapters.

3.1. Introduction

As was described in Chapter I, there is a large body of work, both theoretical [1,2,3,4,5,6] and experimental [7,8,9,10,11,12,13] related to the study of the effect of electric fields on thin films, in particular related to their controlled destabilization and patterning. Studying these self-assembly methods of patterning (self-assembly because the ordered structures are formed spontaneously through the application of an external driving force; the patterns are not manipulated individually) is interesting not only from the viewpoint of pattern formation but also for the potential applications in the coatings industry, where creating uniform films is extremely important. It is particularly difficult to create ultrathin films less than 100 nanometers thick due to the destabilizing van der Waals interactions [14]. Surface patterning is known to impact optical, adhesive, and wetting properties of materials, particularly in soft materials. Carefully controlling these properties is important for technological applications such as biomaterials, microfluidics, coatings, and polyelectrolyte multilayer films. Many of the polymer patterns produced by the EHD instability are on the order of microns, the right length scale for biological applications. For example, an array of polystyrene micron-sized pillars was used to study the effect of three dimensional topologies on cells shape and migration [15]. Biological materials such as proteins and cells often adhere to other biological surfaces. In designing devices for biological applications it is important to improve the adherence properties [16]. In microfluidic devices, surface topography influences the hydrophobicity of a surface [17]. The appearance of coated materials is dictated by the light reflection properties of the coating [18] which is strongly influenced by the surface topography.

Most of the reported experimental work on electric-field induced polymer patterning have used polystyrene or poly(methyl methacrylate), because:

- They are easy to process. PS and PMMA practically do not have a vapor pressure above the entanglement limit. Material loss due to evaporation is therefore not a problem and dissolution of polymers in volatile solvents enables easy processing.

- Their glassy character. The experiment can be performed at elevated temperatures above the glass transition in the liquid state, while the analysis can take place at room temperature where any structure will be frozen in the glassy state.
- Finally, due to the entanglements, the viscosities of polymers are normally rather large resulting in long relaxation times

From the theoretical point of view, EHD instabilities of these polymers are also easy to characterize because at temperatures above the glass transition temperature T_g they can be described as incompressible viscous fluids.

There is still much to learn about these materials and how they interact with their surroundings. In particular, some recent studies support the idea of a heterogeneous dynamic of thin glassy polymer films [19]. The existence of a mobile layer several nanometers thick on top of polystyrene and PMMA polymer films at temperatures well below the glass transition temperature is gaining general acceptance in the polymer physics community [20]. There are some open questions which deserve to be further investigated:

- Can glassy films be easily deformed at room temperature under external electric field?
- Can EFI self-organized patterns be created on glassy polymer films due to interface mobility? If so, which are the parameters that control the surface structuration?

In this chapter I will discuss an experimental study related to these questions.

3.2. Theoretical aspects

The theoretical description of the behavior of thin films subjected to the effect of an external electric field can be very involved; a number of parameters have to be considered. First, the viscoelastic properties of the film need to be characterized: as I will describe below, liquid and solid films show very different responses to an applied field. The electrical parameters of the film also have to be specified. Currents and charge accumulation will be different in perfect conducting, perfect insulators (dielectric) or leaky dielectrics (i.e. poorly conducting) films, determining the effect of an externally applied field on the film. The possibility of dielectric breakdown of the film may need to be considered at sufficiently high field strengths. The intensity and nature of the field may also play a role. In general, DC and AC fields may produce different effects: the frequency of the applied field also needs to be considered. I will briefly outline some relevant theoretical results related to some of the cases mentioned.

3.2.1. Perfect dielectric liquid films

As described in Chapter I, the instability length scale in a purely viscous liquid film has a long-wave character governed by a competition between the destabilizing field strength and surface tension [21,22,23,24,25,26,27,28,29,30].

For thin liquid films the overall pressure distribution at constant temperature at the film surface can be expressed as [31]:

$$p = p_0 - \gamma \frac{\partial^2 h}{\partial x^2} + p_{el}(Z) + p_{dis}(Z) \tag{3.1}$$

with p_0 being the atmospheric pressure. The second term, the Laplace pressure, stems from the surface tension γ and the fourth term, the disjoining pressure p_{dis}, arises from dispersive Van der Waals interactions. The electrostatic pressure for a given electric field in the polymer film according to Landau and Lifshitz is given by [32]:

$$p_{el} = -\varepsilon_0 \varepsilon_p (\varepsilon_p - 1) E_p^2 \tag{3.2}$$

As mentioned before, for large enough values of E_p, only the Laplace and electrostatic terms need to be considered. In a stability analysis, a small sinuscidal perturbation of the interface with wave number q, growth rate t^{-1}, and amplitude u is considered:

$$Z(x,t) = Z_0 + ue^{iqx + t/\tau} \tag{3.3}$$

The modulation of Z gives rise to a lateral pressure gradient inside the film, inducing a Poiseulle flow j

$$j = \frac{Z^3}{3\eta}\left(-\frac{\partial p}{\partial x}\right) \tag{3.4}$$

where η is the viscosity of the liquid. The continuity equation enforces mass conservation of the incompressible liquid:

$$\frac{\partial j}{\partial x} + \frac{\partial Z}{\partial t} = 0 \tag{3.5}$$

Equations (3.3), (3.4), and (3.5) define a differential equation that describes the dynamic response of the interface to the perturbation. In a linear approximation (to order O(u)), a dispersion relation is obtained:

$$\frac{1}{\tau} = -\frac{Z_0^3}{3\eta}(\gamma q^4 + \frac{\partial p_{el}}{\partial Z} q^2) \tag{3.6}$$

As opposed to the inviscid, gravity-limited case ($t^{-1} \propto q$), the viscous stresses lead to a q^2-dependence of in the long-wavelength limit, typical for dissipative systems. Fluctuations are amplified if $\tau > 0$.
Since

$$\frac{\partial p_{el}}{\partial Z} < 0 \tag{3.7}$$

all modes with

$$q < q_c = \sqrt{-\frac{1}{\gamma}\frac{\partial p_{el}}{\partial Z}} \tag{3.8}$$

are unstable. With time, the fastest growing mode will eventually dominate, corresponding to the maximum in Eq (3.6)

$$\lambda = 2\pi \sqrt{\frac{\gamma U}{\varepsilon_0 \varepsilon_p (\varepsilon_p - 1)^2}} E_p^{-\frac{3}{2}} \tag{3.9}$$

To compare the results of the dispersion relation to the experimental data, it is useful to introduce reduced variables:

$$\lambda_0 = \frac{\varepsilon_0 \varepsilon_p (\varepsilon_p - 1)^2 U^2}{\gamma} \tag{3.10}$$

and

$$E_0 = \frac{U}{\lambda_0} \tag{3.11}$$

Equation (3.9) leads to

$$\frac{\lambda}{\lambda_0} = 2\pi \left(\frac{E}{E_0}\right)^{-\frac{3}{2}} \tag{3.12}$$

λ_0 is a characteristic length scale which is connected to the relative strength of the electrostatic and Laplace pressures. In addition, Eq. (3.6) gives a relation for the time constant of the instability:

$$\frac{\tau}{\tau_0} = \pi^4 \left(\frac{E}{E_0}\right)^{-6} \tag{3.13}$$

3.2.2. Perfect dielectric solid and viscoelastic films

Electric field induced mesopatterning can also be achieved directly in soft solid elastic films, but the underlying physics that governs the structure length scale and morphology is quite distinct from that of a liquid film [33,34,35,36,37,38,[39]. In a purely elastic solid, theory predicts a short-wave character with its length scale depending linearly on the film thickness, regardless of the field strength or elastic modulus. The elastic contact instability is understood to arise from a competition between the destabilizing forces (e.g. electrostatic pressure) and the stabilizing restoring elastic forces in the film. As will be described below, the wavelength of this instability is predicted to be about three times the film thickness in the limit of high applied fields, and is essentially independent of all other factors such as the interfacial interactions and the mechanical properties. For the submicron films surface tension also becomes important.

The behavior of viscoelastic films under electric field have been less studied compared with liquid and solid elastic films. However, there are some recent theoretical studies on electric-field-induced instabilities in liquid like viscoelastic films [40,41] and solid films [42]. Recently, Jayati Sarkar and Ashutosh Sharma [43] reported a unified theory of the stability of soft viscoelastic thin films that covers the different regimes of instability in systems of nanoscopic to microscopic thickness. They developed a general linear stability analysis of the film morphology, which gives the following dispersion relation for a visco-elastic thin film with constant viscous and elastic moduli:

$$\left(\frac{\eta\omega}{\mu}\right) = \left[-\left(\frac{\eta}{h\mu}\right)q^2 + (h/\mu)S\right](2qY(q))^{-1} - 1) \tag{3.14}$$

where $q = kh$, $Y(q) = ((1 + e^{2q})^2 + 4e^{2q}q^2)(-1 + e^{4q} - 4e^{2q}q)^{-1}$ and $S = \left(\frac{\partial\pi}{\partial h}\right) = \varepsilon_0\varepsilon_p V^2\left(1 - \varepsilon_p\right)^2(\varepsilon_p d + h)^{-3}$ where ω is the growth coefficient of instability, k is its wave number, γ is the surface tension, μ the elastic modulus, η the viscosity, d the air gap, h the film thickness, π the excess electric pressure at the interface, ε_0 the dielectric permittivity of the free space, ε_p the dielectric constant of the film and V the applied voltage.

The electric field driven surface instability of viscoelastic films was shown to have two distinct regimes: (1) Liquid-like films display long wavelengths governed by applied voltage and surface tension, independent of its rheological properties, and (2) solid-like films require to overcome a threshold voltage for the instability to develop. The characteristic wavelength is proportional to the

film thickness, h, but does not depend of its surface tension, γ, applied voltage (as long as it is higher than the threshold) or rheological properties. They shown that the critical wavenumber of viscoelastic perfect dielectric films, both in wetting and adhesive configurations, have two asymptotic limits of short waves and long waves that are determined only by the parameter γ/μh, where μ is the storage modulus. The solid-like limited is expected at values $\gamma/\mu h<10^{-2}$. In this limit, the critical wavelength remains roughly constant ($\lambda = 2.96h$). In the other limit, where $\gamma/\mu h >1$, the wavelength is close to the long-wave regime of viscous wetting films. As shown in Figure III.1, the transition between short and long waves can be achieved, e.g., by varying the elastic modulus [34,38,42].

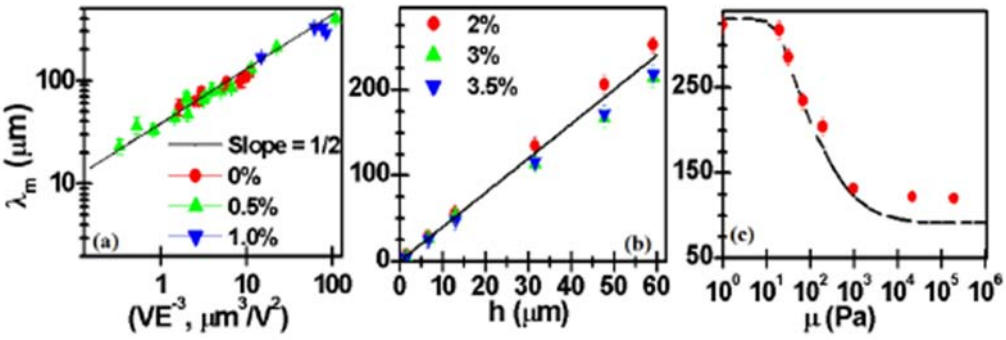

Figure III.1: Characteristic wavelength of field-induced patterns on PDMS thin films. The viscoelastic properties of PDMS films where tuned by varying the cross-linker CL concentration. (a) Liquid-like layers The line represents the viscous film theory (b) solid-like viscoelastic films, the slope of the line is 4.1. (c) Transition between the liquid like and the solid like regimes. Results from [42].

From the above relation, the liquid-like scaling is obtained when the parameter (γ/hμ) is large, whereas the solid-like scaling $\lambda \approx 3h$ is recovered for small (γ/hμ). Interestingly, the wavelength in all cases is independent of viscosity, which only determines the time necessary for the instability to develop. Further, in both the liquid-like and the solid-like regimes, it also becomes independent of the elastic modulus, which remains important only in the transition regime. Basically, in the liquid-like regime, surface tension is the dominant stabilizing mechanism, whereas in the solid-like regime, the elastic strain dominates. The transition is thus governed both by surface tension and elasticity in the form of the parameter, (γ/hμ).

3.2.3. Leaky dielectric films

To describe the behavior of poorly conducting films the possibility of charge movement and accumulation needs to be considered. This case is much more complicated than the discussed above because one needs to consider the field generated by a non-uniform distribution of charges. In addition, the charges-induced field has a shear stress component (not present in the case of conductors or perfect dielectrics) which complicates further the theoretical description. It has been shown that when a leaky dielectric film is subjected to an external field, charges move to the interface resulting in electrically induced stresses substantially larger than for perfect dielectrics: both free and polarization charges are present at the dielectric surface. Even a small surface charge density decreases significantly the voltage necessary to destabilize an interface. [1,2,14]. Therefore, even a poor

conductivity significantly decreases the patterns wavelength (and increases growth rates) of a film destabilized by an electric field compared with the case of perfect dielectrics. This can be inferred from the expressions derived by Pease and Russel to describe leaky-dielectrics. However, to make a quantitative assessment of the lengthy expressions derived in refs. [1,2] requires the knowledge of parameters that are not easily accessible experimentally (surface charge density or potential). For this reason we did not pursue this path in this thesis.

3.2.4. AC vs DC fields

So far I have discussed how DC electrostatic fields can be used to modify the topography of thin films creating patters of controlled λ. It may also of interest to explore the possibilities of applying AC fields for film structuration; it has been theoretically predicted that AC fields could be used to better control the instabilities induced by the field, and to create instabilities not observed with DC fields. [44]. For leaky dielectrics, the frequency of the applied field may have an effect on the charge accumulation, so it could be used to tune the wavelength and growth rate of the instability.

3.3. Experimental setup

We used a modified version of the surfaces forces apparatus (SFA) Figure III.2 (see Chapter II) for our experimental investigation of EFI on polystyrene PS films.

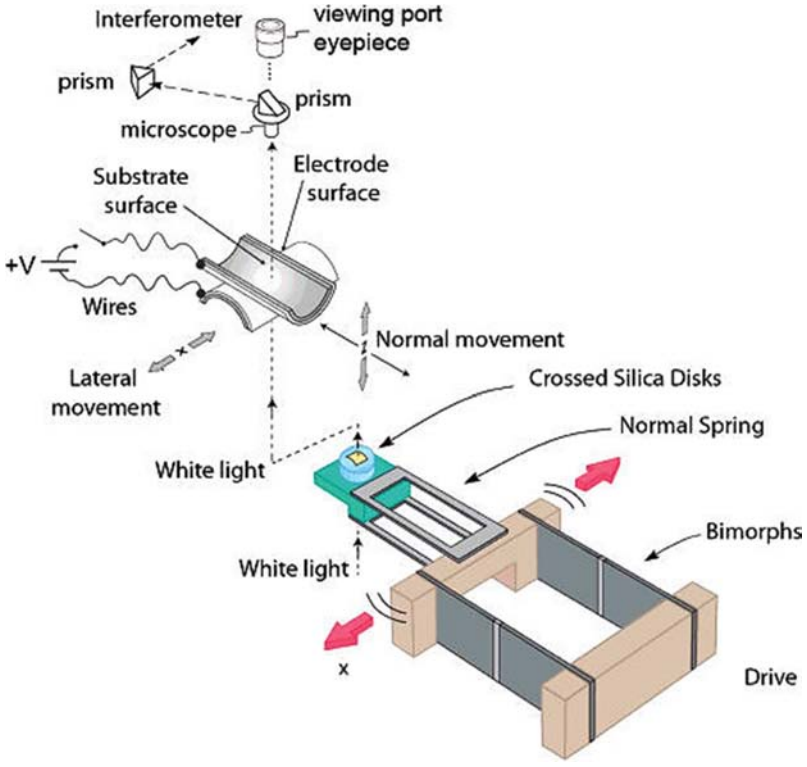

Figure III.2: Experiment setup for applying an electrical field in the SFA [45].

The electric field was applied between two polymer coated conducting (electrode) surfaces in two ways. The first method (method A) involved spin coating PS film from toluene solution on atomically smooth 1 - 4 μm thick sheets of back-silvered muscovite mica. Before spin coating, the mica sheets were glued on cylindrical silica disks (radius R=2 cm) with a small **L** shaped stainless steel connector 0.1 mm thick. (Figure III.3 a). The back-silvered 400 Å thick silver layer in contact with the connector is used as the reflecting layer for the interferometry measurements and also as electrode. In the second procedure (method B), pristine mica sheet were glued on silica disks very close to the thin metallic connector (Figure III.3 b). Then a silver layer of 400 Å thick was deposited by thermal evaporation on top of the mica and the connector. The evaporation was followed by spin coating of a polymer film on top of the silver layer. In both cases the PS film thickness was controlled by varying the concentration of polymer solution and the coating rotation speed (1,000 to 10,000 rpm). The films were then annealed at 95°C for 12 h. Two polymer coated surfaces were then mounted into the disk holders of the Bimorph Slider and Friction Device of the SFA with the axis of the cylinders perpendicularly oriented to each other. As mentioned before, this geometry locally corresponds to a sphere of radius R on a flat surface or two spheres of radius 2R. It was important to arrange the disks such as the protruding conducting **L** shaped connectors did not touch the opposite surfaces during experiments. Shielded wires were used to connect the electrodes to a controlled voltage generator Agilent 3320A, as shown in Figure III.3.

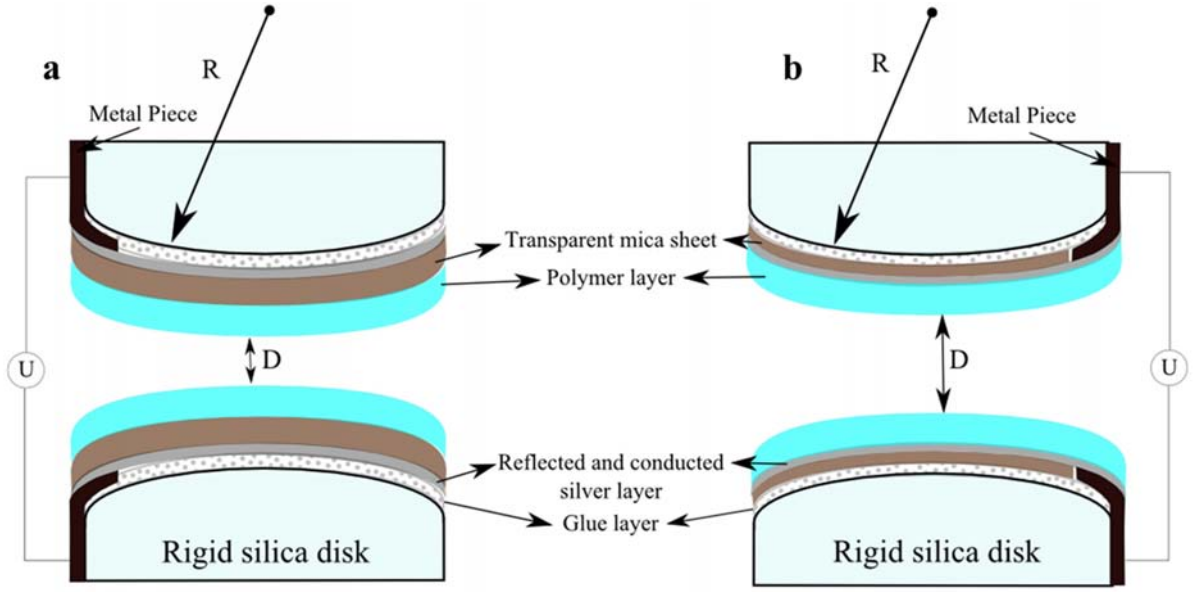

Figure III.3: Procedure to apply an external electrical field in the SFA setup.

The two surfaces were then brought to the desired starting separation or into contact, and different voltages (2-12V) were applied across the opposing silver films to generate the required electric field. For the typical surface radii of R=2 cm used in SFA experiments and at surface separations D, where R >> D, the electric field in the central region of radius ≈3,5 mm can be approximated by the uniform field between two plane parallel plates, with a discrepancy of less than 5% (Supporting Information of reference [45]). FECO were used to determine the thickness and

uniformity of the films (± 1Å) and the surface contact diameter (±3 μm) as described in *Chapter II*. When white light is passed normally through the surfaces (Figure II.25) only certain wavelengths pass through (*see Chapter II*). The emerging light beam consists of discrete wavelengths λ_n (n = 1, 2, 3, ...). In the first method of applying the electric field described before (two polymer films coated on two back-silvered mica pieces separated by a gap distance D) the interferometer contains five layers (Figure III.4). For "symmetric" systems (i.e., when the two polymer layers and two mica films have the same thickness Z, and Y), the gap distance D and refractive index μ_3 of medium can be determined independently by simultaneous measurements the wavelengths of several of FECO, and solving the equation [45,46]:

$$\tan(k\mu_3 D)=(1-r_1^2)\{\sin 2k(\mu_2 Z+\mu_1 Y)-2r_2\sin(2k\mu_2 Z)+ r_2^2\sin 2k(\mu_2 Z-\mu_1 Y)\}[2r_1\{1-2r_2\cos(2k\mu_1 Y)+r_2^2\}-(1+r_1^2)\{\cos 2k(\mu_2 Z+\mu_1 Y)-2r_2\cos(2k\mu_2 Z)+r_2^2\cos 2k(\mu_2 Z-\mu_1 Y)\}]^{-1} \quad (3.15)$$

where $r_1=(\mu_1-\mu_3)/(\mu_2+\mu_3)$, $r_2=(\mu_1-\mu_2)/(\mu_1+\mu_2)$ and $k=2\pi/\lambda$.

In the case $D = 0$ the two polymer films are in contact, the five-layer system becomes a three-layer system consisting of two mica sheets of thickness Y and one central layer interferometer of thickness $2Z$, and Eq(3.1) reduces to the appropriate three-layer formula:

$$\tan(k\mu_2 2Z)=\frac{(1-r^2)\sin(2k\mu_1 Y)}{2r-(1+r^2)\cos(2k\mu_1 Y)} \quad (3.16)$$

where $r=(\mu_1-\mu_2/(\mu_1+\mu_2)$. This is the general equation for a symmetrical three-layer interferometer which can be used to calculate the thickness Z and the refractive index μ_3 of the polymer film. The case where Y=0 represent the second method of applying electric field described above, where the polymer is coated directly on the silver films. D=0 (surfaces are in contact) corresponds to the case of a one-layer interferometer of thickness 2Z; the left hand side of Eq(3.2). is zero and the equation is satisfied by

$$2k\mu_2 2Z=n\pi \text{ or } 2Z=\frac{n\lambda_n}{2\mu_2} \quad n=1,2,3\ldots \quad (3.17)$$

$$1/n=(\lambda_{n-1}-\lambda_n)/\lambda_{n-1} \quad (3.18)$$

n is the order of interference or fringe order. By measuring the wavelengths of any two adjacent fringes λ_{n-1} and λ_n, the thickness of the polymer film Z can be determined using the expression:

$$Z=\frac{\lambda_{n-1}\lambda_n}{4\mu_2(\lambda_{n-1}-\lambda_n)} \quad (3.19)$$

Now if the polymer films are separated to a distance D, the wavelength of a particular fringe will be shifted by $\Delta\lambda_n$ to a longer wavelength λ_n. We can rewrite Eq.3.2 which corresponds to three layer interferometer in the more useful form:

$$\tan(k\mu_3 D)=\frac{(1-r^2)\sin(n\pi\Delta\lambda_n/\lambda_n)}{\pm 2r+(1+r^2)\cos(n\pi\Delta\lambda_n/\lambda_n)} \quad (3.20)$$

where the sign + refers to *n* odd, and the – sigh to *n* even. For small gaps between polymer films we can consider that $\sin(n\pi\Delta\,{}^{\lambda_n}/_{\lambda_\eta}) = n\pi\Delta\,{}^{\lambda_n}/_{\lambda_\eta}$, $\cos(n\pi\Delta\,{}^{\lambda_n}/_{\lambda_\eta}) = 1$ and $\tan(k\mu_3 D) = k\mu_3 D$, and

from Eq.3.6 we obtain:

$$D = {}^{n\Delta\lambda_n}/_{2\mu_2} \text{ for odd-order fringes (n odd)} \tag{3.21}$$

$$D\mu_3^2 = {}^{n\Delta\lambda_n\mu_2}/_{2} \text{ for even-order fringes (n even).} \tag{3.22}$$

Eqs. (3.5)-(3.8) allow the simultaneous determination of D and μ_3 from the measured wavelengths of two consecutive fringes and their wavelength shifts.

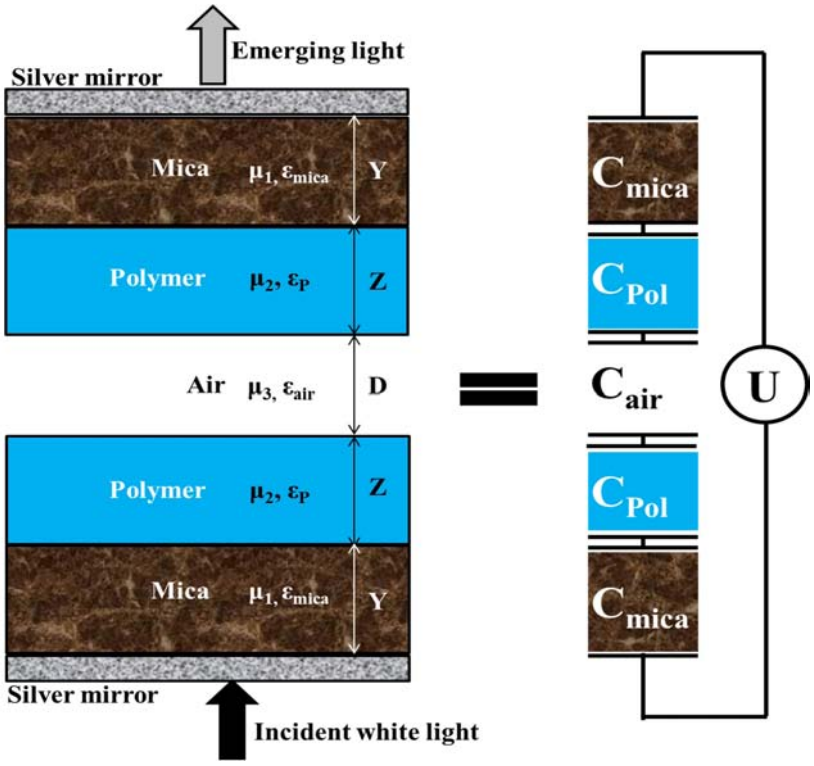

Figure III.4: Schematic representation of five layer interferometer in SFA experiment. The layered system is equivalent to a series of capacitors, as indicated.

A precise measurement of mica thickness, *Y*, polymer thickness, *Z*, and air gap, *D*, between the surfaces allows a precise calculation of the electric field in the polymer *Ep* and in the air gap. They are determined by 4 or 6 parameters: voltage *U*, spacing between polymer films *D*, film thickness *Z*, and dielectric constant of the polymer ε_p (method A) and thickness and dielectric constant of mica *Y*, ε_{mica} (method B). The experimental setup Figure III.3 can be regarded as a three/five capacitors that are stacked in series, as shown in Figure III.4. One capacitor corresponds to the air gap, two correspond to the polymer films and two to the of mica sheets. The capacitance of a dielectric is $C_i = {}^{\varepsilon_0\varepsilon_i A}/_{d_i}$, where ε_0 is the vacuum permittivity, ε_i the dielectric constant of dielectric *i*, *A* the s surface and d_i the layer thickness. The capacitance of the stack, C, is given by:

$$\frac{1}{C} = \frac{1}{C_{mica}} + \frac{1}{C_P} + \frac{1}{C_{air}} + \frac{1}{C_P} + \frac{1}{C_{mica}}$$

$$= \frac{Y}{\varepsilon_0 \varepsilon_{mica} A} + \frac{Z}{\varepsilon_0 \varepsilon_P A} + \frac{D}{\varepsilon_0 \varepsilon_{air} A} + \frac{Z}{\varepsilon_0 \varepsilon_P A} + \frac{Y}{\varepsilon_0 \varepsilon_{mica} A} \quad (3.23)$$

The applied voltage across the plates is the sum of the voltage drop within each layer

$$U = E_{mica} Y + E_P Z + E_{air} D + E_P Z + E_{mica} Y \quad (3.24)$$

Making the assumption that we are dealing with perfect dielectrics, the dielectric displacement d of the system, shown in Figure III.4 caused by an electric field is constant: $d = \varepsilon_0 \varepsilon_{mica} E_{mica} = \varepsilon_0 \varepsilon_P E_P = \varepsilon_0 \varepsilon_{air} E_{air}$.

$$U = \frac{d}{\varepsilon_0} \left(\frac{2Y}{\epsilon_{mica}} + \frac{2Z}{\epsilon_P} + \frac{D}{\epsilon_{air}} \right) \quad (3.25)$$

The induced electric field E_P in the polymer film is obtained by rewriting Eq.(3.11) using $d = \varepsilon_0 \varepsilon_P E_P$

$$E_P = \frac{\epsilon_{air} \epsilon_{mica} U}{D \epsilon_{mica} \epsilon_P + \epsilon_{air} \epsilon_P 2Y + \epsilon_{mica} 2Z} \quad (3.26)$$

In this study the applied voltage was between 1 and 12 V; therefore E_P was typically in the range of 10^5–10^7 V/m.

3.4. Experimental results

In general, we observed that by applying an external electric field (EF) to a smooth glassy PS film (Figure III.5-a) a regular structure (Figure III.5-b) appeared on its surface, even though all the experiments were conducted at room temperature. The formation of these long-lasting patterns on the surface evidence the mobility of the polymer molecules close to the surface of the films. An example of EFI modification of polymer film is presented in Figure III.5. AFM (described in Chapter 2.2.5) was used to characterize the assembled structure. In particular, the distance between the peaks (wavelength) ant their height were determined. For instance, the height cross-profile shown in Figure III.5-c measured along the white line in b) allows to measure peaks 7.0±0.3 nm high, 1.91± 0.01 μm apart. In general, we observe a Gaussian distribution of the measured height and wavelengths. In most cases the size distribution was automatically determined by the AFM software, but in some cases due to edge effects, dirt particles that affect the quality of AFM image, coalescence or only small areas of certain morphology, automatic determination produced inadequate results. In such cases, I measured manually the characteristic pattern sizes, excluding nucleation and coalescence effects. Typically, the averaging included ≈ 10-15 experimental data points.

Results presented in Figure III.5 and Figure III.6 show clearly that it is possible to generate a structure on glassy polystyrene films at room temperature, well below the glass transition temperature of PS. As described before, the appearance of the patterned structures on the PS surface is due to the competition between the destabilizing electrostatic pressure and the combination of capillary pressure at the polymer/air interface and elastic strain on the film, opposing the growth. When the electrostatic pressure overcomes the stabilizing forces, patterns or cells of specific wavelengths and arrangements are generated. The specific morphology obtained depends on the experimental conditions. I will discuss more about the surface morphology later in this chapter.

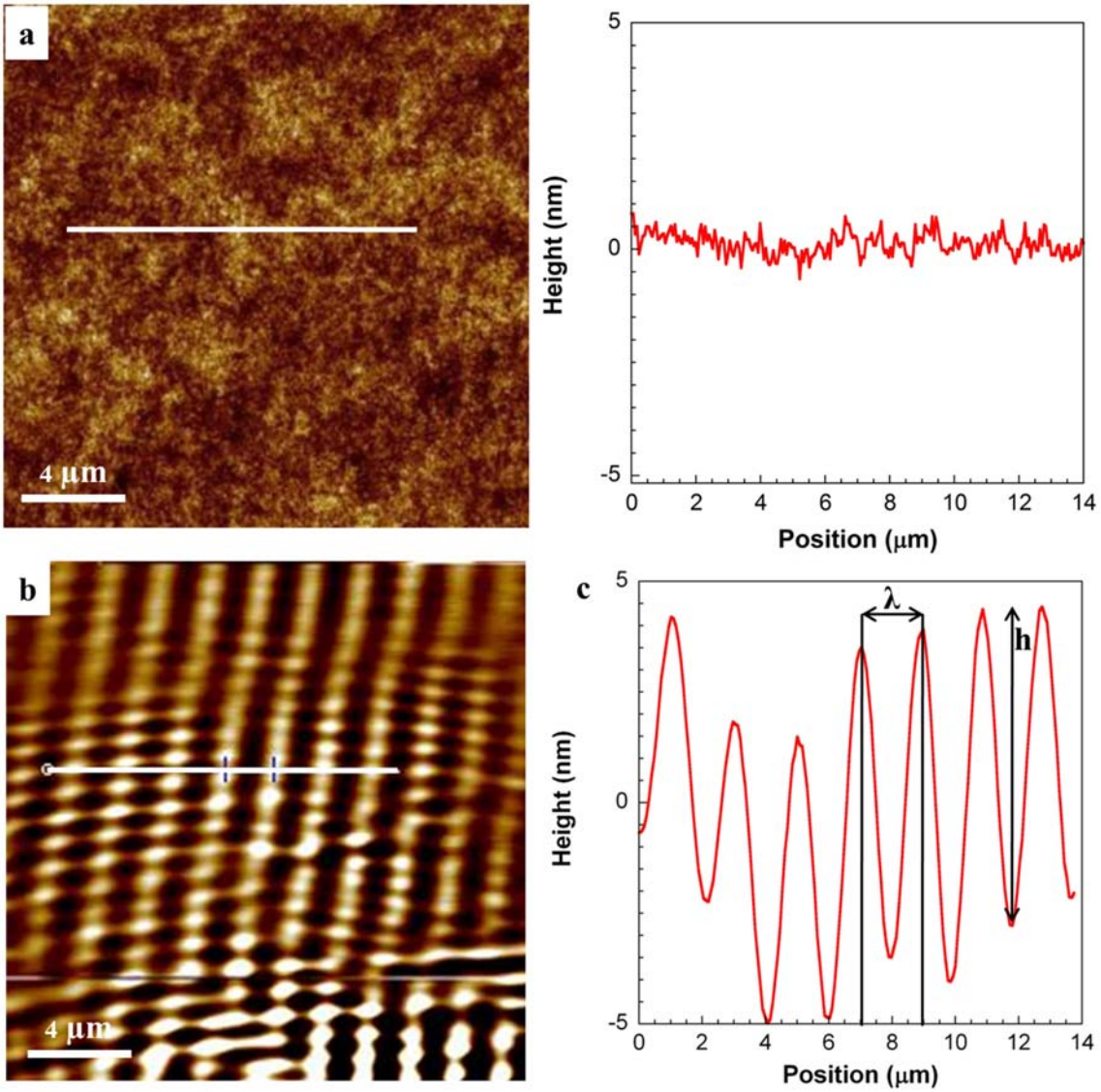

Figure III.5: AFM height images of PS films (a) typical morphology of freshly coated PS film, (b) polymer film destabilized by applying an electric field. The average wavelength λ of the instability and the average peak height h are determined by measuring the distances in (c). The cross-sections correspond to the white lines on the images.

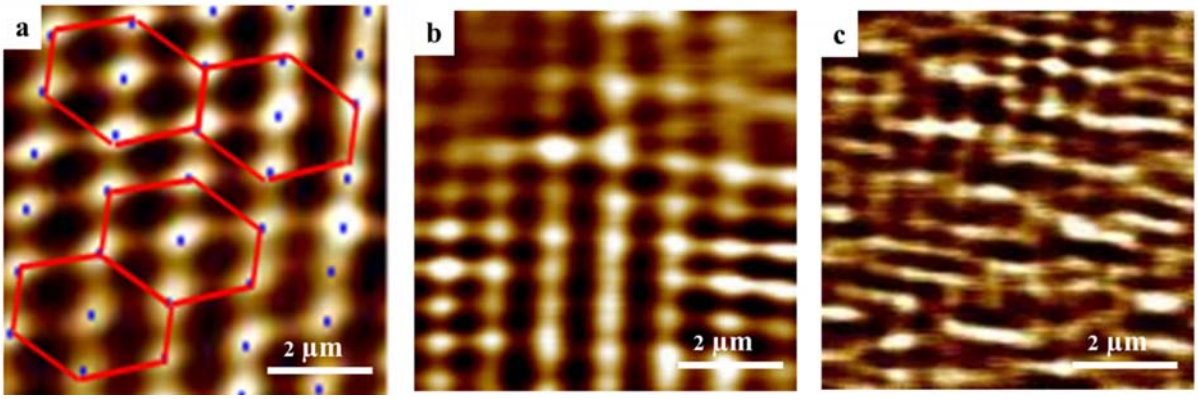

Figure III.6: AFM height micrographs of typical experimentally obtained morphologies of EFI in PS films.

3.4.1. Characteristic Wavelength

As mentioned before, I determined the characteristic wavelength λ by measuring the average distances between peaks from AFM images. Mica (Z) and polystyrene thickness (Y) and surface spacing (D) were determined by interferometry in the SFA. These data allowed us to precisely calculate the applied electric field in the film Ep by using equation (3.13). Figure III.7 summarizes the results of the different experiments performed. It shows the variation of the characteristic wavelength λ of the surface pattern with the applied electric field Ep. It contains results for different PS film thickness, applied voltages, and experiments with DC and AC field (500 kHz). Several important aspects can be observed. First, it is clear that progressively smaller wavelengths are induced as the electric field is augmented: the characteristic size of the pattern can be easily controlled with this method, as have been shown before. Second, AC and DC data seems to follow the same curve: we did not detect an important effect of the frequency of the applied field. This seems to indicate that only polarization effects are responsible for the instability, and there is no accumulation of charges at the interface in case of DC experiments. I will discuss this point again later. Third, it appears that at high E_p an asymptotic λ limit of the order of 600 nm is achieved, which is rather independent of PS film thickness. Finally, we did not observe the existence of a threshold for surface structuration, but a rather progressive increase of λ accompanied by a continuous decrease of the amplitude of the EFI patterns.

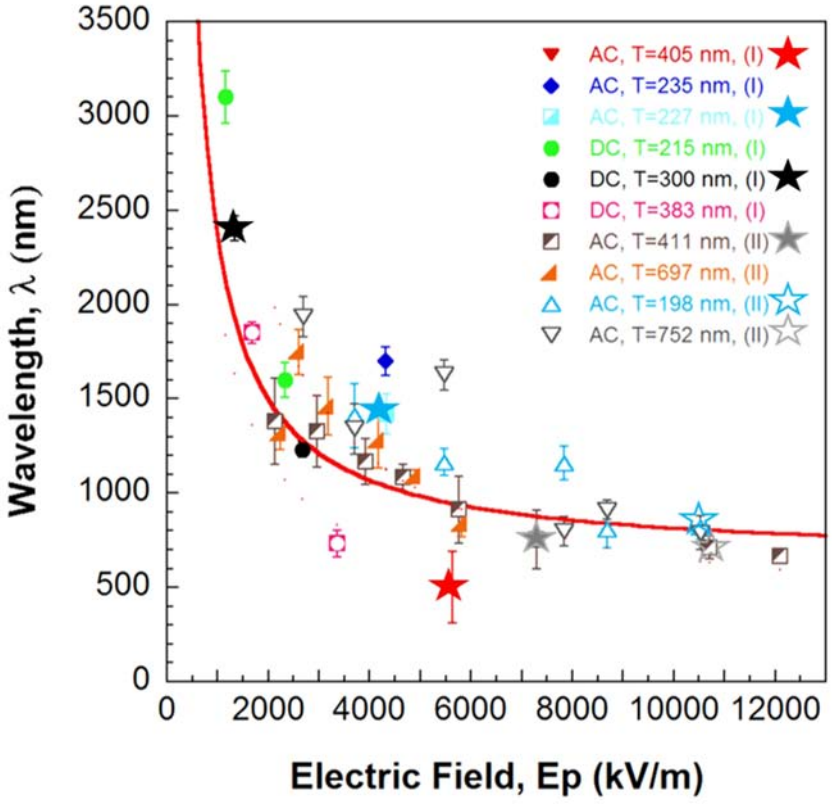

Figure III.7: Variation of the characteristic wavelength λ with the amplitude of the applied electric field E_P. The stars indicate data points corresponding to AFM images presented in Figures 8, 12 and 13. The red line is a guide to the eyes.

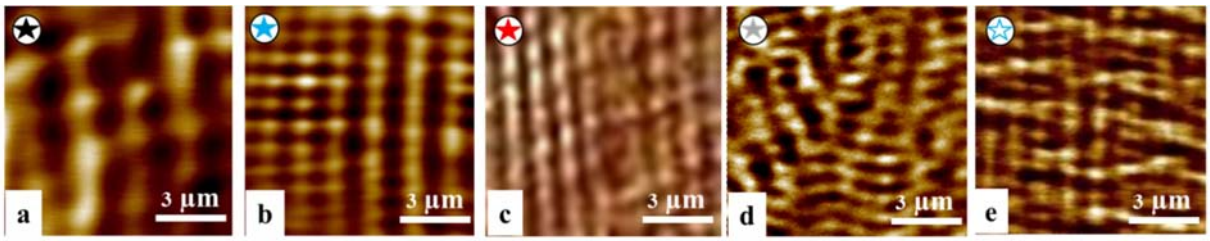

Figure III.8: AFM micrographs representing the evolution of induced patterns of PS films with electric field. By increasing the E_p, the patterns evolve into more disordered morphologies.

As can be observed in the corresponding AFM micrographs presented in Figure III.8, patterns of regular square or hexagonal ordering were typically observed at large and intermediate λ values, corresponding to the weaker applied fields. On the contrary, in the regime of small λ values (higher E_p) an increasingly disordered pattern is observed.

Attempts to describe the experimental data based on perfect dielectric models were fruitless. The assumption of a fluid film leaded to much larger characteristic wavelengths that the ones observed experimentally (cf. Figure III.9, left panel), even though in both cases (experimental results or theoretical prediction for liquid-like behavior) a substantial decreasing of λ with increasing E_p is observed. Similarly, the predictions of eq. 3.14 assuming small $\gamma/h\mu$ values (solid-like film) were not matched by experimental results. Even so, in both cases (experiments and solid-like predictions) an asymptotic λ value independent of E_p is found, and the order of magnitude of the observed wavelength is comparable. It is interesting that the observed λ value at high E_p (around 600 nm) does not seem to depend of the thickness of PS in the range of thickness investigated 200-800 nm. This could be interpreted as a soft-solid film 150-200 nm thick present on top of all the films studied at high E_p. However, this two-layer model would not explain the longer λ values observed at weaker applied fields. The assumption of a perfect-elastic solid seems also incompatible with the long relaxation time of the patterns on the film (of the order of weeks at room temperature) similarly to the scenario I will described in Chapter VI.

It is probably more adequate to describe PS films using the viscoelastic model. Attempts to model the experimental results using Sharma's theory for perfect dielectric were not successful, as can be observed in Figure III.10. The measured wavelength is substantially smaller than the ones that could be calculated for reasonable E_p values (below the dielectrical breakdown of PS, 10^8 V/m). We tried to simulate the measured data by assuming a 200 nm thick soft PS film ($\mu=10^4$ Pa, much lower than the few GPa expected for glassy PS) for all the samples studied. Although the asymptotic limit at high fields matches the experimental data, E_p values 50 times larger than the applied experimentally are required to obtain a similar behavior to the experimentally observed (blue dashed lines). Weaker fields are required to predict λ values of the order of magnitude of the measured data if a thinner liquid film is considered (10 nm). In this case E_p values 5 times larger than the ones observed experimentally are necessary to reproduce the observed λ values (green dashed line in the Figure III.10).

However, in this case no asymptotic finite limit at high E_p is predicted for the liquid-like limit. We can think of several reasons for these discrepancies. First, a description considering the possibility of non-zero conductivity of the film (leaky dielectric) may be necessary. As described before, the accumulation of charges at the interface would induce an additional destabilizing force that would bring closer theoretical prediction and experimental results. Indeed, we observed the formation of black spots on the film surfaces (Figure III.11) at the highest voltages investigated (12V; E_p 6 MV/m), evidencing the degradation of the film, even though the intensity of the field was still well below the dielectric breakdown strength of polystyrene, which is of the order of 10^8 V/m. Leaky dielectrics are more susceptible to breakdown that perfect dielectrics, for a given potential. Nevertheless, we did not observe substantial differences between films structured under the influence of DC or AC fields of similar intensity, which seems to argue against this interpretation. Clearly, more tests need to be performed to clarify this point. A second difficulty to model the experimental results is related to the nature of the PS films. We are attempting to describe it as a uniform isotropic material with regular viscoelastic and dielectric properties. However, as discussed in chapter I, a number of research groups have been reporting results of different experiments that suggest that PS films display are typically non-equilibrium with rather heterogeneous properties. Hence, a more complex multilayer description may be necessary. Efforts to model our data following these two paths are in progress. Finally, the fact that PS films are being structured in both surfaces may play an additional role. The structuration of the films induces a modulation of the dielectric constant between the electrodes, introducing a modulation of the electric field on the films.

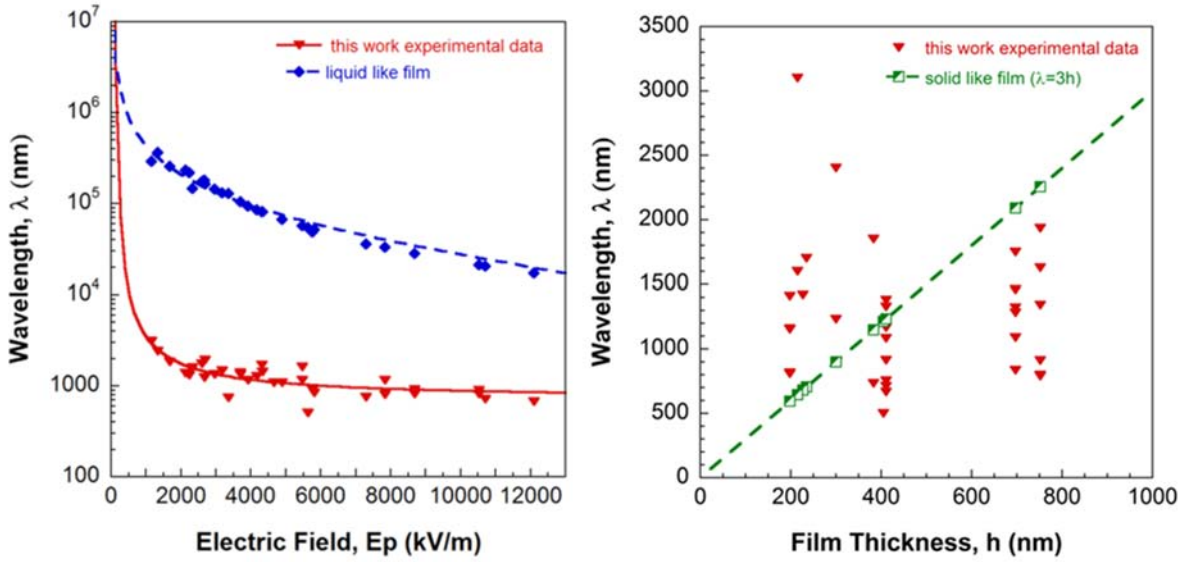

Figure III.9: Left: red line and data points represent results obtained in our experiments. Line and points in blue correspond to expected values for a liquid film at same experimental conditions (eq. 3.12).Right: Line and data points in green correspond to results expected for a solid film (eq. 3.14 at the limit of small for small $\gamma/h\mu$ values).

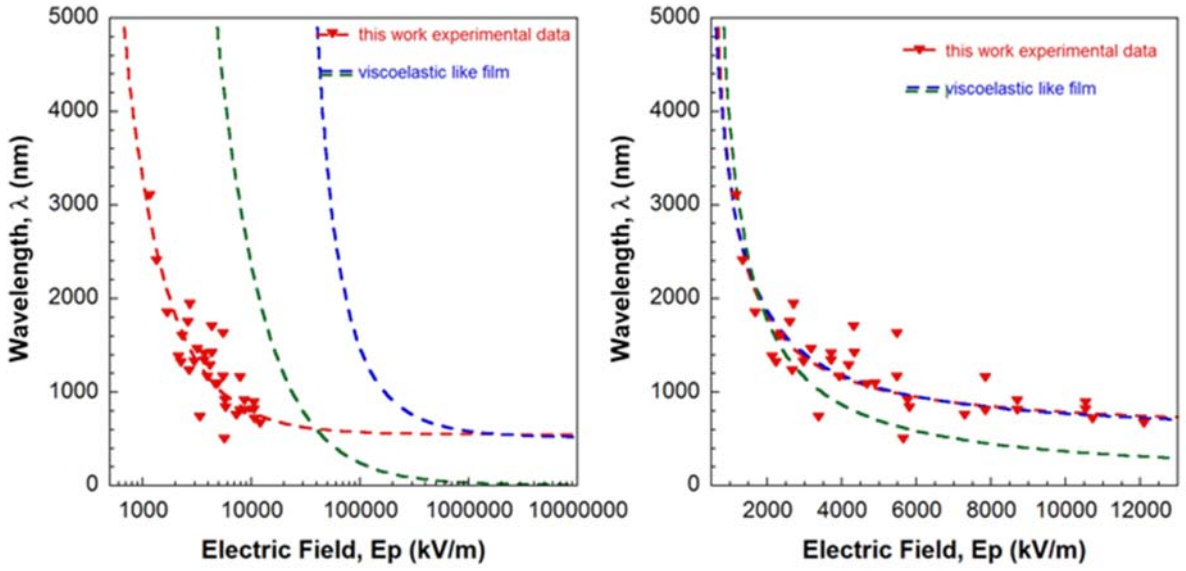

Figure III.10. Left panel: Experimentally measured and calculated λ using eqs.3.14. Blue dashed line: T=200nm, μ 10kPa; green dashed line: T 10 nm; μ= 0 Pa; Right: E_p of theoretical estimations were divided by a factor of 40 (soft solid; blue dashed line), and by a factor of 5 (liquid; green dashed line) to facilitate comparison of the different data sets

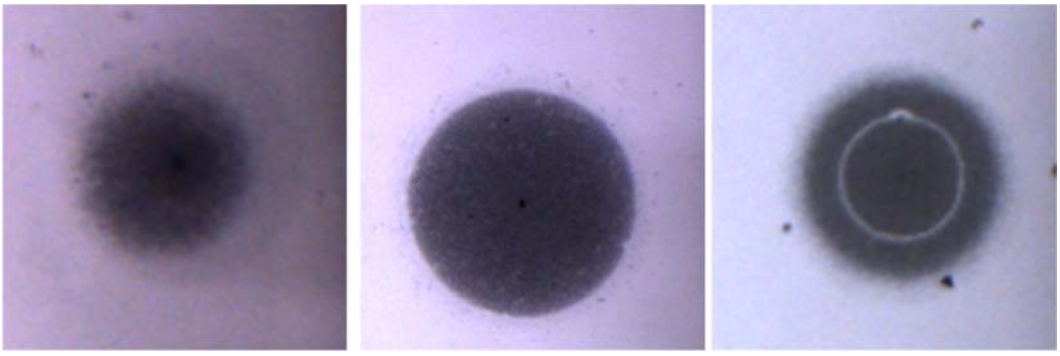

Figure III.11: Optical micrograph displaying zones few tens of micrometers size where EF induced degradation of PS was observed (black areas)

3.4.2. EFI patterns: initial morphology

As mentioned in previous section, we observed a regular morphological evolution of the EFI pattern formed with the strength of the applied field (Figure III.8). At relatively low E_p, (larger λ) a very ordered hexagonal (Figure III.8a) array was generally observed. Upon further increase of the electric field, a morphological transition to a square pattern, above a certain value of the field was observed (Figure III.8b). Sometimes a rectangular symmetry could be detected between the regularly hexagonal and perfectly square arrangements (Figure III.8c). Upon further increase of the applied film, a second transition to a stripes-like morphology was regularly observed ((Figure III.8d). Finally, at even larger applied E_p, a seemingly disordered pattern was observed (Figure III.8e) with the smallest induced λ. I did not attempt to complete a quantitative characterization of the morphological transformations from our limited set of data. However, in Figure III.12 the boundaries between the different morphologies observed are loosely represented.

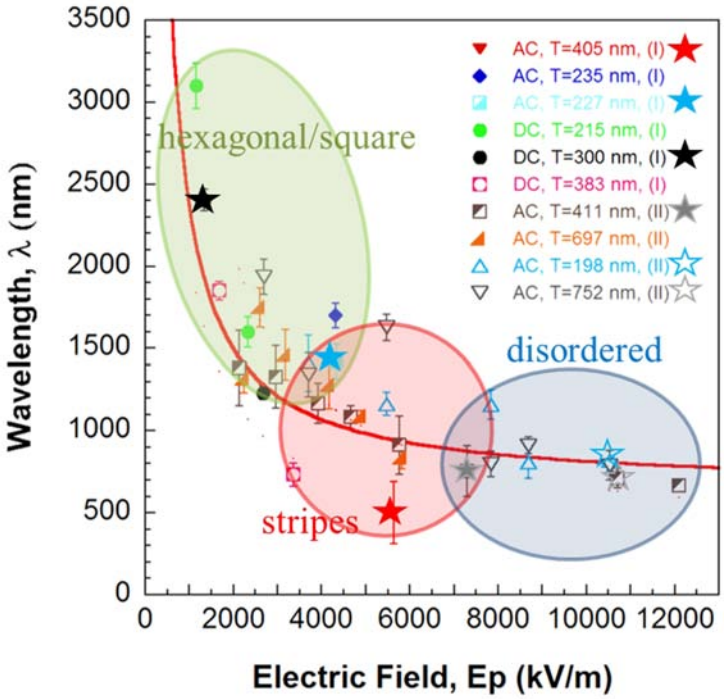

Figure III.12: Variation of the characteristic wavelength λ with the amplitude of the applied electric field E_P. Same data as Figure III.7, indicating the different morphologies observed.

The crossed-cylinders geometry used in our experiment implies a slow variation of the distance between the electrodes, which regularly increases from the point of closest approach (PCA) situated at the center of the sphere-on-a-plate equivalent geometry. Hence, the effect of a continuously varying E_p can be investigated in a single experiment by exploring areas located at different distances from the PCA; larger electric fields are applied at smaller D values, implying a larger destabilizing force. This is illustrated in Figure III.13, which shows the evolution of morphology of induced patterns with the changing E_p in a particular experiment. The region 2 correspond to a region of closest approach of the curved surfaces were we have largest destabilizing force, while in region 1 correspond to a lateral shifted position where D is larger and the applied electric field is weaker. As can observed from experimental obtained morphology on PS film with thickness 227 nm in region 1 we have a column like structures with a square periodic arrangement. Moving in the direction of increasing E_p (towards region 2) we observe that the structure get distorted, columns merge and the morphology changes into stripes-like.

As mentioned before, a more disordered structure is observed in the case of high applied E_p Figure III.14. This evolution has also been observed before in studies of EHI, and has been attributed to the broadening of the dispersion curve. By increasing the applied field, the λ range of wavelengths that are susceptible to be stable increases (i.e. positive ω values in equation 3.14) so it is more difficult for the system to select a characteristic wavelength. As a consequence, the time necessary to reach steady-state morphology increases and the pattern gets less organized.

The morphological evolution observed by us has been partially described in different studies of EHI of liquid films. Pease and Russel [47] described the transitions hexagonal-stripes-disordered in a review of different studies of EHI. They also discussed the possibility of transition square-hexagonal

based on the analysis of a model not restricted to the lubrication approximation. Elastic solid films are also prone to similar morphological transformations. In a theoretical study of the surface instability induced by an external electric field in a soft elastic thin film [48], Sarkar, Shenoy and Sharma have shown that the precise pattern morphology depends strongly on the field parameters and can be classified into three broad morphological phases: columns, stripes, and cavities. They showed that by increasing the electric field the transition from columns to stripes can be induced as presented in their morphological phase diagram (Figure III.15).

Similar morphological transitions (hexagonal-square-stripes) have been extensively documented in the literature in theoretical and experimental studies of ferrofluids subjected to magnetic fields. [49,50]. The role of the magnetic field in these works experiments is equivalent to the destabilizing role of the electric field in the experiments described here.

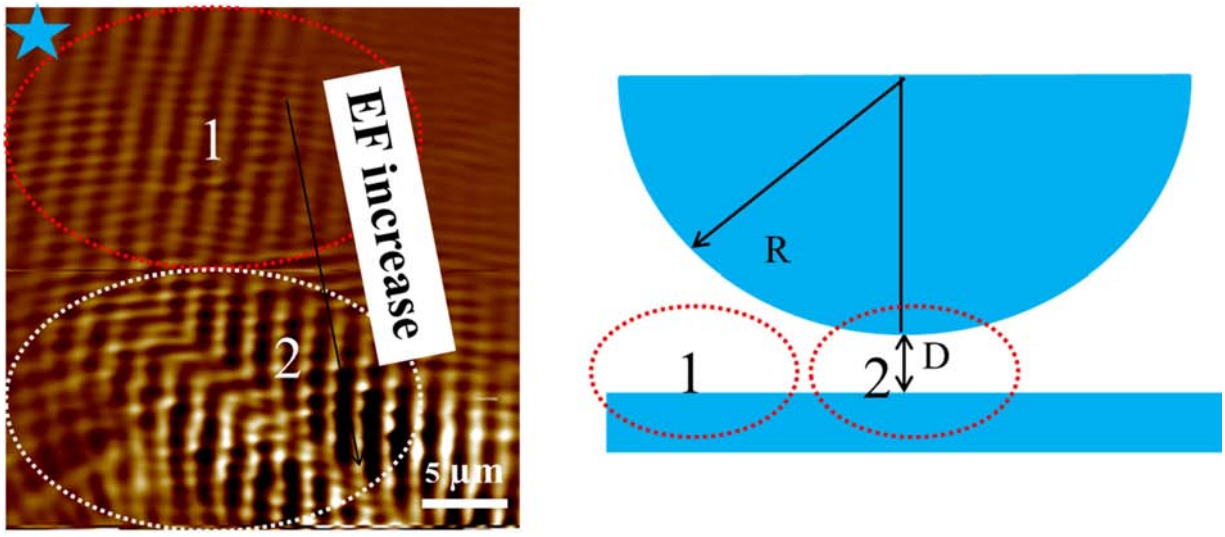

Figure III.13: AFM height micrograph representing the evolution of the patterns induced patterns on PS surface. Starting from the upper part (region 1) with columns in a well-ordered square-like arrangement, the pattern evolves into a more disordered stripe- like morphology (region 2).

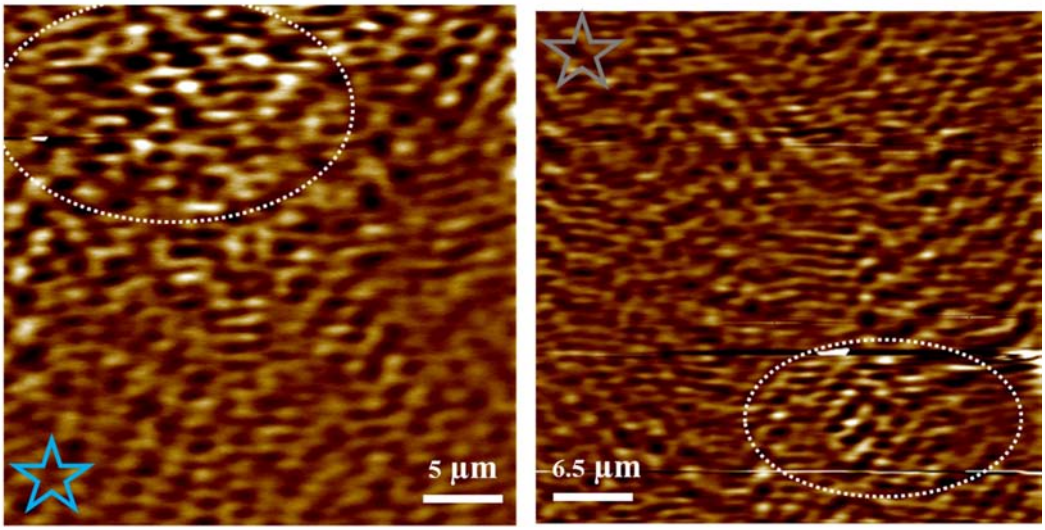

Figure III.14: AFM micrographs representing induced patterns of PS films at high electric fields. A disordered morphology is observed. E_p 5000kV/m

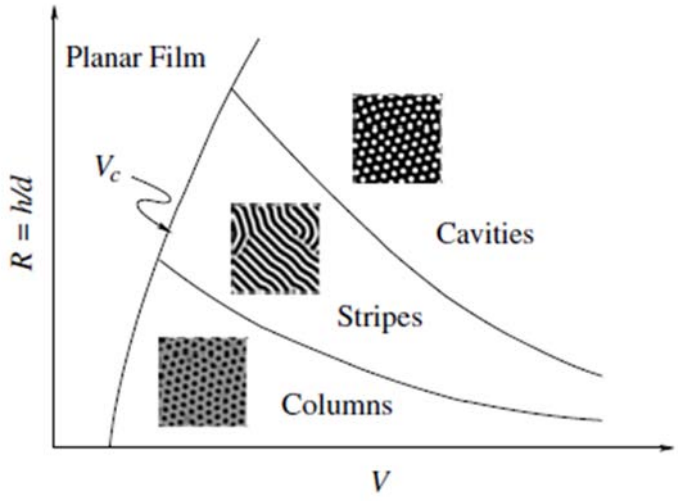

Figure III.15: Schematic morphological phase diagram of the film contactor system in an electric field [48].

3.4.3. EFI patterns: long time evolution and nucleation

In SFA experiment, crossed-cylinders geometry is used, so that the distance between the silver mirrors becomes a slowly evolving function of the lateral position. As we applied a constant voltage between the silver electrodes, changing the distance between the electrodes imply changing the applied E_p (Eq. 3.12). A larger electric field is applied at smaller D values, implying a larger destabilizing force. In addition, as the time constant of instability changes as the 6^{th} power on the electric field (Eq. 3.13), even small variations in E_p can amplify perturbations on a much faster time scale. All this leads to a flow of the polymer material towards the nucleated maximum. In our experiments, the maximum of EF corresponds to the PCA of the curved surfaces, or the contact region if surfaces are in contact (D = 0). Due to mass conservation, this flow depletes its surroundings and triggers a wave propagating outward from the nucleation position. Figure III.16 shows few examples of nucleation. Waves were nucleated in the PCA between two films out of contact (a) or at the rim of contact region (b) and propagated outwards. The wavelength of the nucleate instability was found to correspond to a value $r = 2\lambda$, with an amplitude that decays from the PCA. The observed nucleation wavelength agrees with observations of nucleation instability of Schaeffer et al. [51].

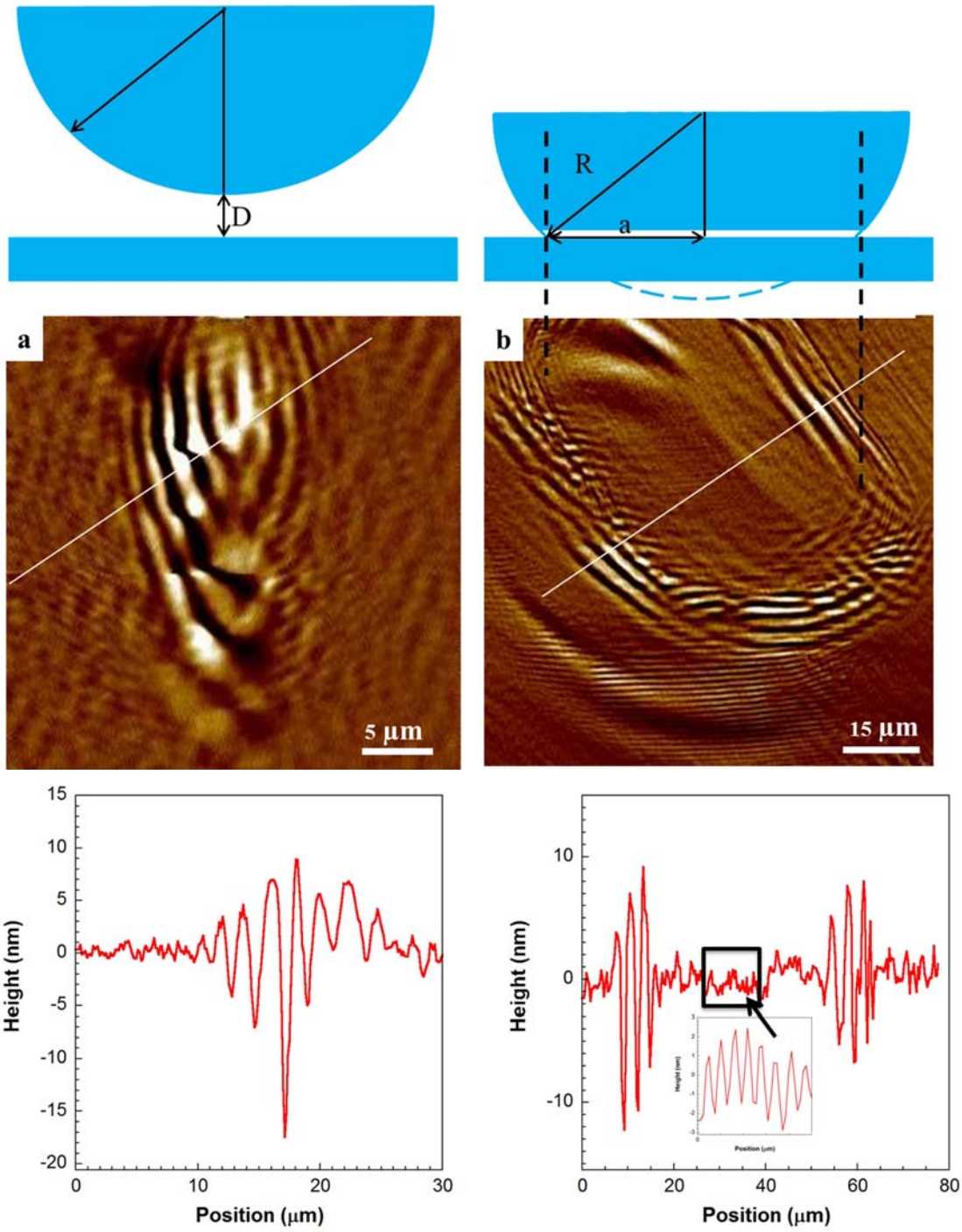

Figure III.16: AFM images of nucleated patterns formed in an electric field for two configurations of SFA surfaces, (a) in close proximity (D=130 nm) and (b) in contact (D=0). *R* is the radius of curvature of surface, *a* is the contact radius.

3.4.4. Evolution of Nucleation Instability

Depending on the value of E_p and the exposing time to electric field, different stages of the nucleated instability are observed. Initially, in the absence of an electric field (Figure III.17-a), the film is smooth and stable. Once sufficiently large voltage is applied to the assembly, surface waves with small amplitude, and a characteristic wavelength λ and arrangement begin to develop, as described before (Figure III.17-b). Later, due to the lateral variation of the imposed electric field due

to the curvature of surfaces, the material starts to flow in the direction of the highest electric field, which in our experiments corresponds to the PCA or the contact region. The characteristic time scale for the development of the nucleated structure is longer than the spontaneous EFI instability. Figure III.17- c shows the formation of elliptical waves (ridges) around the elliptical shape of the contact region, where the electrode spacing is lower than in the surroundings. Eventually secondary order waves are formed from primary annular elevation, and the same process repeats outwards (Figure III.17-c). The average distance *r* between two crests is found to be r = 2λ, with a height that decreases with the distance from the contact region. In the central region of the contact the wavelength of EHD instability remains intact because in this region the distance between the plates is constant and the electric field is homogenous. Finally the amplitude of the waves increases sufficiently to span the air gap between polystyrene films (Figure III.17-d) and eventually made the contact with the opposite surface to form polymer columns with intercolumn distance close to λ.

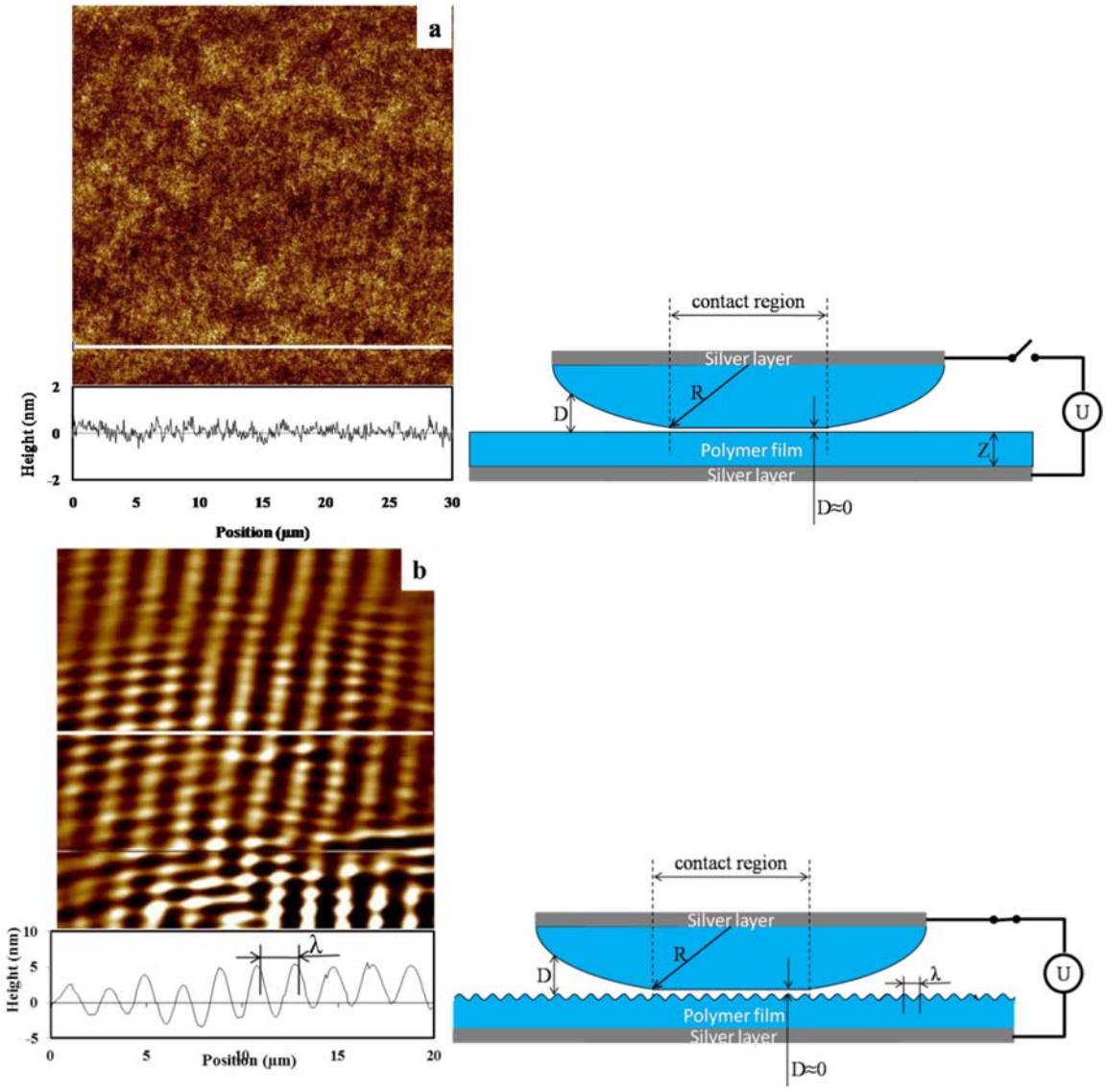

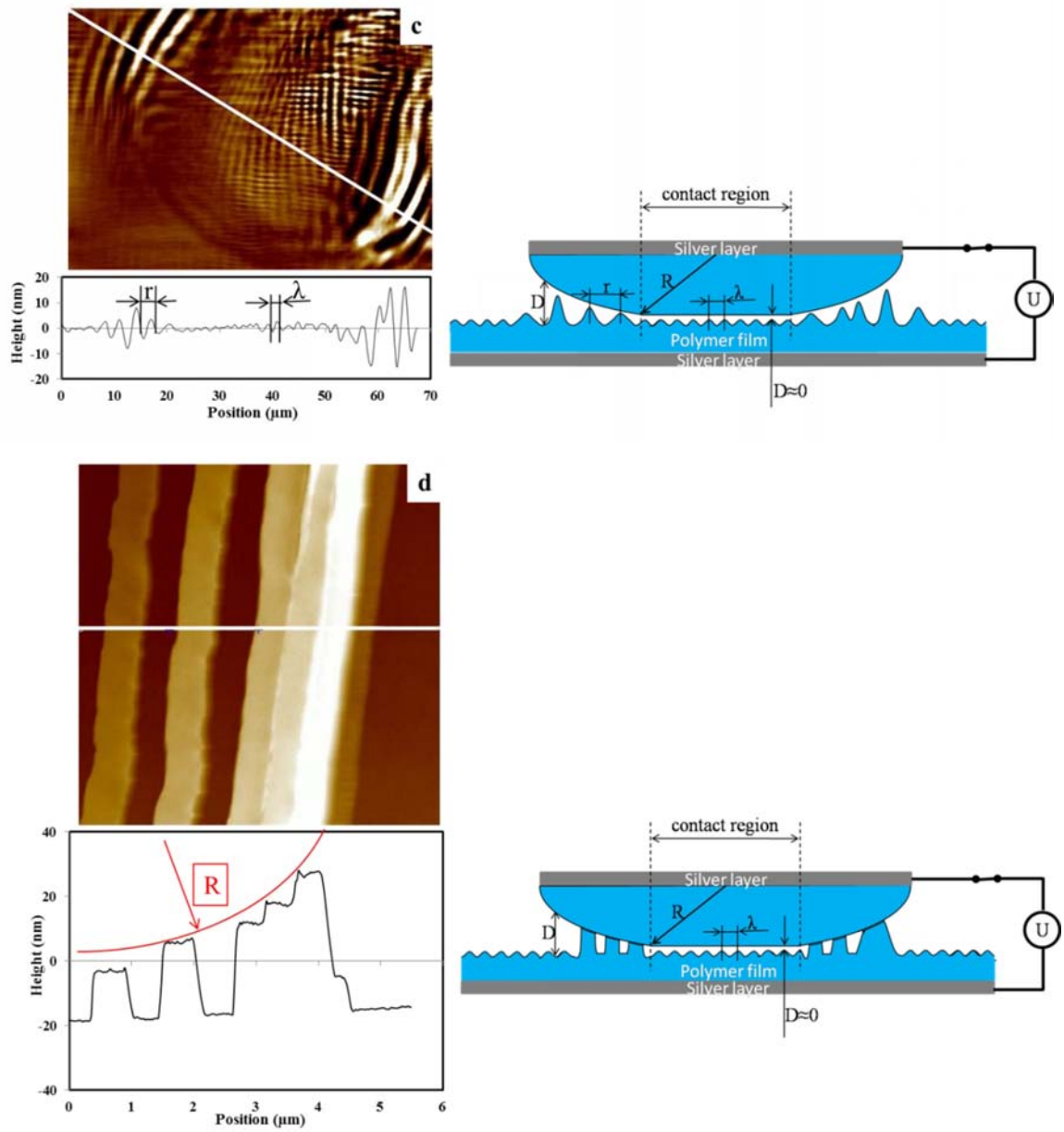

Figure III.17: AFM micrographs of polystyrene (PS) films exposed to EF. (a) The surface of a 227 nm thick PS film is represented as deposited; before exposure to the field the film is very smooth. (b) Spontaneous instability with a characteristic wavelength λ begins to develop. T = 25°C. Applied voltage U = 5 V. (c) Since there is a lateral variation of electric field imposed by the curvature of surfaces, nucleation appears at the edge of the contact region, as illustrated by the cross-sections. (d) Undulations have grown and completely span the distance between the two surfaces. For illustration purposes surface deformation are represented only in the lower surface of the accompanying cartoons. In reality both polymer films are equally modified

Obviously, the nucleation instability may appear even with the surfaces out of contact, as illustrated in Figure III.18. The evolution of the instabilities critically depends on all experimental parameters, in particular on the gap between the surfaces and the time of exposition to EF. As can be observed in the figure, the extension of the nucleation instability critically depends on the exposure time. The initial pattern formed irregular strips that could be described as a sinusoidal surface perturbation, as shown in Figure III.18-a. Then, the pattern evolves as a function of exposure time. Two different exposure times are presented in Figure III.18. It is clear that the nucleated instability is much more developed for the case of the surfaces subjected to the field for longer times. Further

increasing the exposure time induced the formation of columns bridging the surfaces along the rim of previous wave pattern.

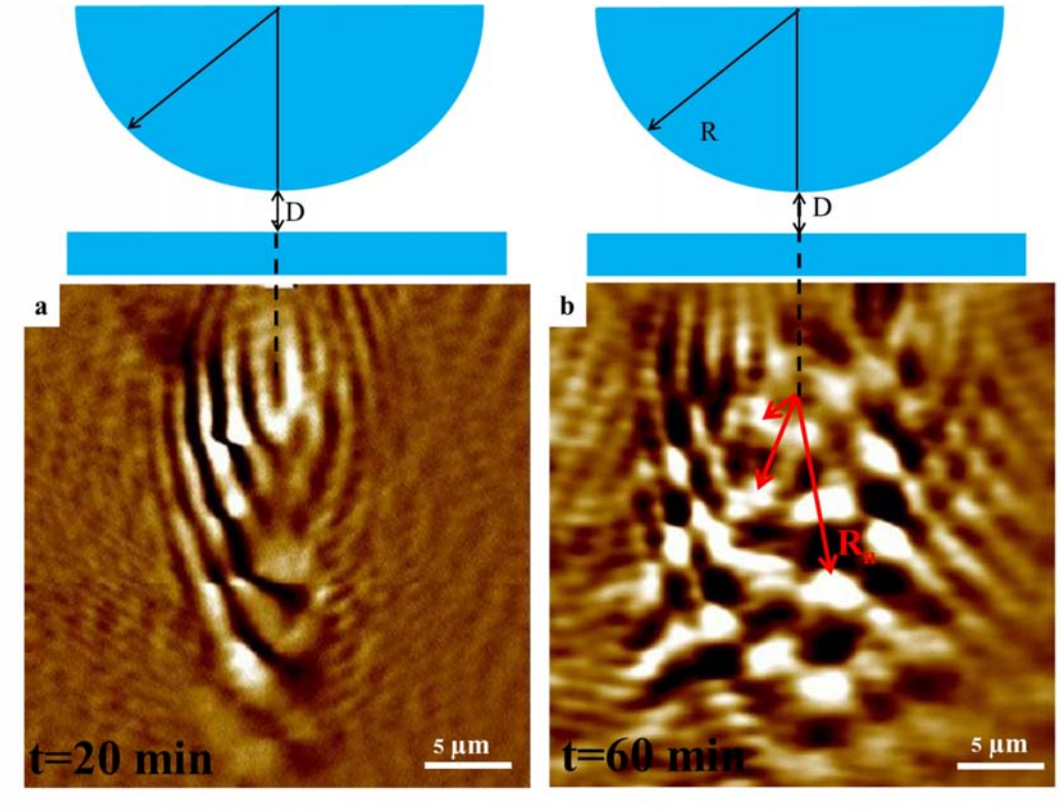

Figure III.18: Spatiotemporal evolution of a 697 nm thick PS film on SFA curved surfaces. Film spacing D = 130 nm. The exposed time to electric was (a) 20 min and (b) 60 min

I did not pursue further the study of film morphology evolution, which has been the subject of numerous studies in the literature. A thorough understanding of how the different parameters (time, D, R, a, film thickness, T, field strength) influence the physics of the nucleation process was beyond the scope of this work. Nevertheless, it is well worthy emphasizing the fact that all the test presented in this chapter were performed at room temperature, evidencing once again the possibility of structuring glassy polymer films without the need of heating above the glass transition. In addition, this technique allows the formation of pattern of smaller wavelengths that the ones typically obtained in liquid films. I will extensively describe in next chapter how the mobility of the topmost layer can be exploited to structure PS films using a completely different technique, which will constitute the central part of the work reported in this thesis.

3.5 Conclusions

The results presented in this chapter described a method to induce and control the structure formation in thin polystyrene films by using an external electric field. Unlikely all the studies of EFI structuration of PS films previously published in the literature, I have shown it is possible to generate a controlled structure on glassy polystyrene films at room temperature under application of electric field. The characteristic size of the EFI patterns, λ, which can be controlled by the strength of the applied E_p, is substantially reduced by this method. The morphology of the induced pattern changes from hexagonal to square to stripes order, to finally acquire a disordered conformation at the highest E_p investigated. The small λ values observed and the fact that a non-zero limit was observed at high E_p argue against a liquid-like description of the films. However, the spatial and temporal evolution of the morphology and the absence of a threshold E_p for the appearance of the instability suggest the opposite. A description involving a leaky dielectric viscoelastic film will certainly be necessary to completely describe our experimental results.

Finally, the appearance of the patterned structures on the PS surface is possible due to the presence of a layer of enchased mobility at the outmost surface of glassy polystyrene films, which can be restructured under external stimuli. The results presented in this chapter show that there are still many interesting aspects to discover regarding the EPI instabilities in thin films, and should pave the way for further studies on the use of electric fields in surface patterning.

3.5. References

[1] Pease, L. F., Russel, W. B., Feb. 2002. Linear stability analysis of thin leaky dielectric films subjected to electric fields. Journal of Non-Newtonian Fluid Mechanics 102 (2), 233–250.

[2] Pease, L. F., Russel, W. B., 2003.Electrostatically induced submicron patterning of thin perfect and leaky dielectric films: A generalized linear stability analysis. Journal of Chemical Physics 118 (8), 3790-.

[3] Shankar, V., Sharma, A., Jun. 2004. Instability of the interface between thin fluid filmssubjected to electric fields. Journal of Colloid and Interface Science 274 (1), 294–308.

[4] Verma, R., Sharma, A., Kargupta, K., Bhaumik, J., 2005. Electric field induced instabilityand pattern formation in thin liquid films. Langmuir 21 (8), 3710–3721.

[5] J. Sarkar and A. Sharma, A unified theory of insabilities in viscoelastic thin films: from wetting to confined films, from viscous to elastic films, and from short to long waves, Langmuir 26, 8464–8473 (2010).

[6] Yang, F. & Song, W. Morphological instability of elastic thin films–effect of electromechanical interaction. *Applied Physics Letters* **87**, 111912 (2005).

[7]Chou, S. Y., Zhuang, L., 1999, Lithographically induced self-assembly of periodic polymer micropillar arrays. Journal of Vacuum Science and Technology B 17 (6), 3197–3202

[8]Chou, S. Y., Zhuang, L., Guo, L., 1999, Lithographically induced self-construction of polymer microstructures for resistless patterning. Applied Physics Letters 75 (7), 1004–1006.

[9]Schaffer, E., Thurn-Albrecht, T., Russell, T. P., Steiner, U., Feb. 2000. Electrically induced structure formation and pattern transfer. Nature 403 (6772), 874–877.

[10] Lin, Z., Kerle, T., Russell, T., Schaffer, E., Steiner, U., 2002.Structure formation at the interface of liquid/liquid bilayer in electric field.Macromolecules 35 (10), 3971–3976.

[11] J. Bae, E. Glogowski, S. Gupta, T. Emrick and T.P. Russell, "Effect of nanoparticle on the electrohydrodynamic instability of polymer/nanoparticle thin film," *Macromolecules***41**(7), 2722-2726 (2008).

[12] Wu, N., Russel, W. B., 2009.Micro- and nano-patterns created via electrohydrodynamic instabilities. Nano Today 4, 180–192.

[13] Arun, N. *et al.* Electric-Field-Induced Patterns in Soft Viscoelastic Films: From Long Waves of Viscous Liquids to Short Waves of Elastic Solids. *Physical Review Letters* **102**, (2009).

[14] Craster, R. V., Matar, O. K., 2005.Electrically induced pattern formation in thin leakydielectric films.Physics of Fluids 17 (3).

[15]M.T. Frey, I.Y. Tsai, T.P. Russell, S.K. Hanks, Y.L. Wang. "Cellular Responses to Substrate Topography: Role of Myosin II and Focal Adhesion Kinase." Biophysical Journal (2006) 90: 3774-3782

[16] Conti, M., Donati, G., Cianciolo, G., Stefoni, S., Samor, B., 2002.Force spectroscopy study of the adhesion of plasma proteins to the surface of a dialysis membrane: Role of the nanoscale surface hydrophobicity and topography. Journal of Biomedical Materials Research 61 (3), 370–379.

[17]Ou, J., Perot, B., Rothstein, J. P., 2004. Laminar drag reduction in microchannels using ultrahydrophobic surfaces. Physics of Fluids 16 (12), 4635 – 4643.

[18] Harrison, C., Stafford, C. M., Zhang, W., Karim, A., 2004.Sinusoidal phase grating created by a tunably buckled surface. Applied Physics Letters 85 (18), 4016–4018.

[19] Inoue, R. et al. Distributions of glass-transition temperature and thermal expansivity in multilayered polystyrene thin films studied by neutron reflectivity. Phys. Rev. E 83, 021801 (2011).

[20] Fakhraai, Z. & Forrest, J.A. Measuring the Surface Dynamics of Glassy Polymers.*Science***319**, 600 -604 (2008).

[21]Schaffer, E., Thurn-Albrecht, T., Russell, T. P., Steiner, U., Feb. 2000. Electrically induced structure formation and pattern transfer. Nature 403 (6772), 874–877.

[22]Schaffer, E., Thurn-Albrecht, T., Russell, T. P., Steiner, U., 2001. Electrohydrodynamic instabilities in polymer films.EurophysicsLetters 53 (4), 518–524.

[23] Morariu, M. D., Voicu, N. E., Schaffer, E., Lin, Z., Russell, T. P., Steiner, U., Jan. 2003. Hierarchical structure formation and pattern replication induced by an electric field.Nature Materials 2 (1), 48–52.

[24] Bandyopadhyay, D., Sharma, A., Jul. 2007. Electric field induced instabilities in thin confined bilayers. Journal of Colloid and Interface Science 311 (2), 595–608.

[25] Reiter, G. Dewetting of thin polymer films. *Phys. Rev. Lett.* **68**, 75 (1992).

[26] Sharma, A. & Khanna, R. Pattern formation in unstable thin liquid films under the influence of antagonistic short- and long-range forces. *J. Chem. Phys.* **110**, 4929 (1999).

[27] Becker, J. et al. Complex dewetting scenarios captured by thin-film models. *Nat Mater* **2**, 59-63 (2003).

[28] Konnur, R., Kargupta, K. & Sharma, A. Instability and Morphology of Thin Liquid Films on Chemically Heterogeneous Substrates. *Phys. Rev. Lett.* **84**, 931-934 (2000).

[29] Zhang, Z., Wang, Z., Xing, R. & Han, Y. Patterning thin polymer films by surface-directed dewetting and pattern transfer. *Polymer* **44**, 3737-3743 (2003).

[30] Seo, S.-min, Park, J.-yong & Lee, H.H. Micropatterning of metal substrate by adhesive force lithography. *Appl. Phys. Lett.* **86**, 133114 (2005).

[31] Erik Schäffer. PhD thesis, University of Konstanz, (2001)

[32] Landau, L.D. (Lev D., Lifshitz, E.M. (Evgenii M. & Landau, L.D. (Lev D. *Fluid mechanics / by L.D. Landau and E.M. Lifshitz ; translated from the Russian by J.B. Sykes and W.H. Reid*. (Pergamon Press ; Addison-Wesley: London : Reading, Mass. :, London : Pergamon Press ; Reading, Mass. : Addison-Wesley, c1959.).
[33] Ghatak, A., Chaudhury, M.K., Shenoy, V. & Sharma, A. Meniscus Instability in a Thin Elastic Film. *Phys. Rev. Lett.* **85**, 4329 (2000).
[34] Shenoy, V. & Sharma, A. Pattern Formation in a Thin Solid Film with Interactions. *Phys. Rev. Lett.* **86**, 119 (2001).
[35] Mönch, W. & Herminghaus, S. Elastic instability of rubber films between solid bodies. *Europhys. Lett.* **53**, 525-531 (2001).
[36] Ghatak, A. & Chaudhury, M.K. Adhesion-Induced Instability Patterns in Thin Confined Elastic Film. *Langmuir* **19**, 2621-2631 (2003).
[37] Sarkar, J., Shenoy, V. & Sharma, A. Patterns, Forces, and Metastable Pathways in Debonding of Elastic Films. *Phys. Rev. Lett.* **93**, 018302 (2004).
[38] Gonuguntla, M., Sharma, A., Mukherjee, R. & Subramanian, S.A. Control of Self-Organized Contact Instability and Patterning in Soft Elastic Films. *Langmuir* **22**, 7066-7071 (2006).
[39] Shankar, V., Sharma, A., Jun. 2004. Instability of the interface between thin fluid filmssubjected to electric fields. Journal of Colloid and Interface Science 274 (1), 294–308.
[40] Tomar, G., Shankar, V., Shukla, S.K., Sharma, A. & Biswas, G. Instability and dynamics of thin viscoelastic liquid films. *Eur. Phys. J. E* **20**, 185-200 (2006).
[41] Tomar, G., Shankar, V., Sharma, A. & Biswas, G. Electrohydrodynamic instability of a confined viscoelastic liquid film. *Journal of Non-Newtonian Fluid Mechanics* **143**, 120-130 (2007).
[42] Arun, N. et al. Electric-Field-Induced Patterns in Soft Viscoelastic Films: From Long Waves of Viscous Liquids to Short Waves of Elastic Solids. *Phys. Rev. Lett.* **102**, 254502 (2009).
[43] J. Sarkar and A. Sharma, A unified theory of insabilities in viscoelastic thin films: from wetting to confined films, from viscous to elastic films, and from short to long waves, Langmuir 26, 8464–8473 (2010).
[44] Roberts, S.A. & Kumar, S. AC Electrohydrodynamic Instabilities in Thin Liquid Films. *Journal of Fluid Mechanics* **631**, 255-279 (2009).
[45] Israelachvili, J.N. Thin film studies using multiple-beam interferometry. *Journal of Colloid and Interface Science* **44**, 259-272 (1973).
[46] Tadmor, R., Chen, N. & Israelachvili, J.N. Thickness and refractive index measurements using multiple beam interference fringes (FECO). *Journal of Colloid and Interface Science* **264**, 548-553 (2003).
[47] Pease, L.F., 3rd & Russel, W.B. Limitations on length scales for electrostatically induced submicrometer pillars and holes. *Langmuir* **20**, 795-804 (2004).
[48] Sarkar, J., Sharma, A. & Shenoy, V.B. Electric-field induced instabilities and morphological phase transitions in soft elastic films. *Phys Rev E Stat Nonlin Soft Matter Phys* **77**, 031604 (2008)
[49] Friedrichs, R. & Engel, A. Pattern and wave number selection in magnetic fluids. *Phys. Rev. E* **64**, 021406 (2001).
[50] Abou, B., Wesfreid, J.-E. & Roux, S. The Normal Field Instability in Ferrofluids: Hexagon–square Transition Mechanism and Wavenumber Selection. *Journal of Fluid Mechanics* **416**, 217-237 (2000).
[51] Erik Schäffer. PhD thesis, University of Konstanz, (2001).

Chapter IV

Intimate contact between polymer surface and water: Electrostatic pressure induced nanostructuration

Table of contents for Chapter IV:

4.1. Introduction

When water is in contact with air, in standard conditions, oxygen and nitrogen are dissolved in concentrations of 0.2 mM and 0.5 mM. It has been shown in the past that reducing the concentration of the dissolved gases may affect several interfacial properties. Despite of the fact that oil and water do not mix, spontaneous emulsification of hydrocarbons occurs after water degassing [1,2,3]. Colloids stability [4], the range of the hydrophobic interaction [5], the conductivity of salt solutions [6], the efficiency of flotation process [7] and the slippage boundary conditions in flowing water are all affected by the amount of gas in solution.

As was described in Chapter I, there is a large body of theoretical and experimental studies suggesting that a region of reduced density is present at the interface between water and hydrophobic surfaces. A number of scanning probe microscopy studies reporting the presence of soft nanometric objects near hydrophobic surfaces in water have been published [8,9,10,11,12,13] after its existence was suggested 15 years ago [14]. Indeed, some reports of the nucleation of micrometric-size bubbles on surfaces were published long before [15]. However, no explanation for the existence of long-lasting nanobubbles that considers the large Laplace pressure inside them has been advanced. Some workers have even suggested that the observed nanobubbles in scanning probe experiments are a consequence of confinement effects or tip-substrate interaction [16,17]. On the contrary, a detailed X-ray reflectivity study on hydrophobic substrates, while supporting the existence of a depleted water layer by the interface, argued against the existence of micro or nanobubbles [18]. Independent reflectivity experiments have also evidenced the presence of a layer of reduced water density near hydrophobic surfaces with an extension determined by the concentration of dissolved gases [18,19,20,21]. However, some ellipsometric and neutron reflectivity studies failed to observed the existence of a water depletion gap [22,23]. Despite of the long list of seemingly contradictory results, consensus is slowly emerging around the idea that a boundary layer of reduced density is indeed present when water is nearby a hydrophobic surface, although its nature is yet to be firmly established [24,25].

In this chapter we explore the effect of dissolved gases in the interface between water solutions and several hydrophobic polymers. We observed that this interface is modified by the degassing of the aqueous phase, showing the influence of dissolved gases and ions present in the water on the interaction between water and a hydrophobic surface. Previously published results have evidenced how the morphology of hydrophobic surfaces can be severely modified in the presence of nanobubbles. We show here how this effect depends strongly on the amount of gas dissolved in the aqueous phase, and more importantly on the nature of the ions dissolved in the water. In addition, the results described in this Chapter clearly evidence the presence of a layer of enhanced mobility at the outermost surface of glassy polystyrene films, in agreement with results presented in Chapter III. This layer makes it possible surface reconstruction at temperatures well below the glass transition temperature, T_g.

4.2. Experimental section

Materials:

Polystyrene (PS) of five different molecular weights (7, 59, 160, 250 and 500 kDa) were investigated. PS of 500 kg/mol (T_g 103°C) and 59 kg/mol (T_g 102°C) were obtained from Sigma-Aldrich. PS of 250 kg/mol (T_g 103°C) was obtained from ACROS Organics. Crosslinkable [26] PS of 160 kg/mol (poly[styrene-co-(4-azidomethylstyrene)) was a generous gift of Dr. Eric Drockenmuller. PS of 7 kg/mol (T_g 90°C) synthesized by ATRP, was a gracious gift from Dr. Antoine Bousquet. PS latex (suspension of PS spheres of radius 400 nm) was obtained from Polyscience.

Film preparation:

Thin PS films were prepared by spin-coating polystyrene solutions in toluene onto small ($1\times1cm^2$) pieces on silicon wafers or mica. As mentioned in Chapter II, the PS film thickness is a function of spin-coating speed, solution concentration and polymer molecular weight. By adjusting these parameters, we prepared PS smooth films of thickness of ≈300 nm for all four M_W's. After spin-coating the PS films were annealed at 95°C for 12 h to remove the residual solvent and release any mechanical stress built up during the spin coating process. Similar results were obtained with films annealed at 150 C for 6 hours. After this treatment the samples were ready for investigations.

To increase the adhesion of the polymer film on the substrates and to avoid the penetration of water between the film and the substrates, in some cases the silicon wafers were coated with a silane layer by exposure to a solution of octadecyltrimethoxysilane (OTS, abcr Specialty Chemicals) in toluene during 2 hours. Identical results were obtained in absence of this primer silane layer.

Films of cross-linkable PS were prepared by spin coating a solution of the polymer in toluene 0.4% w/w. Cross-linking of the PS film was performed by irradiating the film with ultraviolet (UV) light (300-360 nm) during 1 hour, as described in reference [26].

Film characterization: The thickness of the films was determined by ellipsometry (Nanofilm); roughness and morphology were assessed by Atomic Force Microscopy in tapping mode (multimode and Icon, Veeco). The films were also characterized by water contact angle (IDC Concept) and streaming potential measurements (CAD). XPS was performed with 220i-XL ESCALAB, VG, as described in Chapter II,

Water degassing and film treatment: Millipore water with a conductivity of 18 $M\Omega cm^{-1}$ was used for solution preparation. The pH of the aqueous phase was adjusted by adding small amounts of NaOH (Prolabo) or nitric acid (Aldrich) as necessary. Similar results were obtained by using HCl (Aldrich) or KOH (Aldrich). Carefully cleaned Teflon bar stirrers were introduced in the solutions to be degassed to induce the nucleation of gas bubbles. The solutions were subjected to agitation under a pressure of 0.2mbar during two hours. The appearance of macroscopic bubbles in the aqueous phase was observed only during the first 30 minutes of degassing. After the degassing was finished, the air pressure on the flask was gently increased back to atmospheric pressure. The degassed solutions were

put right away in contact with the polymer surfaces for few minutes after stopping the pumping, unless otherwise indicated. The PS films were then dried with a gentle flow of nitrogen gas.

4.3. Contact between water and hydrophobic polystyrene films

As mentioned in the introductory part of this chapter, I will present some experimental results related to the effect of dissolved gases on the interface between water solutions and several hydrophobic polymers. In particular, I will present how the morphology of the surface of some hydrophobic polymer films is modified by degassing of the aqueous phase, showing the influence of dissolved gases and ions present in the water on the interaction between water and a hydrophobic surface. In this section, I present results from experiments aimed to investigate the interface of water with surfaces of different hydrophobicities.

A Nanoscope III MultiMode atomic force microscope (AFM) was used in tapping and contact mode to image the air-solid and the water-solid interfaces. Smooth freshly cleaved mica and polystyrene (PS) film prepared by spin-coating were investigated. Water has contact angle on freshly cleaved mica of ≈5° with water, which indicates that mica surfaces are strongly hydrophilic. On the contrary, a homogenous PS surface gives a contact angle value of ~90° with water, which indicates that a PS surface is hydrophobic in nature.

Figure IV.1-a show the taping-mode AFM height image of a mica surface in air. The surface is very smooth and reveals no spatial structure. To characterize the surface roughness, we will use the root-mean square roughness (R_{RMS} also noted R_q) [27]. R_q is given by the standard deviation of the z-values for the sample area, as given by equation

$$R_{RMS} = \sqrt{\frac{\sum_{i=1}^{N}\sum_{j=1}^{N} Z^2(x_i y_j)}{N^2}} \qquad (4.1)$$

Z is the height deviation taken from the mean image data plane; N is the number of data points in one scan direction. For the image in Figure IV.1-a, R_q = 0.03 nm.

Figure IV.1-b shows the contact-mode AFM deflection image of the same mica sample immersed in water. The image remains featureless. R_q is again 0.03 nm, which is very similar to the value obtained in air. Thus, the surface topography of a clean mica surface remains unchanged in water.

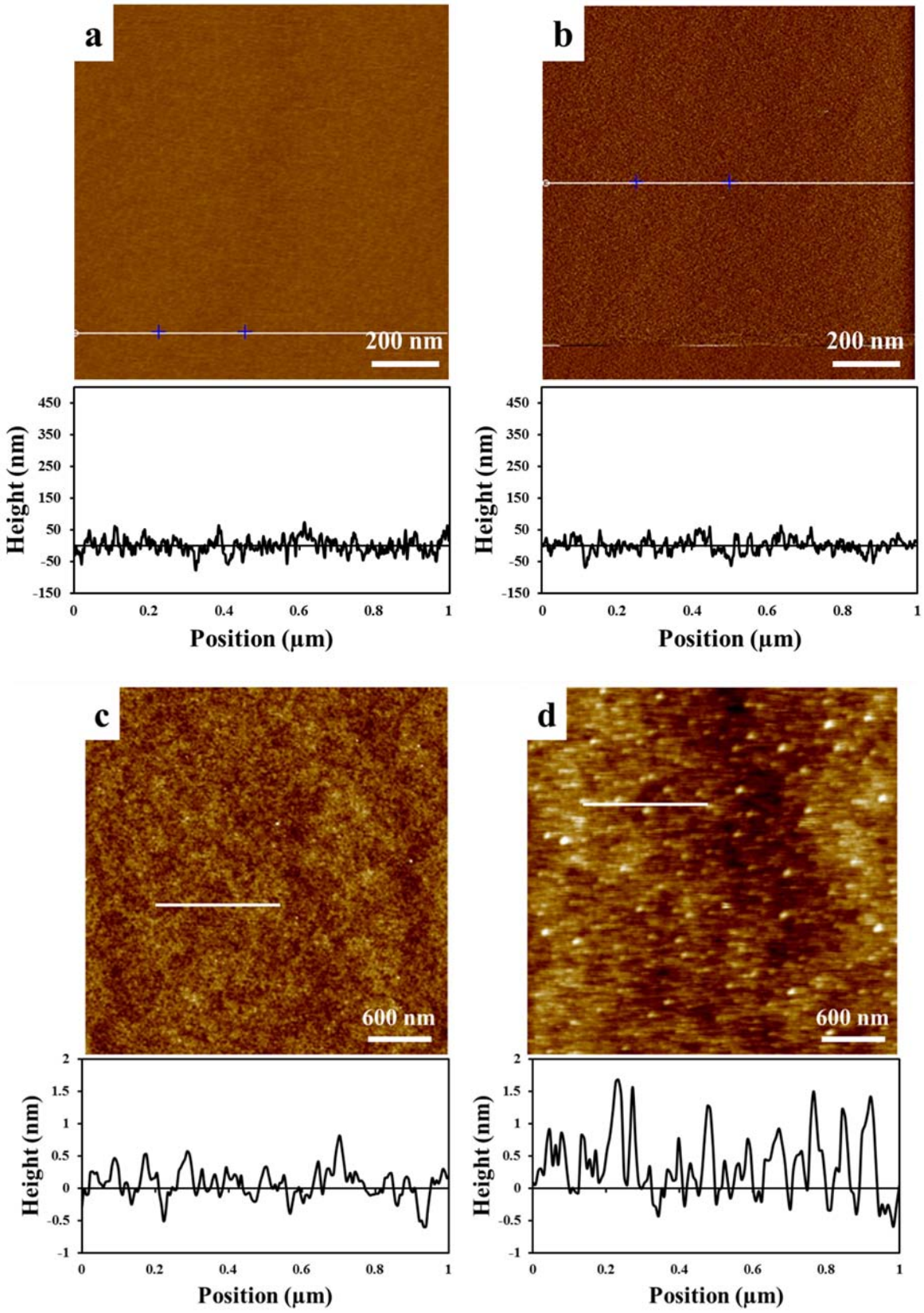

Figure IV.1: Results from AFM study of homogenous PS and mica surfaces: (a) contact-mode AFM height image of mica surface in air, (b) contact-mode AFM deflection image of mica surface in water, (c) taping-mode AFM height image of PS surface in air, (d) contact-mode AFM height image of PS surface in water.

Figure IV.1-c shows the taping-mode AFM height image of a PS surface in air. The image is featureless without any discernable spatial structure, with R_q = 0.27 nm. The cross-sectional view along the line is drawn in Figure IV.1-c. The height profile shows small amplitude oscillations (less than one nanometer). Figure IV.1-d show the contact-mode AFM height image of the same sample in water. This image is markedly different of the one measured in air, in contrast to what was observed with mica. We observe a very compact layer of randomly-distributed spherical objects, in both the deflection and height images. The height and width of these objects are ≈1.5 nm and 40 nm, respectively. These 'soft' objects can be deformed and displaced with the AFM tip (Figure IV.2). The roughness values for the height image in this case are R_q = 0.58 nm, much higher than the values measured in air.

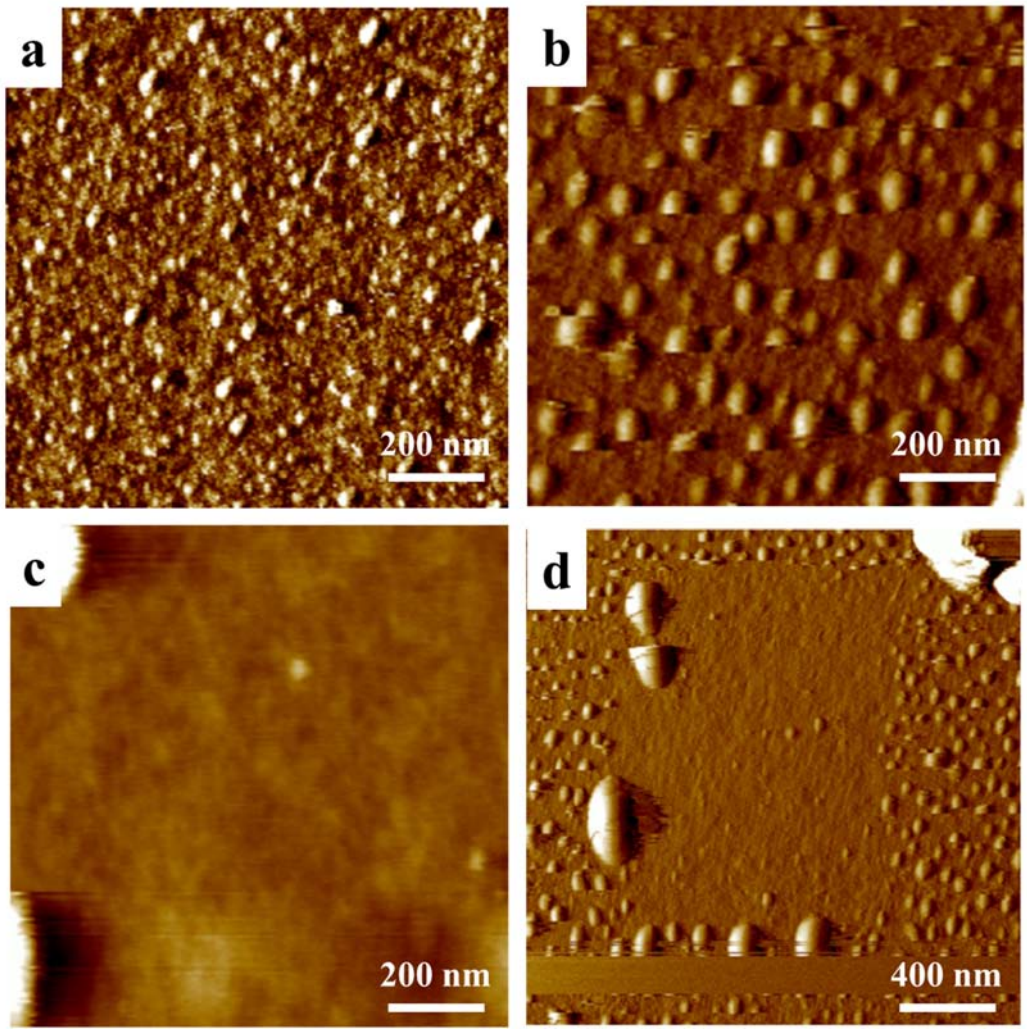

Figure IV.2: Contact-mode AFM deflection images of PS in water (a) initial image, (b) after first scanning the surface once at a increase setpoint voltage (corresponding to a higher force), (c) after scanning the surface once at even higher force, (d) a zoom-out on the same location after a pause of a few minutes.

We also observed a significant effect of the force applied with the AFM tip on the morphology of these objects (Figure IV.2). Figure IV.2-a shows a contact-mode AFM deflection image taken with a very low deflection set point (this set point determines how much force is applied while imaging). Uniformly distributed nanobubbles can be observed. The sample was then scanned with a higher deflection setpoint (higher force) followed by scanning again with a low setpoint voltage. Figure IV.2-b shows the image obtained in this second scanning. The image is markedly different from Figure IV.2-a, and shows that larger objects are now present on the surface. These larger features are formed, in our opinion, due to coalescence of smaller bubbles after being displaced from their original location. Scanning again at an even higher set point, produces a featureless image (Figure IV.2-c) suggesting that, upon much harder pressing with the tip, bubbles can be completely removed from the surface. At this point, the tip was disengaged, and scanning was stopped. After a few minutes, the tip was re-engaged. Figure IV.2-d shows an image of a larger area including the previous spot on the surface. The area which was scanned earlier still remains featureless while the region around the periphery of the scanned area shows features similar to those observed in Figure IV.2-b. From these results we can conclude that the features observed for PS immersed in water are soft air-filled nanobubbles that can be easily manipulated by the AFM tip, and no polymeric contaminants as speculated in a recent study. After the experiment under water, the polystyrene surface was imaged again with AFM in taping mode in air to check for surface topography changes due to the contact with water. As we can observe from Figure IV.3 the morphology is not changed, and the film is as smooth as at the beginning of the experiment.

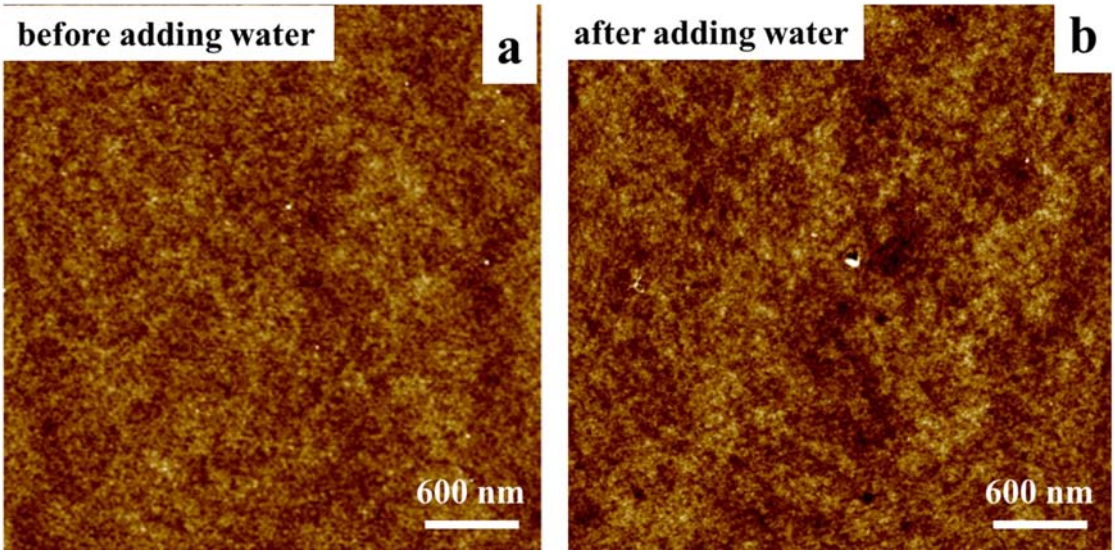

Figure IV.3: Tapping mode height-AFM images of PS coated silicon wafer in air (a) before adding water, (b) after water was removed from the surface.

We did not explore in more detail the properties of these bubbles; we were interested just to verify their presence. Even if the origin of these bubbles is unclear and some debate remains in the literature about their existence [14,28], they have recently been invoked as a possible origin of a number of phenomena, including the long-range attraction between hydrophobic surfaces immersed in

water [29], the stability of an emulsion without a surfactant [30], microboiling behavior [31] and the rupture of wetting films [32]. Nanobubbles on surfaces can also have significant consequences on the motion of particles in liquids or on the flow of liquids adjacent to surfaces or in capillaries. It has also been argued that nanobubbles lead to the frequency-dependent and shear-rate dependent fluid-slip that has been recently observed at partially wetting fluid-solid surfaces [33,34], and which gives rise to considerable reduction in friction of fluid flow past solids. Nanobubbles offer an effective mechanism for drag reduction in micro/nanofluidic applications, in which interfacial properties are expected to dominate the dynamics due to the large surface to volume ratio [35]. In ref. [35] Wang and Bhushan, studied boundary slip and nanobubles in micro/nanofluidic. They also presented a complete review about the properties of nanobubbles on hydrophobic surfaces, including nanobubbles imaging, nanobubles-substate interaction, tip-nanobubles interaction and presented some results showing how the morphology of hydrophobic surfaces can be severely modified in the presence of nanobubbles [36,37].

The aim of our study is not to exploit the properties and dependence of nanobubble formation on hydrophobic interfaces, but to explore the effect of dissolved gases in the interface between water solutions and several hydrophobic polymers. In particular, we investigated how this interface is modified by the degassing of the aqueous phase, showing the influence of dissolved gases and ions present in the water on the interaction between water and a hydrophobic surface. To the best of our knowledge, this is the first experimental study concerning the nanostructuration of hydrophobic polymer surfaces in contact with water solution [38].

4.4. Nanostructuration of hydrophobic polymer surfaces by intimate contact with water.

As described above and in Chapter I, a layer of low water density is formed when water meets a hydrophobic interface (polystyrene). How is this interface modified if gases are removed from water? In this section I describe how under certain conditions this procedure can induce a strong morphology change of the polymer surface. As a first example, let's consider smooth polystyrene thin films (thickness > 200 nm) produced by spin coating from a PS (250Kg/mol)/toluene solution (5%/w) onto surfaces of freshly cleaved mica, glass or silicon wafer, as the one represented in Figure IV.4-a. The smoothness of every film (1×1 μm^2) was checked using AFM. Then the films were immersed in different aqueous solutions with pH ranging from 1.5 (acidified with nitric acid HNO_3) to 12 (by using sodium hydroxide NaOH). Different surfaces were left in contact with the solutions between 5 min to 24 hours, and dried with N_2 gas. AFM pictures were then taken in air on dry surfaces. As represented in Figure IV.4-b,c, the aqueous treatment did not change the texture (morphology)/roughness of the PS surfaces compared with the original sample, and the films conserved their original smoothness.

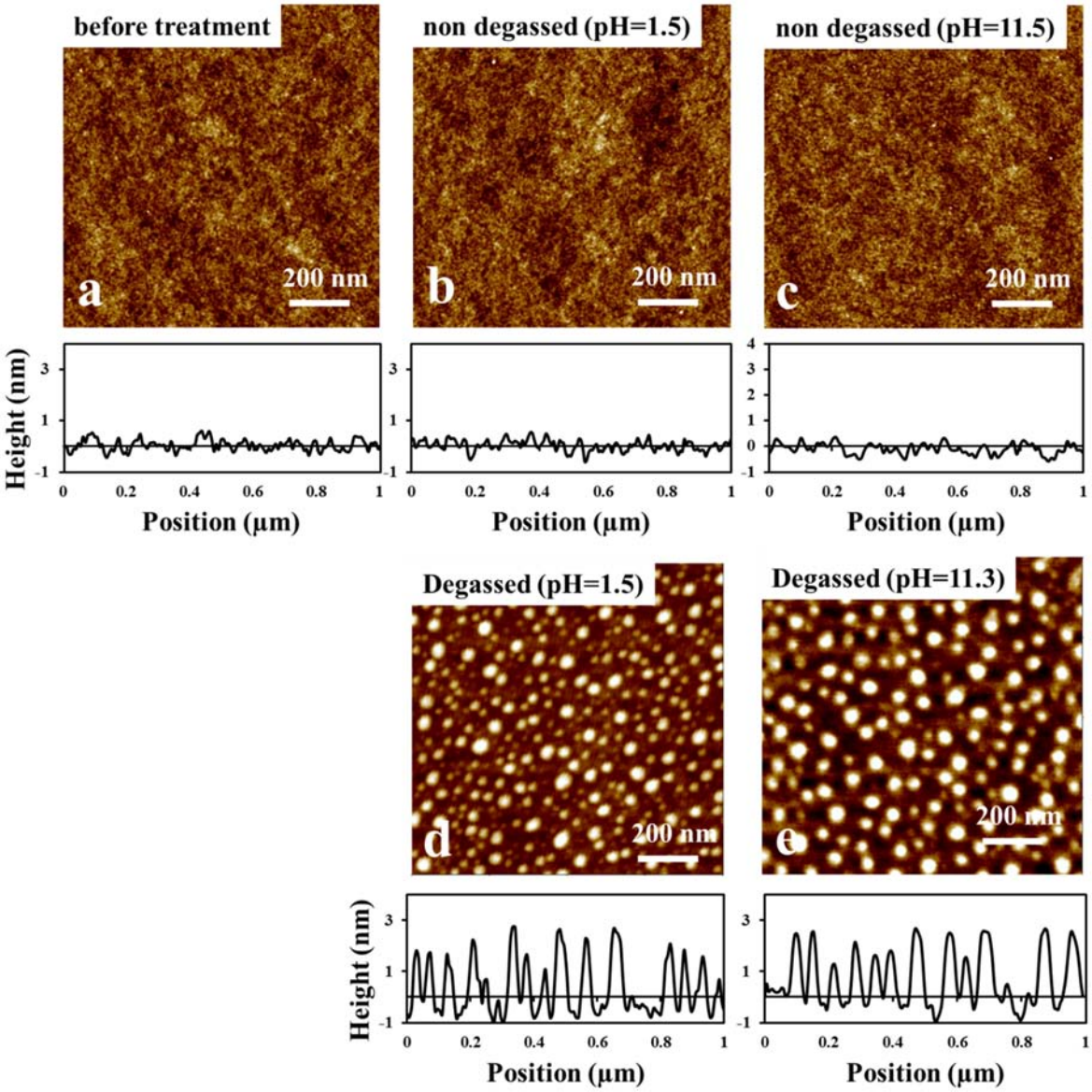

Figure IV.4: 1µm × 1µm height tapping mode AFM micrographs taken in air of 300 nm thick 250 kDa polystyrene films as prepared (spin-coated) (a); after exposure to a non degassed (b) and degassed (c) solution of nitric acid in double distilled water at pH = 1.5 and room temperature. A typical height profile for each condition is presented. The presence of asperities of regular nanometric size is clearly observed on the surface exposed to the degassed solution for 5 minutes. On the contrary, no modification was detected when an identical film was exposed to the same solution under identical conditions (or much longer times) before removing the dissolved gases.

We observed that the results critically changed if the same smooth PS film was exposed to previously degassed solutions. As can be observed in Figure IV.4-d,e, a characteristic nanostructure with a defined wavelength is now clearly seen at high and low pH. These findings show that avoiding the formation of the air interfacial layer by degassing the aqueous phase before it gets in contact with the surface has remarkable implications for the interaction between the two phases. The enhanced proximity between a hydrophobic polymer film and an aqueous solution induces a long lasting self-assembled nanostructure on the solid surface. As will be extensively discussed later, this water

induced self-assembly of hydrophobic polymer surfaces is an indirect validation of three controversial issues: i) the presence of a low density layer at the interface between a hydrophobic surface water, ii) the preferential adsorbtion of hydroxyl and /or hydronium ions at the surface of an hydrophobic surface iii) the presence of a zone of enhanced mobility at the outermost surface of a glassy polymer film. In addition, this approach can be easily tuned to pattern any ‘’mobile’’ polymeric substrate at the nanometric level, opening pathways for producing controlled patterns at the nanoscale in a single simple step.

Since this simple process of nanostructuration of polymer films present scientific and industrial interest and very little work had previously done in this area, we have spent a great deal of effort verifying it and investigating the different variables involved in the process. To this aim, we have explored more than 1500 different films and characterized the behavior of polymers of different nature and molecular weight. We investigated the effect on films and pellets of different polymers, at temperatures above and below the glass transition and molecular weights above and below the entanglement length. We have observed the structuring effect of acidic/basic water on poly(methyl methacrylate) (PMMA), polydimethylsiloxane (PDMS) while crosslinking, films of polystyrene of 5 different molecular weights, PS in the form of colloidal spheres and bulk, and semi crystalline films of polyethylene. We have also looked into the influence of pH, film thickness and film-substrate interaction (Chapter V), temperature of formation and aging (Chapter VI), different salts, acid and bases and degassing, immersion and re-gassing times.

4.4.1. Surface Chemical Analysis: XPS

The first observation of this structuration process was rather surprising; the first hypothesis that came in our mind was that the bumps on the PS surface were due to some form of contamination. Degassing and water exposure could induce the adsorption of impurities. However, after eliminating all possible sources of contamination and thoroughly cleaning our experimental environment, the treatment with degassed solutions would continue to induce the appearance of a long lasting self-assembled nanostructure on the PS surface. We excluded the adsorption of pollutants on the surface, as with non degassed solutions (or after allowing the re-equilibration of previously degassed water phase with air) the nano-structuration would not take place. Moreover, high resolution XPS analysis before and after structuration revealed no change of the treated surface chemical composition. XPS was used to test the exact composition of the PS surfaces before and after treatment with degassed solution. No chemical modification of the films was detected. The atomic composition of non treated, nonstructured (treated with non degassed solution) and structured (treated with degassed solutions) PS films was found to be identical by using XPS.

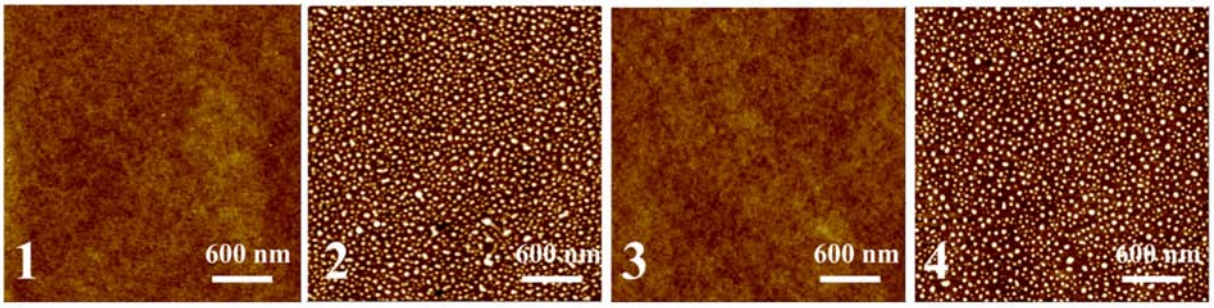

Figure IV.5: AFM micrographs of 300nm thick PS films after 5 minutes exposure to no degassed (1,3) and degassed (2,4) water at pH=1.5 and concentrated salt solutions $NaNO_3$ samples 1,2 and NaCl samples 3,4. AFM show the spontaneous nanostructuration of samples 2 and 4 after treatment with degassed acid solutions. The surface of samples 1 and 3 were very smooth (RMS roughness 0.5 nm) before and after the treatment.

AFM micrographs of some of the studied samples are presented in Figure IV.5. The results of XPS analysis are reported in Table IV.1 All PS films analyzed contains 1-5% oxygen and 95-98% carbon, regardless of their morphology. No traces of sodium, chloride or nitrogen were detected on the samples after treatment with concentrated salt solutions. The XPS results show that no chemical modification of the surfaces has occurred after treatment with degassed or non degassed solutions. The observed blobs observed in Figure IV.5-2,3 are clearly structured PS films, unambiguously eliminating the hypothesis of impurity contamination surface modification.

Table IV.1: Surface composition of some selected samples. No traces of sodium, chloride or nitrogen were detected on the samples after treatment with concentrated salt solutions at low pH. AFM show the spontaneous nanostructuration of samples 2 and 4 after treatment with degassed acid solutions. The surface of samples 1 and 3 were very smooth (RMS roughness 0.5 nm) before and after the treatment.

	Treatment				XPS results (± 5%)					
Sample	Salt	Conc.	pH	Degassing	%C	%O	%Si	%Na	%Cl	%N
1	$NaNO_3$	0.03M	1.5	No	94	5	1	0	0	0
2	$NaNO_3$	0.03M	1.5	Yes	98	2	0	0	0	0
3	NaCl	0.03M	1.5	No	98	1	1	0	0	0
4	NaCl	0.03M	1.5	Yes	99	1	0	0	0	0

If the reported PS surface modification is not due to contamination, the natural question that emerges is “what is the origin of the structure and what determines the size of the bumps”? One possibility may be that some gas is dissolved in the polymer film, which then bubbles the surface upon exposing to a degassed solution.

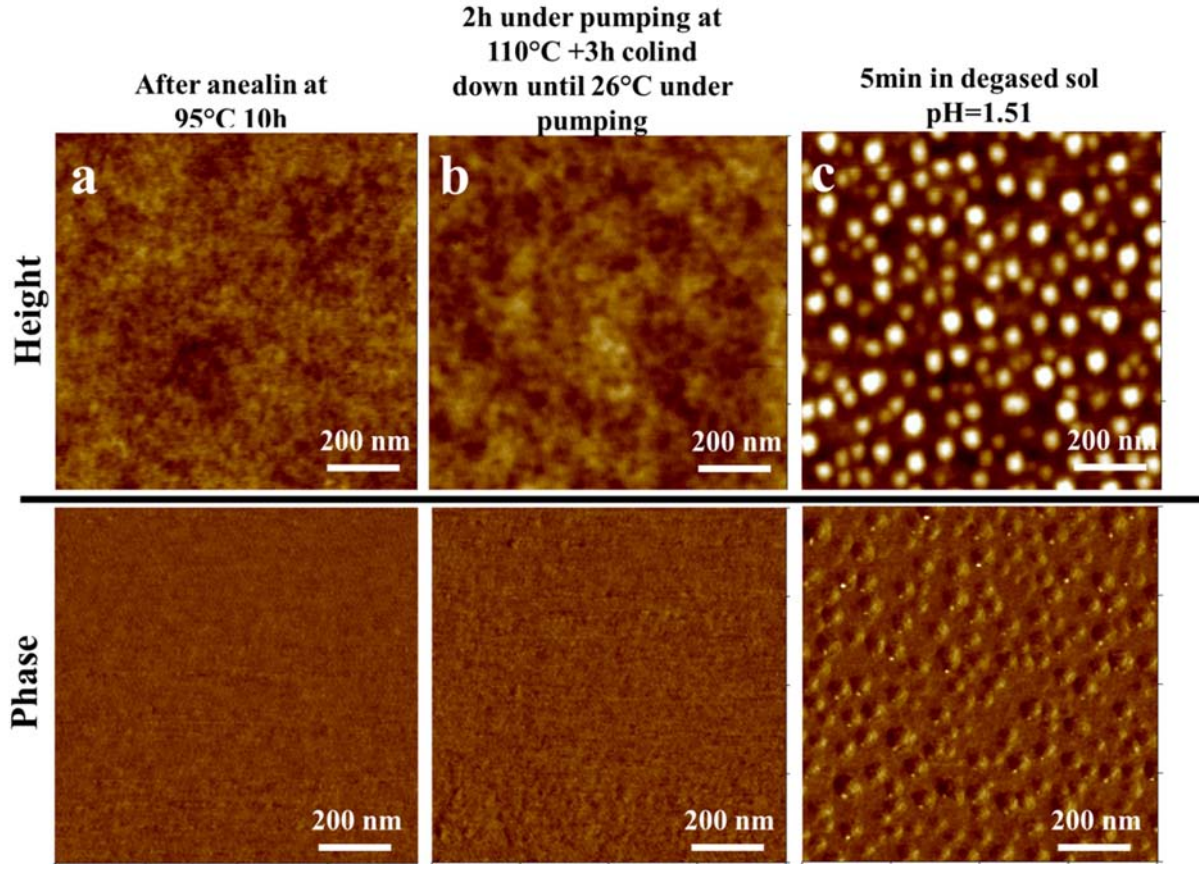

Figure IV.6: AFM micrographs of a 300 nm coated polystyrene -250kDa film on silicon wafer before treatment (a), after sample was heated at 110°C under vacuum (≈0.2 mbar) for 2 hours (b) and after treatment of degassed solution of nitric acid solution of pH = 1.5 (c).

The solubility of gases in the polymer films is certainly very low and not readily accessible, so it is hard to be estimated. Nevertheless, to address this concern, we have performed the following test: a 300 nm thick polystyrene film was spin coated, annealed as usually overnight at 95°C and studied with AFM (Figure IV.6-a), consecutively the sample was heated above T_g (110°C) under vacuum (≈0.2 mbar) for a period of time longer than 2 hours to remove the gas possibly trapped inside the film. After cooling it down (always at low pressure) we verified its smoothness by AFM (Figure IV.6-b) and then treated with degassed acid water for few minutes. We observed the structuration of the film only after treatment with degassed water (Figure IV.6-c). Morphology and size of structuration is similar to that presented before. A less important structuration would be expected if the origin of nanostructuration were the gas dissolved in film.

4.4.2. Effect of nano structuration on wettability of PS films

The contact angle of double distilled water on PS films was measured before and after treatment. As we can observe from Figure IV.7 water contact angle for structured and non structured PS samples behave in very similar way, with an initial slow decrease followed by a plateau near 78°. These values are in good agreement with those reported before for *a*PS [39]. No noticeable change in contact angle hysteresis was observed due to the presence of regular nanosized patterns. Similar

results were obtained for polystyrene samples of different molecular weights. The fact that the wettability of the surface remains unchanged after structuration confirms that the observed blobs are just structured PS; it is unlikely that chemical modification or contamination would not induce any wettability change of the surface.

AFM micrographs of some of the samples used for the wettability tests are shown in Figure IV.8, together with photographs of water drops in contact with the different substrates.

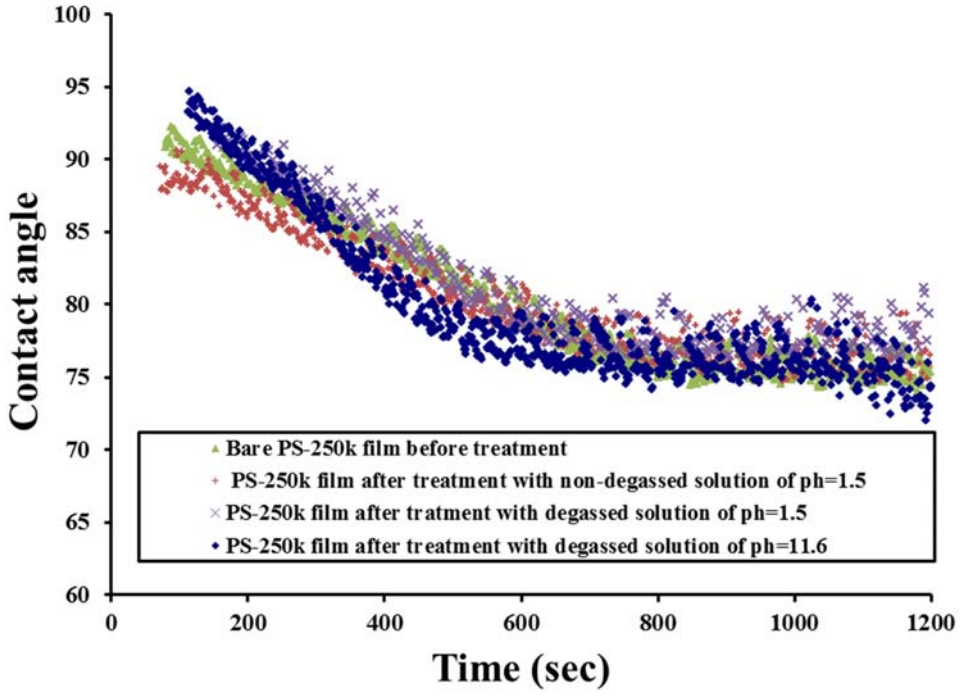

Figure IV.7: Wettability of PS-250k film of thickness 300 nm, before and after treatment with non-degassed and degassed solutions, illustrated as water contact angle as function of time

Table IV.2: Advancing and receding contact angles of PS films after treatment with aqueous solutions

PS sample treatment	θ_{adv}, °	θ_{rec}, °	$\Delta\theta$, °
untreated	90	78	12
non-degassed solution of pH = 1.5	90	78	12
degassed solution of pH = 1.5	90	78	12
non-degassed solution of pH = 11.6	92	78	14

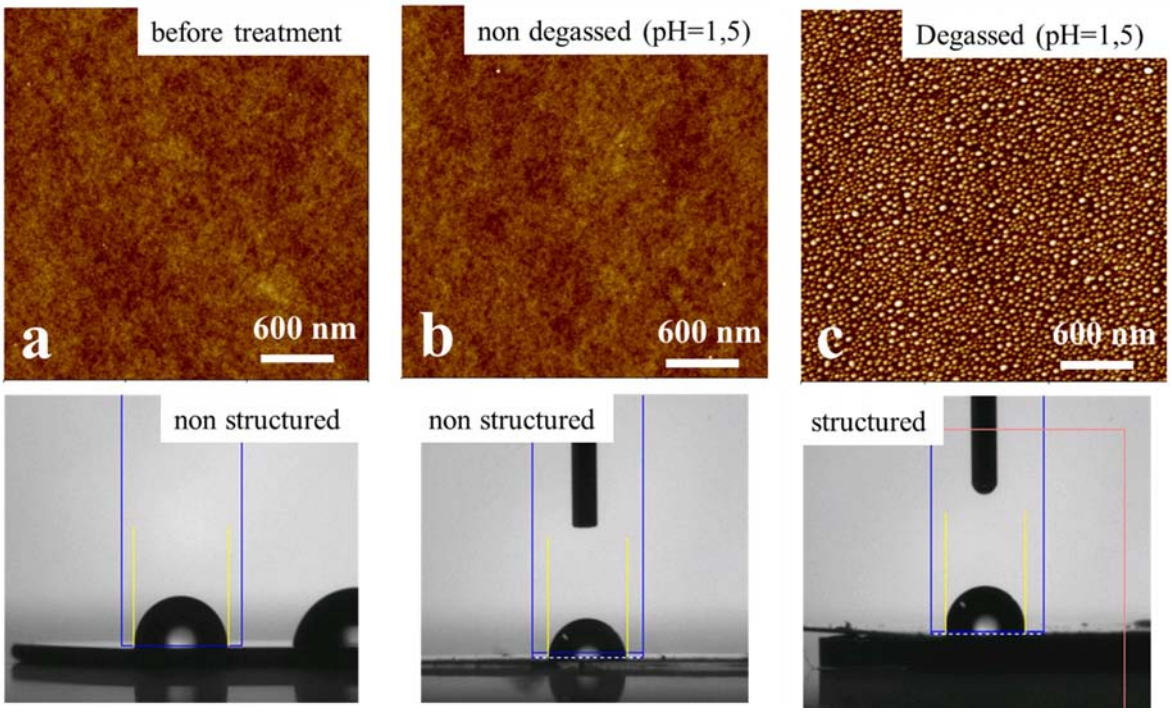

Figure IV.8: AFM micrographs and static contact angle of a 300 nm coted polystyrene-250k film on silicon wafer before and after treatment of with non-/degased solution of nitric acid solution of pH=1.5.

4.5. Variables governing the nanostructuration process

In this section I will describe the effect of different variables on the nanostructuration process described above. In particular, the effect of pH of the aqueous solution, hydrophobicity of the surface, annealing process, film thickness, temperature and supporting substrate will be discussed. Some of these points will be explored in more detail in the following chapters of this thesis.

4.5.1. pH of water solution

One of the most important variables that control the morphology of the structured PS films is the pH of the degassed solution, as can be observed in Figure IV.9. More important modifications are observed at high or low pH values, the size and density of the blobs get substantially smaller under more neutral conditions, and the nanostructure almost disappears between pH values of 6 and 9. Interestingly, streaming potential measurements suggest ionic adsorption on the surfaces at the same conditions. In agreement with previously reported results (*see Chapter I*), [40] we observed a strong variation of zeta potential of the hydrophobic polymer surfaces with pH. The observed surface structuration seems to correlate well with the values of the surface charge density as derived from the measured zeta potential of the surfaces using the Grahame equation (*see Chapter II*) [41,42]: the higher the value of the surface charge density, the larger is the effect of the aqueous phase on the structure of the polymer surface.

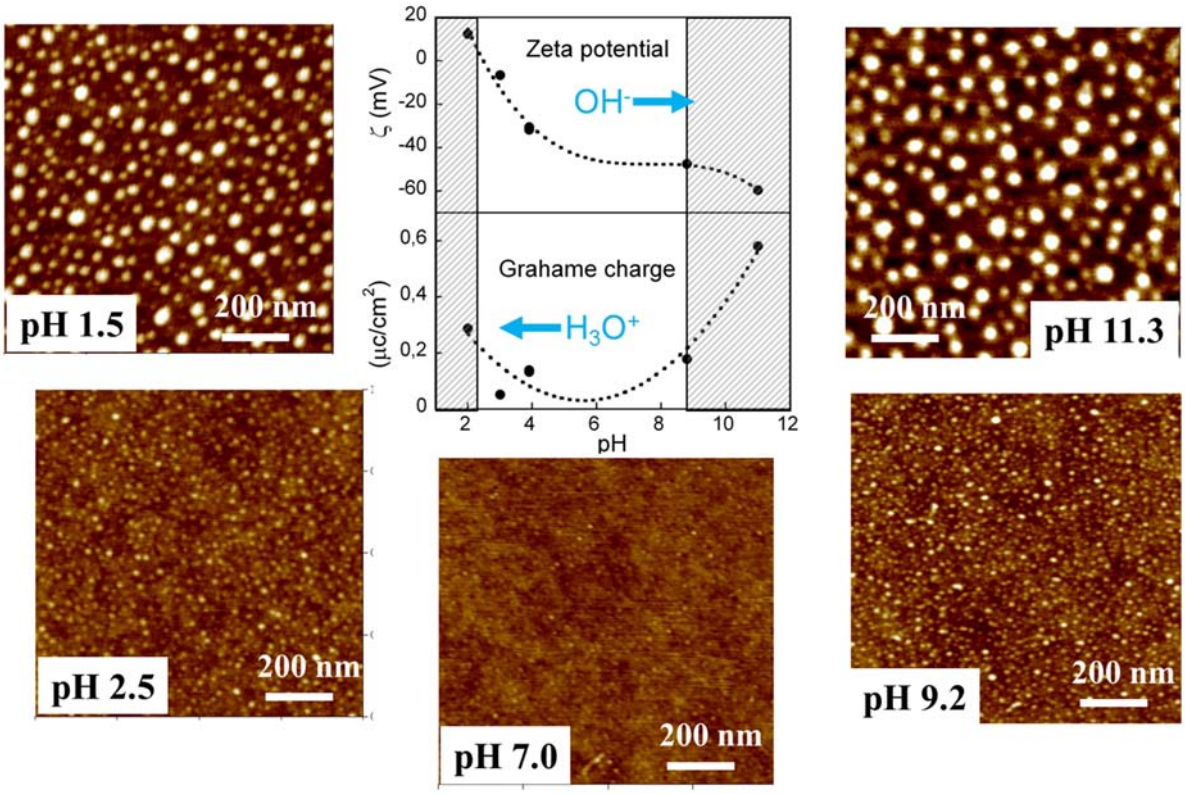

Figure IV.9: 1 µm x 1µm height tapping mode AFM micrographs taken in air of 300 nm thick 250 kDa PS films treated with degassed water at different pH, varied with HNO_3 and NaOH. The graphs show the measured zeta potential and calculated charge density of each substrate. Structuration is observed at pH values in the dashed zones. The modification of the polymer surface in contact with degassed water is determined by the pH of the solution: while relatively large self assembled blobs are observed at low and high pHs, their size and density get substantially smaller under neutral conditions.

This striking result seems to be largely independent of the ionic strength. As can be observed in Figure IV.10-f,g similar patterns were observed by exposure of a polymer film to degassed water at pH = 1.5 (adjusted by adding HNO_3) regardless of the addition of $NaNO_3$ 0.1M. On the contrary, the structuring effect of degassed solutions of sodium chloride, perchlorate or sodium nitrate up to 0.1 M (Figure IV.10-a-e) is not much larger than the one of water at neutral pH.

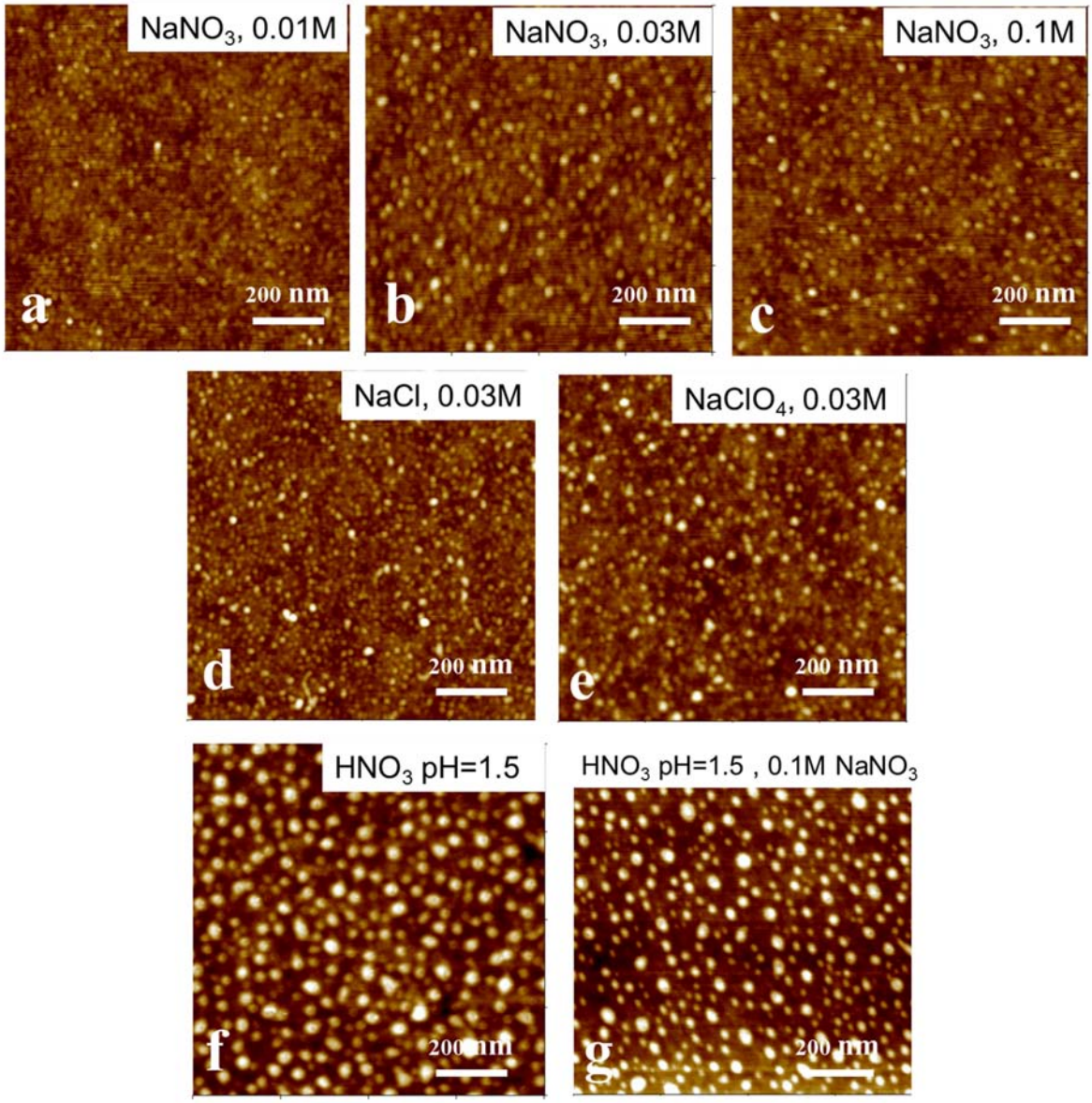

Figure IV.10: AFM micrographs of 300 nm thick PS films after 5 minutes exposure to degassed water at different pH and $NaNO_3$ concentrations. A similar structuration effect is observed at acid pH values in presence or absence of $NaNO_3$. Less significant structuration is observed at neutral pH regardless of the salts concentration of NaCl, $NaNO_3$ and $NaClO_4$

4.5.2. Surface hydrophobicity

As presented above, the surface structuration has no effect on the wettability of the surfaces because the contact angle of water on the substrate is not changed by the process. However, the hydrophobicity of the surface seems to determine the outcome of the process. As we can observe in Figure IV.11, the structuration of the film is not observed if the polymer surface is rendered hydrophilic (θ=30°) before the water treatment by partial UV-oxidation (5 minutes irradiation under an Hg vapor lamp, UVOCS). We used a low pressure mercury vapor lamp which generates UV emissions in the 254 and 185 nm ranges.

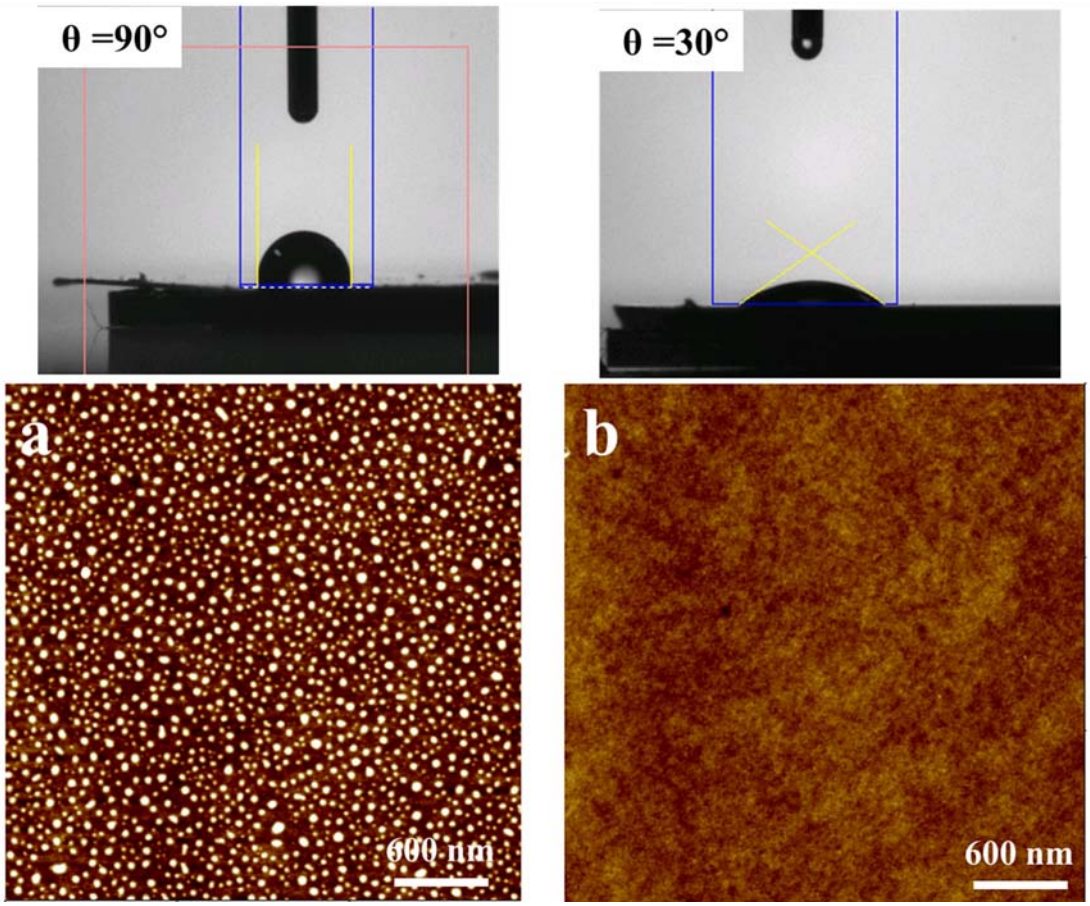

Figure IV.11: AFM micrographs of PS films surface with different wettability after exposure to a degassed acid water of pH=1.5.

We performed a systematic investigation of this point. Films of the same thickness (300 nm) and surface area were placed at 5 cm from the light source, and irradiated for different times. In order to evaluate the effects of UVO treatment, surface morphology, film thickness and water contact angel were measured before and after UVO treatment. AFM and ellipsometry measurements did not revealed significantly changes in the thickness or the morphology of the film with increasing the treatment times (Figure IV.12-a,b). In contrast, the hydrophilic nature of PS was remarkably increased with increasing exposure times, as can be observed Figure IV.12. The water contact angle decreased with increase of UVO treatment time and then became almost constant at about 20°.

After treatment with UVO, samples with of PS of different wettability were simultaneously exposed to a degassed solution of pH = 1.5 during 5 min, and then gently dried with nitrogen and studied again by AFM.

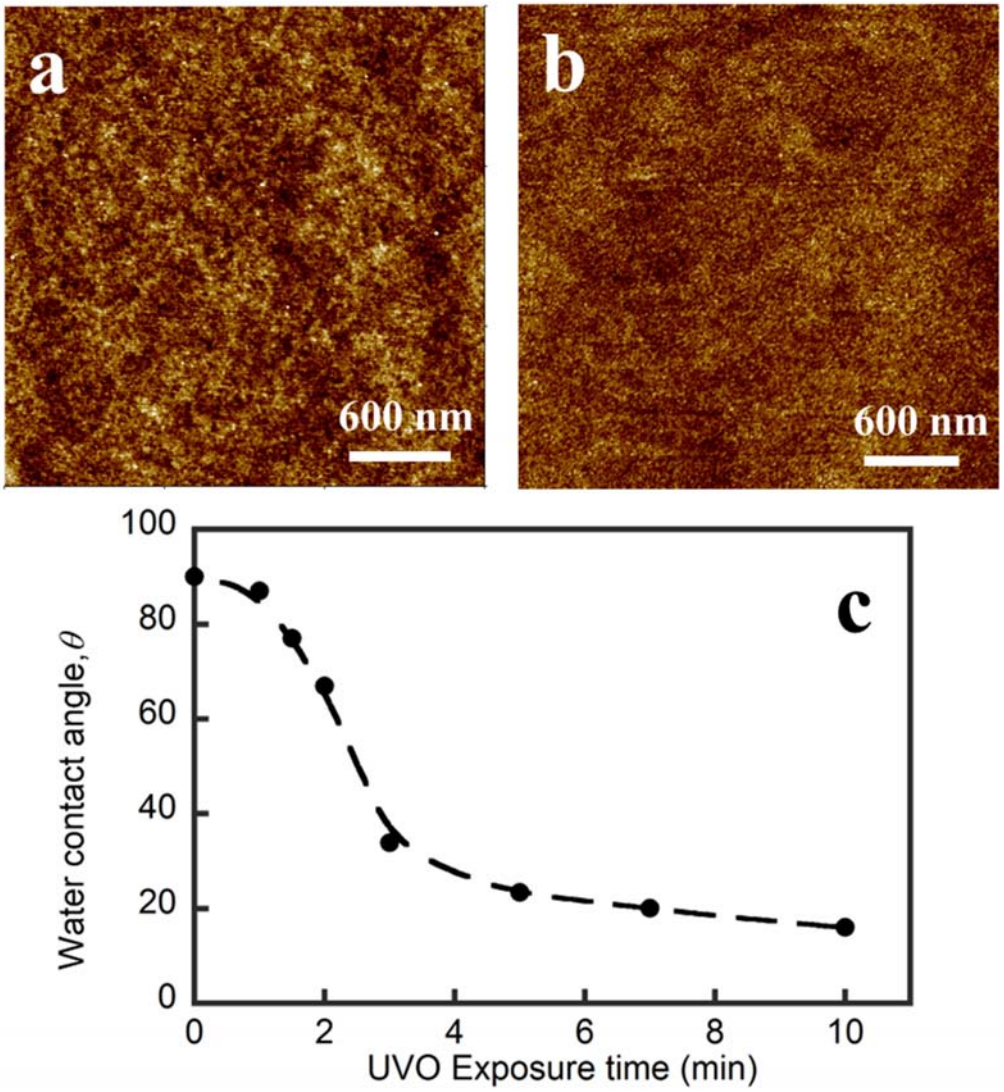

Figure IV.12: a) and b) AFM height images of PS film before and after 10 min UV-oxidation. c) variation of the contact angle of water on PS surfaces after UV-oxidation.

As can be observed in Figure IV.13, the wettability of the PS surface determines the structuring effect of degassed acid water. No structuration was observed for water contact angles smaller than 75°. However, it is known that the UV oxidation reduces the water contact angle on the surface by chain scission and partial oxidation of the PS, but it also enables cross-linking between polymer chains [43], reducing in this way the mobility of the surface layer. As we did a very mild UV treatment, we believed this effect to be minor. Nevertheless, is the reduced structuration observed on the samples represented in Figure IV.13 due to different wettability of the surface or to reduced mobility due to crosslinking? To verify this point and to discard the possible effect of reduced PS mobility by crosslinking we have performed the following test. A smooth 300nm thick PS film (M_w 250kDa) was UV-oxidized 5 min in order to make it hydrophilic (θ=30°). As verified by ellipsomety and AFM, this treatment did not significantly change the thickness or the morphology of the film (Figure IV.14-a). Consistently with our previous tests, no structuration was observed upon treatment

with degassed acid water (Figure IV.14-b). Then we heated the film at 70 °C during 10 hours to promote film reconstruction and the hydrophobicity of the film (the water contact angle after the treatment was θ=85°). This step allowed the reconstruction of the film via conformational changes or chain diffusion reducing the interfacial free energy [44]. Subsequently, a second exposure to degassed acid water effectively provoked the structuration of the film (Figure IV.14-c). This result evidences that is the hydrophilicity of the film and not PS cross-linking that is responsible for the lack of structuration immediately after UV-treatment.

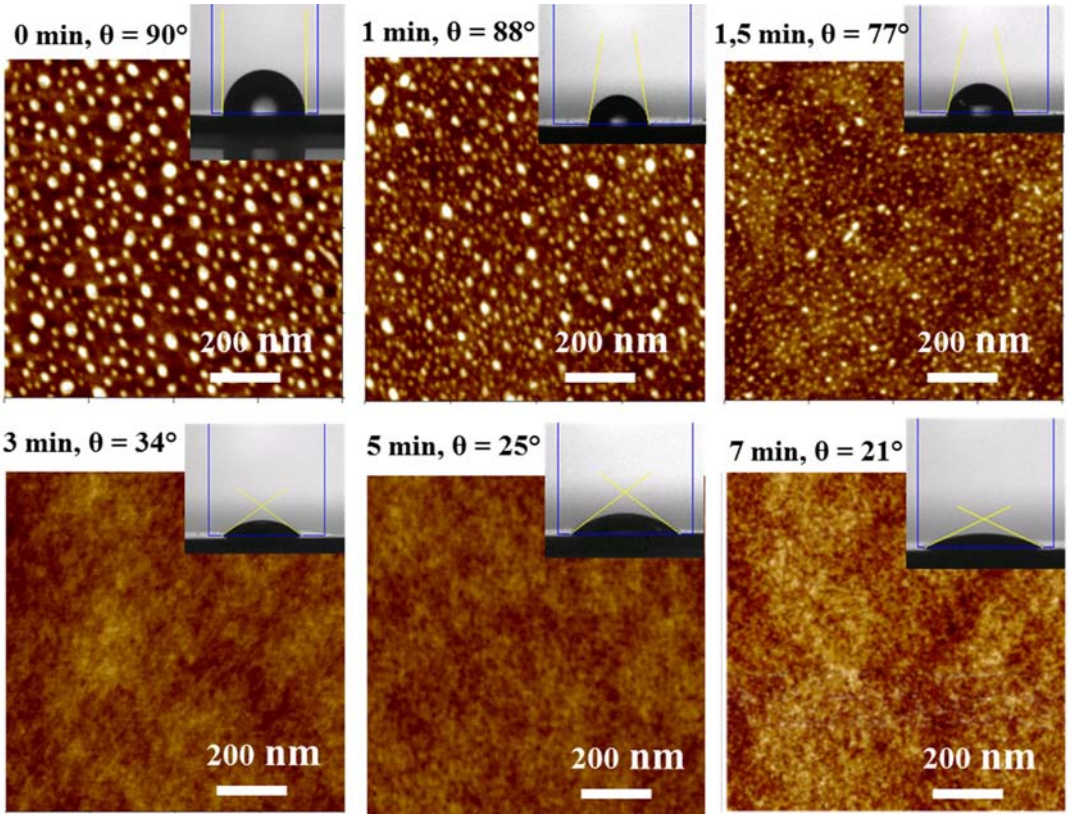

Figure IV.13: AFM micrographs of 300nm thick PS films after different times of UVO treatment and exposure to degassed water at pH 1.5 for 5 min. Water induced structuration is observed only for contact angles greater than 75°

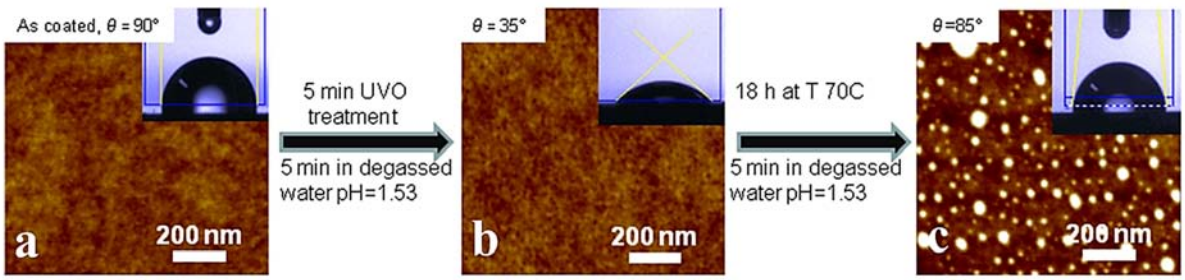

Figure IV.14: AFM micrographs of a 300 nm thick PS film before and after UVO treatment and exposure to degassed water at pH = 1.5 for 5 min. No structuration is observed. The film becomes hydrophobic again after heating it for a certain time. The structuring effect of degassed acid water is then recovered.

Two remarkable conclusions can be drawn from the observed structuration of hydrophobic PS films after exposure to degassed solutions. First, the interaction between the aqueous phase and the hydrophobic substrate is fundamentally modified by the gases dissolved which shelter the hydrophobic substrate from the aqueous phase. Second, there is a mobile surface layer on the polymer which can be restructured under external stimuli, even though we are working at temperatures largely below the glass transition temperature T_g of PS. This indicates that macromolecular chains near the interface have properties which deviate significantly from their bulk counterparts. Indeed, in a recently reported study of relaxation of nanometric deformations on films of PS, Fakhraai and Forrest [45] showed that the mobility of polymer chains is dramatically accelerated nearby the surfaces with respect to the bulk. Although it is still poorly understood, several explanations have been advanced for this enhanced dynamic, related to reduced entanglement density, enrichment of chain ends and increased free volume for the polymer molecules at the surfaces [45].

In order to further demonstrate that the "mobility" of the polymeric surface is a key factor to induce the nanostructuration, the following experiment was performed. Three PS films were prepared with UV cross-linkable azidomethyl-functionalized PS chains [26] by spin coating a solution of the polymer in toluene 0.4% w/w. One was untreated, while to other were partially or completely UV cured, by different times of exposure to UV light. The surfaces were then immersed into degassed acidic solution of pH = 1.5. As expected, the reference sample surface was nanostructured as shown in Figure IV.15-1, on the contrary, the cross-linked sample (Figure IV.15-3) did not present any bump formation (Figure IV.15-2). Cross-linking a polymeric material increases significantly its glass transition (as measured routinely using a Differential Scanning Calorimetry or DSC) and consequently reduces its bulk and surface mobility. This result highlights the importance of mobility to induce nanostructuration; on the other hand, one could take advantage of cross-linking to ''freeze'' a given nanostructure avoiding any subsequent relaxation. To illustrate this point, the nanostructured reference sample (1) was UV cured after structuration. No visible relaxation or disappearance of the bumpy structure was detected after to 1 month in agreement with the lack of mobility. This is not the case for non cross linked samples, as will be shown later.

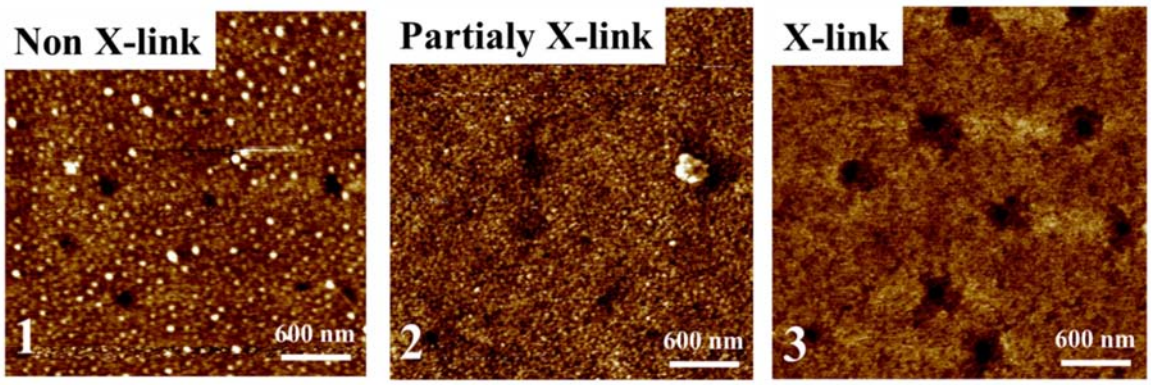

Figure IV.15: AFM micrographs of representing morphology of PS films (M_w-170k) after treatment with degassed nitric acid solution of pH=1.5 of (1) non- cross-linked,(2) partially and fully cross-linked (3)

4.5.3. Influence of annealing

Numerous groups have shown enhanced molecular dynamics relative to bulk values in various organic glass forming material samples confined to thin films [46,47,48,49,50,51,52,53,54]. The cause of these deviations is matter of ongoing debates. One aspect often discussed is related to the thermal-history of the material. Concerning this aspect, a few recent publications pointed out that thin polymer films represent a "highly metastable" state of matter [55] and that considerably large 'residual stresses' persist after their preparation [56,57].It is therefore essential to assess the impact of the preparation and thermal history of the samples.

As already mentioned, for glass forming materials the glassy state is not an equilibrium state and the system in the glassy state always has a tendency to evolve to the potential final equilibrium state through structural relaxations. So, it is important to get the studied systems into the equilibrium state before real measurements. Conventionally, this is achieved by high temperature long time annealing treatments. As were mentioned all thin polymer films in our measurements are thermally treated at 95°C during 12h. But 95°C is a temperature closely to T_g which for sample of M_w 250 kDa is 102°C. In literature usually samples are annealed at a temperature above bulk T_g. The point of such high temperature annealing treatment is to relax polymer chain molecules in the films to reach an equilibrium state, at so high temperature chain molecules can relax completely with fast enough mobility to reach the equilibrium state - one should note that at a temperature above bulk T_g the chain segment characteristic relaxation time is ~0.001 s and accordingly the chain segments can "freely" wiggle around to reach an local equilibrium state. We cannot use very high temperature because if the freshly spin-coated polymer films (especially for ultra-thin films) are exposed to high temperatures some small holes can be formed in the polymer films due to rapid evaporation of the solvent and polymer dewetting from the substrate.

To determine the effect of annealing on the structuration process, the following test was performed. Two samples of the same thickness were spin coated from toluene solution on silicon wafer. Thickness of samples was determined to be around 300 nm and surface was as usually ultraflat (root mean square roughness <0.5 nm). One of the samples was annealed as usually at 95°C during 10 hours, while second one at 150 °C for 6 hours. Then both samples were exposed to a degassed nitric acid solution of pH=1.5. As we can observe from Figure IV.16-a,b water induced structuration is similar in both cases.

It has been known for many years [58,59] that amorphous materials are not in thermodynamic equilibrium at temperatures below their glass transition. As solidified supercooled liquids they have a higher volume, entropy, etc., than they would have in the equilibrium state. Volume relaxation studies reveal that below T_g, the molecular mobility is not quite zero. There is a slow and gradual approach to equilibrium, and this aging process changes some properties of material. During aging the material becomes more and more glassy. It becomes stiffer and more brittle, its damping decreases, and so do its creep- and stress relaxation rates, dielectric constant, loss, etc [60].

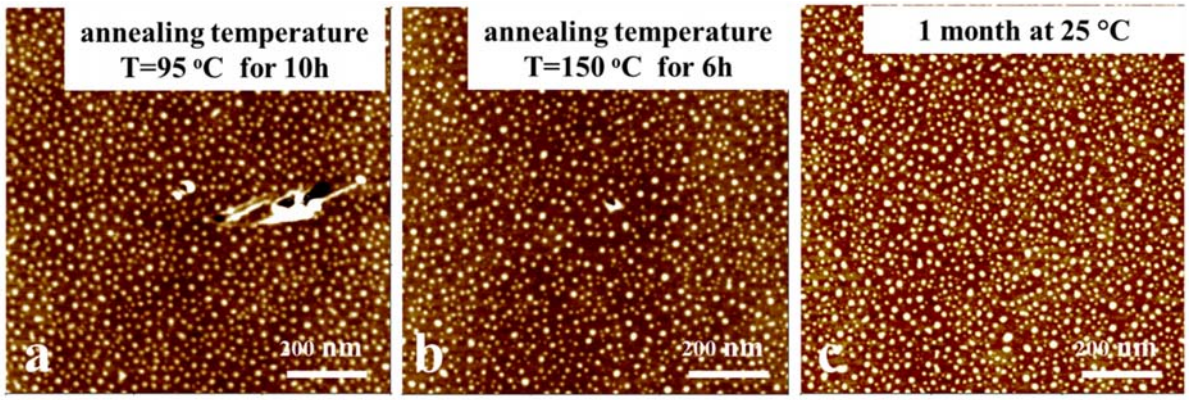

Figure IV.16: AFM micrographs of 300 nm thick PS-250k films after different thermal history and exposure to degassed water at pH = 1.5 for 5 min. Water induced structuration is observed to be similar in all cases.

We were also interested if the surface mobility of polystyrene films changes with time. To explore this, the following experiment was performed. A polystyrene film with M_W = 250 kDa and thickness of 300 nm with same thermal history as sample represented in Figure IV.16-a, was stored at room temperature in a clean environment for 1 month. Then the sample was treated with degassed aqueous solution of pH = 1.5. As we can observe in Figure IV.16-c there are no noticeable changes in the morphology of the induced nanostructuration, compared with a sample treated shortly after preparation (Figure IV.16-a). This result shows that the properties of the upmost layer of PS surface did not undergo substantial changes in time.

4.5.4. Film thickness

As discussed in chapter I, ultrathin polymer films exhibit changes in dynamical and mechanical properties with decreasing film thickness. In particular, the glass transition temperature (T_g), decreases. The essential reason of these confinement effects is matter of discussion. We were interested in investigating if polymer properties of the nanoscale film have any influence on water induced nanostructuration. As shown in Figure IV.17-a,b for films supported on native silicon and mica, the typical diameter and heights of the observed bumps are similar, and are independent of polymer film thickness down to 10 nm. It should be noted that nanostructuration also occurs on a bulky PS substrate made from molten PS pellets, as shown in Figure IV.17-c. These result rules out the influence of the inorganic substrate and /or the thickness of the PS layer on the nanostructuration phenomenon.

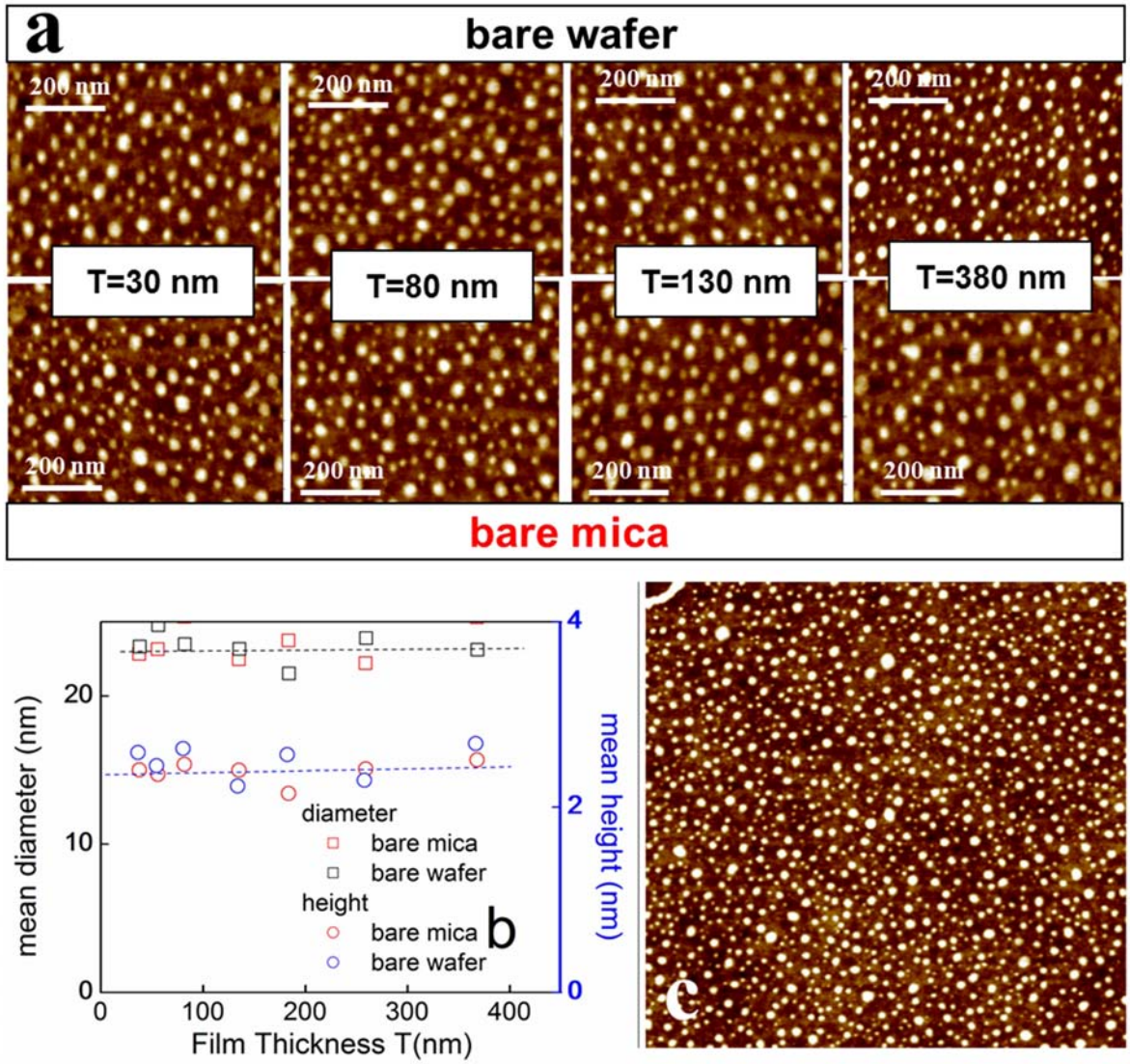

Figure IV.17: (a)-Height AFM micrographs of films of 250 kDa polystyrene films measured in tapping mode in air. The films of indicated thickness were spun coated on bare mica and silicon wafers, and then exposed to a degassed solution of nitric acid in double distilled water at pH = 1.5 at room temperature. The presence of asperities of regular nanometric size is clearly observed on all thickness films exposed to the degassed solution during 5 minutes. (b) Average height (circles) and diameter (squares) of self-assembled bumps observed on the surface of thin polymer films of PS 250 kDa of different thickness treated with degassed water at pH = 1.5. (c) AFM micrograph illustrating how the nanostructuration process was also observed in bulk PS.

4.5.5. Temperature

The size of the nanostructured layer depends also on the temperature; higher temperatures during the process entail larger self assembled blobs. As pointed out above, the ‘’mobility’’ of the polymeric surface is a key factor in the nanostructuration process. An example of the importance of this factor is illustrated in Figure IV.18. A PS thin film was heated to 65 °C and immersed for 5 min in a pH = 1.5 solution previously degassed at 65 °C. As seen in Figure IV.18, the formed bumps are bigger than the ones observed at room temperature, suggesting the presence of a thicker mobile polymer layer.

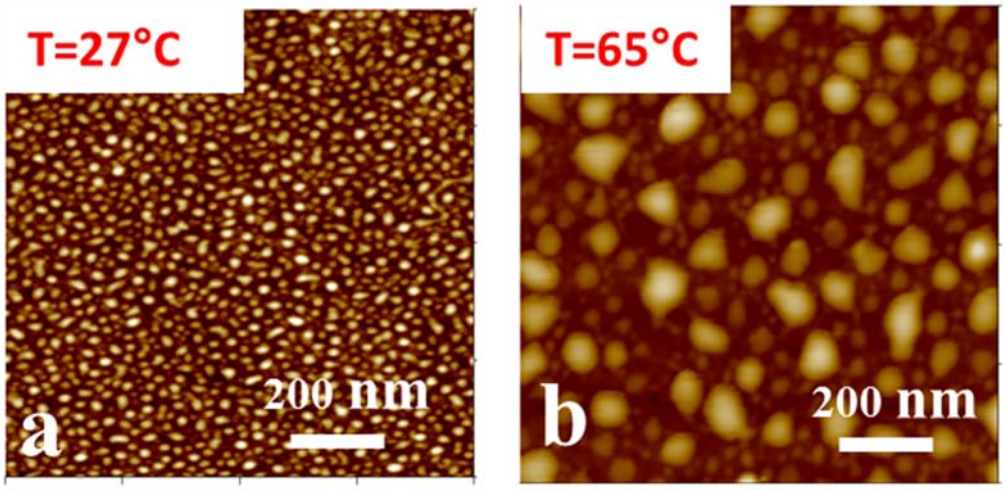

Figure IV.18: Temperature dependence. Nanostructured PS surface produced at (a) 27°C, and (b) 65 °C. Bumps are taller and larger at higher temperatures (h = 7nm, d = 65nm vs. h = 2.5nm, d = 28 nm)

Larger patterns can be also obtained if a previously structured surface with degassed solution of pH = 1.5 is exposed to a second treatment with degassed solution during 1 hour. Bumps are taller and larger (h = 3,7 nm, d = 55 nm) compared with those produced after the first treatment (h = 2.1nm, d = 19 nm).

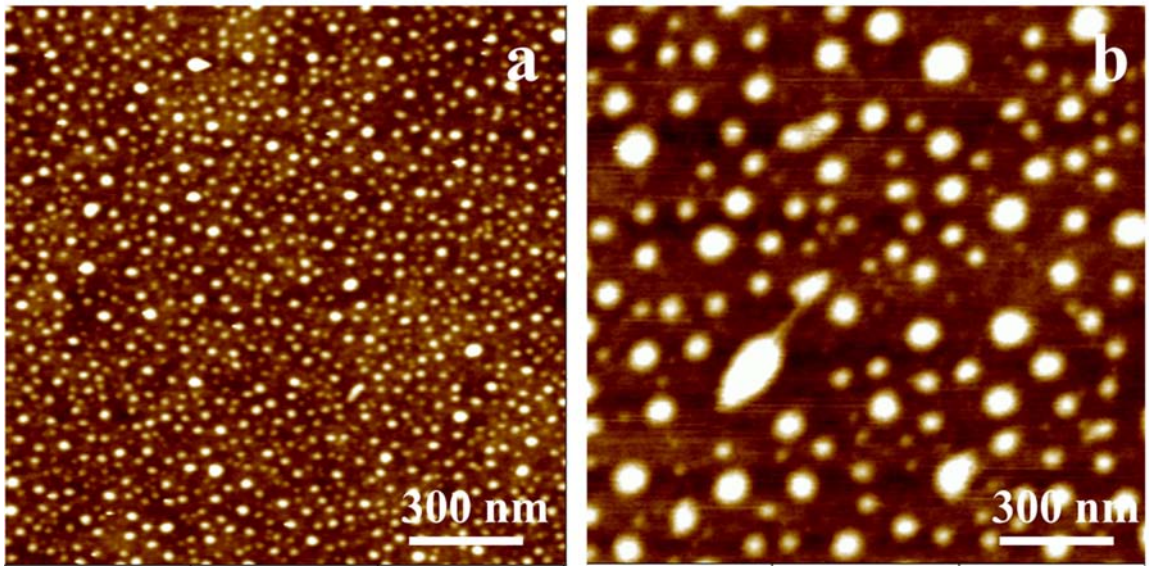

Figure IV.19: (a) AFM height micrograph of 300nm thick PS films after 5 minutes exposure to degassed water at pH = 1.5. (b) AFM height micrograph of a PS film after 1 hour exposure of previously structured film to degassed water at pH = 1.5.

An extensive investigation of the effect of temperature on the formation and relaxation of the structure was performed. It will be described in Chapter VI.

4.5.6. Supporting substrate

For the case of very thin films, the self assembled surface pattern depends also on the type of substrate used. As were described above the typical radii and height of the observed bumps is unaltered in bare mica or oxidized Si wafers for polymer film thickness down to 10 nm. After changing the interaction between the polymer layer and the substrate by modifying surfaces of the same materials with a primer layer, we have found that for very thin films (thinner than few times the radii of gyration of the polymer molecules) the nature of the substrate modifies the structuration process. In particular, the silanization of the silicon wafer and adsorption of smooth monolayer of ceria nanoparticles on mica under the PS layer increases the adhesion between the deposited polymer and the substrate and effectively inhibit the structuration. As can be observed in Figure IV.20, the self assembled surface pattern depends on the type of substrate used. The bumps are substantially reduced - or nonexistent - for films spun on ceria-coated mica or hydrophobized wafers for polymer films thinner than a certain value. We have extensively characterized this phenomenon, which is the subject of discussion in Chapter V.

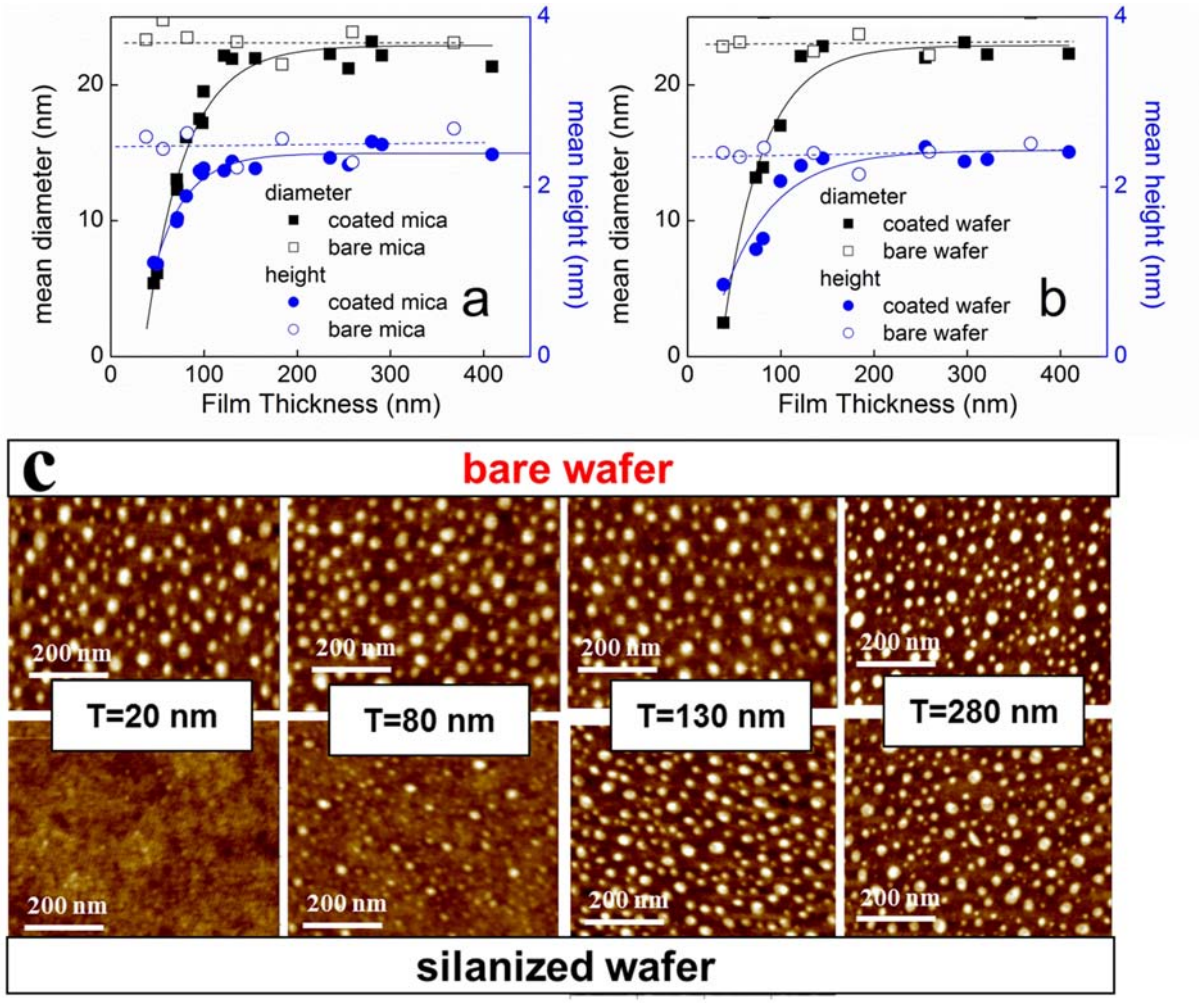

Figure IV.20: Height AFM micrographs of films of 250 kDa polystyrene films measured in tapping mode in air. The films of indicated thickness were spun coated on bare and silanized silicon wafer and then exposed to a degassed solution of nitric acid in double distilled water at pH 1.5 at room temperature.

We can use this method to produce patchy structured surfaces. We performed the following test: we silanized half of a Si wafer by controlled LB deposition of OTS before spin coating a 50 nm thick film of PS on it, and then we treated the film with degassed water at pH 1.5. The resulting morphology is presented in Figure IV.21. As can be observed, the spontaneous structuration appears only in the portion of the film above the non-silanized section of the Si wafer; even though both sections were in contact with the same solution (the film was smooth and featureless before degassed-acid water treatment).

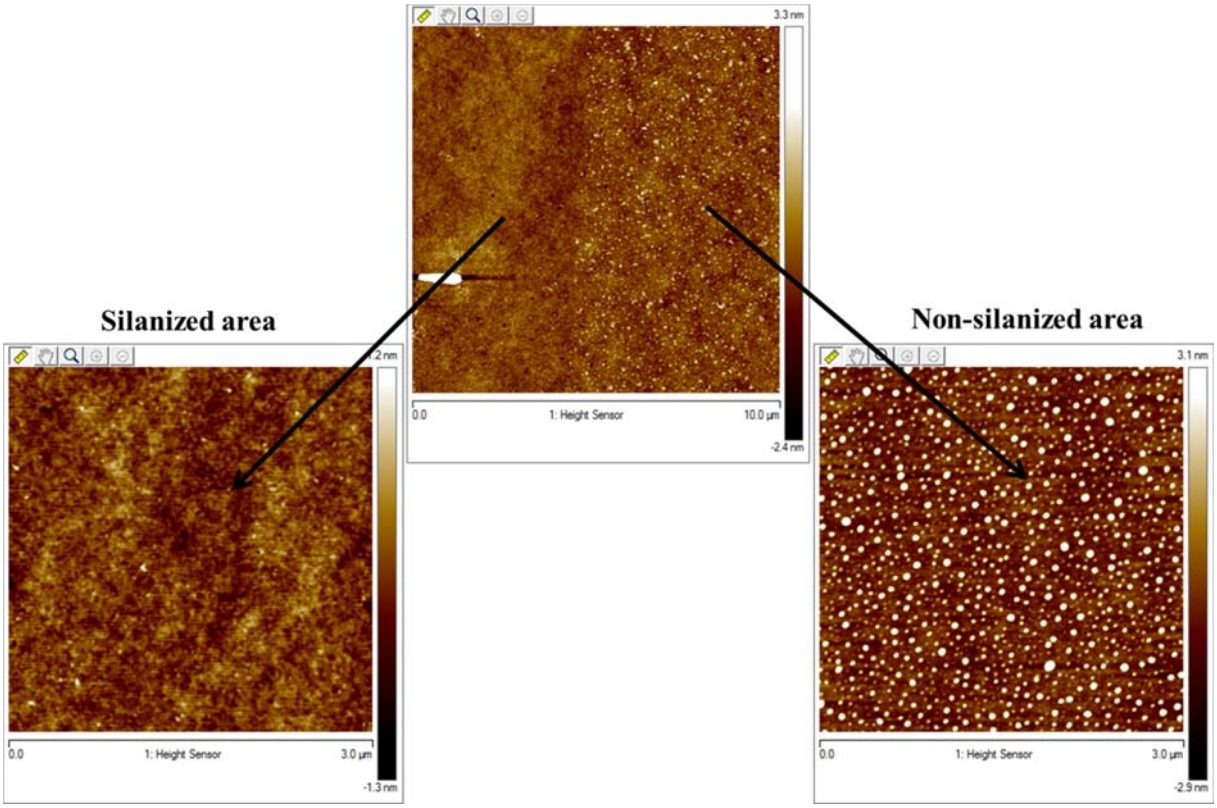

Figure IV.21: Height tapping mode AFM micrographs measured in air of 50 nm thick 250 kDa polystyrene films after exposure to a degassed solution of nitric acid in double distilled water during 5 minutes. pH 1.5; T 25°C. The film was deposited on a half-silanized silicon wafer. The presence of asperities of regular nanometric size is clearly observed on the bare wafer. On the contrary, no modification was detected in the OTS coated region

4.6. Mechanism of formation and temporal evolution of induced nanostructure

4.6.1. Kinetics of nanostructuration process

In order to understand and explain the induced long lasting self-assembled nanostructure on the solid polymer surface we have to clarify which is the mechanism of formation of such nanostructure and how these bumps evolve in water solution and out of solution (air). We attempted to analyze *in-situ* the forming details of such nanostructure using AFM measurements in water, but our

efforts were unsuccessful for several reasons. First, the complete surface structuration is achieved before 1 minute of immersion, while it takes at least that time to engage and start imaging the surface. Second, our AFM does not allow us to safely operate at pH values outside of the range 2-10, while clear structuration is observed outside that range. Finally, we found it difficult to inject the degassed solution in the AFM liquid cell without introducing air. Because of these constraints, we have not been able to study the structuration process in-situ by AFM in liquid. However, we have explored the evolution of the resulting surface morphology by removing the surfaces out of the degassed solutions after different immersion times (from 1 second to few hours). In this way we have determined the morphology of the self-assembled structure as a function of time. AFM micrographs corresponding to different immersion times and a plot representing the average diameter of the observed blobs as a function of immersion time are presented in Figure IV.22.

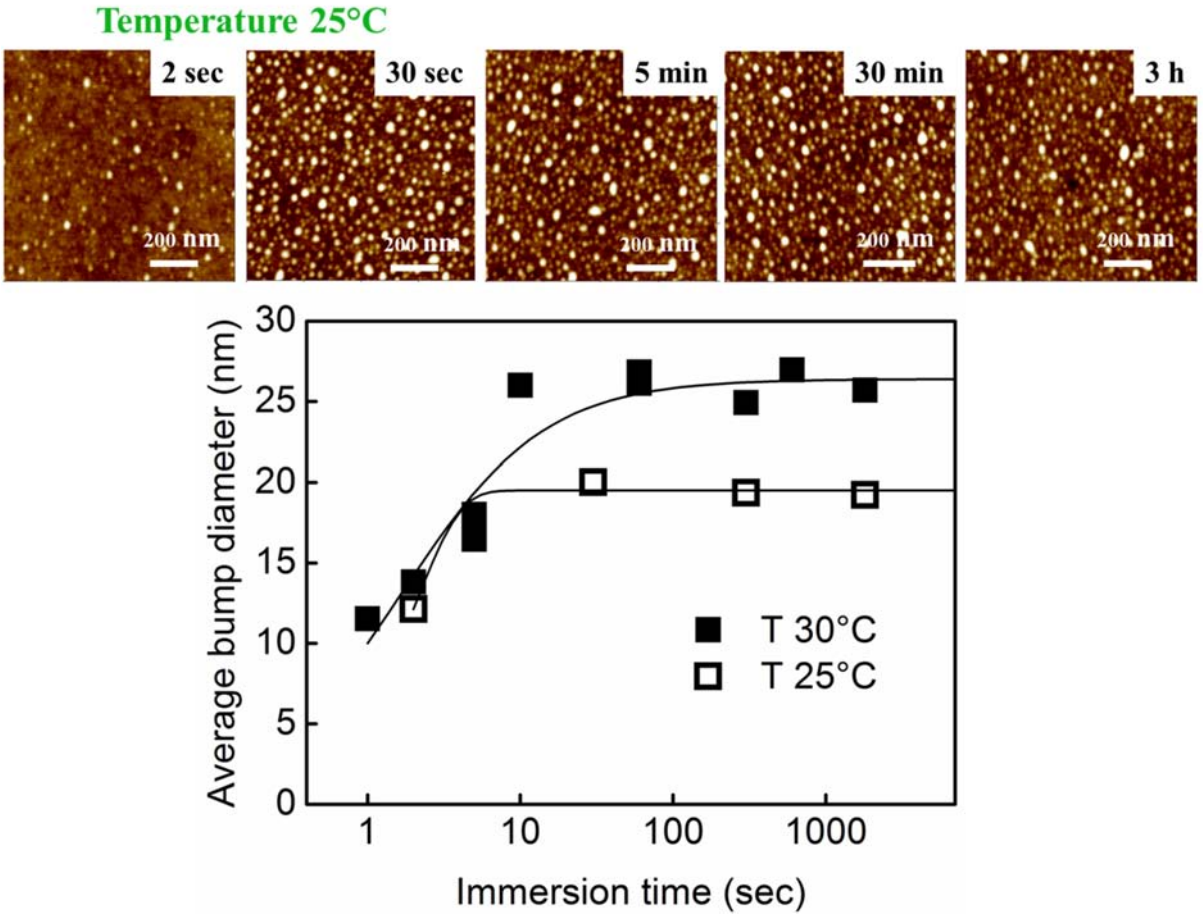

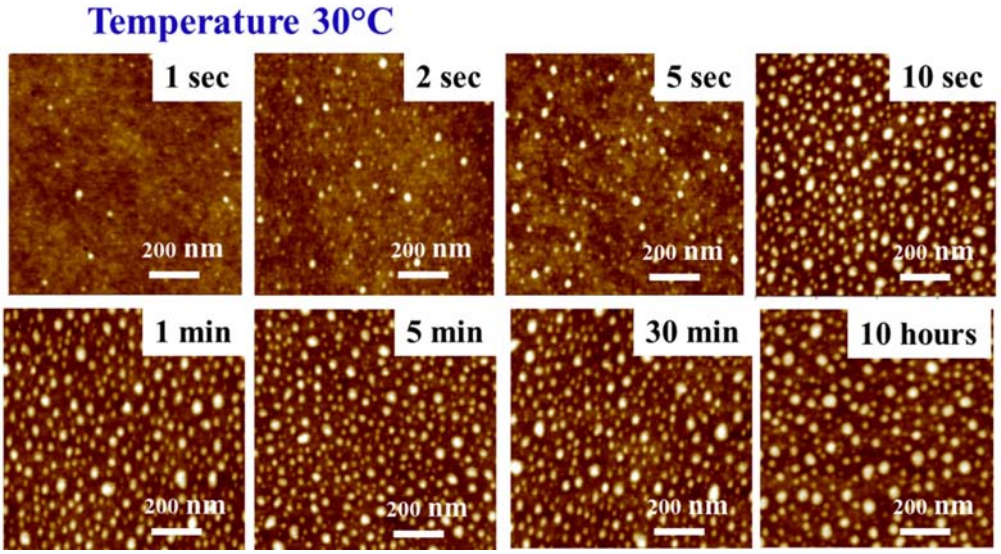

Figure IV.22: AFM micrographs of 300 nm thick PS films after different exposure times to degassed water at pH = 1.5 (with HNO_3) at two different temperatures. No evolution of the structuration morphology is observed after 30 sec of immersion.

From Figure IV.22 we can clear observe that pattern are fully formed after about 30 sec of immersion in degassed solution, and that almost no evolution of the structuration is observed even after keeping samples in solution more than 10 hours.

4.6.2. Evolution of the self assembled structure

The subsequent evolution of the self assembled structure in air is determined by the environmental conditions. As can be observed in Figure IV.23, the blobs disappear after annealing the structured surface at 95°C for few hours. In fact, no heating is necessary for the relaxation of the water-induced nanostructures: the same is observed if the patterned surface is exposed to toluene vapor during 1 hour. We observed a faster evolution of the films of PS of lower molecular weights. Nevertheless, if the ‘’regenerated’’ smooth surface is re-immersed into a degassed acidic solution; a freshly new bumpy surface was generated again.

Indeed, the surface of the film slowly relaxes back to the original smooth condition even when the film is conserved in air at room temperature, well below the glass transition temperature of the polymer. As can be observed in Figure IV.23, one month after the nanostructuration most of the asperities on the film have already relaxed, and the film recovers its original smooth morphology. It is apparent that there is an enormous difference in the time scale of formation and relaxation of the nanostructures. While a well developed structured layer is formed after few minutes of contact between the degassed water solution and the film, the typical time of relaxation of the structure is few weeks, in agreement with a recently published study of temporal evolution of nanoindentation of polystyrene substrates [45]. A complete report of this feature will be presented in Chapter VI.

As can observe in Figure IV.23, two different mechanisms govern the temporal evolution of the nanostructured layer. First, few days after structuration has taken place, clear evidence of surface Ostwald ripening is detected: smaller size blobs disappear at expenses of larger ones which increase further in size (e.g., the region indicated by the arrows) evidencing the mobility of the polymer chains at the surface. The blob number density is then substantially reduced, and big blobs surrounded by a depleted region are often observed. This process obviously coarsens the size distribution of the asperities on the surface, as presented in Figure IV.23. Second, a slow relaxation of the measured blobs is detected. This relaxation is driven by the Laplace pressure on the formed blobs, $\Delta P = 2\gamma/R$, with γ the surface tension of polystyrene and R the radii of the blob, and the elastic strain. The spontaneous relaxation of the structure indicates that the structuration is not a consequence of irreversible plastic deformation of the films, but instead that there is indeed a mobile layer on top of the polymer film that is being reshaped.

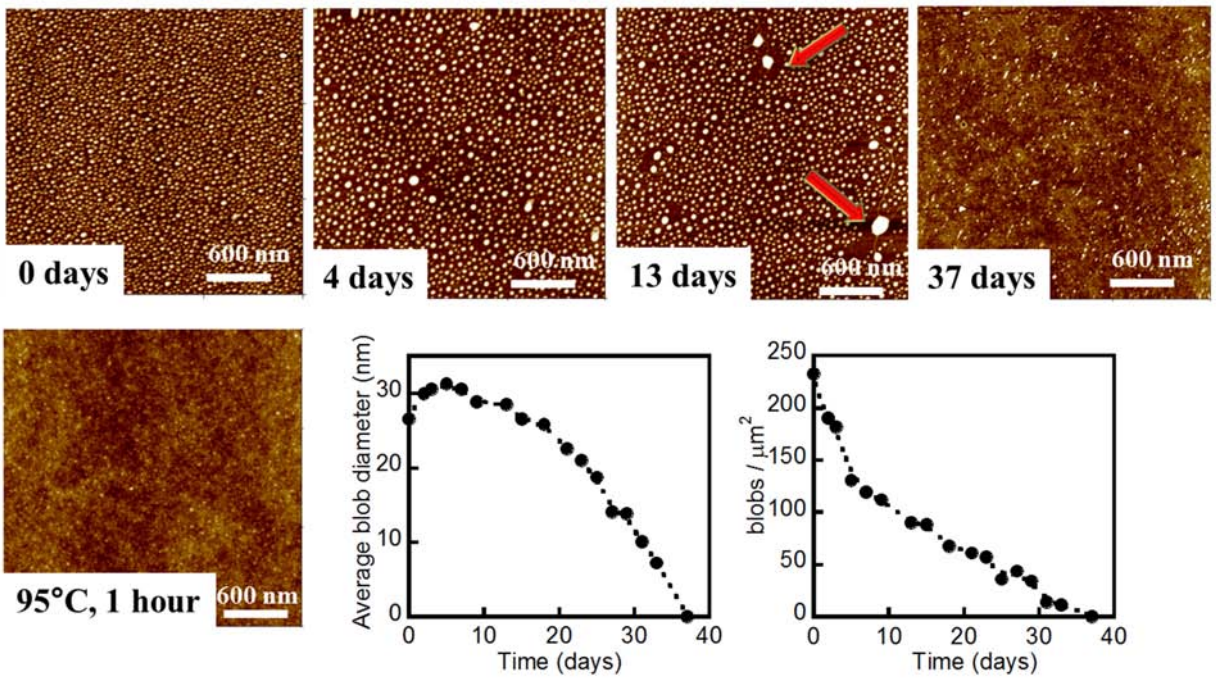

Figure IV.23: AFM height micrographs (3 μm × 3 μm height) measured in air on a film that has been previously in contact with degassed water at pH = 1.5 at different times after water exposure, as indicated. The self-assembled nanostructure on the polymer surface is not at thermodynamic equilibrium. One month after the nanostructuration was induced most of the asperities on the film have already relaxed at room temperature, and the film recovers its original smooth morphology. The relaxation of the structure is greatly accelerated by increasing the temperature.

4.6.3. What is the driving force for the observed nanostructuration?

We have seen that the structuration process described in this chapter depends strongly on the pH and the hydrophobicity of the polymer surface, as well as on the thorough degassing of the water phase. The pH dependence of the process strongly suggests that presence of charged species close to the water/polymer interface drives the instability in the polymer film. Usually, in order to describe the interface between an aqueous solution and a charged surface, one considers the effect of surface

charges due to surface ionization or ionic adsorption on the ionic distribution in the liquid phase. This distribution determines the properties of the material. It seems that a change of paradigm is necessary to understand the phenomena reported in this work. The essence of the problem can be captured through the following question*: what is the influence of the water structure and the ionic distribution on the hydrophobic surface?* It has long being recognized that pristine water/oil interfaces can become charged [61,62]. It is becoming apparent from experiments and simulations that the density of ions in water solutions close to hydrophobic objects is not uniform: some ions are preferentially attracted to the interface [63,64]. The adsorption of water-ions on hydrophobic surfaces has been evoked to explain phenomena as diverse as the electrophoretic mobility of hydrophobic objects [63,64], the nanotube catalyzed etching of silicon dioxide[65], or the electrochemical behavior of grapheme [66]. Different reasons have been evoked for this counterintuitive ionic distribution, which defies straightforward electrostatic considerations. Noah-Vanoucke and Geissier [67] suggested that the entropy gained by placing the ions at the interface more than compensates the energetic costs involved in this process, if ion induced deformation of the interfaces are taken into account**.** In ab initio molecular dynamic simulations, Kudin and Car [68] found that water ions have amphiphilic character because of the asymmetry of the ionic charge distribution, reason why the interface is enriched on those species. Other mechanisms like ionic polarizability [69] and ionic-induced decrement of water polarization fluctuations [63,64] have also been evoked to explain this ionic distribution which defies straightforward electrostatic considerations: ions should strongly partition into the higher dielectric constant aqueous phase.

Despite of the debates around this subject, consensus seems to be emerging around the idea that the interfacial density of hydroxyl or hydronium ions increases nearby water-hydrophobic interfaces, with the respective amount determined by pH [63,64]. This explains why the charge of hydrophobic surfaces in water strongly changes with the pH of the aqueous phase but is less sensitive to the presence of other ions, in agreement with previous experimental and theoretical studies of the physisorption of water ions to hydrophobic surfaces [63,64]. The strong adsorption of these ions at the interface is probably at the origin of the phenomena reported here: they originate an electric field which polarizes the polymer layer, generating an effective surface charge density on the hydrophobic surface. The opposite charges in both sides of the interface result in an attractive force, which is the reason of the rearrangement of the polymer surfaces (Figure IV.24-a). It has already shown in Chapter III that it is possible to pattern a polystyrene film at room temperature by applying an electric field strong enough to induce an electrohydrodynamic instability (Figure IV.24-b). Similarly, surface waves can appear at the interface between water and an immiscible viscoelastic media from the interplay between the stabilizing Laplace pressure and elastic strain and the destabilizing electrostatic pressure; no other force needs to be considered for the films studied here, given that they are sufficiently thick so that the effect of dispersive forces is unimportant [70], and thin enough as to make the influence of gravity irrelevant. This simple picture requires the ions to be very close to the interface, or the

dielectric constant of the media between the ions and the polymer film to be significantly reduced: otherwise a repulsive "image" force between the ions and the low dielectric constant polymer film should be expected [71],which is inconsistent with the structuration reported here.

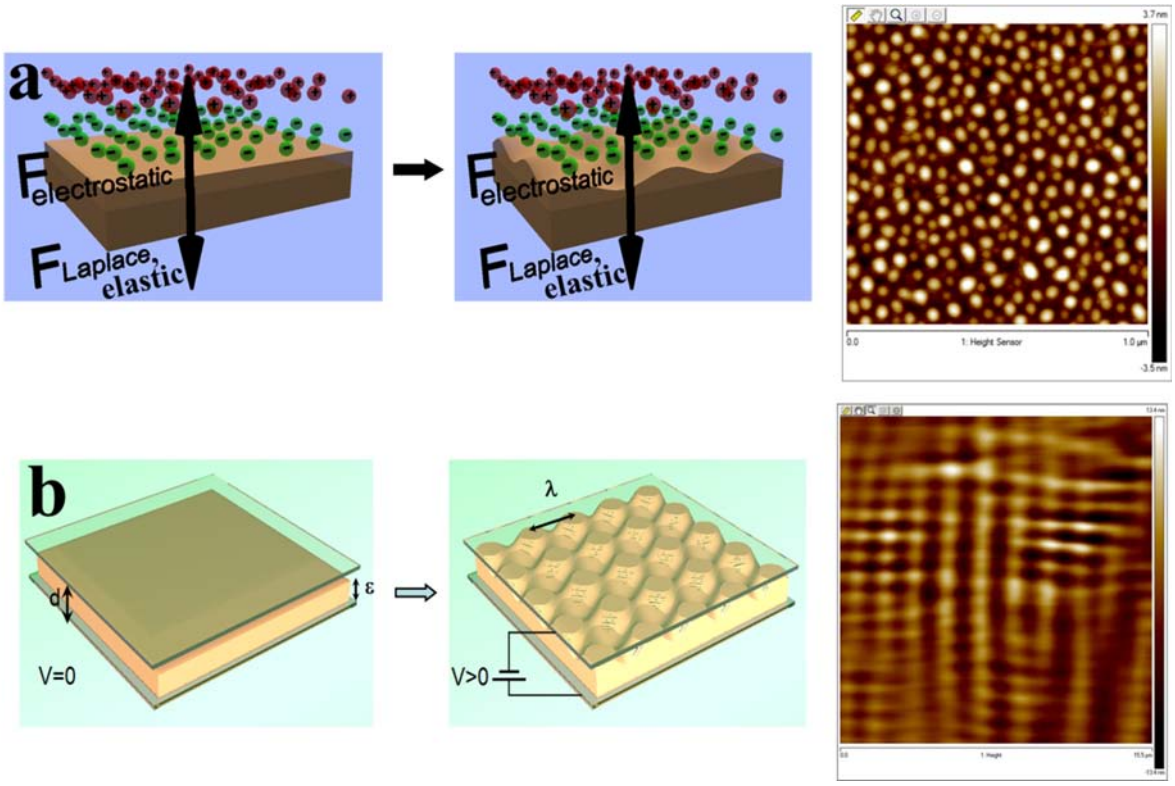

Figure IV.24: (a) 1μm x 1 μm height tapping mode AFM micrographs taken in air of a 300 nm thick 250 kDa polystyrene film after exposure to an degassed nitric acid solution of pH = 1.5 at room temperature for 5 minutes. (b) 15.5 μm × 15.5 μm height tapping mode AFM micrographs taken in air of a 300 nm thick 250 kDa polystyrene film after exposure to an electric field of the order of 1 MV/m at room temperature for 30 minutes. The appearance of motives of regular submicrometric size and nanometric height is clearly observed. The spacing of the pattern is determined by the intensity of the applied field and the temperature. The relaxation time is determined mainly by the temperature.

To determine the effect of the ionic distribution on the polymer films, precise details of the amount and location of the ions in the interface are necessary, which is out of reach even for the largest scale simulations. However, we can make a crude estimation of the electric field in the polymer film by assuming that a certain density of ions is preferentially placed in the water nearby the polymer/water interface. An electric field on the polymer surface of the order of 10^7 V/m can be calculated from the surface charge values presented in Figure IV.9. The real field at the interface is likely to be larger than this conservative estimation: surface charge densities measured by titration of surfactant free oil-in-water emulsions are typically five to ten times larger than the ones we estimate from streaming potential measurements. From the surface charge the electrostatic pressure induced by the field at the polymer-water interface can be estimated as described by Landau and Lifshitz [71], if

the variation of dielectric constant of the polymer is not taken into account [72]. A value of the order of 0.1 MPa is obtained, largely inferior to the yield stress of PS (30 MPa) [45]. The evolution of the polymer surface will then be determined by the competition between the destabilizing effect of the field and the Laplace pressure, which damps the surface fluctuations. A macroscopic description of the problem of the deformation of a viscous liquid bounded by a plane of uniform surface charge has been reported by Killat [73]. If we estimate the wavelength of the fastest growing mode in our films by using the dispersion relation deduced by Killat [73] (Supporting Information) values between 15 and 150 nm are obtained, in agreement with the structures presented in above figures. The kinetic of formation and relaxation of the waves will be determined by the viscosity of the liquid and the interfacial tension. From the same dispersion relationship, a viscosity of the order of 100 MPa·s can be estimated for the mobile layer of the PS films, orders of magnitude lower than the value expected for PS at temperatures below T_g. This macroscopic description cannot be applied if the density of charges at the interface is too low. In that case a description at the molecular level which takes into account the discreteness of the matter is likely to be necessary. This description cannot be built based on the finding reported in this work only. Detailed molecular modeling of the present systems will probably be necessary to reach a complete understanding of the reported phenomena. Nevertheless, it seems apparent that the driving force for the structuration is the preferential presence of water ions at the water/polymer interface.

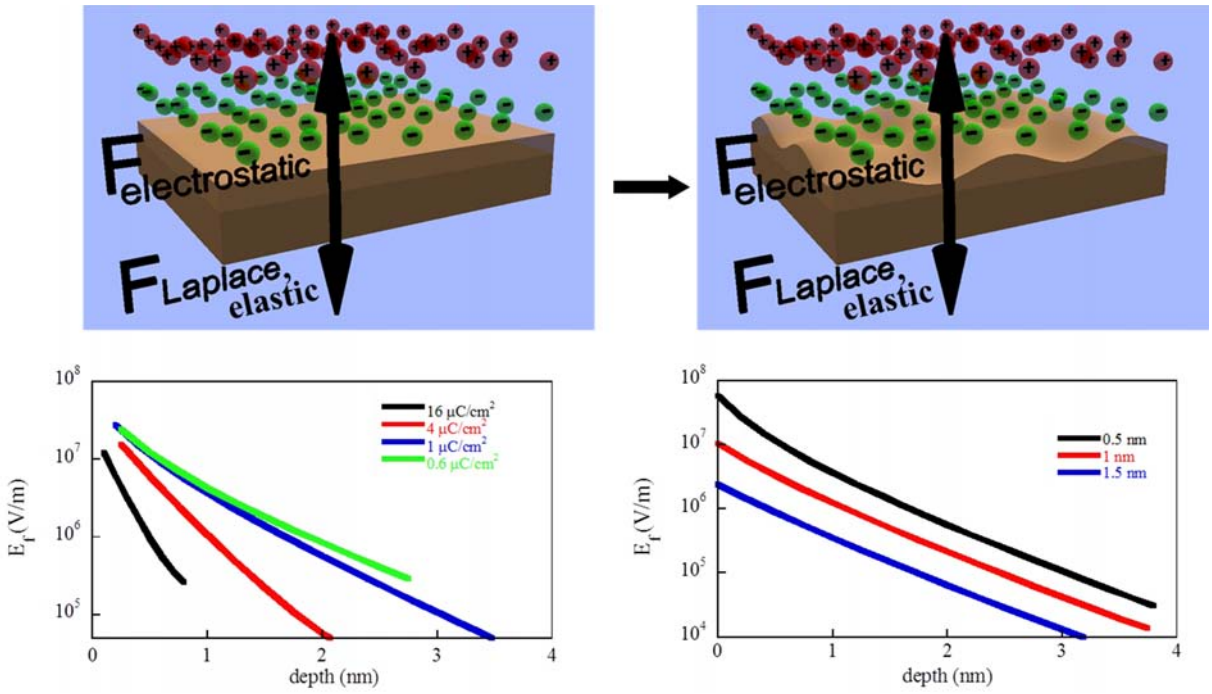

Figure IV.25: The preferential adsorption of ions at the water/polymer interface is likely to be responsible for the observed self-assembled nanostructure. a) the excess charges are placed 0.2 nm away from the interface, at different charge densities. b) the excess charges are placed at different distances from the interface at a constant charge density of 1 μC/cm^2. The electric field in the polymer film in the first few nm from the interface, will depend mainly on the density of charges and the separation of the charges from the interface. The calculated electric field due to the interfacial charges is strong enough to drive the structuration of the polymer film.

As can be observed in Figure IV.25, the electric field on the polymer depends critically on the density of charges and notably on the separation between the charges and the interface. Displacing the position of the charges by a fraction of a nanometer entails a dramatic reduction of the electric field on the polymer, which explains how the presence of a very thin layer of reduced density may deeply modify the interaction between both phases.

4.7. Induced nanostructure by specific ion adsorption

The data discussed above indicate that polymer / aqueous solution interface are charged by the preferential adsorption of hydroxide and hydronium ions. Is the process of nanostructuration possible only in the case of water ions adsorption, or there are other ions that could adsorb to the hydrophobic polymeric surface and generate the structuration? Hofmeister observed, more than 100 years ago, that effective interactions between most charged and neutral objects in aqueous media depend crucially not only on electrolyte concentration but also on ion type. This subject is still intensively studied nowadays [74]. Ion specificity is most drastically revealed at uncharged hydrophobic solid surfaces [75] and at the air-water interface. According to simple electrostatic theory, ions are point-like and interact solely via Coulomb forces. Cations and anions should be equally repelled from hydrophobic interfaces due to image-charge effects leading to ion depletion at the surface, vanishing surface potentials, and increasing the surface tension [76]. However, experimentally it is found that for the air-water interface (i) the surface tension depends sensitively on the ion type and concentration [77], (ii) the surface potential for certain salts reaches values of up to 100 mV relative to pure water [77], and (iii) a negative charge is present at the interface at neutral pH, as inferred from thin-film stability and bubble electrophoresis [78,79]. Likewise, on solid hydrophobic surfaces the zeta potential is strongly negative and depends on ion type and concentration, as described before [80].

We were interested in to explore if ions other than OH^- or H_3O^+ could adsorb to hydrophobic PS surfaces and induce its structuration. In previous sections it was shown that the structuring effect of degassed solutions of sodium chloride, perchlorate or sodium nitrate up to 0.1 M (Figure IV.10-a-e) is not larger than the one of water at neutral pH. In this section we will extend the discussion to a larger number of electrolytes solution containing different ions. Table IV.3 summarize our results of these studies. The salts that have a bigger influence on the nanostructuration ($d > 20$ nm)are emphasized by pink color. All experiments were performed at neutral pH (to avoid structuration dictated by pH and to prevent competition OH^- or H_3O^+ with other ions) using Millipore water with a conductivity of 18 MΩ/cm. The pH of the aqueous phase was measured in all experiments before and after degassing the solution, and was found to be in the range of 6 – 8.5, except for salts containing CO_3^{2-}. The effect of degassed solution on PS films was studied at different concentration of salts ranging from 0.001 to 0.1 M, (only the results obtained at 0.03M are presented in Table IV.3). All the investigated PS films had identical thickness, thermal history and substrate. All the electrolyte solutions were well degassed and

the treatment with degassed solutions was performed at similar temperature. Experiments with each particular salt were performed between 3 and 10 times randomly in time; reproducible results were obtained in all cases. Additionally, it should be mentioned that no change in morphology was ever observed with non degassed solutions. We investigated in greater detail the salts that induced structures at least comparable to the one observed at pH = 11.5 or 1.5. If induced bumps were smaller, we could not distinguish if the effect came from the low concentration of (OH^-) or (H_3O^+), or from specific ions present in solution.

Table IV.3. Average bump size extracted from AFM images of PS films treated with degassed water solutions that contain 0.03 M of different salts. d = diameter, h = height of bumps, Rq = roughness

	OH^-	F^-	Cl^-	Br^-	I^-	NO_3^-	ClO_4^-	SO_4^{2-}	CH_3COO^-	CO_3^{2-}	$B(C_6H_5)_4^-$	$C_{12}H_{25}SO_4^-$ SDS
H_3O^+			d = 25.3 h = 2.6 Rq = 0.9			d = 26.3 h = 2.5 Rq = 0.9						
Li^+		d = 25.9 h = 2.5 Rq = 0.9	d = 14.2 h = 1.7 Rq = 0.4	d = 27.6 h = 2.5 Rq = 0.9	d = 26.2 h = 2.7 Rq = 0.9			d = 7.2 h = 1.2 Rq = 0.2		d = 21.0 h = 2.2 Rq = 0.7		
Na^+	d = 30.0 h = 3.0 Rq = 1.0		d = 12.7 h = 1.4 Rq = 0.4	d = 10.8 h = 1.4 Rq = 0.3	d = 8.7 h = 1.4 Rq=0.4	d = 12.4 h = 1.4 Rq = 0.4	d = 12.0 h = 1.5 Rq = 0.4		d = 9.8 h = 1.5 Rq = 0.3	d = 17.2 h = 1.7 Rq=0.4	d = 32.0 h = 3.2 Rq=1.3	d = 27.1 h = 2.0 Rq = 0.7
K^+	d = 29.7 h = 32 Rq = 1.1		d = 11.2 h = 1.7 Rq = 0.4		d = 13.2 h = 1.3 Rq = 0.3			d = 9.0 h = 1.3 Rq = 0.4		d = 8.5 h = 1.5 Rq = 0.3		
Cs^+		d = 19.1 h = 1.7 Rq = 0.6			d = 9.5 h = 1.5 Rq = 0.4							
Zn^{2+}			d = 8.5 h = 1.5 Rq = 0.3									
Mn^{2+}			d = 8.9 h = 1.4 Rq = 0.2			d = 7.9 h = 1.4 Rq = 0.3						
H_4N^+					d = 20.7 h = 1.7 Rq=0.6							
Me_4N^+					d = 25.4 h = 2.2 Rq=0.7							
Et_4N^+				d = 27.2 h = 2.4 Rq = 0.8	d = 27.4 h = 2.8 Rq = 1.0	d = 23.1 h = 2.2 Rq = 0.8						
$^nBu_4N^+$			d = 22.6 h = 2.2 Rq=0.8									
$As(C_6H_5)_4^+$			d = 31.6 h = 2.9 Rq=1.4									
$(C_{12}H_{25})(CH_3)_2N^+$ DDAB				d = 27.2 h = 2.4 Rq = 0.9								

From the Table IV.3, we can observe that different electrolytes give rise to very different structuring effect:

✓ Similar size and density of bumps is obtained with nitric acid solution of pH=1.5 and sodium hydroxide of pH=11.6. Similar results are obtained with hydrochloric acid (HCl) or potassium hydroxide (KOH) (Figure IV.26).

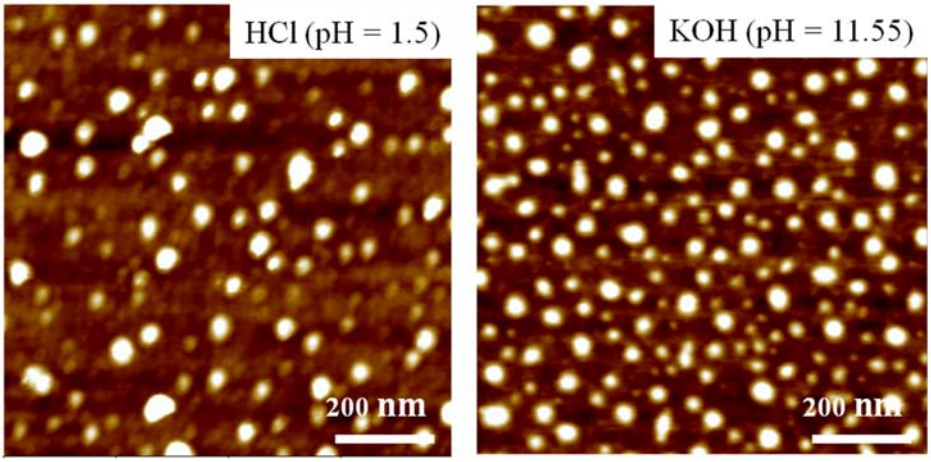

Figure IV.26: AFM micrographs measured in air on a film that has been previously in contact with degassed water at pH = 1.5 and 11.55 acidified with HCl or basidified KOH.

✓ Degassed solution of small size electrolytes, e. g. KCl, NaBr, NaI, or NH_4Cl do not develop large structure on PS surface. As can be observed in Figure IV.27, with this kind of salts bumps are similar in size as those obtained from degassed Millipore water at pH = 7.

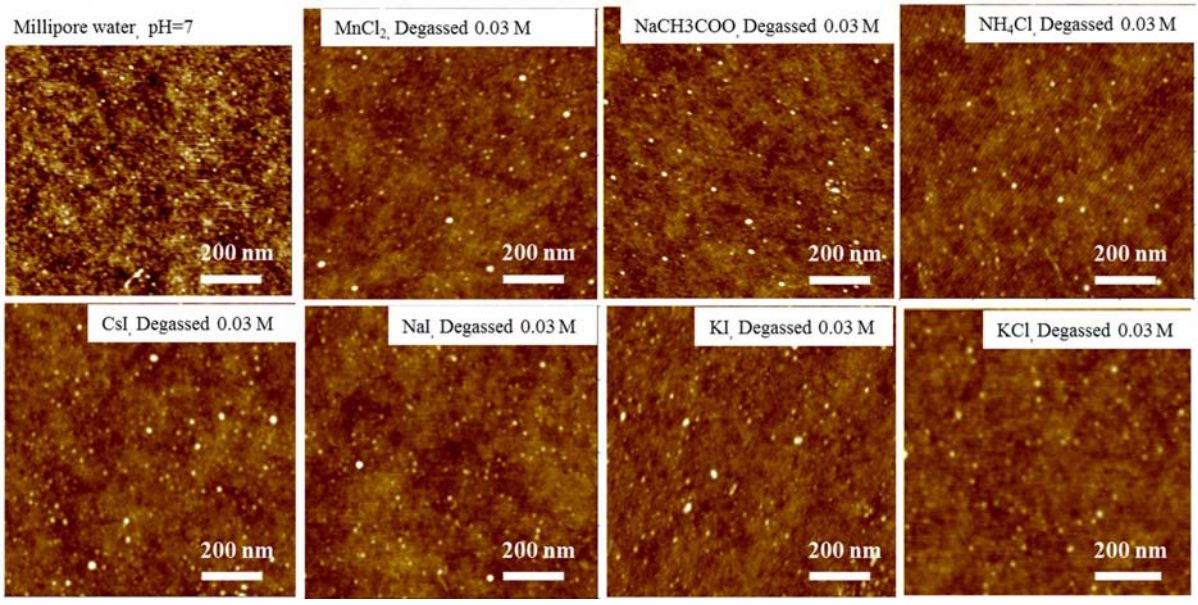

Figure IV.27: AFM micrographs of 300 nm thick PS films after 5 minutes exposure to degassed water at neutral pH and different salts of concentration 0.03 M. A similar structuration effect is observed at neutral pH.

✓ Degassed aqueous solution of large ions, such as tetramethylammonium iodide, tetraethylammonium iodide, tetrabutylammonium chloride, bromide, nitrate or iodide, sodium

tetraphenylborate and tetraphenyl arsonium chloride produce very large blobs on PS surface. Relatively large bumps (although at a lesser density) on PS are also observed after treatment with degassed electrolytes containing lithium ions (Figure IV.28 and pink colored boxes in Table IV.3).

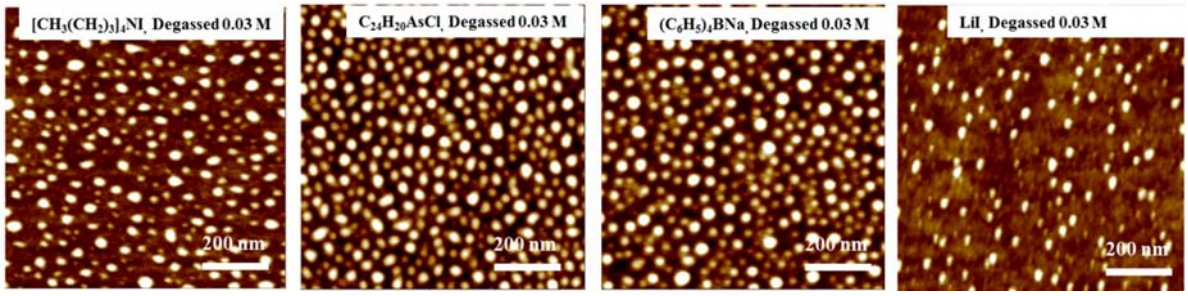

Figure IV.28: AFM micrographs of 300 nm thick PS films after 5 minutes exposure to degassed water at neutral pH and different salts of concentration 0.03 M.

✓ *Effect of counteranions.* Figure IV.29 and Figure IV.30 indicate that surface structuration for tetrabutylammonium salts is different for different counter anions. The surface structuration increases progressively depending on anion, as iodide > bromide > nitrate >chloride. Similar tendency of induced nanostructure regarding the counter anion is observed for lithium salts. It can be observed in Figure IV.30 that degassed LiCl solution induced smaller structure compared with LiI. These results suggest that the effect of structuration is not due to the behaviour of a single ion, but to the combined effect of the different ions present in solution.

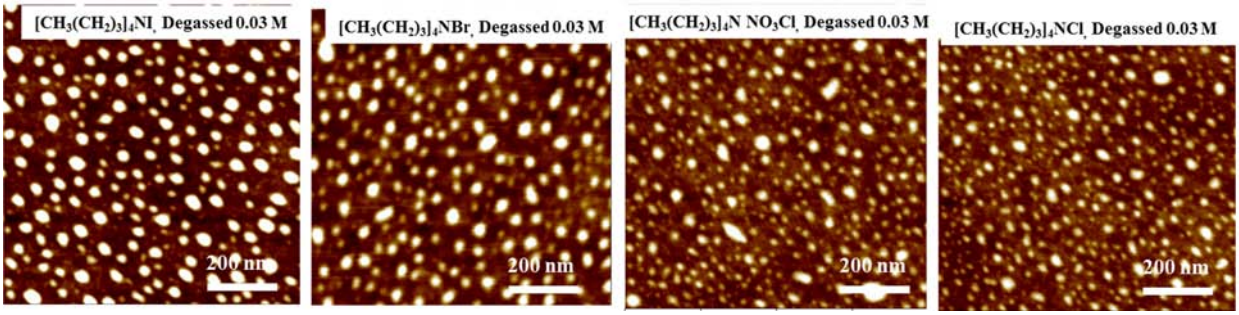

Figure IV.29: AFM micrographs of 300 nm thick PS films after 5 minutes exposure to degassed water at neutral pH and tetrabuthylammonium salts with differ anions, C = 0.03 M.

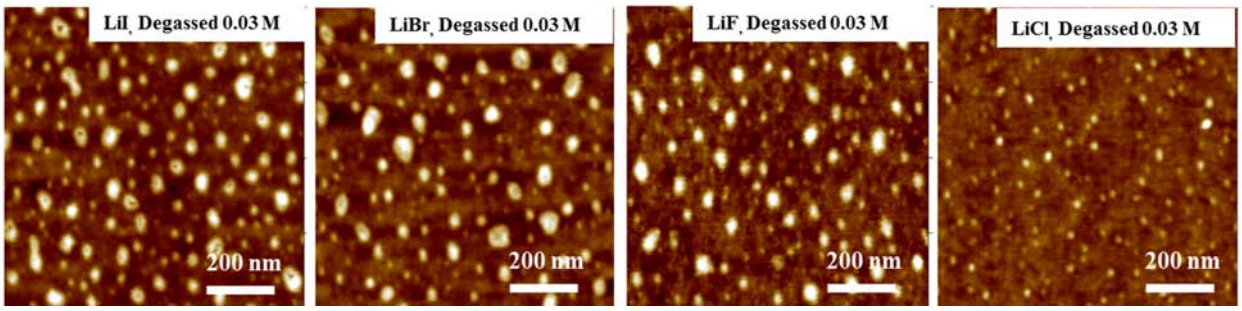

Figure IV.30: AFM micrographs of 300 nm thick PS films after 5 minutes exposure to degassed water at neutral pH and lithium salts with differ anions, C = 0.03 M.

✓ The number of carbons of tetra-alkyl-ammonium iodide salts has a distinctive influence on the nanostructuration. As can be observed in Figure IV.31, the longer is the length of chain of tetra-alkyl-ammonium iodide salts the larger are induced nanostructure, as $CH_3 < CH_3CH_2 < CH_3(CH_2)_3$.

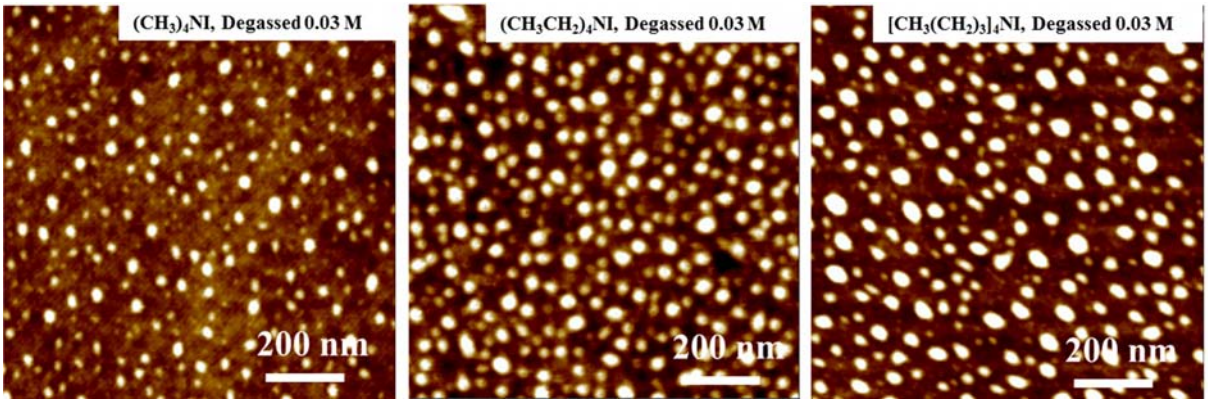

Figure IV.31: AFM micrographs of 300 nm thick PS films after 5 minutes exposure to degassed water at neutral pH and iodide salts with differ ammonium cations, C = 0.03 M.

✓ Similar size ions has the same nanostructuration effect, regardless of ion charge. For example, anionic tetraphenylborate induce same structuration as cationic tretraphenyl arsonium (Figure IV.32).

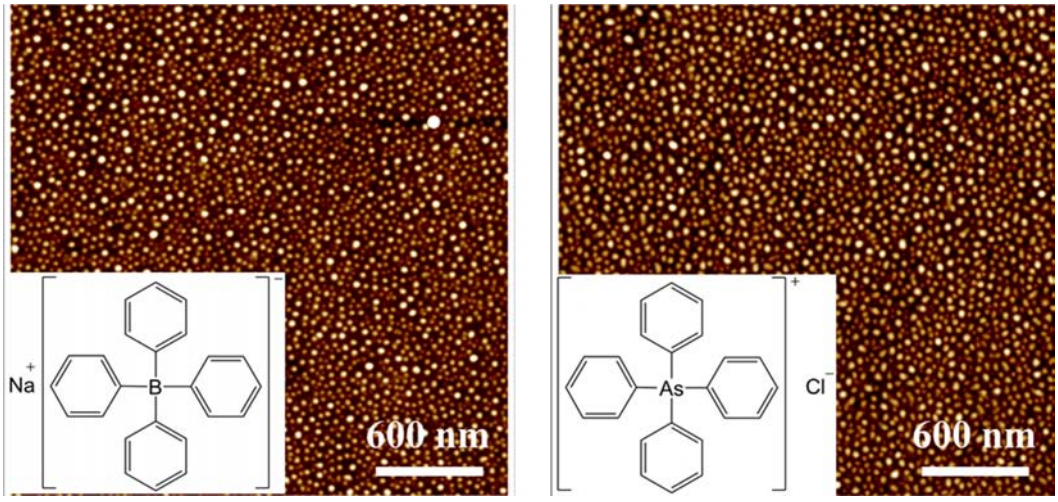

Figure IV.32: AFM micrographs of 300 nm thick PS films after 5 minutes exposure to degassed water at neutral pH and sodium tetraphenylborate (left) and tretraphenyl arsonium chloride (right) salts, C = 0.03 M.

✓ *Concentration of ions.* For the salts that do not develop large structure on PS surface, there is no ion concentration effect. This strongly suggests that the small structuration is influenced only by the small amount of hydroxide ion present in the solutions. Since the pH is maintained constant, concentration of water ions is constant, always inducing the same structuration. On the contrary, the

nanostructuration depends on the concentration of specific ions in the interfacial region, for the salts which influence greatly the structuration (pink colored boxes in Table IV.3, Figure IV.33 bottom). Higher concentrations of these ions result in higher surface charge density, and in a larger effect of the aqueous phase on the structure of the polymer surface.

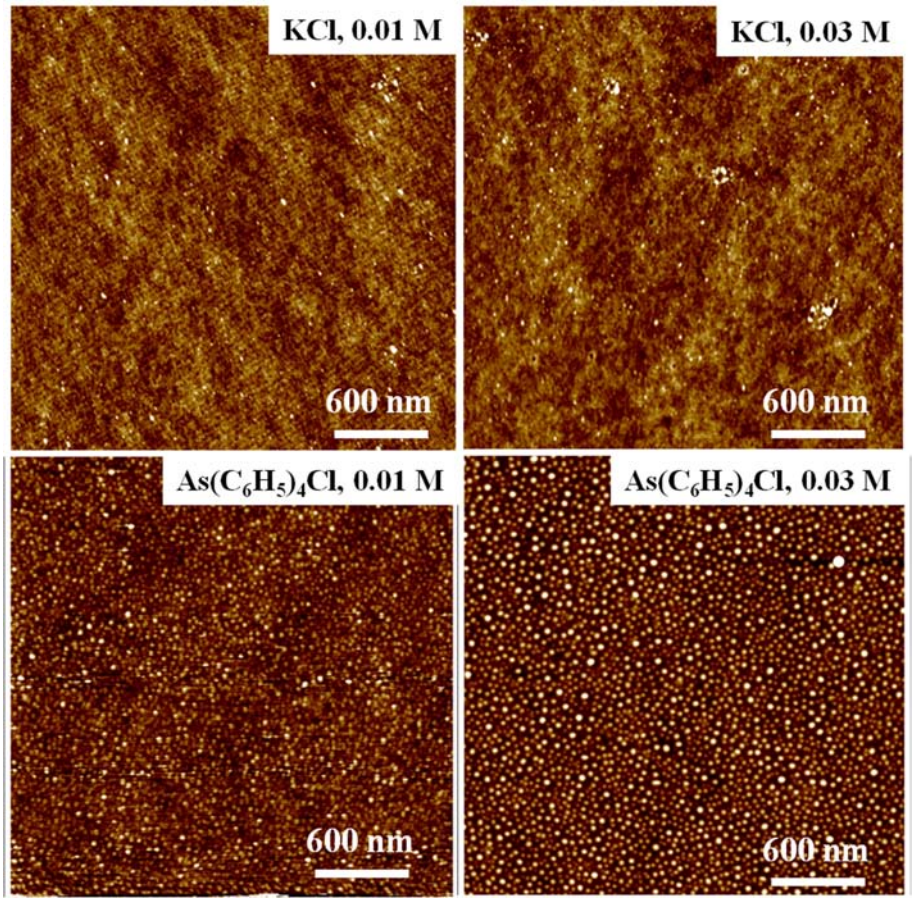

Figure IV.33: AFM micrographs of 300 nm thick PS films after 5 minutes exposure to degassed water at neutral pH and potassium chloride (top) and tretraphenyl arsonium chloride (bottom) salts, at different concentrations, as indicated.

4.8. Effect of gas concentration

It is very revealing to explore the effect of the amount of gas dissolved in water on the structuration process. To investigate this aspect, the following experiment was performed. A series of smooth PS films (300 nm thick, 250 kDa) were immersed for 10 min in water at pH 1.5 and then studied by AFM in air. Before treating the surfaces, the aqueous solution was in contact with air during different periods of time after degassing, to change the amount of gas dissolved. As can be observed in Figure IV.34-a, the size of the observed bumps is larger at short times after degassing. This size is progressively reduced by the increasing amounts of gas in the solution (Figure IV.34-b). Finally after 10 h after degassing, water has regained its equilibrium with the atmosphere, and no structuring effect is detected (Figure IV.34-e). At intermediate times, a seemingly different structuration effect is observed Figure IV.34-c,d: the contact with the aqueous phase induces the

formation of a regular array of shallow holes/rims in the polymer film, with a typical size of 30 nm and depth of 2 nm. The formation of a similar pattern has been reported by Wang and coworkers [81]. They suggested that on PS surface exposed to neutral water solution during 220 min nanoindents could be generated due to high internal pressure of formed nanobubbles combined with surface tension force along the solid−liquid−gas contact line.

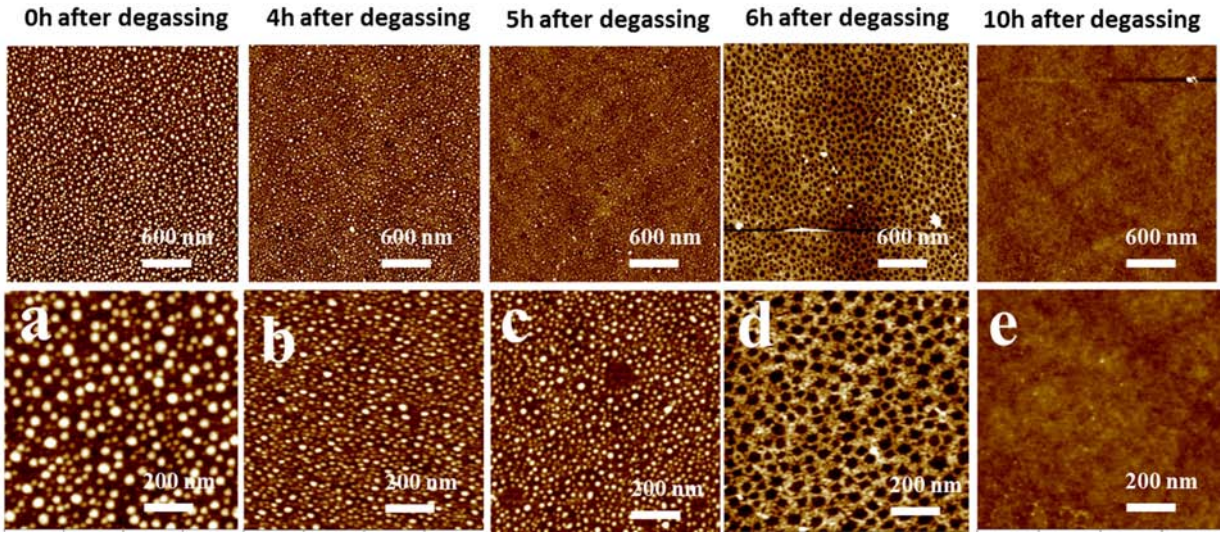

Figure IV.34: The amount of dissolved gas determines the nature and extent of the surface structuration. PS films (300 nm thick, 250 kDa) were immersed for 10 min in water at pH = 1.5 and then studied by AFM in air. Before treating the surfaces, the aqueous solution was in contact with air during different periods of time after degassing as indicated, to change the amount of gas dissolved. (a) Shortly after degassing the preferential adsorption of ions at the water/polymer interface is likely to be responsible for the observed self-assembled nanostructure. Increasing amounts of gas in the solution move the ions away from the polymer surface limiting the structuration.

To elucidate the reason of this morphology change, we tried to reproduce the experiment reported by Wang and coworkers [81]. Smooth films of PS 300 nm thick were immersed in Millipore water at neutral pH. After different periods of time in contact with the aqueous solution (in equilibrium with the atmosphere) the samples were removed, gently dried with nitrogen and studied with AFM in taping mode in air. The resulting morphology is presented in Figure IV.35.

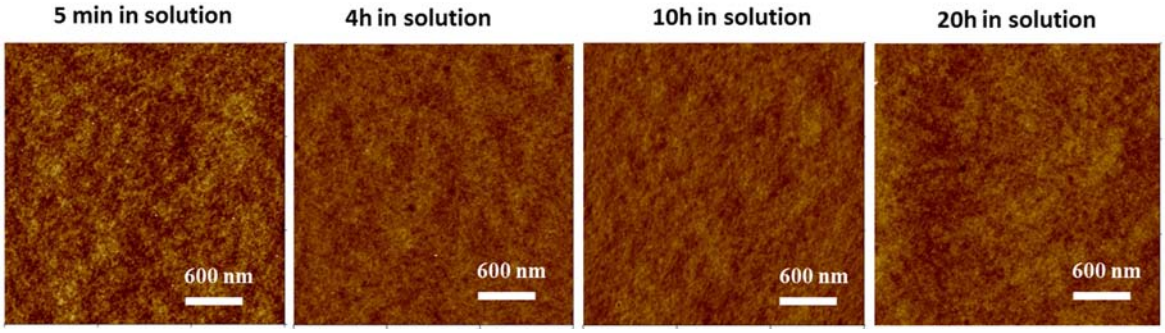

Figure IV.35: Height AFM micrographs measured in air of films that has been previously in contact with Millipore water at neutral pH at different times, as indicated.

As can be observed in the Figure IV.35, the films conserved their original smooth morphology "Nanoindents" were not observed even keeping the films in contact with water for 20 hours. On the contrary, we observe appearance of similar "nanoindents" only at sufficiently low or high pH values at intermediate gas concentrations, as can be observed in Figure IV.36. We do not find any critical difference in the protocol of our experiment compared with Wang's that could explain the disagreement, except that they studied thinner films (30 nm) and that their surfaces were scanning under water.

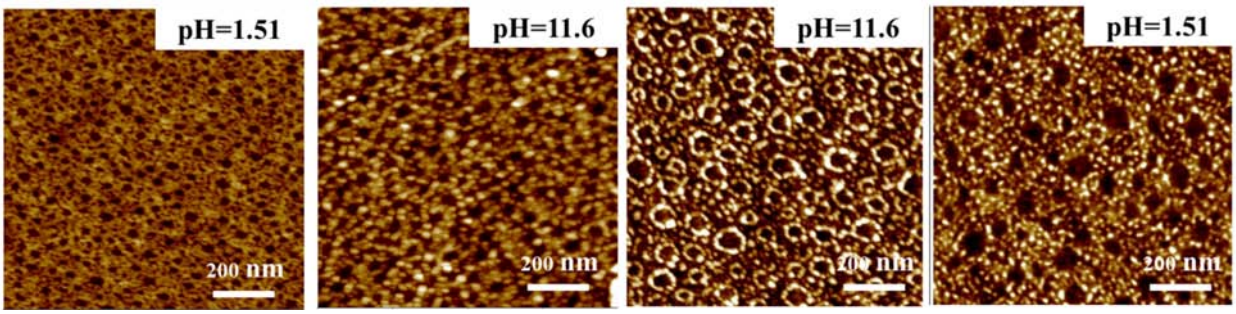

Figure IV.36: Height AFM micrographs measured in air on a film that has been previously in contact with not fully degassed solutions or previously degassed and exposed to air for few hours at different pH, as indicated.

The ensemble of our results suggests the following scenario (Figure IV.37). At low concentration of dissolved gases, the preferential adsorption of ions at the interface generates an attractive force on the polymer molecules at the surface inducing the formation of bumps. At higher gas concentrations a layer of nanobubbles nucleate on the surface. Small bumps are still formed in the region between or at the rim of the nanobubbles, where the air thickness is thin enough; we do not need to evoke a different mechanism to explain the different observed morphologies. In all cases, the thickness of the structured region (between 2 and 3 nm) is consistent with recent reports of the presence of a thin mobile layer on the surface of glassy PS films. At higher gas concentration larger bubbles or even a continuous low-density layer is present at the water-polymer interface and no structuration effect is detected.

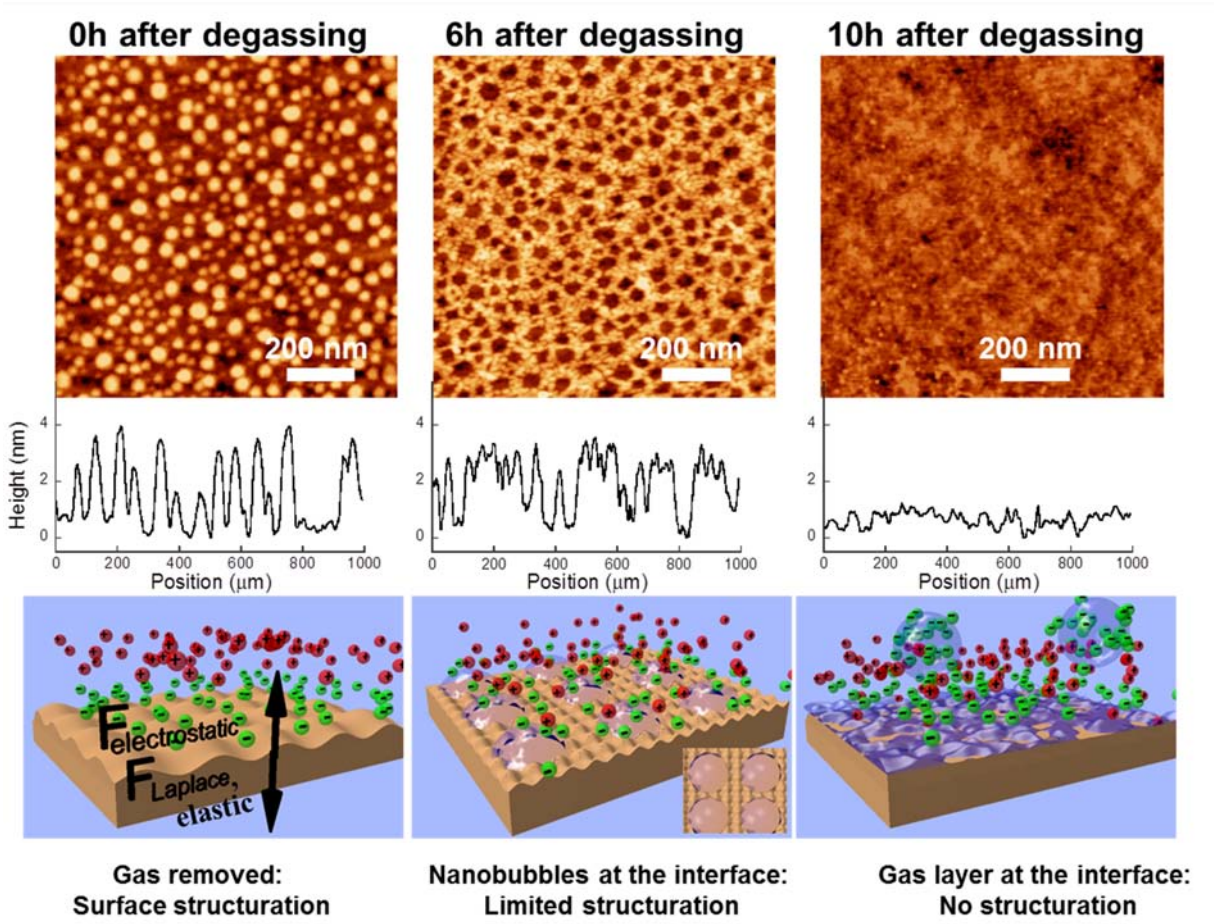

Figure IV.37: The amount of dissolved gas determines the nature and extent of the surface structuration. 300 nm thick 250 kDa PS films were immersed during 10 min in water at pH = 1.5 at different times after degassing, as indicated. A typical AFM height profile for each condition is presented. Shortly after degassing the preferential adsorption of ions at the water/polymer interface is likely to be responsible for the observed self-assembled nanostructure. Increasing amounts of gas in the solution remove the ions from the polymer surface limiting the structuration.

The procedure described in this chapter may be of interest for producing controlled nanostructured structures on flat, nonplanar, or hollow hydrophobic substrates in a single simple step allowing an easy and precise control of the nanopatterns produced. It may find applications in many different scientific and technological fields like nanolithography, microfluidics or flexible electronics. Some realizations of this idea are presented below.

4.9. Perspectives

4.9.1. PS spheres

The goal was to show that nanostructuration was also possible on divided matter, like colloids. For example, it is not possible to pattern PS microspheres with conventional lithographic techniques. Monodispered PS latexes (0.4 µm) were deposited by dip-coating from a concentrated aqueous

solution (10 g/l) on top of a smooth mica substrate. AFM images were taken of the bare surface of those PS spheres. The substrate was then immersed in a in a degassed pH=1.5 nitric acid solution for 5 min. The PS spheres presented a nanostructured surface after the treatment (Figure IV.38).

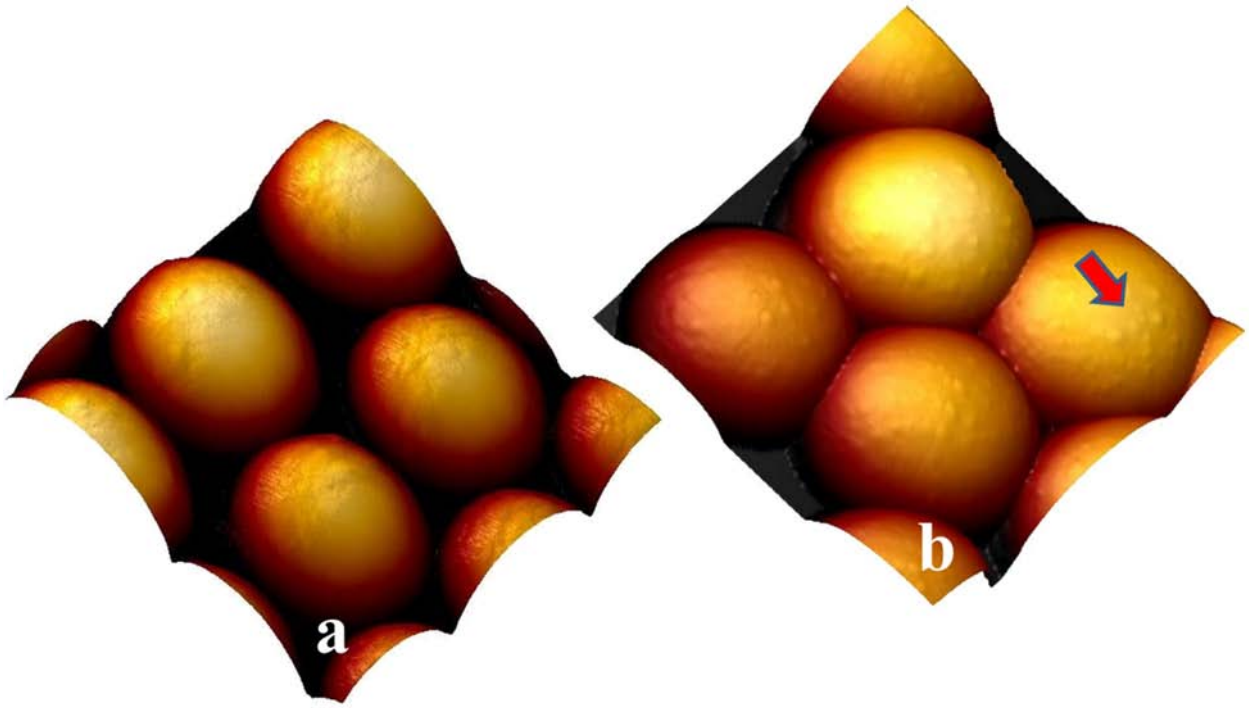

Figure IV.38: 3D Amplitude AFM images of PS latexes deposited onto the surface of smooth mica sheets. (a) Bare PS latexes. (b) Treated latexes where bumps are clearly visible.

4.9.2. Polydimethylsiloxane (PDMS) substrate

PDMS is commonly used as a stamp resin in the procedure of soft lithography, making it one of the most common materials used for flow delivery in microfluidics chips. A PDMS substrate was prepared by pouring the resin (Sylgard 184, Dow) and the cross-linker (10:1) into a Petri dish. The mixture was thoroughly mixed and put under vacuum 20 nm to remove bubbles. This brand of PDMS is known to complete cross-linking in 4 hours at 65 °C. The Petri dish was then put into an oven for 1 hour to give to the layer some mechanical integrity. It was then immersed in degassed pH=1.5 solution and kept in the oven for 3 more hours to fully cross-link the PDMS. AFM images were then taken for a reference PDMS substrate and the treated one. Figure IV.39 shows the surface of the smooth reference sample and the treated one presenting a much rougher aspect.

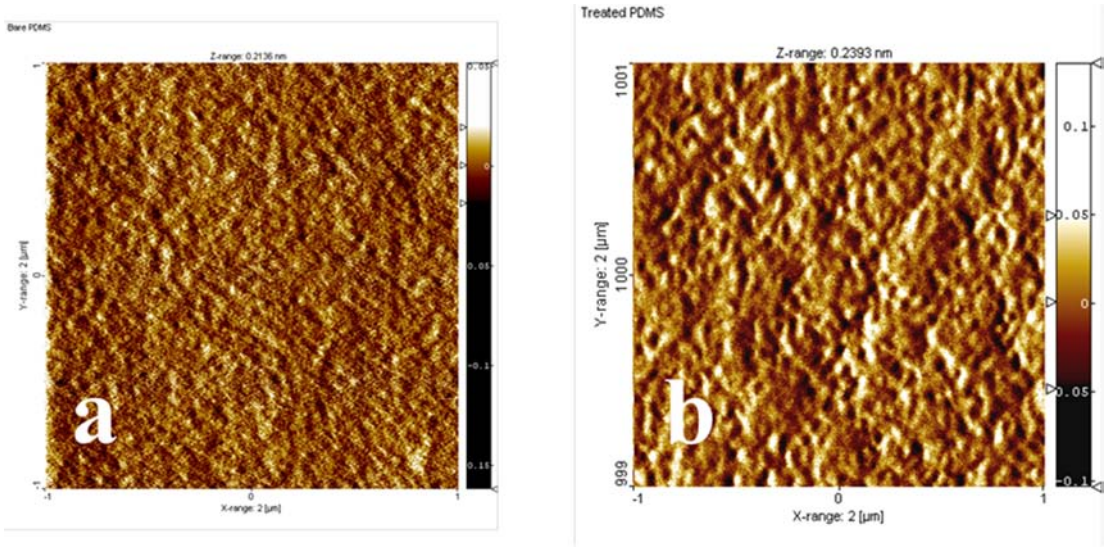

Figure IV.39: AFM amplitude images. (a) Bare PDMS surface x-linked in air at 65 °C for 4 hours. (b) Treated PDMS surface.

Multiscale roughness

The example given here highlights the potential of the *waterborne nanostructuration approach* to generate surfaces with multiscale roughness for different technological applications like adhesion, tribology, microfluidic etc. In a first step, spin coated PS thin films which surface has been previously cross-linked was structured via surface buckling using an osmotic stress approach. PS concentric rings were obtained. A dual roughness was generated in a second step by applying onto the rings the same approach again. Finally, a ternary or multiscale roughness was eventually generated by immersing the previous bi-structured surface to a degassed acidic solution. The multiscale structure is evidenced in Figure IV.40.

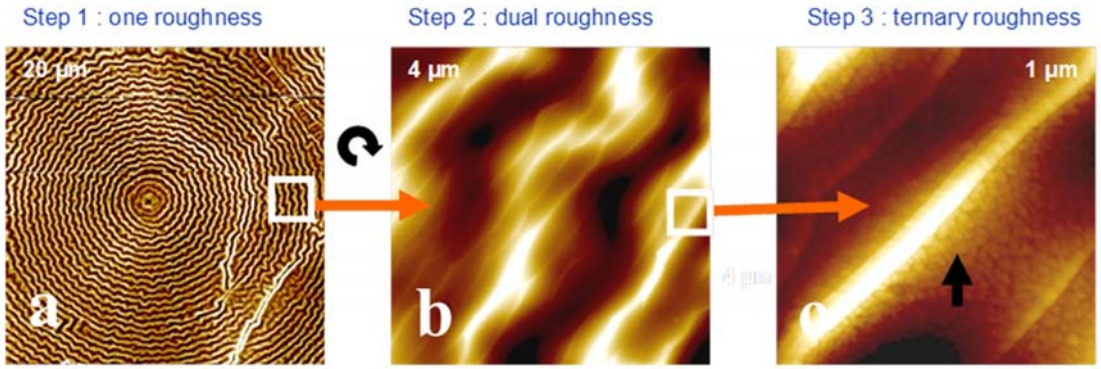

Figure IV.40: AFM images of PS multi-structured PS surface taken in air. Concentric PS rings were obtained via surface swelling induced wrinkling. A second roughness with a smaller wavelength is generated by repeating twice the first approach. A ternary roughness with an even smaller wavelength is generated on top of the previous ones via immersion of the substrate for 5 min into a degassed acidic aqueous solution.

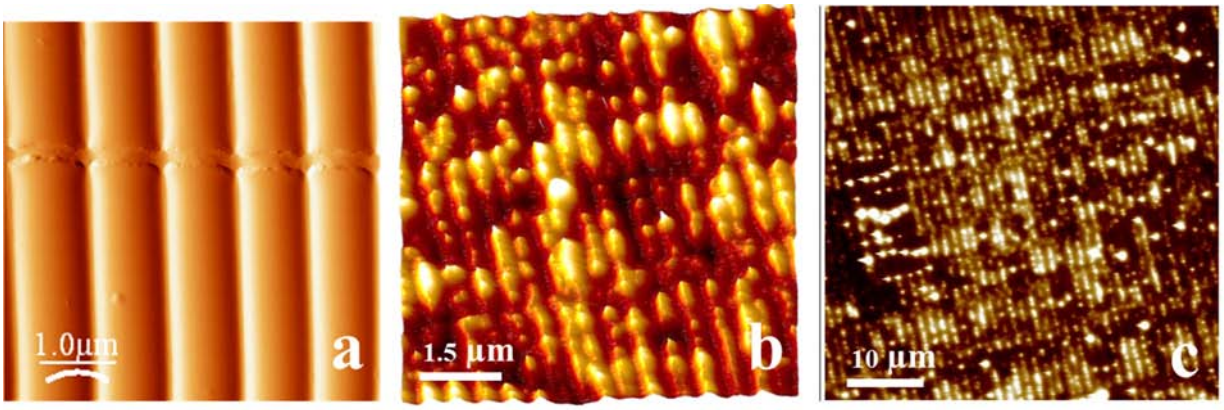

Figure IV.41: AFM image of sinusoidal microwrinkled PDMS-stamp (λ = 2 µm) (a); AFM micrographs taken in air that show the surface nanostructuration on bulk PS partially protected by a sinusoidal microwrinkled PDMS-stamp (b,c).

Selected Patterning by using a PDMS stamp

A ''bulk'' PS substrate was prepared by melting (~ 130 °C) a dozen PS pellets between 2 smooth glass slides. After cooling the system down, the 2 slides were peeled off leaving two smooth PS surfaces. A sinusoidal µ-wrinkled (λ= 2 µm) PDMS stamp obtained by natural buckling was then stuck on top of one PS surface. A couple of glass slides were added above the PDMS to apply a small normal pressure. The sandwich was then dipped into a degassed pH=1.5 nitric acid solution. The aqueous solution was able to ''wet'' the PS surface regions that were not in contact with the stamp. The PDMS was then peeled off and the PS surface dried before taking AFM images. As we can observe in Figure IV.41-b,c after 5 min, bumpy stripes over large areas were generated following the original pattern.

4.9.3. Other hydrophobic polymer surfaces

We have observed that semicrystalline films of polyethylene (PE) are also prone to be structured by this technique (Figure IV.42).

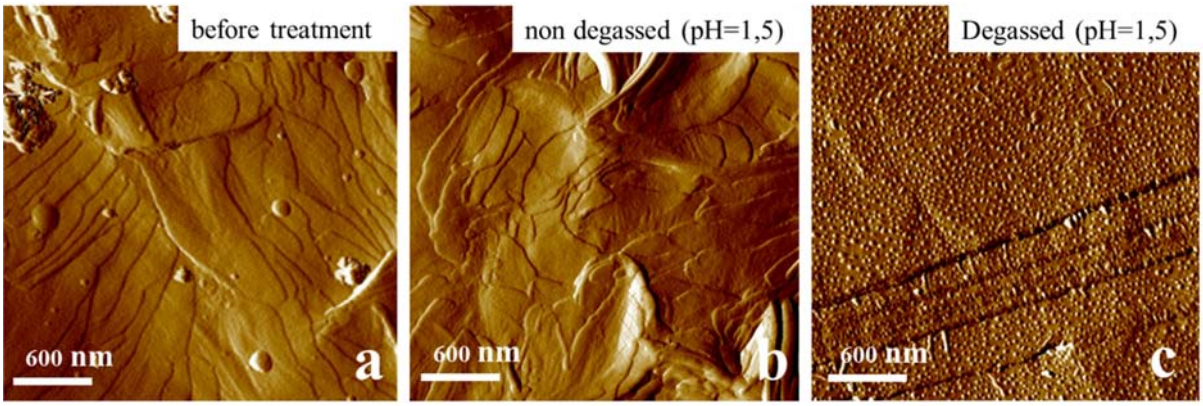

Figure IV.42: 3µm x3µm amplitude tapping mode AFM micrographs taken in air of PE surface as prepared (a); after exposure to a non degassed (b) and degassed (c) solution of nitric acid in double distilled water at pH 1.5 and room temperature. The presence of asperities of regular nanometric size is clearly observed on the surface exposed to the degassed solution for 5 minutes.

A reasonably smooth hydrophobic polyethylene surface were obtained by melting a high density (M_W = 125 k) polyethylene pellets at 170°C on freshly cleaved highly oriented pyrolitic graphite (HOPG) surface. It was kept at this temperature around 20 min after same slight pressing for a good contact. Then polymer surface was cooled down to room temperature at very slow cooling rate on a hot stage. The polymer surface obtained by detachment of the polymer from graphite was investigated by AFM (Figure IV.42-a). No noticeable change of morphology was observed when the films were exposed to an aqueous solution of pH = 1.5 in equilibrium with air. On the contrary, nanopatterns appeared in the surfaces after few minutes of exposure to degassed water solutions, as can be observed in Figure IV.42-c. Similar results were obtained for 312 nm thick spin coated PMMA-120k films exposed to degassed aqueous solution of pH = 1.5 (Figure IV.43-a).

Few tests concerning nanostructuration of hydrophobic copolymer films using the method presented in this chapter were performed with PS-PAA films. Figure IV.43-b,c are presents images of PS-PAA films. The surface topography varies accordingly to the copolymer composition: with PS_{86}-PAA_{70} is rough with sponge-like structure, while with PS_{86}-PAA_{38} the surface was smooth and show worm like features with height of 1.5-2 nm, width about 10 nm and periodicity of about 30 nm. After treatment with non degassed solution the morphology of the films remained unchanged. On the contrary, once the surfaces were treated with degassed solution the appearance of bumpy nanostructure could be observed. For PS_{86}-PAA_{70} we observe that bumps are distributed aver all surface, which can be explained by the fact that the film have a lamellar structure parallel to interface with the surface rich in PS zones that are structured. In the second case things are more complicated; we observe the appearance of bumps only on the particular domains in the worm-like structure. We believe that PS domains are getting structured, while PAA domains remain intact.

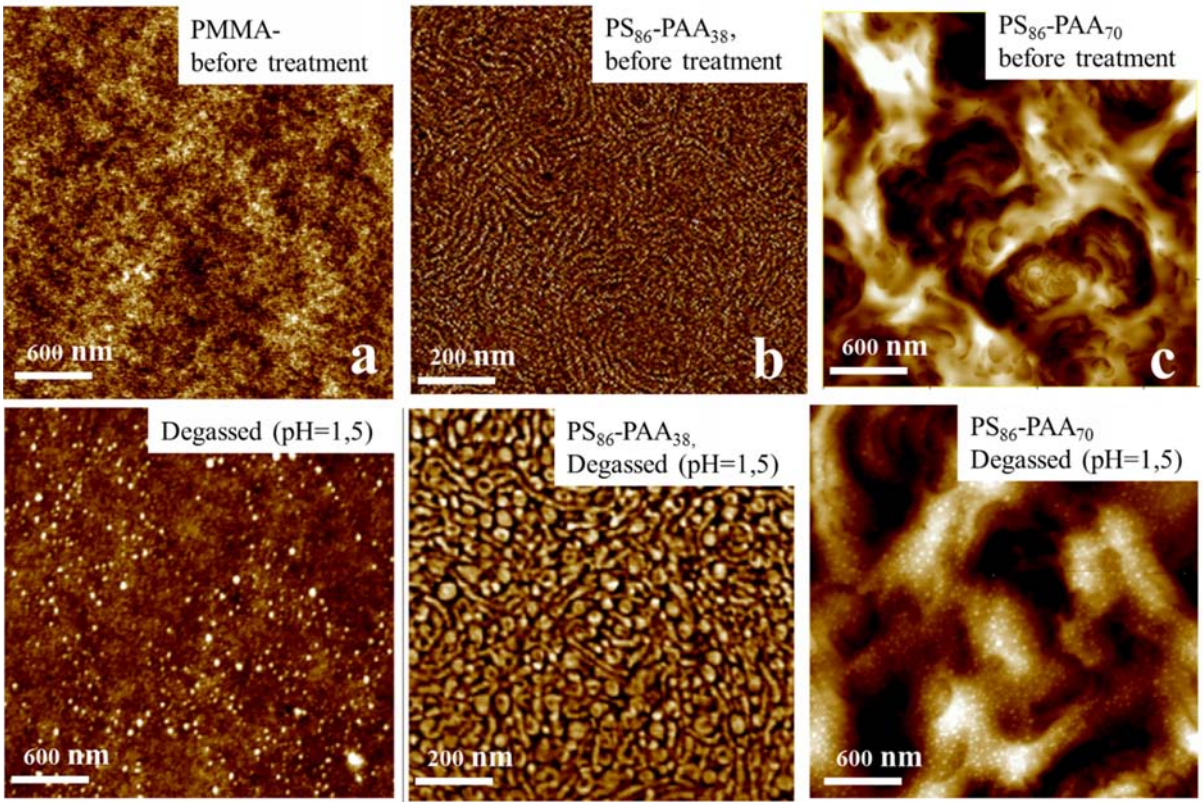

Figure IV.43: AFM micrographs measured in air of PMMA and PS-PAA films as prepared (upper row) and after contact with degassed solution of pH=1.5 (lower row)

4.9.3. Pattern replication

The obtained patterned polymer surfaces can also be replicated by metal thermal evaporation to produce nanostructured metallic films with holes or asperities of controlled size, as illustrated in Figure IV.44. After deposition of a sufficiently thick metal layer, the polymer layer can be cleaved or dissolved away. This procedure allows an efficient and precise control of the metallic surface structure, with possible applications in materials science and photonics.

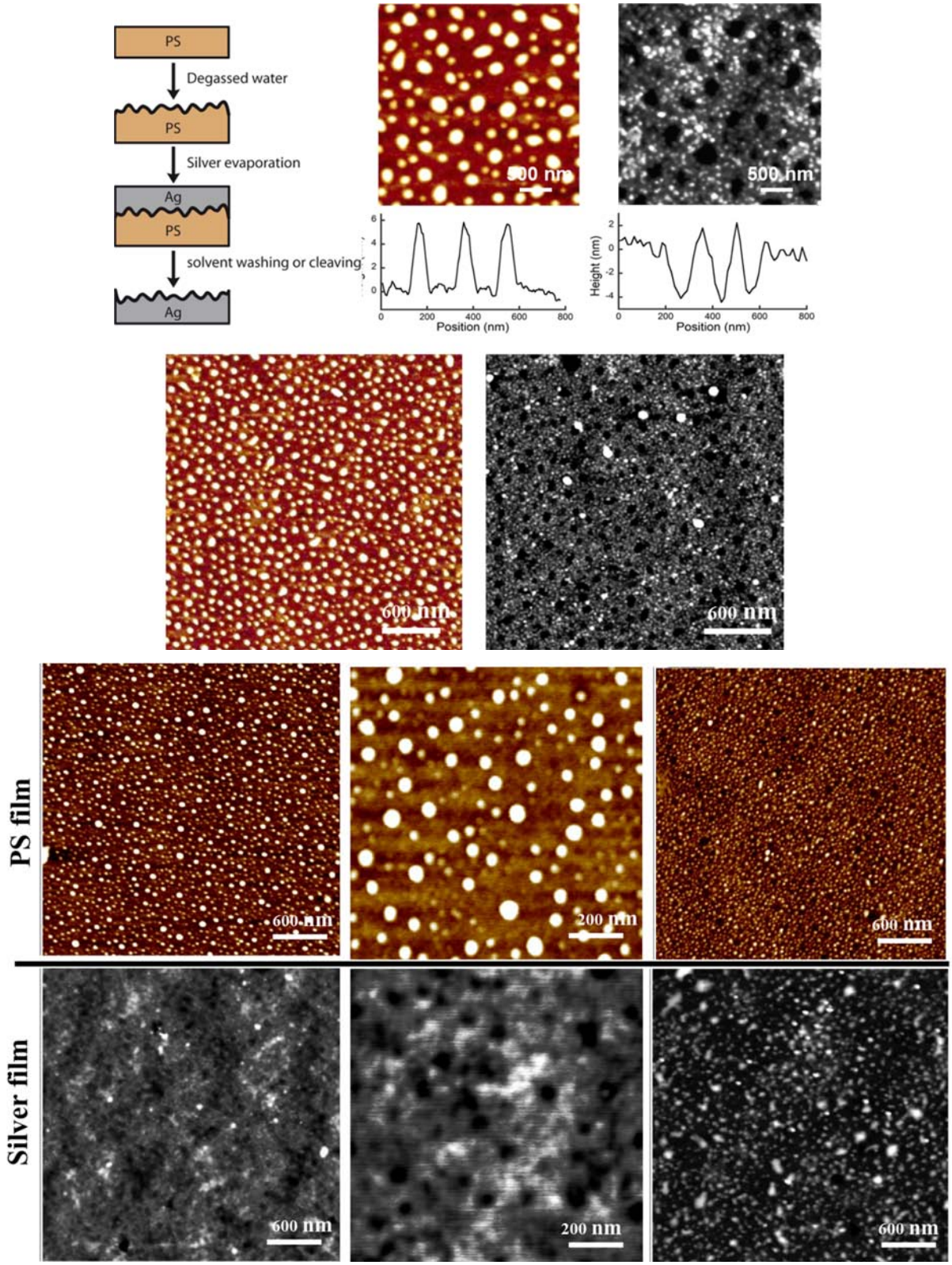

Figure IV.44: The polymer modified surfaces can also be used as a template to pattern metallic films Evaporating a 250 nm thick silver film on a structured PS film and removing the polymer film after gluing the stack onto a convenient substrate, allows production of a metallic film of controlled surface structure as holes or bumps. Brown pictures represent structured PS surface, while black and white images are structures silver films

4.10. Conclusion

We have developed a novel method for producing controlled structured polymer surface with sub–micron and possibly sub–10 nm lateral length scales.

The technique of electrostatic pressure induced nanostructuration presented here is straightforward and does not need any specialized equipment or chemicals. In a laboratory or technological application, this method of structuration can be easily achieved just by controlling with great precision the degassed solution. Furthermore, a combination of the thermic treatment with electrohydrodynamic forces is a promising prospect for a simple, low-cost lithographic technique for the replication of sub–100nm patterns.

We believe that the phenomena described in this chapter are relevant for the interface between water and any hydrophobic object, and should be considered in the description of processes a diverse as protein folding, surfactant aggregation, friction or adhesion. It may find applications in many different scientific and technological fields like nanolithography, microfluidics or flexible electronics [82].

4.11. Supporting information

S - Steps of process of nanostructuration and of AFM characterization method

As summarized in Figure IV.45, the method consists of four main steps: sample and solution preparation, treatment with degassed or non degassed solutions, image acquisition, and image analysis. We will now examine these steps one by one.

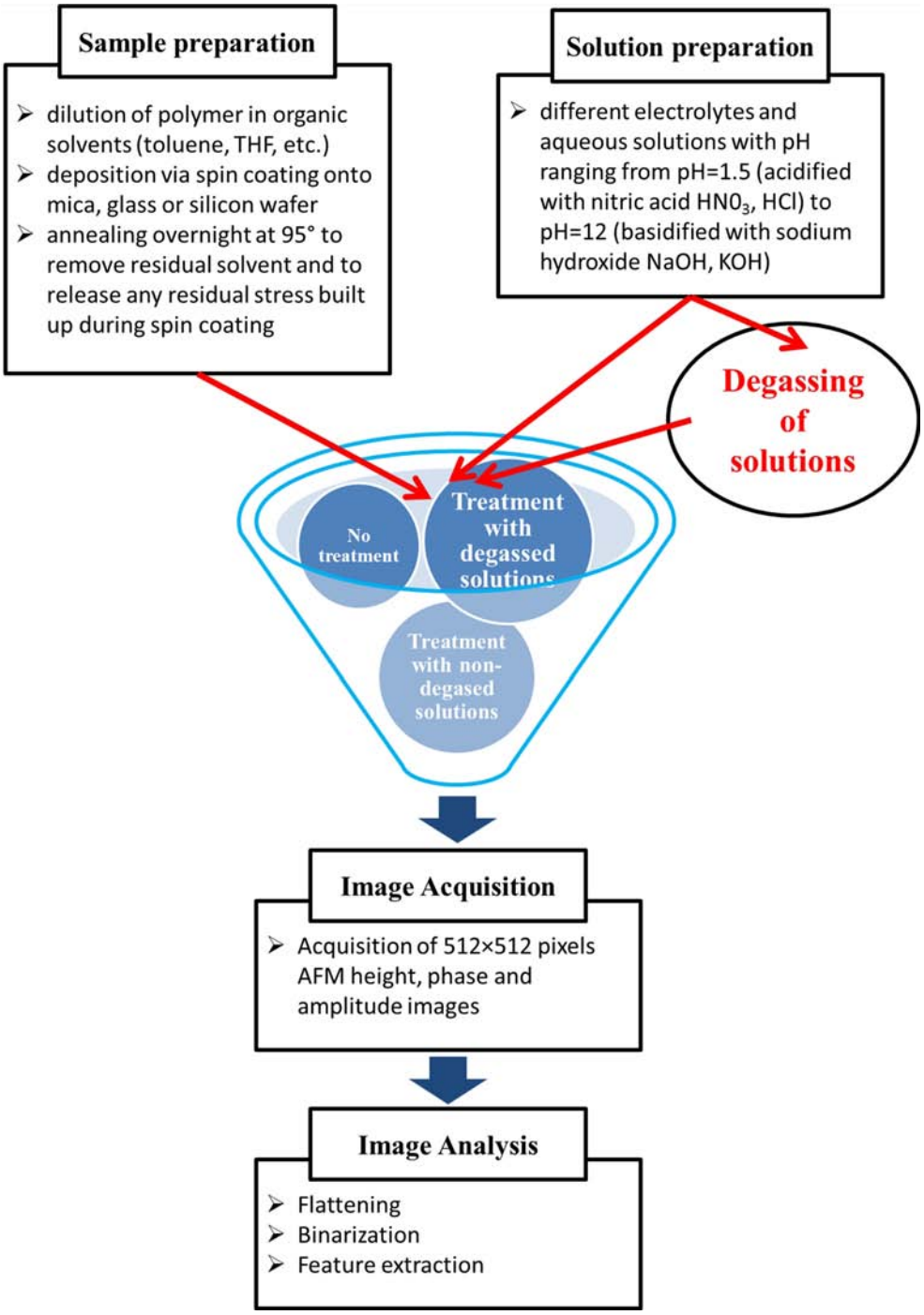

Figure IV.45: Steps of process of nanostructuration and AFM characterization

S.1. Sample (Film) preparation:

First, polymer solutions of concentration 0.5%-10% w/w are prepared. All tools and glassware (magnetic stirrer, pipettes and spatula) are cleaned using absolute ethanol before preparing polymer solutions. To get uniformly dissolved transparent solutions, the polymer-solvent mixture usually were stirred at room temperature for ~1 day. Before depositing the polymer, substrates are properly cleaned (*see Chapter II*). Substrates of $1\times1cm^2$ of silicon wafers, glass or mica were typically used. For spin coating polymer films, two drops of polymer solution are put at the center of the cleaned substrate sitting on the spin coater chuck. To make uniform polymer films it is important to avoid bubbles when depositing polymer solutions; then we start spin-coating at the preset rotation speed and let the spin-coating disc rotate for 60 seconds until the color of the polymer film is stable and uniform. The quality of the polymer films depend on many factors. Specifically, the following factors have to be considered:

- *Solvent choice:* In our measurements, all polymers are dissolved in toluene; We also tried tetrahydrofuran and acetone and found that it can dissolve polystyrene and PMMA quickly but the films made from such solutions are not uniform with some small holes or uinhomogeneities on the film surfaces; the difference between toluene and acetone is that the former solvent evaporates slowly while the later evaporates quickly, perturbing the quality of the film.
- *Air circulation in the spin-coating chamber:* During spin-coating the evaporation of solvent can change the viscosity of the polymer solution and accordingly has an effect on the final film thickness. Therefore, it is important to avoid large fluctuations in the air circulation in the spin-coating chamber.
- *Polymer solution concentration:* In our studies, the polymer concentration was between 0.5% and 10% - if the concentration is too low it is very easy for polymers to de wet and non-uniform films are obtained; on the other hand, if the solution concentration is too high, some corrugations can be formed on the surfaces of the polymer films, especially when preparing relatively thick films.
- *Spin-coating speed:* we used spin-coating speeds within a range of 2000-4000 RPM. For a given polymer concentration, higher spin-coating speeds results in thinner polymer films.
- *Molecular weight M_w of polymers:* For the same concentration, solutions of polymers with higher M_W have higher viscosity. Consequently, the thickness of polymer films made by the spin-coating technique depends on M_W.

After spin-coating, the polymer films were usually annealed at a temperature 95°C abve for more than 12 hours in an oven to remove residual solvent and stress introduced by spin-coating procedure. After annealing, the samples were cooled down to room temperature. After all these treatments the polymer films were kept in clean glass Petri dish in a laminar flow cabinet before use.

In some studies people use high temperature annealing in vacuum to avoid potential chemical attack from the ambient. We did not observe any influence of the annealing procedure on the resulting film structure.

S.2. Solution preparation, water degassing and film treatment

Millipore water with a conductivity of 18 $M\Omega cm^{-1}$ was used for the solution preparation. The pH of the aqueous phase was adjusted by adding small amounts of NaOH (Prolabo) or nitric acid (Aldrich) as necessary. Similar results were obtained by using HCl (Aldrich) or KOH (Aldrich). Once the solution is ready, it is placed in Buhner flask with a rubber cork and stopcock plug to tightly (hermetically) close the flask (Figure IV.46-a). Carefully cleaned Teflon bar stirrers were introduced in the solutions to be degassed to induce the nucleation of gas bubbles. Then the flask is connected to a vacuum pump. As represented in Figure IV.46-b we used an Alcatel 2010 Pascal dual stage rotary vane mechanical vacuum pump. During pumping the pressure inside the flask was lowered to 0.1-0.2 mbar. As we know the solubility of gas obeys Henry's law: the amount of dissolved gas in the liquid is proportional to its partial pressure. Therefore, the reduce pressure inside the flask decreases the amount of gas dissolved in the water. This technique is often referred to as *Vacuum degasification*. The solutions were subjected to agitation (stirring) (also sonication can be used to enhance the efficiency) under a reduced pressure of 0.2 mbar during two hours. The appearance of macroscopic bubbles in the aqueous phase was observed only during the first 30 minutes of degassing. As the process of degasification is long, evaporation of water also take place. Since process of evaporation of water is endothermic process, the water solution under degasification gets cooler (cools down) (Figure IV.46-c). To maintain the temperature constant, the process of degassing is finished (30 min-1h) with the flask placed in water bath temperature controller (Figure IV.46-d). Water bath temperature (temperature of degassed solution) was controlled to closely match to temperature of the sample (polymer films). After the degassing is finished, the air pressure on the flask was gently increased back to atmospheric pressure. The degassed solutions were put right away in contact with the polymer surfaces for few minutes after stopping the pumping (Figure IV.46-e). In experiments presented in this work time to open the flask and pure the degassed solution into a Petri dish and put the sample inside was around 5 sec, unless otherwise indicated. After 5 min in degassed solution (or longer for particular experiments) samples were removed from the solution, dried with a gentle flow of nitrogen gas (Figure IV.46-f) and immediately studied with AFM.

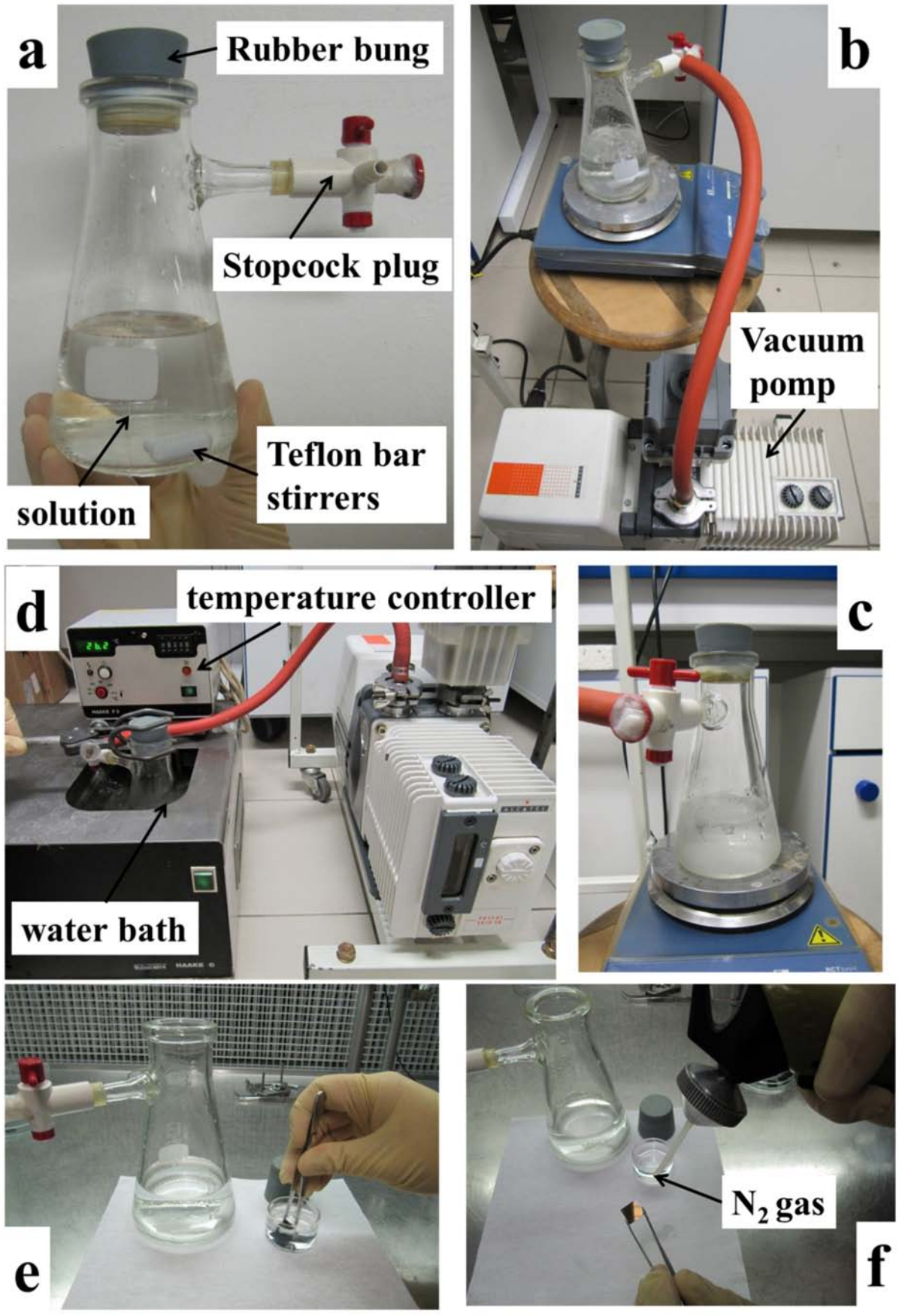

Figure IV.46: Steps of solutions degassing and sample treatment.

S.3. Image acquisition

Like with any other technique, some skill and practice are necessary to correctly operate an AFM and to obtain good quality AFM images. It is not as easy as described in AFM manufacturer's user manual, where it is mentioned that it just takes a few hours of instruction and practice. After sample preparation, setting up the instrument and scanning several images can take few hours. However, if the sample is not well known, or has never been investigated by AFM before, it can take more time to acquire useful data. In this part of the Chapter I discuss the procedure used to measure AFM images. Figure IV.47 shows the major steps involved. After sample preparation, the next step is to place a tip into the AFM. It is possible that a probe will already be inserted, but when beginning with a new experiment, a new probe is usually used.

Figure IV.47: The major steps involved in measuring AFM images.

This step is delicate: great care must be taken when handling the cantilever chips because they are very small and delicate. Usually the tip is placed in he probe holder using clean tweezers with flat ends. After placing the probe in the instrument, the alignment of the optical lever is carried out. This is done in two stages. First, the laser spot is adjusted onto the end of the cantilever. There are two screws for this purpose: one to move the laser parallel to the cantilever axis, and the other perpendicular to it. The goal is to place the laser spot on the cantilever over the position of the tip where highest sensitivity is generally obtained. Visualization and monitoring of the laser spot can be done by placing a piece of white paper in the path of the laser. Note: the user must take care not to look directly into the laser beam, which can be dangerous for the eyes. Proper alignment of the laser is very important in order to obtain best results from the AFM. Poor alignment may reduce the sensitivity and could introduce imaging artifacts. Having aligned the laser onto the cantilever correctly, it must then be correctly aligned in the photodetector. The aim is to translate the photodetector until the laser spot impinges on the center of the detector, i.e. to equalize the signals from all four segments. Sometimes there is a visual display of the photodetector in the AFM software, or just a numeric display of the signals from the photodetector segments. This is a rather similar process to the laser alignment; the only complication comes when the spot is completely off the detector, in which case the user might not know which way to turn the screws. If this is the case, the user simply turns the detector translation screw all the way in one direction, and then all the way in the other until the signal is found, being careful not to apply too much pressure to the screws when the end of the range is reached. In addition, often a third control is inserted in the optical path, which controls

a mirror between the cantilever and the photodetector. This control might be needed in two cases: misalignment by changing the refractive index of the medium, or when a very large realignment of the photodetector is required because the laser spot is in a dramatically different position. If working in tapping mode, the operating frequency must be selected after the tip is loaded and the laser aligned. This is can be done via an automated routine, but often it is done manually. The 'cantilever tuning' window in the AFM software sweeps the oscillation frequency of the driving piezo over a fixed frequency range and displays the amplitude of oscillation at each point. The user should have some idea of the natural frequency of the cantilever, so that it is within the selected range. This information is supplied by the cantilever manufacturer, and typically covers quite a broad range (e.g. 200–400 kHz). Within this range, the cantilever's oscillation should be visible as a single, strong peak. The presence of multiple or misshapen peaks in the frequency spectrum is an indication that something is wrong. The tip could be damaged or not fixed correctly in the probe holder. The resonant frequency represents the point at which the amplitude is maximum. The actual operating frequency is close to the maximum of the amplitude, but a little way off the maximum (on the low-frequency size), to take into account the frequency shift as the tip approaches the sample.

Once the probe is loaded, optical alignment is performed and operating frequency is selected, the next step is to initiate the probe approach (engagement). Depending on the instrument, the automated probe approach may be quite fast or quite slow. Usually the tip is moved close to the sample manually in order not to waste too much time waiting for the automatic approach. This must be done carefully in order to avoid uncontrolled tip–sample contact which can damage the device or the tip. Manual approach depends of the user, but generally involves using the microscope to alternately focus on the probe and sample surface in order to judge (evaluate) their distance from one to another. Once tip is relatively close to the surface, an automated approach is carried out, but not before choosing (inserting) the initial scanning parameters, including scan size (usually zero), scanning speed, gains, and set-point. Note that incorrect approach can easily damage a tip and sample.

Having approached successfully, scanning the sample begins, and we see a line-scan (a two-dimensional plot of the signal the instrument is recording). Often, the height data, as well the phase or amplitude (in contact mode, the cantilever deflection) can be shown, and sometimes both forward and reverse signals are shown. These signals (forward and reverse) can be extremely useful for optimization of scanning parameters. As forwards and backwards scanning lines measure (almost) the same position of the sample, the two height traces should coincide. Large differences between forwards and backwards traces are an immediate indication that something is not right with the scanning. There are a number of possible reasons for forwards and backwards traces not matching but the most common reason is that imaging parameters (gains, set-point, and scanning speed) are not yet optimized. The method to optimize the parameters is an iterative one. The parameters are changed in steps, one at the time, until the tip is properly following the surface (forwards and backwards traces are matching). After optimization, then the slow scan axis movement can be re-enabled and the user

may choose which signals store. There are signals of different types – the height (z piezo voltage signal, and z sensor, if available), amplitude (error signal), and phase. The height signals are the most important, as they are the only signals with a meaningful scale, and the only signals from which we can make useful topographical measurements.

In this study, smooth and structure polystyrene samples were imaged by AFM in air at room temperature using a Digital Instruments Nanoscope IIIa Multimode and an Icon, Veeco. All images were obtained using tapping mode imaging with TESP silicon probes (cantilever spring constant 20-100 N/m and resonant frequency 200-400 kHz). The scan angle was usually maintained at 0°, and the images were captured in the trace direction with a scan rate of 0.5 Hz. Images of 512×512 pixels were acquired. The scan range needed depends on the size of the induced nanostructure, smaller bumps requiring smaller scan sizes for better resolution. All images in the present study were acquired over scan ranges of 1×1 μm^2 or 3×3 μm^2, providing resolutions of ≈0.002 to ≈0.006 μm/pixel respectively. The actual number of images needed depends on the number of bumps that can be identified on the images. AFM images were typically taken near the centre of the sample, but to check that distribution of bumps is uniform the images were also taken at random locations of the sample surface.There is also an inherent sensitivity due to the sharpness of the AFM tip. If the radius of curvature of the AFM tip is much larger than that of the structure, there is a reduced ability to measure correctly the height and diameter of the bumps. This problem is minimized by using sharp tips and/or by frequently changing the tip. The average height/diameter of the nanodeformations were compared to the average before and after changing the tip to ensure that the tips and the imaging resolutions were chosen properly and the parameters of the bumps can be measured accurately and reproducibly.

S.4. Image analysis

Once recorded, AFM data (images) needs to be processed, displayed and analyzed to get the most out of it. AFM data has several advantages over data from other microscopes in terms of data analysis. Firstly, the data is in digital form, therefore there is no digitization step required. As AFM data is already calibrated, there is no need for a scale bar overlaid over the images because the scale is built into the data file. AFM data is by its nature three dimensional, so there are no calculations or guesswork involved in getting three-dimensional data. The data is saved by the AFM software as a file containing all the height and other data recorded by the instrument. Typically, the AFM software provided by the instrument's manufacturer has two main functions, image acquisition, and image processing. These could be separate programs, or may operate together. For analysis of our data we always used the analysis software provided by the manufacturer of the instrument to be sure that the data was correctly interpreted.

S.4.1. Flattening

Artifacts may occur during the image acquisition like "shadowing" due to large structures or image tilt, if the probe and the sample are not perfectly perpendicular. In fact, most images have a

background tilt and/or shadows that are larger than the features of interest. If the background in the image (such as the substrate on which the sample was deposited) has considerable tilt in it, the change in height of the background will mask the changes in height associated with the sample. This concept, along with some examples of flattening operations, is shown in Figure IV.48. AFM is often used to measure samples with very small heights, so even a small tilt in the sample background can have serious effects. Global thresholding techniques cannot be used on uneven (bumpy) images. In addition to tilting in the image caused by the AFM and sample not being perfectly orthogonal, a common problem in AFM images is scanner bow. It occurs mainly in instruments that use tube scanners, and is caused by a swinging motion of the free end of the scanner. This leads to a curve in the image plane as is also shown in Figure IV.48. In such cases, the background must be subtracted from the image. This is often called "leveling" or "flattening" the image, an operation which is commonly performed by softwares provided with AFM apparatus and it is usually the first processing operation carried out on the data. There are a number of different methods that can be used for image levelling, as polynomial fitting, two-dimensional plane fitting and three-point fitting.

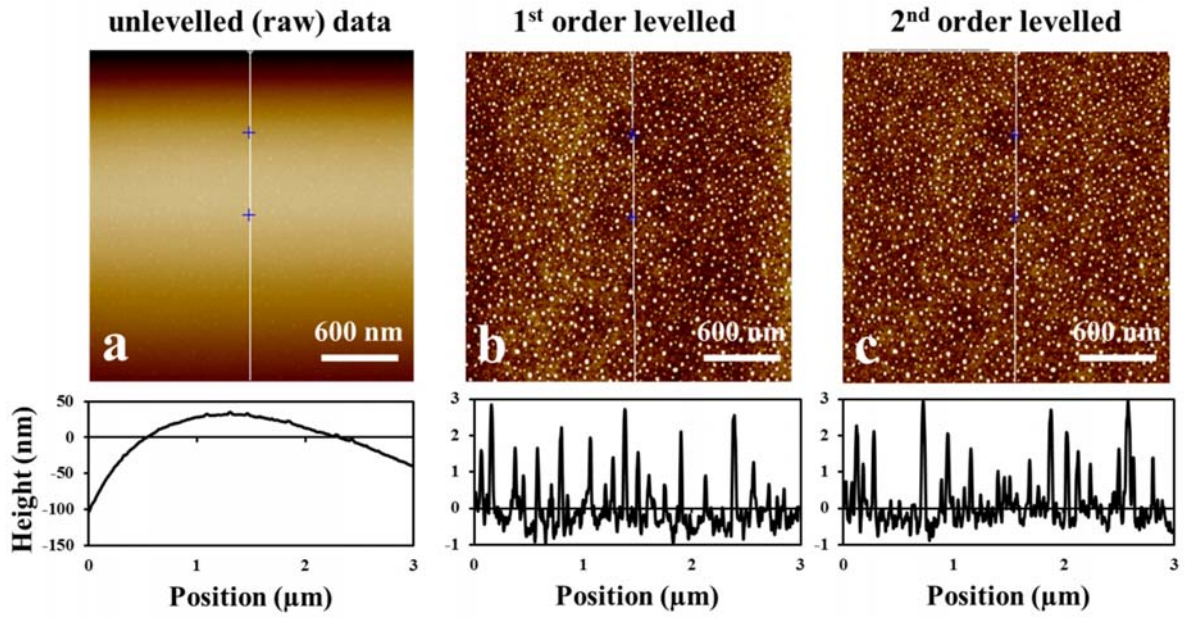

Figure IV.48: Illustration (below: line profiles; top: images) of the effect of first and second order polynomial line levelling. Left: unlevelled (raw) AFM image of structured PS surface showing tilt and scanner bow. Middle: effect of first order horizontal levelling – the bumps are much clear; (curvature of the background due to scanner bow is barely seen). Right: the effect of second order levelling with exclusions, the background is now flat.

To correct the image for the tilt and/or shadowing in our experimental data polynomial fitting were used. Polynomial fitting or 'line-byline' levelling is most common method for flatening AFM images. In this routine, each line in the image is fit to a polynomial equation. Then, the polynomial shape is subtracted from the scan line, which leads to the line being not only flattened, but also shifted such that it is centered on zero height. The order of the polynomial equation can vary from 0 to 3. For

our experimental images a first order fit was normally good enough; occasionally, for larger scans a second order fit was more suitable. It is possible to fit a third order polynomial, but we never used to avoid introducing spurious artifacts on the data.

S.4.2. Displaying AFM images

A large amount of information can be gleaned from AFM images just by observing them. However, the information visible in an image depends on how it is displayed. Furthermore, the AFM user never works in isolation, and needs to communicate the information present in the images to others. There are several ways of displaying images to make them more interesting to view. Images may be displayed by a computer as either 2-dimensional or 3- dimensional projections (Figure IV.49). The standard method and the most used way of representation AFM data in this work shows a two-dimensional (2-D) image, using a color scale to represent height information. The AFM software will normally stretch the color scale to cover the entire range of the z scale. An AFM image displayed in the 2-D format looks much like an image from a traditional microscope. This is not a normal way for humans to see shapes, and can make interpretation difficult. In particular, for viewers not used to AFM data, it can be difficult to determine which features are higher than others, etc. One way to overcome this is to render the height information as a pseudo-three-dimensional image (3-D). An image displayed in a 3-D format gives a rendition of what the surface topography actually looks like. That is, data is displayed in the x y and z axis.

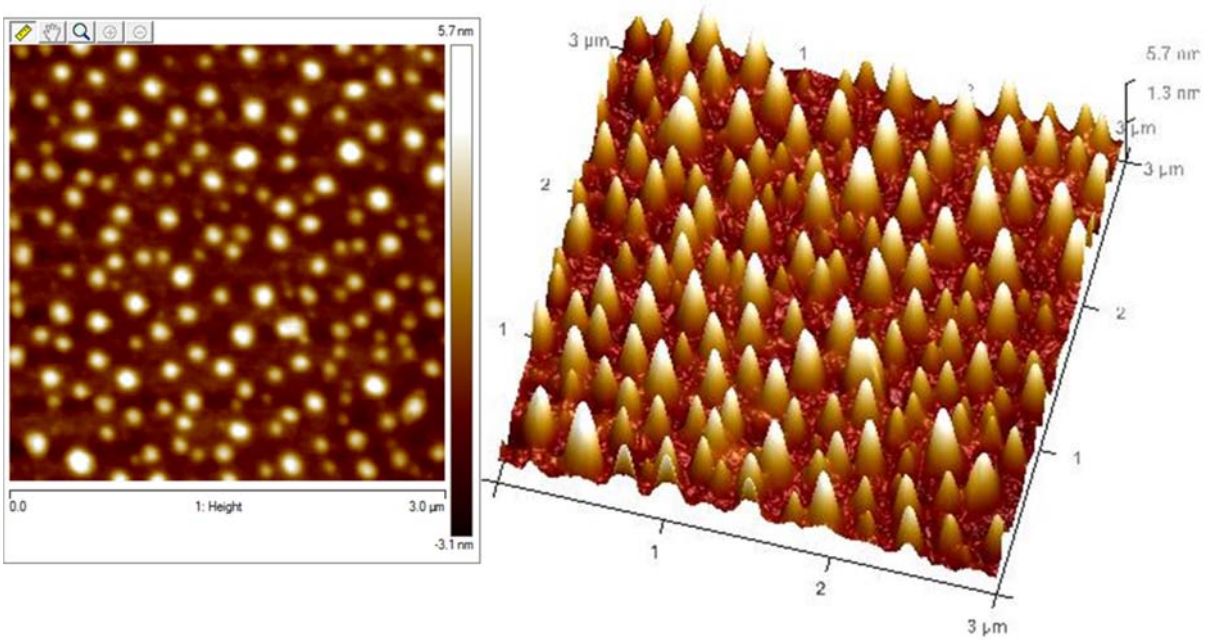

Figure IV.49: Examples of 2D (left) and 3D (right) renderings of height information of structured sample. 3D rendering greatly helps the viewer to visualize the shape of the sample.

S.4.3. Analysing AFM images

AFM images are suitable for further analysis, and it is rare that only displaying the images acquired is sufficient to fully characterize the sample under study. Thus, very commonly further analysis is carried out in order to obtain quantitative information. One of the most common analysis techniques is the extraction and measurement of line profiles. The AFM analysis software allows the user to arbitrarily define lines to be extracted, and these can be horizontal, vertical or at any angle. The software then constructs a new plot, with distance along the chosen line on the *x* axis, and sample height on the *y* axis. In the new plot, the user can easily measure heights, widths, and angles. An example showing an image with extracted line profiles, and measurements of these parameters, is shown in Figure IV.50.

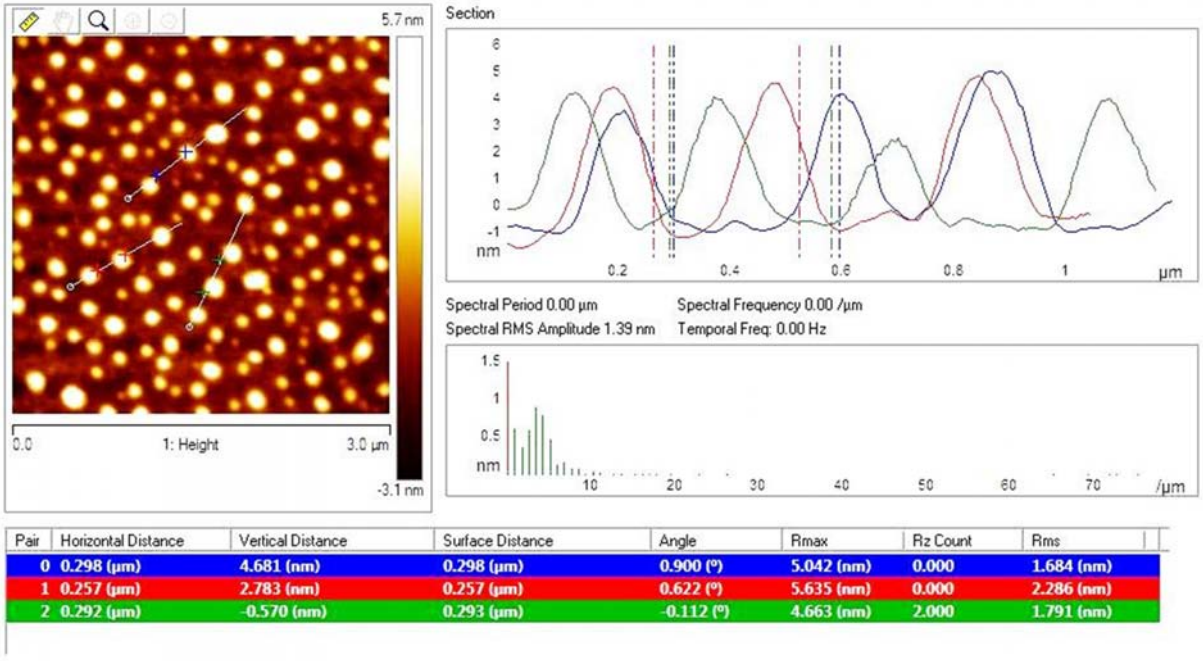

Pair	Horizontal Distance	Vertical Distance	Surface Distance	Angle	Rmax	Rz Count	Rms
0	0.298 (µm)	4.681 (nm)	0.298 (µm)	0.900 (°)	5.042 (nm)	0.000	1.684 (nm)
1	0.257 (µm)	2.783 (nm)	0.257 (µm)	0.622 (°)	5.635 (nm)	0.000	2.286 (nm)
2	0.292 (µm)	-0.570 (nm)	0.293 (µm)	-0.112 (°)	4.663 (nm)	2.000	1.791 (nm)

Figure IV.50: Line profiles analysis of an AFM image of structured PS surface with degased solution.

S.4.4. Bumps Analysis

Manual measurement of line profiles is a very simple and accurate way of measuring features in AFM images. It is useful for measuring a small number of objects. However, for large samples where hundreds of bumps are present, this rapidly becomes tedious and time-consuming. For this reason, most AFM analysis packages include routines for automatic particle counting and analysis. We used the threshold method for identification and analysis of bumps in our samples. In this method it is essential that one can distinguish between the objects of interest (bumps) and the background. After a well-leveled background, a simple thresholding routine was used to isolate the bumps. In this process, the user selects a value above which all features (bumps) are counted as particles. The process of separating the particles from the background is known as image segmentation. A critical issue is the selection of the threshold value. Here, the optimum threshold was selected by looking at the quantity

and the shape of bumps detected for different threshold values. If the threshold selected is too low, not all background is removed, and therefore the count of objects will rise considerably. On the other hand, if the threshold selected is too high, the genuine small particles will be eroded and eventually discarded. Figure IV.51 shows the count of objects as a function of threshold.

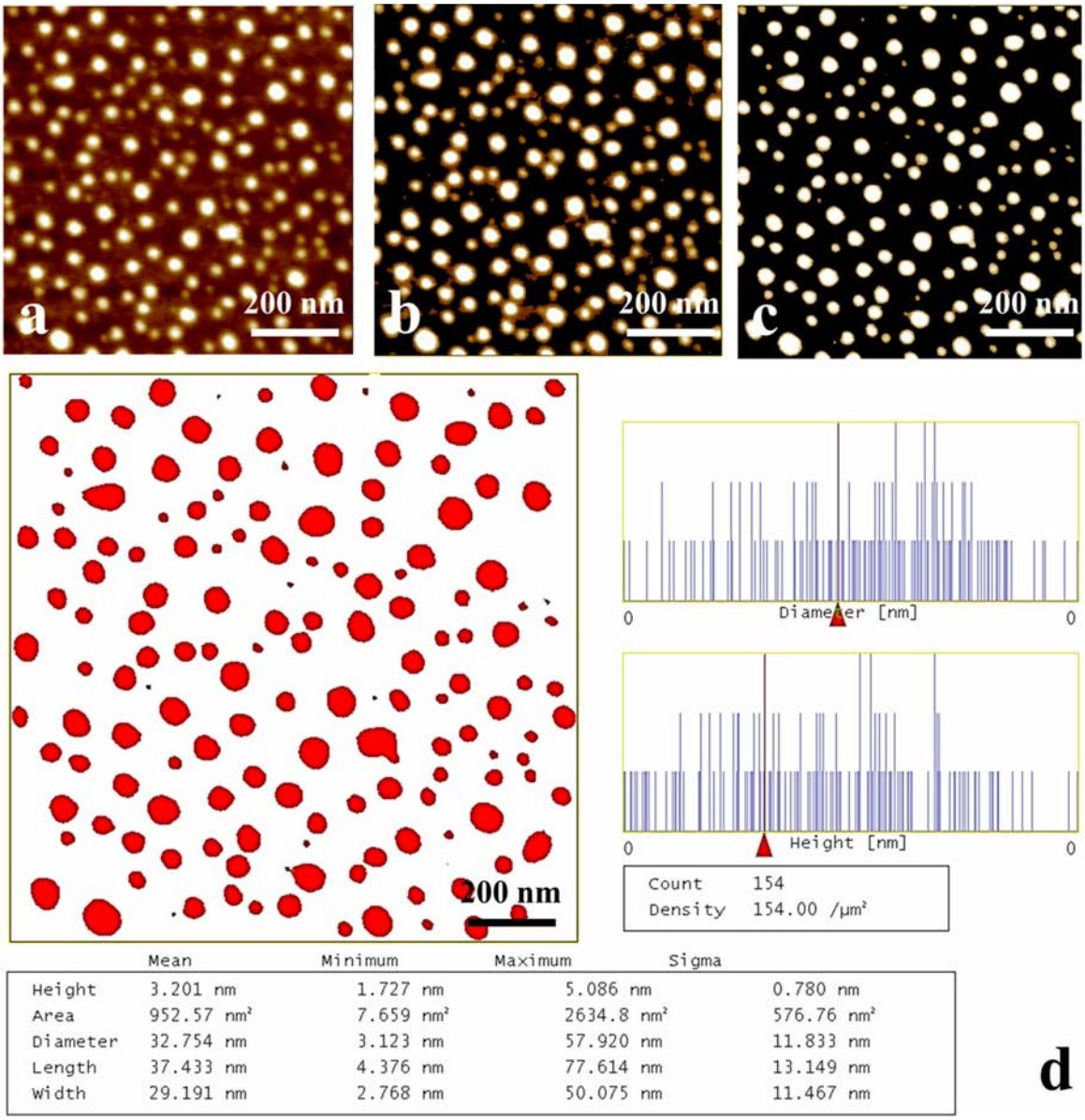

Figure IV.51: An example of a bumps counting routine using threshold

Once the segmentation is complete the AFM analysis software automatically measured height, length, diameter, and area for each particle (or, in our case, bumps). Usually these parameters are presented in a tabular format and it is possible to export all these measurements for further statistical analysis. Some packages also allow direct calculation of the statistics (e.g. mean average, standard deviation, etc.) and plotting of histograms of these parameters. An example of a bumps counting routine and the results are shown in Figure IV.51.

4.12. References

[1] Pashley, R.M. Effect of Degassing on the Formation and Stability of Surfactant-Free Emulsions and Fine Teflon Dispersions. *The Journal of Physical Chemistry B* **107**, 1714-1720 (2003).

[2] Beattie, J.K. & Djerdjev, A.M. The Pristine Oil/Water Interface: Surfactant-Free Hydroxide-Charged Emulsions. *Angewandte Chemie International Edition* **43**, 3568-3571 (2004).

[3] Maeda, N., Rosenberg, K.J., Israelachvili, J.N. & Pashley, R.M. Further Studies on the Effect of Degassing on the Dispersion and Stability of Surfactant-Free Emulsions. *Langmuir* **20**, 3129-3137 (2004).

[4] Snoswell, D.R.E., Duan, J., Fornasiero, D. & Ralston, J. Colloid Stability and the Influence of Dissolved Gas. *The Journal of Physical Chemistry B* **107**, 2986-2994 (2003).

[5] Meyer, E.E., Lin, Q. & Israelachvili, J.N. Effects of Dissolved Gas on the Hydrophobic Attraction between Surfactant-Coated Surfaces. *Langmuir* **21**, 256-259 (2005).

[6] Pashley, R.M., Rzechowicz, M., Pashley, L.R. & Francis, M.J. De-Gassed Water Is a Better Cleaning Agent. *The Journal of Physical Chemistry B* **109**, 1231-1238 (2005).

[7] Dai, Z., Fornasiero, D. & Ralston, J. Influence of dissolved gas on bubble–particle heterocoagulation. *Faraday Trans.* **94**, 1983-1987 (1998).

[8] Mahnke, J., Stearnes, J., Hayes, R.A., Fornasiero, D. & Ralston, J. The influence of dissolved gas on the interactions between surfaces of different hydrophobicity in aqueous media Part I. Measurement of interaction forces. *Phys. Chem. Chem. Phys.* **1**, 2793-2798 (1999).

[9] Ishida, N., Inoue, T., Miyahara, M. & Higashitani, K. Nano Bubbles on a Hydrophobic Surface in Water Observed by Tapping-Mode Atomic Force Microscopy. *Langmuir* **16**, 6377-6380 (2000).

[10] Tyrrell, J.W.G. & Attard, P. Images of Nanobubbles on Hydrophobic Surfaces and Their Interactions. *Phys. Rev. Lett.* **87**, 176104 (2001).

[11] Yang, J., Duan, J., Fornasiero, D. & Ralston, J. Very Small Bubble Formation at the Solid−Water Interface. *The Journal of Physical Chemistry B* **107**, 6139-6147 (2003).

[12] Zhang, X.H., Quinn, A. & Ducker, W.A. Nanobubbles at the Interface between Water and a Hydrophobic Solid. *Langmuir* **24**, 4756-4764 (2008).

[13] Lou, S.-T. et al. Nanobubbles on solid surface imaged by atomic force microscopy. *J. Vac. Sci. Technol. B* **18**, 2573 (2000).

[14] Attard, P. Bridging Bubbles between Hydrophobic Surfaces. *Langmuir* **12**, 1693-1695 (1996).

[15] Newton Harvey, E.; Barnes, D. K.; McElroy, W. D.; Whiteley, A. H.; Pease, D. C.Removal of Gas Nuclei from Liquids and Surfaces *J. Am. Chem. Soc*. **67**, 156– 157 (1945).

[16] Steitz, R. et al. Nanobubbles and Their Precursor Layer at the Interface of Water Against a Hydrophobic Substrate. *Langmuir* **19**, 2409-2418 (2003).

[17] Mezger, M. et al. Water and ice in contact with octadecyl-trichlorosilane functionalized surfaces: A high resolution x-ray reflectivity study. *J. Chem. Phys.* **128**, 244705 (2008).

[18] Doshi, D.A., Watkins, E.B., Israelachvili, J.N. & Majewski, J. Reduced water density at hydrophobic surfaces: Effect of dissolved gases. *Proceedings of the National Academy of Sciences of the United States of America* **102**, 9458 -9462 (2005).

[19] Mezger, M. et al. On the Origin of the Hydrophobic Water Gap: An X-ray Reflectivity and MD Simulation Study. *Journal of the American Chemical Society* **132**, 6735-6741 (2010).

[20] Jensen, T.R. et al. Water in Contact with Extended Hydrophobic Surfaces: Direct Evidence of Weak Dewetting. *Phys. Rev. Lett.* **90**, 086101 (2003).

[21] Poynor, A. et al. How Water Meets a Hydrophobic Surface. *Phys. Rev. Lett.* **97**, 266101 (2006).

[22] Mao, M., Zhang, J., Yoon, R.-H. & Ducker, W.A. Is There a Thin Film of Air at the Interface between Water and Smooth Hydrophobic Solids? *Langmuir* **20**, 1843-1849 (2004).

[23] Seo, Y.-S. & Satija, S. No Intrinsic Depletion Layer on a Polystyrene Thin Film at a Water Interface. *Langmuir* **22**, 7113-7116 (2006).

[24] Kuna, J.J. et al. The effect of nanometre-scale structure on interfacial energy. *Nat Mater* **8**, 837-842 (2009).

[25] Chandler, D. Physical chemistry: Oil on troubled waters. *Nature* **445**, 831-832 (2007).

[26] Al Akhrass, S., Ostaci, R.-V., Grohens, Y., Drockenmuller, E. & Reiter, G. Influence of Progressive Cross-Linking on Dewetting of Polystyrene Thin Films. *Langmuir* **24**, 1884-1890 (2008).

[27] Nanoscope Command Reference Manual for Software Version 5.12 (Digital Instruments/Veeco Metrology Group, Inc., 2001).

[28] Attard, P., Moody, M.P. & Tyrrell, J.W.G. Nanobubbles: the big picture. *Physica A: Statistical Mechanics and its Applications* **314**, 696-705 (2002).

[29] Parker, J.L., Claesson, P.M. & Attard, P. Bubbles, cavities, and the long-ranged attraction between hydrophobic surfaces. *The Journal of Physical Chemistry* **98**, 8468-8480 (1994).

[30] Pashley, R.M. Effect of Degassing on the Formation and Stability of Surfactant-Free Emulsions and Fine Teflon Dispersions. *The Journal of Physical Chemistry B* **107**, 1714-1720 (2003).

[31] Thomas, O.C., Cavicchi, R.E. & Tarlov, M.J. Effect of Surface Wettability on Fast Transient Microboiling Behavior. *Langmuir* **19**, 6168-6177 (2003).
[32] Stöckelhuber, K.W., Radoev, B., Wenger, A. & Schulzet, H.J. Rupture of wetting films caused by nanobubbles. *Langmuir* **20**, 164-168 (2004).
[33] Lauga, E. & Brenner, M.P. Dynamic mechanisms for apparent slip on hydrophobic surfaces. *Phys. Rev. E* **70**, 026311 (2004).
[34] Zhu, Y. & Granick, S. Rate-Dependent Slip of Newtonian Liquid at Smooth Surfaces. *Phys. Rev. Lett.* **87**, 096105 (2001).
[35] Wang, Y. & Bhushan, B. Boundary slip and nanobubble study in micro/nanofluidics using atomic force microscopy. *Soft Matter* **6**, 29 (2010).
[36] Wang, Y., Bhushan, B. & Zhao, X. Improved Nanobubble Immobility Induced by Surface Structures on Hydrophobic Surfaces. *Langmuir* **25**, 9328-9336 (2009).
[37] Wang, Y., Bhushan, B. & Zhao, X. Nanoindents produced by nanobubbles on ultrathin polystyrene films in water. *Nanotechnology* **20**, 045301 (2009).
[38]Siretanu, I.; Chapel, J.-P.; Drummond, C.; Procédé de Formation d'un Motif sur une Surface d'un Support. French patent application PCT/FR2011/000139.
[39] Occhiello, E., Morra, M., Cinquina, P. & Garbassi, F. Hydrophobic recovery of oxygen-plasma-treated polystyrene. *Polymer* **33**, 3007-3015 (1992).
[40] Zimmermann, R., Freudenberg, U., Schweiß, R., Küttner, D. & Werner, C. Hydroxide and hydronium ion adsorption -- A survey. *Current Opinion in Colloid & Interface Science* **15**, 196-202 (2010).
[41] Grahame, D.C. The Electrical Double Layer and the Theory of Electrocapillarity. *Chemical Reviews* **41**, 441-501 (1947).
[42] Israelachvili, J. Intermolecular and Surface Forces. *Academic Press, London* (1992)
[43] Torres, J.M., Stafford, C.M. & Vogt, B.D. Manipulation of the Elastic Modulus of Polymers at the Nanoscale: Influence of UV−Ozone Cross-Linking and Plasticizer. *ACS Nano* **4**, 5357-5365 (2010).
[44] Rouse, J.H., Twaddle, P.L. & Ferguson, G.S. Frustrated Reconstruction at the Surface of a Glassy Polymer. *Macromolecules* **32**, 1665-1671 (1999).
[45] Fakhraai, Z. & Forrest, J.A. Measuring the Surface Dynamics of Glassy Polymers. *Science* **319**, 600 -604 (2008).
[46]Lupascu, V., Picken, S.J. & Wübbenhorst, M. Cooperative and non-cooperative dynamics in ultra-thin films of polystyrene studied by dielectric spectroscopy and capacitive dilatometry. Journal of Non-Crystalline Solids 352, 5594-5600 (2006).
[47] Arndt, M., Stannarius, R., Groothues, H., Hempel, E. & Kremer, F. Length Scale of Cooperativity in the Dynamic Glass Transition. *Phys. Rev. Lett.* **79**, 2077 (1997).
[48] Ellison, C.J. & Torkelson, J.M. The distribution of glass-transition temperatures in nanoscopically confined glass formers. Nat Mater 2, 695-700 (2003).
[49] Keddie, J.L., Jones, R.A.L. & Cory, R.A. Size-Dependent Depression of the Glass Transition Temperature in Polymer Films. *Europhys. Lett.* **27**, 59-64 (1994).
[50] Fakhraai, Z. & Forrest, J.A. Probing Slow Dynamics in Supported Thin Polymer Films. *Phys. Rev. Lett.* **95**, 025701 (2005).
[51] Huwe, A., Kremer, F., Behrens, P. & Schwieger, W. Molecular Dynamics in Confining Space: From the Single Molecule to the Liquid State. *Phys. Rev. Lett.* **82**, 2338 (1999).
[52] Schönhals, A., Goering, H., Schick, C., Frick, B. & Zorn, R. Polymers in nanoconfinement: What can be learned from relaxation and scattering experiments? *Journal of Non-Crystalline Solids* **351**, 2668-2677 (2005).
[53] Sharp, J.S. & Forrest, J.A. Free Surfaces Cause Reductions in the Glass Transition Temperature of Thin Polystyrene Films. *Phys. Rev. Lett.* **91**, 235701 (2003).
[54] Fukao, K., Uno, S., Miyamoto, Y., Hoshino, A. & Miyaji, H. Dynamics of alpha and beta processes in thin polymer films: Poly(vinyl acetate) and poly(methyl methacrylate). *Phys. Rev. E* **64**, 051807 (2001).
[55] Reiter, G. & de Gennes, P.G. Spin-cast, thin, glassy polymer films: Highly metastable forms of matter. *The European Physical Journal E* **6**, 25-28 (2001).
[56] Reiter, G. et al. Residual stresses in thin polymer films cause rupture and dominate early stages of dewetting. *Nat Mater* **4**, 754-758 (2005).
[57] Damman, P. et al. Relaxation of Residual Stress and Reentanglement of Polymers in Spin-Coated Films. *Phys. Rev. Lett.* **99**, 036101 (2007).
[58] Hutchinson, J.M. Physical aging of polymers. *Progress in Polymer Science* **20**, 703-760 (1995).
[59] Strum, L.C.E. Physical aging in plastics and other glassy materials. *Polymer Engineering & Science* **17**, 165-173 (1977).
[60] Strum, L.C.E. Physical aging in plastics and other glassy materials. *Polymer Engineering & Science* **17**, 165-173 (1977).

[61] Carruthers, J.C. The electrophoresis of certain hydrocarbons and their simple derivatives as a function of p H. *Trans. Faraday Soc.* **34**, 300 (1938).
[62] Dickinson, W. The effect of p H upon the electrophoretic mobility of emulsions of certain hydrocarbons and aliphatic halides. *Trans. Faraday Soc.* **37**, 140 (1941).
[63] Gray-Weale, A. & Beattie, J.K. An explanation for the charge on water's surface. *Phys. Chem. Chem. Phys.* **11**, 10994 (2009).
[64] Zangi, R. & Engberts, J.B.F.N. Physisorption of Hydroxide Ions from Aqueous Solution to a Hydrophobic Surface. *Journal of the American Chemical Society* **127**, 2272-2276 (2005).
[65] Liu, H., Steigerwald, M.L. & Nuckolls, C. Electrical Double Layer Catalyzed Wet-Etching of Silicon Dioxide. *Journal of the American Chemical Society* **131**, 17034-17035 (2009).
[66] Ang, P.K., Chen, W., Wee, A.T.S. & Loh, K.P. Solution-Gated Epitaxial Graphene as pH Sensor. *Journal of the American Chemical Society* **130**, 14392-14393 (2008).
[67] Noah-Vanhoucke, J. & Geissler, P.L. On the fluctuations that drive small ions toward, and away from, interfaces between polar liquids and their vapors. *Proceedings of the National Academy of Sciences* **106**, 15125 -15130 (2009).
[68] Kudin, K.N. & Car, R. Why Are Water−Hydrophobic Interfaces Charged? *Journal of the American Chemical Society* **130**, 3915-3919 (2008).
[69] Jungwirth, P. & Tobias, D.J. Molecular Structure of Salt Solutions: A New View of the Interface with Implications for Heterogeneous Atmospheric Chemistry. *The Journal of Physical Chemistry B* **105**, 10468-10472 (2001).
[70] Seemann, R., Herminghaus, S. & Jacobs, K. Dewetting Patterns and Molecular Forces: A Reconciliation. *Phys. Rev. Lett.* **86**, 5534 (2001).
[71] Landau, L. D.; Pitaevskii, L. P.; Lifshitz, E. M. Electrodynamics of Continuous Media; Pergamon: New York; 1960.
[72]The discontinuity in the normal component of the electric field and dielectric constant at the interface are at the origin of a nonzero normal component of the Maxwell tensor.
[73] Killat, U. Revised dynamical theory of thermoplastic deformation. *J. Appl. Phys.* **46**, 5169 (1975).
[74] Kunz, W., Henle, J. & Ninham, B.W. Zur Lehre von der Wirkung der Salze' (about the science of the effect of salts): Franz Hofmeister's historical papers. *Current Opinion in Colloid & Interface Science* **9**, 19-37 (2004).
[75] Horinek, D. & Netz, R.R. Specific Ion Adsorption at Hydrophobic Solid Surfaces. *Phys. Rev. Lett.* **99**, 226104 (2007)
[76] Onsager, L. & Samaras, N.N.T. The Surface Tension of Debye-Hückel Electrolytes. *J. Chem. Phys.* **2**, 528 (1934).
[77] Jarvis, N.L. & Scheiman, M.A. Surface potentials of aqueous electrolyte solutions. *The Journal of Physical Chemistry* **72**, 74-78 (1968).
[78] Karraker, K.A. & Radke, C.J. Disjoining pressures, zeta potentials and surface tensions of aqueous non-ionic surfactant/electrolyte solutions: theory and comparison to experiment. *Advances in Colloid and Interface Science* **96**, 231-264 (2002).
[79] Ciunel, K., Armélin, M., Findenegg, G.H. & von Klitzing, R. Evidence of Surface Charge at the Air/Water Interface from Thin-Film Studies on Polyelectrolyte-Coated Substrates. *Langmuir* **21**, 4790-4793 (2005).
[80] Schweiss, R., Welzel, P.B., Werner, C. & Knoll, W. Dissociation of Surface Functional Groups and Preferential Adsorption of Ions on Self-Assembled Monolayers Assessed by Streaming Potential and Streaming Current Measurements. *Langmuir* **17**, 4304-4311 (2001).
[81] Wang, Y., Bhushan, B. & Zhao, X. Improved Nanobubble Immobility Induced by Surface Structures on Hydrophobic Surfaces. *Langmuir* **25**, 9328-9336 (2009).
[82] Harrison, C. et al. Mechanisms of Ordering in Striped Patterns. *Science* **290**, 1558 -1560 (2000).

Chapter V

Water-ions induced nanostructuration of polymer films: Effect of substrate interaction, film thickness and polymer molecular weight

Table of contents for Chapter V:

5.1. Introduction

Great effort has been devoted to the study of ultrathin (<100nm) polymer films due to their increasing technology importance in sensors, dielectric layers, lubricants and bio-compatible materials. Ultrathin polymer films supported on substrates [1,2,3,4,5,6,7,8,9,10,11,12,13,14,15] or non-supported [1,2] have been studied by a variety of methods, which includes dielectric spectroscopy [3,4,5], X-ray reflectivity [6,7], fluorescence spectroscopy [8,9], positron lifetime spectroscopy [10], Brillouin scattering [11,12], optical waveguide spectroscopy [13], differential scanning calorimetry (DSC) [14] and ellipsometry [15,16,17]. These studies have revealed that many physical proprieties of polymer films such as the glass transition temperature [7,5,15,16,17], dielectric relaxation [3,4,18,19,20] differ from those in bulk samples. Understanding why thin films differ from bulk will help to understand the dynamics in confined glass forming systems, and will lay sound basis for the research of new materials and the development of nano-structures and devices. Despite of the fact that a lot of effort has been devoted to this research area, still many questions remain unanswered.

5.2. Thickness dependence of glass transition in thin polymer films

The pioneering work in this area was the study of thin polystyrene films by Keddie et al. [21]. They found that in films thinner than 40nm T_g was significantly reduced below the bulk value, as is shown in Figure I.13 (Chapter I). One possible reason for to this observation was the argument [6] that in polymer films thinner than the natural size of polymer molecules in bulk samples, the conformation and dynamics of polymer molecules will be different from those of the molecules in bulk samples. However, chain confinement effects do not seem to be responsible for the T_g observed: the thickness dependence of T_g was found to be the same within error for the different molecular weights studied. Keddie et al. proposed that, since the surface-to-volume ratios of those film samples are 6 orders of magnitude larger than that of the bulk samples, the cooperative molecular motion in ultrathin PS films was significantly affected by the free surface and the interface between the polymer films and the silicon substrates. They postulated a sandwich model to describe the ultrathin polystyrene films supported on the silicon wafers. As illustrated in Figure V.1-a, the sample is composed of three layers: the top, the middle and the bottom layers. The top layer has enhanced molecule mobility. The reason is the molecules on the surface have less neighbor molecules surrounding them, which makes the segmental motion easier. On the contrary, the bottom layer may have less molecular mobility because of the solid silicon wall.

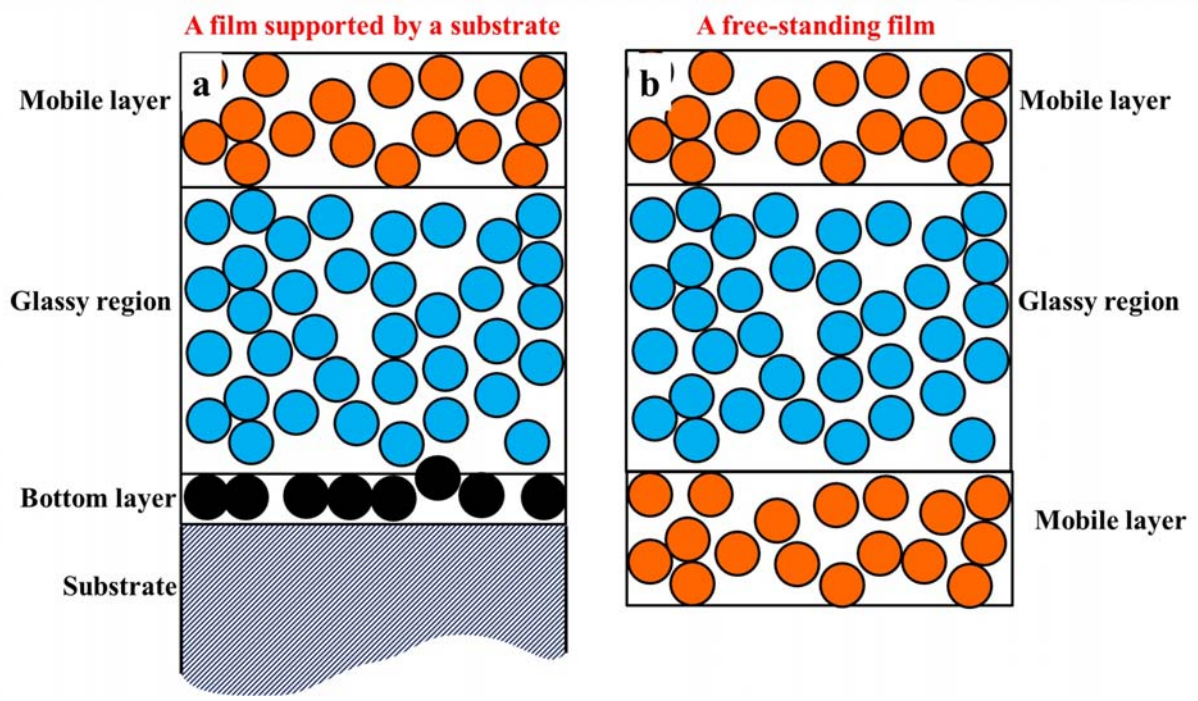

Figure V.1: (a) Sandwich model of an ultrathin polystyrene film supported by a silicon wafer. (b) No supporting substrate exists in a free-standing film, the existence of mobile layer on each surface has been proposed.

Indirect proof of the existence of a mobile surface layer and that the interfacial effects play a key role for the observed dynamics deviations, comes from experiments done on "free-standing" PS films [1,2,11,9,22,23,24,25,26,27]. In this configuration there is no supporting substrate, and it has twice the surface-to-volume ratios of simple supported films, as illustrated in Figure V.1-b. It was observed that T_g reduction in a thin supported film of thickness h is the same as in a free-standing film whose thickness is $2h$. As was discussed in Chapter I, experiments on free-standing PS films [28,2,11] reveal no molecular weight dependence of T_g reduction when $M_w < 514K$ (Figure I.14).

Most research efforts have been conducted in two model polymers, polystyrene (PS) and poly (methyl methacrylate) (PMMA). For thin PS films, studies show that when the film thickness is less than ~60nm the measured T_g values decrease with decreasing film thickness and there is no or very weak substrate dependence [29]. On the contrary for thin PMMA films a strong substrate dependence of T_g is observed, and both positive and negative T_g shifts have been reported depending on the nature of PMMA/substrate interactions. A generally accepted explanation for the observed T_g deviations is based on the air/polymer or substrate/polymer interfacial properties. In cases where there is a strong attractive substrate-polymer interaction which can inhibit molecular motions in the neighboring regions, the substrate/polymer interfacial effects may overwhelm the air/polymer effects and accordingly an increase of T_g may be observed [30,31,32,33,34,35,36,37]. However, how and to what extent the interfacial effects can propagate in thin polymers is still unknown. To study how far the interfacial properties can affect the dynamics of thin polymer films, one should study the T_g

distribution within polymer films as suggest by de Gennes [38]. Probably due to absence of suitable techniques, only one study [9] has been conducted as of today. In that work, Torkelson and coworkers used a fluorescence technique to investigate the polymer mobility spatial distribution, by measuring T_g of dye-labeled PS layers (~14 nm) located in different regions in thin PS films. The authors observed a length scale of ~36 nm over which the vacuum/polymer interfacial properties can affect the polymer dynamics. In addition, when the film is thiner than ~25 nm it seems the polymer dynamics is homogeneous.

In this chapter, we describe our studies of interfacial dynamics of thin polymer films using a novel technique. By measuring surface bumps formation in films in contact with degased water solution of acidic pH as a function of film thickness, the polymer surface dynamics can be measured directly and the length scale over which the substrate/polymer interface affect it can be investigated. We studied isotactic polystyrene films because it is a well studied model polymer and the measured T_g. We measured the near free surface dynamics of thin PS films on four different substrates to determine the range across which the substrate/polymer properties propagate, and different polymer molecular weights (M_w).

5.3. Experimental section

Polystyrene (PS) of four different molecular weights (7, 160, 250 and 500 kDa) were investigated. PS of 500 kg/mol (Tg 103°C) and 59 kg/mol (Tg 102°C) were obtained from Sigma-Aldrich. PS of 250 kg/mol (Tg 103°C) was obtained from ACROS Organics. PS of 7 kg/mol (Tg 90°C) synthesized by by ATRP, was a gracious gift from Dr. Antoine Bousquet.

5.3.1. Film preparation

We prepared films of PS of different molecular weights on four different substrates by spin coating, as described in Chapter II. To make polymer films of different thicknesses solution concentrations ranging from 0.5 wt% to 10 wt% were used. In order to change the polymer/substrate properties, we make PS films on four kinds of substrates. One type of substrate were hydrophilic surfaces of freshly cleaved molecularly smooth mica. The second set of substrates were single side and thoroughly cleaned oxide-coated silicon wafers. We then modified surfaces of the same materials with an adhesion primer layer in order to modify the interaction of the polymer with the substrate. Mica surfaces were coated with a monolayer of 10 nm diameter ceria nanoparticles by dip-coating (see Chapter II, figure II.6). A close-packed monolayer of ceria nanoparticles adsorbez on mica by this procedure, which strongly increases the adhesion between the subsequently deposited polymer layer and the substrate [39]. SiO_2 coated silicon wafers were hydrophobized by coating samples with self assembled monolayers or Langmuir-Blodgett of Octadecyltrichlorosilane (OTS). Figure V.2 shows the schematic anchoring reaction of octadecyl-trichlorosilane (OTS) on OH-terminated surfaces. The OTS

molecules, diluted in chloroform, get hydrolyzed under dissociation of HCl by trace amounts of water present in the deposition solution. These hydrolyzed molecules are adsorbed via hydrogen bonds to the OH-terminated native silicon oxide. In the last step, the silane molecules are covalently bonded to the substrate by water condensation. For a detailed recipe for the OTS-SAM preparation see Sec. 2.2.3.2 Chapter II.

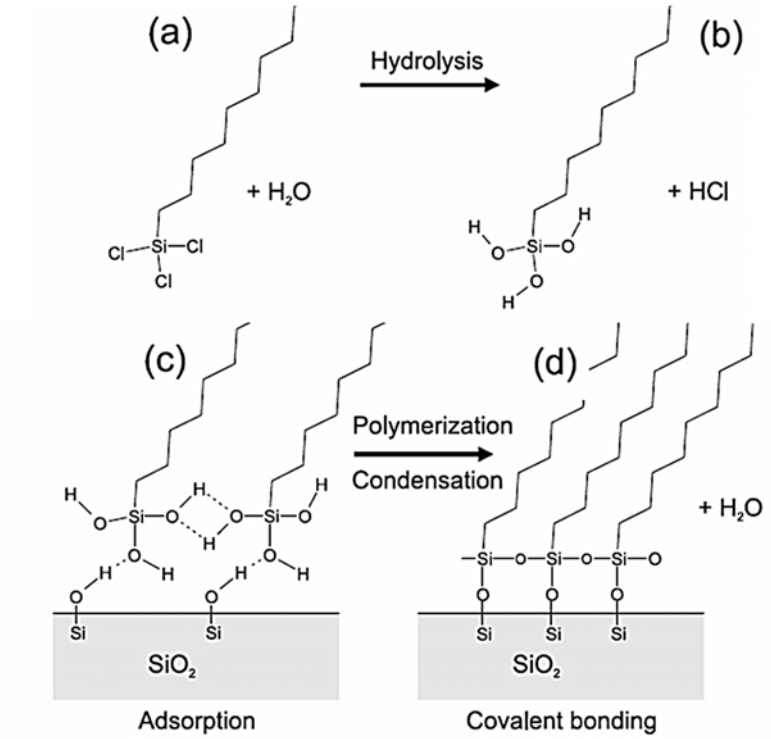

Figure V.2: Anchoring reaction of the octadecyl-trichlorosilane SAM. The OTS molecule (a) is hydrolyzed by trace amounts of water in the deposition solution (b). After adsorption at the SiO_2 substrate (c) the OTS molecules are covalently bound by H_2O condensation (d).

In the SAM method octadecyltrichlorosilane molecules distribute uniformly on the silicon wafer; on the contrary its grafting density can be tuned at different degrees using Langmuir-Blodgett coating technique [40] by varying the imposed surface pressure while film transfer. The grafting density is calculated by the following equation: $\gamma_1 P + \gamma_2(1 - P) = \gamma_3$, where γ_1 is the surface tension of octadecyltrichlorosilane; γ_2 and γ_3 are the surface energies of the silicon wafer and the silanized Si wafer, respectively and P is the grafting density. Contact angles of water on the grafted and bare solid substrates were measured by drop shape analysis at room temperature. These were used to calculate the surface energies of the solid substrates. Figure V.3 and Table V.1 shows AFM measurement and proprieties of silicon wafer before and after OTS coating at different grafting densities and consequently different degree of hydrophobicity. The roughness of the coated samples has also been measured by AFM for 1×1 μm^2 areas.

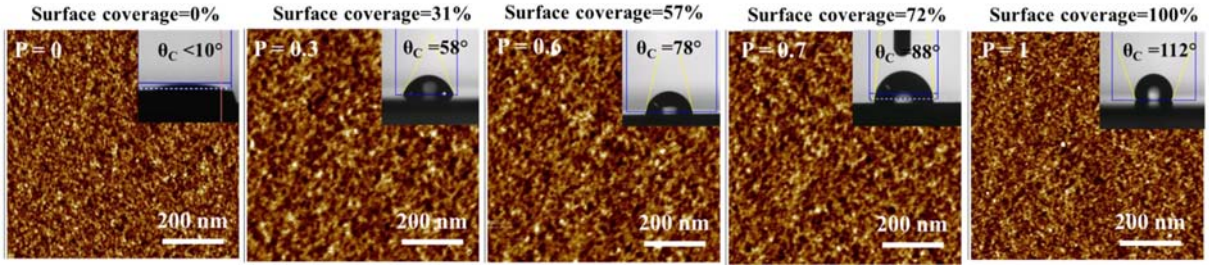

Figure V.3: AFM micrographs of SiO_2 coated with OTS at different grafting densities

Table V.1. Advancing contact angle, receding contact angle and roughness at different densities of SiO_2 coated for OTS.

Sample	θ_{adv}	θ_{rec}	$\Delta\theta$	RMS roughness[nm]	Grafting density (P)
Plane Si (native oxide)	<10°	<10°	-	0.20	0
OTS	58°	39°	19°	0.21	0.3
OTS	78°	68°	10°	0.21	0.6
SAM-OTS	88°	81°	7°	0.21	0.7
OTS	112°	108°	4°	0.20	1

The films were subsequently exposed to degassed double distilled water at pH 1.5 (with HNO_3) at room temperature, and dried with a gentle flow of N_2 gas. The generated structures were examined by tapping mode AFM (Veeco Icon and Multimode) and characterized by the average size and height of the observed self-assembled polymer bumps.

5.3.2. Film characterization

The thickness of the films was determined by ellipsometry (Nanofilm); roughness and morphology were assessed by Atomic Force Microscopy in tapping mode (multimode and Icon, Veeco). The films were also characterized by water contact angle (IDC Concept). Extremely smooth films of thickness 300nm, with a R.M.S. roughness smaller than 0.5 nm were typically obtained. The contact angle of water on the films was around 90° with very small hysteresis.

5.3.4. Water degassing and film treatment

Millipore water with a conductivity of 18 MΩ cm^{-1} was used for the solution preparation. The pH of the aqueous phase was adjusted by adding small amounts of nitric acid (Aldrich) as necessary. Carefully cleaned Teflon bar stirrers were introduced in the solutions to be degassed to induce the nucleation of gas bubbles. The solutions were subjected to agitation under a pressure of 0.2 mbar during two hours. The appearance of macroscopic bubbles in the aqueous phase was observed only during the first 30 minutes of degassing. After degassing is finished, the air pressure on the flask was

gently increased back to atmospheric pressure. The degassed solutions were put right away in contact with the polymer surfaces for few minutes after stopping the pumping, unless otherwise indicated. The PS films were then dried with a gentle flow of nitrogen gas (see Chapter II and IV for more details).

5.4. Surface bumps formation as a function of film thicknesses, substrate materials and molecular weights

As mentioned in Chapter IV, the exposure of the PS films to degassed acid water during few minutes provokes the formation of bumps several nm tall and several tens of nm wide. We studied how this process depended on film thicknesses, substrate materials and polymer molecular weight. Figure V.4 shows the combined results for measurements of surface pattern formation as a function of film thickness and type of substrate used. Selected AFM micrographs we show in Figure V.5.

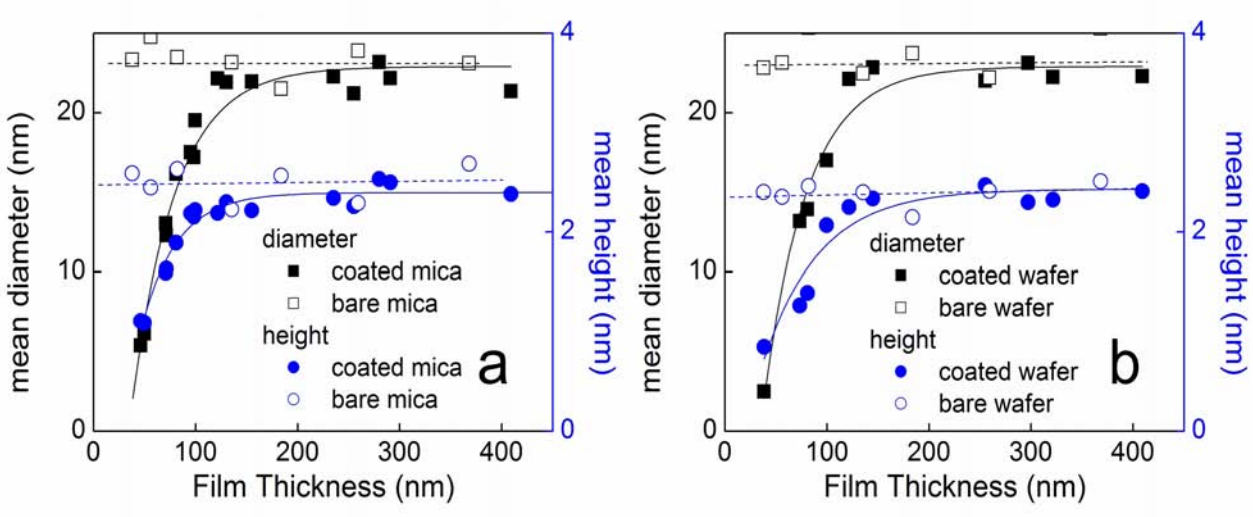

Figure V.4: Average height (circles) and diameter (squares) of self-assembled bumps observed on the surface of thin polymer films of PS 250 kDa of different thickness treated with degassed water at pH 1.5. The films were deposited on (a) bare and ceria-coated mica, and (b) silicon wafers and silanized silicon wafers (fractional surface coverage 0.7). Closed symbols: coated substrates; open symbols: bare substrates.

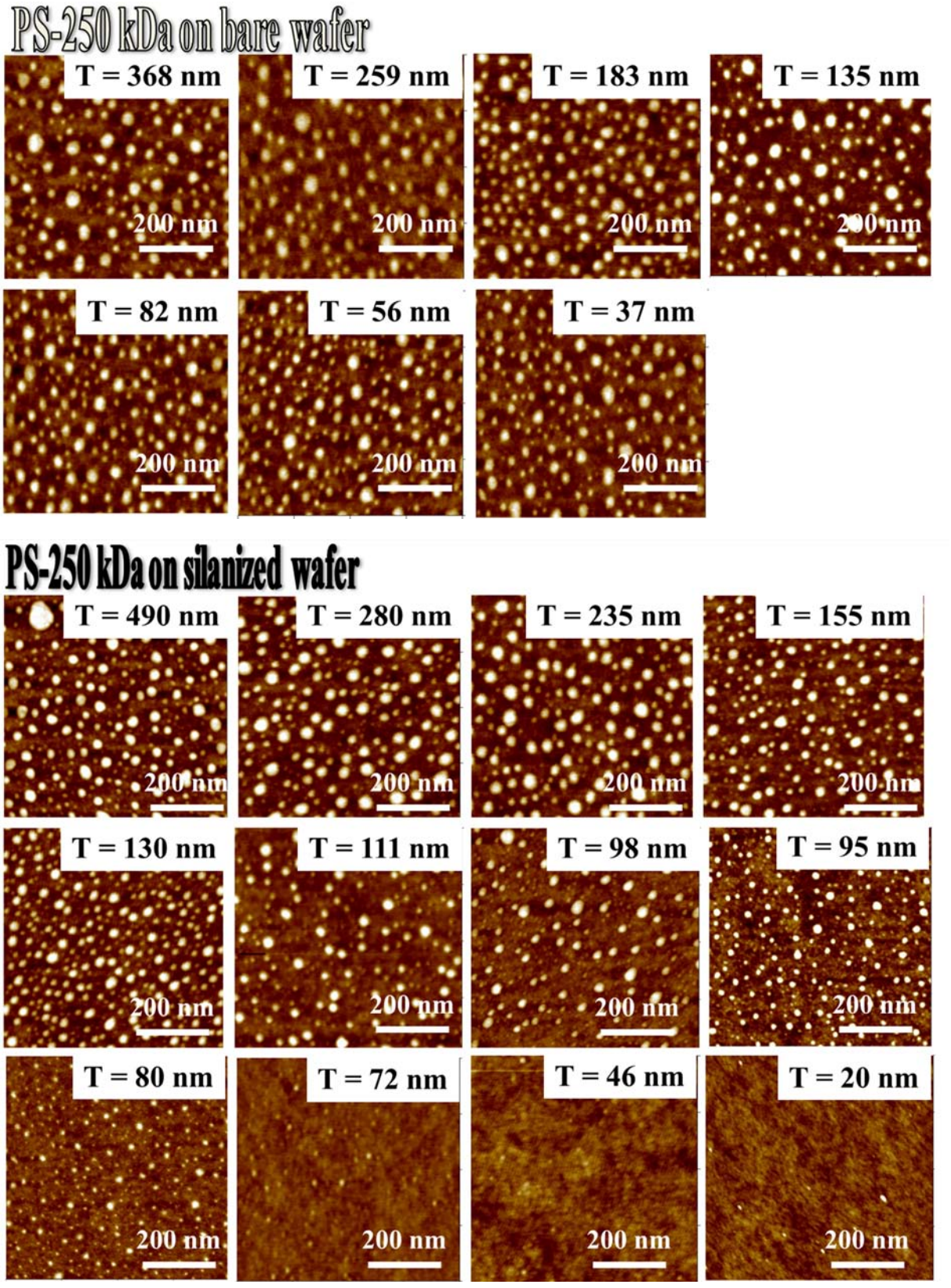
PS-250 kDa on bare wafer
T = 368 nm
T = 259 nm
T = 183 nm
T = 135 nm
T = 82 nm
T = 56 nm
T = 37 nm
PS-250 kDa on silanized wafer
T = 490 nm
T = 280 nm
T = 235 nm
T = 155 nm
T = 130 nm
T = 111 nm
T = 98 nm
T = 95 nm
T = 80 nm
T = 72 nm
T = 46 nm
T = 20 nm
200 nm

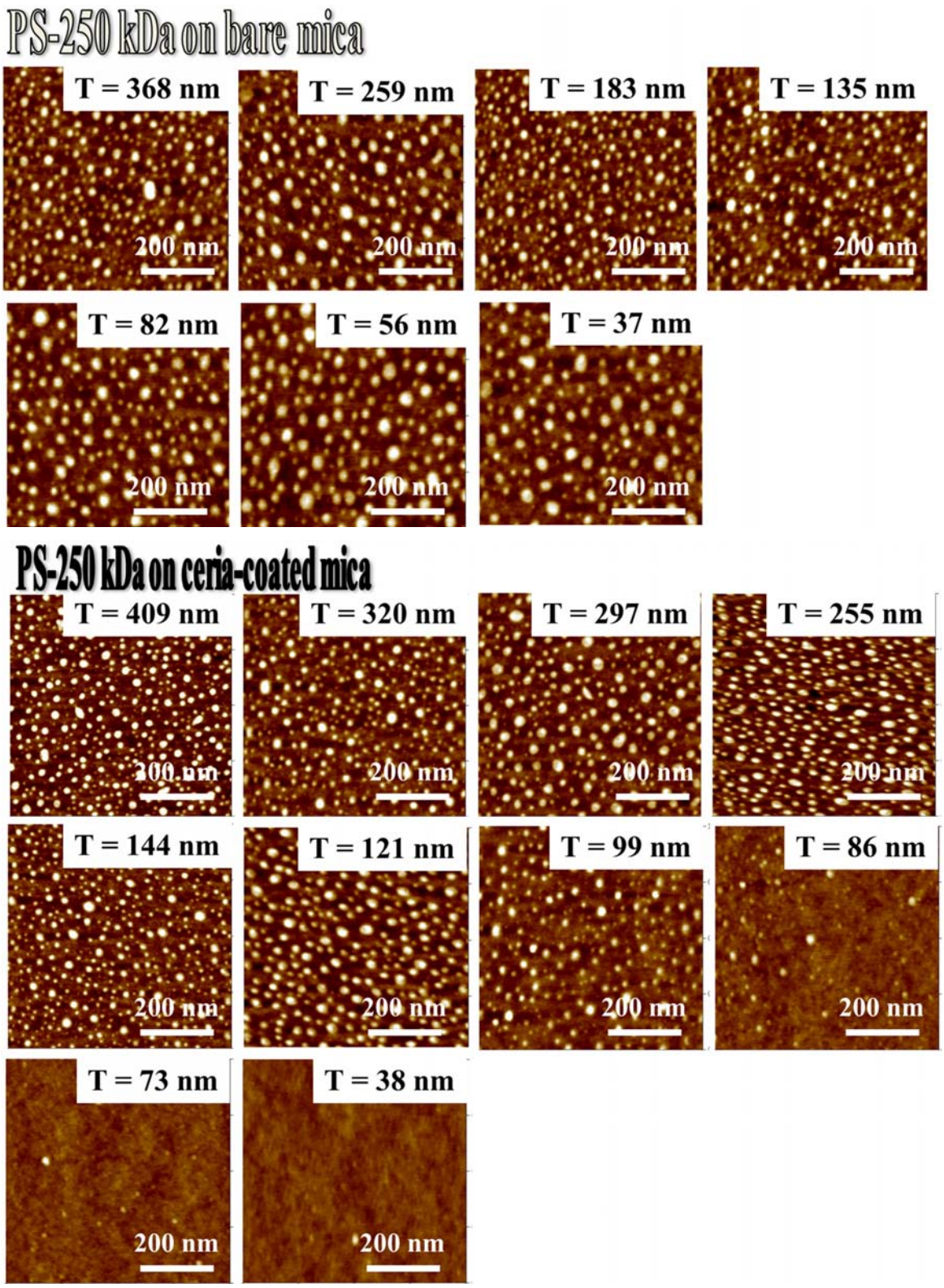

Figure V.5: Height AFM micrographs of films of 250 kDa polystyrene films measured in tapping mode in air. The films of indicated thickness were spun coated on bare and silanized silicon wafers, bare mica and ceria coated mica, and then exposed to a degassed solution of nitric acid in double distilled water at pH 1.5 at room temperature. The presence of asperities of regular nanometric size is clearly observed on some of the films exposed to the degassed solution during 5 minutes. On the contrary, no modification was detected when identical films were exposed to the same solution under identical conditions (or much longer times) before removing the dissolved gases. All the films were featureless before treatment.

From Figure V.4 and Figure V.5, we can observe that there is a clear difference for the PS surface structuration on different substrates: For native silicon and mica supported films, the typical radii and heights of the observed bumps are similar, and are independent of polymer film thickness down to 10 nm. On the contrary, the characteristic size of the structure is substantially reduced —or structuration is not present— for films spun on ceria-coated mica or hydrophobized wafers for polymer films thinner than a certain thickness. The same effect is in general observed after longer times of exposure to degassed water. Because there is a strong polymer/substrate interaction for the case of mica coted ceria, the substrate dependence is very strong compared with the case of bare mica where the polymer/substrate interaction is weak [39]. This bumps formation at temperature where polymer should be glassy suggests very different dynamics between surface properties and whole film.

Observations represented in Figure V.4 and Figure V.5 show that the rheological properties of the first few nm of the PS surface are affected by the substrate, even when it is over 100 nm away from the free surface, and the bulk of the film is in principle completely glassy. It is still an open question how the interfacial effects propagate into or affect the whole polymer film dynamics.

As mentioned above, the idea that polymer segments close to the surface are more mobile that bulk segments is now broadly accepted, although the properties of the mobile layer (thickness, variation with temperature and molecular weight) are still debated. On the contrary, it is not obvious why this excess mobility should be impaired by the influence of the underlying substrate buried down several tens of nanometers below the polymer film surface. This effect can be compared with the reported substrate influence on relaxation time and T_g for i-PMMA [5]. This study showed that, for 20 nm films, the measured T_g value for i-PMMA on a Si substrate is 10–40 K greater than the bulk value, while the surface relaxation time increases by a factor of 3.

Other study of PMMA films on Al interface [41], showed that the substrate dependence of surface relaxation times persists for film thickness of order of ~180 nm.

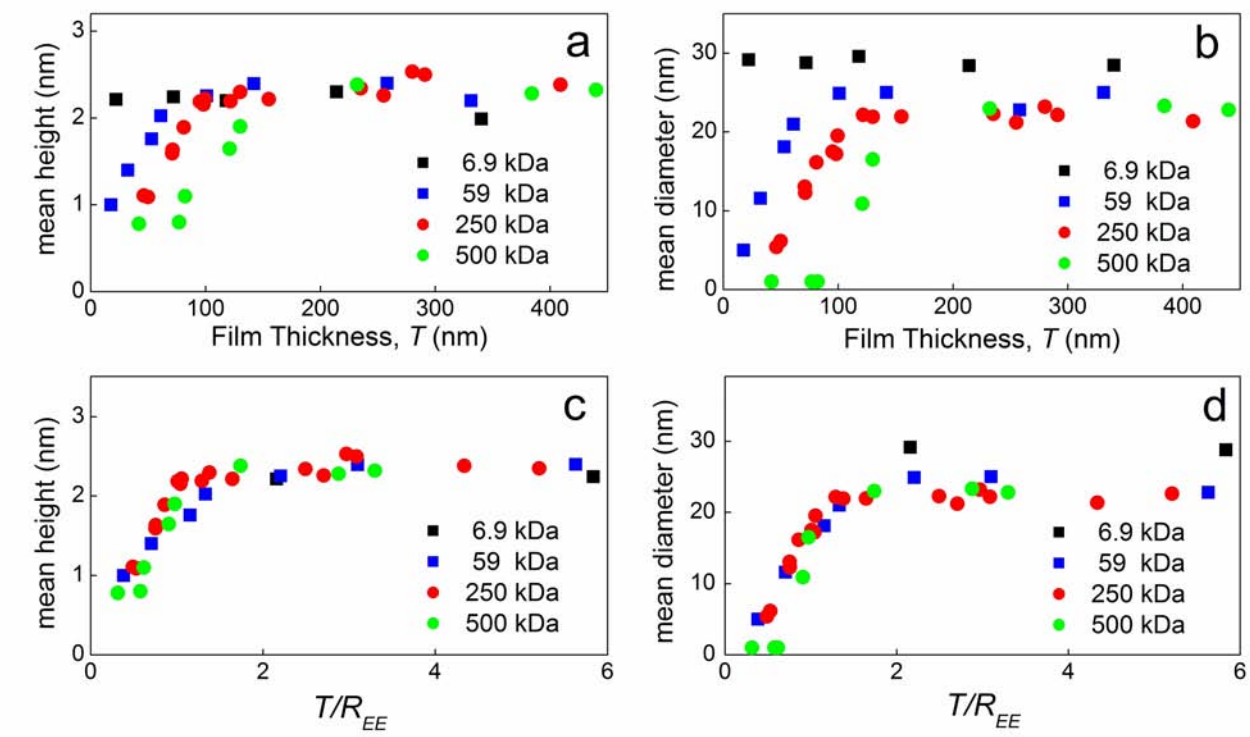

Figure V.6: Effect of polymer molecular weight on the self-assembled structure. Average height (a) and diameter (b) of self-assembled bumps of thin polymer films deposited on silanized silicon wafers (fractional surface coverage 0.7) treated with degassed water at pH 1.5. The results for the different polymer sizes collapse on a single curve if the film thickness is normalized by the polymer end-to-end distance, R_{EE} (c and d)

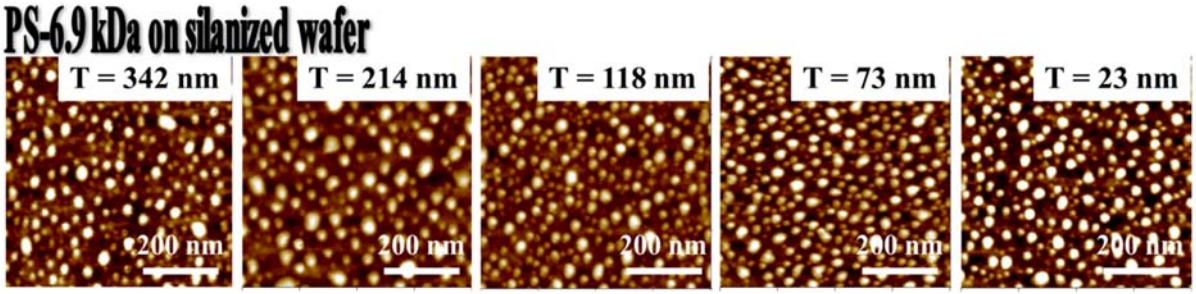

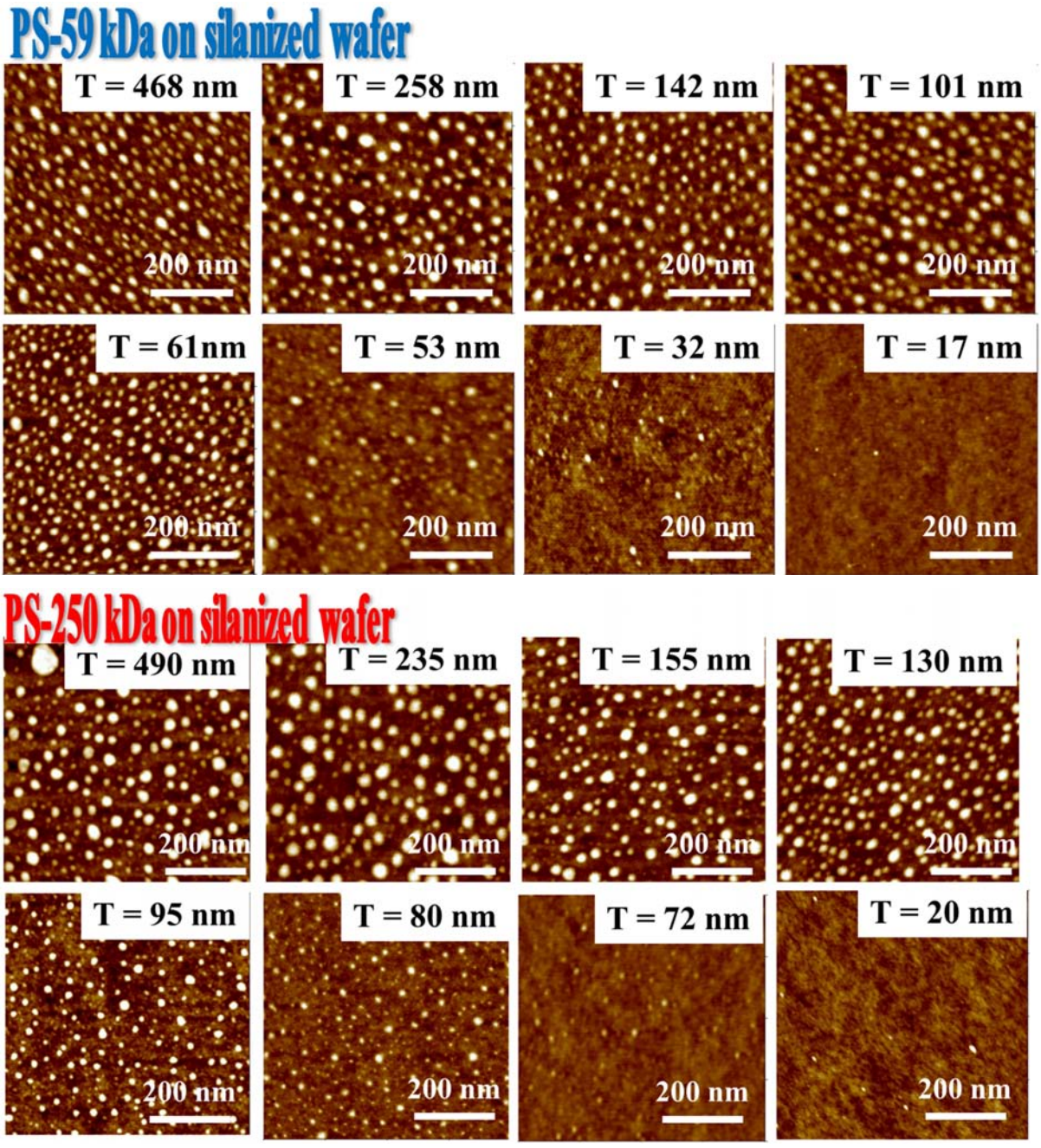
PS-59 kDa on silanized wafer
T = 468 nm
T = 258 nm
T = 142 nm
T = 101 nm
T = 61nm
T = 53 nm
T = 32 nm
T = 17 nm
PS-250 kDa on silanized wafer
T = 490 nm
T = 235 nm
T = 155 nm
T = 130 nm
T = 95 nm
T = 80 nm
T = 72 nm
T = 20 nm
200 nm

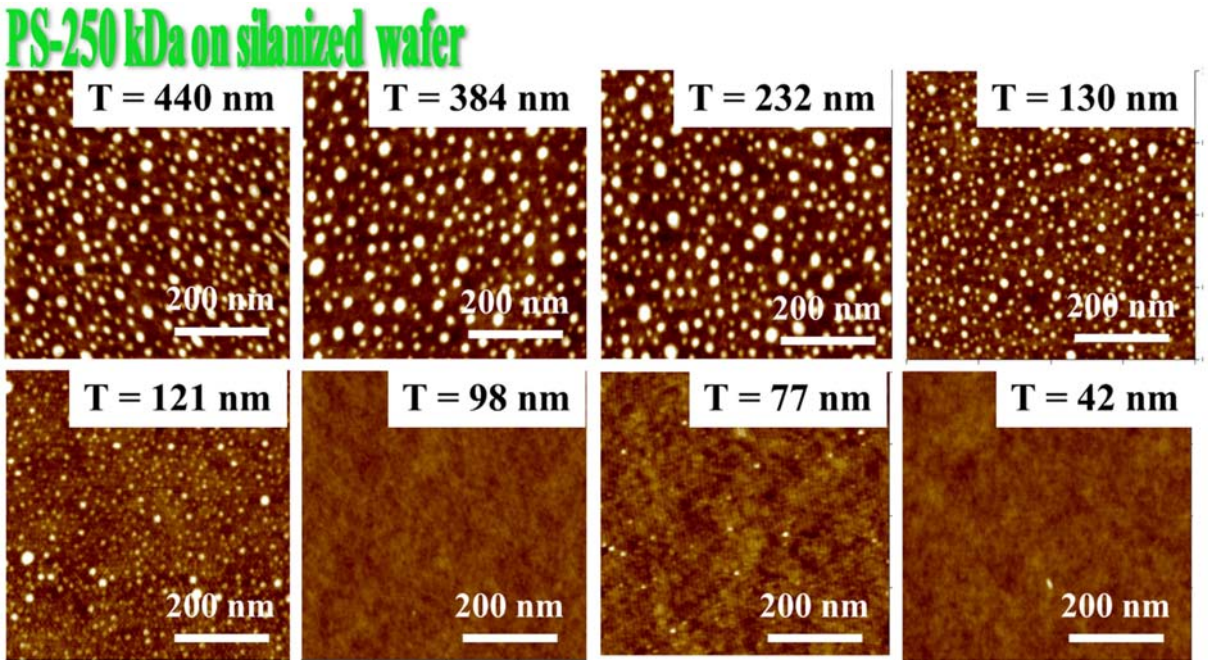

Figure V.7: Height AFM micrographs of indicated thickness films of 6.9, 59,250 and 500 kDa polystyrene films measured in tapping mode in air after exposure during 5 min to a degassed solution of nitric acid in double distilled water at pH 1.5 at room temperature. The presence of asperities of regular nanometric size is clearly observed to be dependent of polymer molecular weight.

It is noteworthy that above certain film thickness the size of the formed bumps seems to achieve a terminal value which is independent of PS molecular weight. On the contrary, the threshold thickness for surface structuration is determined by polymer size, as can be observed in Figure V.6 a-b and corresponding AFM micrographs from Figure V.7. The larger the molecular weight, the longer the range of the effect of the substrate on the structuration of the polymer layer. In all cases the observed effect has a range too large —up to 100 nm for the largest polymer investigated— to be interpreted in terms of the dispersion interaction between the solid substrate and water through the polymer film. The reason for the long-range effect of the substrate on the polymer structuration must be related to the connectivity of the polymer molecules. It is remarkable that by normalizing the film thickness by the mean-square end-to-end distance of the polymer, R_{EE}, the results for the different molecular weights tested collapse on a single master curve, as can be observed in Figure V.6 c-d. This collapse indicates that a mechanism related to the polymer size is responsible for the observed drop of polymer surface mobility.

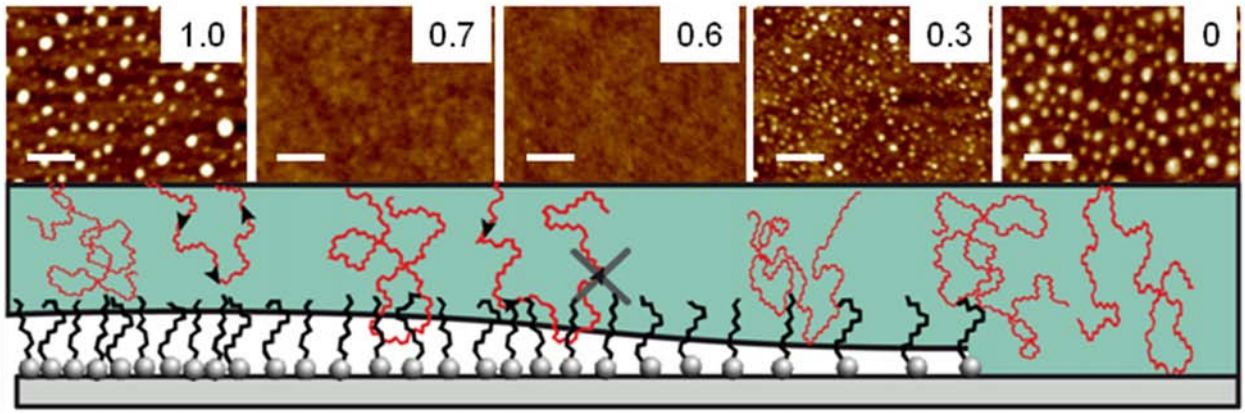

Figure V.8: Height tapping mode AFM micrographs measured in air of 50 nm thick 250 kDa polystyrene films after exposure to a degassed solution of nitric acid in double distilled water during 5 minutes. pH 1.5; T 25°C. The films were deposited on silanized silicon wafers with the surface coverage of OTS indicated on each micrograph. Scale bars correspond to 200 nm. The propagation of a kink (indicated by the black arrows) is slowed by the pinning effect of the OTS layer at intermediated grafting densities, stopping the structuration of the polymer surface.

By exploring different annealing conditions we observed that the effect of the two primer layers investigated is not completely equivalent, but rather process dependent. While ceria-coated mica suppressed the pattern formation in thin films regardless of the annealing process, silanized silicon wafers were effective structuration inhibitors only after annealing of the films. Otherwise, the modification of the supported film resembled the one observed for the case of bare silicon wafers. In addition, we observed that varying the grafting density of OTS on the Si wafer has a strong influence on the inhibitor effect of the primer silane layer, as can be observed in Figure V.8. Very high or very low silane grafting densities produced no effect on the structuration: in these cases the self-assembled structures where observed on polymer films down to 10 nm thick. On the contrary, intermediate grafting densities effectively diminished the surface structuration for thin polymer films, provided that the film has been annealed before treatment with degassed acid water. This effect can be used to remotely control the surface structuration. For example, using L-B, sample of silicon wafer was partially coated with OTS. After exposing to a degased water solution half of sample got structured and the other part, where OTS was grafted remained smooth can be observed in Figure V.9.

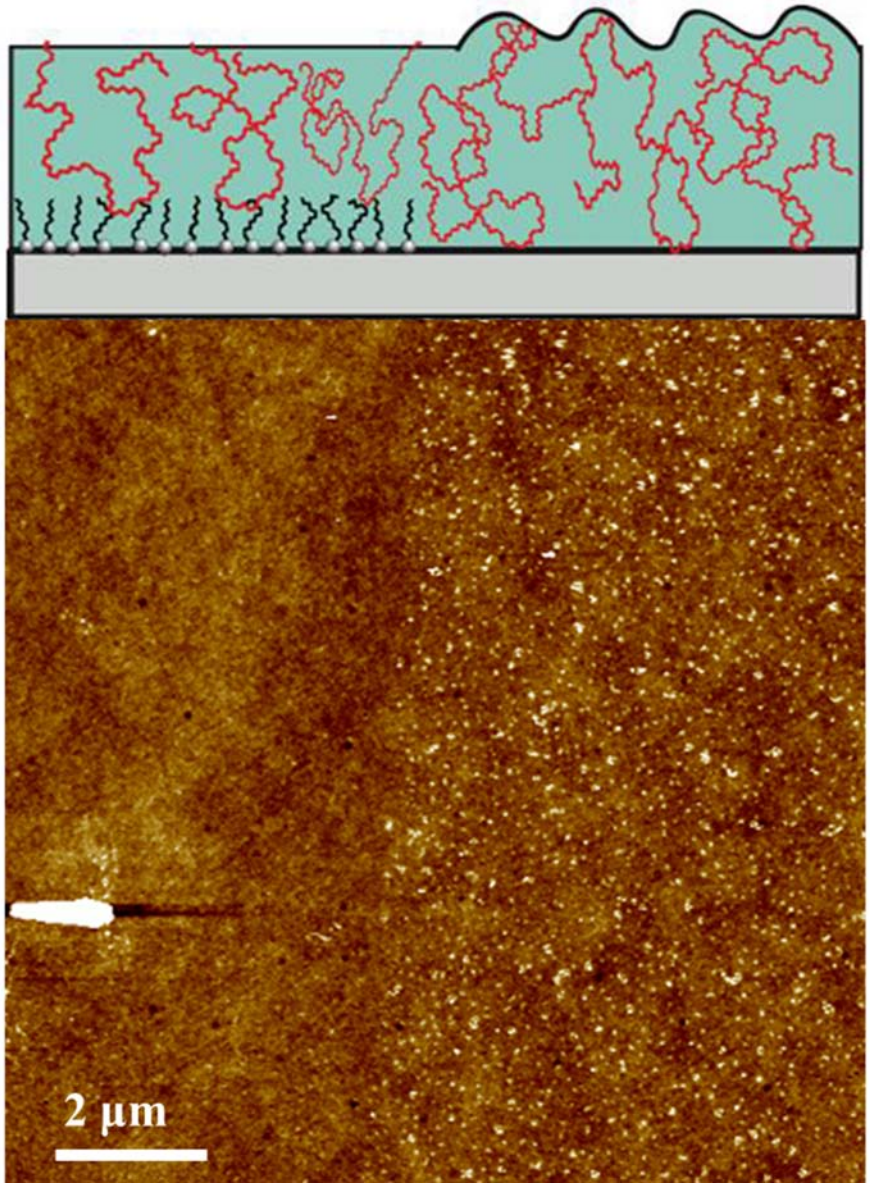

Figure V.9: Height tapping mode AFM micrograph measured in air of a 50 nm thick 250 kDa polystyrene film after exposure to a degassed solution of nitric acid in double distilled water during 5 minutes. pH 1.5; T 25°C. The film was deposited on a half silanized silicon wafer. Scale bar correspond to 10 µm. The presence of asperities of regular nanometric size is clearly observed on region of bare silicon wafer. On the contrary, no modification was detected in the region which previously was coated with OTS, and the morphology of film remains identical as before treatment.

The more puzzling question emerging from the results described above is how the effect of the solid substrate can extend over tens of nanometer up to the polymer surface. We can rationalize our results, at least at a qualitative level, with the help of the sliding mechanism sketched by de Gennes [38], formulated to explain the reduction of T_g in free-standing or supported polymer thin films. This model proposes that the reduced density at the polymer surface confers a greater mobility to the polymer segments: monomers at the polymer surface are less sterically constrained to move. de Gennes proposed that this enhanced free volume then propagates at a certain speed through the polymer chain to depths of the order of the size of the polymer molecules, effectively fluidizing the

polymer layer several nanometers inside the film. The free surface will then act as source and sink of "free volume". The idea behind the model is that the energy barrier for kink (free volume) transport is lower than for segmental motion; polymer loops that start and end at the free surface can then be effectively fluidized, with the chains moving along their own paths. This process is not to be mistaken with the reptation of entangled polymer chains in a melt, which is obviously not possible at temperatures below Tg [42]. This motion is not available for chains with only one "contact" with the free surface: sliding motion would imply entering into volume occupied by other chains. Milner and Lipson ML [43,44] have built on this idea to develop their "delayed glassification model", to quantitatively explain how the effect of a free surface can then fluidize a polymer layer, and have looked into the issue of how deep the influence of the free surface propagates into the sample in a reasonable experimental time scale. Following ML, we can label a certain loop (starting and ending at the surface) as "fast" when the time necessary to cover the distance between the source and the sink of free volume is shorter than a certain characteristic time. ML studied in detail the probability for a chain segment at a given depth in the film to be part of a fast loop, in order to quantify the plasticizing effect of the free surface. They obtained the following expression for the probability P(z) that a segment at a depth z belongs to a fast loop, $P(z) = \exp\left(-\sqrt{\frac{24z^2}{N_{eff}(T)}}\right)$, where N_{eff} is an effective length of the maximum allowed size of a fast loop, which takes into account the effects of finite size chains and temperature [43,44]. Here we are interested in the analogous problem of an otherwise fast loop being in contact or not with the supporting substrate. If the polymer-substrate interaction is sufficiently strong, the presence of the wall can slow down or stop the free volume propagation through the chain, effectively freezing a given loop. If this probability is negligible, the polymer chains at the free surface should not be affected by the presence of the wall. It is obvious than for polymer films substantially thicker than R_{EE}, the effect of the free surface will not be modified by the presence of the solid boundary. On the contrary, for films thinner than R_{EE} the presence of the boundary might affect the propagation of a kink along a polymer chain, as sketched in Figure V.8. The penetrating effect of the substrate will be less pronounced in samples of lower molecular weight. For the two substrate modification methods discussed in this letter (ceria-coated mica and silanized Si wafer) the friction coefficient for the monomers in contact with the modified surface is higher than with the bare substrate, slowing down the polymers movement near the substrate and reducing the structuration. The origin of the slow dynamic seems to be different for each case: for the ceria-coated mica it is due to the enhanced dispersion interaction between polymer chains and the ceria nanoparticles. On the contrary, for the silanized wafers the enhanced friction is probably due to the interpenetration between the polymer molecules and the silane layer, which is enhanced upon annealing and forbidden at very high OTS coverage. Even though these effects are short-ranged (a fraction of an nm) their influence propagates to the polymer surface due to the long-range effects of chain connectivity.

Although conceptually appealing, the sliding model of de Gennes in the ML formulation [43,44] predicts a probability of polymer segments belonging to a fast loop that decays very quickly with depth at room temperature. If that is true, polymer films thicker than few nanometers should not be sensitive to the presence of the solid boundary, which is clearly inconsistent with our results. At least two reasons can be evoked to rationalize the apparent discrepancy between experiments and theory. First, it is possible that the ML model overestimates the temperature decay of the length of the longest fast loop allowed, N_{eff}, which they model as a temperature dependence of the WLF form [45]. This implies $N^*(T) = N^* \exp\left(\frac{C(T-T_g)}{T-T_0}\right)$, with $N^*(T)$ the longest fast loop allowed at a temperature T for infinitely long chains, and T_0 the Vogel temperature. It is obvious that $N^*(T)$ depends strongly on the value of C; ML used the value reported for bulk PS above T_g for illustration purposes, which is certainly not suitable below the glass transition temperature. Indeed, it has been experimentally shown that the dynamic of near-surface polymer chains in glassy PS is substantially faster than the one predicted by extrapolation of liquid PS or the one measured in bulk glassy PS [16]. Results of the temporal evolution of deformed polymer surfaces represented in Chapter VI, entirely agree with this idea. Second, the cooling of the polymer films after annealing might have been carried out too quickly. A very long time may be necessary to reach thermodynamic equilibrium at room temperature, so the polymer chains might effectively be frozen in a configuration which would correspond to a higher temperature. It has been recently reported that the relaxation times of spin-coated polymer films, measured from dewetting experiments, strongly depends on the processing history of the sample [46,47]. It has also been reported that an extremely long time (of the order of weeks) may be necessary to reach final equilibrium in thin viscous polymer films, even at temperatures above T_g [48,49]. In any event, longer fast loops that the ones predicted in [43,44] would account for the behavior observed in this work.

5.5. Conclusion

In conclusion, we have used possibility of structuration of the surface of glassy PS films by contact with degassed water to probe the rheological properties of the near free surface region of PS with different film thicknesses, substrate materials, and M_w values. The results show an enhanced surface mobility compared to the bulk materials under all measurement conditions, but the actual process of formation of self-assembled nanostructure reveals a number of surprising features. This process can be affected by the presence of a solid boundary (up to film thickness of the order of R_{EE}) which may slow down or even prevent the polymer movement. The developing of bumps in the first few nanometer of the surface appears to be affected by the substrate. The substrate dependence of the surface relaxation time persists to a film thickness of ~100 nm. The threshold thickness for surface structuration is observed to be dependent on the M_w of PS.

5.6. References

[1] Forrest & Mattsson Reductions of the glass transition temperature in thin polymer films: probing the length scale of cooperative dynamics. *Phys Rev E Stat Phys Plasmas Fluids Relat Interdiscip Topics* **61**, R53-56 (2000).

[2] Forrest, J.A., Dalnoki-Veress, K., Stevens, J.R. & Dutcher, J.R. Effect of Free Surfaces on the Glass Transition Temperature of Thin Polymer Films. *Phys. Rev. Lett.* **77**, 2002 (1996).

[3] Fukao, K., Uno, S., Miyamoto, Y., Hoshino, A. & Miyaji, H. Dynamics of alpha and beta processes in thin polymer films: Poly(vinyl acetate) and poly(methyl methacrylate). *Phys. Rev. E* **64**, 051807 (2001).

[4] Fukao, K. & Miyamoto, Y. Glass transition temperature and dynamics of α-process in thin polymer films. *Europhys. Lett.* **46**, 649-654 (1999).

[5] Sharp, J.S. & Forrest, J.A. Dielectric and ellipsometric studies of the dynamics in thin films of isotactic poly(methylmethacrylate) with one free surface. *Phys. Rev. E* **67**, 031805 (2003).

[6] Reiter, G. Dewetting as a Probe of Polymer Mobility in Thin Films. *Macromolecules* **27**, 3046-3052 (1994).

[7] See, Y.-K., Cha, J., Chang, T. & Ree, M. Glass Transition Temperature of Poly(tert-butyl methacrylate) Langmuir−Blodgett Film and Spin-Coated Film by X-ray Reflectivity and Ellipsometry. *Langmuir* **16**, 2351-2355 (2000).

[8] Ellison, C.J., Kim, S.D., Hall, D.B. & Torkelson, J.M. Confinement and processing effects on glass transition temperature and physical aging in ultrathin polymer films: Novel fluorescence measurements. *The European Physical Journal E - Soft Matter* **8**, 155-166 (2002).

[9] Ellison, C.J. & Torkelson, J.M. The distribution of glass-transition temperatures in nanoscopically confined glass formers. *Nat Mater* **2**, 695-700 (2003).

[10] DeMaggio, G.B. et al. Interface and Surface Effects on the Glass Transition in Thin Polystyrene Films. *Phys. Rev. Lett.* **78**, 1524 (1997).

[11] Forrest, J.A., Dalnoki-Veress, K. & Dutcher, J.R. Interface and chain confinement effects on the glass transition temperature of thin polymer films. *Phys. Rev. E* **56**, 5705 (1997).

[12] Dalnoki-Veress, K., Forrest, J. & Dutcher, J. Mechanical confinement effects on the phase separation morphology of polymer blend thin films. *Phys. Rev. E* **57**, 5811-5817 (1998).

[13] Prucker, O. et al. On the glass transition in ultrathin polymer films of different molecular architecture. *Macromolecular Chemistry and Physics* **199**, 1435-1444 (1998).

[14] Efremov, M.Y., Olson, E.A., Zhang, M., Zhang, Z. & Allen, L.H. Glass Transition in Ultrathin Polymer Films: Calorimetric Study. *Phys. Rev. Lett.* **91**, 085703 (2003).

[15] Kawana, S. & Jones, R.A.L. Character of the glass transition in thin supported polymer films. *Phys. Rev. E* **63**, 021501 (2001).

[16] Fakhraai, Z. & Forrest, J.A. Probing Slow Dynamics in Supported Thin Polymer Films. *Phys. Rev. Lett.* **95**, 025701 (2005).

[17] Sharp, J.S., Teichroeb, J.H. & Forrest, J.A. The properties of free polymer surfaces and their influence on the glass transition temperature of thin polystyrene films. *Eur. Phys. J. E* **15**, 473-487 (2004).

[18] Fukao, K. Dynamics in thin polymer films by dielectric spectroscopy. *The European Physical Journal E - Soft Matter* **12**, 119-125 (2003).

[19] Hartmann, L., Gorbatschow, W., Hauwede, J. & Kremer, F. Molecular dynamics in thin films of isotactic poly(methyl methacrylate). *The European Physical Journal E - Soft Matter* **8**, 145-154 (2002).

[20] Serghei, A. et al. Molecular dynamics of hyperbranched polyesters in the confinement of thin films. *Eur. Phys. J. E* **17**, 199-202 (2005).

[21] Keddie, J.L., Jones, R.A.L. & Cory, R.A. Size-Dependent Depression of the Glass Transition Temperature in Polymer Films. *Europhys. Lett.* **27**, 59-64 (1994).

[22] Sharp, J.S. & Forrest, J.A. Free Surfaces Cause Reductions in the Glass Transition Temperature of Thin Polystyrene Films. *Phys. Rev. Lett.* **91**, 235701 (2003).

[23] Fakhraai, Z. & Forrest, J.A. Measuring the Surface Dynamics of Glassy Polymers. *Science* **319**, 600 -604 (2008).

[24] Papaléo, R.M. et al. Relaxation times of nanoscale deformations on the surface of a polymer thin film near and below the glass transition. *Phys. Rev. B* **74**, 094203 (2006).

[25] Gasemjit, P. & Johannsmann, D. Thickness of the soft layer on glassy polystyrene surfaces. *Journal of Polymer Science Part B: Polymer Physics* **44**, 3031-3036 (2006).

[26] Teichroeb, J.H. & Forrest, J.A. Direct imaging of nanoparticle embedding to probe viscoelasticity of polymer surfaces. *Phys. Rev. Lett* **91**, 016104 (2003).

[27] Peter, S., Meyer, H., Baschnagel, J. & Seemann, R. Slow dynamics and glass transition in simulated free-standing polymer films: a possible relation between global and local glass transition temperatures. *J. Phys.: Condens. Matter* **19**, 205119 (2007).

[28] Mattsson, J., Forrest, J. & Börjesson, L. Quantifying glass transition behavior in ultrathin free-standing polymer films. *Phys. Rev. E* **62**, 5187-5200 (2000).
[29] Forrest, J.A. & Dalnoki-Veress, K. The glass transition in thin polymer films. *Advances in Colloid and Interface Science* **94**, 167-195 (2001).
[30] Pham, J.Q. & Green, P.F. The glass transition of thin film polymer/polymer blends: Interfacial interactions and confinement. *J. Chem. Phys.* **116**, 5801 (2002).
[31] Grohens, Y., Brogly, M., Labbe, C., David, M.-O. & Schultz, J. Glass Transition of Stereoregular Poly(methyl methacrylate) at Interfaces. *Langmuir* **14**, 2929-2932 (1998).
[32] Fryer, D.S. et al. Dependence of the Glass Transition Temperature of Polymer Films on Interfacial Energy and Thickness. *Macromolecules* **34**, 5627-5634 (2001).
[33] Tsui, O.K.C., Russell, T.P. & Hawker, C.J. Effect of Interfacial Interactions on the Glass Transition of Polymer Thin Films. *Macromolecules* **34**, 5535-5539 (2001).
[34] Bernazzani, P. & Sanchez, R.F. Effect of substrate interactions on the melting behavior of thin polyethylene films. *The European Physical Journal E - Soft Matter* **26**, 8 (2008).
[35] Fryer, D.S., Nealey, P.F. & de Pablo, J.J. Thermal Probe Measurements of the Glass Transition Temperature for Ultrathin Polymer Films as a Function of Thickness. *Macromolecules* **33**, 6439-6447 (2000).
[36] van Zanten, J., Wallace, W. & Wu, W.-li Effect of strongly favorable substrate interactions on the thermal properties of ultrathin polymer films. *Phys. Rev. E* **53**, R2053-R2056 (1996).
[37] Torres, J.A., Nealey, P.F. & de Pablo, J.J. Molecular Simulation of Ultrathin Polymeric Films near the Glass Transition. *Phys. Rev. Lett.* **85**, 3221 (2000).
[38] Gennes, P.G. de Glass transitions in thin polymer films. *The European Physical Journal E* **2**, 5 (2000).
[39] Chapel, J.-P., Morvan, M., PCT Int. Appl. WO 2007126925 A2 20071108 (2007)
[40] Peterson, I.R. Langmuir-Blodgett films. *J. Phys. D: Appl. Phys.* **23**, 379-395 (1990).
[41] Konstadinidis, K. et al. Segment level chemistry and chain conformation in the reactive adsorption of poly(methyl methacrylate) on aluminum oxide surfaces. *Langmuir* **8**, 1307-1317 (1992)
[42] Gennes, P.G. de (Pierre-G. de) *Scaling concepts in polymer physics / Pierre-Gilles de Gennes*. (Cornell University Press: Ithaca, N.Y. :, 1979).
[43] Milner, S.T. & Lipson, J.E.G. Delayed Glassification Model for Free-Surface Suppression of Tg in Polymer Glasses. *Macromolecules* **43**, 9865-9873 (2010).
[44] Lipson, J.E.G. & Milner, S.T. Local and Average Glass Transitions in Polymer Thin Films. *Macromolecules* **43**, 9874-9880 (2010).
[45] Williams, M.L., Landel, R.F. & Ferry, J.D. The temperature dependence of relaxation mechanisms in amorphous polymers and other glass-forming liquids. *Journal of the American Chemical Society* **77**, 3701-3707 (1955)
[46] Raegen, A. et al. Aging of Thin Polymer Films Cast from a Near-Theta Solvent. *Phys. Rev. Lett.* **105**, 227801 (2010).
[47] Reiter, G. et al. Residual stresses in thin polymer films cause rupture and dominate early stages of dewetting. *Nat Mater* **4**, 754-758 (2005).
[48] Barbero, D.R. & Steiner, U. Nonequilibrium Polymer Rheology in Spin-Cast Films. *Phys. Rev. Lett.* **102**, 248303 (2009).
[49] Thomas, K.R., Chenneviere, A., Reiter, G. & Steiner, U. Nonequilibrium behavior of thin polymer films. *Phys. Rev. E* **83**, 021804 (2011).

Chapter VI

Free-surface dynamics of glassy polystyrene films: thermal effects on nanostructure relaxation

Table of contents for Chapter IV:

6.1. Introduction

In physical-chemistry studies, it is often assumed that solid surfaces are rigid and immobile. These assumptions allow one to investigate, for example, adsorption and wettability purely from the point of view of the liquid phase, because it is supposed that the solid substrate does not respond, reorient, or otherwise change in different liquid environments. Such hypothesis may be correct for very rigid solids, but it is not always appropriate for polymers. Polymer structures and properties are very often time, temperature and environment dependent. Solid polymers are, therefore, inherently nonequilibrium structures and, as such, exhibit a range of relaxation times and properties under normal conditions and in response to changing environments. Transition and relaxation phenomena in solids polymers are treated in practically all polymer science textbooks [1,2,3,4,5,6,7,8,9]. The thermal behavior of polymers and the knowledge of their thermal transitions is important in the selections of proper processing and fabrication conditions, the characterization of physical and mechanical properties of materials and hence the determination of appropriate end uses. This aspect is addressed in the present chapter: I explored in detail the dynamic of formation and relaxation of the water-induced nanostructuration process described in previous chapters.

6.1.1. Polymer Transitions and Relaxations

Polymer relaxation has been define by North [10] as "a time dependent return to equilibrium of the system which has recently experienced a change in the constraints acting upon it". If a polymer material is changed or perturbed, it will respond, i.e., relax, to achieve a new state which is closer to equilibrium in the new environment or situation.

Relaxation refers to a time dependent change. Often, this change depends on the time-scale of the observation. A good example of such time-dependent character is "silly putty", an uncrosslinked silicone material. If giving sufficient time it creeps and flows as a liquid, but if throwing it hard against a rigid surface you will observe a highly elastic material bouncing back.

One can also speak of transitions, which are temperature dependent changes [7]. For example, a crystalline material consisting of low-molecular weight molecules will generally exhibit a phase change from solid to liquid at a precise temperature. We will say that that the material has melted. Many thermodynamic properties, such as density and enthalpy, show a discontinuity when heated through their melting or boiling points. Glasses, on the other hand, show no such discontinuity. A window glass, depending on its composition, will go from a rigid, brittle material to a soft, viscous liquid on heating to the vicinity of 1000°C. Glassy or amorphous polymers do the precisely the same thing at lower temperatures; the solid-to-liquid transition occurs very gradually, going through an intermediate "rubbery" state without a discontinuous transformation. The transition from the hard glass into a softer, rubbery state occurs over a narrow temperature range referred to as the glass transition temperature. At higher temperatures they form viscous liquids. The transition that separates

the glassy state from the viscous state is known as the glass–rubber transition. For amorphous polymers the glass transition temperature, T_g, constitutes the most important mechanical property. In fact, upon synthesis of a new polymer, the glass transition temperature is among the first properties to be measured.

6.1.2. Relaxation time

On a molecular scale, when a polymer is at T = 0 K, the chains are at absolute rest. No thermal motions occur and everything is completely frozen in. When the temperature is increased the thermal motions increase and gradually short parts of the chain or side groups may obtain some mobility, which, within the restricted free volume, gives rise to small changes in conformation. Whether this occurs or not it is a matter of competition between the thermal energy of a group (k_BT) and its interaction with neighboring groups. The interaction can be expressed as a potential barrier or activation energy E_a which has to be overcome in order to realize a change in position. As the temperature increases, the fraction of groups able to overcome the potential barrier increases. The jump frequency ν with which the changes occur can be expressed by the Arrhenius equation $\nu = \nu_0 \exp(-E_a/k_BT)$, where υ_0 is the natural frequency of vibration about the equilibrium position and k_B is the Boltzmann constant. The jump frequency governs the time scale τ at which the transition occurs. τ is inversely proportional to υ:

$$\tau = \exp\left(E_a/k_BT\right) \Rightarrow \ln\tau = \ln A + \frac{E_a}{k_BT} \tag{6.1}$$

This equation provides a fundamental relationship between the effects of time and temperature on a transition mechanism. Time and temperature appear to be equivalent in their effect on the behavior of polymers.

As mentioned before amorphous polymers show one or more sub-T_g processes, which are referred to as β, γ, and δ transition as they appear in order of descending temperature. Figure VI.1 shows the influence of the sub-T_g relaxation processes on the damping coefficient (*tan* δ) as a function of temperature.

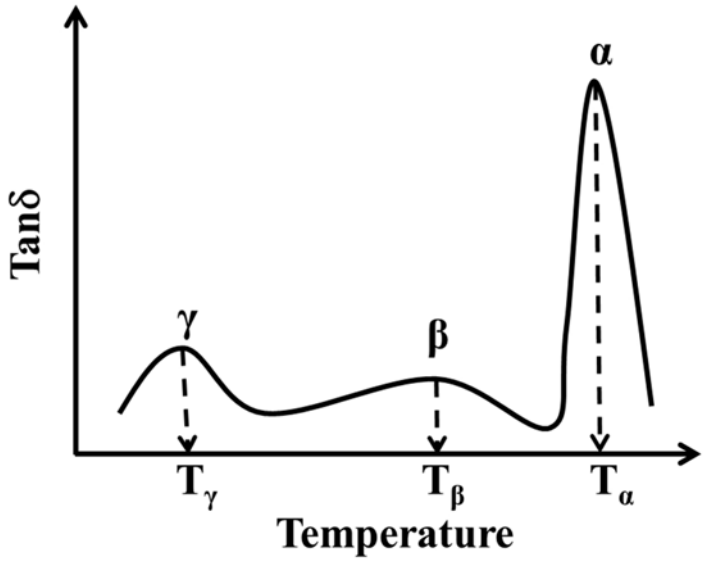

Figure VI.1: Typical *tan δ* of an amorphous polymer as a function of temperature showing the sub-T_g β and γ relaxations at T_β and T_γ below T_g. The magnitude of the mechanical damping at T_g is much larger when compared to the other sub-T_g transitions [7].

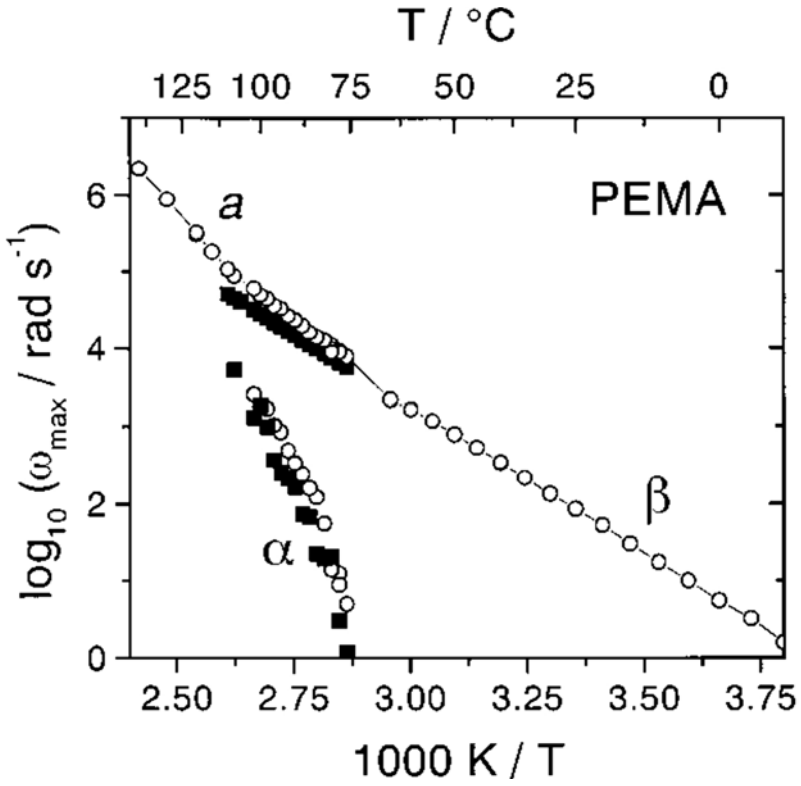

Figure VI.2: Frequency of the loss maxima, ω_{max} for α and β relaxations as a function of reciprocal temperature for PEMA. [11].

The dielectric relaxation of glass forming material well above its T_g time has an Arrhenius dependence to the temperature, and only one relaxation peak is seen in the system. As the temperature is decreased, most materials show two distinct relaxation processes [11]. The slow relaxation time is called α-relaxation and is believed to be from collective motion of particles. This relaxation time

increases rapidly near T_g, such that for every 3-5 degrees decrease in temperature the relaxation time increases approximately one decade. The fast relaxation process which remains at Arrhenius type is called β-relaxation, and is supposed to be due to local vibration of the molecules. The temperature at which the splitting between the two relaxation functions happens is known as the α-β splitting temperature $T_{\alpha\beta}$. Figure VI.2 shows an example of α-β splitting in a glass forming material. It can be observed that at high temperatures there is a single relaxation mechanism. In the moderately supercooled regime the peak splits into α (slow) and β (fast) relaxations. The α-processes exhibit non-Arrhenius temperature dependence and diverges at $T = T_0$. At temperatures below $T_{\alpha\beta}$, the response functions of the system, such as creep compliance and dielectric relaxations deviate from a single exponential relaxation to a behavior that can be roughly described by a stretched exponential function known as Kohlrausch-Williams-Watts (KWW) function.

$$\phi(t) = \exp\left[-(t/\tau)^{\beta}\right] \tag{6.2}$$

where $\beta < 1$. In this equation τ is a temperature-dependent characteristic relaxation time (α relaxation). For fragile glasses the β value is about 0.5. Generally, systems that show a larger deviation from Arrhenius relation also have lower β values and deviate more from a single relaxation behavior.

6.1.4. Bulk vs. surface dynamics

It has been almost fifteen years since the pioneering works on PS films showed a dramatic difference in dynamic properties of films vs. bulk material [12,13]. Since then, many experimental techniques and theoretical approaches have been applied to study the unique properties of polymers in bulk [14,15,16,17,18,19,20,21,22,23,24,25,26,27,28,29,30,31] and surfaces [32,33,34,35,36,37,38,39, 40,41,42,43,44,45,46,47,48]. It is generally accepted that the dynamics of polymers at the nanometer scale are in a plain contrast to those of bulk, as indirectly evidenced by the experimentally measured T_g and relaxation times. There is a continuous growing of evidence showing that interfacial effects play a key role for the observed differences [22,23,24,27,28,45,46,47,49,50,51,52,53,54] (there are also some measurements arguing against this interpretation [55,56]). Specifically, the polymer chain segment motions in the interfacial regions may be enhanced or inhibited compared with those in the bulk parts, based on the nature of air/substrate-polymer interactions, which substantially contributes to the average measured dynamical quantities. Based on this, Forrest et al. proposed a layered on-average dynamics heterogeneity model for thin polymer films [46], which can be used to describe most results of T_g measuring experiments. In ref. [31], Torkelson and Ellison found that the vacuum-polymer interfacial effects can propagate into thin polymer films as far as ~35 nm. In ref. [57] the surface mobile layer in glassy polystyrene films is experimentally observed to be on the order of 3 – 4 nm thick. In ref. [58], Herminghaus et al. observed a molten layer of thickness about 23 nm at a temperature around T_g for 100 nm polystyrene droplets and, in addition, the size of the molten layer increases with temperatures below T_g. The different experimental liquid layer sizes and its temperature

dependence near T_g raise new issues, such as whether the sizes measured by different techniques are comparable or what length scale is more adequate to describe the glass transition. Indeed, it is not known if or how the size of the interfacial region is related to the characteristic length scale involved in the glass transition. The unique nature of long chain structures of polymer molecules may complicate things even further. For example, polymer molecules can be of size of several tens of nanometers and chain confinement effects may contribute to the bulk-film difference. Another important aspect about polymer molecules is that dynamical properties on different length scale may be different, and special attention should be paid when comparing observations of measurements using different techniques.

AFM, nano surface hole/bumps relaxation or fluorescence are powerful techniques in the study of surface properties of thin polymer films, but these techniques are hard to be used to study depth dependence of dynamic properties thin polymer films, or how the size of the interfacial region changes with temperatures. Nano-gold sphere embedding overcomes this difficulty [57,59,60]. In [46], Fakhraai and Forrest observed a rather weak temperature dependence of relaxation of nano surface holes in glassy thin polystyrene films. In [47], molecular weight dependence of the near free surface dynamics was observed for thin i-PMMA films. Unfortunately, there have been some disputes about the interpretation of the embedding results [59,60,61,62,63].

In summary, the studies of the polymer dynamics in local nanometer confined regions are relatively new and require various experiments to confirm the temperature [46] and/or chain size dependence [47] in the near free surface regions of thin polymer films. More theoretical considerations for such dynamical features in nanometer scale confined polymer systems are also necessary. In additions, these studies may improve our understanding of the very nature of the glass transition, in particular by studying finite size effects. Given that polymers can be easily made into amorphous glassy states with varying sample geometries and sizes, if the size of the polymer samples approaches the glass transition characteristic length scale (on the nanometer scale) dynamical deviation may be observed.

In this chapter, I describe our studies of interfacial dynamics of polymer films using a novel technique. By measuring the nanometer scale surface bumps formation and relaxation as a function of time and temperature, properties (surface dynamics) and thickness of this mobile interfacial region were investigated. In addition, we study the dependence of pure near free surface dynamics (without the substrate influence) on polymer molecular weight (M_w).

6.2. Motivation for experiments

Taking together all the results and difficulties of the experimental techniques presented in Chapter I, one can imagine the conditions to be fulfilled by an ideal experiment probing surface polymer dynamics and relaxation:

(i) It should examine the surface directly in a way that is minimally affected by the bulk of the film.

(ii) It should not excessively perturb the surface. Any surface deformation should be as small as possible, without introducing excessive stress, external particles or probes. The driving force in relaxation experiments should be small enough so that observations correspond to a linear response.

(iii) The perturbation should be introduced at temperatures below bulk T_g, to avoid its fast relaxation.

(iv) Measurements should be carried out on a single length scale, if possible, of the order of few nanometers. There is some experimental evidence to suggest the mobile region [8, 19, 20] is of the order of 4 nm. At length scales larger than that this, structural relaxation may never be completed in a reasonable time.

(v) The surface dynamics should be measured over a wide temperature range, especially below bulk T_g.

As we presented in Chapter IV, the method of inducing nanostructuration of polymer film circumvent some of these constraints, allowing to produce ideally perturbed samples for surface relaxation studies. Nanostructuration of the surface takes place at room temperature without inducing particles or other probes. The structuration has a tunable nanometric scale, is well shaped, have a Gaussian size distribution over all surface sample at a length scale of the layer of enhanced mobility. We decided thus to investigate the thermal-relaxation process of nanostructured polystyrene surfaces. The comparison of our results, measured at different temperatures and M_w, with the results measured by other groups using different complementary techniques is presented at the end of the Chapter.

6.3. Experimental section

Samples: Polystyrene (PS) of four different molecular weights (7, 59, 250, and 500 kDa) were investigated. PS of 500 kDa and 59 kDa were obtained from Sigma-Aldrich. PS of 250 kDa was obtained from ACROS Organics. PS of 7 kDa synthesized by ATRP, was a gracious gift from Dr. Antoine Bousquet.

***T_g* measurements**: DSC measurements were performed on a Perkin Elmer Pyris DSC apparatus using a closed aluminum pan containing the polystyrene samples. Temperature and enthalpy calibrations were performed using an indium reference sample. The temperature was raised/decreased from 30°C to 130°C at 10°C/min. The glass transition temperature of the polymers, taken as the midpoint temperature determined in the second run, (Figure VI.3) are compiled in Table VI.1.

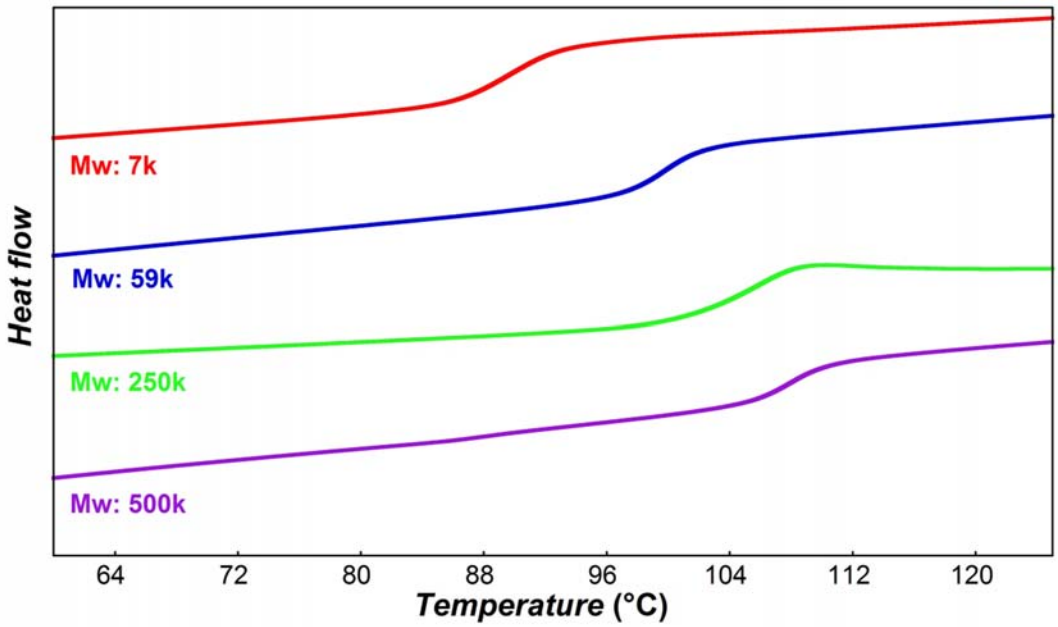

Figure VI.3: DSC traces for different PS samples

Table VI.1: Second run data from heat/cooling flow curves

PS molecular weight	T_g, °C (on heating)	T_g, °C (on cooling)
7k	91	89
59k	103	96
250k	107	101
500k	109	97

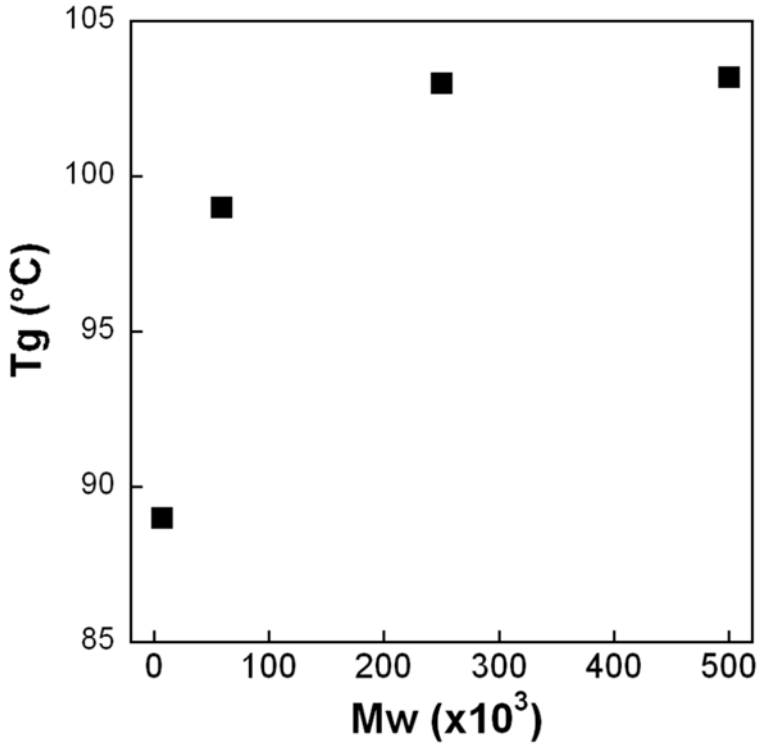

Figure VI.4: Dependence of glass transition temperature on molecular weight.

Film preparation: Thin PS films were prepared by spin-coating polystyrene solutions in toluene onto small ($1\times1cm^2$) pieces on silicon wafers or mica. As described in Chapter II, the PS film thickness is a function of spin-coating speed, solution concentration and polymer molecular weight. By adjusting these parameters, we prepared smooth PS films of thickness of ≈ 300 nm for all M_W's (*see Chapter II*). After spin-coating the PS films were annealed at 95°C for 12 h to remove the residual solvent and release any mechanical stress built up during the spin coating process. After this treatment, the samples were ready for investigations.

The thickness of the films was determined by ellipsometry (Nanofilm); roughness and morphology were assessed by atomic force microscopy in tapping mode (multimode and Icon, Veeco).

6.3.1. Studies of near-free-surface dynamics of glassy polystyrene films

6.3.1.1. Producing and imaging nanostructured PS surfaces

As we described in detail in Chapter III, the method to produce nanometer bumps on PS film consist in exposing flat hydrophobic polymer films to degassed acidic/basic aqueous solution. Figure VI.5 illustrates this technique. It can be observed from Figure VI.5-a and Figure VI.5-b that after exposing a smooth PS film to a degassed nitric acid aqueous solution of pH=1.5 nanobumps with a regular size appear on the surface of PS. Figure VI.5-c shows histograms of bumps diameter and height data from which we determined the number average bump size. The statistics performed on all bumps present on the surface revealed a narrow size/height distribution centered on 25 nm and 2.7 nm,

respectively. As mentioned in Chapter IV, we can tune the typical size of the bumps by controlling the pH of the degassed solution. High reproducibility can be reached by keeping constant the conditions of treatment. This will ensure that structuration present on the surface and average parameters of bumps are similar between different samples.

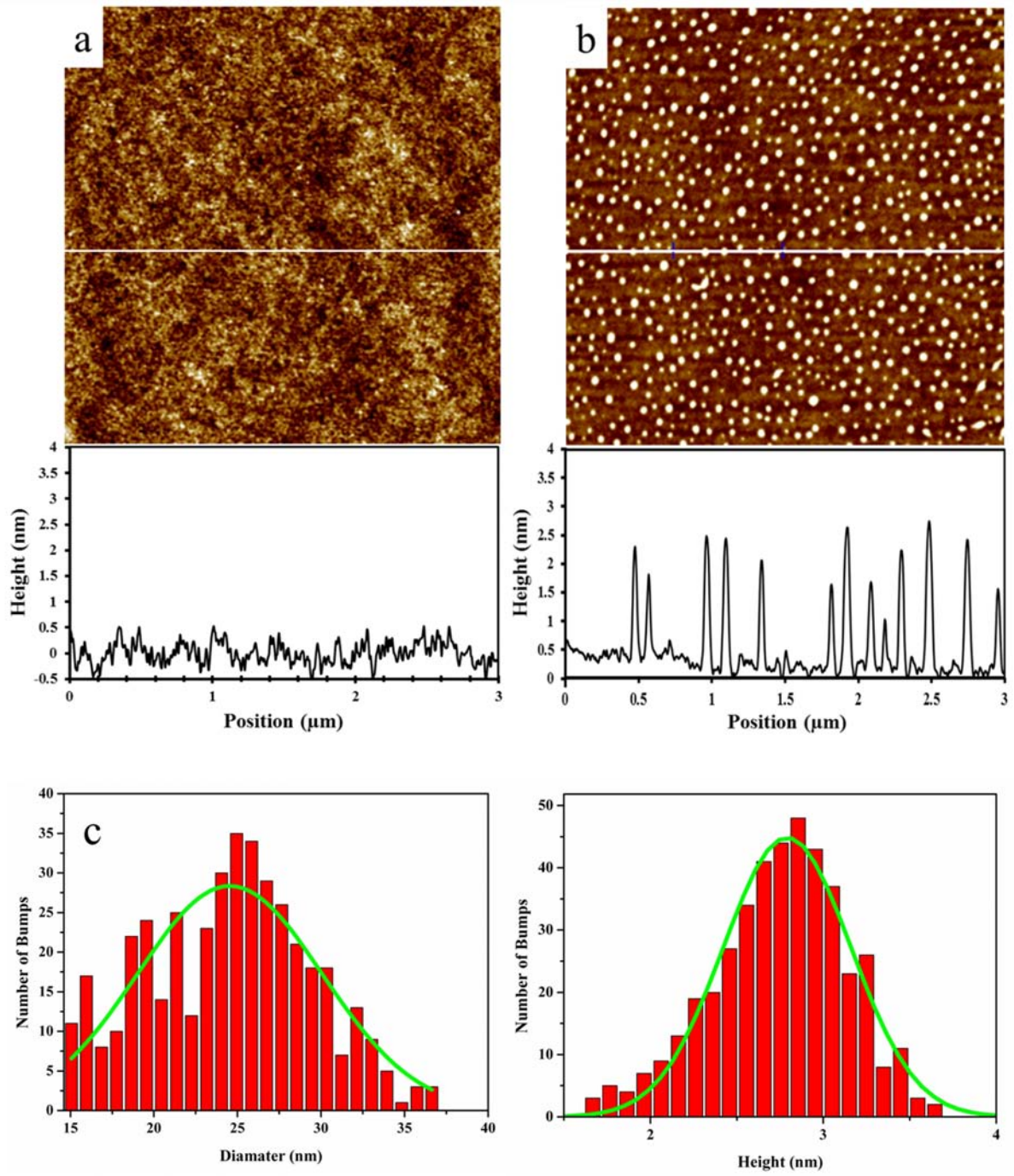

Figure VI.5: Illustration of the process used to create nano-bumps in the PS surface. (a) Taping mode height AFM micrograph (3µm× 3µm) taken in air of 300 nm thick, 250 kDa as prepared; (b) after exposure to a degased solution of nitric acid in double distilled water at pH=1.5 and room temperature. A typical height profile for each condition is presented. (c) Histogram of bumps height and diameter distribution.

6.3.1.2. Surface bumps generation: effect of temperature.

Here we present a new method of tuning the characterization size of induced instability on surface of thin polystyrene films, by changing the temperature of treatment with degassed solution. We performed the nanostructuration process described in Chapter IV at temperatures ranging from 22°C to 70°C. As in previous chapters, fresh spin coated annealed samples of PS were explored. For structuration at controlled temperature, the samples were placed into an oven at the selected temperature for 2h. Simultaneously, a nitric acid solution of pH=1.5 was degassed under reduced pressure (~0.2 mbar) at room temperature for 2h. This procedure is thoroughly described in Chapter IV. After 2h of degassing, the flask containing the solution was placed in a water bath at the selected temperature (without stopping the pumping) for 30 min. Next, the polymer surface was immersed in the solution for 5 min inside the oven, at the selected structuration temperature. Similar results were obtained for longer times in solution, as described later. Subsequently, PS films were dried with a gentle flow of nitrogen gas and immediately studied by AFM. The results of isothermal nanostructuration of 300 nm PS-250k films at temperatures between 22 and 70°C are shown in Figure VI.6.

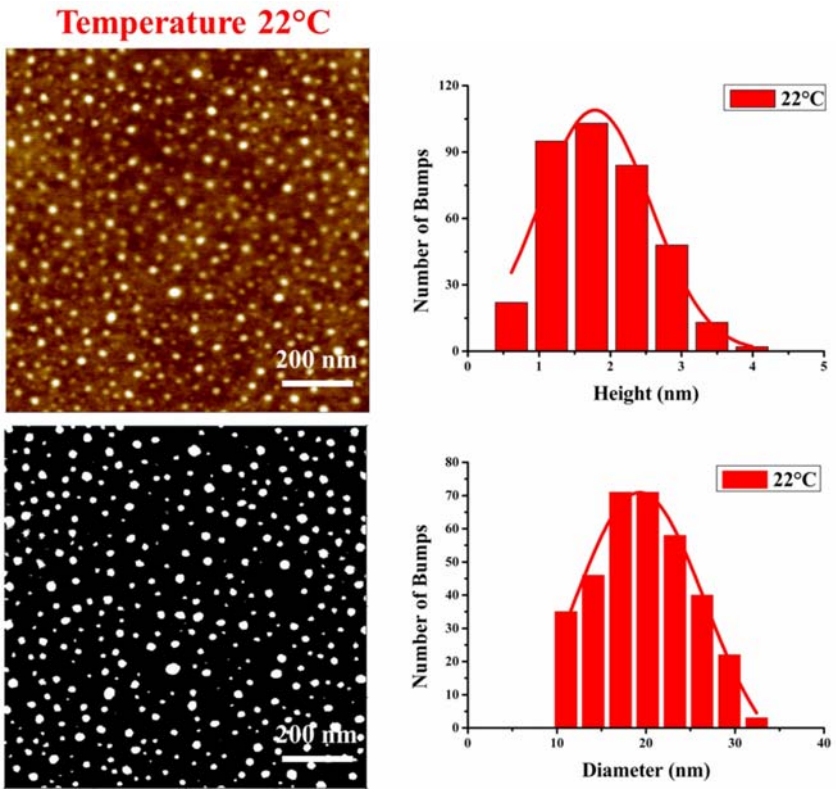

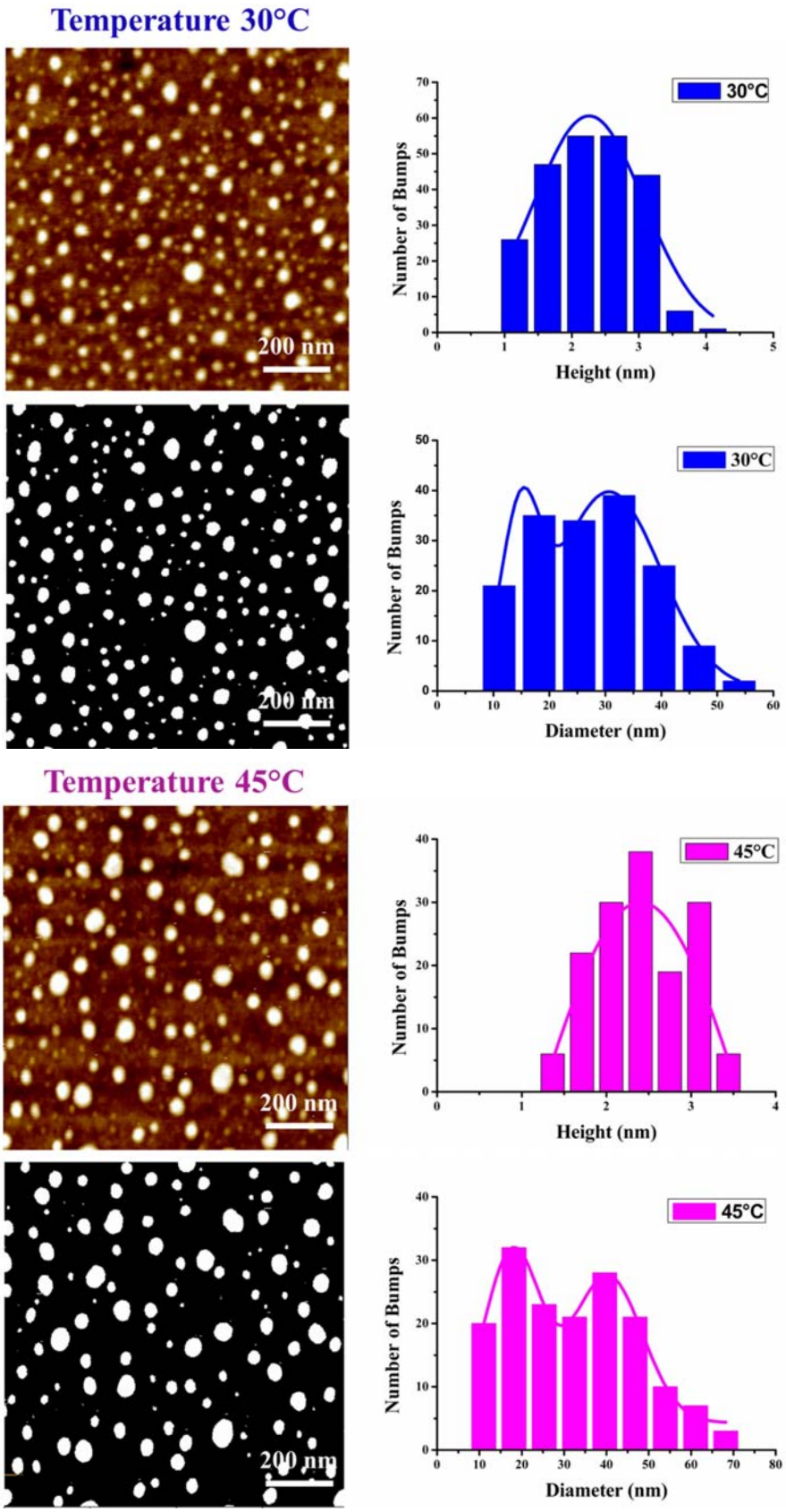
Temperature 30°C
200 nm
30°C
Number of Bumps
Height (nm)
200 nm
30°C
Number of Bumps
Diameter (nm)
Temperature 45°C
200 nm
45°C
Number of Bumps
Height (nm)
200 nm
45°C
Number of Bumps
Diameter (nm)

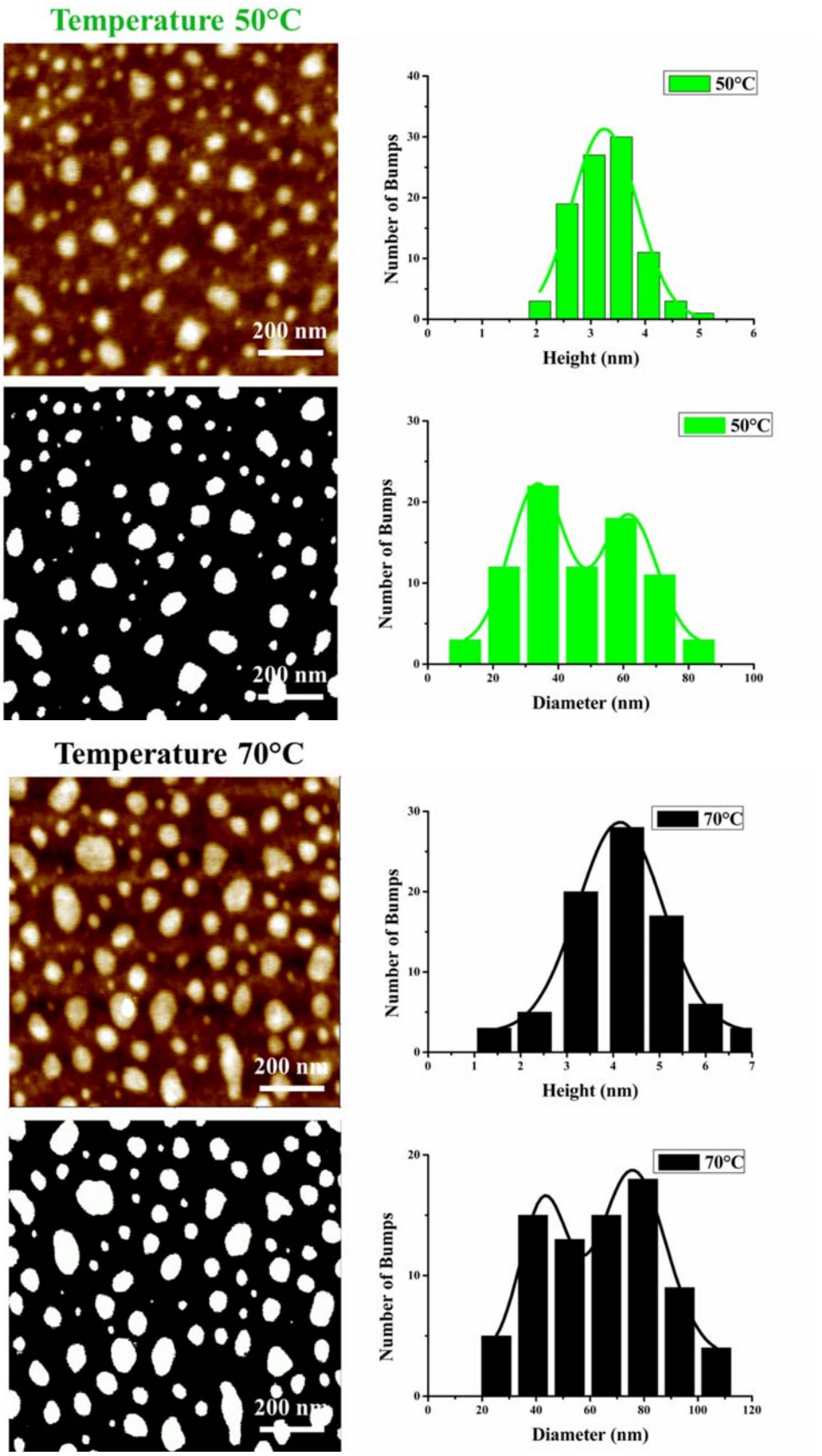

Figure VI.6: Taping mode height AFM images taken in air of isothermal nano-structuration of 300 nm thick, PS-250 kDa films after exposed to a degassed solution of nitric acid water at pH=1.5 at different temperatures.

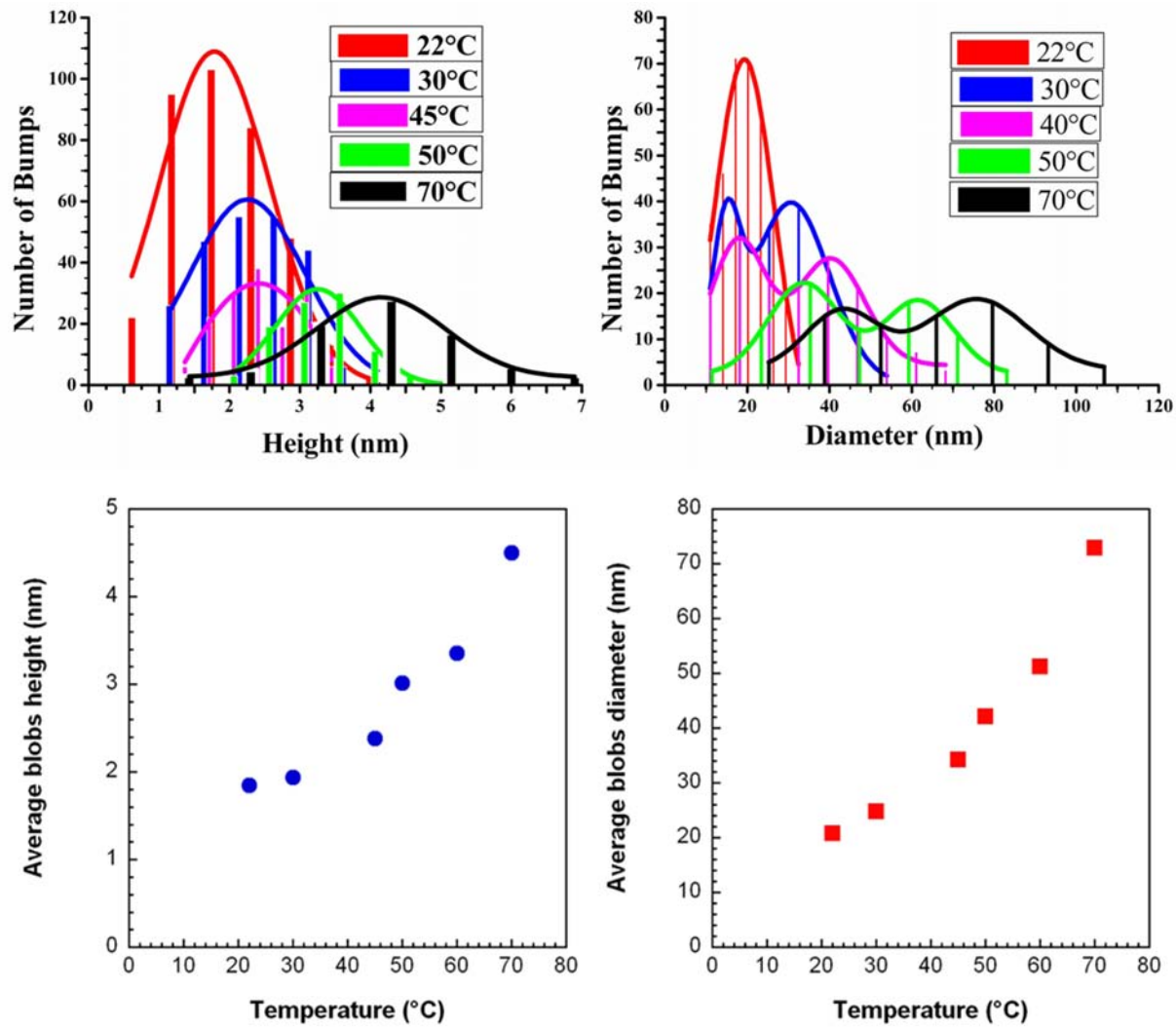

Figure VI.7: Histograms of bumps height and diameter measured in 1×1 μm² areas of the PS films structured at different temperatures. The temperature dependence of number average bump height and diameter are also shown. PS-250 kDa

The size distribution measured at different temperatures together with the variation of number average of bump size is presented in Figure VI.7. By analyzing the characteristic size of induced nanostucturation at different temperatures a number of interesting findings can be noticed. First, these findings indicate once again the presence of a high-mobility layer at the film surface. Second, as represented in Figure VI.6, the created nano-bumps get larger and higher with increasing temperature, which suggests that the thickness of the mobile layer increases with temperature. Thus, the method of nanostructuration can be easily used to create bumps larger in size that those created at very high or low pH. Third, the bump size distribution changes when the temperature increases: at T=22°C the histogram of bump diameters is well-described by a single Gaussian peak. On the contrary, at temperatures larger than 30 °C, a broader, rather bimodal distribution describes better the observed distribution. We can also observe that by increasing the temperatures both peaks shift to larger sizes, and the proportion of small bumps decreases: the number of small bumps decreases with increasing the temperature of treatment. This unexpected observation can be explained in two ways. Either the

larger size is just the result of ripening, which is accelerated by increasing T (the bimodal distribution is explained by the fact that some smaller blobs remain intact), or the dynamics of near surface region of glassy PS films is heterogeneous for T > 30°C [64].

In order to clarify this point, additional experiments were carried out to address the issue of larger bumps. Are they presents immediately after treatment, or are due to Oswald ripening? We investigated the temporal evolution of structured morphology at different temperatures.

As already mentioned in Chapter IV, the surface structuration is completed before 1 minute of immersion. Because of this, we were not able to study the structuration process *in situ* by AFM in liquid. However, additionally to the results presented in Chapter IV (cf. Figure IV.22), we explored the evolution of the surface morphology with time of immersion at different temperatures by removing the surfaces out of the degassed solution after different periods of time (from 1 second to few hours). If bimodal distribution of bumps at temperatures larger than 30°C is due to ripening, at short times of immersion a monomodal distribution is expected, which evolves at longer times of immersion.

The measured temporal evolution of bump size distribution at different temperatures is presented Figure VI.8. It can be observed in the Figure that complete structuration take place in less than 30 sec at all temperatures investigated. As can be observed in the AFM micrographs, the morphology of the samples does not further evolve after 30 sec of treatment, even at high temperatures. Moreover, bimodal distribution of bumps sizes is always observed at high temperatures and not evolves in time, as illustrated for the case of T 50°C. From results presented in Figure VI.8, it seems clear that the larger bumps are forming immediately; their large size and distribution are not dictated by the effect of ripening. These results seem incompatible with a homogeneous distribution of structural properties on the polymer surface (elastic modulus and/or viscosity). We will discuss this interesting finding later in more detail.

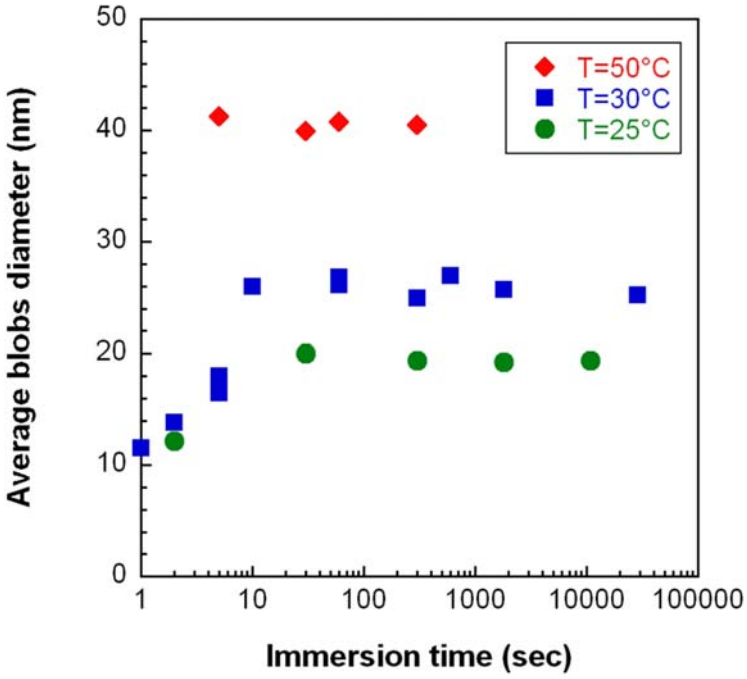
Average blobs diameter (nm)
Immersion time (sec)
T=50°C
T=30°C
T=25°C
0
10
20
30
40
50
1
10
100
1000
10000
100000

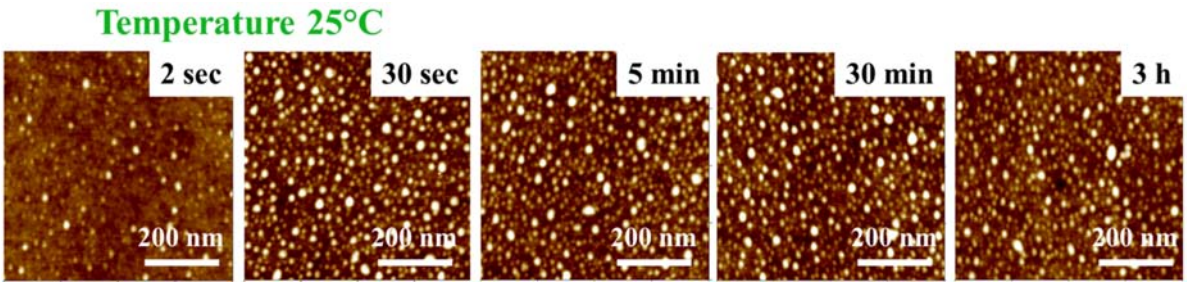
Temperature 25°C
2 sec
30 sec
5 min
30 min
3 h
200 nm

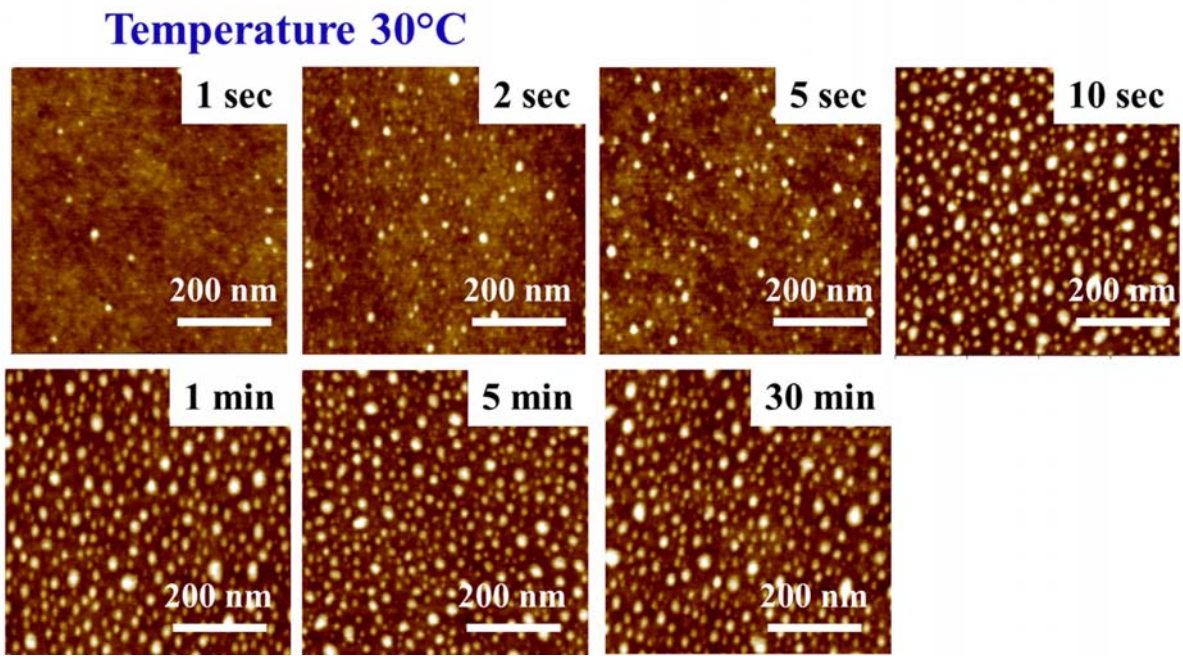
Temperature 30°C
1 sec
2 sec
5 sec
10 sec
1 min
5 min
30 min
200 nm

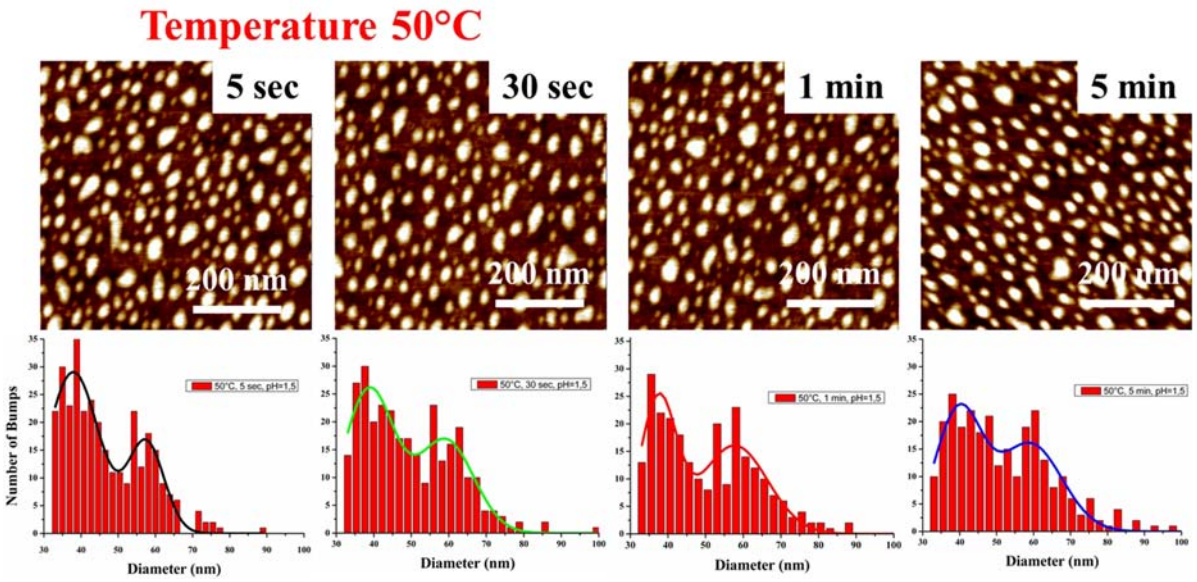

Figure VI.8: AFM micrographs of 300 nm thick PS films after different exposure time to a degassed water at pH=1.5 (with HNO_3) and different temperature of experiment. PS-250 kDa

6.3.1.3. Surface bumps generation: effect of polymer molecular weight.

As was mentioned in the introduction of this chapter, the size of the mobile surface region of glassy thin films of polystyrene was found to be rather independent of molecular weight in most of previously reported works. In this section I describe the influence of this important parameter on the water-induced nanostructuration process. We performed a detailed study of surface bump generation in films of PS of four different molecular weights (7, 59, 250, and 500 kDa) above and below entanglement length.[1] The film thickness for all four M_w's was adjusted around 300 nm to avoid the influence of polymer/substrate interactions described in previous chapter. After spin-coating, the PS films were identically annealed as described before, and then were exposed *simultaneously and during the same period of time* (5 min) to a degassed nitric acid solution of pH = 1.5. Finally, the samples were dried and analyzed by Tapping Mode AFM. Figure VI.9 shows AFM micrographs taken on the different samples after treatment, from which we determined the average bump diameter and height. As can be observed in the figure, there is a slight M_W dependence of bumps average height/diameter on molecular weight at T 30°C. This can be attributed to the fact that the mobility of upmost polymer layer depends on polymer length: lower molecular weight polymers have a higher mobility and consequently larger bumps are formed. However, other than for the case of PS of 7 kDa, the effect is rather minor. A more marked effect of M_W on the nanostructuration process is observed at higher temperatures, as can be observed in Figure VI.10. However, for all studied temperatures, the structuration of films of short (7 kDa), unentangled chains is much more important than for longer chains. These results suggest that chain entanglement constrain the motions of the polymer molecules on the surface, leading to significant reduction of size of induced bumps.

[1] Entanglement molecular weight of polystyrene 19100 Kg/mol

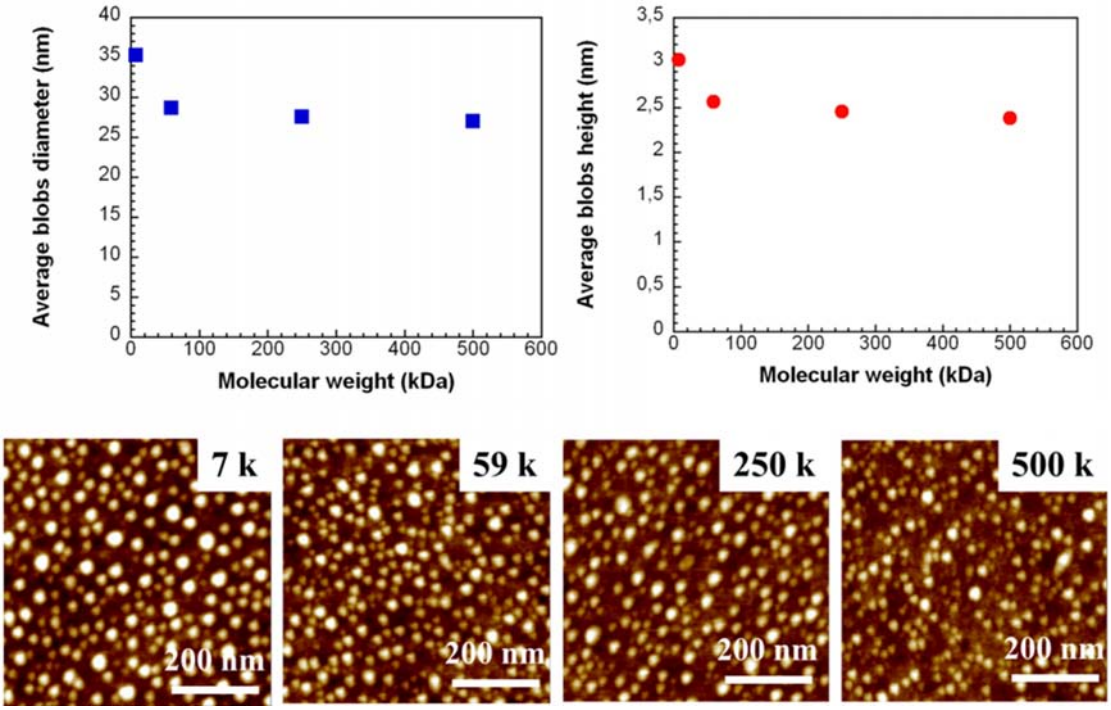

Figure VI.9: Variation of bumps average height (h)/diameter (D) with PS molecular weight

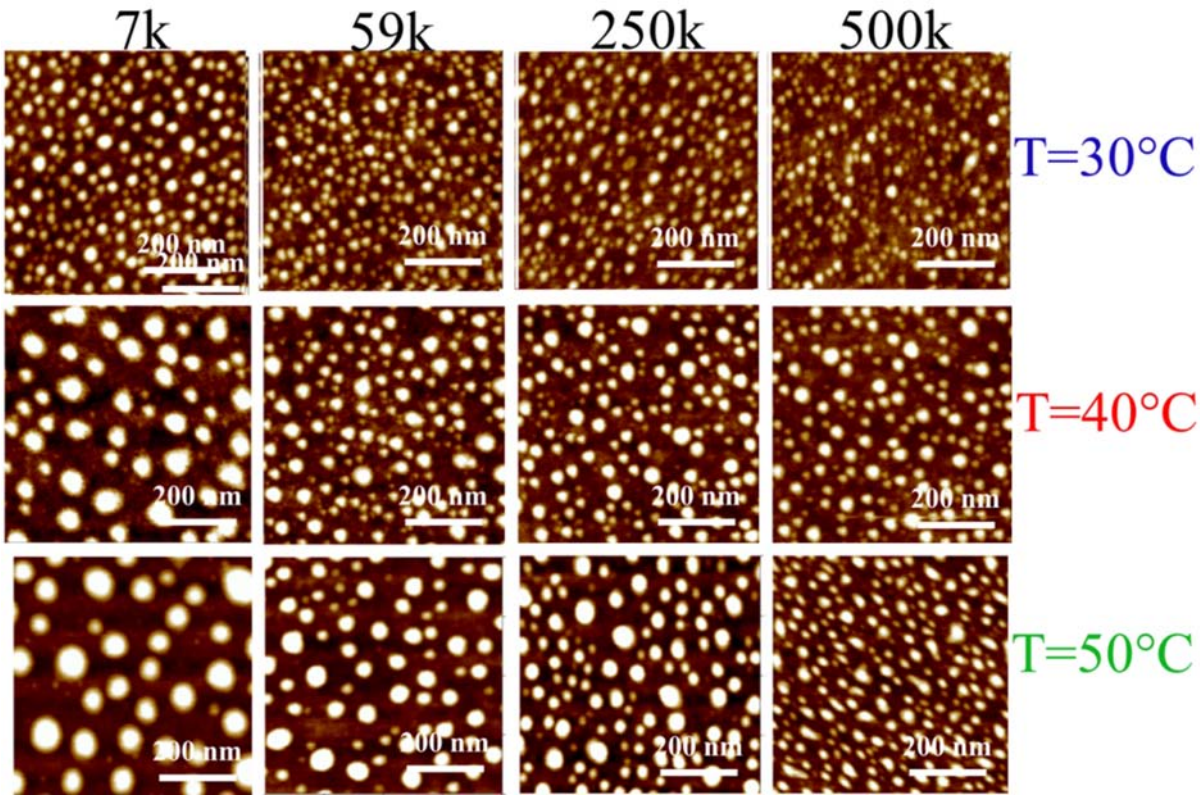

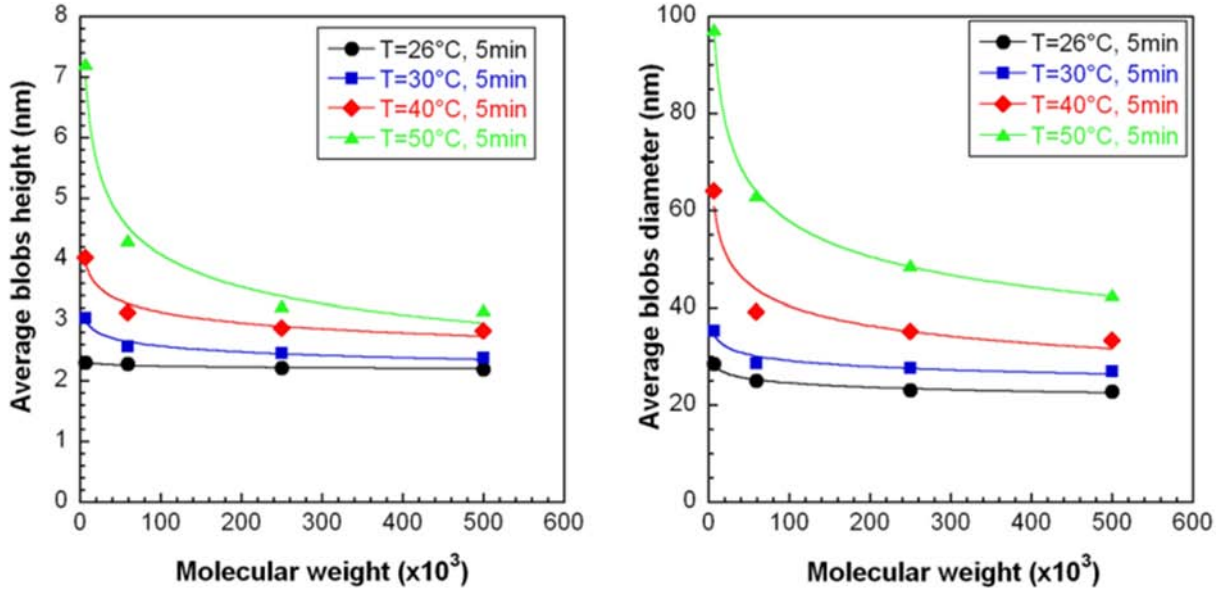

Figure VI.10: Taping mode 1µm×1µm AFM images taken in air of isothermal nano-structuration of 300 nm thick films of PS-7, 59,250 and 500 kDa after exposure to a degassed solution of nitric acid water at pH=1.5 at different temperatures (b) Bump height and diameter number average as a function of M_W for different temperatures

6.3.1.4. Molecular weight variation of thickness of mobile surface layer of PS

As already described in this chapter, there is a large body of studies in literature showing the existence of a mobile layer in the surface of glassy thin polymer films. However, there are only few studies showing experimental evidence of the temperature dependence of the size of this layer [65]. We can estimate its size from the data presented in Figure VI.6, assuming that it corresponds to the volume of the induced bumps. For this purpose, we have calculated the total volume of formed PS bumps at different experimental conditions:

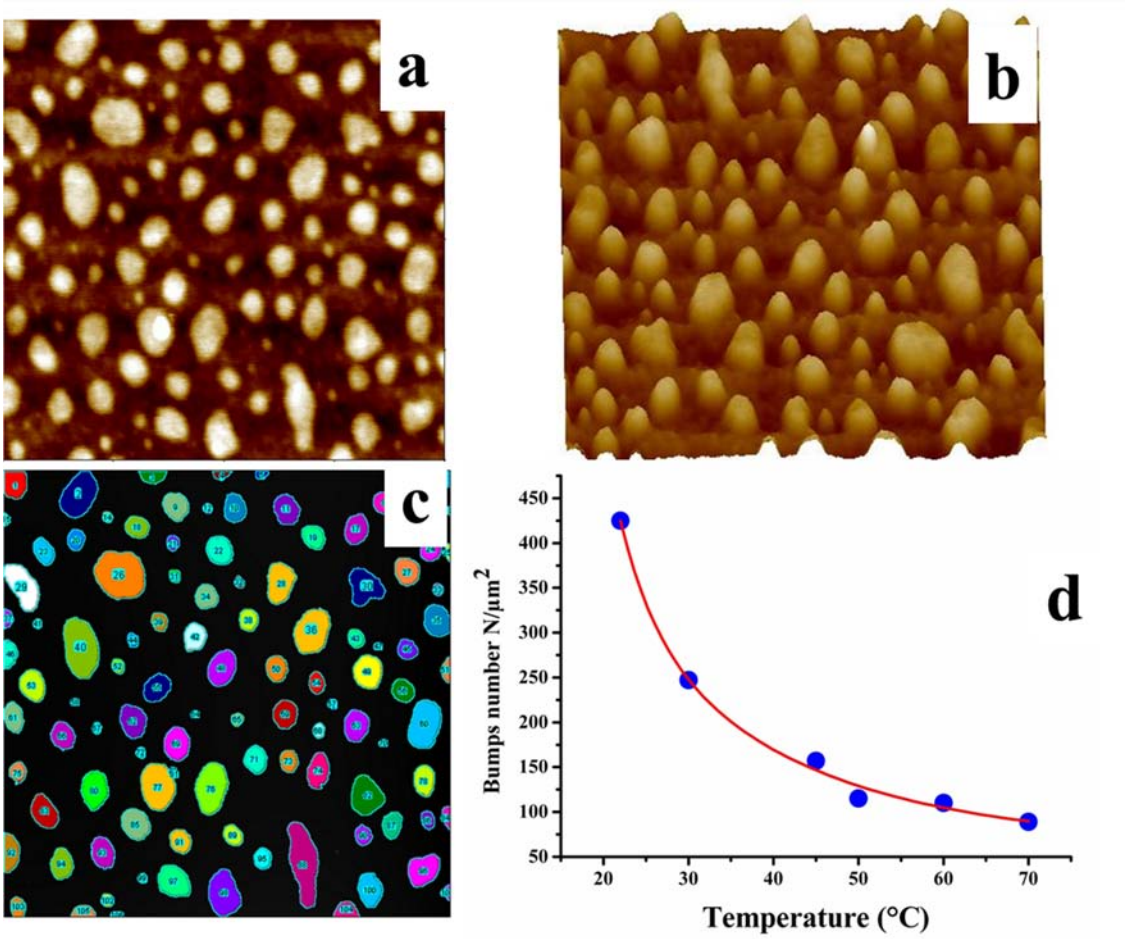

Figure VI.11: (a)-(b) 2D and 3D AFM images of 300 nm thick PS films after 5 min exposure time to degassed water at pH=1.5 at T 70°C. (c) PS bumps counting on its 2D image. (d) Number of bumps present at PS interface after treatment with degsased solution at different temperatures

As shown in Figure VI.6, the morphology of PS surfaces changes with the temperature of treatment from 22 to 70°C: generated bump sizes vary from few nanometers to almost one hundred nanometers. As can be observed for example in Figure VI.12 the shape of the bumps is fairly circular, but PS bumps of more irregular for were also observed at the higher temperatures. If we assume that the bumps are spherical caps, we can calculate its volume as:

$$V = \frac{\pi h(h^2+3R^2)}{6} \tag{6.3}$$

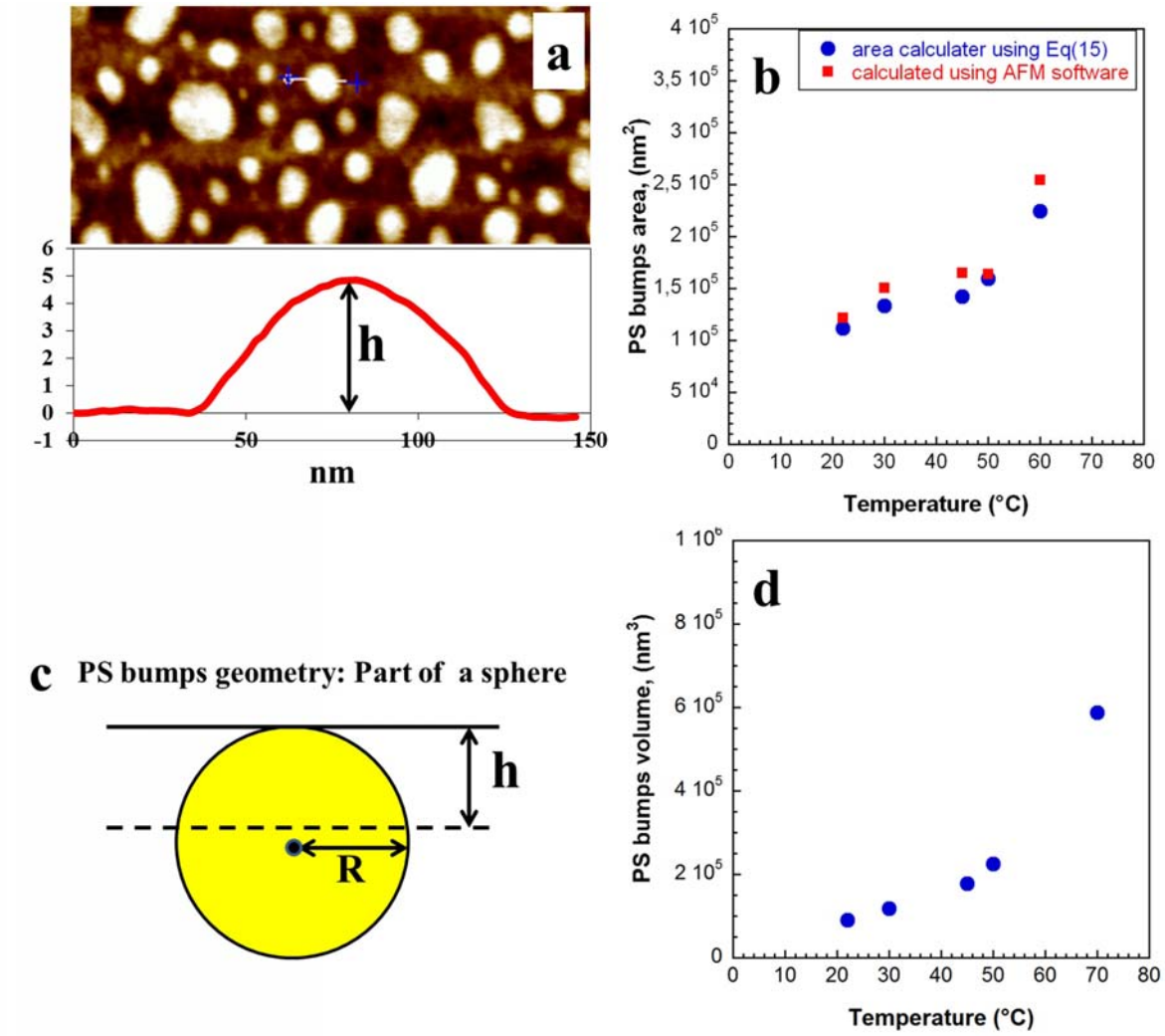

Figure VI.12: (a)-(c) PS bump geometry is considered as a part of sphere; bumps volume (V) and are are calculated using Eq(6.11) by using bump height, *h*, bump radius, *R* and their total number *N*.

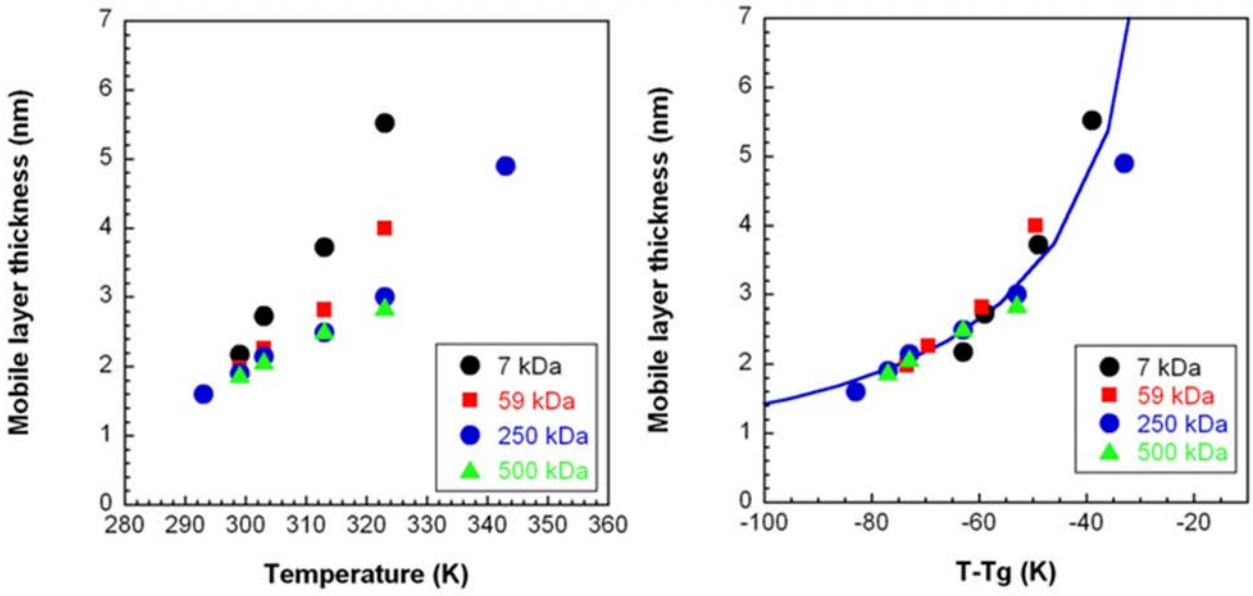

Figure VI.13: (a) Mobile surface layer thickness of PS films of different as a function of temperature (b) Same data represented as a function of temperature deviation from bulk T_g

By using model showing in Figure VI.14 and by adding the volume of all observed bumps, we can obtain the volume (and thickness) of the mobile layer. The value obtained at different temperatures and molecular weights are presented in Figure VI.13. The calculated thickness of the mobile layer increases with increasing temperatures, and decreases with M_w for a given temperature. Qualitatively similar temperature dependence has been reported by Herminghaus et al. [66,67]. They studied polystyrene emulsions by NMR and deduced that $d(T)$ grows continuously according to $d(T) \infty (T_g - T)^{-1}$. The depth to which nanoparticles embed on a polystyrene surface has also been well-described by an exponential growth function [68]. On the contrary, in all above reported works the size of the mobile surface region of thin polymer films at different temperatures was determined to be independent of molecular weight of polystyrene. Interestingly, as can be observed in Figure VI.13, our data for different M_w collapse on a single master curve if it is represented as a function of the deviation from bulk T_g.

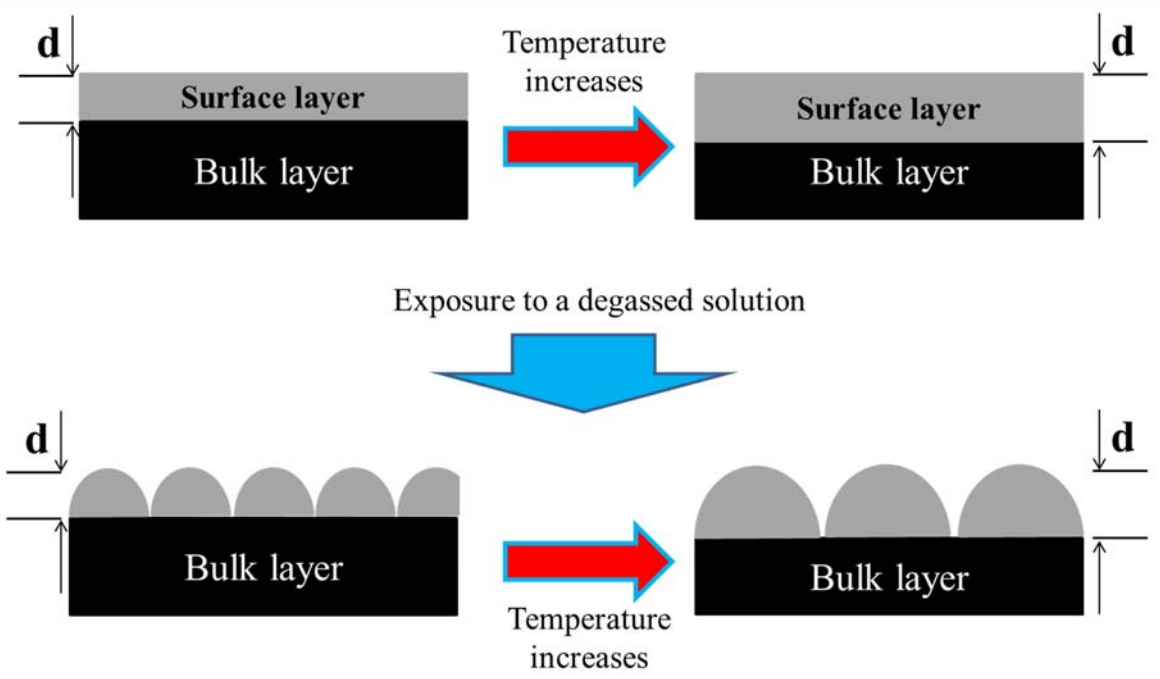

Figure VI.14: Schematic model showing a mobile surface whose thickness grows with temperature. The exposure to a degassed water solution leads to surface nanostructuration

Two models has been advanced to describe the increment in the thickness of a mobile-like layer with temperatures from below bulk T_g [66,69]. Both describe rather well our data, so we cannot select one over the other. In Figure VI.15, the red solid curve is the data fitting to the model proposed in ref. [69]. This model has an empirical prediction of liquid surface size h as a function of T:

$$h = A\left(1 - \frac{T}{T_G}\right)^{v} \tag{6.4}$$

where A and ν are material dependent model constants. In ref. [69] it was reported that values of A and v 3.2nm and 0.56 were adequate for describing PS films. We found that values A 0.4 nm and v = 1 produced the best fit to our data (red line in Figure VI.15).

We also attempted to describe our data by the model presented in [66] (green line in Figure VI.15):

$$h = \frac{h_0 T}{T_g - T} \tag{6.5}$$

where h_0 is a material specific constant. We found that value of h = 0.5 nm fits well our data. Values of h_0 = 0.47 nm [66] and 0.82 nm [67] has been reported in the literature, in good agreement with our results.

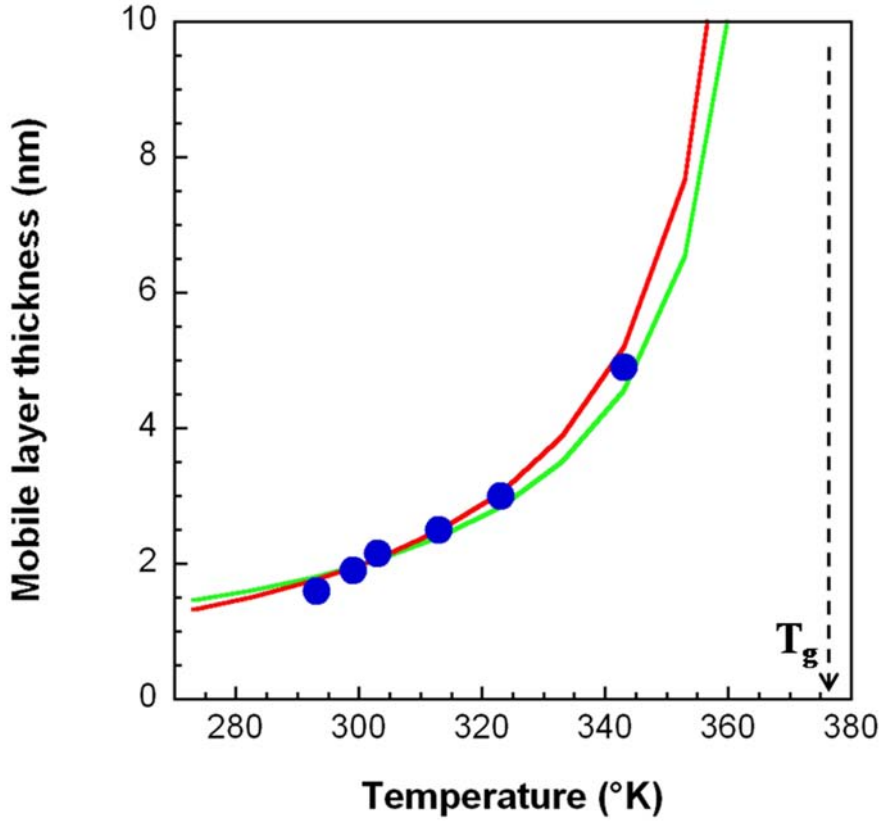

Figure VI.15: Mobile surface layer thickness of glassy PS films as a function of temperature; the red solid curve and the green curve are the fittings to models described in [69] and [66] respectively.

6.3.2. Surface bumps relaxation process

Two methods based on AFM were used for following the dynamics of relaxation of structured polystyrene films. At low annealing temperatures, we follow the size distribution of a number of samples for a certain time (method A). To avoid extra stress caused by repeated heating and cooling of the samples, we measured each sample only once after annealing has begun. This means that we used at least one sample per annealing time. Determination of the relaxation curve for any temperature required then 10 to 20 samples with identical preparation and thermal history (thickness and annealing), the same treatment with degassed solution, which lead to similar initial height (h_0)/diameter (d_0) distributions. This was verified for all the samples by AFM. Then for a given temperature, all of the prepared samples were placed in the oven. After some time, one of the samples was removed, cooled down to room temperature, and then measured by AFM. Each AFM image was analyzed and average diameter and height were extracted. This procedure was repeated at a number of annealing times until bumps were no longer observed and the polymer films recovered their original smoothness. Given that the relaxation of bumps were not followed in a particular sample, average height/diameter of bumps was determined from AFM images taken in several places of the surfaces. The entire experiment was repeated at different annealing temperatures. The temperature was precisely controlled during the duration of the tests in regulated ovens: Bioblok Scientific 45001 (with temperature controlling accuracy 0.5°C) and SalvisLab Vacucenter (accuracy 0.1°C).

The second procedure used to study the thermal relaxation of nanostructured films (method B) was based on the use of Thermo-Microscope Explorer AFM (Veeco). This method permits to follow the morphological changes of the polymer surfaces *in situ*, in real time, and in a wide range of temperatures. The advantage of this method is that relaxation can be studied in the same position of the sample, and individual bumps can be investigated. Following particular bumps eliminates the experimental errors that come from averaging, and the results are more precise. Once placing a nanostructured sample on the heating stage (temperature accuracy of 0.1°C) the relaxation of bumps is followed in real time until bumps disappear completely. All AFM images were analyzed and as in previous cases the dependence h=f(*time*) or normalized h/h_0=f(t) were plotted. The disadvantage of this second method is that long processes require the uninterrupted operation of the AFM till process is finished, which is inconvenient or technically impossible for the case of low T.

Since we are studying the thermal dynamical properties of the near free surface region in thin polymer films, it is important to make sure that real temperature in this region matches the set value. To verify this, we performed several measurements of the surface temperature of silicon substrate supported 300nm thick PS films sitting on the AFM heating stage (heater element includes a Derlin body with a tungsten base and cup; internal components include a multi-stage Peltier element and "K-type" thermocouple) at different setting temperatures. The surface temperature of the PS film was monitored using a thermocouple gently touching the sample. Figure VI.16 shows the results. We observed a systematic deviation from the set temperatures, which was taken into account for data

analysis. Furthermore, after each experiment was finished and the surface already recovered its original smoothness, the surface temperature was verified again with the thermocouple.

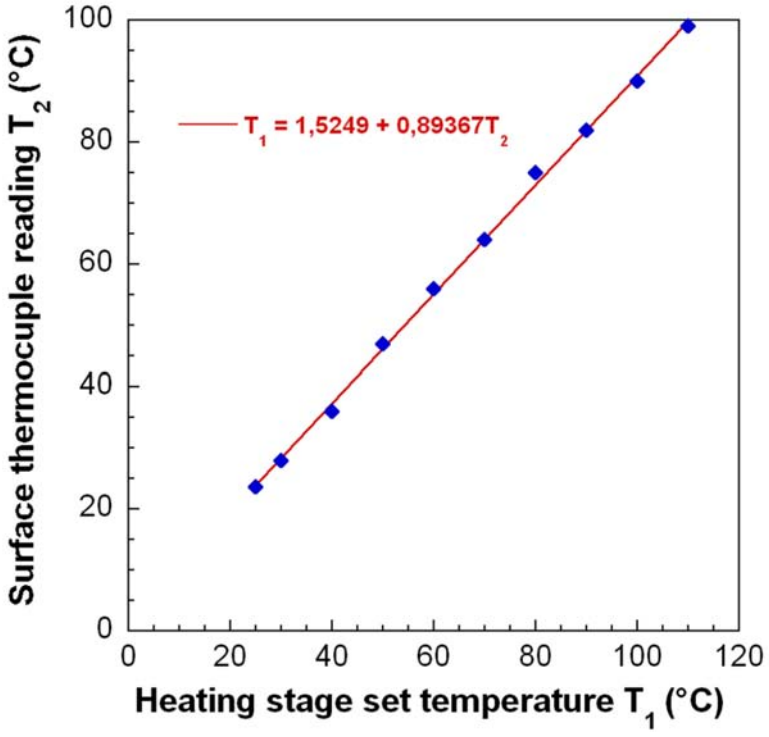

Figure VI.16: Results of polymer surface temperature measurements: blue squares symbols show the measured data using a thermocouple on a thin polymer film surface.

6.3.2.1. Surface structure relaxation at constant temperature

As shown in Chapter IV and mentioned above, a well-developed structured layer is formed at room temperature after a few minutes of contact of PS films with degassed water solution. Nevertheless, the typical relaxation time of the structure at room temperature is of the order few weeks. This relaxation is greatly accelerated by increasing the temperature. Before considering the relaxation process at various temperatures, I will consider the results at 50°C and discuss in detail the temporal evolution of the morphology of structured layers.

Figure VI.17 shows the temporal evolution of a nanostructured 300 nm film of 250k PS at T 50°C. Two mechanisms govern the temporal evolution of the layer. First, smaller size blobs disappear at expense of larger ones which increase further in size (*e.g.*, the regions indicated by the arrows) evidencing the mobility of the polymer chains at the surface. This process, which coarsens the size distribution of the asperities on the surface, suggests the occurrence of surface Ostwald ripening. Second, a slow relaxation of the measured blobs is detected. The principal driving force in the relaxation of the surface roughness is the stress due to the polymer surface tension, which is inversely proportional to the radius of curvature. The magnitude of the initial stress σ_0 will be given by $\sigma_0 = 2\gamma/R$, where γ is the PS surface tension and R is the radius of curvature of the nanobump. For a

spherical cap (bump) with a radius of curvature of 150 nm, σ_0 = 0.5 MPa. This is a factor of ≈ 100 less than the yield stress of PS. The stress gradually decreases as the radii of the nano-bumps decreases. These AFM micrographs clearly show that the self-assembled nanostructure on the polymer surface is not at thermodynamic equilibrium. Due to the presence of a zone of enhanced mobility on top of the polymer surface, the induced nanostructure is able to deform and to reshape. After three weeks, most of the asperities on the film have already relaxed, and the film recovers its original smooth morphology.

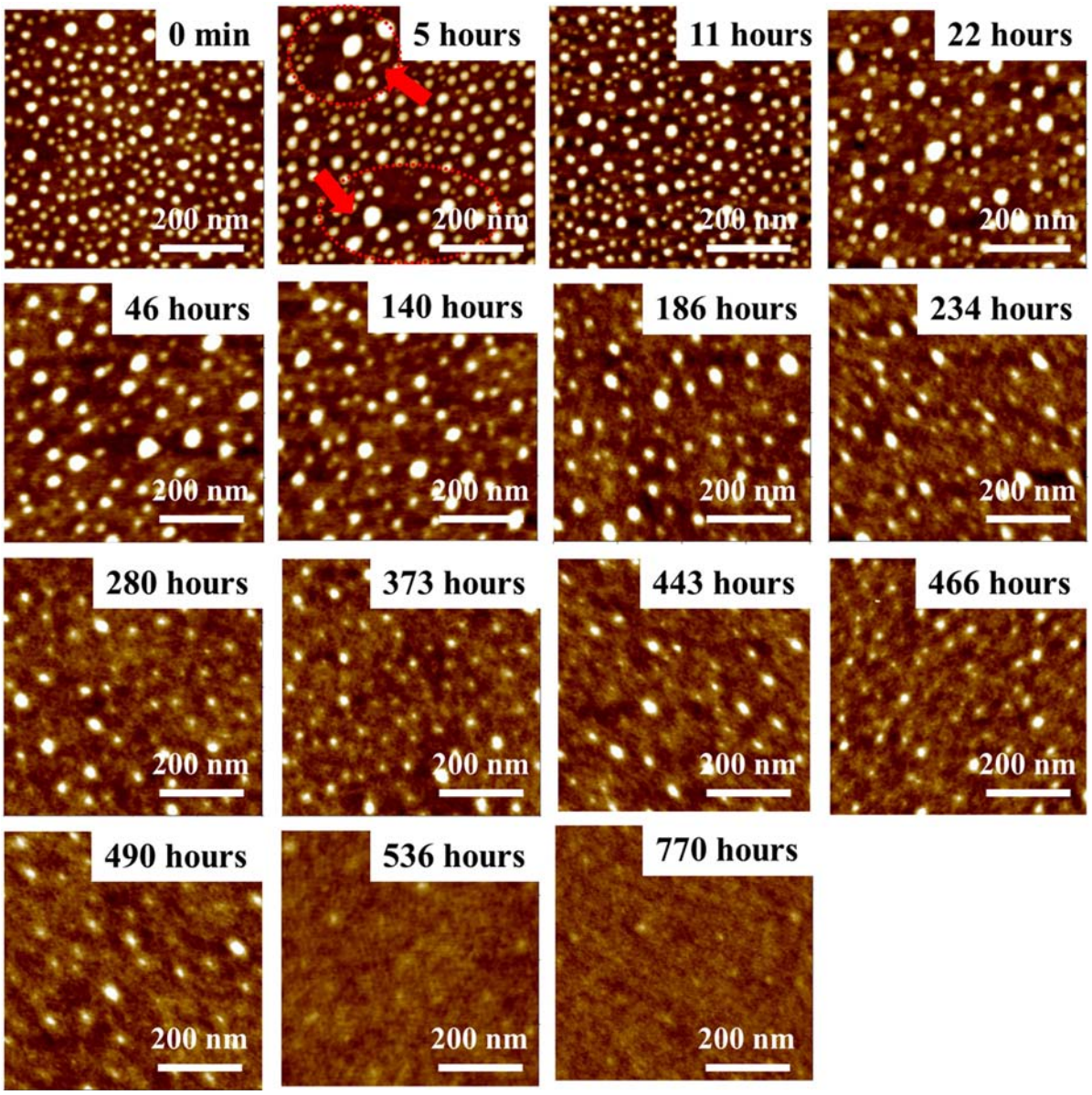

Figure VI.17: PS surface evolution process of bumps at T 50°C. PS-250 kDa

To determine the bump lifetime at constant temperature, each AFM image was analyzed and average diameter and height were extracted. Figure VI.18 represents the histograms of all *n* bumps

height measured on the 1×1 μm^2 area of PS surfaces at specific annealing times. We determined the number average bump height by a Gaussian fit.

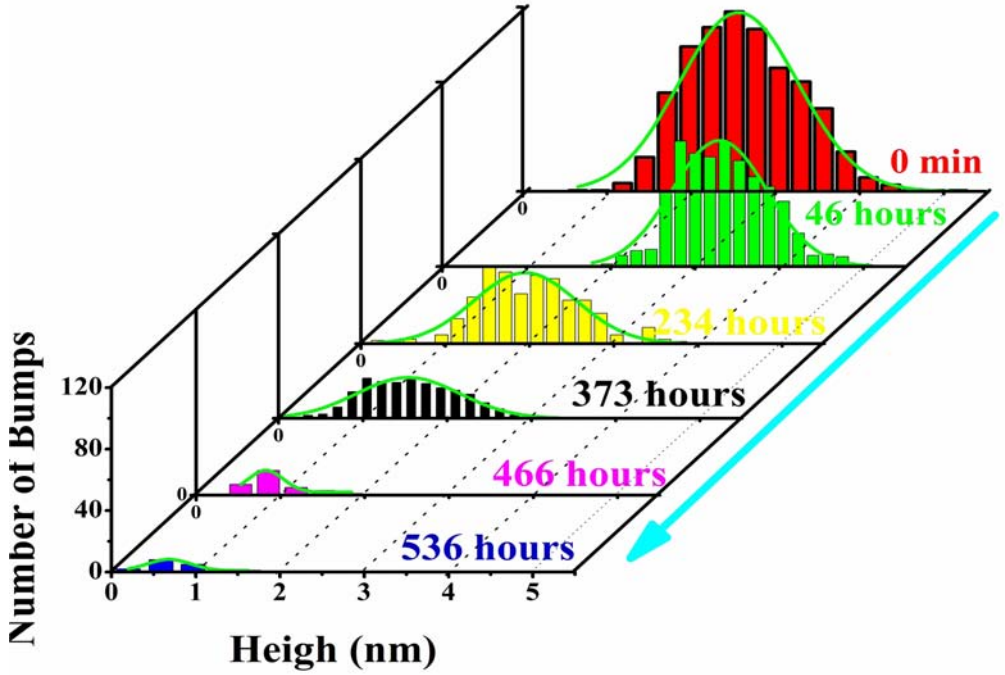

Figure VI.18: Histograms of surface bumps in 1×1 μm^2 areas across the PS interface after annealing bumps at 50°C. The histograms have been shifted both horizontally and vertically for clarity. PS-250 kDa

As can be observed in the figure, the height and number of blobs on the surface progressively decreases at constant temperature (T 50°C). After some time (536 hours) no more bumps are present on the surface (or they are undetectable by the AFM data analysis software).

After analysis of all AFM images, the number average bump height and diameter were extracted from all histograms; the data was used to build a plot of time dependence of the relaxation of bumps, as represented in Figure VI.19. The solid curve in Figure VI.19 is the single exponential fit of the measured time evolution. From Figure VI.19 we can observe that even at 50°C, more than 50°C below the bulk T_g value (103°C), complete surface bumps relaxation is observed in less than 500 hours. Once again, this remarkable result indicates that the PS film surface has enhanced molecular mobility (or is in the rubbery state) while the bulk material is in the glassy state at the same temperature.

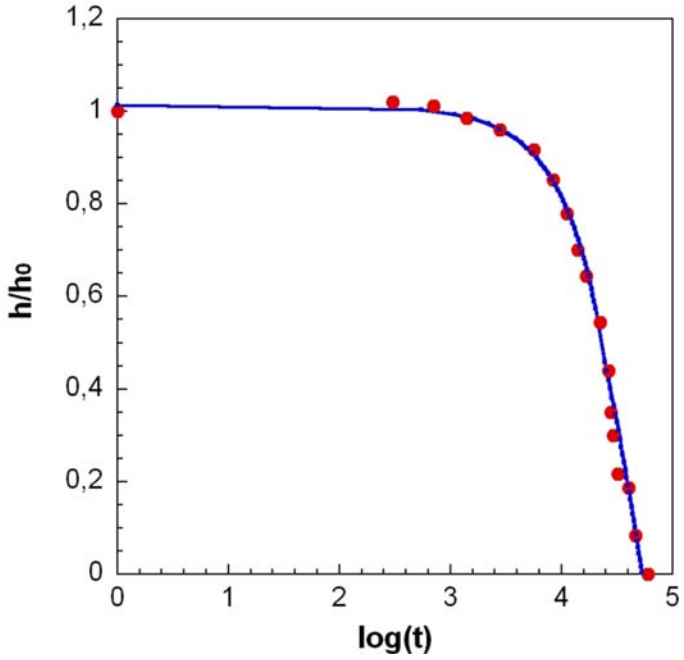

Figure VI.19: Surface bumps relaxation at 50°C for a nanostructured 300 nm thick PS film (M_w = 250kDa) on Si; the solid curve represents a single exponential fit of the data.

The time dependence of the annealing of the surface deformations follows a single exponential relaxation rather than the commonly observed stretched exponential relaxation for bulk PS. In studies of bulk PS dynamic close to the glass transition, the Kohlrausch-Williams-Watts (KWW) equation $\exp(-(t/\tau)^{\beta})$ is frequently applied to fit the experimental data; values of the stretch exponent close to β = 0.4 often provide reasonable fits. In our case, we can find a relationship between the characteristic relaxation time of the surface and the lifetime of the annealing by using the single exponential fit of the nano-deformations size,

$$h = h_0 \exp(-t/\tau) \tag{6.6}$$

where τ is the time constant of the annealing. Taking in account that initial stress on the system is from the surface tension force,

$$\sigma_0 = \frac{2\gamma}{R} \tag{6.7}$$

The characteristic life times of the nano-bumps can be estimated as described in ref. [46]

$$\tau_{\alpha} = \frac{\tau_{life\ time\ (measured)}}{(1+\frac{RG_0}{2\gamma})} \tag{6.8}$$

where $\tau_{life\ time\ (measured)}$ is the experimentally measured surface bumps lifetime, R is the initial radius of curvature of the bumps, G_0 is the longitudinal glassy creep modulus, and γ is the polymer surface tension. The time evolution of the bumps height/diameter can be used to obtain the surface relaxation function for each studied temperature. If the shape of the relaxation function is not temperature-dependent, then it is possible to find a shift factor, a_T, such as the relaxation curves at

different temperatures in time can be superimposed. This is a commonly used technique to describe the temperature dependence of relaxation times in glass-forming materials, as described in Chapter I.

6.3.2.2. Surface structure relaxation: effect of temperature

We measured the nanometer surface bumps relaxation at different temperatures ranging from 30 to 95°C. To exclude potential substrate effects on the near free surface dynamics, the samples used are thick (h>300nm) PS films on silicon. It is important to emphasize that all the samples were generated under identical conditions. In particular, the nanostructuration process was done at 25°C on each case, so a rather monodisperse bump size distribution was regularly obtained. After the surface nanostructure was generated the samples were stored at different temperatures. Samples at temperatures between 70 and 95°C were investigated by tests *in situ* and in real time (method B described above). For samples stored at lower temperatures, method A was employed. As pointed out earlier, lower temperature experiments are time consuming and involve study of multiple samples (10 to 20) with identical preparation and thermal history (thickness and annealing), with the same treatment with degassed solution which lead to similar initial bump size distributions.

Figure VI.20 shows the time dependence of the bump height obtained for the different temperatures investigated. Selected AFM micrographs corresponding to these experiments are presented in Figure VI.21.

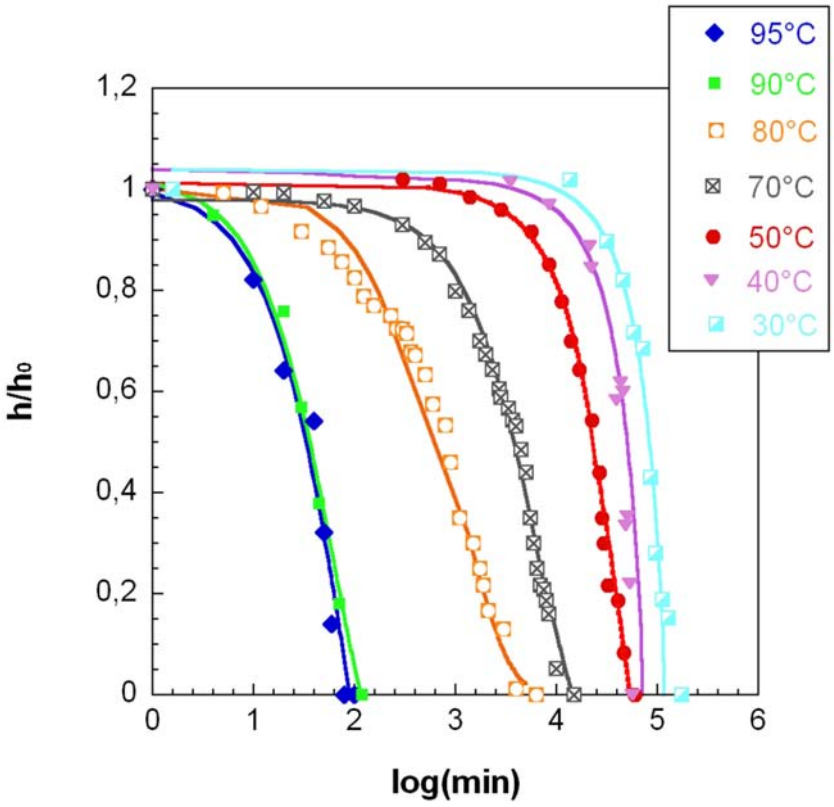

Figure VI.20: Time dependence of the relaxation of bump height at selected temperatures. PS-250 kDa

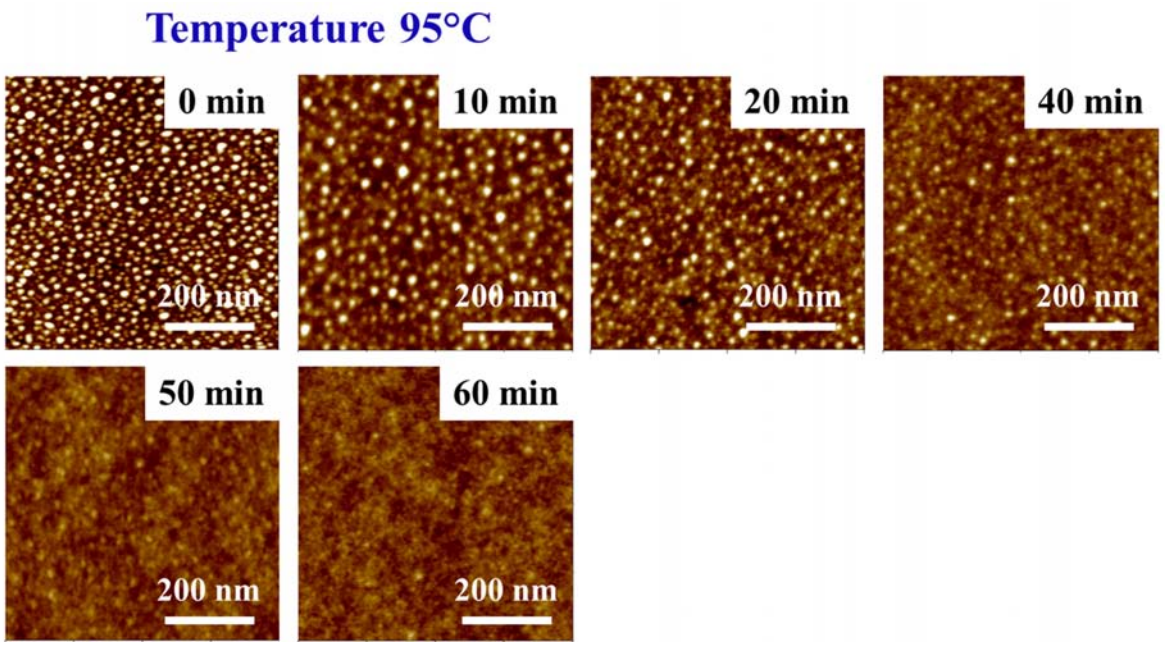
Temperature 95°C
0 min
10 min
20 min
40 min
50 min
60 min
200 nm

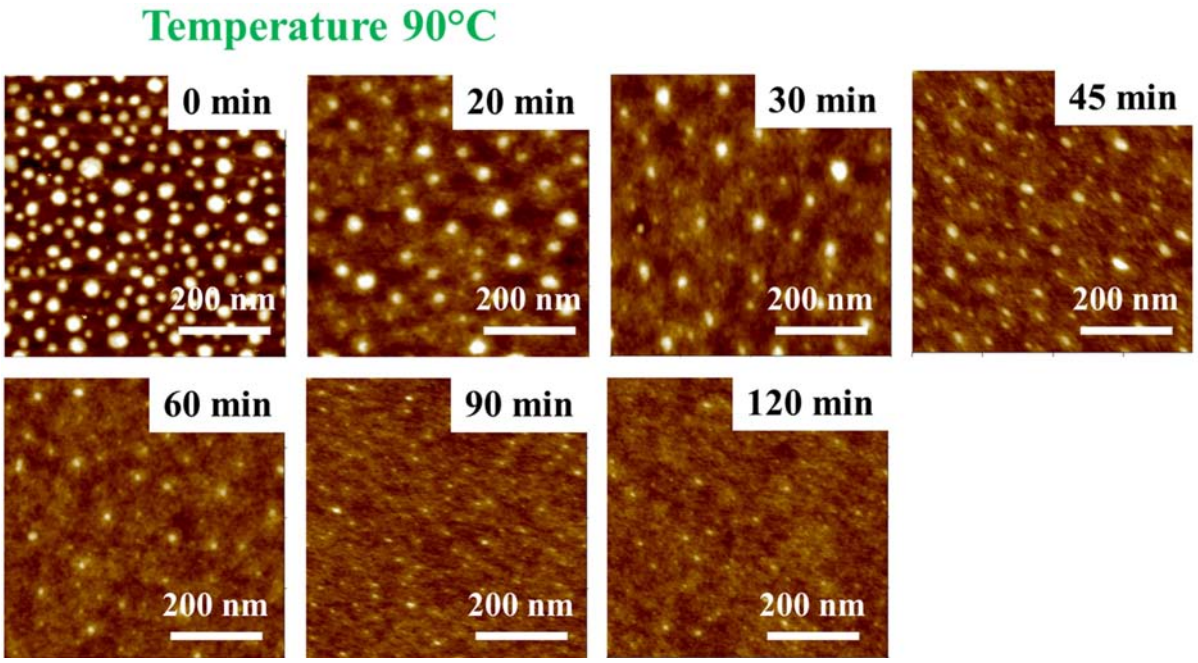
Temperature 90°C
0 min
20 min
30 min
45 min
60 min
90 min
120 min
200 nm

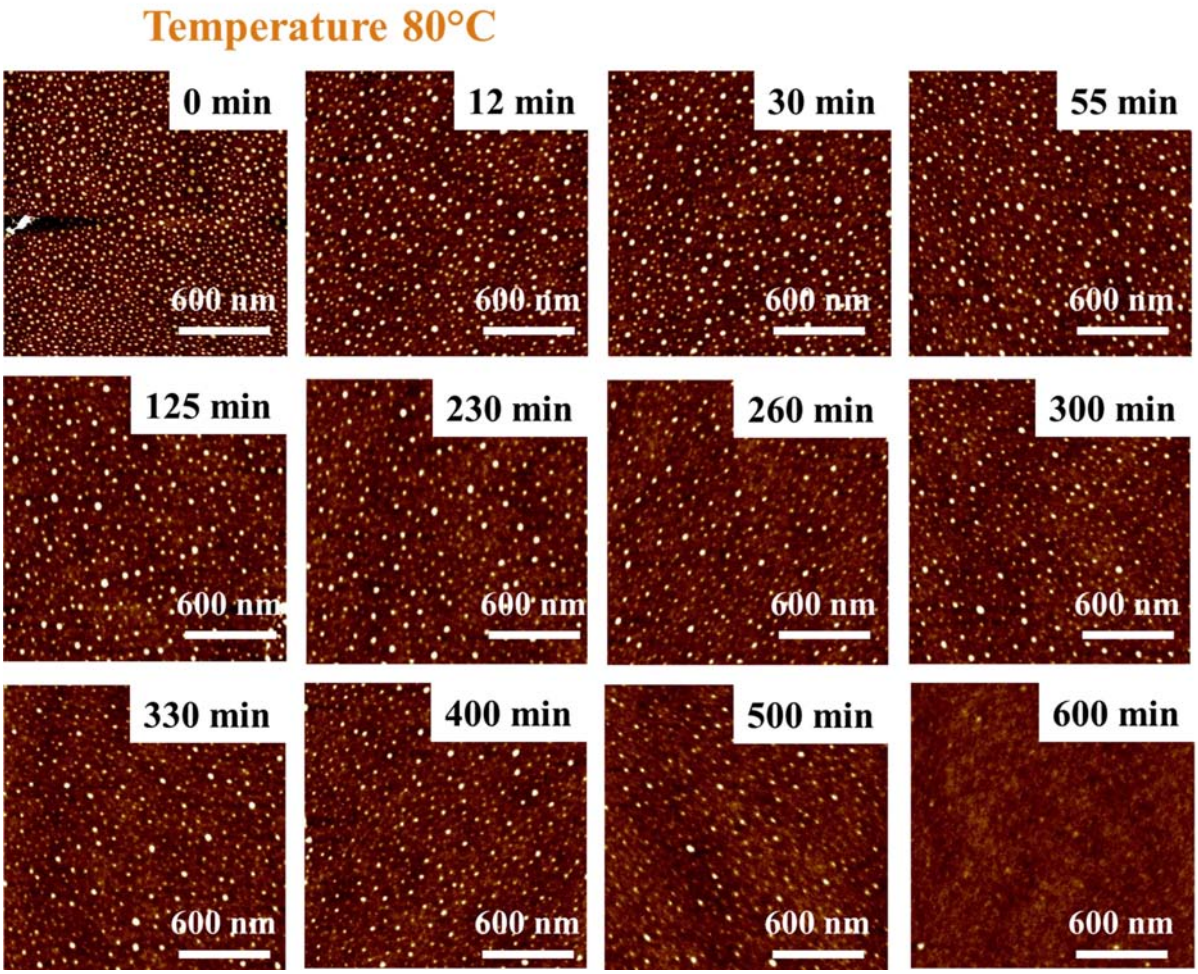
Temperature 80°C
0 min
12 min
30 min
55 min
125 min
230 min
260 min
300 min
330 min
400 min
500 min
600 min
600 nm

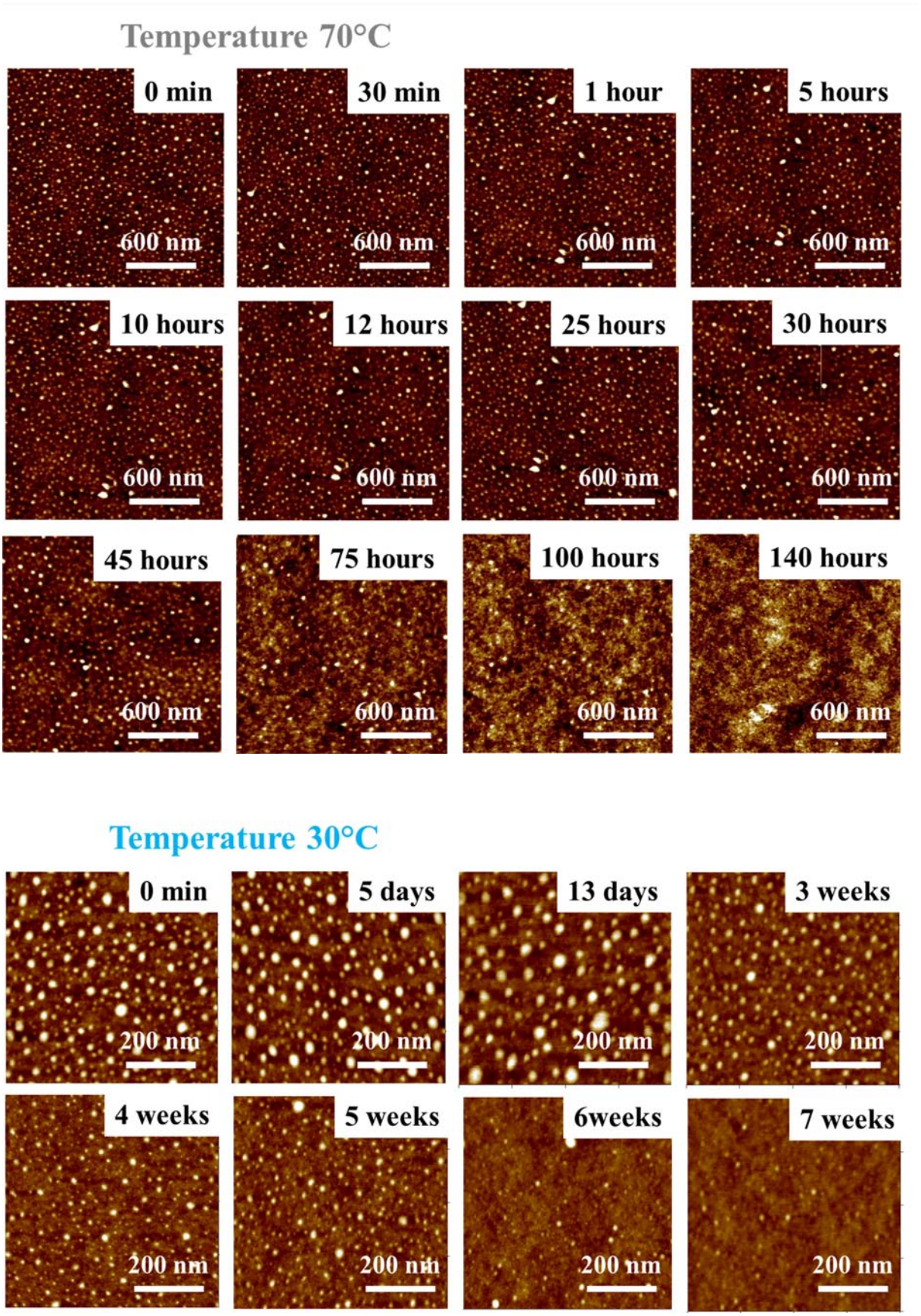

Figure VI.21: Tapping-mode height AFM images measured in air illustrating the evolution of nano-bumps at different temperatures.PS-250 kDa. Film thickness 300 nm

The effect of temperature on the relaxation time of bumps is quite evident: the relaxation time markedly decreases with increasing temperature. This implies that the polymer interface have enhanced molecular mobility with increasing temperature, even though the entire set of experiments was conducted at temperature $T < T_g$, were the material should be in the glassy state.

The time dependence of the bump relaxation functions acquired at different temperatures have been fitted with single exponential decay functions. This single relaxation process was enough to obtain a reasonably good fit of all the curves measured, with the possible exception of T=80°C. As the shape of the relaxation function is not temperature-dependent, we assumed that the system is thermorheologically simple and applied the time temperature superposition method to obtain a master curve containing all the data, as explained in Chapter I. After choosing the reference temperature (T_{ref}) to be 95°C, all the other isotherms were shifted horizontally by a shift factor a_T until they overlapped with the reference isotherm (when an isotherm is shifted to the left, it corresponds to a decrease of the relaxation time, and vice versa). The master curve of the measured bump height relaxation is represented in Figure VI.22. It is obvious that the relaxation data can be well described by a single exponential (solid curve), in manifest contrast to the relaxation function of bulk PS, which is better described by stretching exponential ($f = f_0 \exp[-(t/\tau)^{\beta}]$) with β values ≈ 0.4 (dashed curve in Figure VI.22) [8]. The fact that the relaxation behavior changes from stretched exponential to a single exponential relaxation was also recently observed in studies of nano holes relaxation in the surface of PS films [46]. The strong deviation from bulk behavior suggest either a large change in the relaxations behaviour, or the presence of a new relaxation mechanism near the surface which becomes faster at lower temperatures compared to the bulk α relaxation.

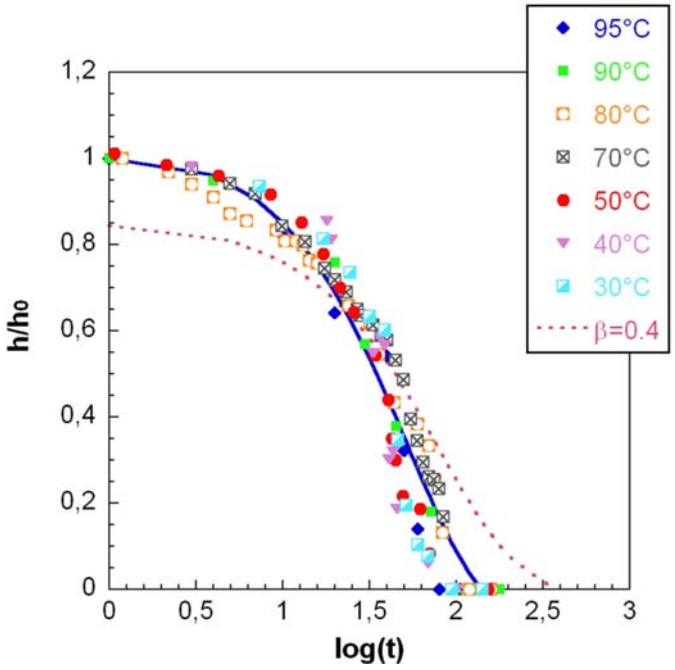

Figure VI.22: Time dependence of the relaxation of bump height for all temperature investigated. The time data were shifted by a factor a_T so that all data collapses into a single master curve, as explained in the text. The solid line is a single-exponential fit; the dashed line is a stretched exponential with bulk value of β=0.4, with the same average lifetime as the single-exponential fit.

The dependence of a_T with temperature is presented in Figure VI.23. Note that two different temperature dependence regimes can be distinguished. At lower temperatures the temperature dependence of the shift factors becomes very weak, while at temperatures closer T_g to it changes much faster. I will discuss this point later in more detail. It is also interesting to compare the a_T values obtained in this work with the ones reported previously. The shift factors reported by Dhinojwala and coworkers for bulk PS below T_g obtained using a second-harmonic generation technique (SHG) [70] and the values resulting from extrapolation of the dynamics of α relaxation [17] to temperatures below T_g, are presented in Figure VI.23. We can easily observe the large difference between bulk and surface shift factors. Both, the results of the extrapolation of the liquid behavior and the bulk glass measurements, point to a much slower dynamics than the one measured from the bump relaxation.

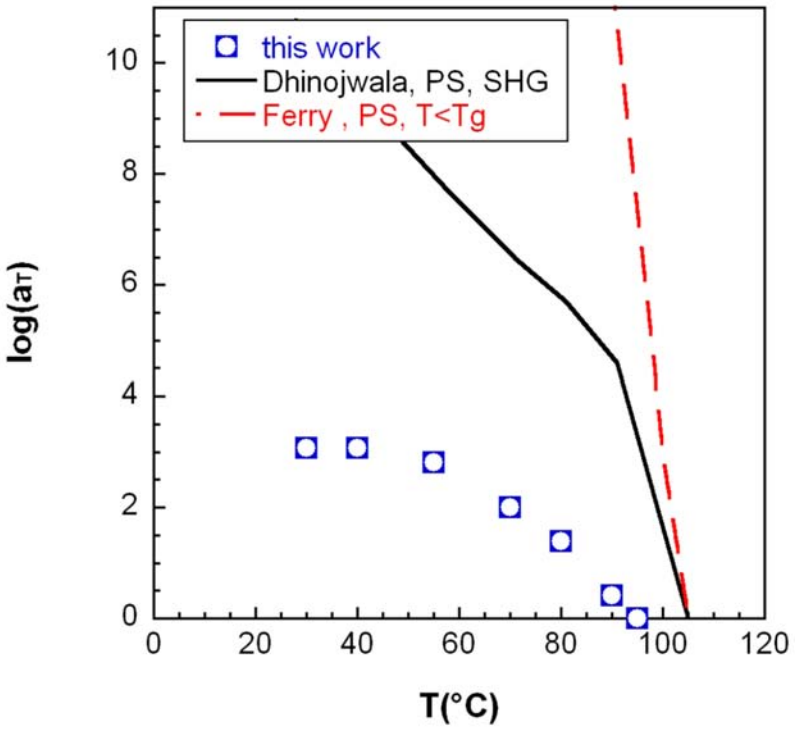

Figure VI.23: Shift factors used to produce superposition of the measured data; the solid curve corresponds to the bulk shift factors of PS obtained by the SHG technique [70]. The dashed line is obtained from the extrapolation of the dynamics of α relaxation [17]

It is also instructive to compare directly the measured relaxation times in different experiments. Figure VI.24 shows the relaxation times of bumps, along with plots of α relaxation times in PS obtained from the SHG technique [70]. Note that as different techniques are used for the bulk and surface measurements, there may be a relative vertical shift with a few orders of magnitude between different data sets, but the temperature dependences is independent of the technique and can be used to compare them. It is again quite clear that the temperature dependence of the dynamics of the near free surface regions of the thin polystyrene films is remarkably different from those of chain segment related α mode (shown as the solid black curve) in bulk polystyrene systems. It is also clear that two different regimes can be distinguished in the data measured from the relaxation of the

nanostructured polymer films. At higher temperatures (60 – 95 °C) the relaxation time can be described by Arrhenius behavior with a single activation energy, as indicated by the red dashed line in the Figure VI.24. Arrhenius-like temperature dependence of τ for $T<T_g$, was observed also in bulk polymeric glasses [71], as the material departs from an equilibrium situation. On the contrary, in the low temperature window, (T<60°C), the temperature dependence is weaker and almost indiscernible.

As has been detailed before [43], different scenarios may account for the Arrhenius behaviour [72,73]. In the Adam and Gibbs model of relaxation of glass formers [72] $\tau(T)=\tau_\infty \exp(C/TS_c)$, where C is a constant and $S_c(T)$ is the configurational entropy. For T<Tg, the temperature dependence of S_c, measured for different glass formers, is weak [74]. If S_c is approximately constant, Arrhenius-type dependence will be obtained. Confinement effects can also be evoked. The dramatic slowing down of structural relaxation of amorphous polymers upon cooling is often attributed to the necessity of cooperative rearrangements [5,72,75] inside regions of size that increases with decreasing temperature. When the cooperativity length comprises the whole object, the effective activation energy becomes independent of temperature and Arrhenius like behavior will be observed. The sub-Arrhenius behaviour observed at low temperature is even more intriguing. At a first sight, the reduced thermal dependence would suggest a decreasing energy barrier with decreasing temperature, which appears completely counterintuitive. At least two hypotheses can be evoked to explain these results. It is possible that there exist different relaxation processes (with different activation energies) responsible for the behavior at high and low temperature. When the fast process is slow down at low temperatures only the slow process is detected. We have already discussed how by changing the temperature of the sample while structuration a very different morphology is obtained (homogeneous vs heterogenous structuration). The heterogeneity of the sample at higher temperatures may be related to an accelerated (thermally activated) relaxation process. A second possibility is related to the actual configuration of the films before treatment. As mentioned before, the structuration of all samples was performed at 25°C under identical conditions. However, as I discussed in previous chapter, the cooling of the polymer films after annealing is carried out in a finite time, while an extremely long time is necessary to reach thermodynamic equilibrium at 25°C. It is easy to imagine that, after cooling, the polymer films become frozen in a configuration corresponding to a higher effective temperature. Thus, heating the relaxing sample at temperatures below its effective structural temperature will have a less significant effect on its temporal evolution. Indeed, this factor may be responsible for the observed heterogeneity on the structural response of the films upon degassed-water treatment.

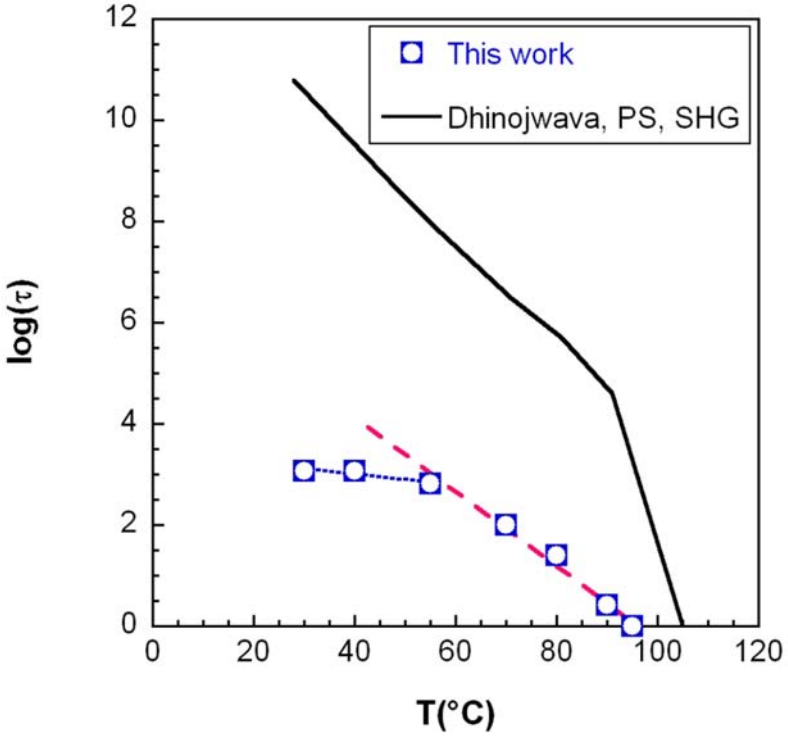

Figure VI.24: Comparison of the calculated surface relaxation times (◘) with bulk α [70] relaxations of PS.

It is also interesting to compare our results of bumps surface relaxation with the results of the dynamic measurements of polystyrene in bulk and at surfaces at temperature below bulk T_g using different techniques. We have compiled the data on relaxation of PS at temperatures below T_g reported by different groups, and converted the relaxation times to shift factors as described before (Figure VI.25) The similarities between the local dynamics of polymers surface on nanometer scales determined by the different groups are evident. We can clearly observe in Figure VI.25 that our results of polystyrene surface bumps relaxation are in good agreement with recent studies of surface holes relaxation [46], results of relaxation processes obtained using temperature-controlled friction force microscopy (FFM) [32] or a lateral force microscopy (LFM) [50], and with the dynamics of free standing films measured by light scattering [32]. This agreement suggests that the sample preparation and the exact structure of thin films are not major causes of reported anomalies in film dynamics or in T_g. On the contrary, dielectric measurements of polymer films show a different behavior (probably because the free surface was covered with Al, and the enhanced dynamics is not detected [51,23,24]) but they match the behaviour reported for studies of relaxation in bulk PS. Interestingly, one AC calorimetric study performed in thin PS films [14] did not match the rest of the film/surface studies. As it was performed at relatively high frequencies, it is possible that the rate of temperature variations was too high to allow the equilibration of the films. Indeed, the authors of this study did not observe any dependence of T_g on film thickness, down to values of 15 nm.

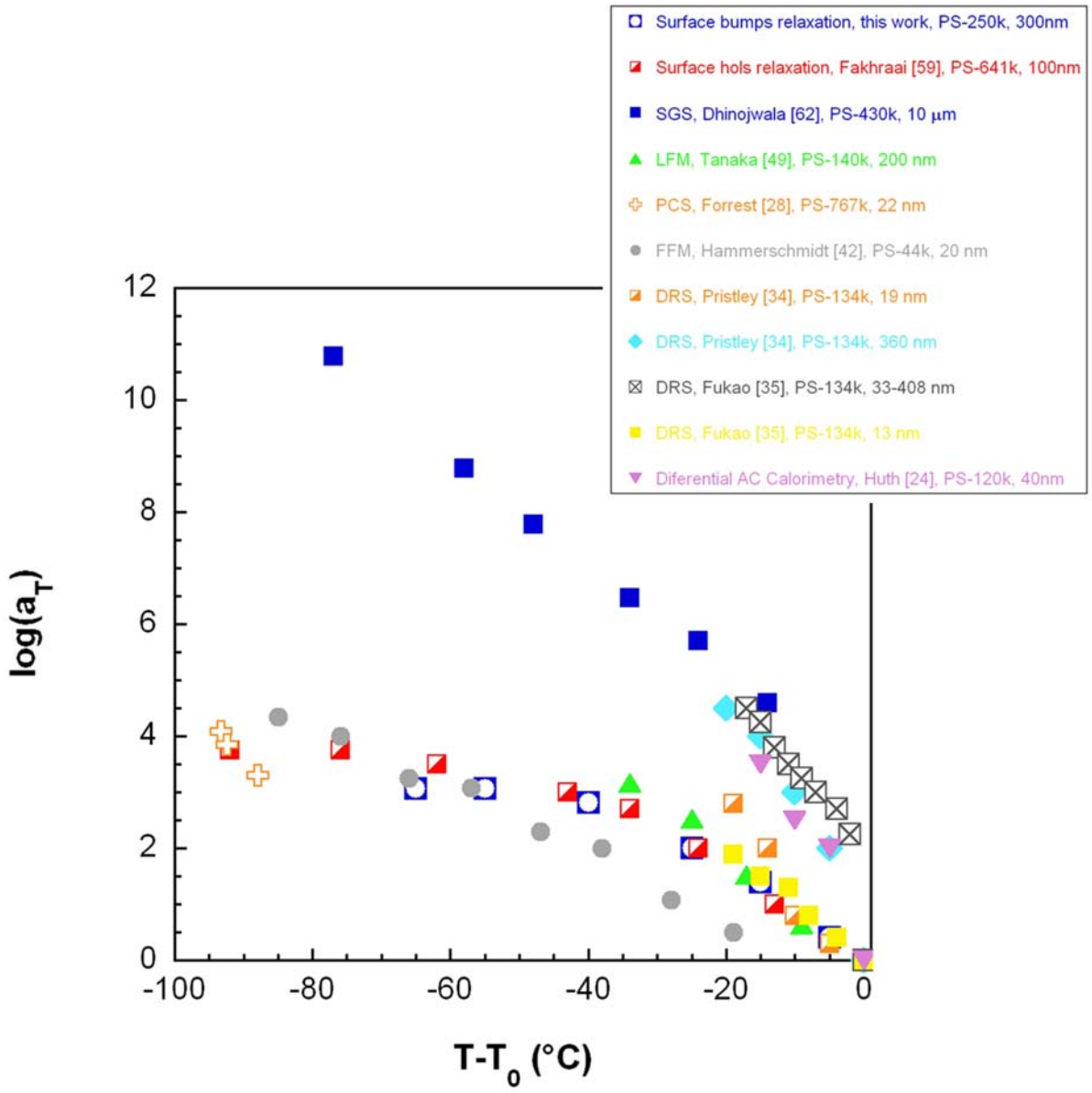

Figure VI.25: Shift factors calculated using WLF equation for PS at different temperatures below T_g; ◘ - from bumps relaxation, ◪ - holes relaxation [46],■ - calculated from second harmonic generation (SHG) [70], ● - temperature-controlled friction force microscopy (FFM) [32] and lateral force microscopy (LFM) [50], ✜ - from photon correlation spectroscopy (PCS) [32] data for supporting film, ■,▲,♦,⊠,◪ - dielectric relaxation spectroscopy (DRS) [23,24] of films with different thickness and ▼ - from differential AC-Chip calorimetry [14].

This compilation of data constitutes strong evidence that near free surface region has enhanced molecular mobility compared to the bulk [70]. The combination of these experimental results strongly suggests the existence of a different relaxation mechanism at the near-free-surface region compared to bulk. This results can also explain the broadening of the transition in thin films, as this new surface relaxation mode in dominant at $T < T_g$(bulk). At $T > T_g$(bulk) the bulk α-relaxation determines the dynamics of the system. On the contrary, at $T < T_g$ (bulk) this surface relaxation mode will be active down to very low temperatures (with a weaker temperature dependence compared to bulk behavior)

causing a broadening of the transition. This can explain the difference between the two sets of data compiled in Figure VI.23. More careful studies on the exact nature of this new mode of relaxation, the influence of polymeric nature or the thickness below which the T_g anomalies can be detected should be performed to verify the universality of this behavior. A complete theoretical description is also required for describing the observe phenomena. As described in previous chapter, the de Gennes theory of sliding motion [76] could be a good candidate in explanation of how the effects of the free-surface are propagated into the bulk of the film, and why it becomes faster than the bulk α relaxation only at temperatures close or below bulk T_g.

6.3.2.3. Surface structure relaxation: effect of polymer molecular weight.

As was shown above molecular weight is one of the parameters that determine the characteristic size of the induced nanostructuration. More precise information about how surface motion of polymer chains is affected by chain length can be extracted from the time-dependent relaxation of surface deformations. In this section I describe how relaxation time of structured surfaces varies with M_w of polymer. Structured samples of four different molecular weights (7, 59, 250, and 500 kDa) above and below entanglement length were prepared by exposing to a degassed solution of pH=1.5 as describe before (Figure VI.26). We performed a detailed study of surface relaxation of the different samples at 40°C.

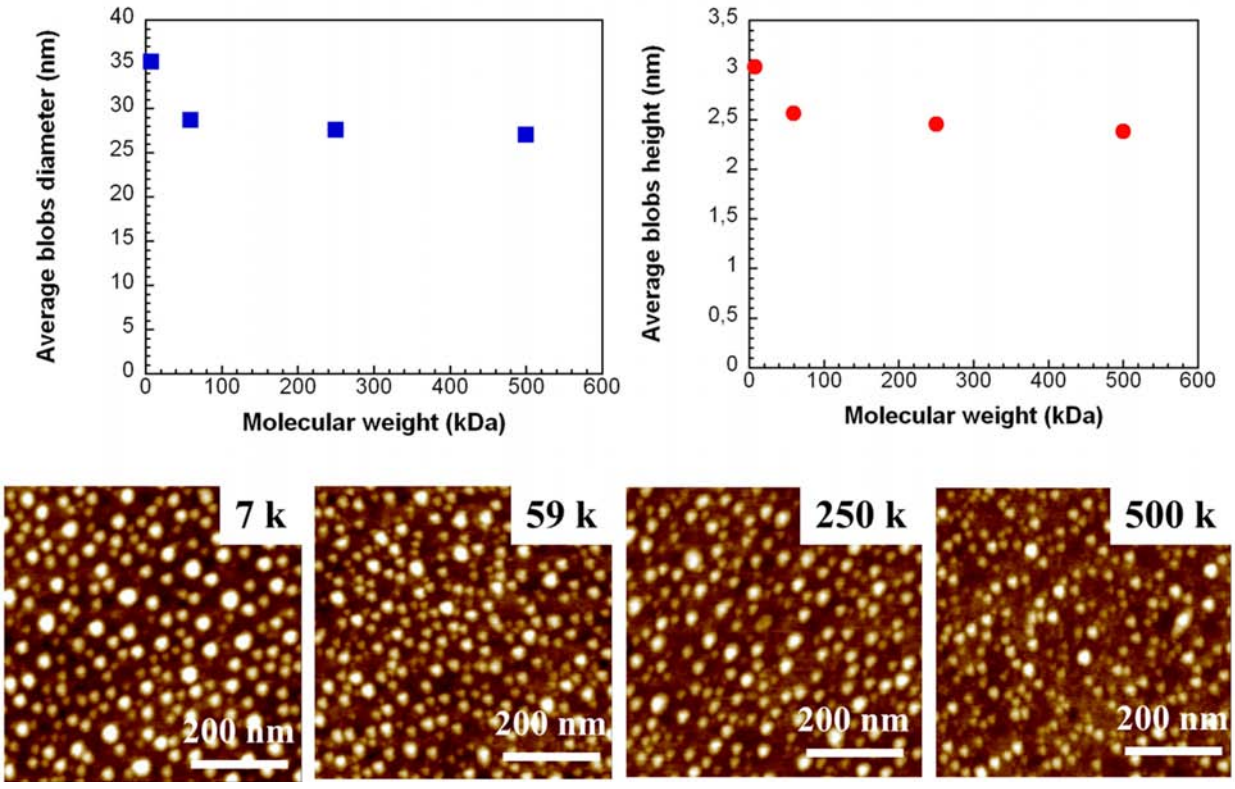

Figure VI.26: Variation of bumps average height (h)/diameter (D) with PS molecular weight

Figure VI.27 and Figure VI.28 show the time dependence of the bump dimensions and selected AFM micrographs measured at constant temperature T = 40°C for the four M_W's samples. As mentioned before, we can distinguish two mechanisms governing the temporal evolution of the nanostructured layers. Ostwald ripening can clearly be observed at short times; for example, for PS sample of 7 kDa, more than ½ smaller size blobs disappear and larger bumps appear after 18 hours. This process is probably responsible for the increase in average bump size observed at short times (obviously, the total bump volume monotonically decreases with time, due to surface relaxation). Moreover, from these plots we can observe that ripening is faster for lower molecular weights, evidencing that the mobility of the polymer chains at the surface is M_W dependent. When ripening is les marked, bumps start to relax under Laplace pressure. From Figure VI.27 and Figure VI.28 it is visible that the relaxation of the polymer surfaces depend strongly on chain length: bumps from short (7 kDa) unentangled polymer chains easily deform and reshape and relaxation is very rapid, while, entanglement seems to constrain the motions of the polymer molecules for long chains samples, leading to a significant increasing in relaxation times.

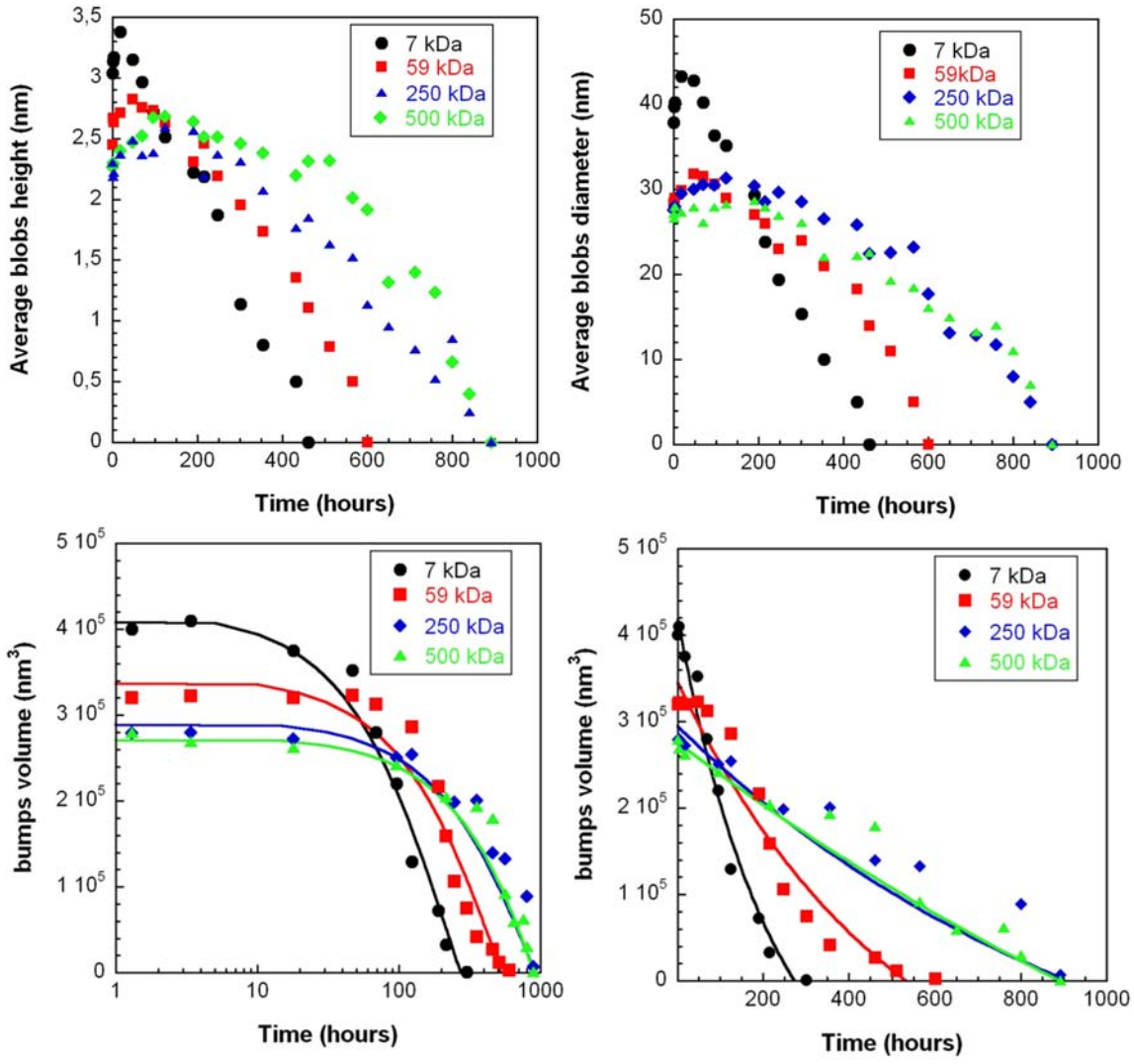

Figure VI.27: Time dependence of the bumps height size and total volume for four M_W at T = 40°C.

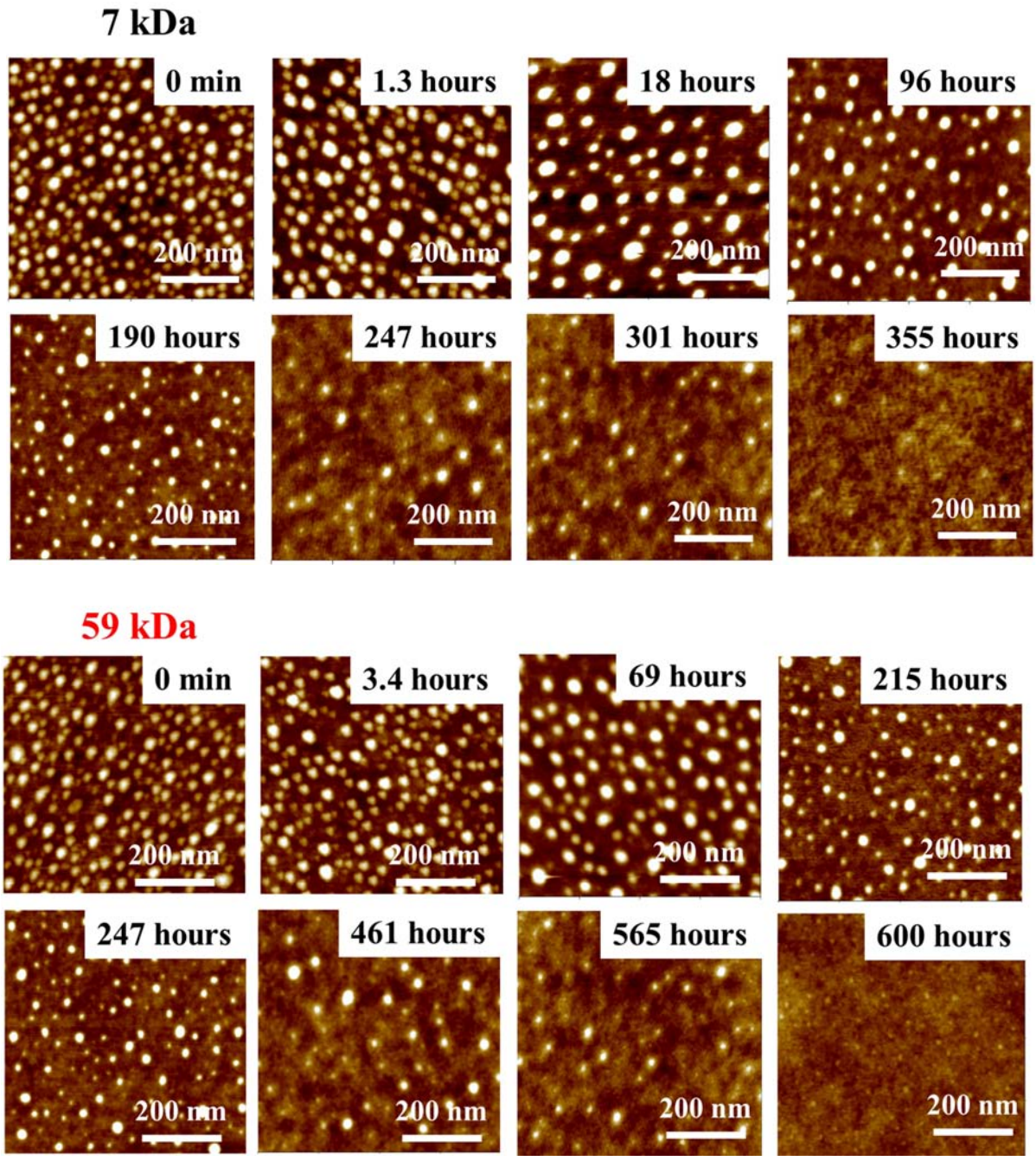
7 kDa
0 min
1.3 hours
18 hours
96 hours
190 hours
247 hours
301 hours
355 hours
59 kDa
0 min
3.4 hours
69 hours
215 hours
247 hours
461 hours
565 hours
600 hours
200 nm

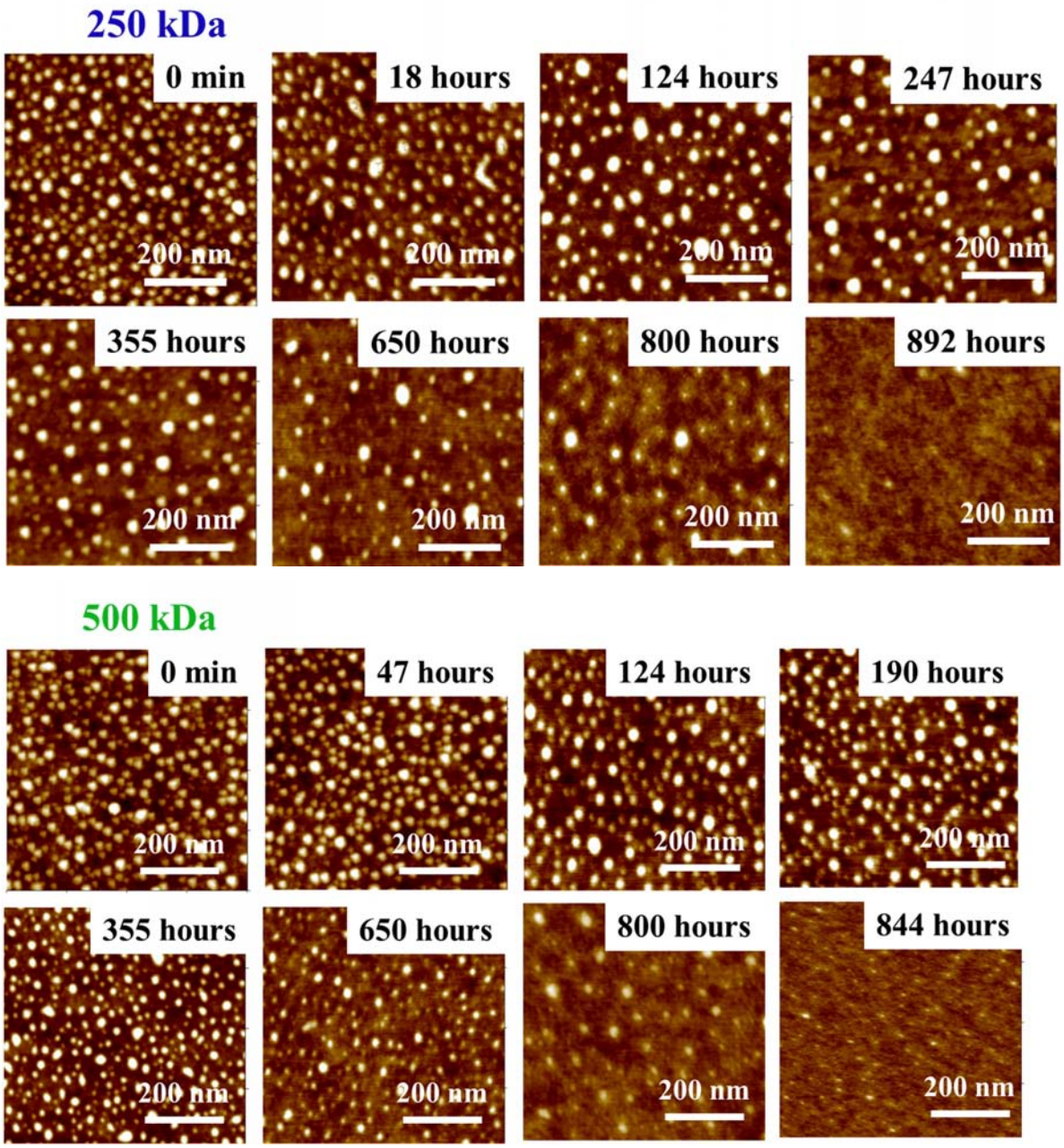

Figure VI.28: AFM images of PS (7, 59, 250, and 500 kDa), illustrating the surface relaxation for different samples T = 40°C.

The temporal evolution of bump dimension for the different M_W's is presented in Figure VI.29. As before, we use a single exponential function $\exp(-(t/\tau))$ to fit the experimental data, where τ is the surface bumps lifetime (solid curves in Figure VI.29). Again, this single exponential relaxation appears to correctly fit the experimental data. Figure VI.30 shows the measured surface relaxation times as a function of molecular weight. We found that the surface relaxation time increases with the M_W of PS. The limited set of data can roughly be fitted as $\tau \propto \log N$, where N is the degree of polymerization; this sublinear dependence of τ on M_W is weaker than what is predicted by Rouse model ($\tau \propto N$) or simple polymer reptation ($\tau \propto N^3$) [4,6,5].

The M_w dependence of polymer dynamics in the near free surface region of PS films has not been extensively investigated in the past. Rouse-like dynamics in the near free surface region in 2 nm confinements for high M_W PS films was reported in ref. [77]. Qi and Forrest [78] also observed a linear dependence of characteristic time of embedding of gold spheres with M_w, for PS samples with $200<M_w<1200$ kDa at temperatures close to bulk T_g; on the contrary, at temperatures lower than bulk T_g (the regimen explored in this work) almost no M_W dependence was observed. These results can be contrasted with the results obtained for i-PMMA films, where even at a temperature of ~36K below the bulk T_g the near free surface region can be treated as a Rouse-like viscous fluid and a linear M_W dependence of dynamics was observed [47]. This dissimilar behaviour of *i*-PMMA and PS probably indicates a structural difference in the near free surface regions of thin polymer films of different nature.

The conclusion extracted from temperature dependence study, that "*near free surface region of PS films comparing to the bulk has its own specific* T_g", has to be enlarged to include the influence of polymer type and M_w.

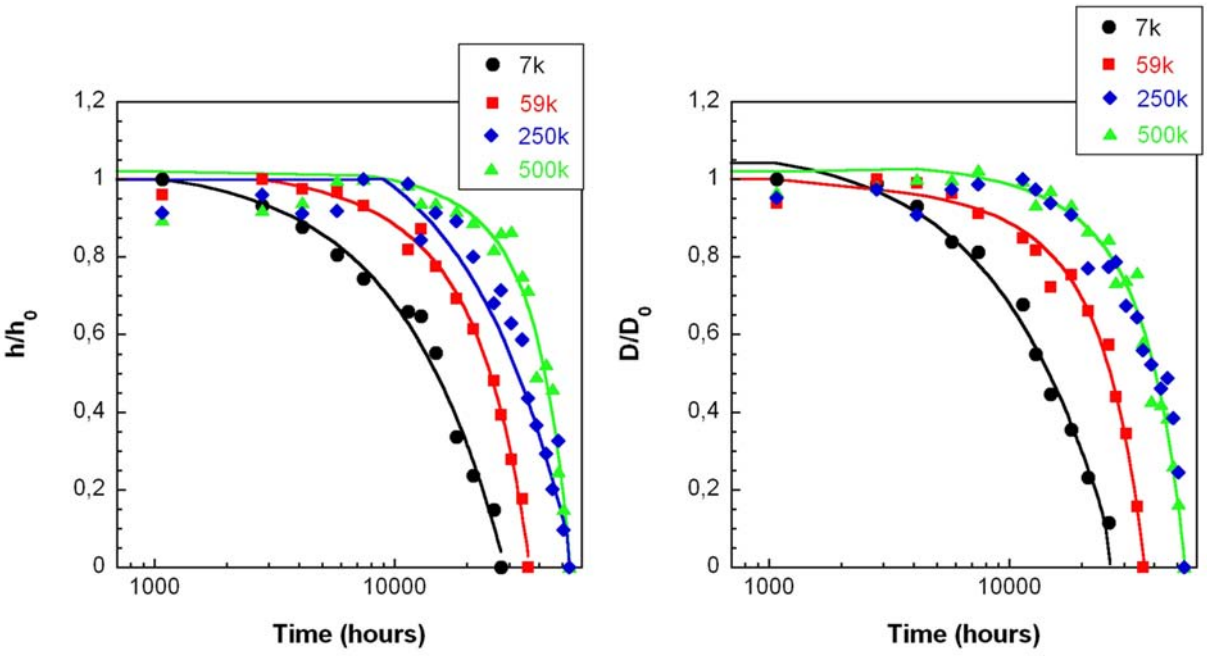

Figure VI.29: Time dependence of the relaxation of bumps for PS (7, 59, 250, and 500 kDa) at T= 40°C.

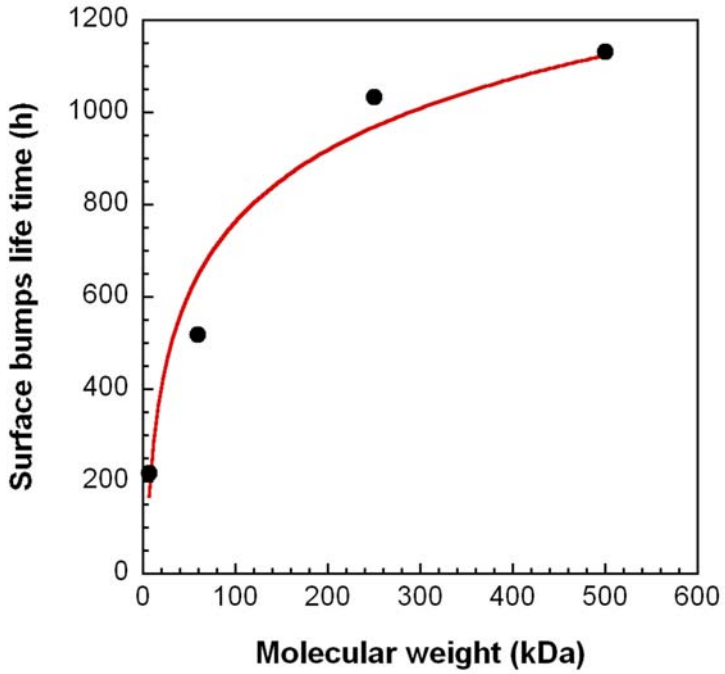

Figure VI.30: Surface bumps life time of PS films (≈ 300 nm) on Si for different molecular weights.

6.4. Conclusion

In this study, we probed the near free surface dynamical properties of thin polystyrene films with the nanobumps relaxation technique. Some interesting observations are found by this simple but powerful technique, which implies the smallest probing perturbations to polymer samples.

- ✓ It is found that there is a mobile surface layer in glassy thin polystyrene films and the mobile surface size increases with increasing temperature.
- ✓ The region of enhanced dynamics in thin polymer films is observed to be dependent on molecular weight of the polymer. This unexpected M_w dependence together with the temperature dependence of the near free surface dynamics of PS films strongly indicate a unique structural difference between the free surface region and the bulk part, which warrants more experimental and theoretical studies.
- ✓ We have devised and carried out a simple experiment that enables us to unambiguously measure the temperature dependent relaxation time for the mobile surface region of polystyrene films. The surface region shows relaxation at all temperatures measured (down to 30°C), and the resulting relaxation times display a surprisingly weak temperature dependence at low T.
- ✓ The surface relaxation time is observed to be weakly dependent on M_W.
- ✓ The surface relaxation obtained results shows a remarkable consistency to recently reported works concerning thin film relaxation data.

6.5. References

[1] Mark, J.E. *Physical properties of polymers*. (Cambridge University Press: 2004).
[2] Ferry, J.D. *Viscoelastic properties of polymers*. (John Wiley and Sons: 1980).
[3] Andrade, J.D. Surface and interfacial aspects of biomedical polymers. Vol. l. *New York: Plenum Press* (1985).
[4] Jones, R.A.L. & Richards, R.W. *Polymers at surfaces and interfaces*. (Cambridge University Press: 1999).
[5] Karim, A. & Kumar, S. *Polymer surfaces, interfaces and thin films*. (World Scientific: 2000).
[6] Tsui, O.K.C. *Polymer thin films*. (World Scientific: 2008).
[7] Haward, R.N. & Young, R.J. *The Physics of glassy polymers*. (Springer: 1997).
[8] Boyd, R. & Smith, G. *Polymer Dynamics and Relaxation*. (Cambridge University Press: 2010).
[9] Sperling, L.H. *Introduction to physical polymer science*. (John Wiley and Sons: 2006).
[10] Ledwith, A. & North, A.M. *Molecular Behaviour and the Development of Polymeric Materials*, 368-403, Chapman and Hall: (1975).
[11] Schröter, K., Unger, R., Reissig, S., Garwe, F., Kahle, S., Beiner, M., Donth E. Dielectric Spectroscopy in the αβ Splitting Region of Glass Transition in Poly(ethyl methacrylate) and Poly(n-butyl methacrylate): Different Evaluation Methods and Experimental Conditions, *Macromolecules* **31**, 8966-8972 (1998).
[12] Beaucage, G., Composto, R. & Stein, R.S. Ellipsometric study of the glass transition and thermal expansion coefficients of thin polymer films. *Journal of Polymer Science Part B: Polymer Physics* **31**, 319-326 (1993).
[13] Keddie, J.L., Jones, R.A.L. & Cory, R.A. Size-Dependent Depression of the Glass Transition Temperature in Polymer Films. *Europhys. Lett.* **27**, 59-64 (1994).
[14] Efremov, M.Y., Olson, E.A., Zhang, M., Zhang, Z. & Allen, L.H. Glass Transition in Ultrathin Polymer Films: Calorimetric Study. *Phys. Rev. Lett.* **91**, 085703 (2003).
[15] Efremov, M.Y., Olson, E.A., Zhang, M., Zhang, Z. & Allen, L.H. Probing Glass Transition of Ultrathin Polymer Films at a Time Scale of Seconds Using Fast Differential Scanning Calorimetry. *Macromolecules* **37**, 4607-4616 (2004).
[16] Huth, H., Minakov, A.A. & Schick, C. Differential AC-chip calorimeter for glass transition measurements in ultrathin films. *Journal of Polymer Science Part B: Polymer Physics* **44**, 2996-3005 (2006).
[17] Ferry, J.D. *Viscoelastic properties of polymers. Second Edition*. (John Wiley & Sons Inc: 1970).
[18] Kim, H. et al. X-ray photon correlation spectroscopy on polymer films with molecular weight dependence. *Physica B: Condensed Matter* **336**, 211-215 (2003).
[19] Kim, H. et al. Hydrodynamic surface fluctuations of polymer films by coherent X-ray scattering. *Thin Solid Films* **515**, 5536-5540 (2007).
[20] Erichsen, J., Dolgner, K., Zaporojtchenko, V. & Faupel, F. Glass Transition Temperature in Thin Polymer Films Determined by Thermal Discharge in X-ray Photoelectron Spectroscopy. *Macromolecules* **37**, 8813-8815 (2004).
[21] Forrest, J.A. et al. Relaxation dynamics in ultrathin polymer films. *Phys. Rev. E* **58**, R1226 (1998).
[22] Fukao, K. & Miyamoto, Y. Slow dynamics near glass transitions in thin polymer films. *Phys. Rev. E* **64**, 011803 (2001).
[23] Fukao, K. & Miyamoto, Y. Dielectric and dilatometric studies of glass transitionsin thin polymer films. *Le Journal de Physique IV* **10**, 4 (2000).
[24] Fukao, K. & Miyamoto, Y. Glass transitions and dynamics in thin polymer films: dielectric relaxation of thin films of polystyrene. *cond-mat/9907110* (1999).doi:doi:10.1103/PhysRevE.61.1743
[25] Priestley, R.D., Broadbelt, L.J., Torkelson, J.M. & Fukao, K. Glass transition and alpha -relaxation dynamics of thin films of labeled polystyrene. *Phys. Rev. E* **75**, 061806 (2007).
[26] Sharp, J.S. & Forrest, J.A. Free surfaces cause reductions in the glass transition temperature of thin polystyrene films. *Phys. Rev. Lett* **91**, 235701 (2003).
[27] Hartmann, L., Gorbatschow, W., Hauwede, J. & Kremer, F. Molecular dynamics in thin films of isotactic poly(methyl methacrylate). *The European Physical Journal E* **8**, 10 (2002).
[28] Forrest, J.A., Dalnoki-Veress, K. & Dutcher, J.R. Brillouin light scattering studies of the mechanical properties of thin freely standing polystyrene films. *Phys. Rev. E* **58**, 6109 (1998).
[29] Keddie, J.L., Jones, R.A.L. & Cory, R.A. Size-Dependent Depression of the Glass Transition Temperature in Polymer Films. *Europhys. Lett.* **27**, 59-64 (1994).
[30] Sharp, J.S. & Forrest, J.A. Free Surfaces Cause Reductions in the Glass Transition Temperature of Thin Polystyrene Films. *Phys. Rev. Lett.* **91**, 235701 (2003).
[31] Ellison, C.J. & Torkelson, J.M. The distribution of glass-transition temperatures in nanoscopically confined glass formers. *Nat Mater* **2**, 695-700 (2003).
[32] Hammerschmidt, J.A., Gladfelter, W.L. & Haugstad, G. Probing Polymer Viscoelastic Relaxations with Temperature-Controlled Friction Force Microscopy. *Macromolecules* **32**, 3360-3367 (1999).

[33] Ge, S. et al. Shear Modulation Force Microscopy Study of Near Surface Glass Transition Temperatures. *Phys. Rev. Lett.* **85**, 2340-2343 (2000).
[34] Schwab, A.D. & Dhinojwala, A. Relaxation of a rubbed polystyrene surface. *Phys. Rev. E* **67**, 021802 (2003).
[35] Kerle, T., Lin, Z., Kim, H.-C. & Russell, T.P. Mobility of Polymers at the Air/Polymer Interface. *Macromolecules* **34**, 3484-3492 (2001).
[36] Gasemjit, P. & Johannsmann, D. Thickness of the soft layer on glassy polystyrene surfaces. *Journal of Polymer Science Part B: Polymer Physics* **44**, 3031-3036 (2006).
[37] Meyers, G.F., DeKoven, B.M. & Seitz, J.T. Is the molecular surface of polystyrene really glassy? *Langmuir* **8**, 2330-2335 (1992).
[38] Du, B., Tsui, O.K.C., Zhang, Q. & He, T. Study of Elastic Modulus and Yield Strength of Polymer Thin Films Using Atomic Force Microscopy. *Langmuir* **17**, 3286-3291 (2001).
[39] Weber, R. et al. X-ray reflectivity study on the surface and bulk glass transition of polystyrene. *Phys. Rev. E* **64**, 061508 (2001).
[40] Rudoy, V.M. et al. Metal Nanoparticles on Polymer Surfaces: 1. A New Method of Determining Glass Transition Temperature of the Surface Layer. *Colloid Journal* **64**, 746-754 (2002).
[41] Hutcheson, S.A. & McKenna, G.B. Nanosphere Embedding into Polymer Surfaces: A Viscoelastic Contact Mechanics Analysis. *Phys. Rev. Lett.* **94**, 076103 (2005).
[42] Kerle, T., Lin, Z., Kim, H. & Russell, T. Mobility of Polymers at the Air/Polymer Interface. *Macromolecules* **34**, 3484-3492 (2001).
[43] Papaléo, R., de Oliveira, L., Farenzena, L., de Araújo, M. & Livi, R. Probing thermomechanical behavior of polymers at the nanometer scale with single-ion bombardment and scanning force microscopy. *Phys. Rev. B* **62**, 11273-11276 (2000).
[44] Farenzena, L.S., Livi, R.P., de Araújo, M.A., Garcia Bermudez, G. & Papaléo, R.M. Cratering and plastic deformation in polystyrene induced by MeV heavy ions: Dependence on the molecular weight. *Phys. Rev. B* **63**, 104108 (2001).
[45] Teichroeb, J.H. & Forrest, J.A. Direct imaging of nanoparticle embedding to probe viscoelasticity of polymer surfaces. *Phys. Rev. Lett* **91**, 016104 (2003).
[46] Fakhraai, Z. & Forrest, J.A. Measuring the Surface Dynamics of Glassy Polymers. *Science* **319**, 600 -604 (2008).
[47] Qi, D., Fakhraai, Z. & Forrest, J.A. Substrate and Chain Size Dependence of Near Surface Dynamics of Glassy Polymers. *Phys. Rev. Lett.* **101**, 096101 (2008).
[48] Papaléo, R.M. et al. Relaxation times of nanoscale deformations on the surface of a polymer thin film near and below the glass transition. *Phys. Rev. B* **74**, 094203 (2006).
[49] Kajiyama, T., Tanaka, K. & Takahara, A. Surface Molecular Motion of the Monodisperse Polystyrene Films. *Macromolecules* **30**, 280-285 (1997).
[50] Tanaka, K., Takahara, A. & Kajiyama, T. Rheological Analysis of Surface Relaxation Process of Monodisperse Polystyrene Films. *Macromolecules* **33**, 7588-7593 (2000).
[51] Fukao, K., Uno, S., Miyamoto, Y., Hoshino, A. & Miyaji, H. Dynamics of alpha and beta processes in thin polymer films: Poly(vinyl acetate) and poly(methyl methacrylate). *Phys. Rev. E* **64**, 051807 (2001).
[52] Pham, J.Q. & Green, P.F. The glass transition of thin film polymer/polymer blends: Interfacial interactions and confinement. *J. Chem. Phys.* **116**, 5801 (2002).
[53] Sharp, J.S. & Forrest, J.A. Free Surfaces Cause Reductions in the Glass Transition Temperature of Thin Polystyrene Films. *Phys. Rev. Lett.* **91**, 235701 (2003).
[54] Torres, J.A., Nealey, P.F. & de Pablo, J.J. Molecular Simulation of Ultrathin Polymeric Films near the Glass Transition. *Phys. Rev. Lett.* **85**, 3221 (2000).
[55] Wang, X.P., Tsui, O.K.C. & Xiao, X. Dynamic Study of Polymer Films by Friction Force Microscopy with Continuously Varying Load. *Langmuir* **18**, 7066-7072 (2002).
[56] Ge *et al.* Shear modulation force microscopy study of near surface glass transition temperatures. *Phys. Rev. Lett.* **85**, 2340-2343 (2000).
[57] Teichroeb, J.H. & Forrest, J.A. Direct Imaging of Nanoparticle Embedding to Probe Viscoelasticity of Polymer Surfaces. *Phys. Rev. Lett.* **91**, 016104 (2003).
[58] Herminghaus, S., Seemann, R. & Landfester, K. Polymer Surface Melting Mediated by Capillary Waves. *Phys. Rev. Lett.* **93**, 017801 (2004).
[59] Sharp, J.S., Teichroeb, J.H. & Forrest, J.A. The properties of free polymer surfaces and their influence on the glass transition temperature of thin polystyrene films. *Eur. Phys. J. E* **15**, 473-487 (2004).
[60] Ochoa, J.G.D., Binder, K. & Paul, W. Molecular dynamics simulations of the embedding of a nano-particle into a polymer film. *J. Phys.: Condens. Matter* **18**, 2777-2787 (2006).
[61] Hutcheson, S.A. & McKenna, G.B. Erratum: Nanosphere Embedding into Polymer Surfaces: A Viscoelastic Contact Mechanics Analysis [Phys. Rev. Lett. 94, 076103 (2005)]. *Phys. Rev. Lett.* **94**, 189902 (2005).

[62] Hutcheson, S.A. & McKenna, G.B. Nanosphere embedding into polymer surfaces: a viscoelastic contact mechanics analysis. *Phys. Rev. Lett* **94**, 076103 (2005).
[63] Sharp, J.S. et al. Reply to comment on "The properties of free polymer surfaces and their effect upon the glass transition temperature of thin polystyrene films" by S.A. Hutcheson and G.B. McKenna. *Eur. Phys. J. E* **22**, 287-291 (2007).
[64] Qi, D., Ilton, M. & Forrest, J.A. Measuring surface and bulk relaxation in glassy polymers. *The European Physical Journal E* **34**, 7 (2011).
[65] Herminghaus, S. Polymer thin films and surfaces: Possible effects of capillary waves. *The European Physical Journal E - Soft Matter* **8**, 237-243 (2002).
[66] Herminghaus, S., Jacobs, K. & Seemann, R. The glass transition of thin polymer films: some questions, and a possible answer. *The European Physical Journal E* **5**, 8 (2001).
[67] Herminghaus, S. Polymer thin films and surfaces: Possible effects of capillary waves. *The European Physical Journal E* **8**, 7 (2002).
[68] Ilton, M., Qi, D. & Forrest, J.A. Using Nanoparticle Embedding to Probe Surface Rheology and the Length Scale of Surface Mobility in Glassy Polymers. *Macromolecules* **42**, 6851-6854 (2009).
[69] Keddie, J.L., Jones, R.A.L. & Cory, R.A. Size-Dependent Depression of the Glass Transition Temperature in Polymer Films. *Europhys. Lett.* **27**, 59-64 (1994).
[70] Dhinojwala, A., Wong, G.K. & Torkelson, J.M. Rotational reorientation dynamics of disperse red 1 in polystyrene: α -relaxation dynamics probed by second harmonic generation and dielectric relaxation. *J. Chem. Phys.* **100**, 6046 (1994).
[71] O'Connell, P.A. & McKenna, G.B. Arrhenius-type temperature dependence of the segmental relaxation below T[sub g]. *J. Chem. Phys.* **110**, 11054 (1999).
[72] Adam, G. & Gibbs, J.H. On the Temperature Dependence of Cooperative Relaxation Properties in Glass-Forming Liquids. *J. Chem. Phys.* **43**, 139 (1965).
[73] Erwin, B.M. & Colby, R.H. Temperature dependence of relaxation times and the length scale of cooperative motion for glass-forming liquids. *Journal of Non-Crystalline Solids* **307-310**, 225-231 (2002).
[74] Richert, R. & Angell, C.A. Dynamics of glass-forming liquids. V. On the link between molecular dynamics and configurational entropy. *J. Chem. Phys.* **108**, 9016 (1998).
[75] Priestley, R.D., Ellison, C.J., Broadbelt, L.J. & Torkelson, J.M. Structural Relaxation of Polymer Glasses at Surfaces, Interfaces, and In Between. *Science* **309**, 456 -459 (2005).
[76] Gennes, P.G. de Glass transitions in thin polymer films. *The European Physical Journal E* **2**, 5 (2000).
[77] Manias, E. et al. Intercalation Kinetics of Long Polymers in 2 nm Confinements. *Macromolecules* **33**, 7955-7966 (2000).
[78]Dongping Qi. PhD thesis, University of Waterloo, Ontario, Canada, 2009.

Concluding remarks and future work

In this thesis I investigate novel methods of structuring and control structure formation process in thin polymer films, particularly at temperatures lower than their glass transition. I have found that the surface of glassy polystyrene can be reconstructed at room temperature either by direct or indirect application of an electric field, strongly suggesting that a layer of enhanced mobility indeed exists at the surface of this glassy polymer. However, the direct study of properties of this specific near free surface region of thin polymer films is very rare due to the limited suitable experimental techniques. For this reason, I have completed an extensive study of the temporal relaxation of polymer surfaces previously structured by our methods. I think our results suggest a number of interesting lines of research that are well worth pursuing. I will mention the ones that I feel are the most promising.

Some future work

- A more complete characterization of the surface modification under direct application of an electric field seems interesting. In particular, it would be interesting and useful to know how the wavelength and morphology of this instability depend on temperature of the sample and molecular weight. Theoretical analysis will improve our understanding of the physical proprieties of this process.
- In my opinion, many doors are open related to the nanostucturation of hydrophobic polymer surfaces by simple treatment with degassed aqueous solutions. Elucidation of the details of the mechanism responsible for this process and ion specificity effects require a large body of theoretical and experimental work.
- The findings of our study of bump relaxation suggest specific properties in the near free surface region of PS films. In particular, the resulting relaxation times display surprisingly weak temperature dependence at low T. The influence of aging and annealing process on this result should be elucidated. In addition, it is worthwhile to conduct more studies to investigate any potential dependence of polymer material and M_w dependence in this temperature region.
- We observe heterogeneous dynamics in glassy polymer films with nanometer resolution. It will be interesting to conduct some more studies around this subject (a hard task due to the limited experimental techniques and studies available).